Impacts of agroforestry on microclimate for grape and wine production: assessment in Southern France

Juliette Grimaldi

Université Fédérale
Toulouse Midi-Pyrénées

THÈSE

En vue de l'obtention du

DOCTORAT DE L'UNIVERSITÉ DE TOULOUSE

Délivré par :

Université Toulouse 3 Paul Sabatier (UT3 Paul Sabatier)

Présentée et soutenue par :
Juliette GRIMALDI
le vendredi 5 octobre 2018

Titre :

Impacts microclimatiques de l'agroforesterie en viticulture :
étude de cas dans le Sud de la France

Impacts of agroforestry on microclimate for grape and wine production:
assessment in Southern France

École doctorale et discipline ou spécialité :
ED SDU2E : Surfaces et interfaces continentales, Hydrologie

Unité de recherche :
CESBIO

Directeur/trice(s) de Thèse :

Vincent BUSTILLO (UMR CESBIO, UPS)
Thomas HOUET (UMR LETG, CNRS)

Jury :
Nathalie OLLAT (rapporteur - UMR EGFV, INRA)
Hervé QUENOL (rapporteur - UMR LETG, CNRS)
Emmanuelle VAUDOUR (rapporteur - UMR ECOSYS, AgroParisTech)
Dominique COURAULT (examinateur - UMR EMMAH, INRA)
Jean-Philippe GASTELLU-ETCHEGORRY (examinateur et président - UMR CESBIO, UPS)
Vincent BUSTILLO (directeur de thèse - UMR CESBIO, UPS)
Thomas HOUET (co-directeur de thèse - UMR LETG, CNRS)

ABSTRACT

Agroforestry practices may be a sound strategy towards agroecological and climate-resilient strategies for grape and wine production but have almost never been referenced. The thesis work participated in the project Vitiforest and focused on the positive interactions/competitions between grapevine and trees through the local impacts of trees on the energy, air and water fluxes. In this context, three objectives were targeted: (i) documenting the microclimatic impacts from trees in vineyards, (ii) assessing their consequences on grape production, and (iii) discussing the impacts according to the morphological characteristics of the vegetation.

Three study sites where grapevine is intercropped with trees were selected in Southern France in order to sample diverse contexts of "terroir" and vegetation structure. Experimental data were collected in 2015 from vine veraison to harvest and in 2016 from a few weeks before budburst until harvest. The collected data set gathers meteorological records, microclimatic records distributed within the vineyards together with measurements of yield and grape quality for wine making, and a set of UAV images which covers the visible, near infrared and thermal infrared spectral domains. In order to characterize the morphology and the arrangement of the vegetation, an image analysis approach was tested. It notably consisted in mapping the land cover, the top canopy heights (internal metrics) and the landscape grain of the vegetation (landscape metrics).

The temperatures measured in the bunch zone of grapevines were analyzed in the young and NE/SW oriented study vineyard. It showed that the trees from forested borders and the topography together contribute the most to the spatial variability of temperatures. In this context, no assumed effect from the shade of the trees was observed on the northern side of the alleys of trees which are planted within vine rows. Unexpectedly, specifically at the first vine rows located on the southern side of these tree rows, a significantly cool pattern was observed and was the most pronounced on days of summer with high evaporative demand. This cold pattern coincided with the highest yields measured. In addition, the overall spatial variability of temperatures explained 30 to 50 % of the variability of some of the qualitative variables, namely the pH, the concentrations of malic acid and polyphenols.

In order to further investigate the magnitude of competition for light between trees and grapevine, three-dimension mock-ups of vineyards were built. They were used together with a meteorological time series running from budburst until harvest for simulating the 3D radiative budget using the model DART developed at CESBIO. Thanks to the advanced functionalities of this model for representing heterogeneous vegetated landscapes and for accurately simulating the state of the atmosphere, current and future shading patterns were addressed. The total quantity of energy absorbed by grapevine was cumulated in time over the whole season and was mapped in 2D. The results obtained showed that the potential impact from trees on the photosynthesis of grapevine is negligible for all the tested arrangements, while the architecture of grapevine itself greatly contributes to its light interception regime.

This thesis provides first references and opens many further perspectives of research. Improvements in the modeling of cloud cover during radiative budget simulations are proposed and could lead to higher estimations of light interception. Also an analysis of the thermal infrared imagery for assessing patterns of grapevine water stress has been initiated. Finally, the collected data set and the tested methodology will allow widening the scope of references to other contexts of agroforestry vineyards.

RESUME

Bien que prometteuse face au double défi agro-écologique et climatique, la pratique de l'agroforesterie en viticulture n'a fait l'objet que de très peu d'études. Adossée au projet Vitiforest, la thèse présentée dans ce manuscrit vise à documenter les avantages et limites de l'arbre à travers ses effets sur les flux d'énergie, d'air et d'eau. Dans ce cadre, trois objectifs ont été plus spécifiquement ciblés : (i) caractériser l'effet des arbres sur le microclimat d'un vignoble ; (ii) évaluer les répercussions en termes de rendement et de qualité des raisins ; (iii) comparer les résultats selon la nature et l'agencement des arbres.

Trois vignobles associant vignes et arbres ont été sélectionnés dans le sud de la France de manière à couvrir différents terroirs et structures de végétation. Une campagne expérimentale a été menée de la véraison aux vendanges en 2015 puis du débourrement de la vigne jusqu'aux vendanges en 2016. Le jeu de données acquis regroupe des suivis météorologiques, des suivis microclimatiques, des mesures de rendement et de qualité des baies distribués spatialement au sein des vignobles, et un jeu d'images de très haute résolution (< 10 cm), couvrant les domaines du visible, proche infrarouge et infrarouge thermique acquis par drone. Afin de caractériser la morphologie et l'agencement de la végétation en lien avec ses effets climatiques potentiels, une méthode basée sur l'analyse d'image a été testée. Elle inclut notamment la cartographie de l'occupation du sol, des hauteurs de végétations (métrique interne) et du gradient d'ouverture du paysage (métrique paysagère).

L'analyse des températures en zone des grappes a révélé que, dans le cas d'un vignoble jeune, orienté NE/SO et à larges espacements, les arbres de bordure se combinent à la topographie et contribuent le plus à la variabilité des températures. A ce stade du développement des rangs d'arbres qui sont intercalés entre les rangs de vigne, aucun effet n'a été observé sur les vignes localisées au Nord des arbres et pouvant être attribué à l'ombrage par les arbres. De manière inattendue, spécifiquement sur le premier rang au sud des arbres, un patron significativement plus frais a été observé, d'autant plus marqué les journées estivales à forte demande évapotranspiratoire. Ce patron coïncide spatialement avec les plus forts rendements mesurés au sein du vignoble. Aussi, la variabilité générale des températures explique autour de 30 à 50 % de la variabilité de certains critères qualitatifs notamment le pH, la concentration en acide malique et celle en polyphénols.

Afin d'évaluer plus spécifiquement l'ombrage des arbres sur la vigne, la carte de végétation de l'un des trois vignobles étudiés a été utilisée pour construire différentes maquettes de vignobles en agroforesterie. Celles-ci ont été implémentées dans le modèle 3D de bilan radiatif DART développé au CESBIO, accompagnée d'une série météorologique annuelle. Grace aux fonctionnalités avancées de ce modèle, notamment pour représenter des paysages hétérogènes et l'état de l'atmosphère, l'ombrage présent et futur a été simulé et l'énergie résultante absorbée par la vigne a été cumulée sur l'ensemble d'une saison végétative. Les résultats de cette approche méthodologique inédite montrent que l'influence des arbres sur la photosynthèse de la vigne est très faible dans les configurations testées, tandis que l'architecture de la vigne elle-même a naturellement une influence forte sur son interception lumineuse et sur le microclimat au sein de sa canopée.

Le travail mené apporte des premières références et ouvre de nombreuses perspectives. L'amélioration de la représentation des nuages lors des simulations d'ombrage et l'utilisation de l'imagerie infrarouge thermique pour documenter l'effet des arbres sur le stress hydrique de la vigne sont notamment en cours de test. Aussi le jeu de données collecté et l'approche méthodologique développée permettront d'élargir les références à d'autres contextes.

REMERCIEMENTS

Je voudrais exprimer toute ma gratitude envers celles et ceux qui, en plateau comme en coulisse, ont contribué à l'aboutissement de ces travaux de thèse. Je vais tacher de n'oublier personne mais si tel était le cas, je vous prie de ne pas m'en tenir trop rigueur.

Je remercie tout d'abord Nathalie Ollat, Emmanuelle Vaudour et Hervé Quénol qui ont rapporté ce manuscrit avec exigence et sincérité. Mes remerciements s'adressent également à Dominique Courault et Jean-Philippe Gastellu. Tous ensembles, je vous remercie de m'avoir fait l'honneur de participer au jury de cette thèse et pour les riches échanges que vous avez suscités le 5 octobre. Un merci particulier à Hervé Quénol pour le décalage horaire Néo-Zélandais.

L'envie de faire une thèse me tenait depuis plusieurs années. Elle s'est affirmée au contact de Rainer Hienerwadel, Olivia Aubriot, Marc Moraine et Christine Aubry que je remercie pour leurs travaux inspirants et leurs encouragements à suivre leurs pas. Entre des crues népalaises, des moutons Pyrénéens, des légumes parisiens ou des modèles multi-agents franco-québécois, fallait-il encore faire un choix. L'idée de cette thèse-ci a germé sur un air de Neil Young et je tiens à remercier Marc Deconchat à Dynafor de m'avoir aidée à affiner ma candidature. J'ai eu le plaisir de te retrouver en conférence et séminaire et suis à chaque fois sortie très inspirée par nos rencontres.

Ce sera donc les arbres agroforestiers et leurs effets micro-climatiques, ou devrais-je dire, les « *Arbres des villes et arbres des champs : effet climatique des continuités de végétation à l'échelle locale* ». En effet, tel été l'intitulé de la demande de financement envoyée à la Fondation de France. Par une généreuse donation de leur héritière, les stylos BIC nous sponsorisent. Je remercie Thierry Gissinger et l'ensemble du comité scientifique pour l'agroforesterie tempérée de la dotation qui m'a été accordée durant trois années. Je vous remercie également d'avoir accepté les réajustements successifs du sujet lorsque j'ai pris conscience du caractère pharaonique de mes premières ambitions. L'acceptation du CASDAR Vitiforest a également été une grande chance et je remercie le ministère de l'agriculture pour avoir financé dans ce cadre mes expérimentations et huit mois supplémentaires de contrat.

A l'initiative de ce projet de thèse il y a bien sur Vincent Bustillo que je remercie pour avoir élaboré le volet microclimatique de Vitiforest et pour m'avoir acceptée à ses côtés. Vincent, je salue aussi ta grande curiosité et maitrise scientifique et l'autonomie laissée tout au long de la thèse. Vaille que vaille, ce sont des expériences formatrices. Puis il y a Thomas Houet que je remercie d'avoir accepté de compléter le tandem des encadrants, même avec une plus petite roue. Lorsque plus d'un an s'était écoulé tu évoquais l'idée de faire voler des drones je n'aurai pas parié beaucoup de chapitres là-dessus. Mais voilà que seulement quatre mois plus tard tu étais licencié pour le pilotage et nous étions à Lagardère aux côtés de deux ailes volantes aux allures d'abeille ! Merci à toi pour ce superbe jeu d'images, pour avoir été de toutes les relectures, même en pleins congés, et pour tes conseils tant pragmatiques que bienveillants que j'ai plusieurs fois sollicités.

Je remercie Yann Kerr puis Laurent Polidori, successivement à la direction du CESBIO, de m'avoir accueillie dans cette belle demeure scientifique et de m'avoir accordé de multiples bureaux.

Au fil des ans, Eric Ceschia, Benoit Coudert, Marie Gosme et David Sheeren m'ont beaucoup aidée à élaguer le sujet de la thèse et à dimensionner/réajuster son volet expérimental. Merci à chacun.e pour le suivi de mes travaux et pour avoir partagé vos connaissances de manière très éclairante.

Je remercie aussi tous les collègues et membres du projet Vitiforest auquel j'ai pris beaucoup de plaisir à participer. Merci tout particulièrement à Emilie Bourgade, Thierry Dufourcq, Josépha Guenser et bien sur

Virginie Montagne pour nos riches échanges « multidisciplinaires » et pour nos collaborations qui tendent à perdurer.

Après un passage à *Brico*, voilà la Logan pleine de piquets et boitiers, filons sur le terrain :

A Lapouyade je remercie bien évidemment Delphine et Benoit Vinet qui sont des vignerons agroforestiers aussi passionants que passionés. Merci pour votre porte très grande ouverte et votre enthousiasme aussi délicieux qu'un verre d'Emile Grelier. Merci aussi à Marc Vergnes de l'IFV.

A Lagardère, je remercie à nouveau Thierry Dufourcq et toute l'équipe gersoise de l'IFV pour ces belles journées de vendanges. Merci aussi à Patrick et Clément Dubos pour leur accueil, leurs coups de main et leur indulgence face aux capteurs en tout genre disséminés dans leurs vignes.

A Restinclières je remercie Thierry Vacher pour cette même indulgence. Je remercie bien chaleureusement William Trambouze de la CA34, de m'avoir encouragée à venir sur ce mythique Domaine et pour tous les enseignements tirés de nos échanges. Je remercie aussi Christian Dupraz et Lydie Duffours de l'unité System pour leurs conseils scientifiques aguerris et pour la mise à disposition des données météo.

A Aalbecke (en Belgique une fois) je remercie Pierre Scheercousse d'AP32, Robert Flamand pour sa sagesse et l'étudiante Mélissa Wachs pour sa témérité et son indulgence.

A Barran, site de tous les déboires, je remercie Caroline Thill, cheffe d'exploitation du lycée agricole de Beaulieu, pour la mise à disposition de la parcelle.

A mes côtés sur le terrain, un immense merci aux biscotos affutés de Rémy, Manon, Mélissa, Mathis, Benoit & Benoit. Et c'est sans parler de ceux de Renaud car je te dois, à toi tout seul, une fière chandelle. Il faudra encore bien des *give it back challenge* pour être quittes. Merci pour ton aide à taper, ramper, désosser, réparer mais surtout pour ton humour et ton amitié à toute épreuve.

Toutes ces pérégrinations n'auraient pas non plus été possibles sans le travail averti des gestionnaires du CESBIO que je tiens à saluer. Je remercie tout particulièrement Emilie Bastie, alias La Patronne, pour son génie administratif et sa bienveillance quotidienne.

Je remercie tous les membres du GEODE pour leur accueil ainsi que pour la mise à disposition des DGPS et du laser par l'intermédiaire du DIPEE. Merci tout particulièrement à Hugues Barcet et Hugo Jantzi pour leur aide technique. Puisque je suis au GEODE, merci aussi à Zoé pour ses conseils en gestion de projet et à Fanny Rhoné pour ses conseils de doctorante-warrior. Lorsque nous plantions la haie chez Yvan et toi, j'en ai conclu que l'histoire finissait bien !

C'est en cassant qu'on apprend à rafistoler et souder. Merci à Philippe Rabier de l'IUT puis à Bartosz et Franck au CESBIO pour les heures passées sur les stations endolories.

Il est grand temps d'analyser toutes ces données :

« … mais la modélisation ce n'est pas pour moi ! ». Heureusement que seuls les imbéciles ne changent pas d'avis, sans quoi je serai passée à côté de DART. Un immense merci à Jean-Philippe pour m'avoir mis ce bijou de science entre les mains, pour avoir cru en moi et pour toutes ces heures de travail et d'échange qui m'ont passionnée. Mes remerciements vont aussi bien sur à Eric, Nicolas, Jordan, Lucas, Christopher et Yingjie qui constituent l'équipe DART. Merci pour votre soutien, pour le travail accompli et pour votre remarquable efficacité. Si vous le voulez bien, on se dit à très bientôt.

Merci à Julie Betbeder de m'avoir introduite à l'écologie du paysage et à Jacques Baudry pour son aide à l'utilisation de Chloé.

Benoit Coudert, te revoilà car merci pour les voyages dans l'infrarouge thermique et pour ta remarquable pédagogie qui a tout éclairé. J'espère qu'à partir des briques déjà posées nous auront l'occasion de poursuivre

sur ces questions. Rémy Fieuzal, te revoilà aussi car je tiens à te remercier pour la belle épopée statistique. J'ai aussi grandement appris et apprécié de co-écrire avec toi alors j'espère à tout bientôt en article.

Merci à Claire et Pierre-Alexis pour votre aide à l'analyse d'images par ACP et autres stat, j'ai fort appris. Merci à Mireille et Tiphaine pour votre expertise sur les données météo et votre sympathie. Arnaud et Phil, un très grand merci pour vos explications en analyse de données, en dé-méli-mélo de séries temporelles et pour ce mémorable hacking..! Dawa je te remercie aussi pour les nombreux coups de pouce OTB (magnifique !), bash, LaTeX (ce sera pour la prochaine). Merci encore à Hervé Gibrin et à Vincent Rivallant pour l'aide logistique apportée à tous les doctorant.e.s du CESBIO.

Mon ordinateur a bien failli, ne pas suivre la cadence. Je tiens à remercier Laurent Merlet à l'IUT puis Clément Vergnes et Yann Robert au CESBIO pour toutes les opérations chirurgicales. Aussi Yann, un grand bravo et merci pour le magistral déploiement de serveurs qui m'a été fort utile.

Ma-te-la-be, qu'est-ce que c'est ?! Trouvez une super-ChaCha et prenez quelques bières à l'Evasion, et ces syllabes n'auront plus de secret ! Charlotte, merci pour tous les cours du soir si pédagogues, et puis bien au-delà, merci pour ton entrain et pour toutes les peines et les joies partagées. Cher Flo, merci mille fois pour ta chaine de classif dont l'installation t'a valu bien des « bordel ! ». Je te remercie aussi un peu pêle-mêle pour l'initiation à python, à Gdal (fantastique !), au ski de rando et aux réconfortantes patates à l'ail. Merci aussi et surtout pour ton soutien durant ces derniers mois et pour m'offrir la chance d'apprendre à te connaitre.

Arrive alors l'heure de l'écriture et de la déconfiture.

Je remercie très sincèrement Laurent Polidori, Valérie Desmarez, Gilles Boulet, Mehrez Zribhi, Ahmad Albitar, Simon Gascoin et de nouveau Jean-Philippe Gastellu pour leur soutien et conseils pour amorcer et tenir le sprint final. Merci aussi à David pour les pauses plan-de-thèse et plante-à-thèse ! Merci bien sur à toi Béa, ma super-coach, parée à tous les dépassements de plannings, pour tes innombrables conseils, pour ta propre thèse devenue mon livre de chevet et surtout pour ton grand cœur. C'est grâce à toi si nous voilà toutes Licornes !

Je remercie les collègues des unités Dynafor et de System pour leurs invitations à présenter mes travaux. Je remercie la Fondation de France pour les annuelles journées des doctorants qui ont toujours été de très bons moments d'apprentissage et d'échange.

Je remercie mes futurs collègues du RMT d'avoir patienté quand je faisais durer le plaisir et tout particulièrement merci à Delphine Mézière pour son amical soutien.

Quitte à faire très long, je terminerai ces remerciements par une pensée envers tou.t.e.s les collègues et proches qui m'ont joyeusement entourée et soutenue au fil de ces quatre ans.

Les matins il y avait le quai de la gare endormie, les coteaux gersois qui défilent, la cathédrale de calcaire, la rue de la poste qui n'en finit pas de grimper et enfin les portes de l'IUT, nous y voilà. Je remercie toute l'équipe d'irrésistibles Auccitains pour ces années à vos côtés : merci à Enguerrand et Julie les co-bureaux de jeunesse, merci à Nathalie, Sébastien, Fred, Amidou, Constance pour leur sympathie, à Manon pour son super stage, Maël pour les bières et rescapades de station en péril, Benoit deuxième du nom pour l'hospitalité et nombreux coups de pouce, Mathis pour ta gaieté inébranlable et ton accompagnement dans toutes mes folies déménageuses, la team Solen-Benoit pour son très grand cœur, les footing-mont-d'Or et barbecue amicaux ! C'est la rentrée sur l'IUT : au sein des équipes d'HSE et GéBio je remercie tout particulièrement Valérie et Christelle pour leur enthousiasme, Perrine pour sa force inspirante, Coralie pour le rattrapage de microbio, Philippe, Eliane et toute l'équipe technique qui fonctionne du tonnerre, Claire-Em pour les blagues sur les étudiants (Oooh !) et Babeth pour nos moments de partage.

A présent le canal et les platanes défilent, nous voilà dans la ville rose. Je remercie Eric et Milena pour leur accueil chaleureux dans le bureau 109 puis Dawa, Marvin et Flo pour les derniers mois dans le bureau 100, « ça ne devrait pas être long » ! Merci à Sylvain Mangiarotti pour l'inspiration. Dans les bureaux voisins, un grand merci également à toute la clique fort sympathique composée de Thierion, Steph&Alex, Colette, Marie, Arnaud, David, Erwan, Renaud, César, EmilieD, PA, Christopher, Flo, Le Flamboyant, ChaCha, Béa, la Patronne, Landiou, sans oublier Hoaaaa !

Non loin de là, il y a aussi des GETiens organisant la prochaine ACDC. Pour toutes ces escapades pyrénéennes, gersoise et au jardin, merci à Alex, BrianCoco, Antonin&Jessy, Gillou, Jeune-Max, Ratichon, Mélo, Jing, Alice, Alexandra et ThomasLeleu l'entremetteur. Au-delà de ces rencontres, Msieur Leleu je te remercie pour tout ce que tu m'as fait partager, pour Capi, pour qui tu es, avec ou sans barbe, et pour cette magnifique caisse à outils qui en dit long.

Aux Crivini, Marco, Arnaud, Alex et Laurène, mes « amis du lindy », mille merci pour tous ces *bounce* et rires à vos côtés. Côté canal, merci à Emilie Jacq, Floriane, Emma, Berta and co pour les demi-pliers toujours de bonne humeur. Merci à Julien pour l'invitation à Dynafor et pour les discussions amicales à vélo.

Merci à Rémi le coloc activiste puis aux colocs adoptifs de la rue du Taur qui m'ont accueillie, moi et mon bureau ambulant. Merci d'avoir supporté chaleureusement ma rédaction. Je remercie aussi tout spécialement Jo de m'avoir fait partager l'épopée estivale d'une fromagerie et pour tous les épisodes de Martine à la ferme. Vivement les prochains. Merci aussi à tous les autres vieux de la vieille, Mumuth, Raph, MarieMarie, Nico, Bill et Albane pour nos retrouvailles et l'amitié qui dure. Merci tout particulièrement à madame boulette #1/#2 pour tes visites et la joie de te connaitre.

Merci à ma famille, composée de Grimaldi et de Duchmöll-Ouin-Ouin, pour toutes leurs marques d'affection. J'ai une pensée particulière pour Rém, merci de ton réconfort avisé dans les coups durs ainsi qu'un immense merci à Mine qui m'a fait la grande joie de venir assister à ma soutenance. Ma Célou, je te remercie pour être chaque jour une sœur si tendre et inspirante. J'ai tenté de suivre tes pas mais on me dit dans l'oreillette que ce n'est pas le même doctorat…oh la boulette ! Merci à mon lutin, jeune pousse estivale et baigneur du dimanche soir qui me remplit de bonheur. Enfin je termine bien sur par vous, Papou et Mounita, car vous êtes mes piliers. Je vous remercie pour votre amour et votre soutien sans faille depuis le tout premier jour.

Auprès de mon arbre, je vivais heureux

GEORGES BRASSENS

CONTENTS

List of figures

List of tables

Abbreviations and acronyms

AF	Agroforestry
AOD	Aerosol Optical Depth
Avg	average
BOA	Bottom Of Atmosphere
DEM	Digital Elevation Model
DSM	Digital Surface Model
DTM	Digital Terrain Model
ET0	Reference Evapo-Transpiration
E	Irradiance
Max	maximum
Min	minimum
NH	Northern Hemisphere
NIR	Near Infrared Radiation – wavebands from 800 nm to 1 500 nm
PAR	Photosynthetically Active Radiation – wavebands from 400 nm to 700 nm
P0	Mean sea level pressure
Qt.	Quantile
Patm	Local Atmospheric pressure
R	Rainfall
R_a^{LW}	Atmospheric Longwave radiations
Rg	Global Solar Radiation
RH	Air Relative Humidity
TIR	Thermal Infrared
Tair	Air temperature
Tg	Ground temperature
Ts	Surface temperature
UAV	Unmanned Aerial Vehicle
WD	Wind direction
WS	Wind speed

CHAPITRE I
Introduction générale

Les systèmes agroforestiers seront capables d'imiter ou de reproduire les nombreux cycles nutritifs et les influences environnementales favorables que l'on observe dans les écosystèmes forestiers tout en garantissant des systèmes agricoles productifs.

(Kidd and Pimentel 1992)

I.1 Vers des pratiques durables en viticulture

I.1.1 Un double défit agro-écologique et climatique

Maintenir une biodiversité fonctionnelle, socle de nombreux services écosystémiques, est un enjeu actuel majeur en viticulture dans la perspective de réduire l'utilisation d'intrants et de garantir la préservation des sols tout en maintenant des performances socio-économiques élevées. (Gary et al. 2017). S'ajoutant au défit environnementale, le changement climatique représente un défit majeur en viticulture car les températures et la contrainte hydrique ont un impact fort sur la production de raisin et la typicité du vin (Malheiro et al. 2010; Fraga et al. 2012; Quenol 2014; van Leeuwen and Darriet 2016). Les températures moyennes sont en cours d'augmentation, de même que la fréquence et l'intensité des phénomènes extrêmes, notamment des périodes de canicule et de sécheresse (Pachauri et al. 2015). Dans de nombreuses régions viticoles du monde, ces nouvelles tendances affectent déjà la production de raisin et de vin (Jones et al. 2005; Jones and Webb 2010; van Leeuwen and Darriet 2016) : (i) des températures plus élevées provoquent une accéleration de la succession des stades phénologiques qui décale la maturation des raisins au cœur de l'été, et (ii) le manque d'eau prononcé certaines années réduit les quantités de raisin récoltées et modifie la composition des baies.

Bien que la culture de la vigne soit pratiquée dans de nombreuses régions du monde celle-ci se caractérise par une très grande diversité de contextes géographiques, de pratiques et d'objectifs qualitatifs (Vaudour 2002; Van Leeuwen and Seguin 2006). En conséquence, la recherche de stratégies de production alternatives et adaptées à ce nouveau context est très attendue mais doit tenir compte de cette diversité intrinsèque à la viticulture (García de Jalón et al. 2017).

I.1.2 Pratiques anciennes et actuelles d'agroforesterie en viticulture

Parmi des stratégies agro-écologiques vers une production de raisin et de vin plus durable et résiliente face aux changements climatiques, des pratiques modernes d'agroforesterie voient le jour en viticulture et attirent l'attention de la communauté scientifique (Trambouze and Goma-Fortin 2013). Selon Nair (1991), "*agroforesterie*" est le nom général donné aux systèmes de production qui associent des arbres avec n'importe quel type de cultures et / ou d'animaux sur une même unité de terre. Dans de tels systèmes, la composante ligneuse interagit écologiquement et économiquement avec les cultures et / ou les animaux. Ces interactions peuvent prendre de multiples formes et évoluent dans le temps. A partir des ressources disponibles, l'objectif intrinsèque de l'agroforesterie consiste à optimiser les interactions positives, à maximiser la quantité, la diversité et la durabilité des productions (Lundgren 1982). Bien que la *science* de l'agroforesterie soit relativement nouvelle, l'*art* lui, est ancien (Nair 1991). Cette affirmation s'applique particulièrement à la viticulture car des cas de vignes cultivées en présence d'arbres ont été mis en évidence dès les premières références à la culture de la vigne dans l'Antiquité, en contexte méditerranéen (Plinius Secundus (Plines l'Ancien) 79). Amouretti (1988) fait état en particulier de deux formes principales pratiquées dans l'Antiquité : (i) des vergers mixtes constitués de vignes (buissonnante ou en gobelet) intercalées avec des arbres fruitiers ou *oullières* (**Figure 1a**) et (ii) des vignes grimpantes sur des arbres ou *hautain* (**Figure 1b**). Dans ce second cas, les vignes grimpaient notamment sur des ormes (*Ulmus*), des érables (Acer), des peupliers (*Populus*) ou des frênes (*Fraxinus*), pratique notamment recherchée dans les plaines et les basses terres en tant que stratégie de protection contre le risque de gel (Sirven et al. 2016). Les formes traditionnelles de vignobles agroforestiers étaient communes jusqu'au XIX^{e} siècle dans les régions de la culture de la vigne méditerranéennes et continentales humides d'Europe, mais ont rapidement décliné après la crise du phylloxera (Fabre 2015).

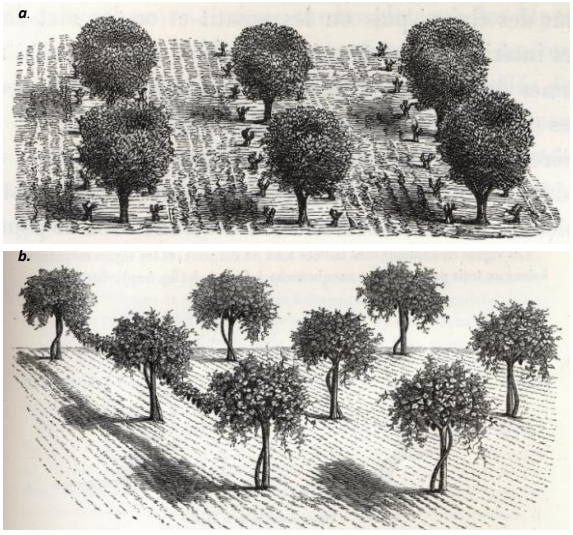

Figure 1: Deux formes principales d'association arbre-vigne pratiquées depuis l'Antiquité. L'illustration *a* montre un verger mixte ('oullière') regroupant trois productions: céréales, vigne et oliviers. L'illustration b montre des vignes grimpant sur les arbres ('hautain') dans la plaine de Tarbes (sud de la France) - Source: Ministère français de l'agriculture

Inspirées à la fois par l'héritage des pratiques anciennes et par des pratiques émergentes de cultures de céréales entre des allées d'arbres en régions tempérées, (Mosquera-Losada, M.R. et al. 2012), les cas modernes rencontrées de vignobles agroforestiers se composent d'alignement d'arbres d'essence forestière ou fruitière, intercalés entre les vignes. Les arbres sont généralement plantés à une très faible densité par rapport aux plantations forestières (**Figure 2**). Contrairement aux vignobles agroforestiers de l'Antiquité, ces plantations «modernes» sont conçues de manière à permettre la mécanisation complète des opérations culturales sur la vigne, à savoir la récolte, la protection et lutte phytosanitaire et le rognage des sarments. Ces systèmes sont à la fois peu nombreux et frappent par leur grande diversité en termes d'essences, de dispositions et de pratiques, qui rappelle celle marquant la viticulture de manière générale.

Dans ce contexte, (i) évaluer les avantages et les limites de l'association vigne-arbre et (ii) identifier les dispositions et les pratiques de gestion optimales en regard des objectifs de production, se présente comme une double opportunité pour soutenir le développement de pratiques agro-écologiques performantes en viticulture.

Figure 2 : Formes modernes d'associations vigne-arbre ou "vignobles agroforestiers". (a.) Vigne intercalée avec des oliviers en Sardaigne (Italie). (b.) *Vitis vinifera* cv. Grenache associée à des cormiers (*Sorbus domestica*) âgés de vingt ans dans l'Hérault (France). (c.) *Vitis vinifera* cv. Merlot associé à des arbres fruitiers divers (pommier, cerisier, poirier, etc.) en Gironde (France). (d.) *Vitis vinifera* cv. Cabernet-Sauvignon associé à des alisiers (*Sorbus domestica*) âgés de huit ans dans le Gers (France). (e.) Vigne intercalée avec des oliviers avec irrigation dans la région d'Ombrie (Italie).

I.2 Pourquoi et comment interroger la contribution microclimatique des arbres dans un vignoble ?

I.2.1 Contexte scientifique

À l'instar de tout type de système en agroforesterie, l'introduction d'arbres dans un vignoble peut avoir un impact sur la vigueur de la vigne et la production de raisin puis de vin via de multiples facteurs, parfois interdépendants (Nair 1993). Des interactions entre la vigne et les arbres peuvent notamment se mettre en place et prendre la forme de compétitions / complémentarités directes pour l'accès aux ressources (lumière, eau, nutriments) (Ong et al. 1996; Bayala and Wallace 2015; Bayala et al. 2015; Noordwijk et al. 2015), la modification du climat (Baldy and Stigter 1998; Stigter 2015), la modification des propriétés de sol (Pinho et al. 2012; Lorenz and Lal 2014) ou la fourniture de nouveaux habitats et ressources pour la biodiversité aérienne et sous-terraine (Batish 2008). Ainsi, cet ensemble constitue un système complexe à étudier.

Adoptant une approche pluridisciplinaire, le CASDAR Vitiforest (2014-2018) vise à améliorer les connaissances sur les vignobles agroforestiers modernes dans le contexte du sud-ouest de la France (**Figure 3**). Le travail de thèse présenté dans ce manuscrit participe au projet Vitiforest en se concentrant sur les impacts microclimatiques de l'arbre.

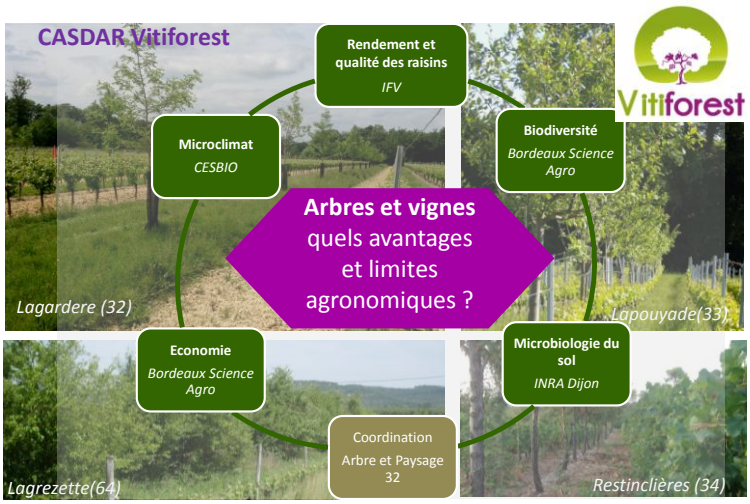

Figure 3: Le CASDAR Vitiforest (2014-2018) : thématiques et partenaires

I.2.2 Définition des composantes du climat et des échelles d'intérêt

Dans le cadre de ce manuscrit, les manifestations climatiques sont définies comme l'ensemble des phénomènes se produisant à l'interface entre l'atmosphère et la surface terrestre (**Figure 4**). Ceux-ci correspondent principalement à des transferts d'énergie, de quantité de mouvement et d'eau, tous initiés par l'apport énergétique issu du soleil. Le rayonnement solaire global (R_g) arrive à la surface terrestre sous la forme d'un rayonnement courte longueurs (domaine solaire) composé (i) d'une fraction directe et (ii) d'une fraction diffuse qui résulte de réflexions et de diffusions par les composants de l'atmosphère.

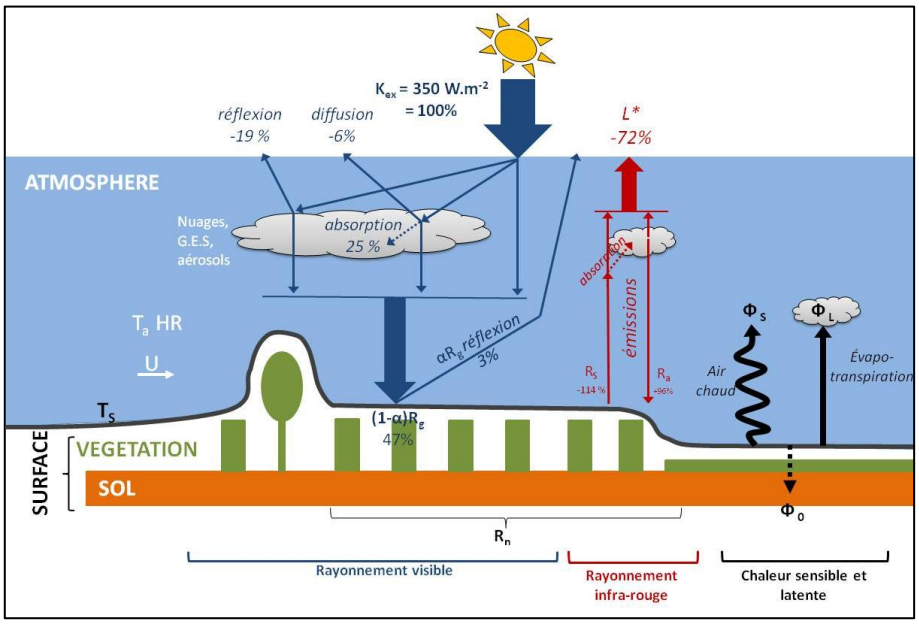

Figure 4: Bilan d'énergie et de masse à l'interface entre l'atmosphère et la surface de la Terre. Les notations utilisées sont définies dans les équations ci-dessous.

Eq. 1: Termes du bilan radiatif de surface

$$\boldsymbol{R_n + \Phi_L + \Phi_S + \Phi_O = \delta E}$$

avec

R_n	Rayonnement net
Φ_L	Flux de chaleur latente émis par la surface vers l'atmosphère (échanges convectifs)
Φ_S	Flux de chaleur sensible émis par la surface vers l'atmosphère (échanges convectifs)
Φ_O	Flux de chaleur dans le sol (échanges conductifs)
δE	Energie convertie par la surface sous des formes chimiques (ex : photosynthèse)

Eq. 2: Rayonnement net absorbé

$$\begin{aligned} \boldsymbol{R_n} &= \mathbf{R_{SW\downarrow} - R_{SW\uparrow} + R_{LW\downarrow} - R_{LW\uparrow}} \\ &= \boldsymbol{(1-\alpha)Rg + (1-\rho_S)R_a - R_S} \end{aligned} \quad [2]$$

avec

$R_{SW\downarrow} = \mathrm{R_g}$	Rayonnement global [W.m^{-2}]
$R_{SW\uparrow} = \alpha \mathrm{R_g}$	Rayonnement global réfléchi
$R_{LW\downarrow} = \epsilon_a \sigma \mathrm{T_a^4}$	Rayonnement atmosphérique incident grandes longueurs d'ondes (loi de Stefan Boltzmann)
$R_{LW\uparrow} = (1-\epsilon_S)\epsilon_a \sigma \mathrm{T_a^4} - \sigma \mathrm{T_S^4}$	Réflexion du rayonnement atmosphérique et émission propre de la surface grande longueur d'onde.
α_s	Albédo de la surface
R_a	Rayonnement thermique incident émis par l'atmosphère (grandes longueurs d'onde) [W.m^{-2}]
ρ_s	Coefficient de réflexion thermique de la surface dans les longueurs d'onde du rayonnement thermique
R_s	Rayonnement émis par la surface (grandes longueurs d'onde) [W.m^{-2}]
σ	Constant de Stefan-Boltzmann (5.67:10^{-8} W.m^{-2}.K^{-4})
ϵ_c	Emissivité de l'atmosphère vers le sol
T_a	Température radiative du compose atmosphérique [K]
ϵ_s	Emissivité de la surface
T_s	Température radiative de la surface [K]

Eq. 3: Flux de chaleur latente

$$\boldsymbol{\Phi_L = -L_V E = \frac{\rho C_P (e_s - e_a)}{\gamma (r_s + r_a)}}$$

avec

L_V	Chaleur latente d'évaporation de l'eau [W.m^{-2}]
E	Quantité d'eau évaporée par unité de temps
$\rho . C_P$	Capacité calorifique de l'air (1212 J.K^{-1}.m^{-1})
γ	Constant psychrométrique (66,1 PaK^{-1})
r_s	Résistance stomatique [s.m^{-1}]
r_a	Résistance aérodynamique de l'air [s.m-1], variant avec la vitesse du vent U
e_s	Pression de vapeur d'eau de la surface
e_a	Pression de vapeur d'eau de l'air au voisinage de la surface

Eq. 4: Flux de chaleur sensible

$$\boldsymbol{\Phi_s = h(U)(T_a - T_S) \text{ avec } h(U) = \rho C_P h'(U)}$$

avec

T_a	Température de l'air [K]
T_s	Température de la surface [K]
$\rho . C_P$	Capacité calorifique de l'air (1212 J.K^{-1}.m^{-1})
U	Vitesse du vent à 2 m au-dessus du sol [m.s^{-1}]
$h'(U)$	Coefficient de résistance aérodynamique de l'air variant en fonction de la vitesse du vent

Eq. 5: Conduction heat flux from the ground

$$\boldsymbol{\Phi_o = \lambda_g(z) \frac{\partial T_g(z,t)}{\partial z}}$$

avec

T_g	Température du sol à la profondeur z [K]
$\lambda_g(z)$	Conductivité thermique du sol à la prof. z [W.m^{-1}.K^{-1}]

L'énergie radiative absorbée par la surface et par les composants de l'atmosphère contribue à augmenter leur température (T_s et T_a). Selon la loi de Stefan Boltzmann, ils émettent en retour des rayonnements de grande longueur d'onde (domaine infrarouge thermique 3 à 100 μm), dans toutes les directions (**Eq. 2**). De plus, des gradients de température et de teneur en eau entre l'atmosphère et les composants de surface déclenchent (i) des flux turbulents (déplacements moléculaires dans les compartiments gazeux) qui correspondent à des flux de chaleur sensible (**Eq.4**) ou de chaleur latente (**Eq. 3**), qui correspondent au déplacement respectivement d'air chaud et de vapeur d'eau, d'un compartiment *source* ayant une température / teneur en vapeur d'eau élevée vers un compartiment *puit* de température /teneur plus faible; et (ii) des flux de conduction (diffusion moléculaire se produisant dans des compartiments solides ou liquides) qui correspondent à la transmission de chaleur d'un matériau de température élevée à un matériau de plus faible température (**Eq. 5**). Une très petite quantité d'énergie reste également temporairement stockée dans des molécules organiques par des processus biochimiques (photosynthèse, oxydoréduction, etc.). La conservation de l'énergie à l'interface entre le sol, la végétation et l'atmosphère est donnée par **Eq. 1**. Par convention, l'atmosphère est utilisée comme référence et les flux doivent donc être comptés positivement lorsqu'ils augmentent les apports énergétiques de l'atmosphère.

Principalement en raison de la structure intrinsèque de l'atmosphère, les phénomènes climatiques agissent comme un continuum couvrant une très large gamme d'échelles spatiales et temporelles (Oke 1992) (**Figure 5**). Le macroclimat, le mésoclimat et le climat local sont généralement distingués en considérant les phénomènes ayant une étendue spatiale couvrant respectivement les continents, les grandes régions géographiques et les petites régions agricoles. De plus, à l'échelle climatique locale, l'échelle microclimatique correspond spécifiquement à des variations notables sur une échelle spatiale variant de 1 m à 1 ha et une échelle de temps variant de la minute à la journée.

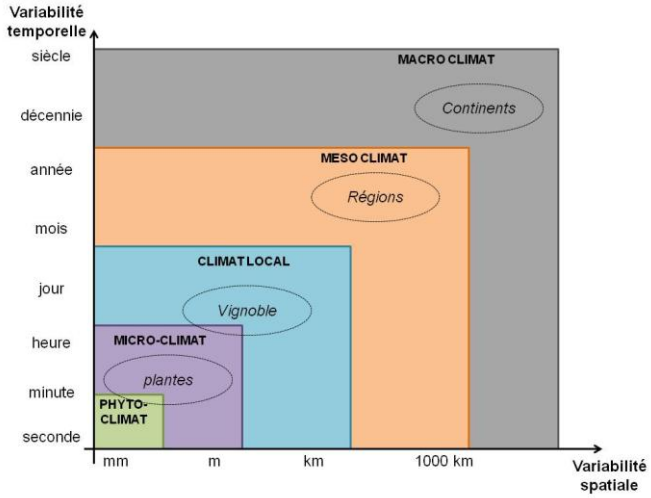

Figure 5: Continuum d'échelles spatio-temporelles composant le climat– d'après Oke (1992)

Dans ce continuum, les phénomènes climatiques de grandes échelles sont principalement déterminés par l'état des couches supérieures de l'atmosphère et par des causes extraterrestres, tandis que l'influence de la surface est croissante plus l'on tend vers les petites échelles (Choisnel 1977; Quenol 2011). Selon cette représentation, les conditions climatiques se produisant à une échelle donnée peuvent être considérées comme une distorsion des tendances climatiques s'exprimant à l'échelle supérieure en raison des variations des caractéristiques locales de surface. Parmi les caractéristiques de surface, la topographie, les ressources en eau, les zones urbanisées et l'utilisation du sol en général sont les principaux facteurs d'impact (Quenol 2011). En effet, tous ces composants de la surface terrestre interagissent localement avec le flux d'air et les flux d'énergie (Oke 1992). Concernant la végétation, la contribution climatique des arbres est plus particulièrement due à leur architecture aérienne et sous-terraine, ainsi qu'à leur importante évapotranspiration pour garantir leur croissance et métabolisme. En conséquence, les arbres introduisent localement de la variabilité au sein des flux radiatifs, d'air et des bilans d'eau. Les effets climatiques des arbres sont observés aux échelles locales (Chiapale 1975; Gross 1987; Guyot 1989; Geier-Hayes et al. 1995; Grant 1997) mais aussi à méso échelle (Mitchell et al. 2004; McPherson 2007; Eiseltová et al. 2012) et aux échelles continentales et globales (Makarieva et al. 2013; Ellison et al. 2017; Otto et al. 2014; Bonan 2008). Cependant, on peut s'attendre à ce que les impacts les plus directes s'observent dans leur proche voisinage, c'est-à-dire à l'échelle microclimatique, qui coïncide avec l'échelle de décision et de questionnement des agriculteurs, notamment en ce qui concerne l'agencement et les pratiques de gestions de la végétation les plus optimales en agroforesterie.

I.2.3 Questionnements méthodologiques

L'introduction d'arbres dans les vignobles peut générer des interactions directes ou indirectes entre la vigne et les arbres à travers une modification des flux d'énergie, d'air et d'eau. L'évaluation de l'impact microclimatique des arbres consiste à documenter l'effet des arbres sur ces flux et les rétroactions pouvant découler des variables d'état de la vigne et du sol. Plusieurs questions méthodologiques sont alors soulevées : comment évaluer le microclimat d'un vignoble de manière systémique et en extraire la contribution des arbres ? Quelles variables d'état devraient être ciblées au vu de la sensibilité de la vigne aux facteurs environnementaux ? Comment appréhender la variabilité des impacts liée aux caractéristiques de la végétation et à la diversité des pratiques ? Répondre à ces questions constitue les principaux défis méthodologiques identifiés.

I.3 Contributions attendues

I.3.1 Lacunes de connaissance

Il existe à ce jour très peu de références documentant les performances des vignobles agroforestiers et ceux d'autant plus concernant le volet microclimatique. A ma connaissance, on citera

de manière exhaustive deux études rapportées dans la littérature grise, qui ont toutes les deux été conduites sur le domaine expérimental agroforestier de Restinclières, dans le sud de la France (43,7258 ° N -3,8573 ° E), en contexte méditerranéen. Pour la première étude, Gomma-Fortin et Trambouze (2009) ont effectué des mesures d'éclairement au niveau des feuilles de vigne situées à 3,75 m et 6,25 m de pins (*Pinus brutia*) âgés de dix ans (**Figure 6**). Cependant, ces mesures ne couvrant qu'une seule journée estivale, leur extrapolation dans le temps, sur l'ensemble du cycle végétatif et reproductif de la vigne, ainsi que dans l'espace semble déconseillée.

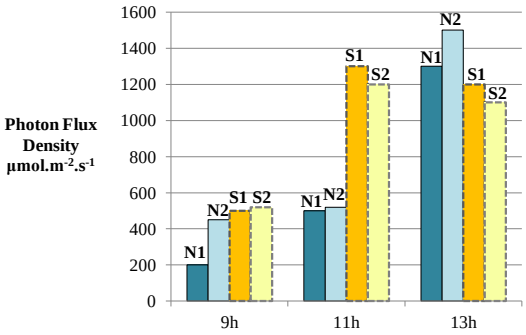

Figure 6: Mesures de densité de flux de photons à la surface de feuilles de vignes le 18-Aug. 2009 effectuées de part et d'autre d'un rang de Pins Brutia orienté EW (parcelle B10), Domaine expérimental de Restinclières. Les heures sont données en heure locale (UTC +2 hrs). Abréviations: *N1/N2* = 1er/2è rang de vigne au Nord des arbres – *S1/S2* = 1er/2è rang de vigne au Sud des arbres – Adapté de Gomma-Fortin et Trambouze (2009)

La deuxième étude, réalisée par Gouttesoulard (2015) cherche a évaluer les conséquences de l'ombrage par des mesures de températures effectuées dans la zone des grappes au sein rangs de vigne situés à 2,5 m et 3,75 m d'arbres (deux densités de plantation). Au niveau des rangs situés au Nord des arbres, une diminution moyenne des températures maximales journalières de 4 °C et 5,5 °C a été observées, respectivement) proximité de cormiers (*Sorbus domestica*) et de cyprès (*Cupressocyparis leylandii*), ces vignobles en agroforestiers étant orientés Ouest/Est. Pour les orientations Nord/Sud, une diminution moyenne maximale de 4,5 °C est rapportée le matin sur le premier rang de vignes situé à l'Ouest de cormiers, et de 3 °C l'après-midi du côté Est.

Ces deux références suggèrent que l'introduction d'alignement d'arbres dans un vignoble génère des patrons microclimatiques contrastés qui sont essentiellement liés à l'ombrage par les arbres. Néanmoins, la variabilité de ces tendances dans le temps, au long des saisons et des années, ainsi que leur impact potentiel sur la production de raisins et de vin demeurent inconnus.

I.3.2 Objectifs de la thèse

Cette thèse vise à améliorer les connaissances générales concernant l'impact microclimatique d'arbres dans un vignoble. Trois objectifs scientifiques sont plus spécifiquement retenus: (i) caractériser l'effet des arbres sur le microclimat d'un vignoble, (ii) évaluer les répercussions en termes de rendement et de qualité viticole des raisins, et (iii) comparer les résultats selon la nature et l'agencement des arbres.

I.3.3 Structure du manuscrit

Ce manuscrit est organisé en sept chapitres distincts, qui incluent une introduction et une conclusion générale.

Cette introduction générale a permis de poser les enjeux et objectifs de la thèse et de définir les concepts essentiels relatifs au climat repris au long du manuscrit.

Les chapitres deux et trois fournissent successivement un état des connaissances concernant l'impact microclimatique des arbres dans diverses formes d'agroforesterie et sur la sensibilité de la production de raisin et de vin aux facteurs climatiques. Ils permettent d'identifier les mécanismes les plus centraux et les variables d'état à évaluer pour l'étude des vignobles agroforestiers ainsi que la méthodologie la plus adaptée.

Le chapitre quatre présente le matériel d'étude, à savoir (i) les terrains d'étude qui ont été sélectionnés afin d'échantillonner divers contextes de «terroir» et de végétation, ainsi que (ii) le jeu de données collectées, qui regroupe des suivis météorologiques, des suivis microclimatiques distribués dans les vignobles, des mesures de rendement et de composition des baies ainsi qu'un ensemble d'images de très haute résolution, acquises par drone, dans les domaines spectraux du visible, du proche infrarouge et de l'infrarouge thermique. Ce chapitre présente ensuite les méthodes d'analyse d'images qui ont été développées pour caractériser la morphologie et l'agencement de la végétation.

Le chapitre cinq décrit la méthode puis les résultats d'analyse des patrons de température au sein de l'un des trois vignobles sélectionnés, puis présente les corrélations observées entre la variabilité de température et des critères quantitatifs et qualitatifs à la récolte.

Le chapitre six étudie plus spécifiquement l'impact présent et futur liés à l'interception de la lumière par une approche de modélisation 3D du bilan radiatif de vignobles agroforestiers.

Enfin, la conclusion générale synthétise les principaux résultats de la thèse en lien avec les connaissances existantes. Aussi elle permet une prise de recul sur la pertinence des méthodes développées au cours de la thèse et propose des perspectives de recherche méritant d'être poursuivies.

I.3.4 Supervision et valorisations de la thèse

Les travaux de thèse présentés dans ce manuscrit ont bénéficié du soutien financier de la Fondation de France (Bourse jeune chercheur "Agroforesterie tempérée") et du CASDAR Vitiforest. Ils ont été effectués au sein de l'UMR CESBIO et l'Université Toulouse 3 sous la co-direction de Vincent Bustillo[1] et Thomas Houet[2]. Aussi, ils ont bénéficiés de réunions annuelles d'un comité de suivi constitué par Eric Ceschia[1], Benoit Coudert[1], Marie Gosme[3] et David Sheeren[4].

[1] UMR CESBIO, Université Toulouse 3

[2] UMR COSTEL, CNRS

[3] UMR System, INRA

[4] INRA UMR DYNAFOR

Les éléments présentés dans ce manuscrit ont par ailleurs été valorisés sous diverses formes académiques et vulgarisées :

(i) Un article de recherche a été soumis au journal *Agricultural and Forest Meteorology*, qui porte sur l'analyse des patrons de microclimat sur le site d'étude de Lagardère ;

(ii) En co-écriture avec les partenaires de Vitiforest, un article de revue a été soumis au journal *Agronomy for Sustainable Development*. Il propose un état de l'art inédit et multidisciplinaire sur les performances et les limites de l'agroforesterie en viticulture;

(iii) Aussi, j'ai effectué une présentation orale à la 3ème Conférence Européenne d'Agroforesterie (23-25 Mai 2016, Montpellier, France) et à la Conférence d'Ecologie du Paysage de l'IUFRO (24-29 September 2017, Halle, Allemagne), axées respectivement sur la variabilité des températures et sur les méthodes d'analyse d'images permettant de comprendre l'impact microclimatique de la végétation ;

(iv) J'ai présenté un poster à la Conférence "Agriculture and Climate Change" (26-28 March 2017 Sitges, Espagne) donnant une vue d'ensemble de la thèse ;

(v) J'ai effectué une présentation orale auprès de viticulteurs lors des Journées techniques "Agroécologie au vignoble" (Vitinnov et Bordeaux Sciences Agro, 14-15 Nov. 2017, Bordeaux, France) ;

(vi) Enfin j'ai répondu à une courte interview pour la revue technique "Réussir Vigne".

CHAPTER I
General introduction

Agroforestry systems will be able to mimic or replicate many of the nutrient-cycling and favorable environmental influences found with forest ecosystems, while generating the exportable outputs achieved with agricultural systems.

(Kidd and Pimentel 1992)

I.1 Towards sustainable production of grapes and wine

I.1.1 Current challenges of viticulture

Increasing biodiversity and the provision of ecosystem services is highly at stake in viticulture in order to decrease the use of chemical inputs and to guarantee the conservation of the soil properties while maintaining high socio-economic performances (Gary et al. 2017). Adding to environmental issues, climate change is of prime concern for grape and wine production as temperatures and water availability directly impact both grape yield and grape quality for wine making (Malheiro et al. 2010; Fraga et al. 2012; Quenol 2014; van Leeuwen and Darriet 2016). Average temperatures are increasing as well as the frequency and intensity of extreme events, notably of heat weaves and droughts (Pachauri et al. 2015). In many grapevine growing regions around the world, these new trends are already impacting grapevine production (Jones et al. 2005; Jones and Webb 2010; van Leeuwen and Darriet 2016): (i) higher temperatures have been triggering earlier phenological succession which notably shifts the ripening of berries into the warmest days of summer and (ii) increased water stress have been reducing yields and modifying the fruit composition at harvest.

Though grapevine cultivation is spread all around the world, it is characterized by a very wide diversity of geographical contexts and of production objectives in terms of wine style (Vaudour 2002; Van Leeuwen and Seguin 2006). Consequently, the search for alternative and adaptive strategies of production are greatly expected but should take into account this intrinsic diversity (García de Jalón et al. 2017).

I.1.2 From past to present forms of agroforestry vineyards

Among agroecological strategies towards more sustainable and climate-resilient grape and wine production, modern forms of agroforestry vineyards are emerging and are raising the attention of the scientific community (Trambouze and Goma-Fortin 2013). As defined by Nair (1991), "agroforestry" is a collective name for land-use systems involving trees combined with any type of crops and/or animals on the same unit of land. In such systems, the woody component interacts ecologically and economically with the crop and/or animal components. Such interactions can take many different forms and these may change over time. The intrinsic aim behind agroforestry practices is to optimize the positive interactions, to obtain the highest total, the most diversified and/or most sustainable production from the available resources (Lundgren 1982). While the *science* of agroforestry is fairly new, the *art* is old (Nair 1991). This statement particularly applies to viticulture as signs of grapevines being cropped together with trees were found since the first references of grapevine cultivation in the Antiquity, under Mediterranean context (Plinius Secundus (Plines l'Ancien) 79). Amouretti (1988) notably reports two main practices from the Antiquity: (i) mixed orchards constituted by bushy or gobelet trained vines which were intercropped together with fruit trees (**Figure 1a**) and (ii) vines that were highly trained upon trees (**Figure 1b**). In this second case, vines notably grew on elm trees (*Ulmus*), maple trees (*Acer*), poplar trees (*Populus*) or ash trees (*Fraxinus*) on plains and lowlands, notably as a protective strategy against frost risk (Sirven et al. 2016). Traditional forms of agroforestry vineyards used to be common in the Mediterranean and humid-continental grapevine growing regions of Europe until the XIXth century but rapidly declined after the phylloxera crisis (Fabre 2015).

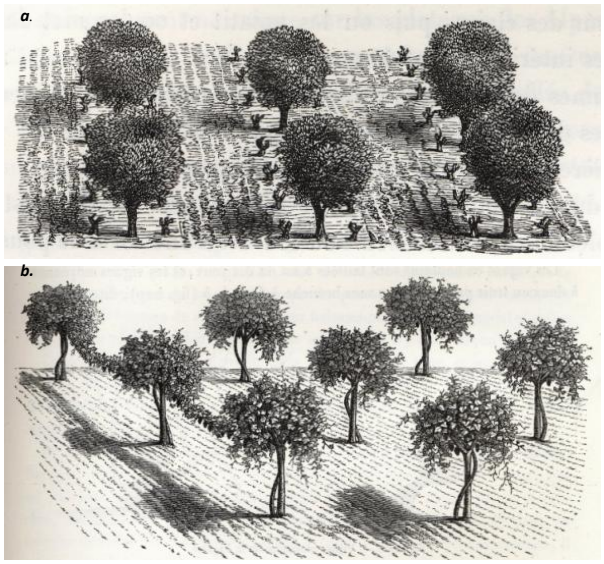

Figure 7: Two main forms of tree-grapevine intercropping from the Antiquity. Illustration *a* shows a mixed orchard (French '*oullière*') with three producing stories: crop, grapevine and olive trees. Illustration *b* shows grapevines highly trained upon trees (French '*hautain*') in the Plain of Tarbes (Southern France) - Source: French Ministry of Agriculture

Inspired by both the heritage from past practices and by cases of tree-crop alley-cropping systems which are developing in temperate regions (Mosquera-Losada, M.R. et al. 2012), the modern forms of

agroforestry vineyards can present rows of timber wood/fruit trees planted within grapevine rows at a very low density compared to forestry practices (**Figure 2**). Contrary to the Antique agroforestry vineyards, the 'modern' forms of agroforestry vineyards are designed so as to allow full mechanization of the management operations on grapevine, namely harvest, crop protection and canopy pruning. Striking is the very wide diversity of tree species, of arrangement and of management practices of these systems, which recalls the one that characterizes viticulture in general.

In this context, (i) assessing the advantages and drawbacks of intercropping trees together with grapevine and (ii) identifying the optimum arrangements and management practices in regards to the production objectives stand as a twofold sound opportunity to support the development of efficient agro-ecological practices in viticulture.

Figure 8: Modern forms of grapevine and tree intercropping or "agroforestry vineyards". (a.) Grapevine intercropped with olive trees in Sardinia (Italy). (b.) Grenache grapevine together with twenty-year old sorb trees (*Sorbus domestica*) in Herault (France). (c.) Merlot grapevine intercropped with mixed fruit trees (apple, cherry, pear, etc) in Gironde (France). (d.) Cabernet-Sauvignon grapevine intercropped with eight-year old sorb trees (*Sorbus domestica*) in Gers (France). (e.) Grapevine intercropped with irrigated olive trees in Umbria region (Italy).

I.2 Why and how addressing the microclimatic contribution of trees in vineyards?

I.2.1 Scientific context and objectives

Similarly to any kind of agroforestry systems, introducing trees within a vineyard potentially impact the performances of grape and wine production through multiple and interlinked factors (Nair 1993). It may notably set interactions between grapevine and trees in the form of direct competitions/complementarities for accessing resources (light, water and nutrients) (Ong et al. 1996; Bayala and Wallace 2015; Bayala et al. 2015; Noordwijk et al. 2015), of climatic modifications (Baldy and Stigter 1998; Stigter 2015), of soil properties modifications (Pinho et al. 2012; Lorenz and Lal 2014) and of the provision of new habitats and resources for above and below ground biodiversity (Batish 2008). The ensemble constitutes a complex system to study.

In order to improve knowledge concerning modern agroforestry vineyards in the context of South-western France, the research project named Vitiforest has been conducted following a multidisciplinary approach (**Figure 9**). The thesis work presented in this manuscript took part in Vitiforest focusing on the microclimatic impacts from trees.

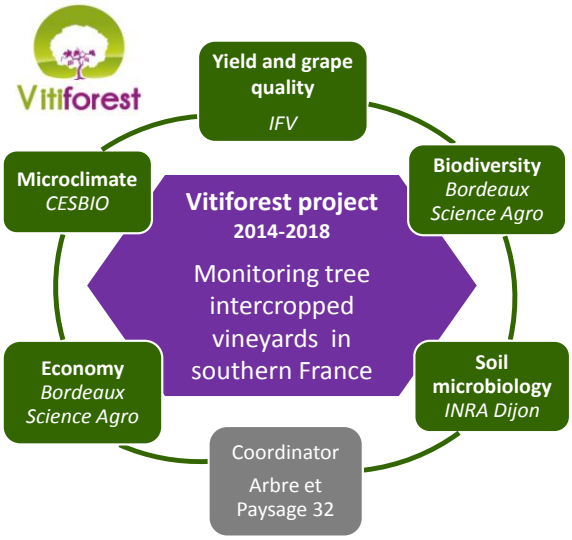

Figure 9: Research objectives, subjects and partners of *Vitiforest CASDAR* (French).

I.2.2 Definition of climate components and scales of interest

For the purpose of this work, climate manifestations are defined as the ensemble of phenomena occurring at the interface between the atmosphere and the Earth surface (**Figure 10**). They mainly correspond to transfers of radiations, momentum and water triggered by the incoming energy from the sun. The global incoming solar radiation (R_g) arouses at the ground surface as a combination of direct light and diffuse light which results from reflexions or diffusions from the components of the atmosphere.

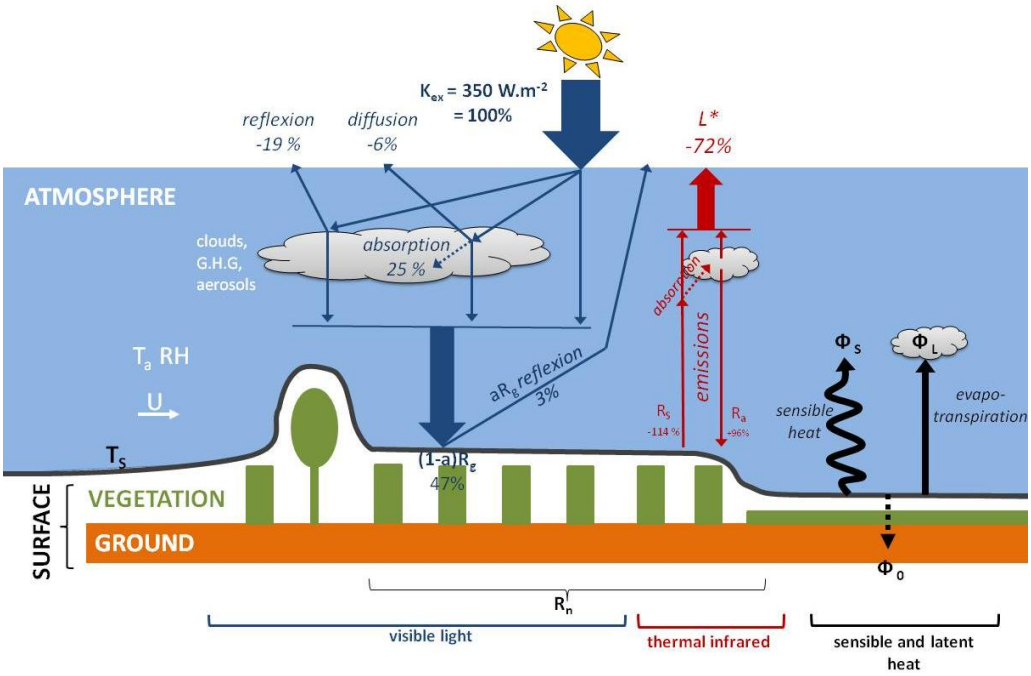

Figure 10: Energy and mass budget at the interface between atmosphere and the Earth surface. Notations are defined in the equations below.

Eq. 6: Components of the radiative budget at the Earth surface

$$\boldsymbol{R_n + \Phi_L + \Phi_S + \Phi_O = \delta E} \quad [6]$$

ith

R_n	Net radiation
Φ_L	Latent heat flux (turbulent exchange of water) towards the atmosphere
Φ_S	Sensible heat flux (turbulent exchange of air) towards the atmosphere
Φ_O	Conduction flux from the ground towards the atmosphere
δE	Fraction of energy biochemically converted by the vegetation into organic compounds (e.g. photosynthesis)

Eq. 7: Net radiation components

$$\boldsymbol{R_n = R_{SW\downarrow} - R_{SW\uparrow} + R_{LW\downarrow} - R_{LW\uparrow}} \quad [7]$$
$$\boldsymbol{= (1-\alpha)Rg + (1-\rho_S)R_a - R_S}$$

with

$R_{SW\downarrow} = R_g$	Global radiation [W.m^{-2}]
$R_{SW\uparrow} = \alpha R_g$	Reflected global radiation
$R_{LW\downarrow} = \epsilon_a \sigma T_a^4$	Downward atmospheric long wave exitance (Stefan Boltzmann law)
$R_{LW\uparrow} = (1-\epsilon_S)\epsilon_a \sigma T_a^4 - \sigma T_S^4$	Upward long-wave radiation includes the atmospheric exitance reflection and the surface proper emission
α_s	Surface albedo
R_a	Long-wave radiation coming from the atmospheric emission [W.m^{-2}]
ρ_s	Surface factor of reflexion of long wave radiations
R_s	Long-wave radiation emitted by the surface towards the atmosphere [W.m^{-2}]
σ	Stefan-Boltzmann constant (5.67:10^{-8} W.m^{-2}.K^{-4})
ϵ_c	Atmosphere emissivity of long-wave radiations towards the ground
T_a	Atmosphere temperature [K]
ϵ_s	Surface emissivity of long-wave radiations
T_s	Surface temperature [K]

Eq. 8: Latent heat flux

$$\boldsymbol{\Phi_L = -LE - -L_V E = \frac{\rho C_P (e_s - e_a)}{\gamma (r_s + r_a)}}$$

with

L_V	Water latent heat of vaporization [W.m-2]
E	Quantity of water evaporated per unit of time
$\rho . C_P$	Air specific heat capacity (1212 J.K-1.m-1)
γ	Psychrometric constant (66,1 PaK-1)
r_s	Stomata resistance [s.m-1]
r_a	Air aerodynamic resistance [s.m-1], varies with U (wind speed)
e_s	vapor pressure in vegetation
e_a	vapor pressure in the stomata air

Eq. 9: Sensible heat flux

$$\boldsymbol{\Phi_s = h(U)(T_a - T_S) \text{ with } h(U) = \rho C_P h'(U)} \quad [9]$$

with

T_a	Air temperature [K]
T_s	Surface temperature [K]
$\rho . C_P$	Air specific heat capacity (1212 J.K-1.m-1)
U	Wind speed at 2 m above ground[m.s-1]
$h'(U)$	Air aerodynamic factor. It varies positively with U powered between 0.5 and 1, depending on the air flow regime

Eq. 10: Conduction heat flux from the ground

$$\boldsymbol{\Phi_o = \lambda_g(z) \frac{\partial T_g(z,t)}{\partial z}} \quad [10]$$

with

T_g	Ground temperature at depth z [K]
$\lambda_g(z)$	Ground thermal conductivity at depth z [W.m-1.K-1]

The radiative energy absorbed by the surface and by the atmosphere components contribute to increasing the temperatures of these two compartments (T_s and T_a). In return they emits long wave radiations in the thermal infrared wavebands (3 to 100 μm), in all directions, according to Stefan Boltzmann Law (**Eq. 7**). Additionally, gradients of temperature and water content between the atmosphere and the surface components trigger (i) turbulent fluxes (molecular displacement occurring in gaseous compartments) or sensible (**Eq. 9**) and latent (**Eq. 8**) heat, which correspond to air or water vapor displacement from a source compartment with high air temperatures /water vapor content to a sink with lower content; and (ii) conduction fluxes (molecular diffusion occurring in solid or liquid compartments) which corresponds to the transmission of heat from material with high temperature to a material with lower temperature (**Eq. 10**). A very small amount of energy also remains temporary stocked into organic molecules through biochemical processes (photosynthesis, oxidation-reduction, etc.). The energy conservation at the Soil-Vegetation-Atmosphere interface leads to **Eq. 6**. By convention, the atmosphere is used as a reference thus the fluxes should be counted positively when they increase the energy inputs of the atmosphere.

Mainly because of the intrinsic structure of the atmosphere, climatic phenomena work as a continuum covering a very wide range of space and time scales (Oke 1992) (**Figure 11**). The macroclimate, the mesoclimate and the local climate are commonly distinguished considering phenomena with a spatial extent covering continents, large geographical regions and small agricultural regions respectively. In addition, within the local climatic scale, the microclimatic scale specifically corresponds to variations noticeable at 1 meter to 1 ha spatial scale and minute to day time scale.

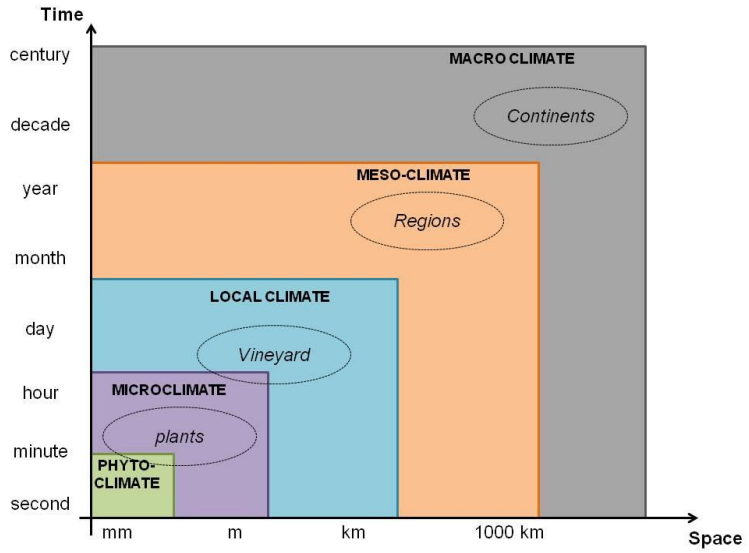

Figure 11: Continuum of time and spatial scales composing the climate on Earth – adapted from Oke (1992)

Within this continuum, the largest scale phenomena are mainly driven by the state of the upper layers of the atmosphere and by extraterrestrial causes, while the contribution from the surface increases at smaller scales (Choisnel 1977; Quenol 2011). Following this representation, the climate conditions occurring at a given scale can be considered as a distortion of the climatic trends applying at the upper scale because of variations of the surface characteristics. Among surface characteristics, topography, water resources, vegetation urbanized areas and the land uses in general are the main contributing factors (Quenol 2011). Indeed, all these land surface parameters locally interact with the air flow and with the energy fluxes (Oke 1992). More specifically, the climatic contribution from trees is mainly due to their above and below ground architecture and roughness as well as their high transpiration demand to sustain tree growth. As a consequence, they introduce variability in radiation patterns, on air fluxes and on the water budgets. On the one hand, the climatic effects of trees have been observed at local scale (Chiapale 1975; Gross 1987; Guyot 1989; Geier-Hayes et al. 1995; Grant 1997), meso scale (Mitchell et al. 2004; McPherson 2007; Eiseltová et al. 2012) and continental to global scales (Makarieva et al. 2013; Ellison et al. 2017; Otto et al. 2014; Bonan 2008). On the other hand, most direct impacts can be expected in the very close vicinity of trees, i.e. at the microclimatic scale, which matches with the scale of farmers' decision, notably with their questioning concerning best tree planting structure in an agroforestry system.

I.2.3 Arousing methodological issues

Introducing trees in vineyards may set direct or indirect interactions between grapevine and trees through the energy, air and water fluxes. Assessing the microclimatic impact from trees consists in documenting the impacts of trees on these fluxes and the potential retroactions it may triggers from grapevine and ground state variables. This raises several methodological issues: How assessing the microclimate of a vineyard in a systemic way and identifying the specific contribution from trees? Which state variables should be targeted in regards to the sensitivity of grapevine to environmental factors? How apprehending the variability of impacts which is due to the characteristics of the vegetation as well as the wide diversity of practices? Answering these questions represents the main identified methodological challenges.

I.3 Expected contributions from this thesis

I.3.1 Gaps of knowledge

Very few references already exist concerning agroforestry vineyard performances and even so concerning their microclimate. To our knowledge, one can exhaustively cite two experimentations reported in the grey literature, both carried out at the agroforestry experimental Domain of Restinclières in southern France (43.7258°N -3.8573°E), under Mediterranean context. In the first study by Gomma-Fortin and Trambouze (2009), measurements of irradiance arousing to the leaves of

grapevines located at 3.75 m and 6.25 m from ten-year-old *Pinus brutia* were carried out (**Figure 12**). This assessment only covered half a single day of summer. As a consequence, extrapolation throughout grapevine vegetative and reproductive cycle or in space is not recommended.

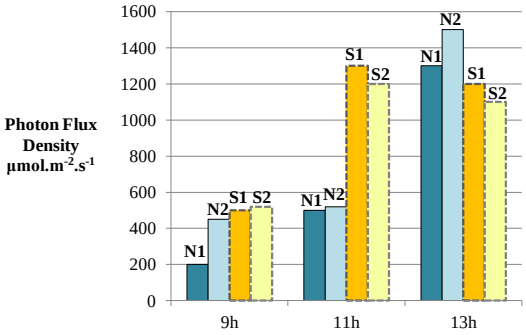

Figure 12: Measurements of photon flux density arousing to grapevine leaves on the 18-Aug. 2009 on either sides from a EW oriented row of *Pinus brutia* (B10 plot) at the experimental Domain of Restinclières. Hours are given as local time (solar time +2 hrs). Abbreviations: *N1/N2* = 1st/2nd northern row from tree row – *S1/S2* = 1st/2nd southern row from tree row – Adapted from Gomma-Fortin and Trambouze (2009)

The second study by Gouttesoulard (2015) assessed the consequences of shading on the air temperatures which was measured inside vine rows, in the bunch zone of grapevine, at either 2.5 m or 3.75 m from trees, depending on the planting density. At the first vine row on the northern side of trees, their results reported an average depletion of the maxima daily temperatures at veraison of 4 °C and 5.5 °C with respectively *Sorbus domestica* and *Cupressocyparis leylandii* species, considering a West/East oriented plantation. For North/South orientations, an average maximum depletion of 4.5 °C was reported in the morning on the first vine row on the western side of *Sorbus domestica* trees and of 3 °C, in the afternoon on their eastern side. These two references suggest that intercropping trees within a vineyard does generate contrasted microclimate patterns which are due in this case to light interception. Nonetheless, very little is known concerning the variability of these patterns in time throughout the season and years and concerning their potential impact on the production of grapes.

I.3.2 Objectives of this thesis

In order to fill in some of these knowledge gaps, this thesis aims at improving the general knowledge concerning the microclimatic impacts of trees in vineyards. Three main objectives are more specifically retained: (i) documenting the local microclimatic impacts from trees in vineyards, (ii) assessing the consequences they entail on grapevine physiology and production, and (iii) discussing the impacts according to the morphological characteristics of the vegetation.

I.3.3 Structure of the manuscript

This manuscript is structured in seven chapters including this general introduction and conclusion.

This introductive chapter highlights the main research challenges and objectives and provides the useful concepts regarding climate mechanisms.

Chapter two and three successively provide a state of the art of the current knowledge concerning the microclimate impacts from trees in diverse forms of agroforestry systems and on the sensitivity of grape and wine production to microclimatic factors. They allow identifying the most central mechanisms and state variables to be assessed for the study of agroforestry vineyards as well as the most adapted methodology.

Chapter four presents the material: (i) the study sites which were selected in order to sample diverse contexts of "terroir" and vegetation; (ii) the collected data set, which gathers meteorological records, microclimatic records distributed within the vineyards together with measurements of yield and grape quality for wine making, and a set of Unmanned Aerial Vehicle (UAV- drone) images which covers the optical, near infrared and thermal infrared spectral domains. Then it presents the image analysis methods which were developed for characterizing the morphology and the arrangement of the vegetation.

Chapter five describes the methods and the results from the analysis of temperature patterns in one of the study vineyard and the correlations they presented with quantitative and qualitative traits at harvest.

Chapter six more specifically investigates the current and future impacts due to light interception through the 3D modeling of the radiative budget of agroforestry vineyards.

Finally the general conclusion (chapter seven) summarizes the main findings of the thesis in regards to the literature, discusses the relevance of the methodological developments which were tested and proposes perspectives for further research.

I.3.4 Supervision and additional productions

The Ph D work presented in this manuscript benefitted from the financial support of the Fondation de France (Bourse jeune chercheur "Agroforesterie tempérée") and from the CASDAR Vitiforest. It was based at the UMR CESBIO and Université Toulouse 3. It was co-directed by Vincent Bustillo[5] and M. Thomas Houet[6] and benefited from yearly meetings with an advisory board constituted by Eric Ceschia[1], Benoit Coudert[1], Marie Gosme[7] and David Sheeren[8].

Parts of the work presented in this manuscript were presented under various materials:

(i) A research paper was submitted to the Agricultural and Forest Meteorology journal concerning the analysis of microclimate patterns at the study site of Lagardere;

[5] UMR CESBIO, Université Toulouse 3
[6] UMR COSTEL, CNRS
[7] UMR System, INRA
[8] INRA UMR DYNAFOR

(ii) In collaboration with partners of Vitiforest, a revue paper was submitted to the Agronomy for Sustainable Development journal which offers a multidisciplinary state of the art concerning the performances and limits of agroforestry vineyards;

(iii) Two presentations were performed at the 3rd European Agroforestry Conference, (23-25 May 2016, Montpellier, France) and the IUFRO Landscape Ecology Conference (24-29 September 2017, Halle, Germany). They respectively focused on temperature patterns and image analysis methods for comprehending the microclimatic impact of the vegetation;

(iv) A poster was presented at the Agriculture and climate change Conference (26-28 March 2017 Sitges, Spain);

(v) A presentation was made to vine growers and wine makers at the Journées techniques "Agroécologie au vignoble" (Vitinnov et Bordeaux Sciences Agro, 14-15 Nov. 2017, Bordeaux, France);

(vi) and a short interview was made for the professional journal “Réussir Vigne”.

CHAPTER II
Microclimatic impact of trees: a state of the art

II.1 Introduction

Vegetation impacts the climate as it interferes with the heat and the mass transfers between the earth surface and the atmosphere. Because of the specific shape and roughness of woody vegetation, plus the high transpiration demand to sustain tree growth, trees can have a significant impact on the local climate of a land (Oke 1992; Quenol 2011).

Climatic effects of trees have been observed at local scale (Chiapale 1975; Gross 1987; Guyot 1989; Geier-Hayes et al. 1995; Grant 1997), meso scale (Mitchell et al. 2004; McPherson 2007; Eiseltová et al. 2012) and continental to global scales (Makarieva et al. 2013; Ellison et al. 2017; Otto et al. 2014; Bonan 2008). In order to limit the scope of the thesis, the focus is made on the microclimatic scale (1 m^2 to 1 ha areas and day to year timeframes) where main processes listed hereafter occur and also because it matches with the scale of farmers' decision (i.e. their practices in an agroforestry system). Indeed, at this scale, mechanisms involved in tree / climate interactions are:

1. shading (interception of direct sunbeams),
2. sheltering (interference with the air flow),
3. water cycle modifications (through precipitation and runoff interception, underground redistribution, ground evaporation and tree transpiration),
4. reflection of sun beams by the sunny sides of dense canopies
5. and heat release as thermal infrared radiations emitted by trees.

Within an agroforestry vineyard, grapevine canopy also interacts with sun beams, airflow and water flows and thus generates a specific microclimate in its vicinity (Smart 1973, 1985, English et al. 1989, 1990). Nevertheless, the microclimatic mechanisms induced by trees may significantly differ in intensity and in spatial footprint from that induced by grapevine because trees and grapevine supposedly present differences of physiology and architecture. Also the microclimatic influence of trees, strongly depends on the tree type, planting structure and canopy management choices.

This first chapter provides a state of the art of the current knowledge concerning the microclimatic impacts from trees and proposes methodological recommendations for their assessment in the context of agroforestry vineyards. Based on a vast review of literature, the main characteristics of these mechanisms sorting them by type are firstly described. Then, their potential consequences on the microclimatic variables within an agroforestry vineyard are analyzed. Finally, the contribution of the vegetation structure to the observed trends is reported.

II.2 Mechanisms

II.2.1 Radiative effects of trees

Figure 13 shows that trees modify the incoming radiation in their vicinity through three types of radiative mechanisms:

i) trees **intercept** a fraction of the direct sunlight incoming radiations thus generating shading patches;

ii) trees **reflect** a fraction of the direct sunlight incoming radiations with preferential orientation;

iii) trees **emit** energy through longwave radiations, which partly substitutes to the downward radiations emitted by the atmosphere.

Concerning shortwave radiations, it must be kept in mind that the incident light available for plants comes from several radiation sources: the sky, which emits a direct and a diffuse fraction of the incident radiation, as well as the vegetation canopy components and the soil surface in its vicinity, because the two latter scatter a fraction of the radiation they intercept (Sinoquet et al. 2001).

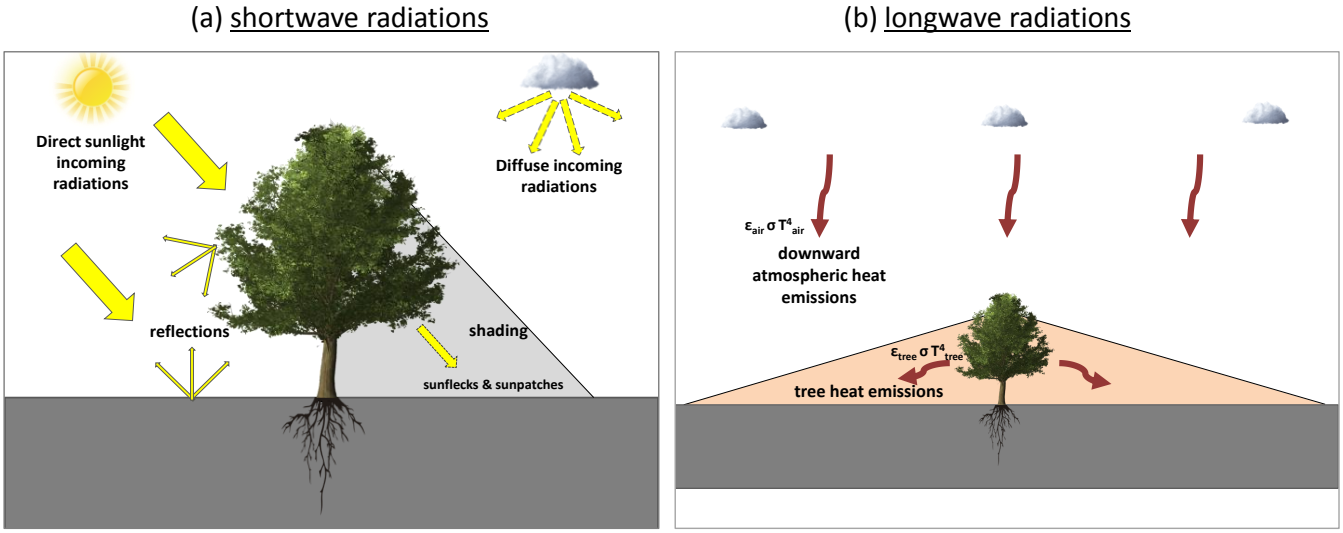

Figure 13: Modifications of the incoming radiations for an understory crop in the vicinity of a tree. (a) shows interception and reflections of the solar shortwave radiations. (b) shows the contribution of longwave radiations emitted by trees instead of the atmosphere in part of the solid angle.

II.2.1.1 Shading

Within agroforestry plantings, the canopy of trees intercepts sunlight and so partially reduces the irradiance for the understory crops. Shadows correspond to the horizontal projection of tree canopy. In a time frame of seconds to minutes, shadows composed by total shade, penumbra or sunflecks alternatively appear and disappear with wind induced movements of the tree leaves and branches (Chazdon 1988). In a time frame of hours, days and seasons, patterns of juxtaposed shadows and sunpatches move forward and change form as the sun runs in the sky with different angles of

incidence (Artru et al. 2017). The available light at the bottom of the atmosphere originates from the sun from either direct sourcing or diffuse sourcing after scattering on the atmosphere, ground, and vegetation components (**Figure 10**). From all the available light, the Photosynthetically Active Radiations **(PAR)** correspond to the wave bands used by plants for their photosynthesis. They fall within the spectral range of 400 nm to 700 nm and will be used for measuring the intensity of the light irradiance of plants. Addressing the instantaneous PAR irradiance and its integration in time over the vegetative growth period is essential in the scope for understanding the productivity of grapevine when intercropped with trees. The existing knowledge concerning these aspects is reviewed in the following subsections.

Intensity of light interception

Agroforestry plantings are sparse compared to forest tree plantings. The amount of interception at a given time is given by two separate and additive components (Jackson and Palmer 1979):

- the light which has passed between the trees,
- the light which has passed within the canopy.

Consequently, the intensity of light depletion mainly results from the combined effect of

$$I_c * A_{shade}$$

where I_c is the fraction of intercepted light and A_{shade} is the extent to which it applies (Meloni and Sinoquet 1997).

INSTANTANEOUS BUDGET

The instantaneous spatial extent of a shadow corresponds to the planar projection of the volume occupied by the tree canopy. When projected horizontally, the spatial extent of shadows increases with solar angles, tree heights and tree density at the plot scale (Jackson and Palmer 1979; Reifsnyder 1989; Chirko et al. 1996b; Leroy et al. 2009; Talbot and Dupraz 2012; Dufour et al. 2013). In addition it varies with the shape of the tree crown, e.g. trees with rectangular cross section showed greater interception than that with triangular cross-section (Jackson and Palmer 1972). The spatial extent of shadows exhibits an important variability in time which is directly due to the influence of the solar angle (Satterlund 1983). This is illustrated in **Figure 14** showing the shadow cast of a hypothetical evergreen ash tree. The simulated shadow cast assumes constant tree height and canopy volume and firstly confirm that during the day, a tree casts its shortest shadow at solar noon, when the sun reaches its highest altitude angle, corresponding to zenith 0° in the Northern Hemisphere (NH), producing a shadow that points toward due north *i.e* azimuth 0° (Geier-Hayes et al. 1995). Secondly, during the year, in NH, a tree casts its longest shadows about December 21st, on the winter solstice, and its shortest shadows about June 21st, on the summer solstice. From the summer to the winter solstice, shadows lengthen, while from the winter to the summer solstice shadows become shorter (Geier-Hayes et al. 1995).

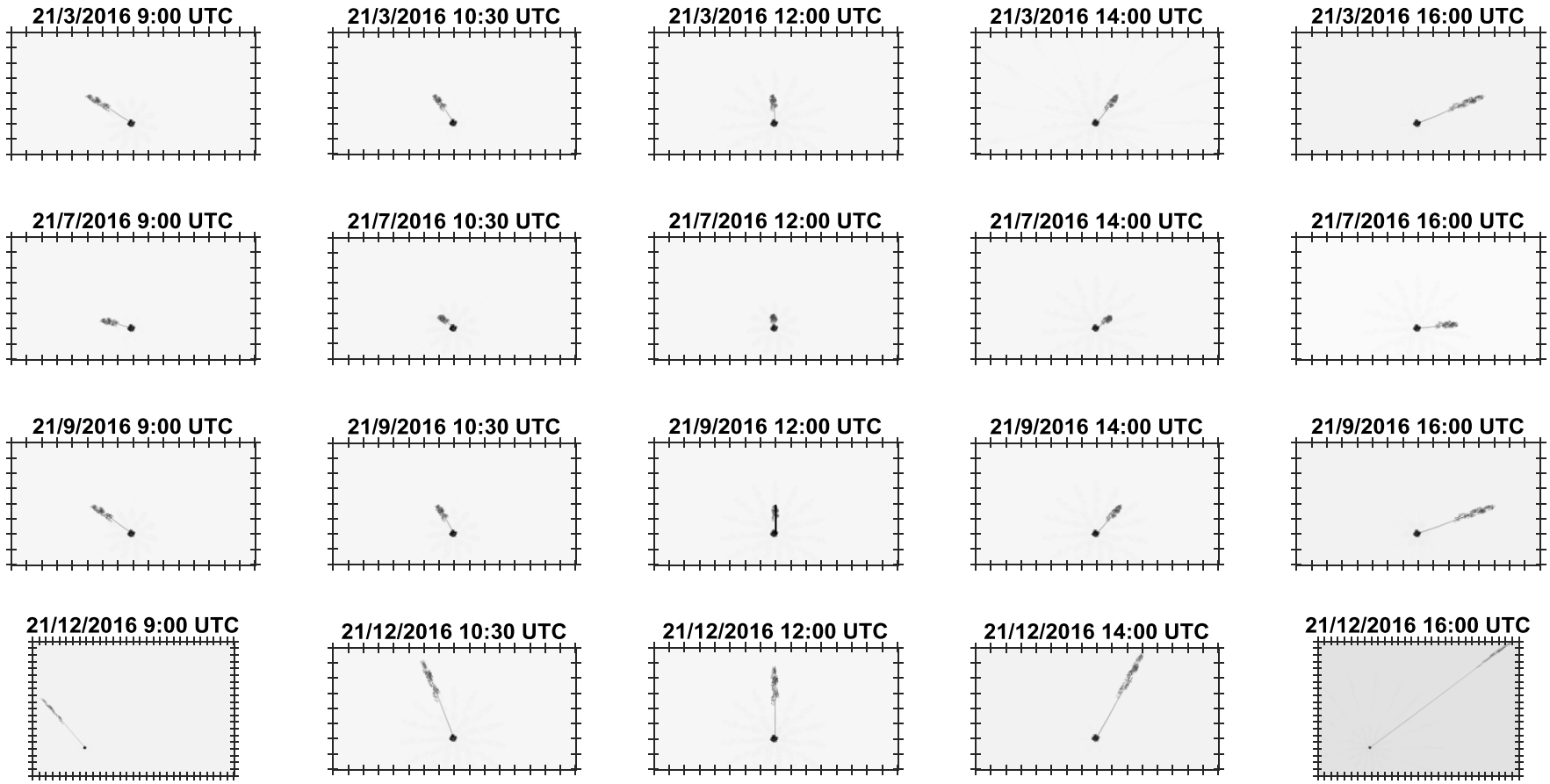

Figure 14 : Simulations of a single tree shadow cast throughout the year obtained with DART model (Gastellu-Etchegorry et al. 1996). A tree of height H = 10 m was considered using a 3D mock-up of common ash tree (*Fraxinus excelsior*) available in DART database. The topography is completely flat and the site is located at latitude 43.82°N, longitude -0.35 °E and 175 m of elevation above sea level (Lagardère (32), France). Images are graduated every 0.5 H = 5 m. Dates and times are given in UTC corresponding to minus 1 hour to the local winter time.

The intensity of light transmission through a tree canopy shows an almost logarithmic decay with depth of penetration (Oke 1992). In order to quantify sun light interception through tree canopies, the Beer's Law (equation 1) has been applied in many mechanistic models (Jackson and Palmer 1972; Prentice and Leemans 1990; Sinoquet and Bonhomme 1992; Mobbs et al. 1999; Sinoquet et al. 2001). For sake of simplification, these models consider the vegetation canopy as a turbid medium: the incoming light is extinct proportionally to the cumulated leaf area met through the length of the path ray within the canopy.

$$PAR\downarrow_z = PAR\downarrow_0 \; e^{-KL'_z} \qquad [1]$$

with

$PAR\downarrow_z$	average PAR radiation at the level z from top of the canopy
$PAR\downarrow_0$	PAR received at the top of the tree canopy
K	coefficient of extinction by the tree leaves
L'_z	leaf area accumulated from the top of the canopy down to the level z

Nonetheless, within an actual tree shadow, the intensity of incoming light consistently varies. A single point can alternatively fall:

i) in **full umbra** i.e. without direct incomes of PAR when the canopy elements totally absorbed the direct fraction of PAR,

ii) in **penumbra** when the canopy elements partially absorbed the direct fraction of PAR,

iii) in **sunflecks** i.e in full sun light when no canopy element has intercepted the direct PAR.

The occurrence of a sunfleck at a particular location and time depends on interacting factors: the coincidence of the solar path with a canopy opening; the movements of clouds that obscure or reveal the sun; and the wind-induced movement of foliage and branches (Chazdon and Pearcy 1991).

In addition, the **cloud cover** induces great variations of the intensity of shading from the trees: light relative depletion is higher on clear sky days, as incident radiations are mostly direct than on fully overcast days when most of the beams come from diffuse reflections (Jackson and Palmer 1979; Grant 1985; Reifsnyder 1989; Leroy et al. 2009; Talbot and Dupraz 2012; Artru et al. 2017). A few examples taken from the literature give an order of magnitude of the resulting quantity of light within shadows. **Figure 15** presents the quantity of PAR received at the bottom and at the top of a walnut tree on the 17th of August, 1996 with clear sky conditions, at Plauzat, France (45°N, 2°E), from simulations and measurements performed by Sinoquet et al., (2001). Striking is the important contribution of the diffuse radiations: it maintains a constant 'background level' of light of about 80 to 120 µmol.m^{-2}.s^{-1} in the shaded area. Thanks to this contribution, the relative fraction of transmitted light is very high at both the early and the late hours of the day. Also striking is the non negligible amount of PAR due to the occurrence of sunflecks, corresponding to random peaks. The amount of PAR received in the shaded area temporarily reaches about 45 % of that received in full sun. Similar results illustrated in **Figure 16** were obtained by Gay et al., (1971) within the shadow patches of Loblolly Pine (*Pinus*

taeda), a rather low density species given its rather tall height and canopy architecture. In this latter example, the assessed tree was part of a forest ecosystem (stands were uniformly spaced about 3.7 m). It may explain a rather smaller diffuse 'background' level of radiation in the early morning and late afternoon as well as at the base of the midday peaks.

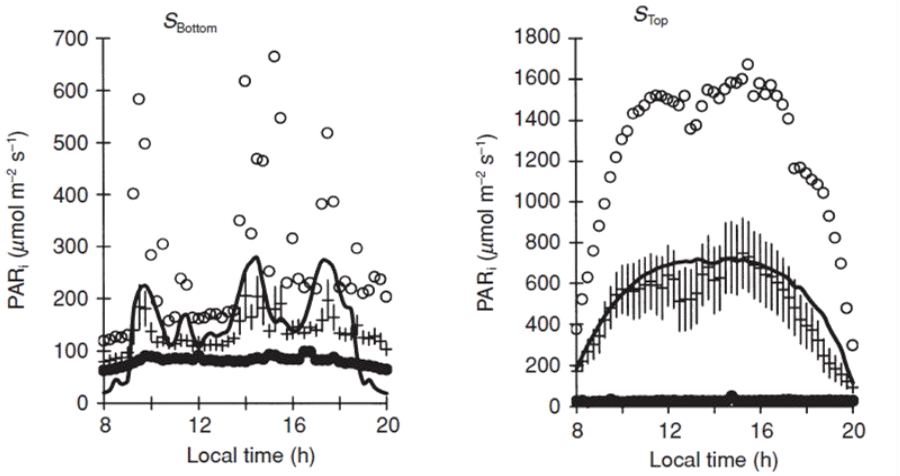

Figure 15: Diurnal PAR irradiance of shoots located at the bottom (left) and at the top (right) of the tree crown of a 20 year old walnut tree (*Juglans regia L.)* on the 17 August 1996 at Plauzat, France (45°N, 2°E): mean value (+), standard error (bars), maximum (o) and minimum (•) measured irradiance over 12 leaflets sampled per shoot, irradiance simulated by the RATP model (bold line) – From (Sinoquet et al. 2001)

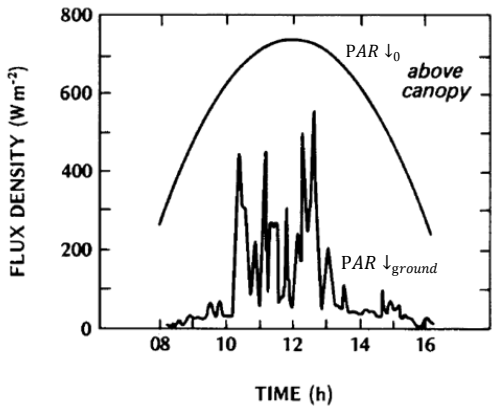

Figure 16: Irradiance in Photosynthetically Active Radiations (PAR) measured above the tree canopy and at one point on the ground below a 23 m stand of Loblolly pine (*Pinus taeda L.*) near Durham, North Carolina, USA (36°N, 79 °W) on 30 October 1965 – From the experiment of (1971) as reviewed by Oke (1992)

In winter, in the case of deciduous trees, only the remaining branches and stems intercept light. With Paulownia trees growing in China, Chirko et al. (1996a) reported a winter interception in PAR by the woody parts of about 10 to 15 % of the incoming light. It applied over a distance from the tree of 80 % of the tree height. Similar results were obtained by Dupraz et al. (2005) considering walnut trees in France. Their approach was based on the analysis of hemispherical pictures of the canopy with the Gap Light Analyze (GLA) software (Frazer et al. 1999).

Let's now consider the amount of light reaching the understory strata of canopy when integrating the shade extent in space (considering the whole planting area) and in time (yearly, over the whole vegetative period). As mentioned before, both the size of the tree shadow and the irradiance distribution within the shaded area are time functions (Meloni and Sinoquet 1997). Considering an isolated tree, **Figure 17** shows a schematic representation of the whole area submitted to light depletion when integrating the shade cast throughout the year. The resulting bean shape is similar to the results obtained by Dupraz et al. (2005) but contrary to these authors, this representation does not consider a progressive fading border. The tree height H is the vegetation morphological factor contributing to this area. Its borders would have been slightly narrower considering an evolution of the canopy volume over seasons. **Figure 17** also gives estimations of the cumulated incident radiation as a fraction of the incident radiation in full sun. The irradiance in PAR may equal 10 to 40 % and 40 to 50 % of the irradiance in full sun, respectively towards North and towards the East/West. The lowest values appear the closest to the tree trunk as shade projects there most of the time throughout the year (Chirko et al. 1996a; Dupraz et al. 2005; Artru et al. 2017).

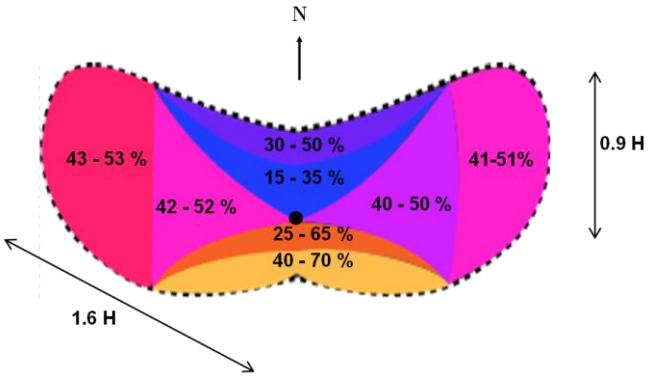

Figure 17: Schematic representations of potential light availability patterns around a single tree when integrating the shadow cast of a single tree from 1st April to September 21st in the Northern hemisphere. The width and length of the longest shadow cast were calculated applying trigonometrical relationships (Satterlund 1983) on the solar altitude and azimuth angles of the 21 September at a latitude of 43.8°N and assuming a tree of height H and ellipsoid canopy shape The estimations of PAR cumulated irradiance are given as a fraction of the incident PAR measured in full sun using the experimental and modeling work of (Dupraz et al. 2005).

Considering now several scattered trees, unless their canopies have reached full closure, the combination of their shadows in space generates alternating sunpatches and light depleted areas. The relative proportion of these two patterns depends on tree spacing, tree arrangement within the plot and tree row orientation if applicable (Jackson and Palmer 1979; Reifsnyder 1989; Leroy et al. 2009). Modeling results obtained by Artru et al. (2017) considering alleys of walnuts intercropped together with cereals are showed in **Figure 18**. During the first decade, whole ground area receives from 80 to 100 % of the light received without trees. Later on, the proportion of horizontal area affected by a reduction of light irradiance increases with tree growth, whatever the orientation of the tree row. Nevertheless, Artru et al. (2017) results show that the distribution of light irradiance is more

heterogeneous under a East-West (E-W) row orientation than that with a North-South (N-S) row orientation. With a E-W orientation, they observed a strong gradient of irradiance from 20 to 100 % in the fourth decade while with a N-S orientation, light availability never reached below 40 % of that of a full sun plot. In addition, these authors underline that the area undergoing the strongest light reduction are mainly that located in the uncropped zones i.e on the tree rows.

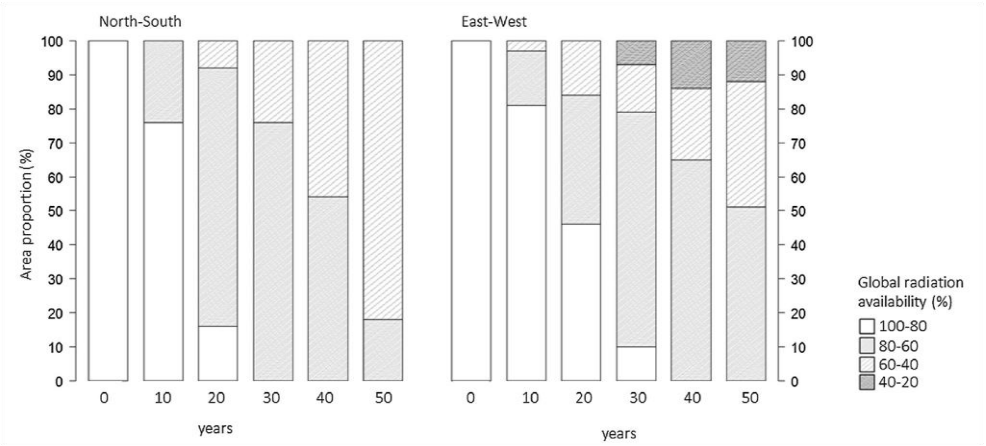

Figure 18: Estimations of the proportion of the ground area concerned by light interception and the resulting total irradiance through decades of tree growth in an alley-cropping system. Global radiation availability is given as a proportion of the full sun value. Both North to South (left) and East to West orientations (right) of the tree rows are considered. - From Artru et al. (2017).These authors used the HiSaFe model (Mobbs et al. 1999; Dupraz et al. 2005). They modeled a site in Belgium (50°33'N) planted with walnut trees organized in alleys. Trees were spaced by 7 m on a given row and by 35 m between two rows. Their crowns were represented by ellipsoids with dimensions set according to the tree trunk height respecting allometric relationships. Tree heights were not mentioned for any of the considered decades.

KNOWLEDGE GAPS

Several knowledge gaps and uncertainties remain concerning light interception by trees.

First, References concerning isolated trees and alley-cropping systems in general have shown that both the morphology of the trees and their spatial organization within a plot are involved. These studies led to very varied results depending on the type and organization of the trees, on their age, on the season and on the management practices. Consequently, no general extrapolation can be made to the case of agroforestry vineyards. Also, similarly to other agroforesty systems (Meloni and Sinoquet 1997), the spatial and temporal variability of irradiance within an agroforestry vineyard should be high but remain to be documented considering various arrangements of agroforestry vineyards.

Secondly, most of the accounted references consider quantities of light reaching horizontal surfaces. It is the case for alley-cropping references (Frazer et al. 1999; Talbot and Dupraz 2012; Artru et al. 2017) with homogeneous crop canopies. Nonetheless, considering an horizontal surface of interception may not be relevant for many cases of grapevine architectures (**Figure 34**). When grapevine exhibits an architecture in rows with discontinuous and high lateral planes of foliage, the contribution from vertical plans in light interception should be considered as well (Mabrouk et al. 1997, 2015). A few authors considered the quantity of light intercepted by plants organs, e.g. Sinoquet

et al. (2001) considered it on specific leaves or branches. Unfortunately these did not specify the contribution of the incidence angle of the light relatively to the organ.

In terms of methodology, most of the time the heterogeneity of irradiance was addressed using a transect approach (Chirko et al. 1996a, b). Only a few recent work proposed time and 2D space integrated assessments (Dupraz et al. 2005; Artru et al. 2017). This latter approach should be further developed as it allows more meaningful estimations at the plot scale and on the long term.

In addition, many references suffer from a lack of indication or consideration of the time context i.e. of the date, phenological stage of trees and/or crops and the age of the planting. Reviewed results provide either instantaneous/daily snapshots or cumulated light budgets over a whole cycle of development of the understory crop. Thus their extrapolation to other days, seasons or years of growth are not recommend. Two exceptions stand out: (i) Chirko et al. (1996a) distinguished energy budgets according to the phenological stage of the understory wheat, and (ii) Artru et al. (2017) considered energy budgets according to the age in decades since planting. At both the short and long term, the two highlighted an important time variability of the light regime induced by trees. Similarly, the meteorological conditions were either unspecified at all or specified by authors but not considered as a variability factor. Indeed, many of the cited references do not mention the percentage of diffuse light in their context of study, and most of the authors who eventually did so, performed extrapolations seasons based only on references acquired on cloudless days. Not considering cases of overcast skies i.e the contribution of diffuse light is identified as a source of overestimating the attenuation of light.

Composition of incident light

MAIN SUNLIGHT PROPERTIES

Solar radiations at the bottom of the atmosphere range from wavelengths of 250 nm to 2500 nm (**Figure 19**).

The Photosynthetically Active Radiations (PAR) correspond to the wave bands actually used by plants for their photosynthesis. They correspond to the spectral range from 400 nm to 700 nm so typically comprise 45 % of the incident solar radiation.

Below this range, the wavelengths from 290 nm to 400 nm correspond to the **solar ultraviolet radiations (UV)**. They roughly represent 4 % of the solar radiation. They present damaging properties for living cells as they convey such amount of energy that they interact with organic molecules and notably generate disturbances in the DNA of animals, plants and micro-organisms (Hockberger 2007). Three main impacts on grapevine are identified:

1. when solar irradiance is very high, UV radiations may cause sunburnt damages on leaves and berries (Carbonneau et al. 2015);
2. UV radiations trigger the synthesis of flavonoid components notably anthocyanins and flavonols, that positively impact the wine quality of berries (Harborne and Williams 2000);

UV radiations protect grapevine against microbial diseases: (i) they directly damage fungi conidia (Austin and Wilcox 2012), (ii) and they indirectly protect against fungi infection through triggering the synthesis of flavonoid, which play a barrier effect (Azuma et al. 2012).

Plants have developed chemical sunscreen against UVs consequently the UV they absorb are mostly dissipated harmlessly without contributing to their photosynthesis (Evans and Von Caemmerer 2010).

Beyond 700 nm (**infrared band**) absorption drops to near zero as an adaptation strategy against too much heating up of the leaves (Evans and Von Caemmerer 2010).

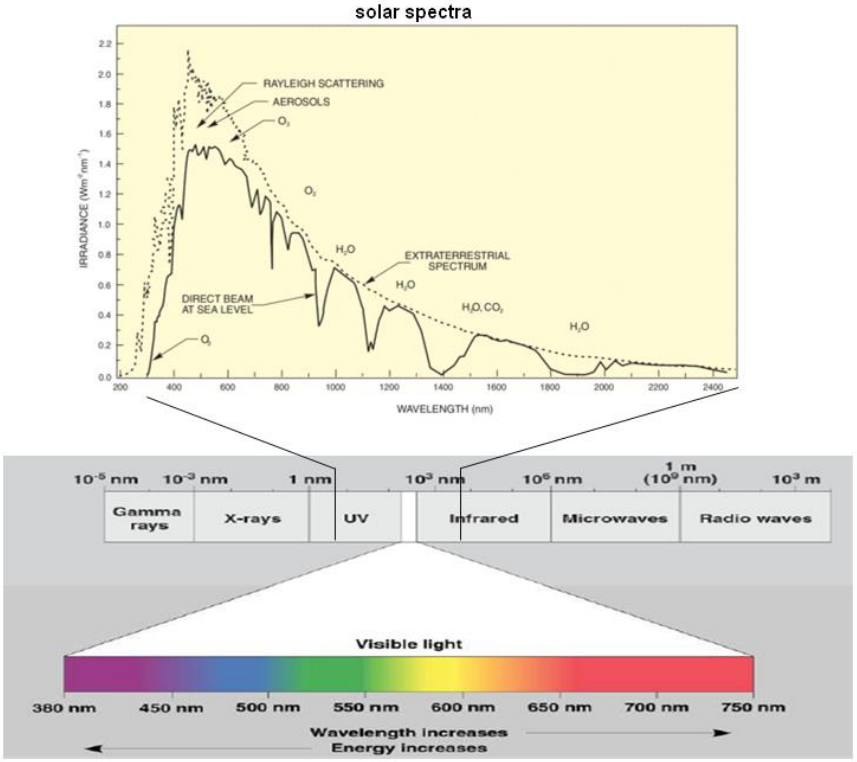

Figure 19: Solar spectrum. The solid line shows composition of direct incident radiation at sea level on a clear sky day. the dotted curve shows the extraterrestrial spectrum i.e. before absorption and scattering by the constituents of the atmosphere - From (Evans and Von Caemmerer 2010; Newport 2018)

Within the PAR, radiations do not equally fuel the photosynthesis as it depends on the optical properties of the photosynthesis pigments (**Figure 20**). For most plants and notably for grapevine (*Vitis* species), spectral bands from 400 nm to 500 nm (blue and a few green light) and from 600 to 700 nm (red light) are the most efficiently captured by the chlorophyll pigments, which are the main photosynthesis pigments. Only few of the radiations from 500 nm to 600 nm (green light) are absorbed, the latter process being assumed by accessory pigments, such as carotenes and xanthophylls, which pass it to the photosynthetic process (Champagnol 1984; Whitmarsh and Govindjee 1999). Nonetheless there are evidences that the contribution of green light to photosynthesis at the plant level is significant and that it may even play essential role for the photosynthesis of plants grown under shade conditions (Sun et al. 1998; Terashima et al. 2009).

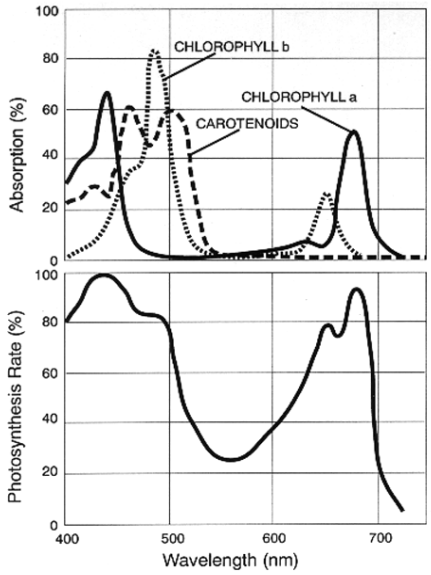

Figure 20: Photosynthesis efficiency within the PAR. Top graphic shows the absorption spectra of chlorophyll and carotenoid pigments in chloroplasts. Bottom graphic gives the rate of photosynthesis (over the 400-700 nm spectral range) that is measured as the variation of the oxygen quantity for a given incident photon flux density (oxygen evolution / incident photon). – From (Whitmarsh and Govindjee 1999)

IMPACTS FROM TREE INTERCEPTION

The composition of incident light reaching an understory crop slightly differs from the one on top of the tree canopy since scattering on phytoelements is selective. Indeed, scattering of the wavebands above 700 nm (Near Infrared - NIR), and especially of the far-red wavelengths (700-800 nm), are the largest. Also, within the PAR, the chlorophyll pigments filter out the red and blue wavelengths while it reflects and transmits most of the green ones (495–570 nm) (Gommers et al. 2013). Consequently, the NIR and the green wavebands dominate in the resulting spectra reaching understory vegetation while the red and the blue are lower than in the solar spectra (Ross 1981). It may not significantly disadvantage the efficiency of photosynthesis for the understory crop for two reasons:

(i) as mentioned above, the absorption from secondary pigments may compensate;

(ii) also recent evidence demonstrates a role for green light in sensing a shaded environment and engagecompensating response at the chloroplast and at the whole canopy level (Zhang and Folta 2012).

In addition, the **red/far red ratio** drops below 1.1 under the shade or next to plant canopies while it is usually greater than this value for direct sunlight. This typical signature is involved in shade perception by plants and is reported to trigger two types of adaptations (Gommers et al. 2013):

(i) either shade avoidance i.e. extra growth of plant vegetative parts,

(ii) or shade tolerance i.e. an increase of light use efficiency at cell scale..

According to Parsons et al (1998), UV radiations are less intercepted in a tree shade than the other wavelengths of the solar spectrum, notably than the PAR (Grant 1997). They appear with unusually high proportions in the spectra from under a forest canopy notably due to a particularly

important contribution from diffuse UV radiations (Parisi et al. 2000). These observations applied the most when the surface intercepting sun light was vertical (Parsons et al. 1998), which is the case of most of grapevine canopy with vertically trained shoots by trellis system (**Figure 34**).

II.2.1.2 Reflections of shortwave radiations by dense canopies

During portions of the day, radiation is reflected off the tree canopy surfaces which face the sun as illustrated on **Figure 13**. This "mirror effect" may be amplified by secondary reflections of the radiations scattered by the ground, depending on the ground cover type. In the presence of tree canopies that are very dense, contiguous and oriented east-west reflections from tree hedges may significantly increase the radiant flux density in their immediate southern side (Guyot 1989; Brandle et al. 2004). The amount of reflected radiant flux is dependent on time of the day, season of the year, and the albedo of the vertical parts of the canopy (Brandle et al. 2000). No specific observations of these phenomena could be found in the case of trees in agroforesty systems. References concerning photosynthesis of grapevine suggest that reflection mechanisms contribute to the photosynthetic rate of grapevine in very limited proportions: reflections within the canopy of grapevine itself, i.e. at phytoclimate scales are the most contributing ones (Smart 1974) while reflections from sides of neighboring vine comprises for less than 5 % of the light vine absorbs in total (Smart 1973).

II.2.1.3 Thermal infrared emissions from trees

Both trees and air in the vicinity of grapevine emit an amount of heat that is proportional to their temperature powered by four, according to Stefan-Boltzmann law (**Figure 4**). These emissions occur as thermal infrared emissions (8 to 11 µm) and may modify the radiative budget of neighboring vines. As illustrated in **Figure 13,** the atmospheric infrared radiations received at the ground level in the surrounding area to a tree are partly substituted by thermal infrared emissions from the trees. As the thermal properties of the atmosphere differ from that of the tree canopy and of the tree woody parts, the amounts of energy that trees and air supply significantly differ. Indeed, surface temperature of the trees is higher than the apparent radiative temperature of the air, especially with clear sky and dry air conditions (Guyot 1989). Estimations show that:

- at 0 °C the tree canopy releases 360 W.m^{-2} whereas the air releases 236 W.m^{-2};
- at 25 °C, they respectively release 434 W.m^{-2} and 336 W.m^{-2}.

The former estimations were made according to Brutsaert (1982), assuming the following thermal emissivities respectively for the air in winter, for the air in spring and for tree leaves: $\epsilon_{a_{winter}} = 0.64$, $\epsilon_{a_{spring}} = 0.75$ and $\epsilon_{leaves} = 0.97$. These estimations of tree thermal emissions are of the same magnitudes of those observed by Chiapale (1975) reviewed by Guyot (1989). In the case of rather dense tree hedgerows, these authors state that the extra energy input occur at the ground level over a radius of 3*H* to 4*H* times, where *H* is the height of the hedge. At a given site at located at a

distance *d* from trees the relative contribution from the hedge varies with the *d*:*H* ratio as it depends on the skyview factor of the hedge at this location.

II.2.2 Aerodynamic effects of trees

II.2.2.1 Wind flow in the landscape

Definitions

Brandle et al. (2004) recalls that wind is air in motion or convection. It is caused by differences of pressure in the atmosphere which result from variations of heating of the Earth's surface. Wind flows may be observed from (i) the global synoptic scale, where atmospheric circulations drive climatic patterns, to (ii) the millimetric scale (i.e inside the laminar boundary layer that wraps every surface on Earth), where transfer processes by diffusion constantly arise. In between, within the atmospheric boundary layer that extends from the ground to about 200-1000 meters above the Earth's surface, the **surface winds** correspond to horizontal and vertical air displacements (Oke 1992; Brandle et al. 2004).

Surface winds result from simultaneous free convection, which is induced by differences of air temperature between air layers, and forced convection, which is due to the external force of the winds blowing at the regional scale and meeting the elements on the earth surface. Both mechanisms result in the transfer of sensible heat (warm air) and latent heat (water vapor), between the earth surface and the atmosphere (Guyot 1999). At local scale, most of the convective heat transfer operates through a turbulent flowing regime (i.e. his interpenetration and mixing of the moving layer of air with the neighboring ones, at a chaotic pace) as opposed to a laminar regime (no interpenetration) (Oke 1992; Guyot 1999). **Turbulence** corresponds to important variations of the horizontal and vertical speed illustrated by the blue ellipses in **Figure 21.** These happen at the time scale of 10^{-3} to 10^{4} seconds and spatial scales of 10^{-3} to 10^{4} meters within the air that flows near the ground surface (Guyot 1999).

Although surface winds can be quite variable and the flow highly turbulent, the main component of the wind moves parallel to the ground (Brandle et al. 2000). As illustrated in **Figure 21**, the vertical profile of **the horizontal wind speed** mainly follows a logarithmic increase with the altitude z above ground. This is due to a strong influence of the surface on the first layers of the wind flow.

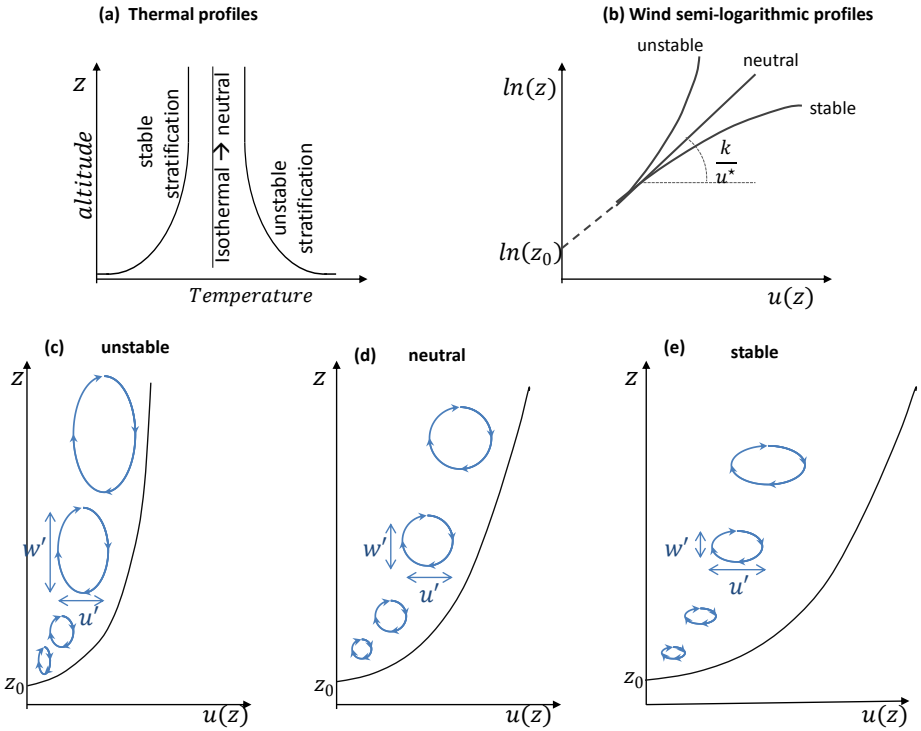

Figure 21: Schematic representations of the vertical profiles of the wind flow close to a bear ground, considering various conditions of air stability. z_0 represents the roughness length of the surface. (a) shows stable, neutral and unstable thermal profiles of air temperature near the ground. (b) shows their consequences on the vertical profiles of the horizontal wind speed u represented in semi-logarithmic coordinates. The theoretical logarithmic relationship given by equation 1 applies in neutral conditions. The vertical gradient of u is amplified in stable conditions while it is reduced with an unstable air. (c), (d) and (e) show the vertical profiles of the horizontal wind speed and the shape of the eddies for each stability case. u is the horizontal wind speed, u' is the horizontal acceleration, w' is the vertical acceleration. Unstable conditions lead to an increase of the buoyancy. – from Guyot (1999)

Summarizing Oke (1992) and Guyot (1999), the local wind regime in place within a given landscape results from the combination of three main parameters:

- the mean wind speed and direction of the air flow at the regional scale,
- the atmospheric stability,
- and the surface roughness.

In the following sub-sections, the influence of the state of the atmosphere on the air flow regime is first explained. Then, the specific influence of vegetation considering information that applies for vineyards and tree plantations is detailed.

Atmospheric stability

The atmospheric stability is mainly qualified as stable, unstable or neutral, depending on the thermal profile of the air. As shown on **Figure 21**, the atmospheric stability influences both the turbulence and the vertical profile of the wind speed. When dense cold air is located near to the ground, typically during a clear sky night, the atmosphere exhibits stable stratified conditions which tend to diminish the vertical accelerations of air in motion. On the contrary, when warm and light air is located near the ground surface (unstable stratification), typically during a clear sky day, the

accelerations of the vertical wind speed are amplified. In between, neutral atmospheric conditions correspond to situations where there is no significant variation of the air temperature between the bottom and the upper layers. Neutral atmospheric stability is typical of cloudy days or strong wind conditions, which do not permit atmospheric stratification (Oke 1992). In this latter case, turbulence is only generated by mechanical friction of the air with the surface.

As a counterbalance of turbulence, the vertical gradient of wind speed is enhanced in stable conditions and reduced in unstable ones compared to the neutral case. The theoretical logarithmic rise mainly applies for neutral atmospheric stability conditions while additional corrective factors must be applied for stratified conditions (stable or unstable). In equation 2, the implication of the state of the atmosphere is summarized by the stability term Φ_z. For neutral atmospheric conditions, this term equals unity and allows a simplification.

Vertical profile of wind speed above vegetated landscapes

The general profile of horizontal wind speed (u) in a vegetated landscape is illustrated in **Figure 22**.

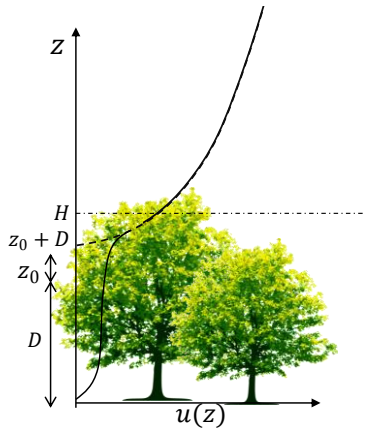

Figure 22: Vertical profile of horizontal wind speed u at an height z above the ground. H is the height of the vegetation, D is its zero plane displacement and z_0 is the roughness length of the surface - From (Oke 1992; Guyot 1999). Above the height $z_0 + D$, the horizontal wind speed follows a logarithmic increase with the height z above ground. Below this height, within the vegetation cover, the vertical profile of wind speed follows a rather exponential trend (Zhu et al. 2004).

When the ground is covered by a dense vegetation of height H the logarithmic profile is 'displaced' and starts from an height $z_0 + D$. Above this height, the following equations apply, from (Guyot 1999; Zhu et al. 2004):

$$u(z) = \frac{u^\star}{k}\left[ln\left(\frac{z-D}{z_0}\right) + \Phi_z\right] \quad [2]$$

with

$$u^\star = \sqrt{\frac{\tau_0}{\rho}} \quad [3]$$

and

$$\tau_0 = k\,\rho\,\frac{\partial u}{\partial z} \qquad [4]$$

$u(z)$	: mean wind speed [m.s^{-1}] at the height z [m]
D	: zero-plane displacement [m]
z_0	: roughness length [m]
$u^\star$	: friction velocity [m.s^{-1}]
$k \approx 0.4$	: von Karman's constant
Φ_z	: atmospheric stability term
τ_0	: shear stress at ground level i.e drag force exerted by the surface [kg.m^{-1}.s^{-2}]
ρ	: air density [kg.m^{-3}]

Equations 2 to 4 highlight a strong implication of the vegetation cover on the wind profile through the roughness length z_0, the zero-plane displacement D and the friction velocity $u^\star$.

- The **roughness of the surface z_0** applies a drag force on the bottom part of the air flow. Above a bare ground, a dense grass rye, an orchard and a forest, it is estimated at 0.001 m, 0.02 m, 0.5 to 1 m, and 1 to 6 m respectively (Oke 1992; Guyot 1999). In the case of vegetated surfaces, this parameter essentially represents the roughness of the upper layers of the vegetation. It increases with the vegetation height by a multiplicative factor of about 0.05 (grapevine) (Sene 1994) to 0.15 (Arya 2001). It also depends on the leaf area density and on the leaf density distribution in space. For low values of leaf area density, the roughness firstly increases with the leaf vegetation index until a threshold of density is reached, above which the roughness then decreases with vegetation closure (Guyot 1999).
- The **zero-plane displacement D** increases with the vegetation height by a multiplicative factor of about 2/3. Also it increases with the vegetation leaf area, without any inflection point, contrary to the roughness parameter.
- The geometry of the surface also influences the viscosity of the air at the boundary layer with the surface. It operates through the **shear stress τ_0** which applies on the air flow and generates turbulence (Guyot 1999).

Vertical profile of wind speed inside vegetation canopy

Within the vegetation cover, from the height $z_0 + D$ to the ground level, the horizontal wind speed follows a rather exponential decrease (Guyot 1999; Zhu et al. 2004). This is due to the interception of the air flow by the leaves and branches, which absorb the kinetic energy of the flow. Most of the drag occurs in the upper part of the canopy. Contrary to the air flow around a tree, the air flow passing through a tree is no more vertically conservative.

A general formulation was firstly proposed by Inoue (1963) for crop canopies, from which the following equations applied to tree canopies by Zhu et al. (2004) are derived.

$$u_{in}(z) = u_{out}(z)\,.\,exp\left[-\alpha(z)\,(1-\tfrac{z}{H})\right] \qquad [5]$$

with $$\alpha(z) = l(z).C_d.LAI(z) \quad [6]$$

and $$l(z)^2 = -\rho\,.\tau(z).\left(\frac{\partial u}{\partial z}\right)^{-2} \quad [7]$$

$u(z)$	: mean wind speed [m.s^{-1}] at the height z above ground, either within (in) or outside (out) the canopy [m]
H	: vegetation height [m]
C_d	: canopy drag coefficient
LAI	: Leaf Area Index
$l(z)$	: mixing length [m]
τ	: shear stress i.e. drag force [kg.m^{-1}.s^{-2}]
ρ	: air density [kg.m^{-3}]

The latter equations highlight that the resistance generated by the vegetation depends on the leaf density at height z and on the canopy drag coefficient, which itself depends on the dimensions, orientations and organization of the leaves in space. The resolution of this system of non linear differential equations is complex and often leads to simplifications depending on (i) the turbulency context (eq. 7) and (ii) depending on the vegetation type. The homogeneity of the canopy in space, can notably be considered (Raupach and Thom 1981). For more details, we refer to Zhu et al. (2000) concerning single trees, to Zhu et al. (2004) concerning forests and to Wang (2012) concerning the specificities to take into account in sparse canopies.

II.2.2.2 Consequences of trees on the air flow

The two previous subsections highlight that trees modify the characteristics of the air flow above and within their canopies through mechanical drag and obstruction. For continuity reasons, the characteristics of the air flow leeward and windward of trees are also impacted. In the case of agroforestry practices, the wind regime undergone by crops in the vicinity of trees is impacted.

The mean horizontal wind speed, the wind direction and the turbulence of the air flow are all together concerned. The mechanisms involved depend on the characteristics and the morphology of the vegetation. In the case of an **isolated tree** (Gross 1987), it is observed that:

(i) The air preferentially gets around the obstacle rather than through the canopy **(Figure 23)**;

(ii) a reverse flow forms on the lee side of the tree **(Figure 23)**;

(iii) wind velocity increases at the tree top;

(iv) the wind velocity is reduced in the area beneath the treetop at the upstream side of the tree or *quiet zone*;

(v) a large vertical turbulent eddy or *wake zone* forms behind the tree, tree acting as a generator of turbulence (Ruck and Schmitt 1986; Gross 1987).

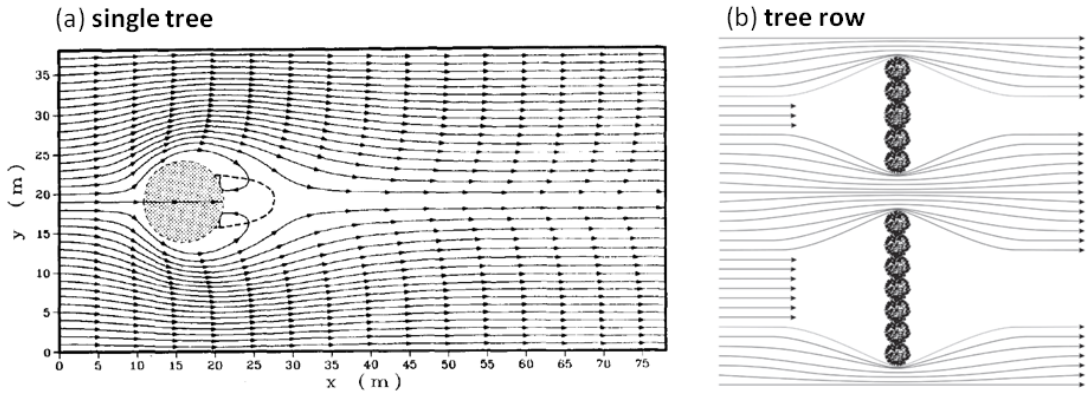

Figure 23: Wind flow patterns around a single tree (left) from 3D modeling simulations by Gross (1987), and around a tree row (right), from the review of Brandle et al. (2000). On the left, streamlines were simulated in a horizontal cross section 1 m above ground. The scene contains an isolated ellipsoidal-shaped tree (dotted contour) which measures a total height of H = 16 m, with a canopy going from the top to the bottom of the tree (no stem pruning) and a largest crown diameter equaling 13 m. The drag coefficient of the tree was set to 1 which corresponds to a leaf area index of 10 and an average canopy porosity of 0.93 according to the estimations by Ruck and Schmitt (1986). The dashed line indicates a region where the horizontal wind vector is going back-wards. On the right, the areas of preferential and accelerated wind flow are indicated by the close spacing of the lines.

The morphology of the tree contributes to the variability of these observations. The numeric simulations of Gross (1987) showed that the length of the quiet zone increases with the tree height (*H*) while the lateral dimensions remain nearly constant. In addition, the width of the wake zone increases with the tree crown diameter and with its length and height but to lesser extent. A stem-pruned tree generated a longer and more intense turbulent flow than a tree with no stem (bushy shape), due to the wind jet beneath the canopy in the first case (**Figure 24**).

When trees are organized as a **contiguous canopy forming a row** or ***hedgerows*** or ***windbreaks***, similar patterns are observed but with even greater intensity and footprints. The following observations are based on the very abundant literature concerning the sheltering effects of natural windbreaks or shelterbelts (Jensen 1954; Caborn 1957; Plate 1971; Raine and Stevenson 1977; Oke 1992; Brandle et al. 2004; Wang and Takle 1996, 1997; Cleugh 1998; Forman and Baudry 1984). Considering a windbreak of height *H*, the air in the layer below the top of the windbreak ($z < H$) begins to slow and diverge at a location of about five windbreak heights upwind of the windbreak (at $x = -5H$). Some air continues to flow through the porous windbreak creating a region of *bleed flow* immediately to the lee with reduced velocity because of the drag exerted by the vegetation in the windbreak. A *quiet zone* of lower wind speed also goes on in the lee of the windbreak. It has a roughly conic shape, its boundaries being formed by the windbreak, the ground surface and a line sloping downwards and downwind from the top of the windbreaks that intersects the ground between 3 and 8H from the windbreak (**Figure 24**). The rest of the air - the amount depends on the porosity - actually flows over the top of the windbreak (see streamline deflection in **Figure 24**) where its velocity increases. This increase is imposed by vertical continuity demand, the flow being conservative. This

upper layer of air or *displacement zone* extends at least 1.5 H above the windbreak (McNaughton 1988). In addition, a turbulent layer of air also called *mixing layer* or *wake zone* initiates where the wind profile is inflected by the meeting point of the quiet and the displaced flows. From a thin layer initiated at the tree top of the windbreak, it grows downward above and behind of the quiet zone, and eventually intersects the ground surface, at about 5 to 10 H from the tree row, marking the limit of the quiet zone.

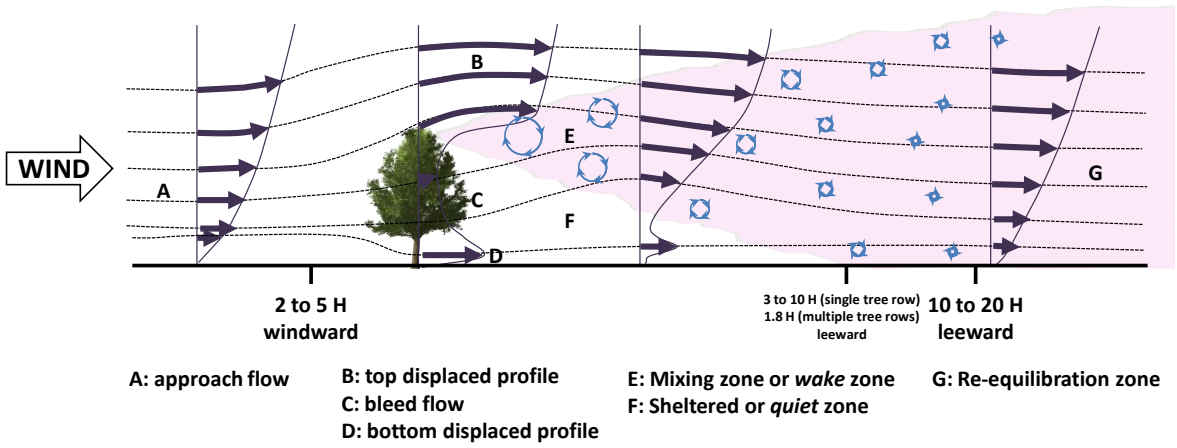

Figure 24: Schematic of vertical airflow regime above and through a vegetated wind break oriented normal to the flow, in neutral atmospheric conditions. The arrows indicate hypothetical vertical profiles of mean horizontal wind speed. H is the total height of the tree. - Adapted from (Judd et al. 1996; Cleugh 1998; Brandle et al. 2000).

The porosity of the windbreak is stands as a key parameter of effectiveness as it physically determines the proportion of air actually passing through the windbreak. It results that the reduction of the wind speed behind a windbreak compared to before the windbreak is of same range as the windbreak porosity (**Figure 25**): for example, in the case of a 10% porosity windbreak the wind speed approximately equals u_0*10% in the quiet zone downwind. Conversely, the extent of the sheltering effect decreases as the porosity of the windbreak increases: with windbreaks of 10% porosity and 73% porosity, the maximum wind speed reduction is reached between [0 – 2H] and [0 – 8H] respectively (Wang and Takle 1996; Cleugh 1998).

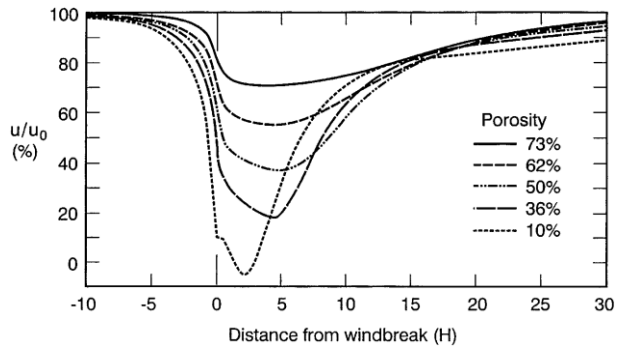

Figure 25: Spatial variation of average horizontal wind speed expressed as a percentage of the upwind wind speed, with varying windbreak porosity. Height of wind speed was not specified, but it is less than 0.5H. After (Wang and Takle, 1997) cited by (Cleugh, 1998)

When a succession of **several tree rows** combine in the landscape and referred as ***multiple windbreaks***, the wind that is forced up over the first hedgerow drops rather sharply before being forced up again over the next hedgerow in the wind path. On the one hand, the turbulence of the approach flow is thus generally higher than with a single windbreak. As a consequence the *quiet zone* only extends to 1.8 H according to (Judd et al. 1996) or to 5 H according to Guyot and Verbrugghe (1976) and the local velocity reduction is lower than with a single windbreak. On the other hand, multiple windbreaks also increase the roughness of the surface at the regional scale (recall equation 2). This additional roughness term provokes a sheltering effect at the landscape scale. In other words, if considering one of the windbreaks among a multiple windbreak grid, the upwind mean velocity of the approaching air flow is lower than that for a single windbreak. Because this non-local effect more than compensates the decrease in local shelter, wind speed is lower in overall wind speed is lower behind a windbreak under multiple windbreak configuration than behind a single windbreak (Forman and Baudry 1984; Judd et al. 1996; Cleugh 1998).

As explained in the previous **subsection 'Atmospheric stability'**, a stratified atmosphere either amplifies or depletes turbulent exchanges compared to a neutral atmosphere. At the same time it provokes the opposed effect on the horizontal wind speed. As a consequence, the wind patterns in the vicinity of trees that were previously described actually apply in near-neutral stability conditions with moderate to strong winds (Oke 1992). In stable conditions, the sheltering effect of trees exhibits a larger footprint, i.e. the quiet zone extends further behind the hedge than that with neutral atmospheric conditions (Gross 1987) but turbulence (longitudinal windspeed fluctuations) can propagate on a much longer distance behind the hedgerow (McNaughton 1988). On the opposite, under unstable conditions, wind speed recovery arises sooner, the minimum velocity is increased but surface shear stress (turbulence generator) is reduced, compared to under neutral atmospheric conditions (McNaughton 1988).

II.2.3 Water budget modifications

The **Figure 26** inspired by Bayala and Wallace (2015) illustrates the modifications of water balance induced by trees in an agroforestry system compared to monocropping. Inputs of water in the ground, soil water holding capacity and water uptakes both due either to ground evaporation or tree transpiration are all together concerned. The following subsections present basic processes that control the individual water balance components of an agroforestry system and give orders of magnitudes found in the literature.

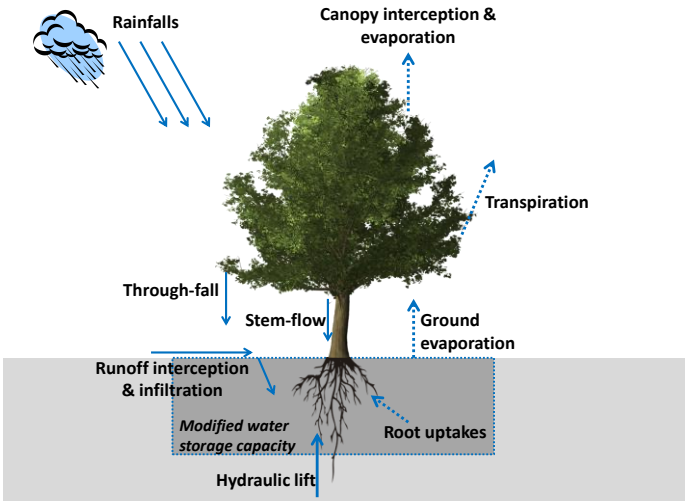

Figure 26: Modifications of the water balance in the vicinity of a tree. Solid lines represent water inputs in the ground while dashed lines represent water losses. On the one hand, the distribution of rainfall in space and in time is modified by the tree canopy because the canopy intercepts the air flow during rain events and preferentially allocate the intercepted fraction with through-fall (dripping from the leaves) and stem-flow (along the branches and stem). On the other hand, a fraction of the gross rainfalls which is intercepted by the tree canopy is lost by evaporation. Water inputs beneath the tree may also differ from that beneath the crop because i) their rates of surface runoff and infiltration differ, ii) and because trees redistribute water from relatively wet deeper soil horizons to drier surface layers, a process called hydraulic lift. In addition, trees may have different rate of root uptakes that supply the tree transpiration, compared to the crop usual uptakes for its own transpiration. Finally, trees may play an indirect effect on the ground water content in two ways: it may modify the soil water storage capacity (through modifying the soil porosity and organic matter content) and it may modify the rate of the ground evaporation (through modifying the climatic demand).

II.2.3.1 Rainfall regime and distribution

Trees in agroforestry systems may significantly modify the pattern, the quantity and the energy of rainfall received by crops in their very vicinity (Bayala and Wallace 2015). Two main mechanisms are involved:

i) Tree canopy acts as an obstacle which intercepts the air flow and provokes unequal lateral distribution of the rain falling in its immediate surroundings,

ii) Tree canopy interferes with the rainfall by holding back a part of the precipitation in the canopy, a process hereafter called interception.

Spatial distribution of rainfalls

The spatial distribution of rainfalls shows a canopy edge effect that is due to the wind interception by the canopy during rainfall events (Darnhofer et al. 1989). On the leeward side of the trees, the amount of precipitation reaching the surface may be slightly reduced. The converse is true on the windward side where the canopy may function as a barrier that catches water and distributes it to the ground or to the canopy of the understory vegetation through increased stem flow and increased dripping from the canopy (through-fall) (Woodall and Ward 2002; Brandle et al. 2004). In the semi-arid context of Kenya, the experimental design of Darnhofer et al. (1989) included dense multiple rows of *Cassia siamea* trees (8 tree rows formed a 12 m wide hedge with trees staggered by 1.5 m on each row), with a tree height of 3 m in average. Leeward from the tree, it showed a deficit of rainfall

over a distance of approximately the tree height. The main factors were the wind speed and its direction relative to the tree/crop interface, and the tree canopy architecture. Reductions of 27 % in average and up to 50 % were observed with heavy storms with an orientation that maximized the wind-break effect of the tree hedge. Considering storms with winds from all direction, the same area experienced a total rainfall deficit of only 18 %. In temperate climatic context, networks of hedgerows surrounding agricultural plots also generate a spatial pattern of precipitation that matches with the one of wind speed, (Merot and Ruellan 1980) as cited in (Forman and Baudry 1984).

Rainfall interception and evaporation loss

INTERCEPTION BY TREE CANOPIES

Interception of rainfall by tree canopy and its subsequent evaporation has long been identified as an important component of the water balance in forests (Linhoss and Siegert 2016). During precipitation, some rainfall is temporarily held on tree canopy. If the canopy receives sufficient solar energy or thermal energy from the atmosphere, evaporation occurs. Otherwise, when rainfalls exceeds evaporation, water accumulates until it drips from the leaves (fall-through) or runs down the stem (stem-flow) (Bayala and Wallace 2015). In other terms, the fraction of gross precipitation that is temporarily intercepted by the tree canopy (P_{tree}) diverges into three different flows:

- a sub-fraction that reaches the ground through stem-flow (P_{stem}),
- a sub-fraction that reaches the understory crop or the ground through dripping from the leaves or through-fall ($P_{through}$)
- a sub-fraction that remain intercepted and then lost by evaporation from the leaves (I).

Site-based observational studies as well as modeling approaches estimate forest interception loss around 10 to 30 % of the gross incoming rainfall (Crockford and Richardson 2000; Miralles et al. 2010; Linhoss and Siegert 2016). It even reached 40 % in the case study of a dense forest of mixed Spurce and Pine trees in a temperate climate (in Great Britain, 2250 mm per year), (Calder and Newson 1979). The intensity of interception losses highly depend on the canopy and trunk storage capacities. **Figure 27** from Linhoss and Siegert (2016) illustrates that both are dynamic parameters that increase with the volume and the intensity of rainfall until a saturation threshold is reached. Also, the partition between relocation ($P_{stem} + P_{through}$) and losses (I) is sensitive to tree geometrical properties, namely to leaf shape and inclination, leaf area index, branch angle, crown height, and to the nature and thickness of the bark layer - (Crockford and Richardson 2000; Miralles et al. 2010).

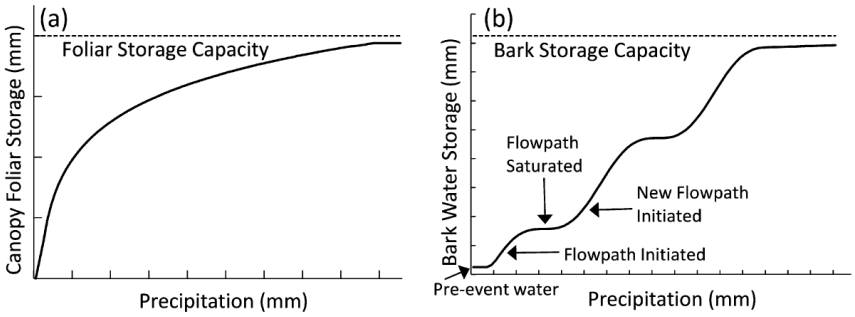

Figure 27: Theoretical relationships between (a) canopy storage capacity and precipitation and (b) bark storage capacity and precipitation, from (Linhoss and Siegert 2016)

Assuming agroforestry plantings equivalent to sparse forests, the evaporation per unit area of tree canopy in an agroforestry vineyard can be estimated from the *Gash model* (Gash et al. 1995) or the *Rutter Sparse model* (Valente et al. 1997). The analytic equations of both models were initially developed for dense forests, respectively by Gash (1979) and by Rutter et al. (1971, 1975), and were then reformulated in order to better take into account the specificities of interception by sparse forests. Indeed Tecklehaimanot and Jarvis (1991) report that a greater tree spacing increases the rate of evaporation from wet canopies, as a result of an increase in the boundary layer conductance of the trees. They also found that with a tree spacing of 8 m or more, the amount of water stored by individual trees becomes independent from the tree density. Using the equations of the Gash model (Gash et al. 1995), theoretical estimations can be obtained for sparse canopies, which are typical of agroforestry systems. For example, the analysis presented in **Figure 28** suggest that interception losses are likely to range between 3 to 10 % of the annual rainfalls (Bayala and Wallace 2015). Measurements of same range were obtained by Maruti et al. (2012) in an agroforestry coffee planting with 230 trees.ha^{-1}. Though these densities are low for tropical agroforestry systems, they are higher than most of that in the agroforestry vineyards found under temperate and Mediterranean climates.

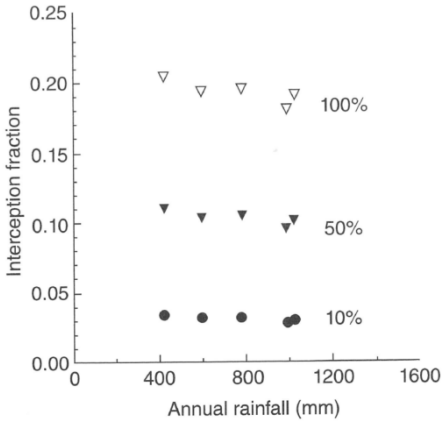

Figure 28: Estimates of the annual fraction of rainfall lost as interception (*I*) obtained by (Bayala and Wallace 2015) using a sparse forest model (Gash et al. 1995) for rainfall data between 1984 and 1988 at Machakos, Kenya. Different degrees of canopy cover were used to simulate dense (▽ 100 %), intermediate (▼50 %) and sparse (● 10%) canopies.

A tendency for annual interception losses to decrease as rainfall increases has been observed in both the semi-arid Kenyan climatic context, where a dry and rain season alternate (Bayala and Wallace 2015), and the British temperate climate context (Calder and Newson 1979). It may be partly explained by the fact that for individual storm events, through-fall increases with the intensity of the precipitation, while stem-flow and interception together decrease (Darnhofer et al. 1989). For example, for storms with less than 10 mm or more than 20 mm precipitation gross, these authors reported proportions of through-flow respectively of 79 % (i.e. $P_{stem} + I = 21$ %) and of 89 % (i.e. $P_{stem} + I = 11$ %).

SPECIFICITIES OF INTERCEPTION IN AGROFORESTRY VINEYARDS

Because of the row structure of grapevine canopy, some specificities regarding rainfall interception may apply in an agroforestry vineyard. The consequences of this phenomenon in terms of water loss will depend on the planting structure. Two cases must be considered:

i) When tree canopy falls right above that of grapevine, occlusion is complete.

ii) But when tree canopy is positioned close to that of grapevine, the effect of trees is indirect, through a reduction of the effective rainfalls wetting the ground in the vicinity of grapevine. In this case, the quantity of intercepted and lost water due to tree should be assessed relatively to that usually intercepted by grapevine canopy. (Myburgh 2004)

Kinetic energy of rainfalls

As well as modifying the quantity and the spatial distribution of rainfall, tree canopies may also impact its kinetic energy by altering the size and the velocity of raindrops. These latter parameters are notably at stake in vineyards where hailstone events or soil erosion may be intense. For a given type of tree canopy, the kinetic energy of the through-falling drops either increase or decrease, depending on the rainfall characteristics (Calder 1986). For example, during heavy storms, tree canopies may disaggregate the drops initially of large size and reduce their kinetic energy, whereas during storms of low intensities, the tree canopy may amalgamate the initially small drops into bigger drips falling from the tree (Bayala and Wallace 2015).

Nonetheless, the observations of Hall and Calder (1993) in tropical forests suggest that the intensity of the rainfall is nearly negligible parameter compared to the implication of the tree canopy properties. Indeed, the tree species in place may be the main factor for kinetic impact of the trees, notably the width and spatial distribution of their leaves. For example, the large and flat leaves of *Tectona grandis* showed a "break-even" threshold in rain intensities of 3000 $mm.hr^{-1}$, while the smaller leaves of *Eucalyptus camaldulensis* and the thin needles of *Pinus caribaea* showed thresholds of 100 $mm.hr^{-1}$ and 50 $mm.hr^{-1}$ respectively. It means that through-fall within *Tectona grandis*

systematically increased the kinetic energy of the drops while the through-fall within the two other species had a reducing effect when heavy storms occurred. A difference of up to nine-fold was reached with the two most contrasted cases of kinetic effects.

Consequently, when vine growers adopting agroforestry practices are willing to prevent soil erosion, special care must be taken to select species with leaf characteristics and canopy heights that reduce, rather than increase, the risk of erosion.

II.2.3.2 Root systems of grapevine (Vitis vinifera) and trees

Roots drive water and nutrient uptakes by plants. Root growth, distribution and activity within the ground are essential information in order to address competition between grapevine and trees in an agroforestry vineyard and their potential complementing.

Main characteristics

Although woody plants are said to be deep rooted, the majority of their roots are located close to the soil surface (Schenk and Jackson 2002). As illustrated in **Figure 29**, a negative exponential relationship has been used to describe the root density (L_v) distribution with depth (z) for isolated trees (Landsberg and McMurtrie 1984; Eastham and Rose 1990), as cited by (Crosbie et al. 2008). A negative exponential function can also be used to describe the lateral spread of tree root density, which applies for both isolated tree or a tree belt (Sudmeyer 2002). As a result, the root length density per unit of soil volume can be estimated from the following equation proposed by Landsberg and McMurtrie (1984).

$$L_v(z,r) = L_0 \,.\, e^{-k_1 z}\, e^{-k_2 r} \qquad [8]$$

$$L_{tot} = \frac{2\,\pi\,L_0}{k_1 k_2^2} \text{ and } V_{tot} = \frac{\pi\, r_0^2}{2\,k_1} \qquad [9]$$

with

$L_v(z,r)$	Root density [L.L^{-3}] per unit of soil volume at depth z and radius r for any point in the rooting volume
L_{tot}	Total length root [L]
V_{tot}	Total volume of soil explored [L^3]
r_0	Radius of the root system near the surface (z ≅ 0)
L_0	Root density at the base of the tree
k_1 *and* k_2	Downward and outward extinction coefficients. Values may be obtained by setting $k_1 d_{max} = k_2 r_0 = 3$, where d_{max} is the deepest soil depth reached by the roots.

Though this representation is crude for studying physiological processes, it is well suited for hydrological purposes i.e. for estimating water uptakes from isolated trees (Landsberg and McMurtrie 1984). For a given transpiration rate by a tree, the rate of water uptake from any particular unit of volume of wet soil may be proportional to $L_v(z,r)$ though the relationship is certainly not linear (Landsberg 1999). This latter author assumes an asymptotic relationship based on research in

agricultural crops but also states that it could be different for trees since they exhibit widely separated roots which penetrate deep into the soil.

The size and shape of tree root systems present a very high variability which is noticeable from variations in the deepest soil depth reached by the roots (d_{max}) and in the maximal lateral root spread (l_{max}) (Schenk and Jackson 2002). This variability can partially be estimated from observations of the tree canopy: under water limited conditions, Schenk and Jackson (2002) observed significant correlations between d_{max} and l_{max} and the volume V_c of the tree canopy, assuming an ellipsoid shape ($V_c = \pi . H_c . W_c^2/6$, H_c and W_c being respectively the height and the width of the canopy). More precisely, differences in the canopy volume explained 11 % of d_{max} and more interestingly, explained 53 % of the variability of l_{max} .

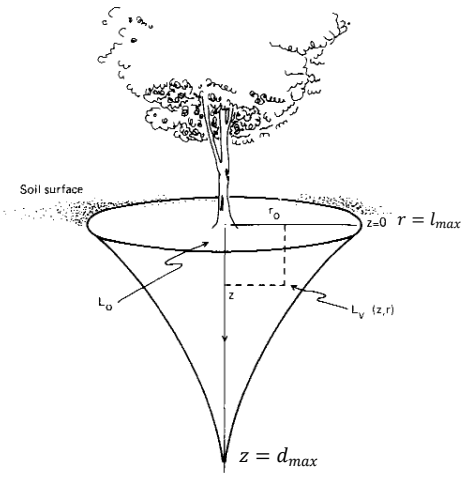

Figure 29: Schematic representation of the root volume of an isolated tree. Root length density L_y is assumed to decrease exponentially from the base of the tree ($L_v = L_0$) both outwards (r -axis) and downwards (z-axis) – from (Landsberg and McMurtrie 1984)

Compared with most woody species, deciduous fruit plants (Atkinson 2011) and grapevine (*Vitis vinifera*) present the capacity to develop very deeply rooting system which strongly contributes to their capacity to survive under severe water-stress conditions or xeromorphism (Van Rooyen et al. 1980), as reviewed in Smart and Coombe (1983). Also, compared to many other species, grapevine develops root system of very low density, which is expressed in terms of root length area density and volumetric density in **Table 1** from Smart and Coombe (1983).

Table 1: Average root length density per unit of area and per unit of volume for different crops under field conditions – From the review by Smart and Coombe (1983). Data were gathered from the review of Atkinson (1983) except data for grapevines from Freeman B (comm. pers.)

	Root length $(cm_{root} . cm_{soil}^{-2})$	**Root density** $(cm_{root} . cm_{soil}^{-3})$
Grapevines	0.9 - 4	0.002 - 0.03
Apple trees	0.8 - 24	0.01 - 0.2
Pear trees	7 - 69	0.12 - 0.56
Prune trees	15 - 68	0.13 - 0.56
Conifers	5 - 126	0.5 - 0.69
Cereals	100 - 4000	

Environmental x genetic factors

The 3D architecture of grapevine root system presents a very high variability in the field. Several environmental factors are involved which are relevant for gaining insight on grapevine response to agroforestry practices.

Firstly the soil texture, the soil porosity and the continuity of soil horizons have a major influence. They impact the maximum depth of grapevine roots, their density and their distribution. For grapevine growing in deep coarse sandy soils or gravels, roots may be found at depths of 10 m and more, but the deep roots are few and the majority of roots concentrate in the first 6 meters (Van Zyl and Weber 1981). Similar root architectures are found in Bordeaux vineyards, with especially dense root systems in porous and gravelly zones (Seguin 1972) as reviewed by Smart and Coombe (1983). In contrast, in a soil with restrictive hardpan at 70 cm, grapevine roots are strongly limited to the first horizon and are distributed at a uniform density throughout the 10- to 70-cm zone (Van Zyl and Van Huyssteen 1980).

Secondly, the density and architecture of grapevine roots is strongly influenced by the magnitude of already existing competitions between grapevines, (planting density), or between grapevine and grassy cover (ground management practices). This point is specifically developed in the following subsection (see **Grapevine and tree roots facing competition**).

Thirdly, the root architecture of grapevine is influenced by the soil water regime. The periodicity of root growth and its response to irrigation treatments was notably studied by Freeman et al. (1982). They observed a greater root production with a relatively dry treatment than with a wet treatment, reflecting the well-known phenomenon of phenological plasticity. Their results are similar to those of many studies reviewed by Smart and Coombe (1983), except that of Magriso and Tonchev (1972) who reported that the cumulative length of roots actually increased with increasing water supply in the top 2-3 m of soil.

The variability induced by environmental factors combines with that induced by scion genotype. The genetic variability among grapevine species (*Vitis vinifera*) in terms of root biomass allocation and root development is well documented by Tandonnet et al. (2009).

Developments concerning the variability of tree root systems, especially in agroforestry systems, can be found in the review of Noordwijk (2015). Also, the experimental work carried out in orchard walnut trees by Contador et al. (2015) illustrates the strong specificity of tree root responses depending on water supply and tree management practices. However, at the scale of climatic regions, Schenk and Jackson (2002) observed no significant correlation between the mean annual precipitations or the precipitation seasonal distribution and the vertical and lateral dimensions of tree root systems (vertical and lateral maximal extensions were considered). It suggests that more complex and specific

relationships are involved at the local and micro scale. Accessibility to water table could notably be a key parameter (Crosbie et al. 2008).

Growth and effectiveness of roots

The root systems of woody plants differ from that of annual plants because these are perennial. Against first thought, being perennial does not imply to be fixed. On the contrary, striking is the plasticity of rooting systems for many woody perennial plants: from a primary thickened framework that arises from the original cutting, they develop a framework of ramified roots. At least the fourth ramification order is reached in the case of grapevine (Smart and Coombe 1983). The volume of soil being explored evolves in time with the initiation of later-formed roots which does not require further growth from the plant base. Consequently, the root system of woody plants at a given time consists in a mixture of roots of different types and ages (Atkinson 1983).

Over the life cycle of grapevine, the extent of grapevine root framework is established within the first few years after planting (Smart and Coombe 1983). Under agroforestry practices, the extent of grapevine root may thus vary depending whether grapevines were planted simultaneously with trees, prior to trees or later than trees. Over a year, a striking property of grapevine roots is their delay in starting root growth activity in spring, whereas most deciduous fruit trees (Glenn and Welker 1993; Atkinson 2011; Contador et al. 2015) and forest tree species (Lyr and Hoffman 1967) initiate root growth before renewed shoot activity, a delay of 3 to 10 weeks after bud burst is observed for grapevine (Freeman and Smart 1976; Lilov and Andonova 1976). Once initiated, grapevine root growth is rapid and exhibits two peaks: the first one occur when shoot growth ceases and the second one occurs after the fruit harvest (Freeman et al. 1982). Similarly the growth kinetics of fine tree roots for trees can follow a uni-modal or a multi-modal pattern with respect to the vegetative and reproductive cycle of the tree, which itself depends on the tree species (Contador et al. 2015).

Most contribution for water uptakes by grapevine during its vegetative growth comes from its largest and suberized roots, despite their lower conductance compared to the other roots (Smart and Coombe 1983). Pine trees may be similar to grapevines in this respect (Winter 1974).

Grapevine and tree roots facing competition

Managing competition with other stocks or with a grassy cover is a well-known concern for viticulturists. Similarly, experiments carried out on other types of agroforestry systems can give us some clues about the possible responses of the trees in sparse plantings and under varied management practices.

PLANTING DENSITIES

Under favorable soil conditions, low planting densities of grapevine increase grapevine vigor and consequently increase the density of the deep roots of grapevine (Morlat et al. 1984). In the experimental work of these latter authors, the deepest exploration zone was obtained with row spacing of 2.60 m, but for a given row spacing, large spacing along the row actually decreased the root number. These authors also concluded that planting grapevine at a low density increases the proportion of deep roots while high densities increase the proportion of shallow roots. With wines planted at a spacing of 3.1 m between rows on a shallow calcareous loam and under irrigation, Stevens and Nicholas (1994) reported lateral extensions of the main root systems that are smaller than half of the width of the middle row.

Concerning tree root systems, in a tree-pasture agroforestry system under an assumed Mediterranean climate (Australia), Eastham and Rose (1990) observed deeper and denser tree roots when the trees were planted at high densities, although total length and mass of roots produced per tree decreased with increasing tree density. Also "root/shoot" ratio of trees increased as tree density decreased owing to greater root production at low tree densities.

GRASSY COVER

Depending on the soil management practices, a grassy cover can add to the intra-species competition and constitutes an important component to take into account in agroforestry practices within a vineyard. In vineyards with middle-rows covered with grass-rye, the amount of grapevine roots in the middle row and especially in sub-surface is reduced while deep roots are enhanced compared to a chemically weeded vineyard. This tendency is reinforced when the planting density of grapevine is low (Morlat et al. 1984).

Soil management also affects the balance of short (lateral) to long (extension) roots in fruit trees orchards. Atkinson (1983) reports that fruit trees develop a more important proportion of lateral roots under grass than under a chemically weeded ground. Nevertheless this may be directly due to the presence of irrigation in the trials they refer to, while the converse may be expected for non irrigated systems where the highest soil humidity generally occurs deep in the ground.

ROOTS OF TREES IN AGROFORESTRY SYSTEMS

Concerning agroforestry vineyards, only the study by Goma-Fortin and Trambouze (2012) could be found, and is from grey literature. At the experimental domain of Restinclières, the *Pinus brutia* species provoked vine dieback with low to null yield at distances of 2.25 m and 3.25 m from the trees due to root invasiveness in this context of shallow soil. No equivalent competition could be observed for the other timber wood species present at this site.

The root response of trees and crops under any other types agroforestry practices were reviewed by Noordwijk (2015). Given the soil and climatic context of the study by Livesley et al. (2000) – a kaolinitic oxisol under a tropical savannah climate - their observations could be eventually

transposable to that in a Mediterranean grapevine growing region. In this latter study, both maize and trees (hedgerow of *Grevilla robusta* or alley cropped *Senna spectabilis*) planted 0.75 cm apart presented a decrease in root length at their meeting point. Also the spatial extent of tree roots showed lateral redistribution: root density reached a maximum at about 3 m from the tree row while after maize cultivation, the tree root densities kept decreasing over a distance of 0.5 m to 5.5 m from the tree row.

EFFICIENCY OF MANAGEMENT PRACTICES ON ROOT SYSTEMS IN AGROFORESTRY SYSTEMS

Canopy pruning is either effective or not on reducing root competition depending upon tree species. This has been observed for stem pruned trees (Jones et al. 1998; Livesley et al. 2000) and for hedgerows (Korwar and Radder 1994).

In addition, **root pruning** is practiced in various agroforestry systems, as well as in forestry, using a plough device, in order to limit the lateral spreading of superficial tree roots (Yadav and Khanna 1992; Sudmeyer 2002; Ghezehei et al. 2015). For example, Woodall and Ward (2002) observed that root pruning of *Pinus radiata/Schinus areira* belt in a Mediterranean climate reduced but did not cancel tree competition with wheat, though significantly increasing soil moisture on a lateral distance of about 10 m from the trees. Striking is the lateral extent of water competition estimated to a distance of 20 to 30 m from the trees without tree pruning. In addition, from an experiment on sorghum and tree hedgerows (*Leucaena*) grown during the rainy season of a monsoon climate, Korwar and Radder (1994) conclude that the competition between hedgerows and arable crop can be considerably reduced by the combined effect of root pruning and frequent canopy pruning (at one to two months interval) of the hedgerows.

Nonetheless, more recent observations identify two potential serious drawbacks to root pruning. Firstly, it seems to stimulate a quick re-growth of lateral roots, preferentially in the 0-30 cm soil horizon, making it necessary to repeat pruning prior to each cropping season (Ong et al. 2007). Secondly, pruning lateral roots interrupts bi-directional flows of water through the process of hydraulic redistribution, which is presented further in this chapter (see **Hydraulic redistributions**). For both trees and crops in their vicinity, this could deplete the ability to maintain transpiration under dry conditions (Ong et al. 2007).

II.2.3.3 Hortonian runoff interception

Hortonian runoff happens at the ground surface of an unsaturated soil when the intensity of rainfall exceeds the infiltrability of soil, leading to overland flow. Strategies for capturing Hortonian runoff are sought after in order to promote the soil recharge, especially in Mediterranean grapevine production areas. Hortonian runoff interception is also highly at stakes for soil and water conservation through erosion control and pesticide runoff reduction (Prosdocimi et al. 2016). Introducing trees in sloping vineyards, may improve Hortonian runoff interception and water infiltration in the soil through

mechanical reduction of flow velocity (Folorunso et al. 1992; Ruiz-Colmenero et al. 2013) and through the enhancement of surface soil macro-porosity (Pellek 1992).

According to the review of Mekonnen et al. (2015), the most effective runoff breaking effects is reached, by decreasing order, with:

1. trees or shrubs associated with grass buffers,
2. spontaneous or sown grassy covers,
3. highly shaped tree rows over mulched or bare ground.

Weed management practices in the vineyard which leads to bare ground - through either deep tillage or chemical spraying - practically cancel the beneficial effect of the trees, especially on silty soils, which are prone to crusting (Maetens et al. 2012; Prosdocimi et al. 2016). In one given system, the efficiency of water runoff interception also varies in time through the season according to the state of the vegetation and to the simultaneous rainfall regime (Pan et al. 2017).

Also the efficiency of interception from trees highly depends upon the orientation of tree rows relatively to the slope, when applicable. In a hilly vineyard, a tree row tends to form a bank due to sediment accumulation. If the bank is perpendicular to the slope, it segments the hillslope and forces the runoff to infiltrate while a bank with same orientation as the slope could concentrate the surface runoff instead of capturing it (Burel et al. 1993; Merot 1999).

II.2.3.4 Drainage processes

Trees may also generate a redistribution of the water below ground through both horizontal and vertical drainage processes. Both processes result from spatial variations of the soil water content. Multiple types of processes can be involved and the main ones are presented in the following sub-sections

Preferential infiltration along roots

Plant roots contribute to create soil macropores and thus they increase infiltration rates at the soil surface and redistribution rate from upper soil layers to deeper ones, through a process called preferential flow (Mapa 1995). Preferential flow of water corresponds to the non homogeneous movement of water through the ground. More details on the different mechanisms involved and on the contribution of tree roots to this phenomenon are given by Lange et al. (2009).

Within an agroforestry vineyard, the rate of preferential infiltration and its overall contribution to the water budget could vary compared to that in a monocropped vineyard. The intensity of the changes depends whether the root systems significantly differ from that in a monocropped vineyard, which itself notably depends on the tree species, on environmental factors and on management choices.

Lateral flow interception

Under certain conditions of water table lift and rainfall, the sub-surface layers of ground may saturate. Then, the excess of water flows laterally along the slope and may form saturated areas that contribute to surface runoff (as Dunnian runoff) and/or feed perched temporary groundwater that contribute to interflow. The presence of trees may intercept saturated lateral flows by generating dryer sub-surface patches or "sink areas", where water is preferentially stored (Bayala and Wallace 2015).

Hydraulic redistributions

The passive movement of water via roots from wetter to dryer portions of soil used to be called hydraulic lift (Caldwell et al. 1998). Since more recently it is known as hydraulic redistribution (Burgess et al. 1998) because it has been found that water can flow passively through plant roots both upward, downward or laterally, following water potential gradients (Brooks et al. 2006). The number of studies documenting hydraulic redistribution indicates that the process is common in plants whose roots are subject to significant water potential gradients (Caldwell et al. 1998; Jackson et al. 2000), as cited by Brooks et al. (2006).

A few recent propositions for integrating the hydraulic redistribution mechanism into water budget mechanistic models were found (Mendel et al. 2002; Lee et al. 2005; Siqueira et al. 2008). All conclude to the significant impact of this mechanism on regional and meso-scale climates.

Introducing trees within a vineyard could modify grapevine access to water resources to an extent which depends on both grapevine and trees ability to redistribute water. In the following subsections, the existing knowledge concerning the upward, downward and lateral redistribution by both grapevine and trees is reported.

HYDRAULIC LIFT (UPWARD WATER FLUXES)

Trees within a vineyard may redistribute water upward through a process called hydraulic lift. It corresponds to the vertical transfer of water through the roots from relatively wet deeper soil horizons to drier surface layers (Siqueira et al. 2008; Bayala and Wallace 2015). This mechanism is supposedly a trait from evolution which enables to delay the onset of plants' water stress, to extend root lifespan and to increase plants capacitance during periods of high transpiration demand: if the soil is dry, roots do not only take up water but also release water in the dry horizons (Williams et al. 1993; Mendel et al. 2002). Over the year, hydraulic lift occurs mainly during the driest period (Lee et al. 2005). During the day, it usually occurs at night when tree transpiration rate is low (Caldwell et al. 1998). The hydraulic lift mechanism suffers from controversy though it has been observed for more than 50 tree species and climatic contexts. For example one can cite the hydraulic lift of eucalyptus trees under a Mediterranean climate (Burgess et al. 2001), of maple trees under a humid continental 'Dfb' climate (Emerman and Dawson 1996), of broad leave evergreen trees under a monsoon tropical climate (Oliveira et al. 2005), as well as that of desert ecosystems (Yoder and Nowak 1999; Hultine et al. 2003; Hao et al. 2010).

Hydraulic lift is not specific to trees as it is observed for bushy species and grassy species as well (Caldwell et al. 1998). Nonetheless, no reference could be found concerning the hydraulic lift of either grapevine or agroforestry plantings. For tree plantings, a few orders of magnitude can be found from natural ecosystems. For example, for a douglas-fir forest in a humid continental climate, Brooks et al. (2006) observed the maximum hydraulic lift by late summer, when soil water potential was approximately −1 MPa. Also for forest ecosystems, hydraulic lift increases transpiration during the driest period of the year in a range between 19 % in a humid continental context (Dawson 1993) and 40 % in tropical monsoon context (Lee et al. 2005).

RECHARGE OF DEEP HORIZONS (DOWNWARDS REDISTRIBUTION)

The reverse behavior to hydraulic lift i.e. downwards redistribution happens when water gradient is inversed: usually at the end of dry seasons, if the surface soils are partially rewetted by rainfalls but the deeper layers remain dry, water is passively transported by roots from the surface and released into deeper soil horizons. Similarly to the upward transport, this mechanism has a significant role in maintaining root viability and facilitating plant growth in dry soils. One can cite a few examples of tree downward redistribution: in a semi-arid context by *Grevillea robusta* trees (Smith et al. 1999); in Mediterranean context, by eucalyptus with essential role in the deep recharge of the ground water resources (Burgess et al. 2001). No specific reference could be found concerning the downward hydraulic redistribution by grapevine.

LATERAL REDISTRIBUTIONS

Lateral redistributions from tree roots have been mentioned by Brooks et al. (2006). Also the description of tree root physiology from Siau (1984) suggests a tremendous variability according to taxa.

Lateral gradients of subsurface soil moisture can besignificant in a vineyard for notably two reasons. Firstly because plant canopies (of grapevine and eventually of grassy cover) is structured in rows. Indeed, as vine rows and middle-rows alternate, so do various patterns of evaporative demand and evaporation trends. Secondly, water availability can be temporally and spatially constrained when micro-irrigation is in place (Araujo et al. 1995). For example, in California, it is estimated that well over 150 000 ha of grapevine (*Vitis*) are cultivated using drip or micro-irrigation systems (Larry Schwankl et al. 1998). Such micro-irrigation systems restrict water availability to localized soil zones of often less than 20 % of the volume of soil being explored by the entire root system of grapevines (Smart et al. 2005). Most of the literature documenting lateral redistribution by grapevine roots only concern irrigated grapevine (Smart et al. 2005; Bauerle et al. 2007), in the goal of improving irrigation efficiency. Smart et al. (2005) performed experimental work in real feed conditions. They considered *Vitis riparia* cv. V. berlandieri grapevine trained in bilateral/quadrilateral cordons, grown under Mediterranean climate in a sandy clay loam with no gravel. In this context, lateral redistribution from

wet areas to dry areas occured over a distance of at least 1.8 m and at a relatively short time frame of 36 h.

II.2.3.5 Transpiration

Plants uptake water to supply their transpiration, in quantities and rate that depend on the climatic demand (i.e. on the energy budget of the canopy), on the biomass of their canopy and on the volume of wet soil that their roots can explore (Landsberg and McMurtrie 1984; Black et al. 2015). The risk of competition between grapevine and trees for their own transpiration mainly depends on:

i) the architecture of the root systems which results from the agroforestry practice

ii) and on the amount and timing at which both grapevine and trees capture water for transpiration.

All these variables being dynamic, agroforestry vineyards may be characterized by heterogeneous spatial and temporal patterns of water use.

Transpiration drivers within time

Plant transpiration constantly depends on the water and energy transfers from the plant canopy to the atmosphere. To calculate the transpiration rate (λE) of an homogeneous canopy with full ground cover, Monteith et al. (1965) considers plants as a sole 'big-leaf' and proposes the following expression:

$$\lambda E = \frac{\Delta R_n + \rho C_P \frac{e_s - e_a}{r_a}}{\Delta + \gamma(1 + \frac{r_s}{r_a})} \quad [10]$$

with

$$r_s = \sum_i \frac{r_{st}^i}{LAI_i} \quad [11]$$

and

$$r_a = \frac{ln\left(\frac{z_m - d}{z_{0m}}\right) . ln\left(\frac{z_h - d}{z_{0h}}\right)}{k^2 u(z)} \quad [12]$$

λE	Transpiration rate, λ being the latent heat of vaporization of water
R_n	Above canopy net radiation
$e_s - e_a$	Vapor pressure deficit of the air
γ	Psychrometric constant
Δ	Slope of the saturation vapour pressure temperature relationship
$\rho \; and \; C_P$	Density and specific heat of the air
r_s	Mean (bulk) surface resistance of the whole canopy
r_a	Aerodynamic resistance
r_{st}^i	Bulk stomatal resistance of the canopy elements (i)
LAI_i	Leaf area index of the canopy elements (i) [$m^2_{leafarea}.m^2_{soilsurface}$]
$u(z)$	Wind speed a height z above ground
D	zero-plane displacement (recall eq. 2)
$z_{0m} and \; z_{0h}$	Roughness length governing momentum transfer (recall eq. 2) / heat and vapour transfer
z_m	Height of humidity measurement
z_h	Height of wind measurement
k	Von Karman constant

Equations 10 to 12 highlight a strong control of both the climatic variables and the plant physiological state, on the evaporation of a single plant. The stomatal resistance of plants responds to the gradient of humidity from the soil to the air continuum according to a relationship which is very species-specific. Two main patterns of transpiration can be opposed:

(i) When plants are sufficiently supplied in water to meet the climatic demand, the stomatal resistance is generally near the physiological minimum and the rate of transpiration depends mainly on meteorological conditions. The plant releases the energy it absorbed through water transpiration (latent heat) with a rate that increases with the net incoming radiation, the water pressure deficit of the air (eq. 10), as well as the wind speed (eq. 12). At the plant level, the quantities of water being transpired also increases with the leaf area (eq. 11).

(ii) When the plant water loss exceeds uptake, plant control over transpiration at the stomata level and at the whole plant level can become the main driver of the plant water budgets. If the stomatal resistance switches to a significantly high level, transpiration can cease so the plant releases the energy it absorbed essentially through sensible heat. Depending on the plant's strategy facing water scarcity, many varied responses can occur.

The latter developments support the idea that transpiration is a key process regarding the climatic effects of trees and their potential impacts on grapevine under agroforestry practices. Firstly, the trees directly impact the water budget of a vineyard through capturing water for their transpiration. But the converse is also true as the rate of transpiration from trees depends on the degree of competition with grapevine. Secondly, adding complexity, both trees and grapevine impact the microclimatic variables in their vicinity, which is precisely the purpose of this whole chapter. As a consequence, the transpiration patterns occurring within an agroforestry vineyard directly responds to the specific light, air flow and water flow regimes in place within the vineyard. Thirdly, transpiration rate has a feedback effect on the climatic variables in place, notably on the temperature of the canopy elements (depending on the balance between latent and sensible heat emissions) and on the air humidity.

Transpiration model adapted to discontinuous canopies

There has been several attempts for adapting the 'big leaf' model of transpiration from Penman-Monteith (Monteith et al. 1965) to the mixed and discontinuous canopies in agroforestry systems (Bayala and Wallace 2015). One of the key points is to take into account the light interception mechanisms in place. In addition, Wallace et al. (1990) showed that it is essential to take into account the mutual climatic influences of the different components of the system. In the case of agroforestry systems with discontinuous canopies, the contribution of the ground to water and heat fluxes reinforces this stake. Not taking into account the microclimatic factor led to underestimation of the tree transpiration by up to 20 % when the stomatal resistance of the subcanopy is high and to

overestimation by up to 15 % when the resistance is low. From this basis, Wallace et al. (1990) proposed a model suited for agroforestry systems with discontinuous canopies. The model is presented in **Annexe A**. In first approximation, it could be applied for estimating the transpiration from an agroforestry vineyard. Indeed, grapevine presents a canopy structured in rows as well as a rather high height, similarly to millet under alley-cropping management for which the model of Wallace et al. (1990) exhibited good performances (Bayala and Wallace 2015).

Sensitivity of transpiration to environmental factors

Under **non limited water supply**, plants transpiration is mainly driven by climatic variables. The sensitivity of response depends on species main physiological traits, e.g. deciduous versus evergreen leafing, and on morphological traits of their canopies and root systems (Aranda et al. 2012), which are both under a strong genotype x environmental and/or management control. At the leaf level, maximal rates of transpiration occur from isolated, healthy leaves that are well supplied with water and exposed to high evaporation demand (i.e. in conditions of dry air, high wind speed and full sunlight). But for a whole canopy, the interior leaves are generally cooler, absorb less radiation and are in a more humid microclimate, thus their transpiration rate is lower than for peripheral leaves. This strong implication of the canopy structure on the potential transpiration of plants was notably studied for grapevine by Van Zyl and Van Huyssteen (1980): **among various trellis systems, bush vines presented both the highest rooting densities and consumption of water.** Concerning tree species**,** the following very general rules apply: tree water needs and transpiration rate are correlated to the tree productivity and biomass (Eagleson 2005). Fast growing evergreen tree species such as pines and eucalypts present the highest annual transpiration while native deciduous will generally present lower rate and needs (Aranda et al. 2012).

Comparison of grapevine and tree behaviors facing water scarcity

Plants can face periods of water scarcity on a seasonal basis and on a daily basis, a depression of sap flow being observed at midday for many climatic contexts and species. Under water scarcity conditions, plant transpiration is driven by leaf stomatal conductance. Similarly to most plants, stomatal control by woody species regulates the flux of water through the soil-plant continuum. Nevertheless, unlike herbaceous species, woody species must not only achieve sufficient hydration of above ground organs, but also ensure a continuity of the water column from soil to leaves (Smart and Coombe 1983; Aranda et al. 2012).

Plants' water use strategy and response to droughts involve physiological and anatomic responses at the tissue, the leaf and the plant scales. They may be classified along a spectrum ranging from isohydric to anisohydric behaviors. In the first case, also called *drought avoidance*, a decrease of the soil water content triggers a tight stomatal control of the sap flow. On the one hand, it ensures the

maintenance of the plant water potential to a high level. On the other hand, it limits photosynthesis and biomass production. In the second case, also called *drought tolerance*, stomatal control is loose and there is no discernible threshold of water scarcity for water potential maintenance. The plant keeps transpiring but with high risk of desiccation of its organs. The tendency of plants towards either isohydric or anisohydric strategies highly depend upon species and upon the climatic context where the cultivars were selected (Smart and Coombe 1983; Aranda et al. 2012).

Grapevine presents a pronounced isohydric behavior and an overall very high resistance to droughts compared to most woody, deciduous fruit plants (Atkinson 2011). Among the mechanisms listed by Kozlowski (1976) for drought avoidance by tree crops, grapevine exhibits the following: reduced leaf area and number, leaf shedding, leaf orientation, high leaf cuticular resistance, stomatal size and frequency modification, control of the stomatal resistance with water stress, presence of epiderm and modification of root-shoot ratio. In addition, grapevine displays photosynthetic activity from its stems (Kriedemann and Buttrose 1971), as reviewed by Smart and Coombe (1983).

Grapevine tolerance to drought presents an important genetic variability. The implication of the root stock type and that of the cultivar combine (Serra et al. 2014; Ollat et al. 2016; Simonneau et al. 2017).

In an agroforestry vineyard, depending on the tree species, the trees undergoing drought may either reduce, maintain or increase their transpiration rate per unit leaf area (Maseda and Fernandez 2006). In the latter case, it could reinforce competition with grapevine for water and thus affect grapevine biomass production. Literature from forest ecosystems gives a few clues of the inter species variability of tree responses to drought by comparing the transpiration trends of two species grown in the same forests. For example, in humid continental context, oak species showed a very pronounced isohydric response on the short term whereas Sugar maple, Tulip poplar and Sassafras trees showed anisohydric short term responses and pronounced tendency to biomass reduction on the long term (Roman et al. 2015). Another interesting example is provided by Aranda et al. (2012) in a Mediterranean context: in June, (Northern hemisphere) average transpiration of about 4.5 $L.h^{-1}$ for both *Quercus Ilex* and *Pinus Nigra* growing in the same forest. In August, *Quercus Ilex* maintained a transpiration of at least 75 % of that in June while the transpiration of *Pinus Nigra* fell to null almost permanently.

II.2.3.6 Indirect modifications of the soil content in water

IMPACTS ON SOIL WATER INFILTRATION AND HOLDING CAPACITY

For forested areas, Lange et al. (2009) reported that water holding capacities vary depending on the type of forests, the greatest storing capacity being met under forests the closest to their natural stage. Similarly, Kammer et al. (2013) observed that the water holding capacity of the soil is positively correlated with plant species diversity. These observations suggest that introducing trees within a

vineyard could increase the water holding capacity by means of an increase in both above and below ground biodiversity. Notably a long term increasing effect on the organic matter content notably on humic acids can contribute to elevating the water holding capacity in soils – around 14 mm_{water}/m_{ground}/ % MO, (Rawls et al. 1991). Observations of different types of agroforestry systems go in the sense of this hypothesis (Lorenz and Lal 2014). For example, alley cropping is recognized as sound strategy for improving the fertility of degraded, low-activity clay soil in the tropics. The key to its success is the use of tree pruning as green manure or mulch (Ong et al. 1991). Tree pruning also enhances tree root senescence which may also provide a source of organic matter and nutrients for the crop and rhizosphere micro-organisms (Smucker et al. 1995; Lehmann and Zech 1998) as cited in (Livesley et al. 2000).

IMPACTS ON THE EVAPORATION FROM THE GROUND

Evaporation from the soil surface as well as the transpiration from a cover crop can represent a significant source of water loss in the water budget of a vineyard. For example, in semi-arid climate, since water in topsoil layers evaporates within 1-2 days, it was proposed that rainfall less than 25 $mm.day^{-1}$ should be ignored in the water balance (Van Zyl 1981; Myburgh 2004). Similarly, for contrasted climatic and agronomic contexts, both Cancela et al. (2012) and Füri (1977) reviewed in Smart and Coombe (1983) estimated at 30 % the contribution of evaporation from bare ground to the total evapotranspiration of a vineyard when the climatic demand is high. These losses of water are highly at stakes in grapevine production regions facing summer droughts, namely in Mediterranean and in semi-arid climates.

In addition, the soil evaporates water at a rate controlled by meteorological and ground context (Lebon et al. 2003): (i) when the soil has been rewetted above field capacity by rains evaporation occurs at potential rate E_{s0}. and the cumulated quantity of water loss is directly controlled by the climatic demand (Allen 1998, chap. 7); (ii) when soil moisture is scarcer, the rate of soil evaporation is also limited by the soil water diffusivity, which is a constant for any particular soil (Black et al. 1969).

In short, introducing trees in a land modify the amount and rate of water evaporation from the ground and from other crops transpiration (**Figure 26**). Local modification of the climatic demand is the main lever involved. Indeed, through the radiative and air-flow effects of trees, the climatic demand for water transfer from the ground to the atmosphere is modified. The impact of a tree row relatively to that of a grapevine row is complex to predict, notably because the evaporation from the ground of a vineyard already presents an important variability depending on extrinsic parameters, namely, the climatic context and the soil type, and on intrinsic parameters, namely the vine type, the vine architecture, the soil management practices, and the eventual irrigation practices (Smart and Coombe 1983). Also the resulting impact of introducing trees in a vineyard may depend on the soil management practices which are adopted on the tree row as well. A grassy cover below trees may notably respond differently than a mulched or bare ground (Van Leeuwen et al. 2009).

II.2.3.7 Conclusions on potential effects of trees on the overall water balance of a vineyard

To sum up, ligneous plants influence the soil water content in their vicinity through both direct effects:

- interception by canopy and roots,
- aerial and underground redistributions,
- uptakes for tree transpiration;

and indirect effects:

- soil structure modifications that influence the soil water storing capacity,
- modifications of the climatic demand which controls soil evaporation and grapevine transpiration.

Because trees and grapevine differ in their morphologies and physiological functioning, introducing trees within a vineyard can locally modify the water balance. The references formerly presented notably highlight that trees capture water to sustain their transpiration with a rate and from an explored volume of soil that can significantly differ from that of grapevine, depending on species. Consequently, water competition between trees and grapevine may occur depending on the combination of the amount of available water, the water requirements to sustain their respective transpiration and the volume of soil their roots explore. All these factors vary in space and time, through phenological stages of grapevine and trees, and through the meteorological years. Consequently, heterogeneous spatial and temporal patterns of water use may appear in agroforestry vineyards. No reference concerning the water status of grapevine in agroforestry vineyards could be found, and only very few references were found when widening the scope to any type of agroforestry systems under temperate climates. In the case of hedgerow networks, two main patterns combine in space during the vegetative seasons:(i) in the vicinity of hedges, the soil water content increases in inverse proportion to the distance to the hedge, (ii) while at the closest distances to the hedge a competition for water between the trees and the neighboring crop is noticeable, (Mette and Sattelmacher 1994) as cited in (Merot and Ruellan 1980).

Also, water redistribution, water needs and root architectures all together vary with the soil type, the climatic context and the species in place. Consequently, multiple and even divergent answers may be met in terms of water competition, depending on the type of agroforestry vineyard being considered.

A few methodological recommendations can be made. Firstly it seems important to precise the time scale of the phenomenon involved in the water budget of an agroforestry vineyard. For example,

the budget of groundwater recharge can vary if considered on the short or on the long term. Secondly, observations should systematically be interpreted in regards to the seasonal factor, i.e. whether they apply under a rather dry or wet season. Similarly, it is central to take into account the environmental extrinsic factors (the soil type and the climatic context). Thirdly, in the specific case of agroforestry vineyards, experimental protocols should take into account the variability of soil management practices under the tree row, the vine row and on the middle rows. Surface runoff interception, hydraulic redistribution and evaporation from the ground all together greatly vary depending if the ground is covered with grass, is mechanically weeded or is chemically weeded.

I.3 Microclimate variations in space and time

In the previous part of this chapter the effects of trees on radiations (light and heat) have been detailed, on the air-flow and on the water flows at the plot scale. The previous mechanisms are linked together by the energy and water budgets at the soil-vegetation-atmosphere interface (Oke 1992; Pokorný 2001; McPherson 2007). Their combination in space and time modifies the microclimate in the vicinity of the trees, notably the amount of solar radiations, the availability of water in the ground, the ambient temperature, the air humidity and the wind regime. The microclimate of agroforestry vineyards have seldom been studied (Trambouze and Goma-Fortin 2013; Grimaldi et al. 2016, 2017; Trambouze et al. 2017), though it is essential information for understanding tree impact on physiological processes underlying grapevine yield and berry composition. Thus, the literature review has been enlarged to the meteorology of tree-crop agroforestry systems (Monteith et al. 1991; Dupraz et al. 2005; Talbot and Dupraz 2012; Dufour et al. 2013; Lecomte and Dupraz 2015; Stigter 2015; Artru et al. 2017), of forests (Gash et al. 1995; Crockford and Richardson 2000; Denyer et al. 2006), of orchards (Jackson and Palmer 1972; Mc Aneney et al. 1990, 1992; López-Olivari et al. 2016) and of windbreaks and hedgerows (Caborn 1957; Forman and Baudry 1984; Bagley 1988; McNaughton 1988; Guyot 1989; Brandle et al. 2004) in temperate climate context. From this literature review, it is concluded that five potential microclimatic zones may combine within agroforestry vineyards (**Figure 30**).

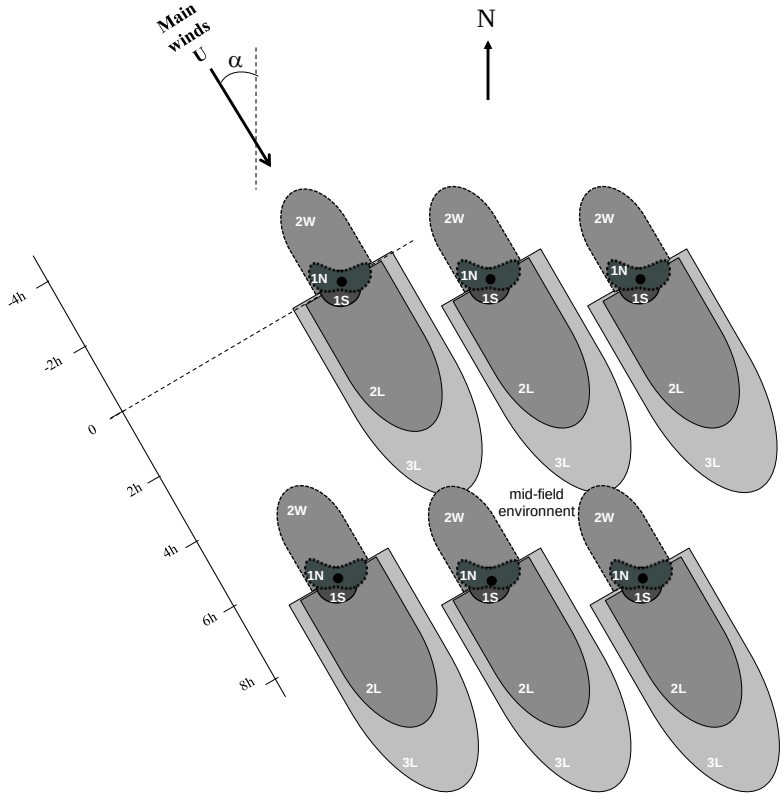

Legend

● Location of tree stem. H = tree total height α = air flow approach angle relatively to the tree row

Zone	P.A.R	Wind U	Day temperatures (T_v: vegetation temperature – T_G: ground temperature – T_a: air temperature)	Night temperatures	Atmospheric moisture	Soil moisture	Leaf humectation
1N *Shaded North*	– – to –	= or – (depending on α)	– T_v[2] T_G[1,2]	+	?	?	+
1S *Insolated South*	+	= or – (depending on α)	+ to ++ (depending on α)	+	?	- ?	– to =
2W *Quiet windward*	=	–	+ [1] T_a	– ?	+	+	+
2L *Quiet leeward*	=	– –	+ T_v[2] T_a[1] T_G [2]	– ?	+ in average – temporarily	+	= to +
3D *Wake*	=	+ (turbulence)	– to =	– to =	–	–	–

Figure 30: Theoretical microclimate zoning around alleys of trees and main expected variations of microclimatic variables. On the map, the maxima cast shadow lengths (i.e. the dimensions of zone 1N) were calculated applying trigonometrical relationships (Satterlund 1983) on the solar altitude and azimuth angles of the 21st September at latitude of 43.8°N, assuming a tree of height *h* and with an ellipsoid canopy shape. In the table, each microclimatic variable may increase (+), unsignificant change (=), or decrease (-) relatively to that in the mid-field, or be unknown (?). P.A.R stands for photosynthetically active radiations.

Ref: [1] (Caborn 1957) - [2](Monteith et al. 1991)

II.3.1 Zone 1N or shaded North (in NH)

The *zone 1N* is the whole area submitted to shading when integrating shade cast of a single tree throughout the year. Its area increases with tree height (H), reaching 0.9 H towards North and 1.6 H towards East/West, according to estimations made on the 21st September at a latitude of 43.8°N. The irradiance in PAR may equal 10 to 40 % and 40 to 50 % of the irradiance in the mid-field, respectively towards North in the Northern Hemisphere (NH) and towards the East/West, the lowest values

occurring the closest to the trees (Chirko et al. 1996a; Dupraz et al. 2005). In addition, as the sun daily runs in the sky, shading is located within zone 1N, at western, northern and eastern orientations to the tree respectively in the morning, at mid-day and in the afternoon. For the overall zone, shading is generally more intense on clear sky days as incident radiations are mostly direct compared to overcast days when most of the beams come from diffuse reflections (Jackson and Palmer 1979; Leroy et al. 2009; Talbot and Dupraz 2012; Artru et al. 2017).

Temperatures in the 1N zone result from the combination of the cooling effect of shading and the warming effect due to tree TIR heat emission (Chiapale 1975; Guyot 1989). At night, only this latter mechanism operates which leads to warmer temperatures in the vicinity of trees, and so potentially to a lower risk of radiation frost during clear sky nights in winter and spring (Guyot 1989), compared to the outfield. During the day, one can infer a prevalence of the cooling effect due to shading, especially on clear sky days with low to medium wind speed (Corlett et al. 1989; Monteith et al. 1991). Consequently dew deposition and morning frost happening at sun rise may last longer in the western part of zone 1N. Also because of shading, leaf wetness duration is greater after dew or rainfall events. Air relative humidity might be greater as well but with more uncertainty due to reduced ground and crop transpiration.

Part of the zone 1N is located directly under the tree canopy and consequently submitted to specific rainfall regime according to the through fall and stem flow of water. Underground, part to the entire zone 1N coincides with the area of tree rooting system which strongly impacts the amount of water available. In summer, water stress tendency is hard to predict as the inputs of water in soil, the uptakes by trees and by grapevine and the climatic demand for transpiration are all together under the tree influence and may compensate (Stigter 2015). The intensity of grapevine water stress and its dynamics also depends on the meteorological context: after a rain-induced recharge, the soil moisture may remain high longer than in the mid-field while during drought it may decrease lower and quicker because of tree-grapevine root competition for water uptake.

II.3.2 Zone 1S or insolated South

Zone 1S corresponds to the southern areas submitted to intense reflection of short wave radiations from the southern side of rather high and vertical tree canopies. Due to this additional energy inputs, day and night temperatures are warmer than in the mid-field environment (Guyot 1989). This pattern will be even more intense when tree canopy is dense, contiguous and with high albedo. It may also combine with heating up effects of sheltering in case dominating winds are blowing from the North. In winter, the risk of radiation frost may be lowered whereas on the warmest days of summer, the risk of extreme heat damages may be enhanced (Guyot 1989). The amount of water captured to supply the transpiration of a tree very dense canopy is also very high resulting in higher risk of water

competition with grapevine in *zone 1S* compared to the mid-field environment (Mette and Sattelmacher 1994).

Once shading and direct competition effects gone, windbreak effects might be the most influencing factor on the resulting microclimatic patterns.

II.3.3 Zone 2W (quiet windward) and zone 2L (quiet leeward)

Zone 2W and 2L are located near the trees, respectively windward and leeward, in the main wind blowing direction. They are characterized by respectively a slightly and an intensively lower wind speed compared to the mid-field environment but homogenous energy incomes through direct and diffuse sun radiations. Consequently, compared to the mid-field environment, near-surface air temperatures tend to be higher by day (Forman and Baudry 1984; McNaughton 1988; Guyot 1989; Mc Aneney et al. 1990; Brandle et al. 2000). By night, air temperatures within 1 m of the ground are eventually 1 to 2°C warmer in the wind-sheltered areas than in the mid-field environment (Zhang et al. 1999; Hodges and Suratman 2004) as reviewed by Brandle et al. (2000), while in contrast, they tend to be slightly cooler 2 m above the surface (Brandle et al. 2000). Igounet et al. (1995) observed that berry temperature positively respond to wind speed reduction, especially during final phase of maturation. In their experiment, sheltered clusters reached daily mean temperatures 4 to 10°C higher than the surrounding air while berry heat accumulation disappeared with average wind speed greater than 3.5 – 4 $m.s^{-1}$. Temperature patterns in sheltered zones are even more pronounced on clear sky days and nights or when the ground is dry (Guyot 1989). On the one hand, the risk of frost from cold air drainage may be higher during winter and early spring clear sky nights, and so even more if the sheltered zones are located on slopes or down part vineyards (Caborn 1957). On the other hand, the vineyards that are usually exposed to strong winds may be protected from mechanical damages on leaves and berries. In addition, in spring, the soil of sheltered areas warms up quicker than in the open-field: temperature differences of 0.5 °C to 3 °C were observed between sheltered and unsheltered zones at 10 cm deep in the ground (Van Eirman et al. 1964; Guyot 1989). As a consequence, earlier budburst may occur. Also, owing to the reduced air-movement, the water evaporated from the soil and transpired by growing crops is retained longer in sheltered areas causing thus a slight increase of air humidity notably during the second half of the day, when energy balance on the vegetation is negative (reviewed by Caborn (1957); (Cleugh 1998; Brandle et al. 2000). More significant, dewfall is considerably enhanced in sheltered areas due to a number of factors including reduced wind speed, greater humidity, and colder nocturnal temperatures. Dew tends to form earlier and to evaporate later, and can represent as much as a 200 % gain compared with deposition in the open aera (Oke 1992, chap. 7). The extra dew formation at night and lower climatic demand conditions in sheltered areas result in a significantly longer leaf wetness duration following dew deposition or rainy events (authors

reviewed by Caborn (1957); (Cleugh 1998; Brandle et al. 2000). Summarizing the effects of shelter upon evapotranspiration, Oke (1992, chap. 5) concludes that daytime water losses are reduced while nocturnal water gains are increased in wind-sheltered zones. Nonetheless, the consequences on grapevine water status remain complex to predict notably because it is greatly influenced by the climatic context. When considering all together temperature, wind speed, air humidity and the amount of water available in the ground, it can be hypothesized that the risk for water stress on grapevine in the sheltered zones may indeed be lower under conditions of dry-air advection (McNaughton 1988) whereas it may actually rise in summer during very hot days of low wind speed. This latter assumption may have applied in the Mediterranean climate of the Salina Valley (US), where Freeman et al. (1982) observed more grapevine under water stress in a sheltered area under the influence of a windbreak than without windbreak.

II.3.4 Zone 3 or turbulent wake zone

A zone 3 or *wake zone* may eventually form leeward of some trees which have very dense and contiguous canopies and are organized in a network of hedgerows. The air flow forced up over the first tree row may drop rather sharply in a turbulent flow and so generate enhanced turbulence (Caborn 1957; Guyot 1972; Brandle et al. 2000). The wake zone location and dimensions are in debate as they strongly depend on both tree height and canopy porosity. Because of enhanced turbulence compared to the mid-field environment, a higher risk of advection frost during windy nights of winter and spring is expected. As turbulence drives the aerodynamic resistance of the vegetation, it increases the intensity of heat, water and CO_2 fluxes. Consequently, it can be also expected shorter leaf wetness, stronger soil desiccation and higher evaporative demand in wake zones (McNaughton 1988; Guyot 1989) potentially responsible for a more intense water stress in summer, in conditions of dry-air advection (McNaughton 1988).

II.4 Implication of the vegetation structure

Morphological properties of the trees stand as a major variability factor influencing the intensity and spatial extent of their radiation, wind-breaking and water cycling effects. The following subsections summarize knowledge concerning the variability in tree-induced microclimatic patterns depending on the main morphological traits of the vegetation, considering these individually. It allows drawing a few conclusions concerning appropriate choices of planting and management practices in order to partly control the microclimatic effects of trees.

II.4.1 Tree height

As illustrated on **Figure 30**, the higher the trees will grow, the larger the *1N*, *2W* and *2L zones* will extend. Indeed, the tree height is a major factor of spatial extent of shade (Dupraz et al. 2005; Talbot and Dupraz 2012; Artru et al. 2017) and of the wind speed reduction, beside isolated trees (Gross 1987) or hedgerows (Jensen 1954; Caborn 1957; Plate 1971; Raine and Stevenson 1977; Oke 1992; Brandle et al. 2004; Wang and Takle 1996, 1997; Cleugh 1998; Forman and Baudry 1984). Potential drawbacks to understory grapevine during the mature phase of trees may be addressed through tree pruning and thinning (Sudmeyer and Flugge 2005; Rivest and Vézina 2015), with likely positive effects on wood quality (Cutter et al. 2007).

II.4.2 Foliage density

The foliage density increases with the amount of leaves and branches and with the thickness of the canopy, and consequently increases throughout the tree full leaf enlargement in the case of deciduous trees (Chirko et al. 1996a). The denser it is, the lesser the light irradiance within zone 1D (Leroy et al. 2009; Talbot and Dupraz 2012) and the lower the wind speed within zones 2U and 2D (Figure 25)(Wang and Takle 1996, 1997; Cleugh 1998) . It also increases the extent of turbulence (zone 3), in the case of very dense canopies (Perera 1981; Schwartz et al. 1995; Wang and Takle 1996; Vigiak et al. 2003). Very dense tree canopies designed for a total wind-breaking effect would at the same time lead to intense shading, extreme temperatures and enhanced turbulence patterns within vineyards. Consequently wide hedgerows of very low porosity are not recommended except in the particular case of vineyards exposed to strong winds. Hedgerow and windbreak effects are most effective with semi-porous plantings (Guyot 1972) as they will maintain a moderate air flow within a vineyard. It is a sound strategy for alleviating the temperature extrema and so to prevent both frost and extreme heat damages.

II.4.3 Orientation of the tree rows

In the case of a perennial crop such as grapevine, possibilities of orientation for the tree rows may be limited by the orientation of already planted rootstocks and by the topography of the vineyard. Nevertheless, when trees are organized in rows, the azimuth angle of the tree row has several climatic impacts.

Some references concluded that the orientation of the tree row impacts the total amount of light: with an east-west (EW) orientation, *zone 1N* is more extended but the integrated interception may actually be lower than with a north-south (NS) one (Chirko 1993; Dupraz et al. 2005; Artru et al. 2017) (**Figure 18**). These conclusions disagree with those of Jackson and Palmer (1979) and Leroy et al (2009) who did not observe significant quantitative effects of the tree row azimuth. More significantly, the azimuth angle of the tree row impacts the spatial and seasonal distribution of the light at the plot scale (Leroy et al. 2009): EW orientation generates more variability in light interception throughout the year while the impact of a NS orientation remains more homogenous at the plot scale: in the first case the shade cast is longer from August to September than from May to July, considering the Northern hemisphere (Jackson and Palmer 1979). Orientation of the tree row relatively to the prevailing wind direction also affects the efficiency of wind speed reduction in the 2W and 2L quiet zones. As the length of the sheltered areas varies with cos α (Heisler and De Walle 1988) – α being the angle between the air flow and the tree row – shelter effects don't noticeably fade for angles below 20° to the normal. With larger angles, sheltered areas reduce in size but are still effective with angles as much as 45°(Bean et al. 1974; Cleugh 1998).

II.4.4 Tree spacing and overall density at the plot scale

The morphological aspects of a given tree combine all together, notably the tree height, the tree foliage density and the canopy shape. Also at the plot scale, the trees may be organized as either contiguous or disconnected canopies and together with the understory crop, they constitute an ensemble of specific aspect in 3D.

For sparse tree canopies such as agroforestry plantings, the total interception of light increases with planting density at the plot scale. Nonetheless, planting trees aligned in rows reduce the total footprint of shadow cast on grapevines compared to scattered tree arrangements (Jackson and Palmer 1972, 1979).

Torita and Satou (2007) found strong negative correlation between, on the one side, the product of tree rows width (W) with total tree density (Ad), and on the other side, the minimum relative wind speed in 2W and 2L zones. Also, the shelter distance generally increased with W x Ad.

Moreover, in the case of agroforestry vineyards, it seems that the whole woody vegetation within a vineyard, including grapevine, and that at the hedges, should be taken into account when considering consequences on the microclimate. On the one hand, the canopy architecture of grapevine showed a strong influence on the light, the temperature and the water regime of a vineyard (Morlat et

al. 1984; Smart 1985; English et al. 1989). On the other hand, border effects from hedgerows or forested borders showed impacts in terms of water competition, insolation or wind sheltering effects of intensity by far greater than that of isolated trees (Freeman et al. 1982; Landsberg 1999; Brandle et al. 2004).

In order to calculate light interception and vegetation water use of agroforestry systems with very varied spatial arrangements (block plantings, windbreaks, timberbelts, scattered trees of varied densities, alley cropping), Landsberg (1999) sought for an aggregating vegetation metrics. He concluded that in the case of dense plantations, the most important parameter is the leaf area index LAI $[m^2_{leaves}.m^{-2}_{ground}]$ - the area of leaf surface per unit of ground area, while, in scattered trees the important parameter is leaf area density ρ_f $[m^2_{leaves}.m^3_{canopy}]$ - leaf area per unit canopy volume

II.4.5 Shape of the tree canopy

To secondary extents, the overall shape of the tree canopy influences microclimatic patterns.

Firstly, it influences the spatial footprint of both shading and sheltering. Jackson and Palmer (1972) observed that interception decreases with the angle of the hedge surface to the horizontal which explains a greater PAR interception by trees with rectangular, then truncated, then triangular canopy shapes. The *2L quiet zone* also goes on further away with a ball-shaped tree than that with a cone-shaped tree (Gross 1987). In the case of agroforestry vineyards, tree canopy positioned at an height comprised between the ground and the height of grapevine has very reduced effects on the air flow regime as the grapevine itself already has strong windbreak effects that vary with grapevine management choices (Brenner et al. 1995; Hunter et al. 2016). Nonetheless, once trees become significantly taller than grapevine, Chirko et al. (1996a) and Dupraz et al. (2005) recommend stem pruning over half the total tree height in order to minimize light interception by trees.

Secondly, the peripheral branches contribute the most to the whole tree transpiration as the transpiration from the tree leaves exposed to sun light is about six times greater than that of shaded leaves (Hanson 1917). Consequently, pruning the tree canopy in 3D shape that maximizes the exposure of leaves to sun radiations (i.e. canopy shapes with high “width/length” ratio and facing South, in NH) will maximize the quantities of water transpired by the trees. On the contrary, compact canopy shapes may be privilege in order to reduce competition for water.

The 3D distribution of tree leaves presents high inter-species and intra-species variability depending on the climatic and soil context and canopy management practices. Various 3D shapes of tree canopy can result in the same overall foliage density but has differing impacts on the light, air and water fluxes (Eagleson 2005). The occurrence of sunflecks is notably greatly influenced by the 3D distribution of the leaves (Meloni and Sinoquet 1997).

II.5 Conclusions

Woody vegetation impacts the energy and water budget of a land because it mechanically intercepts the shortwave radiations (light) from the sun, modifies the air flow regime and redistributes water above and below ground. In addition, woody vegetation emits longwave radiations (sensible heat) and releases water vapor through the transpiration process (latent heat). In the context of agroforetsry vineyards, the climatic mechanisms generated by trees may differ in intensity, in spatial extent and in timing from those generated by grapevine (*Vitis Vinifera*) because of differences in their anatomy, physiology and management. The main features of trees that have climatic significance are:

- the very high standing architecture;
- a denser top canopy while the trunk zone may eventually be devoid of foliage in the case of single highly pruned tree rows;
- the combination of tree height, shape and foliage density that leads to greater radiation trapping and a rougher surface;
- the elevated volumetric biomass density that enables heat and mass storage over short periods of time;
- a potentially deep rooted and plastic rooting architecture, though little is known under tree-grapevine intercropping context;
- a different stomatal control of their water status, especially in the case of permanent leaf or coniferous species.

Consequently, introducing tree in a land potentially generate significant local modifications of the energy and water budgets which would manifest through significant modifications of the microclimate variables. Several climatic patterns may combine and apply with an intensity that may evolve with the age of the planting. Light competition seems present but limited if a sparse planting structure is adopted and with adapted canopy management practices. A reduction of the wind speed may appear on the long term with a main consequence of increasing the leaf wetness duration. The aerial temperatures may not show such significant variations in terms of seasonal means but could be significantly impacted in their extreme values. The maxima temperatures during warm and quiet days of summer as well as the risk of increased frost occurrence by late spring should be investigated in priority. The risk of water competition between trees and other crops notably grapevine remains equivocal. From the literature review presented in this chapter, striking is the complexity of this question as multiple factors are involved, both extrinsic (the meteorological context, the soil type, the tree and grapevine species), and intrinsic (management practices), Also, mutual influences occur between trees, grapevine, ground and the atmosphere components, adding to the complexity of this question.

On the one hand references considering agroforestry vineyards are greatly expected. On the other hand, one should note that they will only apply in the context, timeframe and for the type of agroforestry plantings that will be assessed. More globally, this latter observation applies for all the

climatic variables likely to be assessed in an agroforestry vineyard. Thus, methodological approaches for studying the microclimate of an agroforestry vineyard should take it into account. A way to do so could consist in systematically selecting a monocropped vineyard and including it into the experimental trial as the reference situation. In this configuration, the microclimate generated by a grapevine + tree disposition could be compared to that generated by a grapevine + grapevine disposition, all other things being (as) equal (as possible).

The structure of the vegetation from the individual tree scale to the plot scale stands out as a key factor of variability to document. At the same time, it meets expectations of vine growers willing to adopt agroforestry practices. They raise the question of the preferential planting choices and the management strategies in order to adjust as best as possible the microclimatic effects of the trees to the objectives and to the context of production.

The response of grapevine to microclimatic changes induced by trees will depend on its sensitivity to environmental factors. The following chapter reviews and discusses this issue.

CHAPTER III
Environmental responses of grapevine: A state of the art

III.1. Introduction

From a state of the art on the microclimatic impacts of trees, chapter II concludes that introducing trees in a vineyard may modify the light, the air and the water fluxes all together, thus generating specific microclimatic conditions of important spatial and temporal variability. In order to document the acceptability of agroforestry practices in viticulture, this latter observation addresses the issue of grapevine sensitivity to environmental factors. Which state variable are the most impacting on grapevine physiology? What are the impacts of microclimatic modifications on grape and wine production? In order to anticipate experimental and modeling works presented chapters IV, V and VI, the objectives of this chapter III are double:

- Firstly, the microclimate variables the most likely to influence grape and wine production should be identified and quantified;
- Secondly, a relevant methodological approach for assessing the microclimate of agroforestry vineyards and the consequences on grapevine production should be proposed.

In order to meet these goals, the following content of this chapter provides a revue of literature structured in three parts. The first part introduces relevant elements of viticulture in regards to the bio-climatology of grapevine. The second part chronologically describes the contribution of various climatic variables to the vegetative and reproductive cycle of grapevine. The third part considers one by one the main state variables the most likely to be impacted by trees and gives a focus on integrated experiments which assessed their consequences on the yield and or the berry quality for wine making.

III.1.1 Grapevine (Vitis vinifera L. ssp. vinifera) characteristics and cultivation

III.1.1.1 Physiology and phenology

The genus Vitis (Grapevine) belongs to the family of *Vitaceae* and comprises about 79 different species of perennial vines (Carbonneau et al. 2015). Among them, *Vitis vinifera* L. ssp. *vinifera* was domesticated for wine production in the Neolithic times from wild species originating from the Himalayas to the Atlantic coast, between the 43th and 49th northern parallels (Bouby et al. 2013). It is further referred as grapevine in this manuscript. Grapevine is now cultivated in most of the wine producing regions in Europe and the New Word (**Figure 31**).The area of extension of its cultivation is mainly defined according to heat and water constraints (Hedrick et al. 1919; Bonnefoy 2013). On the one hand, insufficient cumulated amounts of heat, late spring frost and early autumn frosts are the main limiting factors for its Northern extension. To secondary extent, too prolonged periods of wetness in regards to disease risks are also involved. On the other hand, too severe water stress

because of too seldom and scarce precipitations, and damages from extremely high temperatures are the most limiting factor of its extension in Southern regions.

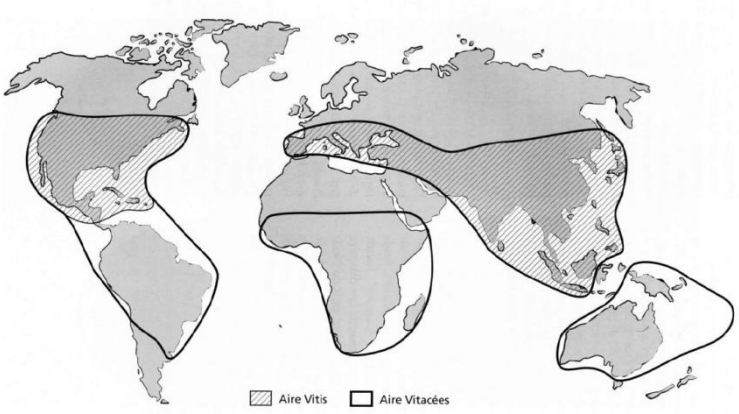

Figure 31: Area of extension of *Vitis* cultivation in the world – Source Blouin (2007)

In 2010, the total harvested area of grapes in the world was estimated, by FAOSTAT, at about 7.1 million ha and all together, the table grape, dried grapes, grape juice and the wine industries represented the most important fruit economy in the world (Vivier and Pretorius 2002).

From ancient species, grapevine has evolved from a bushy, sun-loving plant to a trailing climber (**Figure 32**). In addition, since *Phylloxera* massive attack in the late XIX^{e}, modern producing vines are now systematically grafted on a resistant rootstock from different species.

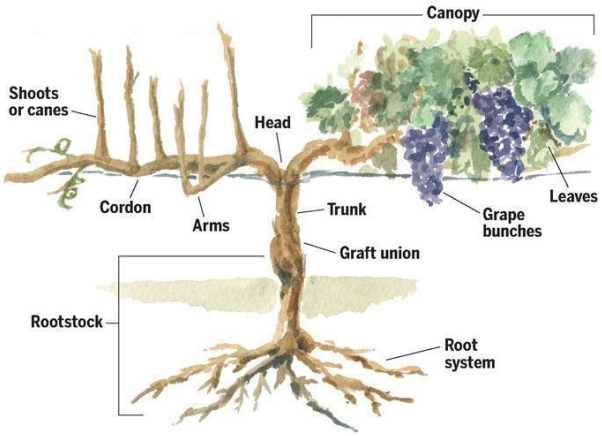

Figure 32: Overview of grapevine components and architecture, by Dave Johnson for Bay Area News Group (https://www.evineyardapp.com/blog/2017/05/30/overview-of-grapevine-structure-and-function/)

Throughout a year starting from winter *N* and finishing in winter *N+1*, the phenological succession of grapevine divides in height principal growth stages (**Table 2**).

Table 2: Principal phonological stages of grapevine (*Vitis vinifera* L. ssp. *vinifera*)

Principal growth stage	*Description from Lorenz et al.*(1995)	*BBCH Code*	*Visible aspect from Bloesch and Viret (2008)*
Dormancy	Rest state during winter.	00	
Sprouting	The dormancy of winter buds breaks. Buds begin swelling and then greening until budburst happens corresponding to the appearance of visible green shoot tips.	01 →09	  
Leaf development	From one to nine unfolded leaves appear and spread away from shoots.	11 →19	  
Inflorescence emergence	Inflorescences become clearly visible, swell and then show separating flowers.	53 →57	  
Flowering	From 1 to 100 % of the flower hoods detach from their receptacle and fall.	60 →69	  
Development of fruits	Fruits begin to swell (fruit set), then bunches start hanging and berries progressively adopt a pea-size until they touch completely.	71 →79	  
Ripening of berries	Veraison corresponds to the first stage of berry ripening: berries brighten in color and become more compact. The main evolutions concern berry composition: sugar content rise while organic acids drop. In the mean time berry soften. It finally ripes for harvest when sugar and acids stabilize.	81 →89	  
Senescence	After harvest, maturation of woods stops, the leaves discolor and fall.	91 →99	 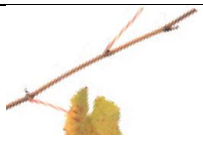

III.1.1.2 Management practices

Management of grapevine canopy

The architecture of grapevine canopy is managed through complementary choices of pruning and shoot positioning (**Figure 33**) together with trellis system and trimming (**Figure 34**). The choices of the vine growers are mainly driven according to their final objectives in terms of shoot to fruit ratio

(Kliewer and Dokoozlian 2005), light interception efficiency (Schultz 1995; Gladstone and Dokoozlian 2003; Louarn et al. 2007), temperature and aeration in the bunch zone (Carbonneau and Casteran 1986; English et al. 1990).

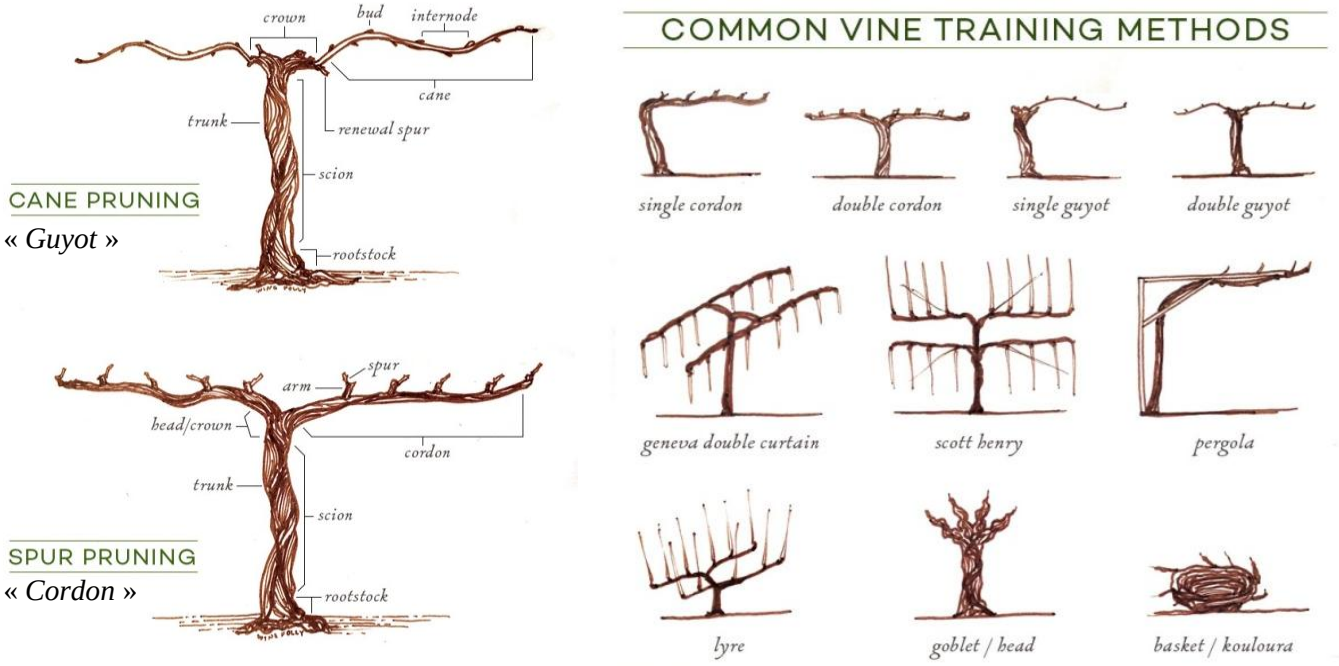

Figure 33: Pruning and training methods.
Source: Wine Folly (https://winefolly.com/review/grape-vine-training-methods-illustration)

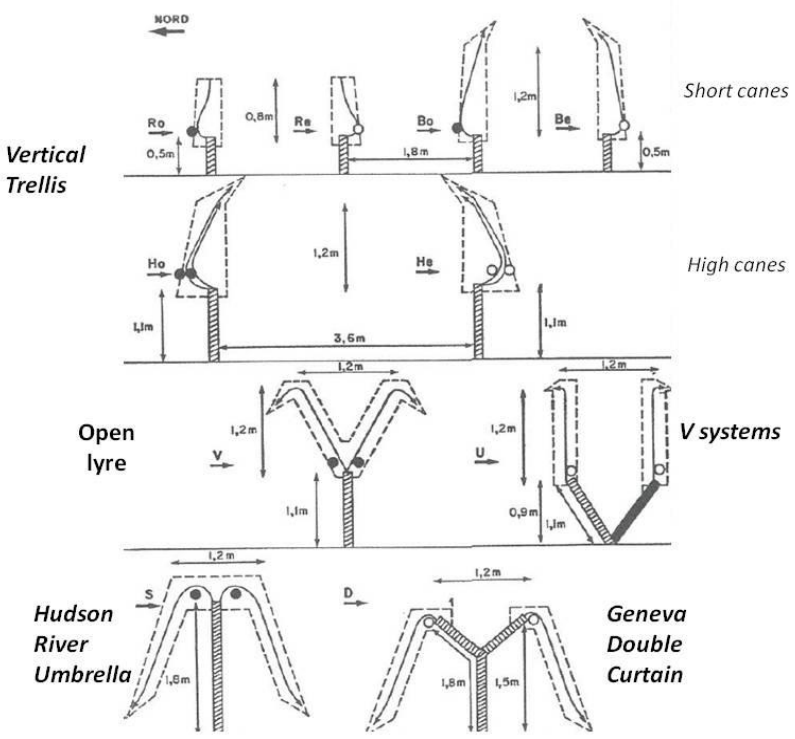

Figure 34: Common trellis systems - (Carbonneau et al. 2015)

Design of vineyards

The following elements are summarized from Hedrick et al. (1919). Convenience in vineyard operations makes alignment imperative most of the time. Some vine-growers attach importance to the direction in which rows run, holding either that the full blaze of the sun at mid-day is desirable for vine, soil and fruit, or is detrimental. On the one hand the fullest exposure of plants to the sun is obtained with:

(i) West and East orientation of the rows when (most commonly) the spacing between vines on a given row is lower than the distance between rows,

(ii) or from North and South orientation when (eventually) the spacing between vines is higher than the distance between rows.

When shade seems more desirable, these directions are reverse. However, most often the rows are laid out in accordance with the shape of the vineyard and the topography.

Water management

Depending on the climatic context and to secondary extent on the soil type, grape growers adopt different strategies for managing grapevine access to water. Schematically three cases can be distinguished from seldom to systematic water deficit.

1) In grapevine growing regions under temperate oceanic climate and/or with deep soils, water is sufficiently available all throughout the period of grapevine development and the competition from a cover-crop can be tolerated by the mean of adapted management practices (Celette et al. 2010; Ripoche et al. 2011). Cover crop can eventually contribute to imposing a mild-water stress with positive effect on grapevine production and berry quality for wine making.

2) In grapevine regions with a more pronounced summer drought, namely ‘Csb and Csc’ Mediterranean climates (Peel et al. 2007), losses of water from evaporation by a cover crop become intolerable. Viticulturists seek to limit water losses by keeping the soil bare and mulching has been recommended (Medrano et al. 2015; Prosdocimi et al. 2016).

3) In grapevine production regions of ‘Csa’ Mediterranean climate and semi-arid climates (Peel et al. 2007), water deficit is endemic. It can be enhanced by shallow and sandy soil types with poor retention. In these contexts, rainfalls cannot sustain grapevine needs for commercial production and are complemented by irrigation. Irrigated vineyards are common in the *New World* and are increasing in the terroits from the *Old world*, though with controversy They rise could tend to stabilize with changes in productive strategies (Acevedo-Opazo et al. 2010).

In addition, grapevine tolerance to drought can be managed on the long term according to the choice of rootstock (Serra et al. 2014; Ollat et al. 2016).

Adaptative strategies against climate change

Average temperatures and CO_2 concentrations are increasing, plus local threats are emerging (Jones et al. 2005; Malheiro et al. 2010; Pachauri et al. 2015) notably more frequent and intense heat waves and droughts in Southern Europe (Jones 2003; Malheiro et al. 2010; Quenol 2014; Pachauri et al. 2015). All around the world, grape and wine production is showing signs of impacts from these new trends (Jones et al. 2005). Phenological stages notably come earlier and are shorter than before (Jones and Davis 2000), and berry composition is changing (Jones and Davis 2000; Duchêne et al. 2010). Also, little is known concerning the evolution of more indirect effects notably on the evolution of the pest and disease risk.

At regional scale new grape cultivation "terroirs" may appear while some of the current ones won't persist unless some changes are adopted (Quenol 2014). For coping with increased temperatures, more frequent droughts and more intense light, both adaptative and resiliency strategies can be considered in viticulture. On the long term, the adaptation strategies mainly consist in varietal changes towards late ripening or drought resistant clones and rootstocks (Jones and Davis 2000; Duchêne et al. 2010; Fraga et al. 2012; Ollat et al. 2016; van Leeuwen and Darriet 2016). On a shorter term, the resiliency strategies consists in modifying the phytoclimate of the vines notably by training the vines on higher trunks, late pruning, sooner harvesting, maintaining the presence of one leaf layer in front of the grape bunches and eventually using UV-B filtering screens (Fraga et al. 2012; Van Leeuwen and Destrac-Irvine 2017). Though irrigation is already increasing, its benefits are more equivocal as it infers important technical and social drawbacks such as high investment costs, soil salinization, competition with food crop and environmental impacts (Van Leeuwen and Destrac-Irvine 2017).

Grape growers tolerance to competition

Woody vegetation surrounding vineyards such as forest or hedges is present in many vineyards but may be considered with mistrust by vine growers on an agronomical basis (Branas 1974). Risks of light reduction and of too severe competitions for water and nutrients with a potential decrease in yield and vigor are notably feared. Nevertheless, some vine growers are also willing to adopt agroecological practices in order to improve the landscape and ecosystem services in their land. The advantages and drawbacks for adopting such practices highly depend upon the winegrower's goals in terms of grape yield and wine style. These factors determine the level of tolerance of the negative impacts from the trees. Three main considerations are successively developed.

First, the grass cover management practices already in place in the vineyards is an important factor to consider. Indeed, grass coverage of the soil is very developed in viticulture under temperate climate. It allows a good conservation of the soil properties reduces the use of herbicides, reduces soil erosion, facilitates the entry of machines, improves the soil water stock replenishment and rises the organic matter content (Celette et al. 2008). Nonetheless, the two main agronomical restricting factors regarding covers are the risks of competition for nitrogen and for water, this latter being intensified under arid climates. Thus the management choices of a grass cover, species, percentage of the surface, duration of the presence, are usually made according to the climatic context, soil type, grape variety and wine style, in order to control the competition for water and nutrients.

Second, when considering intercropping trees in a vineyard, soil type should be considered as well, as it plays a specific and important role in wine production. Indeed, soil type is part of the concept of "terroir" (Vaudour 2002) which identifies the capability of a geographical area to provide distinctive characteristics for the wine product. For an expression of terroir at full potential, the required optimal conditions are both moderate nitrogen and moderate water supplies. These conditions allow an optimal ripening of the grapes (Van Leeuwen and Seguin 2006) and are obtained either naturally in rainfed vineyards of temperate climates or with drip irrigation (Cifre et al. 2005) or fertigation (Fuentes et al. 2008) under semi-arid climates. In general, the rootstock material, the cultivar and the training system of grapevine are all chosen according to soil and environment in order to insure a precocity and sufficient maturity for the grapes.

Third, to develop modern agroforestry vineyards at a large-scale, tree arrangement should allow full mechanization for the main operations on grapevine, namely harvest, crop protection and canopy management. In coming years, these operations could also include the mechanization of the winter vine pruning, knowing the specific equipment and training system currently under development (Gatti et al. 2011).

Consequently, when considering the introduction of trees within a vineyard, the climate, the soil type, the existing practices for vineyard management, and the economic goals of the grape growers already narrow the scopes of possibilities. For research purposes, these factors should all be taken in consideration for accurately comprehending the competition/complementarities between grapevine and trees.

III.2 Sensitivity of grapevine to microclimate throughout its vegetative and reproductive cycles

III.2.1 Overall chronology

As for other crops, microclimate greatly impacts both the vegetative and the reproductive cycle of grapevine through direct and indirect processes. Specifically in the case of viticulture, microclimate

impact must be considered regarding the yield in berries (quantitative criteria) but also regarding berry composition traits impacting wine making (qualitative criteria) (Jackson and Lombard 1993).

The sensitivity of grapevine to microclimate variables evolves throughout the succession of phenological stages.

Prior to budburst, only extremely low temperatures may damage the ligneous part of the vine while a few successive cold days are necessary for releasing latent buds from dormancy. In spring, activated buds burst as soon as exposed to sufficient heat. The temperature threshold for budburst ranges from 8 °C to 11 °C depending on the grape cultivar (Carbonneau 1992). Once budburst occurred, damages from late frost events are feared notably when air temperatures reaches below 2 °C (Mosedale et al. 2015).

After budburst, latent buds grow from the stalk until they reach the stage of 6 spread out leaves. The sum of active temperatures above 10 °C or growing degree day, shows strong correlation with the vegetative growth speed of grapevine, especially when it is weighted by the length of the day (Tonietto and Carbonneau 2004) and is commonly used for predicting key phenological stages such as budburst and veraison (Parker et al. 2013). Photosynthesis of grapevine operates from budburst to leaf fall according a C_3 photosynthetic pathway. It directly contributes to the whole plant biomass, notably to the yield, and indirectly to the sugar content in grapes. Light intensity and leaf temperature are the two main environmental factors controlling the photosynthesis efficiency of grapevine leaves (Kriedemann 1968, 1977; Stoev and Slavcheva 1979; Stoev and Slatcheva 1982). The typical photosynthetic light response of grapevine can be separated into two stages: the first at low photon flux densities (PFD), typically when 9-23 < PFD < 150 $\mu mol\,(photons).m^{-2}.s^{-1}$ where photosynthesis occur but is strongly light-limited, and the second at high photon flux densities, typically above 600 to 1000 $\mu mol.m^{-2}.s^{-1}$, depending on grapevine cultivar, where photosynthesis becomes light-saturated (**Figure 35**).

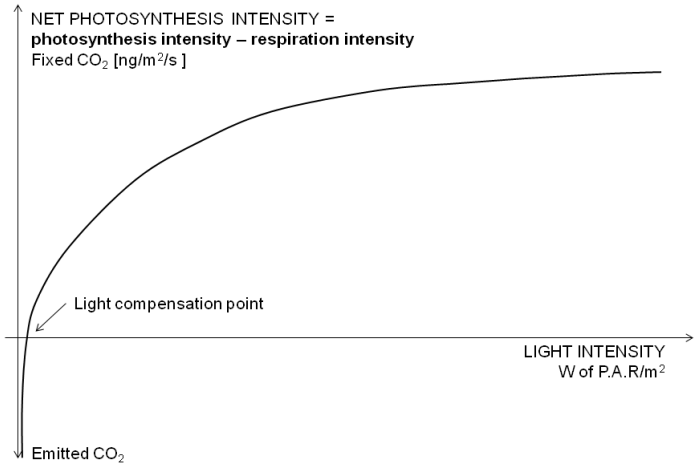

Figure 35: General influence of light intensity on photosynthesis activity (from Champagnol, 1984)

The leaf temperature effect is complementary (**Figure 36**): it controls both photosynthesis rate and saturation point, with an apparent threshold around 10 °C and an optimum estimated at 24°C and 28°C for northern and southern grapevine type respectively (Motorina 1958; Kriedemann and Smart 1971; Greer 2017). Photosynthesis also showed a rapid decline above 35 °C (Kriedemann 1968).

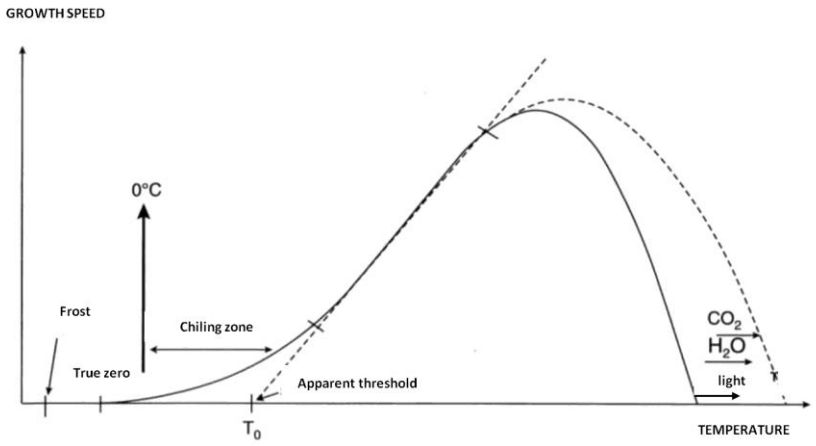

Figure 36: Temperature control on vegetative speed growth – source De Parcevaux and Huber (2007)

The optimal temperature for grapevine flowering, pollination and germination success ranges between 20°C and 30°C depending on grapevine cultivar (Motorina 1958). Flowering is shortened when flowers reach quite high temperatures (25 °C – 35 °C), nevertheless pollination may be depleted either if above 35 °C temperatures suddenly occur, or in case of mean temperatures below 14 °C-15 °C (autorhors reviewed by Vasconcelos et al. 2009). Once flower is fecundated, young fruits grow during summer in several phases and the mitotic growth phase (phase 1) is very proportional to growing degree day accumulation (Parker et al. 2013).

Then berry ripening starts at the end of berry growth which matches with the *veraison* stage: sugar accumulates in berries while organic acids are being degraded. Until harvest, temperature and plant water status are the two main contributing factors to the ripening of berry. In addition, secondary metabolites of particular interest are synthesized in berry skins after veraison. Notably the anthocyanins, the flavonols and the tannins are molecules of phenolic type – flavonoids – with essential role in the color of grapes and wines, in juice reductive-oxydation mechanisms and in the structure and bitterness of wines. Authors reviewed by Downey et al. (2006) observed that their synthesis increases with increasing light and most of all increasing berry temperatures but to a certain maximum above which synthesis is inhibited. Blockage of the synthesis is estimated to occur at 30 °C and 35 °C for night and day temperatures respectively (Kliewer and Torres 1972; Azuma et al. 2012). Free aroma compounds or aroma precursors in grapes are also sensitive to light and temperature like pyrazines (Roujou de Boubée et al. 2000), terpenols and norisoprenoids (Reynolds and Wardle 1993; Marais et al. 1999) or rotundone (Zhang et al. 2015).

III.2.2 Bioclimatic indexes to assess climatic potential for grapevine cultivation

III.2.2.1 Annual trends

Temperature stands as the main climatic variable contributing to the timing of yearly phenophases of grapevine. Indeed, it is a very integrated variable which shows strong correlations with both the yield and the quality of berry composition for wine making at harvest time. As a consequence, several bioclimatic indexes which are based on average temperatures, extreme temperatures or sums of temperatures have been developed in order to compare the climate of various grapevine growing regions and to model grapevine response to regional climate (Le Roux 2017). Following the recommendations of Tonietto and Carbonneau (2004), three bioclimatic indexes, were used for comparing the climatic potential of the three studied vineyards, namely the Heliothermal Index of Huglin, the cool night index and a dryness index. For each studied sites the indexes that were computed using the SAFRAN data recorded from 1990 to 2016 are presented in **Table 6**. These indexes can be interpreted according to the classification of grapevine growing regions from Tonietto and Carbonneau (2004) and shown in **Table 1**. The following subsections provide the characteristics of these indexes and justify choosing them.

Table 1: Classification of the climate of grapevine growing regions according to their heliothermal index, night cold index and dryness index. – From Tonietto and Carbonneau (2004)

Bioclimatic Index	*Type of climate*	*Acronym*	*Class interval*
Heliothermal index of Huglin (HI)	Very warm	HI +3	$HI > 3000$
	Warn	HI +2	$2400 < HI \leq 3000$
	Temperate warm	HI +1	$2100 < HI \leq 2400$
	Temperate	HI -1	$1800 < HI \leq 2100$
	Cool	HI -2	$1500 < HI \leq 1800$
	Very cool	HI -3	$HI \leq 1500$
Night cold index (°C) (CI)	Very cool nights	CI + 2	$CI \leq 12$
	Cool nights	CI + 1	$12 < CI \leq 14$
	Temperate nights	CI – 1	$14 < CI \leq 18$
	Warm nights	CI - 2	$CI > 18$
Dryness index (mm) (DI)	Very dry	DI + 2	$DI \leq -100$
	Moderately dry	DI + 1	$-100 < DI \leq 50$
	Sub-humid	DI-1	$50 < DI \leq 150$
	humid	DI - 2	$DI > 150$

The Heliothermal Index of Huglin

As formerly explained, grapevine vegetative growth occurs between a range of minimum and a maximum temperature, and at a rate which also depends on the temperature. Thus the concept of growing degree-days is commonly used for modeling the phenological succession of grapevine. It consists in cumulating the surplus of daily average temperatures which are above the minimum temperature required for budburst (Galet 2000), photosynthesis and cell division processes. The

minimum threshold of 10 °C is usually used for grapevine though the actual minimum temperature highly depends upon grapevine cultivar (Leeuwen et al. 2008). On the basis of the degree-days principle, Huglin (1978) proposed a slightly modified index, called the Heliothermal Index of Huglin (HI) which takes into account daylight duration as well. It is a very useful index for comparing grapevine growing regions regarding the global heliothermal (heat and light) conditions during the whole vegetative cycle of grapevine (Tonietto and Carbonneau 2004).

The Heliothermal Index of Huglin (HI) is calculated using:

in the Northern hemisphere:

$$HI = \sum_{1^{st}Apr.}^{30^{th}Sept.} \frac{[\,(Tmean_d - 10) + (Tmax_d - 10)] * k}{2} \quad [°C] \qquad [1]$$

with
$Tmean_d$: Daily mean temperature (greater than 10 °C) $[°C]$
$Tmax_d$: Daily maximum temperature (greater than 10 °C) $[°C]$
k : Length of day coefficient – It depends on the latitude. According to Vaudour (2003) the following values are to be used :

Latitude (°N or °S)	
Below 40°00’	$k = 1.00$
from 40°1’ to 42°0’	$k = 1.02$
from 42°1’ to 44°0’	$k = 1.03$
from 44°1’ to 46°0’	$k = 1.04$
from 46°1’ to 48°0’	$k = 1.05$
from 48°1’ to 50°0’	$k = 1.06$

Note that in the Southern hemisphere, the Heliothermal Index is calculated from the 1st October to the 31th March.

Cool night index

The cool night index focuses on the mean minimum night temperatures during the month when ripening usually occurs. This index allows comparing wine-growing regions according to their qualitative potential, notably in relation to the development of secondary metabolites (polyphenols, pigments, aromas) in grapes (Tonietto and Carbonneau 2004). In the Northern hemisphere, the cool night index (CNI) is calculated as the average daily minimum temperature in September:

in the Northern hemisphere:

$$CNI = \frac{\sum_{1^{st}Sept.}^{30^{th}Sept.} Tmin_d}{30} \qquad [2]$$

with
$Tmin_d$: Daily minimum temperature $[°C]$

In the Southern Hemisphere, the cool night index is calculated considering the month of March.

Dryness index

The severity of summer drought and its potential impact on berry ripening and wine tipicity can be assessed using the dryness index proposed by Tonietto and Carbonneau (2004), which has also been recently used by Pedrosa et al. (2017) for comparing grapevine growing regions. The dryness index is based on a simplification of the potential water balance of the soil index of Riou et al. (1994). It takes into account the climatic demand of a standard vineyard, the evaporation from bare soil and rainfalls without considering surface runoff or drainage.

The index is calculated the following way. For each month from April to September (northern hemisphere) the soil water reserve at the end of the month is estimated by:

in the Northern hemisphere:

$$W_m = W_{m-1} + P_m - T_{v_m} - E_{s_m} \quad with\ m = April\ to\ September \qquad [3]$$

with

$$T_{v_m} = ETP_m * k \qquad [4]$$

and

$$E_{s_m} = \frac{ETP_m}{N} * (1 - k) * JP_m \qquad [5]$$

and

$$JP_m = minimum\left(\frac{P_m}{5}, N\right) \qquad [6]$$

W_m : Soil water reserve at the end of the month m (mm)

P_m : Monthly cumulated precipitations (mm)

T_{v_m} : Potential evapotranspiration of the vineyard (mm)

E_{s_m} : Direct evaporation from the soil (mm)

ETP_m : Monthly cumulated potential evapotranspiration (according to Penman method) (Penman 1948) (mm)

k : Coefficient of radiation absorption by grapevine, which depends on grapevine architecture. The adopted values of *k* are:

m = April	$k = 0.1$
m = May	$k = 0.3$
m = June to Sept.	$k = 0.5$

N : Number of days in the month

JP_m : Rainfall per month, if below N (mm/5)

In the present study, $W_0 = W_{March}$ was computed as the average water content in the root soil horizon over the last seven days of March. For the whole period from 1990 to 2016, the median value and the standard deviation of $W_{March}^{1990\ to\ 2016}$ at the three study sites are provided in **Table 6**.

III.2.2.2 Risk of extreme temperatures

Heat risk

The risk of extreme heat was assessed considering three indices:

- Hot days: the total number of days in the year when the maximum daily temperature (T_{max}) is greater or equals 30 °C.

- Very hot days: the total number of days in the year when the maximum daily temperature (T_{max}) is greater or equals 35 °C.
- The severity of heat stress: accumulated degree days above 28°C. The severity of heat stress (SHS) was calculated the following way:

in the Northern hemisphere:

$$SHS = \sum_{1^{st}Apr.}^{30^{th}Sept.} T_{mean_d} - 28 \quad [°C] \qquad [7]$$

with $Tmean_d$: Daily mean temperature above 28°C [$°C$]

Frost risk

Similarly to Mosedale et al. (2015), frost risk was assessed considering three indices:

- Days of frost: the total number of days in the year when the minimum daily temperature (T_{min}) is lower or equals 0°C.
- Frequency of late frost: the number of days after budbreak when the minimum (T_{min}) is lower or equals 0°C. As no information concerning budbreak time was available, the 1st April was used as an approximation for all years and study sites.
- The severity of late frost: accumulated degree days below 2°C after budbreak. As for the frequency of late frost, the period used for cumulated was from 1st April to the 30th September for every years and study sites. The severity of late frost (SLF) was calculated the following way:

in the Northern hemisphere:

$$SLF = \sum_{1^{st}Apr.}^{30^{th}Sept.} |2 - Tmean_d| \quad [°C] \qquad [8]$$

with $Tmean_d$: Daily mean temperature below 2°C [$°C$]

III.2.3 Fungi disease risk

II.3.1 Environmental control of fungi diseases

Fungi diseases are of great concern in viticulture as they may reduce plant growth and vine yield and may affect the fruit and wine quality (Thind et al. 2004; Williamson et al. 2007; Gadoury et al. 2012). In response, important amounts of fungicides are spread with economical costs as well as sanitary and environmental damages.Whether introducing trees in a vineyard could increase the risk of fungi diseases is a frequently and legitimately raised question from viticulturists Indeed, meteorological conditions are one of the main drivers of their occurrence and specific microclimatic conditions within a vineyard may generate patterns of prevailing occurrence. Microclimatic variables directly influence fungi disease risk in three ways:

- they trigger prime infection from survived mycelium in the ground and dead organs,
- they control the growth and germination rate of conidiophores,
- and they fuel the propagation of conidia from one plant to another (intra-plot spreading) and from one plot to another (local spreading).

In addition, the influence of the microclimate on fungi disease risk is also indirect,

i) through impacting the phenological state and vigor of grapevine,

ii) through influencing the composition in flavonoids (anthocyanins and flavonols) which are recognized as antifungal agents (Harborne and Williams 2000),

iii) and through extending or shortening the duration of efficiency of treatments, notably as wind and water drops can wash away the contact fungicides.

Given the heterogeneous patterns of microclimate that trees may generate within a vineyard (**Figure 30**), the following paragraph assesses the potential impact of agroforestry on the risk of fungi diseases. For sake of concision, it focuses mainly on the potential direct impacts of trees. Among fungi diseases affecting grapevine, Downy Mildew, Powdery Mildew and Grey Mold diseases are found in most grape growing areas in the world. They reduce plant growth and vine yield and may affect the fruit and wine quality (Thind et al. 2004; Williamson et al. 2007; Gadoury et al. 2012).The specific risk of development of these three diseases within an agroforestry vineyard is successively considered. Risk assessment will be performed knowing that the gravity of diseases jointly depend of the rate of infection, the rate of growth of the mass of mycelium and the rate of sporulation i-e of dispersion (Gadoury et al. 2012).

II.3.2 Downy Mildew disease (Plasmopara viticola)

Plasmopara viticola is grapevine pathogen responsible for **downy mildew.** As illustrated on **Figure 37,** its prime occurrence and survival necessitate high humidity and soaked plant organs, while mild temperatures also have a positive effect but of secondary importance (Rouzet and Jacquin 2003; Rossi et al. 2008). Its dispersion relies on the action of rainfall water drops (Rossi et al. 2008; Rossi and Caffi 2012). Based on this knowledge, the two following assumptions can be made concerning the risk of downy mildew in an agroforestry vineyard:

(i) The shaded areas (zone 1N) and sheltered areas (zones 2W and 2L) of the vineyard may be at higher risk of survival of the zoospores after dew or rain events because of the longer wetness duration than that in the rest of the vineyard.

(ii)Grapevine stocks located directly under the tree canopy are submitted to the throughfall of water while and after rainfalls occurrence. The decrease of the raindrop kinetic energy as well as the longer dripping of rain drops than that in the rest of the vineyard may increase disease dispersion from this area.

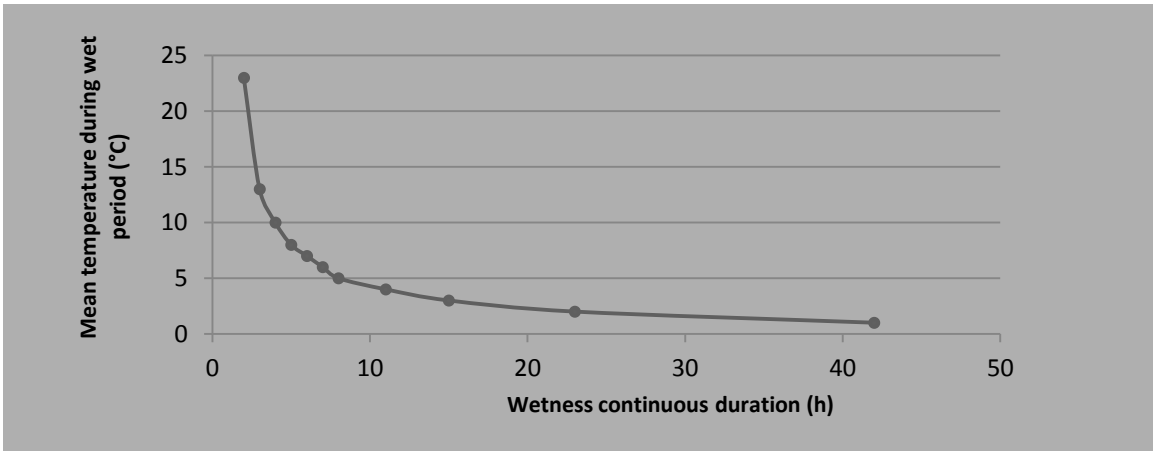

Figure 37: Thresholds of temperature and leaf wetness duration for dispersion of the conidia of *Plasmopara viticola*, the fungal pathogen agent of Downey Mildiou, according to the mechanistic model of Rossi et al (2008)

II.3.3 Powdery Mildew disease (Uncinula necator)

Uncinula necator is a biotropic ascogenous fungus responsible for grapevine powdery mildew disease. It affects all the green parts of vine, leaves, inflorescence and berries. Its reproductive cycle is particularly sensitive to moderate temperatures, with a minimum, optimum and maximum temperatures for infection and colony growth of respectively 10 °C, 22 °C and 30 °C (Calonnec et al. 2005, 2008). On the contrary light inhibits its development through the combined deleterious effects of warm temperatures and UVs (Austin and Wilcox 2012). Eventually dry conditions may trigger the release of conidia (Willocquet and Clerjeau 1998; Thind et al. 2004). Both wind and raindrops from light rainfalls (tap and puff effects) have major effects in dispersing conidia at the intra-plot scale (Willocquet and Clerjeau 1998; Willocquet et al. 1998). By combining the latter review of knowledge with the potential climatic patterns identified in **Figure 30**, the following assumptions can be made:

(i) In the shaded zone (zone 1N), the risk of development of powdery is ambiguous: on the one hand, it could be higher than in the rest of the vineyard due to the combined effect of lower day time temperatures and light depletion (Halleen and Holtz 2001; Zahavi et al. 2001; Austin and Wilcox 2012). Also within this zone, grapevine stocks located bellow the tree canopy may be characterized by a faster spreading of the disease from one to another of their leaves because of the reduced kinetic energy of the raindrops (Willocquet and Clerjeau 1998). On the other hand, the increased wetness duration of leaves and more humid conditions may temper the disease.

(ii) In the insolated zone (zone 1S), the risk is ambiguous as well: the dry conditions may trigger the disease but the rate of conidia release would deplete as soon as the temperatures would reach above the optimal temperature of 22 °C (Halleen and Holtz 2001; Calonnec et al. 2008).

(iii) Finally sheltered zones (zones 2W and 2L) the risk could be reduced due to the long leaf wetness duration, the warm temperatures and a reduced dispersion by the air flow (Willocquet et al. 1998).

II.3.4 Grey Mold disease (Botryotinia fuckelina)

Botryotinia fuckelina (*Botrytis cinerea* teleomorph) is the airborne fungi pathogen with necrotrophic lifestyle responsible of the Grey Mold disease of grapevine. In grape, the conidia infect mainly the flower receptacle where it can remain as masses of mycelium in a quiescent state. When its germination and sporulation is reactivated by environmental conditions, these latter provoke the death of grapevine flowers, the mummification of fruits and trigger secondary infections within the vineyard (Williamson et al. 2007). Long wetness duration and low temperatures of the plant organs are the main parameters triggering infection and conidia survival (Broome et al. 1995). Also, in the absence of water droplets, very high air relative humidity (above 93 %) could also trigger conidial germination and infection of flowers (Williamson et al. 2007).

Consequently, the risk of Grey Mold disease development could be significantly higher in an agroforestry vineyard than in a monocropped vineyard as both wind sheltered areas and shaded areas may create preferential spots of prime infection and fungi sporulation. In both areas it is due to the longer wetness duration on top of grapevine organs. In the shaded area, it combines with a positive effect on the fungi of chill temperatures, light depletion and light composition in shade (Schumacher 2017). Interestingly, Broome et al. (1995) mention that in Chile, by the time of their publication, most table grapevines were trained onto overhead arbors, a *traditional* form of agroforestry vineyard, the term "arbors" being though ambiguous. Because of shade and shelter, the fruit in theses canopies experience high humidity, low temperatures and low light infiltration conditions so the risk of bunch rot is very high. As a consequence *Botrytis* fungus is controlled by applying from 8 to 10 fungicides spays per year.

Nonetheless spreading of the disease may eventually be reduced within the vineyard because of reduced air flow. Also, the impact of Grey Mold will actually depend on the very specific microclimate undergone by berries. Consequently, the microclimate generated by the architecture of grapevine itself may be on greater influence on the risk of disease than that of intercropping trees (English et al. 1989).

II.3.5 Conclusions on the potential fungi disease risk in agroforestry vineyards

In short, tree canopy covering grapevine canopies, shaded grapevines or sheltered grapevines may create preferential spots of prime infection and fungi sporulation in an agroforestry vineyard. In the case of many fungi diseases such as the Grey Mold disease, the Downy Mildew and Anthracnose disease (Thind et al. 2004) it is mainly due to the lack of ventilation under humid conditions, leading to longer wetness duration on top of the plant organs. The case of Powdery Mildew is more specific: trees could have a neutral to unknown effect on this disease as it requires relatively dry conditions and moderate temperature and these two conditions may seldom be simultaneously met in the vicinity of

trees. Finally, at the inter-plot scale, spreading of fungi diseases might eventually be delayed because trees can slow down the air flow.

From these latter developments, two recommendations can be made regarding the prophylaxis of an agroforestry vineyard. Firstly, it suggests that on-site monitoring of disease occurrence to preferentially target the zones in the very vicinity of the trees, namely the shaded northern zones (zone 1N) and insolated southern zones (zone 1S). Secondly, when the risk of fungi disease is already high, planting dense and continuous tree rows (dense hedges) as well as planting grapevine directly under the tree canopy are discouraged.

Finally, the previous assumptions seems important to be considered in light that the architecture of grapevine itself has a major impact on the microclimate undergone by the leaves, the flowers and the berries of grapevine. Consequently grapevine canopy management may actually play a greater influence on the risk of disease than that of intercropping trees (English et al. 1989).

III.3 Consequences on yield and berry quality

III.3.1 Overall view of existing knowledge

As for other crops, climate is a major factor of grapevine cultivation. Both its vegetative and reproductive cycles respond to solar radiation, wind regime, temperature, humidity and plant water status (Carbonneau et al. 2015). Through the microclimatic effects mentioned previously, intercropping trees with grapevine may impact both grape yield (the amount and weight of berries) and the grape quality for wine making (berry composition in sugar, polyphenols, aromatic components and organic acids)

The main climatic patterns expected within an agroforestry vineyard were presented in Grapevine response is complex to assess because (i) several factors combine, (ii) climatic patterns vary in space and time and (iii) some thresholds and optimum values, notably of temperature and PAR, may or may not be crossed, depending on the location and season. Nevertheless the very exhaustive literature on the agrometeorology of grapevine may give some clues. For each microclimate pattern identified in **Figure 30**, **Table 3** summarizes the most likely yield and berry composition patterns, based on a selection of experiment results and reviews from the literature. Precisions concerning the context of validity of these references are given below the table.

Impacts on grapevine phenology might also appear in the area of climatic influence of trees but do not figure in **Table 3**. In the case of evergreen trees, budburst may happen earlier in insolated or wind sheltered zones whereas it may be delayed in the wake zone (Carbonneau et al. 2015). Also, with any kind of trees, grapevine vegetative growth might be more rapid and flower sooner for grapevine located in sheltered zones due to the higher amount of accumulated degree days (Van Eirman et al. 1964; Guyot 1989). In addition, ripening of berries could start sooner for grapevines submitted to a more intense water stress (Carbonneau 1992; Carbonneau et al. 2015) i-e potentially for grapevine located in the insolated zone 1S, in the wake zone 3, and eventually in the competition zone (zone 1N), depending on the tree water regime. Nevertheless there is little information concerning the importance of such potential variations notably in terms of time difference and spatial resolution. Also these hypotheses are mainly based on general knowledge at local scale. For these reasons, they remain more hypothetical at the microclimatic scale and do not figure in **Table 3**.

Table 3: Most likely expected agronomic consequences within an agroforestry vineyard. Literature references are classified per microclimatic zones which are likely to appear within an agroforestry vineyard. The tendencies of quantitative and qualitative criterion compared to that in a monocropped vineyard are symbolized as a rise (↑),as equivalent (=) or as a decrease (↓).Precisions concerning the context of validity of these references are given below the table, notably the grapevine cultivar – if provided-, the main features for experimental work and the main topic for reviews.

WS = Water stress	Plant & organ biomass			Berry composition		
	Extreme event damages	**Berry and Cluster number (BN / CN)**	**Biomass, Cluster Weight (CW), Berry weight and volume (BW/BV)**	**Soluble solids (°B), Sugars, and nitrogen (N)**	**pH / Titrable Acidity (TA)**	**Secondary metabolites Anthocyanins (As), Flavonols (F)**
ZONE 1N Shaded	↓ Radiation frost risk ↑ risk of flower buds fall [1]	↓ Bud fruitfulness [2–5] ↓ BN [2,6]	↑ Leaf density, [7] ↓ total, root and stems biomass [8] ↓ BW [7–11], ↓ BV [9], CW ↓ [7]	↓ °B [7,11,12] ↑ N and arginine [11]	↑ pH [7], ↓ pH[11] ↑ TA as malate concentration ↑ [7,9–11]	↓ As [7,9,12–14] , ↓ As for Pinot Noir, = for Cardinal [15] Modified composition in As [10,13,16–21] Lower phenolic accumulation [9,22] ↓ F content [19,20,23] ↓ Overall wine ranking [7]
ZONE 1S Insolated	↓ Radiation frost risk [24,25] ↑ Extreme heat damages	↑ flower initiating [1] ↑ BN [1]	Until 30°-35°C: ↑ shoot growth, ↑ total biomass and ↑root biomass proportion [8] ↑ BV [1],	↓ °B [12]	↓ TA [12] and ↓juice pH [12]	↓ As [12,13,19,26–29] Modified composition in As [17–20] ↓ total phenolics [12] ↑ F [19]
ZONE 2W Quiet windward	↑ pollen soaking risk [1]		↑ BW [12]	↑ °B [12]	↓ TA especially for cabernet sauvignon [12] = pH for Grenach and ↑ pH for Cabernet Sauvignon [12]	↓ As, notably in sunny and warm climates [12] ↓ total phenolics, notably in sunny and warm climates [12]
ZONE 2L Quiet leeward			↑ BW [12]	↑ °B [12]	↑ TA [12] ↓ TA especially for Cabernet Sauvignon [12] = pH for Grenach and ↑ pH for Cabernet Sauvignon [12]	↓ As, notably in sunny and warm climates [12] ↓ total phenolics, notably in sunny and warm climates [12]
ZONE 3 Wake	↑ drought			Sugars ↑ if mild WS at ripening Sugars ↓ if severe WS at ripening [1,30–32]		↑ As [26–28,33] whereas ↓As [29]

Sources

a [1] (Carbonneau 1992)
s2 [2] (May 1965) *Sultana*
s2 [3] (May and Antcliff 1963) *Sultana*
s1 [4] (Sánchez and Dokoozlian 2005) *Chardonnay* and *Cabernet Sauvignon*
d2 [5] (Wagner 1966) *Sultana*
d1 [6] (Baldwin 1963) *Sultana*
s1 [7] (Archer and Strauss 1989) *Cabernet Sauvignon*
d2 [8] (Buttrose 1969) *Muscat, Gordo Blanco, Rhine Riesling, Shiraz, Ohanez , Sultana*
d2 [9] (Dokoozlian and Kliewer 1996) *Cabernet Sauvignon* and *Pinot noir*
s2 [10] (Koyama and Goto-Yamamoto 2008) *Cabernet Sauvignon*
d2 [11] (Kliewer and Lider 1970) *Cardinal* and *Pinot noir*
s1 [12] (Bergqvist et al. 2001) *Cabernet Sauvignon* and *Grenache*
d2 [13] (Azuma et al. 2012) *'Pione'* (*V. x labruscana*)
s2 [14] (Niu et al. 2013) *'Jingxiu'*
d2 [15] (Kliewer 1970) *Pinot noir* and *Cardinal*
s3 [16] (Tarara et al. 2008) *Merlot*
s1 [17] (Price et al. 1995) *Pinot noir*
s1 [18] (Haselgrove et al. 2000) *Shiraz*
d1 [19] (Spayd et al. 2002) *Merlot*
a [20] (Downey et al. 2006)
s2 [21] (Downey et al. 2008) *Shiraz*
s2 [22] (Keller and Hrazdina 1998) *Cabernet Sauvignon*
d2 [23] (Buttrose et al. 1971) *Cabernet Sauvignon*
m [24] (Chiapale 1975) Hedges
b [25] (Guyot 1989)
d1 [26] (Mori et al. 2005) *Pinot noir*
d1 [27] (Mori et al. 2007) *Cabernet Sauvignon*
d1 [28] (Yamane et al. 2006) *'Aki Queen' (Vitis labrusca x V. vinifera)*
d1 [29] (Kliewer and Torres 1972) 'Cardinal', 'Pinot noir', 'Cabernet Sauvignon' and 'Tokay'
w [30] (Hardie 1980) ?
c [31] (Smart and Coombe 1983)
c [32] (Kuhn et al. 2013)
w [33] (Ojeda et al. 2002) *Syrah*

Notation

a review on agro-meteorology of grapevine (*Vitis vinifera*)
b review on natural windbreaks microclimatic effects
c review on water stress effects on grapevine
s1 shading experiments on grapevine: natural shade generated from trellis system / pruning / orientation / selection at harvest
s2 shading experiments on grapevine: net above vines / cloth or boxes around bunches
s3 experiment focusing on light effect on grapevine with grapevine grown on field with different orientations and forced convection for cancelling temperature effect
d1 assessment of temperature/light effect on grapevine: through correlation tests with meteorological conditions over several years of growth
d2 assessment of temperature/light effect on grapevine: through vine cultivation in phytotron - or in vitro berry cultivation in case of Azuma et al. (2012)
m Modeling of radiation budget
w water stress effect on grapevine assessed through irrigation scheme experiment

III.3.2 Shading experiments

The consequences of incident light reduction on vine and grapes were analyzed through experiments reported in **Table 3 (row 1 Zone 1N Shaded**). Modifications of the light regime were applied either naturally (natural shade from shading system, canopy pruning, orientation of the rows, selection of naturally shaded plants), or by artificial installations (net applied above vines, cloth or boxes put around part of the plants notably bunches, growth in phytotron).

Among these references experiments from Archer and Strauss (1989) stands particularly informative as it considered the natural shade from vegetation in the vicinity of vines. Two levels of shade were distinguished, a light shade (0.8 Compensation Point) and an intense shade (0.1 C.P).They were compared to a full sun control (1.4 C.P.). In this context, the density of the canopy showed an increase of a twofold and threefold factor respectively, suggesting that light reduction triggered compensating response from the vine. In addition, the yield was depleted by 25 % and 50 % respectively, because of the combined effect from decreased berry masses and bunch masses. These authors also reported a reduction of skin color, of sugar content (by 8 % and 12 % respectively), a rise of pH (by 3 % and 17 % respectively), a rise in malic acid (by 16 % and 22 %) but no change in tartric acid. Applying a standard procedure from the Viticultural and Oenological Research Institute, an experienced panel also measured a decrease in the wine ranking.

In addition, Kriedemann (1968) focused on mechanisms at leaf scale on *Sultana* grape. This author reported that a partial illumination of 8.5 % of the total leaf area enabled a photosynthetic rate equivalent to 25 % of the rate when the entire lamina was illuminated. Also, applying shade specifically on berries had a negative impacts during stages I and II of fruit developments but not necessarily on the third and final stage (Dokoozlian and Kliewer 1996). It systematically generated a decrease in berry size and weight while at the whole plant level, elevated durations of bright sunshine and of sums of daily maximum temperatures had a positive effect on berry weight through their control of the mitotic cellular divisions occurring in the initial stages of berry development (May 1965; Wagner 1966; Champagnol 1984).

III.3.4 Intense wind / sheltering experiments

Air movements within the vineyard affects the growth and development of grapevine as well as the insect activity, the population growth and the development and dispersal of diseases. The effects of wind can be divided into two categories. Firstly, the air flow regulates the microclimate of grapevine. It operates through (i) controlling the exchanges of heat and water vapor at the leaf surfaces and (ii) through the diffusion of heat and water vapor between the air spaces located inside the canopy and the free air. Secondly, the air flow can play a direct mechanical action on the organs of grapevine itself, as well as on soil particles, insects, fungi and pollen.

Experiments reported in **Table 3 (row 3&4 Zones 2W and 2L**) synthezise the effects of wind speed reduction. Strong wind and turbulent air flows can cause mechanical damages on grapevine especially on the upper leaves (Branas 1970). In addition, grapevines grown on windy sites show undesirable characteristics such as stunted growth, malformation and actual breakage at the graft or bud union (Carbonneau et al. 2015). Contrary to wind protected fruit orchards, yet little is known on the performances of wind-protected vineyards. In wind protected fruit orchards, early fruit tree growth is enhanced especially on dwarf and semi-dwarf rootstocks. In this case, an early development of the sheltered plants is critical in meeting early production objectives which maximize economic return (Norton 1988). The wind sheltering effect of trees may have ambiguous impact regarding plant water regime. In a windbreak protected vineyard, Freeman et al (1982) observed higher stomatal conductance which allowed a longer photosynthetic period during the day compared to non sheltered areas. Nonetheless, more negative leaf water potential also suggested a more intense water stress.

III.3.5 Consequences of grapevine water stress

Similarly to light and temperatures, the impact of water stress on vine is ambiguous as well. It notably depends on the time of its occurrence and on the intensity of the stress **(Figure 38)**. In short, existing results agree that a moderate water stress is profitable to grapevine production and wine quality while an intense water stress and an early occurrence can affect the net carbon assimilation rate of grapevine and consequently the yield and the wine quality, particularly in rainfed vineyards. For further details, the excellent revue by Smart and Coombe (1983) is recommended to the reader.

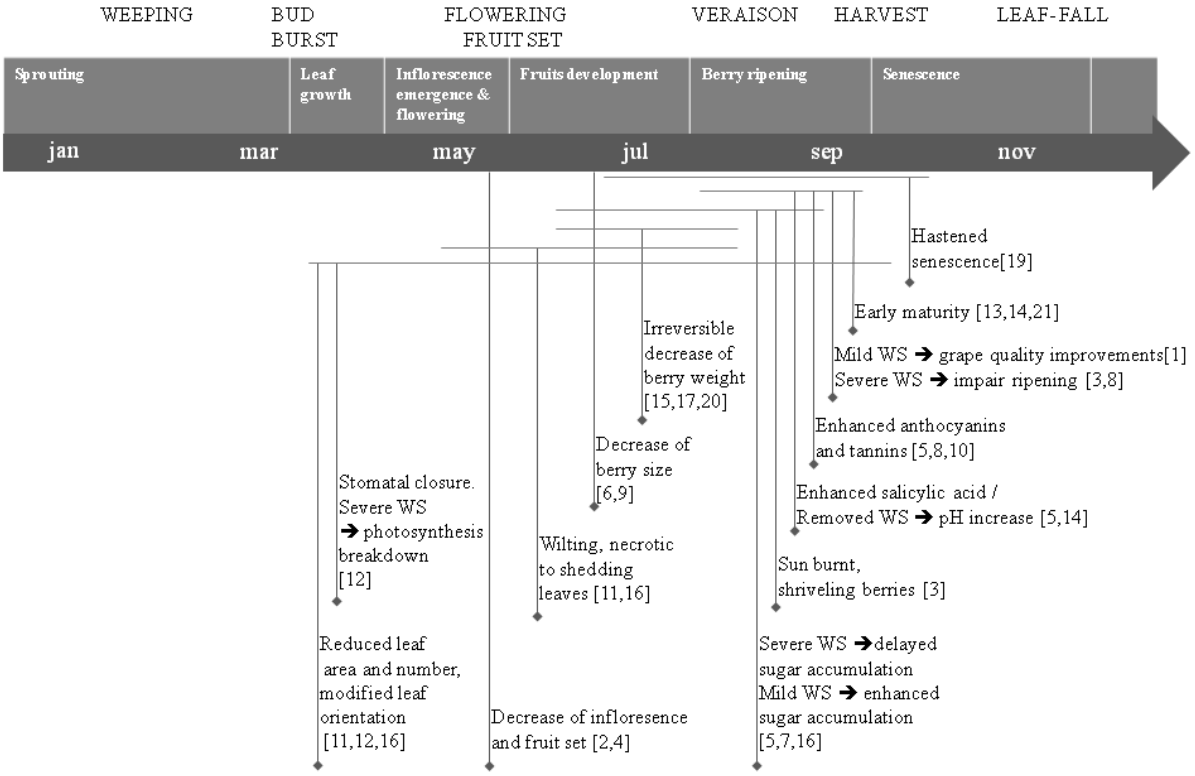

[1] Acevedo-Opazo C, Ortega-Farias S, Fuentes S (2010) Effects of grapevine (Vitis vinifera L.) water status on water consumption, vegetative growth and grape quality: An irrigation scheduling application to achieve regulated deficit irrigation. Agric Water Manag 97:956–964. doi: 10.1016/j.agwat.2010.01.025
[2] Alexander DM (1965) The effects of high temperature regimes or short periods of water stress on development of small fruiiting Sultana vines. Aust J Agric Res 817–823.
[3] Ashizawa M (1964) Studies on drought damage to grapevine in the region of Kagawa prefecture. Kagawa University
[4] Buttrose MS (1974) Fruitfulness in grapevines: effects of water stress. Vitis 299–305.
[5] Carbonneau A (ed) (1992) Agrométéorologie de la vigne en France. Commission of the European Communities, Brussels
[6] Coombe BG (1960) Relationship of growth and development to changes in sugars, auxins, and gibberellins in fruit or seeded and seedless varieties of Vitis vinifera. Plant Physiol 241–250.
[7] Hardie W. (1980) The influence of vine water status on development of grape berries (Vitis vinifera L.). Universiy of California
[8] Hardie W., Considine J. (1976) Response of grapes to water-deficit stress in particular stages of development. Am J Enol Vitic 55–61.
[9] Harris J., Kriedemann P., Possingham J. (1968) Anatomical aspects of grape berry development. Viitis 106–119.
[10] Hendrickson A., Veihmeyer F. (1951) Irrigation experiments with grapes. Bull Californian Agric Exp Stn 1–31.
[11] Kozlowski T. (1976) Water relations and tree improvement. In: Cannell MC., Last FT. (eds) Tree Physiology and Yield Improvement. Academic Press, New York, pp 307–327
[12] Kriedemann P., Buttrose MS (1971) Chlorophyll content and photosynthetic activity within woody shoots of vitis vinifera. Photosynthetica 22–27.
[13] Neja R., Wildam W., Ayers R., Kasimatis A. (1977) Grapevine response to irrigation and trellis treatments in the Salins Valley. Am J Enol Vitic 16–26.
[14] Seguin G (1975) Alimentation en eau de la vigne et composition chimique des moûts dans les grands crus du Médoc. Phénomènes de régulation. Connaiss Vigne Vin 22–34.
[15] Smart RE (1974) Photosynthesis by Grapevine Canopies. J Appl Ecol 11:997. doi: 10.2307/2401759
[16] Smart RE, Coombe BG (1983) Water relations of grapevines. In: water deficits and plant growth. Academic Press, pp 137–196
[17] Vaadia Y, Kasimatis A. (1980) Vineyard irrigation trial. Am J Enol Vitic 88–98.
[18] Van Rooyen F., Weber H., Levin I (1980) The response of grapes to a manipulation of soil-plant-atmosphere continuum. I. Growth, yield, and quality responses. Agrochemophysica 59–68.
[19] Van Zyl J., Weber H (1977) Irrigation of Chenin Blanc in the Stellenbosch area within the framework of the climate-soil-water-plant continuum. In: Procedure Symposium on Quality Vintage. Stellenbosch, South Africa, pp 331–350
[20] Veihmeyer F., Hendrickson A. (1950) Grapes and decidious fruits. Calif Agric 13–18.
[21] Wildam W., Neja R., Kasimatis A. (1976) Improving grape yield quality with depth controlled irrigation. Am J Enol Vitic 168–175.

Figure 38: Review of knowledge concerning the consequences of water stress on grape and wine production depending on its occurrence throughout the vegetative and reproductive cycle of grapevine.

III.4 Conclusions

This review of literature highlighted that as for other crops, climate is a major factor of grapevine cultivation. Both its vegetative and reproductive cycles respond to solar radiation, wind regime, temperature, humidity and plant water status in an integrative way. Climate factors operate either directly through controlling cellular growth, metabolism, transpiration and physical damages, or indirectly through influencing pest and diseases occurrence and pollination success. As a consequence, microclimatic modifications from trees in an agroforestry vineyard may impact both grape yield (the amount and weight of berries) and the grape quality for wine making (berry composition in sugar, polyphenols, aromatic components and organic acids) but in indeterminate/ambiguous proportions. Indeed, grapevine yield and quality traits respond to the aerodynamic, radiative and water status of grapevine which may either amplify or compensate each other.

Similarly to other agroforestry system, too severe competitions for light and for water stand as the two prime concerns for intercropping trees within vineyards. In order to relevantly document these risks, the meteorological and soil context as well as the practices in terms of the vine canopy and grape growers objectives should all be taken into consideration. In addition to direct competition for resources, impacts from trees can be expected from modifications of the microclimatic variables. For methodological purposes, the temperature stands as a synthetic proxy of prime interest.

On the one hand, temperature reacts to variations in the visible light regime (typically shading), to the emission of long wave radiations, to variations in the wind regime through the wind contribution in the heat fluxes in the soil-plant-atmosphere continuum and to the plant water status. Concerning this latter case, two main cases can be opposed: the plant temperature is regulated through transpiration of water (dissipative flux of latent heat) when there is sufficient water in the ground to supply the climatic demand, whereas the plant temperature rises (dissipative flux of sensible heat) when stomata closure happens as a protective mechanisms against desiccation. On the other hand, the temperature is involved in most of the physiological, reproductive and metabolic processes responsible for the vine vigor, the yield in berries and berry composition. It also indirectly impacts the physiology of the vine and the yield in berries through impacting the biological cycles of pests and diseases.

Finally it can be concluded that both the dynamics of the microclimate variables and the occurrence of extreme events are worth considering. In order to understand their impacts on grapevine production, they should be put in regards to the phenological stage of grapevine at the time of their occurrence. Concerning the potential impacts of trees on extreme events, our review motivates us to assess in priority the risk of late frost after budburst and the risk of heat chock or severe droughts during berry ripening.

CHAPTER IV
Experimental approach

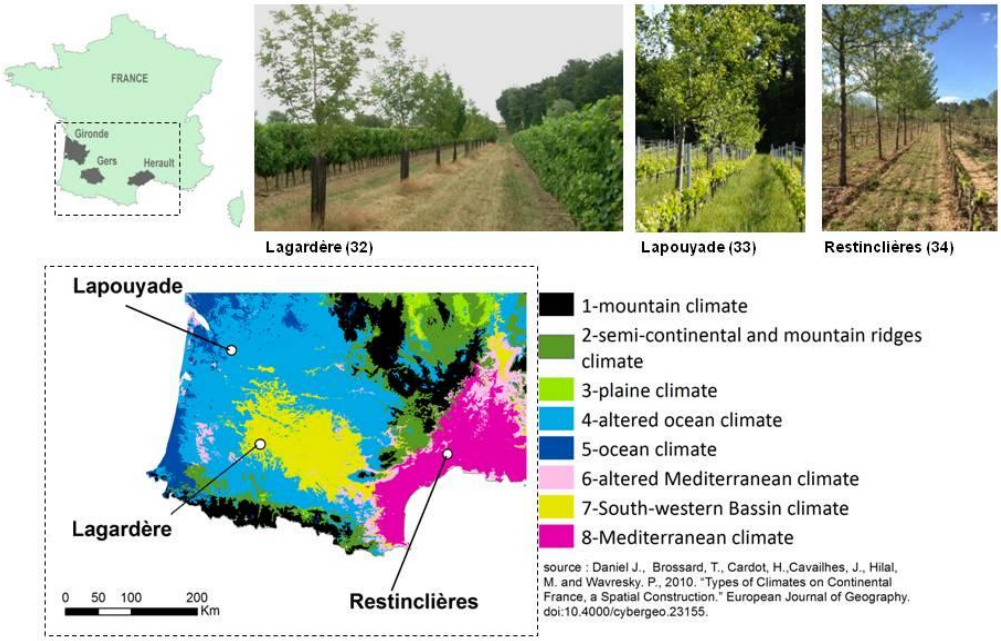

	Lagardère (32)	Lapouyade (33)	Restinclières (34)
Location	Gers 0°19'14,513"E/43°49'34,996"N EARL Dubos	Gironde 0°17'29,417" E/45°5'9,559''N Domaine Emile Grelier	Prades-Le-Lez, Hérault 3°51'28,317"E / 43°43'33,02"N Domaine de Restinclières
Climate	Oceanic to humid continental	Oceanic	Mediterranean
Altitude Slope Selected area	175 m 3.0 % 3.4 ha	70 m 4.6 % 7 ha	85 m 5.4 % 11 ha
Soil	Silty clay loam 1:2 middle row with grassy cover 1:2 middle row with bare ground	sandy loam All with grassy cover	sandy clay loam with 50 % calc. rocks All bare ground
Vine Root-stock Density Year of plantation Orientation	Vitis vinifera cv. Sauvignon gris (W) 3309C 2.5 m x 1 m (4000 stocks/ha) 2008 W/E (-22°W)	Vitis vinifera cv. Merlot (R) 101-14 and Riparia 1.5 m x 1 m (6600 stocks/ha) 2002 N/S (- 9.8°N)	Vitis vinifera cv. Grenach (R) R 110 2.5 m x 1 m (4000 stocks/ha) 1997 B3:W/E (+18.3°W) - B4: N/S (+19.4°N)
Trees Year of plantation Arrangement Planting spacing	*Sorbus domestica*, *Sorbus torminalis* and *Pyrus pyraster* 2008 alleys d_1 =10 m - d_2 = 20m – d_V = 3.25 m	Mixed fruit and timber wood trees 2009 inside vine rows, replacing one stock d_1 =5 m - d_2 = 60m – d_v = 1.5 m	*Sorbus Domestica* (plot B3 and B4) Other timber wood trees 1997 alleys d_1 =3 m - d_2 = 15m – d_V = 3.75 m (LD) / d_V = 2.5 m (HD)
Terroir	« Côtes de Gascogne»	"Bordeaux Supérieur" Organic label	« Languedoc»

Figure 39: Three study vineyards in Southern France: climatic trends, vine and trees characteristics, spacing and soil management. Abbreviations: *d1*: distance between trees on the same tree row; *d2*: distance between tree rows; *N/S*: North/South oriented; *W/E*: West/East oriented

IV.1 Introduction

The first months of Ph D were dedicated to the identification of relevant study sites and the design of an experimental campaign. three study vineyards with agroforestry practices were selected in Southern France - thanks to the advises of Emilie Bourgade (A&P 32), Thierry Duffourcq (IFV 32), Josepha Guenser (Vitinnov), William Trambouze (CA 34), Lydie Duffours (INRA UMR System) and Christian Dupraz (INRA UMR System). They are respectively located at Lagardère (Gers-32), Lapouyade (Gironde-33) and Domaine de Restinclières (Prades-Le-Lez, Hérault, 34) (**Figure 39**) and are further referred as *Lagardère (32), Lapouyade (33)* and *Restinclières (34)*. This panel covers diverse climatic context, diverse vine production practices and agroforestry arrangements

In 2015, from vine veraison to harvest, a short campaign of data acquisition serving much as a trial was carried out at Lagardère (32). Then longer and more complete campaigns were carried out in 2016, from a couple of weeks before budburst until harvest at the three study sites. The collected data set mainly gathers (i) meteorological records, (ii) distributed records of temperatures measured in the foliage/bunch zone/root zones of grapevine, (iii) distributed measures of the yield and composition of grapes at harvest and (iv) a stack of very high resolution images from punctual drone flights, which covers the visible-near visible and thermal infrared spectrum. Much efforts were put into the settlement of data loggers and data collection in order to provide the most unbiased and useful data.

The following content of this chapter is structured in three parts:

- (i **Setting context**) first it presents the geographical and meteorological context of the three study sites and exposes their main characteristics regarding the vegetation characteristics and management practices;
- (ii **Justifying experimental choices**): then it presents sensors specifications and the strategy of distribution of the acquisitions in space and time for each type of targeted variable.
- (iii **Proposing an image analysis approach**): finally it presents methodological developments based on image analysis in order to characterize the morphological characteristics of the vegetation in regards to its microclimatic impacts.

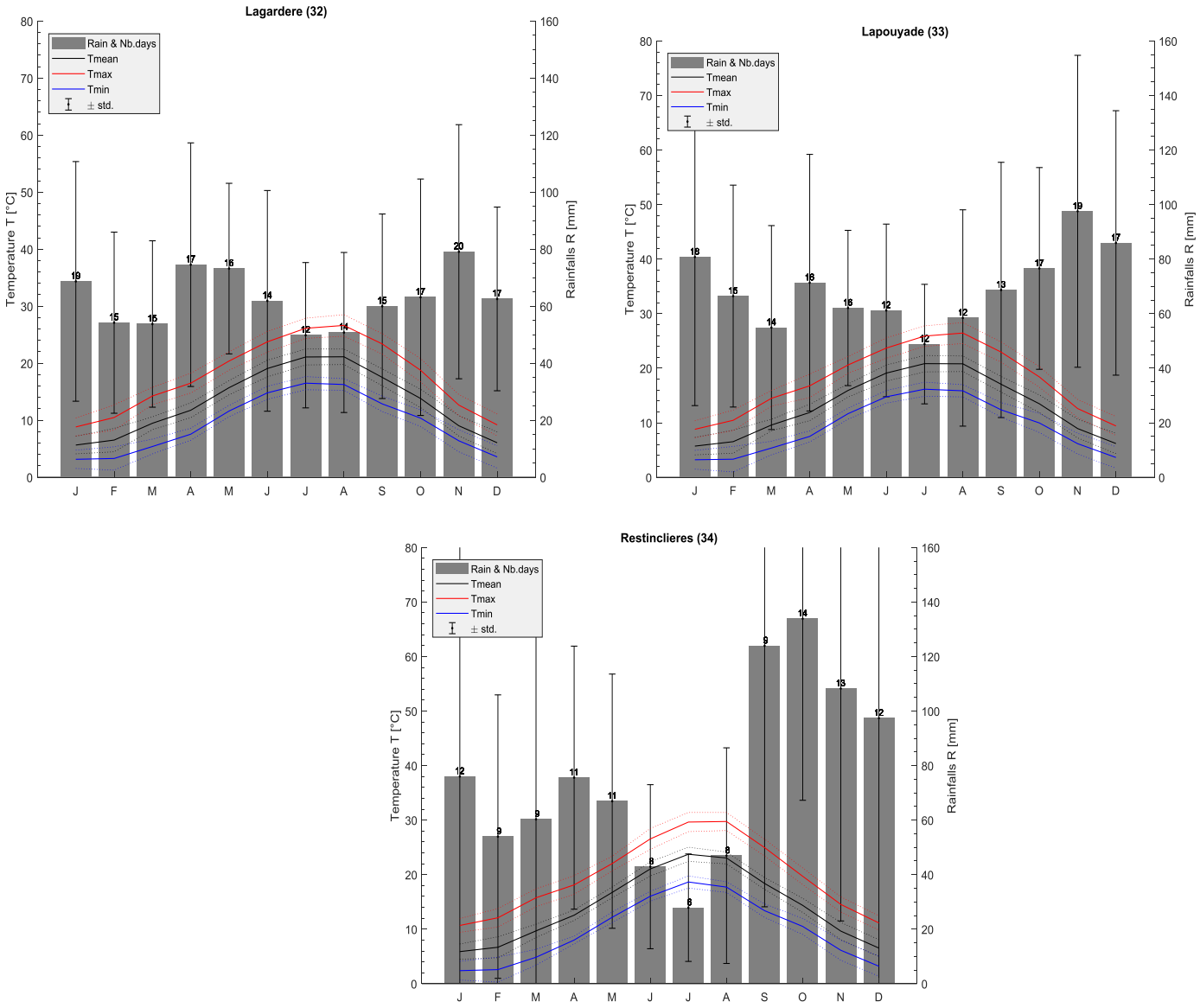

Figure 40: Monthly cumulated rainfalls, number of days of rainfall, and temperatures at Lagardère (32), Lapouyade (33) and Restinclières.(34) Averages and standard deviations are provided – Source of data: SAFRAN from 1990 to 2016.

Table 4: Bioclimatic indexes and risk of frost and heat stress for grapevine cultivation at Lagardère (32), Lapouyade (33) and Restinclières (34). Table gives the median and the 10 % and 90 % quintiles 10 % (in brackets) obtained from SAFRAN data from 1990 to 2016. The severity of late frost shows a not applicable result when there was no day with T_{mean} below 2°C. Abbreviations: Nb. Number of. - n.a: not applicable.

Median (qt.10 % - qt. 90 %) from 1990 to 2016	**Lagardère (32)**	**Lapouyade (33)**	**Restinclières (34)**
Mean daily temperature [°C]	13.1 (12.2-13.9)	13.0 (12.3 – 13.8)	14.1 (13.5 – 14.6)
Cumulated precipitations per year [mm.yr^{-1}]	741 (625-892)	824 (674 - 998)	844 (643 - 1204)
Nb. days of rainfalls per year [days.yr^{-1}]	197 (175 - 220)	181 (167 - 213)	122 (101 - 151)
Nb. hot days (Tmax > 30°C) [days.yr^{-1}]	15 (9 - 29)	17 (8 - 28)	41 (24 - 56)
Nb. very hot days (Tmax > 35°C) [days.yr^{-1}]	0 (0 – 5.2)	1 (0 – 4.8)	2 (0 - 7)
Severity of heat stress [°C]	0 (0 – 1.0)	0 (0 – 4.7)	0 (0 – 3.8)
Nb. cold days (Tmin < 0°C) (days) [days.yr^{-1}]	27 (10 - 40)	26 (12 - 42)	35 (16 - 47)
Nb. late cold days (between 1st April and 31th Sept.) [days.yr^{-1}]	0 (0 - 1)	0 (0 - 1)	0 (0 - 0)
Severity of late frost [°C]	n.a	n.a	n.a
Heliothermal Index of Huglin [°C]	1956 (1783 - 2134) Temperate	1927 (1768 - 2095) Temperate	2330 (2181 - 2520) Temperate warm
Cool night index [°C]	13.1 (11.0 – 14.6) Cool nights	12.5 (10.4 – 14.1) Cool nights	13.2 (11.8 – 15.0) Cool nights
Dryness index [mm]	191 (130 - 250) Humid	154 (98 - 214) Humid	100 (24 - 173) Sub-humid
W_{March} [mm]	312 (285 - 333)	282 (260 - 301)	312 (290 - 352)

IV.2 Study sites

IV.2.1 Lagardère (32)

IV.2.1.1 Regional context: the Côtes-de-Gascogne

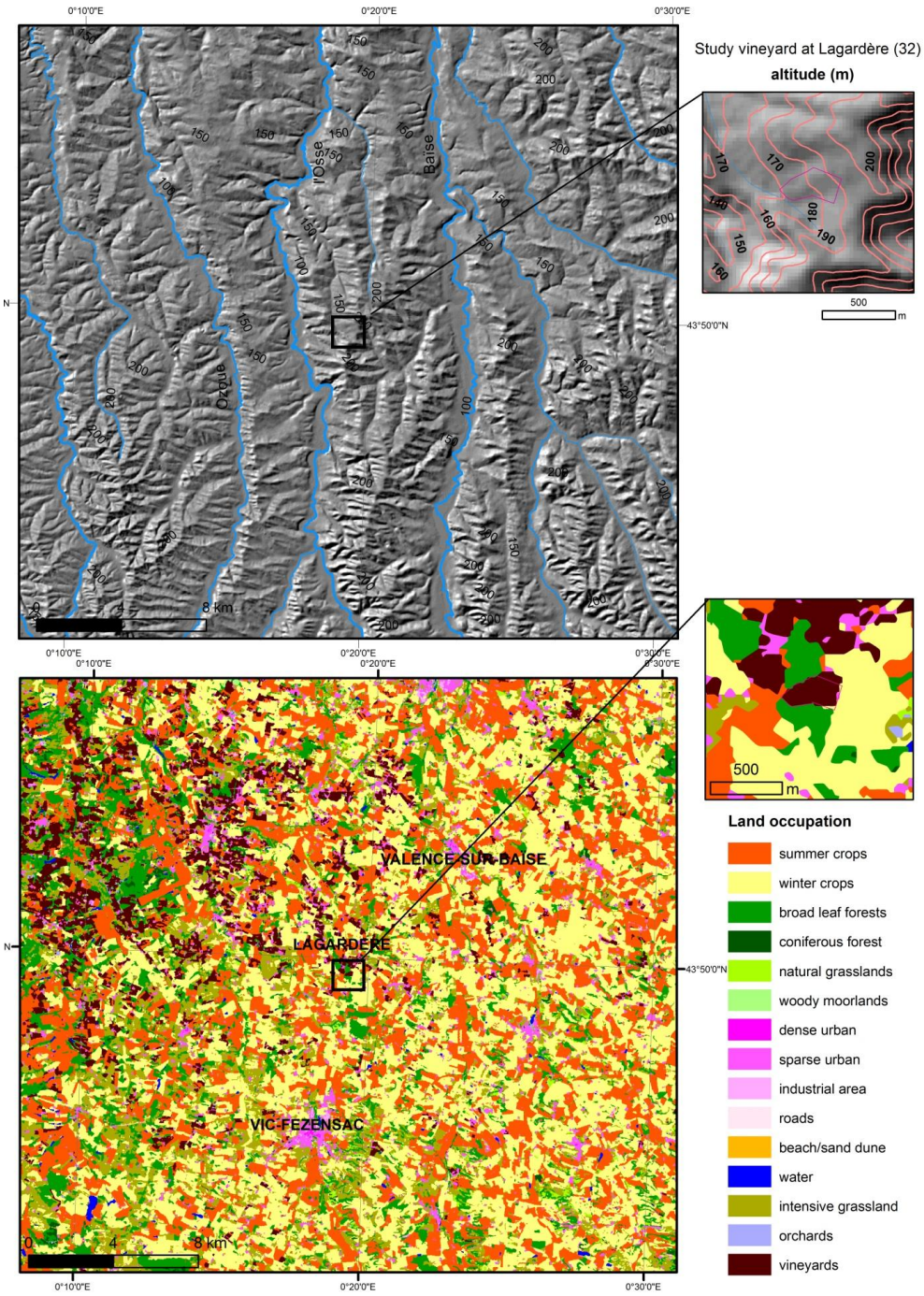

Figure 41: Topography and land occupation of the Côtes-de-Gascogne region and zooms on the study vineyard at Lagardère (32) - Source of data: BD TOPO 25 m (IGN) and Land cover map 2017 by Inglada et al. (2017)

The EARL Dubos is located in the French municipality of Lagardère (43.8264 °N, -0.3507 °E, in the department of Gers (32), at a mean altitude of 175 m above sea level. It is located in the area of

production of the Sud-Ouest wines and more precisely in the northern part of the geographic region of Côtes de Gascognes in the southern part of the Bassin Aquitain. The geology of this region corresponds to a deep alluvial fan which was built by the deposit of sediments (clay, sands, molasses) from the erosion of the Pyrenees in the Eocene and Pleocene (Geoportail 2018). The topography is made by hills with gentle slopes separated by valleys which are oriented N/S where several tributary rivers of the Garonne, notably the Baïse, flow towards the North, (**Figure 41**). Soils of the hillsides are mostly calcareous clays and can be very varied in depth (MAAF 2014). The "Côtes de Gasognes" is a rural region with varied landscapes gathering crops, pasture, mixed-forests and vineyards (**Figure 41**) (Inglada et al. 2017)[9].

The regional climate is oceanic to humid continental according to the classification of climates at global scales from Peel et al. (2007). Over the year, the mean average temperature is 13.1°C, the temperature amplitude is 15 °C and the total cumulated rainfalls are 741 mm (**Table 4**), which is rather low for France (Joly et al. 2010). Nonetheless, there is no dry season as precipitations are rather fairly distributed throughout the year (**Figure 40**). Rainfall regime is seasonal (Joly et al. 2010):

i) in autumn and winter, rainfalls are under the influence of the Atlantic Ocean. They are rather frequent but of moderate intensity.

ii) in spring and summer, stormy disturbances come from Spain or the Mediterranean sea and provoke less frequent but rather intense rainfalls.

For both rainfalls and temperatures, the year-to-year variability is moderate and seems higher in winter than in summer (**Figure 40**). The regional climatic potentialities for wine production in Lagardère (32) are given in **Table 4**. The heliothermal index of Huglin takes part to the temperate class. Most of the years, berry ripening occurs under cool night and humid conditions (Tonietto and Carbonneau 2004). Concerning extreme temperatures, in spring, the risk of late frost is small (once every ten years) while in summer, the risk of heat stress is also low but presents an important year-to-year variability.

Lagardère vineyard is part of the 'Côtes-de-Gasgogne' terroir, which is one of the European Protected Geographical Indication for the wines from South-Western France. Most of the planted vines (80 %) are white cultivars (*colombard*, Ugni *blanc*, *petit manseng* and *Sauvignon*) and a few are red cultivars (*tannat*, *merlot*, *Cabernet-sauvignon*) (FranceAgrimer 2012).

[9] The Land Cover Map of France in 2017 produced at CESBIO is available at http://osr-cesbio.ups-tlse.fr/~oso/

IV.2.1.2 Characteristics of the vineyard

Topography and vegetation arrangement

Within the vineyard of P. Dubos at Lagardère (32), a study site of 3.4 ha was selected for assessment. It is located at an average altitude of 175 m. The study vineyard is planted with North-West/South-East oriented rows of *Vitis vinifera* cv. *Sauvignon gris* (white grapes) grafted on 3309C. Vines are spaced by 1 m on a row and by 2.5 m between vine rows, which corresponds to a medium theorical density of 4000 stocks per hectare (**Figure 42**).

The north-western part of the study vineyard only contains vine rows, which were planted in 2006, while the south-eastern part contains vine rows and tree rows, which were together planted in 2008 (**Figure 43**). A total of 40 timber wood trees stand within vine rows. They are organized in three rows of same species, namely *Sorbus domestica* further referred as 'C' - for *Cormier* in French – *Sorbus torminalis* as 'A' - for *Alisier* in French - and *Pyrus piraster* as '*P*' for pear tree, separated by six vine rows i.e. 19 m. Trees are spaced by 10 m from one to another and by 3.25 m from the immediate northern and southern neighboring vine rows. This agroforestry arrangement corresponds to a theoretical density of 3158 vines and 53 trees per hectare.

The northern and southern zones are separated by a ditch and a discontinuous bushy tree hedge. The borders of the plot are occupied by mixed forest (on the North-West, NW, and South-East, SW), by grapevine rows (NE), a road and then a large pasture (E) and by a pond and then a young red oak planting (SE) (**Figure 41**). The whole area presents a smooth continuous slope of 3 % which mainly flows from NE to SW, towards the pond (**Figure 41**).

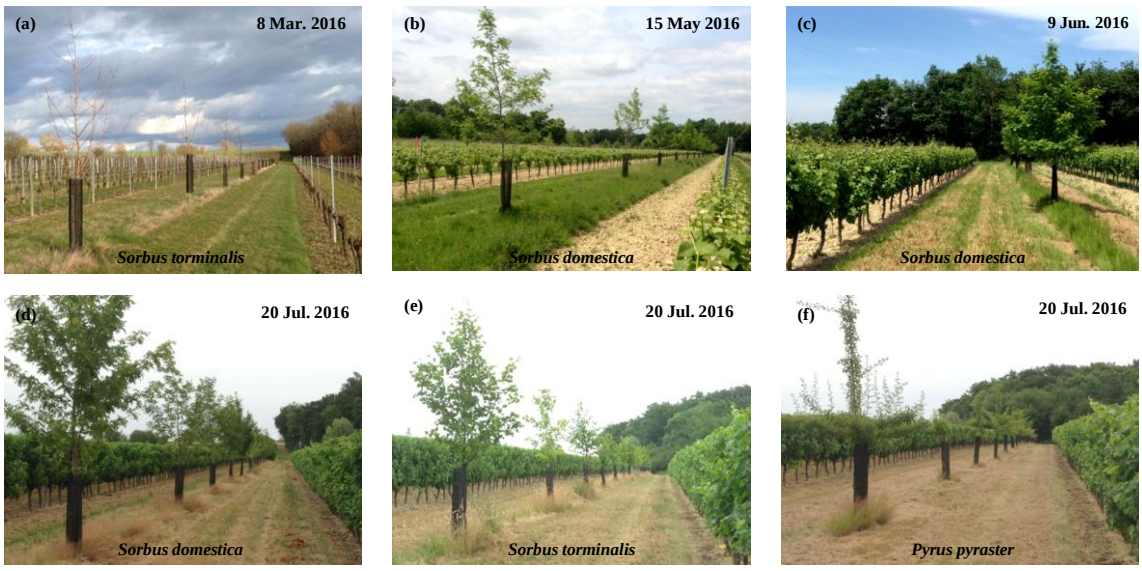

Figure 42: A modern case of agroforestry vineyard at Lagardère, Gers, France (43.8264 °N, -0.3507 °E). Rows of timber wood trees (Sorbus domestica, Sorbus torminalis and Pyrus pyraster) were planted in 2008 together with Vitis vinifera cv. Sauvignon gris.

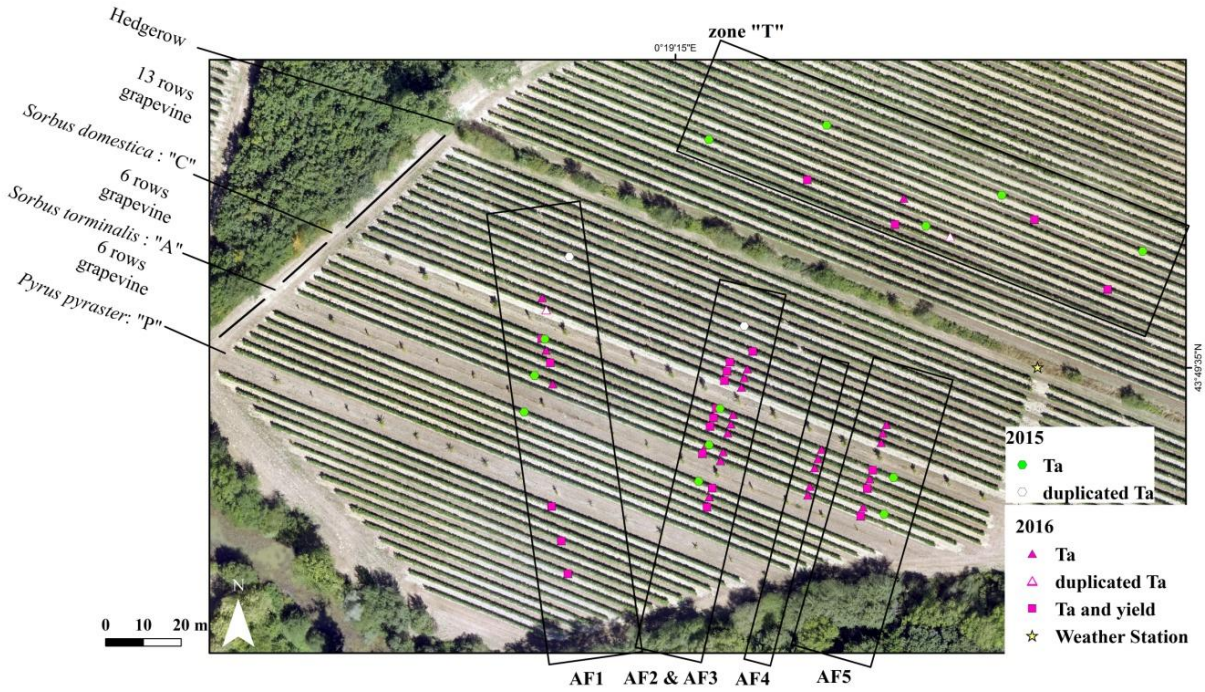

Figure 43: Vegetation arrangement and distribution of experimental plots at the study vineyard of Lagardère (32), France. Measurements of air temperature (Ta) were carried out simultaneously at 15 plots from 29 Jul. to 2 Sep. 2015 (●) and at 49 plots from 10 Mar. 2016 to 2 Sep. 2016 (▲ and ■). In 2015, the measurements were duplicated at AF1_Cn7 and AF2_Cn7 locations (white ○), while in 2016, they were duplicated at AF3_Cn1 and T4 locations (white △). Also, the grapes from 22 plots (pink ■) were collected as individual batches at harvest in 2016. The names of the plots are given according to their position either in the northern zone "T" or in one of the five southern transects named "AF1" to "AF5". Both T plots and transects are numbered from NW to SE. Tree rows planted with *Sorbus Domestica*, *Sorbus torminalis* and *Pyrus piraster* are designated respectively as *'C', 'A' and 'P'*. Also '*si*'/'*ni*' stands for the ith vine row on either the southern/northern side of a tree row. Background picture was acquired by drone flight on 23 Aug. 2016 by T. Houet.

Cultivation practices

Soil type and management

The soil is a deep silty-clay loam. One out of two grapevine middle rows and tree rows are sown with a grassy cover. The grassy cover on grapevine middle rows is regularly mowed while that on tree rows is mowed only once over the whole vegetative growth season. The bare soil on one out of two grapevine middle rows is mechanically weeded while the bare soil under grapevine rows is chemically weeded.

Grapevine

The fruit branches of grapevines are pruned (Guyot pruning), their canopy is trained in vertical shoot position by a trellis system and trimmed at 2 m above ground. Except grapevine pruning, all the interventions on grapevine are done mechanically.

Grape production follows the specifications for the 'Côtes de Gascogne' wines consequently the yield cannot exceed 120 hL.ha^{-1} and grape must present a minimum of 9 % of alcohol by volume after fermentation (MAAF 2014). Win making and wine selling is operated by a cooperative wine cellar and 70 % of the white wine which is produced is sold abroad (Syndicat des Vins Côtes de Gascogne 2018).

TREES

Since tree planting in 2008, trees have been pruned at their trunk once every year in order to shape them as blocks of wood. According to lasermeter measurements performed in 2016, the average height of the trees was 3.8 m, 3.3 m and 3.0 m in row C, A and P respectively (**Figure 42**).

In addition to the potential economical benefit from timber wood production, the vine grower was motivated for co-planting trees in the vineyard mainly in order to improve the landscape aspect of its land and the biodiversity (Madrid 2015).

IV.2.2 Lapouyade (33)

IV.2.2.1 Regional context of the 'Bordeaux Supérieur' region

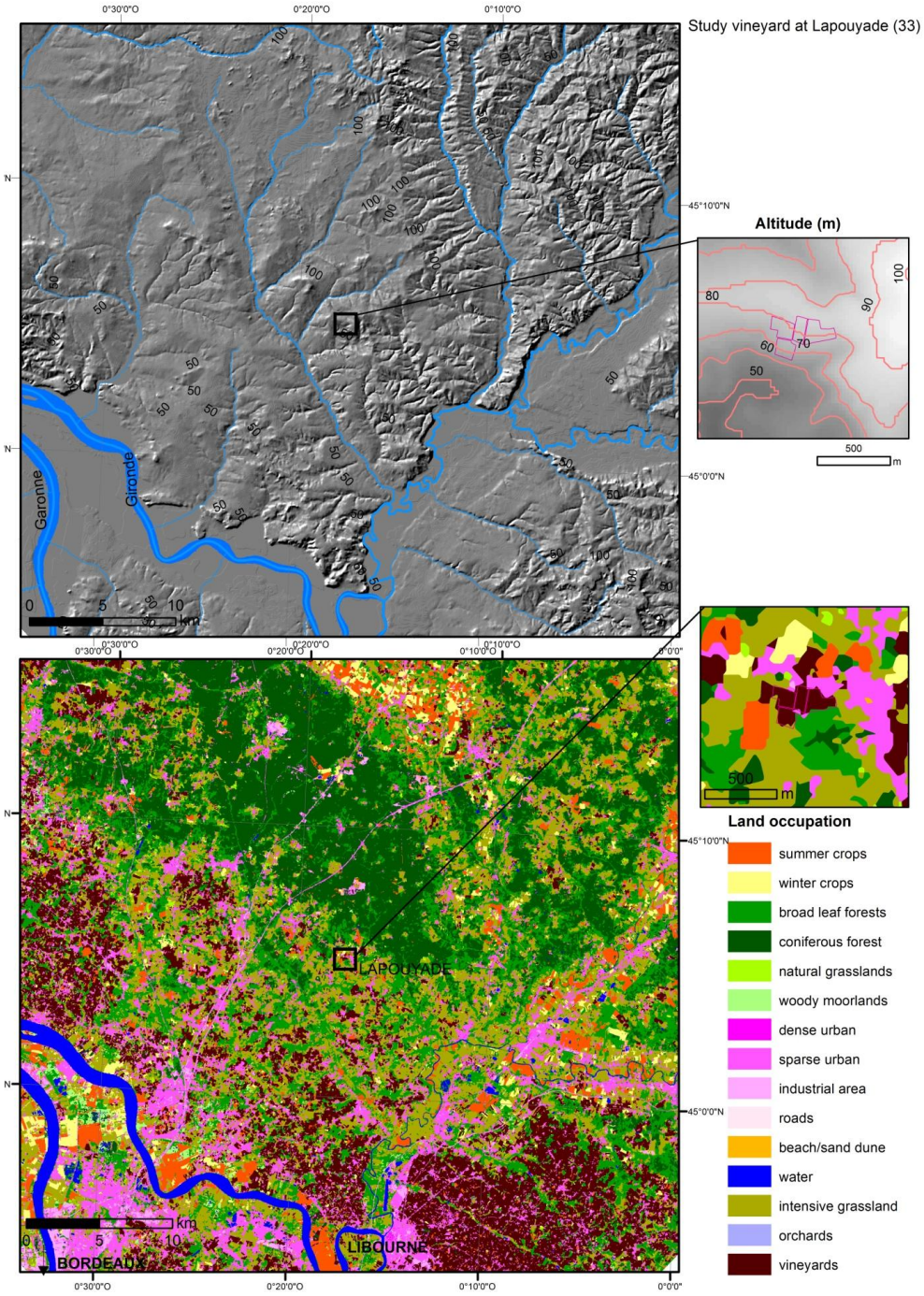

Figure 44: Topography and land occupation in the Bordeaux Supérieur vine growing region and zooms on the study vineyard at Lapouyade (33) - Source of data: BD TOPO 25 m (IGN) and Land cover map 2017 by Inglada et al. (2017)

The Domain Emile Grelier is located in the French municipality of Lapouyade (45.086°N, -0.2915°E) in the department of Gironde (33). Lapouyade is located in the area of production of the Bordeaux wines, at 25 km inland from the estuary of the Gironde, where the Garonne and the Dordogne rivers meet, and at 40 km North-East from the city of Bordeaux (**Figure 44**). In terms of

geology, this area corresponds to the northern part of the Aquitaine Basin, which is named the Aquitaine Plateau. It is a relatively shallow sedimentary platform gently undulating and occasionally faulted (Geoportail 2018). Above a limestone foundation, the soils of this area are mainly calcareous clays or sandy loams, with a neutral or alkalin pH (MAA 2017).

Urbanization is quite important at Lapouyade because of the proximity of the city of Bordeaux and the town of Libourne. Mainly habitations, vineyards as well as pasture and deciduous forests occupy the land (**Figure 44**).

Vineyards of Lapouyade are located in the 'Bordeaux Supérieur' Protected Geographical Indication which is mainly planted with vines of red cultivars (*Merlot, Cabernet-franc*) and a few white cultivars (*Semillon, Sauvignon*) (FranceAgrimer 2012).

Lapouyade shows an oceanic climate (Peel et al. 2007) which is under the strong influence of the Gironde estuary and the Atlantic Ocean. Over the year, the mean average temperature is 13.0 °C, the temperature amplitude is 15 °C and the total cumulated rainfalls are 824 mm (**Table 4**). Rainfalls are the greatest in late autumn and winter and the lowest in summer while the converse is true for the temperatures. Nonetheless there is no dry season at Lapouyade as rainfalls are quite fairly distributed throughout the year (**Figure 40**). Both spring and summer show a minimum of 12 days of rainfalls per month. The regional climatic potentialities for wine production at Lapouyade are given in **Table 4**. The heliothermal index of Huglin takes part in the temperate class most of the years. There is a non negligible risk of late frost at Lapouyade due to the forests which are located inland further North-East. They tend to counterbalance the protection from the Ocean and limit the extent of grapevine cultivation further inland (MAA 2017). Berry ripening occurs in average under cool night and humid conditions (Tonietto and Carbonneau 2004). Nevertheless, the year-to-year variability of rainfalls and most of all of temperatures in August and September is high (**Figure 40**) which generates a strong vintage effect (MAA 2017).

IV.2.2.2 Characteristics of Emile Grelier vineyard

Vineyard topography and vegetation arrangement

Emile Grelier vineyard is located at an average altitude of 70 m above sea level. It occupies a contiguous total area of 7 ha on a hillside of gentle slope (4.6 %) facing South (**Figure 44**). The vineyard was planted with vines of *Vitis vinifera* cv. *Merlot* (red grapes) in 2005. Grapevine was planted at a rather high density (6600 stocks per ha.): there is a distance of 1.5 m between vine rows and 1 m between stocks on a given row. In addition, Delphine and Benoit Vinet, the two vine growers, have been co-planting rows of trees in their land since 2008. Three types of agroforestry arrangements have been progressively introduced (**Figure 45**):

- Mixed fruit trees (2/3) and timber wood trees (1/3) were planted in 2008 (one row) and then in 2014/2015 (two rows) directly within vine rows. The trees on a given

row are spaced by 9 m and each of them replaces one vine stock. The most eastern tree row presents the highest trees as it was planted in 2008 while trees are still quite short on the two other rows as they were planted in 2014/2015.

- Two rows of *Sorbus domestica* trees were planted in 2014/2015 along a central alley. Trees are located at a distance of 1 m from grapevine rows and are spaced by 9 m from each other.
- Mixed bushy hedgerows were planted in 2014/2015, along the ditch and the road at the northern border of the vineyard and along the ditch at the western border.

Except the northern hedgerow, rows of grapevine and rows of trees are oriented N/S, in the same direction as the main slope.

The whole area is surrounded by a road and habitations on the northern edge, by a dense oak forest on the eastern and southern edges and by a pasture on the southern and western edges.

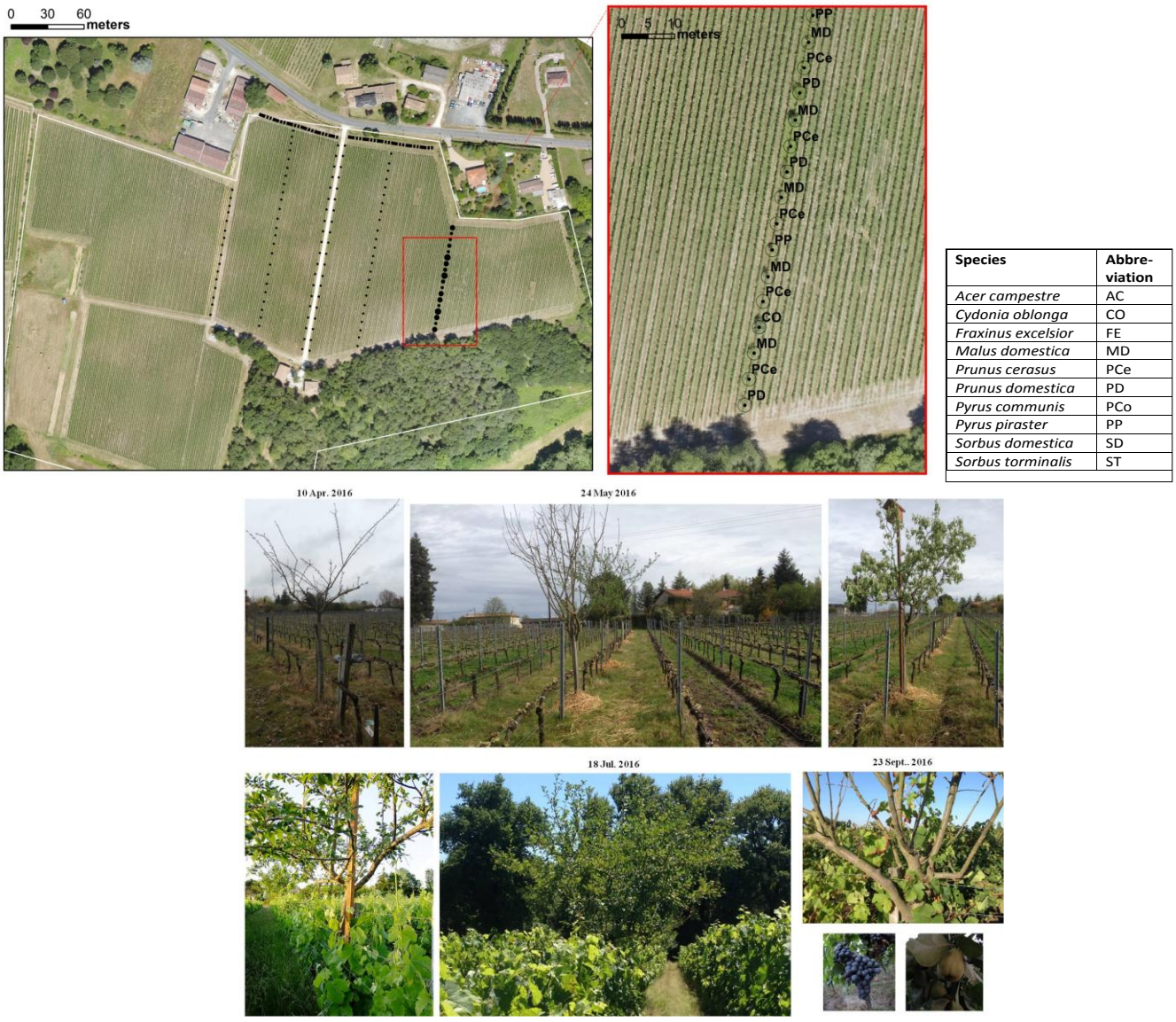

Species	Abbre-viation
Acer campestre	AC
Cydonia oblonga	CO
Fraxinus excelsior	FE
Malus domestica	MD
Prunus cerasus	PCe
Prunus domestica	PD
Pyrus communis	PCo
Pyrus piraster	PP
Sorbus domestica	SD
Sorbus torminalis	ST

Figure 45: Tree species and arrangement at Domain Emile Grelier, Lapouyade (33)- photo sources: J. Grimaldi & D. Vinet.

Cultivation practices

Soil type and management

The soil texture is of sandy loam type. All the middle rows are covered by a grassy cover of mixed species which was either sown in 2015 (2/3) or results from natural grass covering (1/3). The bare soil under grapevine rows is mechanically weeded through ploughing the ridges about 4 to 5 times a year.

Grapevine

Vines of *Vitis vinifera* cv. *Merlot* are grafted on R101-14 and Riparia high quality rootstocks. The fruit branches are pruned (Guyot pruning) according to a short size cordon de Royat pruning and the canopy is highly trained by a vertical shoot positioning system with trellis. Grapevine canopy is regularly trimmed after flowering. The foliage is approximately maintained with an eight of 0.9 m i.e. at a maximum of 1.4 m above ground.

The grapevine rows which contain trees are manually spread against diseases and manually harvested because of the presence of trees standing as obstacles, while the rest of the vine rows are mechanically managed and harvested. Grapevine is cultivated under the specifications for the organic labels. In addition, grape production follows the specifications for the '*Bordeaux Supérieur'* wines consequently the yield cannot exceed 50 $hL.ha^{-1}$ and the grape must present a minimum of 11 % of alcohol by volume after fermentation (MAA 2017). Vinification of the grapes from the Domain Emile Grelier is operated as a separated batch by a cooperative cellar under the supervision of grapevine growers. Then the wine is sold directly at the domain.

Trees

Since tree planting in 2008, the trees in tree rows have been stem pruned once a year. The timber wood trees are shaped as blocks of wood while the fruit trees are shaped in goblets. In addition, the woody hedges at the border of the vineyard have been laterally pruned so as to remain outside the limits of the vineyard. Increasing the biodiversity, protecting the soil from organic matter losses, wind breaking and improving the visual aspect of the vineyard were the main motivations for agroforestry in this vineyard (Madrid 2015).

IV.2.3 Restinclières (34)

IV.2.3.1 Geography and climate of the Languedoc region

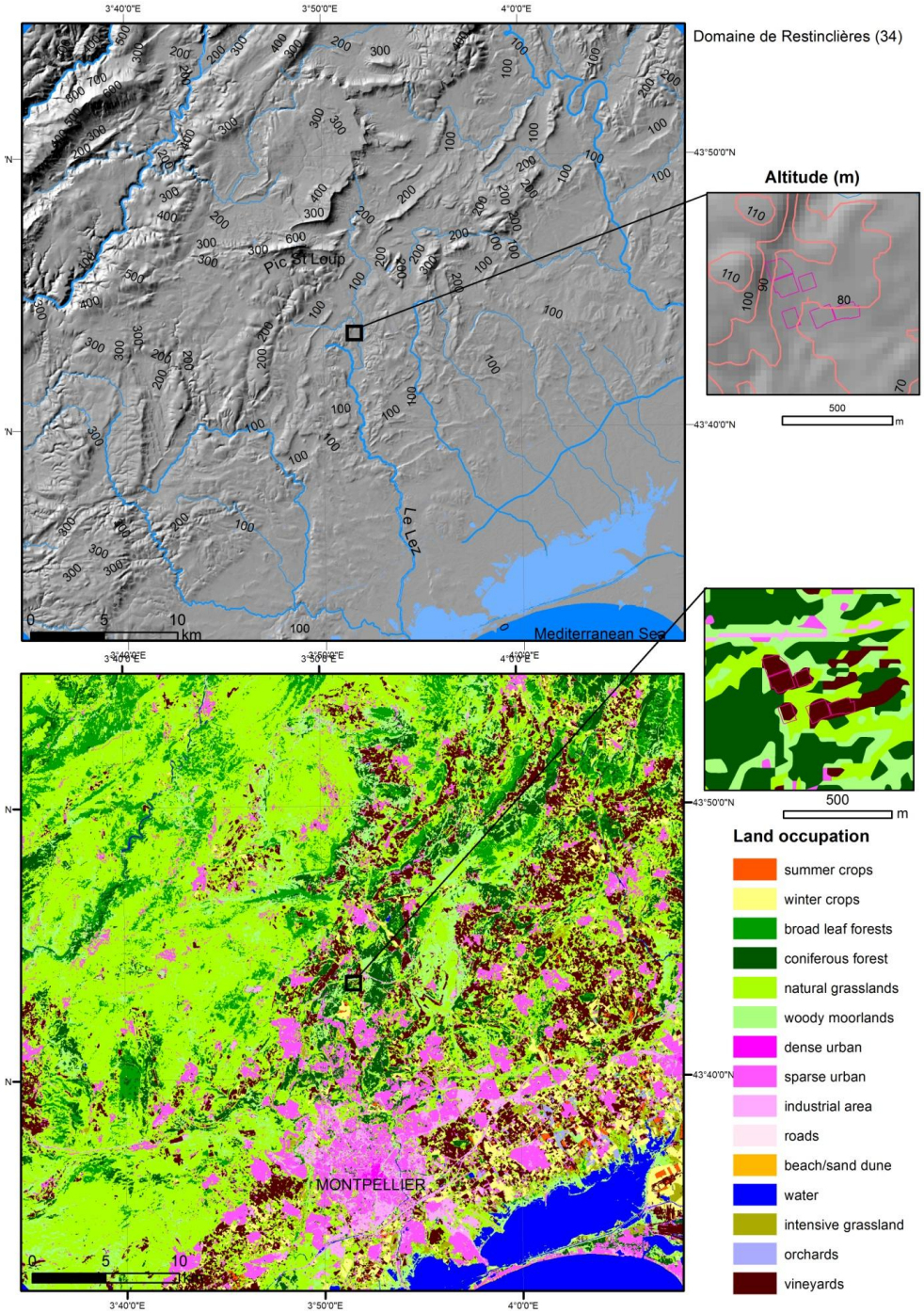

Figure 46: Topography and land occupation in the 'Languedoc' vine growing region and zooms on domain of Restinclières at Prades-Le-Lez (34) - Source of data: BD TOPO 25 m (IGN) and Land cover map 2017 by Inglada et al. (2017)

The Domain of Restinclières is located in the French municipality of Prades-Le-Lez (43.7258°N, -3.8573 °E), in the department of Hérault (34), and falls in the area of production of the Languedoc wines. It is located at 15 km North from the city of Montpellier, at 25 km from the Mediterranean sea, at an altitude of 185 m above sea level. The area corresponds to the southern part of the calcareous massif of the Pic Saint Loup Mountain which is crossed by the valley of the Lez, flowing to the South

towards the sea (**Figure 46**). The calcareous bedrock was formed in early cretaceous while the valley stands on sandstone and marls from the quaternary (Geoportail 2018). From North-West to South-East, the topography of the area is marked by a succession of ridges and valleys oriented NE/SW which is progressively replaced by terraces and then karstic basins (**Figure 46**). Most of the land is occupied by guarrigues of *Pinus halepensis* and bushy *quercus ilex* (MAAF 2017), by patchy vineyards on the terraces and by urbanization (habitations and roads) in the valleys (**Figure 46**).

The Domain of Restinclières is located right next to the 'Pic Saint-Loup' Protected Geographical Indication to the North and the 'Grès de Montpellier' Protected Geographical Indication to the East. Most of the vineyards in this area are mainly planted with vines of red cultivars (*Syrah, Grenach, Mourvedre*) (MAAF 2017).

The regional climate is Mediterranean (Peel et al. 2007), i.e. rather warm and strongly marked by a warm and dry summer (**Figure 40**). The severity of drought is qualified as 'sub humid' according to the dryness index (**Table 4**).

Over the year, the mean average temperature is 14.1 °C and the cumulated rainfalls are 844 mm. Nonetheless, both temperatures and rainfalls show a great variability with the season:

temperature amplitude is the highest for France (18 °C) (Joly et al. 2010) as both the number of hot days in summer and the number of cold days in winter are high (**Table 4**).

More than 55 % of the annual precipitations occur in autumn while less than 110 mm of rain falls during summer (**Figure 40**). The amounts of days of rainfalls per year and per month are quite low as the rain often falls as intense storms. It is notably the case at the beginning of autumn with very intense episodes of stormy rains which arrives from the warm Mediterranean Sea and generally last from 2 to 4 days.

The heliothermal index of Huglin belongs to the 'temperate warm' class (**Table 4**), illustrating that grapevine vegetative growth and phenological succession happens relatively faster in the Languedoc wine producing region than at the two other study sites. In addition, berry ripening occurs under cool to temperate nights, depending on the year.

Temperature regime is particularly constant from one year to another compared to other grapevine growing regions from France (Joly et al. 2010). As a consequence, vintage effect in this region is mostly due to the high variability of rainfalls.

The risk of grapevine damages from extreme heat is the highest at Restinclières out of the three study sites. Also, though the number of days of frost is also the highest, it did not happen from 1990 to 2016 (**Table 4**).

IV.2.3.2 Characteristics of the selected plots

Topography and vegetation arrangement

The domain of Restinclières has been an experimental domain dedicated to on field experimentation regarding agroforestry systems since 1994, on the initiative of the departmental council (*Conseil Départemental de l'Hérault*) and INRA (Montpellier Center). Over a total area of 215 ha, the site includes 30 ha of alley-cropped plots (rapeseed, wheat, peas) and 7 ha of tree-intercropped vineyard (wine grapes), further called 'agroforestry vineyard' (INRA and CRPF 2000). Since tree planting in April 1996 and then grapevine planting in 1997, the agroforestry vineyard has been cultivated by M. Thierry VACHER, under a land rent contract. In addition, it has been the object of a long term experimental assessment supervised by the chamber of agriculture of Hérault (CA 34) in order to document the impacts of the trees on the productivity of grapevine and on the grape quality for wine making through above and below ground mechanisms of competition/complementarity (Duffours 2011; Goma-Fortin and Trambouze 2011, 2012; Trambouze and Goma-Fortin 2013; Gouttesoulard 2015; Trambouze et al. 2017).

The agroforestry vineyard was planted inside the guarrigues (mostly *Pinus halepensis* and bushy *quercus ilex*) on the hilly part of the Domain, which presents very shallow and rocky soils. It is located at an average altitude of 85 m. The slope is the highest (5.4 %) on the Western area where it flows from West to East while it becomes gentler and flows North to South on the eastern part of the vineyard (**Figure 46**).

The vineyard was designed for experimental purposes: it divides in height agroforestry plots (**Figure 47**) which vary from one to another by tree species, by row orientation and/or by planting density (**Table 5**). Each agroforestry plot subdivides into four different areas which correspond to two modalities of red grape cultivar, either *Syrah* or *Grenach*, multiplied by two planting densities, either a 'low density' where tree row occupies the width of two vine rows, or a 'high density' where tree row occupies the width of one vine row (**Figure 48**). In addition, there is a forested reference plot (sole tree rows – 'RefTree') and a monocropped grapevine reference plot (sole vine rows – 'RefVine') matching with each agroforestry plot (**Figure 47**).

Targeted plots

For the purpose of this PhD, ***in situ* microclimate measurements** were performed inside the B3 and B4 agroforestry plots. These two plots are both planted with *Sorbus domestica* trees but differ by orientations of the rows (**Table 5**). Within these plots, only the vine rows with the *Grenach* cultivar were targeted as the *Syrah* cultivar is very impacted by wood disease. In B4, the two planting densities of grapevine were assessed while in B3 only the high density was targeted (**Figure 47**). The limited amount of data loggers and workload were the two limiting factors for this selection.

UAV born images were captured in visible, multispectral and thermal infrared wave lengths. The overall footprint of the images only covered the western part of the agroforestry vineyard (B3, B4, B5 plots and the western part of the B7 plot) and was centered on plots B3 and B4 plots. The autonomy of the drone battery was the main limiting factor for further extending the area of capture to the overall vineyard. A compromise was made between the area of extent and the spatial resolution of the images of about 10 cm, for an accurate observation of grapevine canopy.

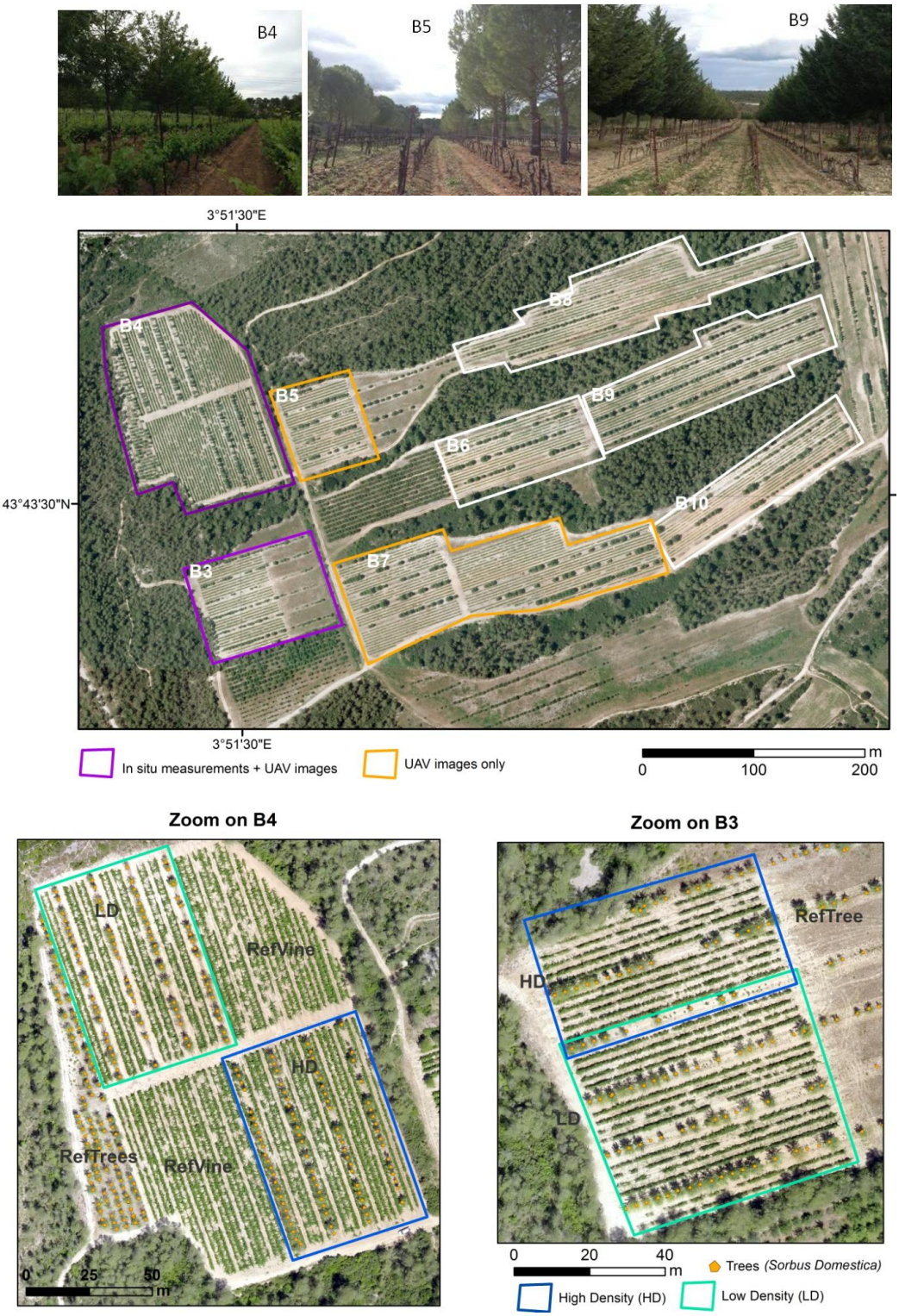

Figure 47: Overall view of the Domain of Restinclières (34) (viticulture part) and zooms on the targeted B3 and B4 plots - Back ground images: BD ORTHO 2016 from IGN (all) and drone RGB image on the 19/07/2016 (bottom).

Table 5: Vegetation type and arrangement per plots at Restinclières (34). Abbreviations: AT = After thinning out one out of two trees originally planted – MC= *in situ* microclimate measurements, I = UAV born images - Source: (Goma-Fortin and Trambouze 2011)

Plot	Tree species	Grapevine cultivar	Row orientation	Tree spacing d_R * d_T	Assessment in 2016
B3	*Sorbus domestica*	Black *Grenach* and *Syrah*	W/E (+18.3°W)	15 m * 3 m	MC, I
B4	*Sorbus domestica*	Black *Grenach* and *Syrah*	N/S (+19.43°N)	15 m * 3 m	MC, I
B5	*Pinus pinea*	Black *Grenach* and *Syrah*	W/E (+18.1°W)	15 m * 6 m AT	I
B6	*Pinus pinea*	Black *Grenach* and *Syrah*	W/E (+19.2°W)	15 m * 6 m AT	
B7	*Pinus brutia*	Black *Grenach* and *Syrah*	W/E (+34.8°W)	15 m * 6 m AT	I
B8	*Aulnus cordata* and *Calocedrus decurrens* (all dead)	Black *Grenach* and *Syrah*	W/E (+17.6°W)	15 m * 6 m AT	
B9	*Cupressus sempervirens* and *Cupressocyparis leylandii*	Black *Grenach*	W/E (+22.4°W)	15 m * 4 m AT	
B10	*Pirus communis*	*Syrah*	W/E (+33.6°W)	15 m * 6 m AT	

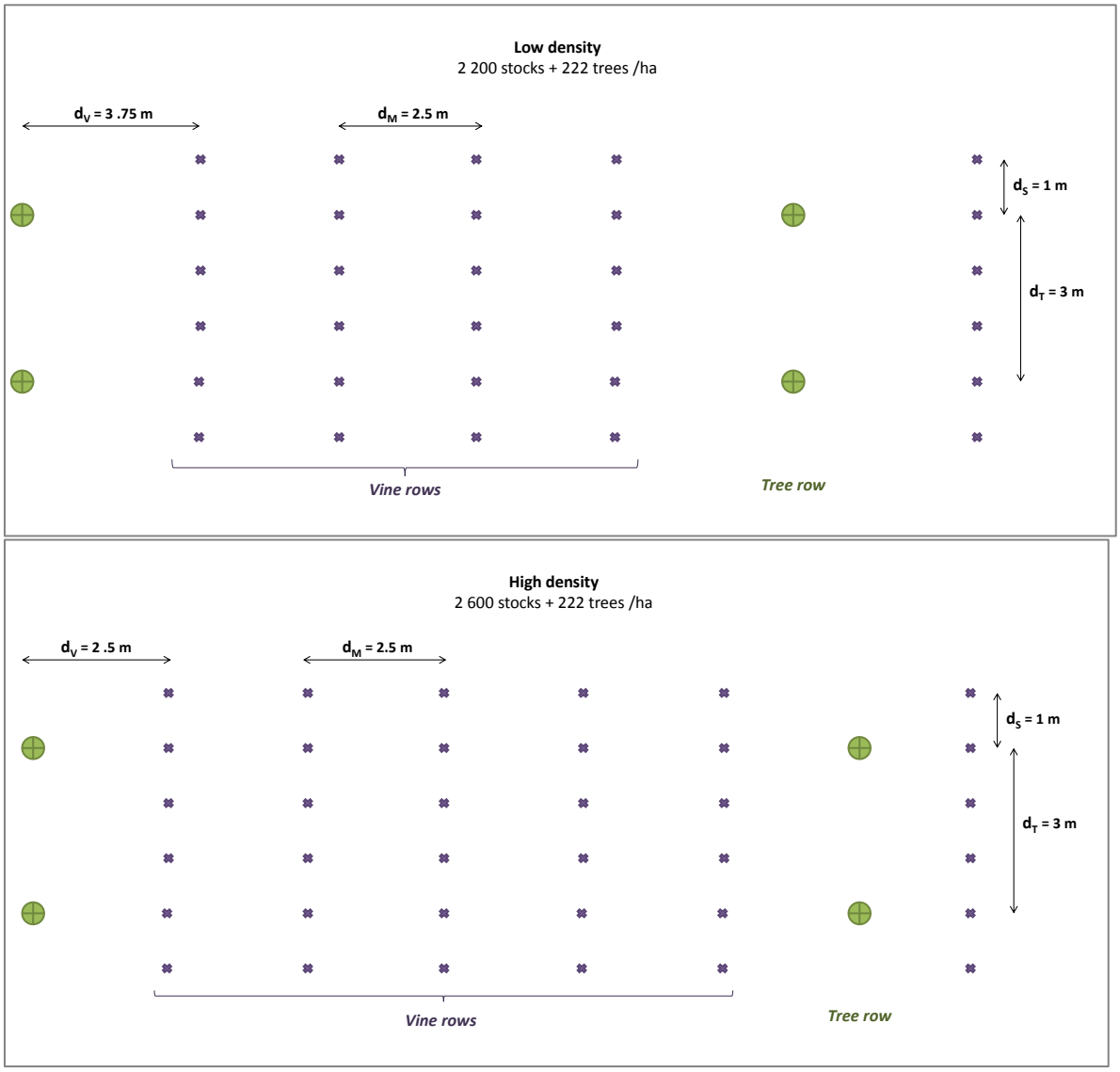

Figure 48: Low density and high density of grapevine and tree planting in the plots B3 and B4 at Domaine de Restinclières (34)

Cultivation practices

Soil type and management

The soil presents the textural composition of a clay-sandy loam and contains more than 50 % of calcareous rocks (Trambouze and Goma-Fortin 2013). It is particularly shallow in the studied plots (Gouttesoulard 2015). The soil of the whole plot is kept entirely bare during the whole vegetative growth of grapevine. The middle rows used to be mechanically weeded but are now chemically weeded while grapevine and tree have always been chemically weeded. The soil of the middle rows shows significant signs of erosions such as deep gullies which form in several middle rows of the B4 plot.

Grapevine

Vines of *Vitis vinifera* cv. *Syrah* and *Grenach* are grafted on 110 Richter rootstocks. They were planted in April 1996 at an equivalent density of 4000 stock.ha^{-1}. In winter, the vines are cordon trained and pruned as a Royat cordon while in spring suckers are chemically removed from the trunk. Grapevine canopy is usually highly trained with trellis system and pruned once a year, around mid-July. Nonetheless, during the experimental campaign of 2016, many vine rows in the B3 and B4 plots were left untrained with branches falling down to the ground as a net (**Figure 49**).

Over the last decade, the *Syrah* cultivar has shown an important mortality due to wood disease while the Grenach cultivar remained saved.

Trees

During the years following the tree planting, trees of all plots have been stem pruned once every year in order to shape them as blocks of wood. In addition, except for the *Sorbus domestica* species (plot B3 and B4), about 50 % of the trees were thinned after five years of growth in order to lower competition with grapevine. Similarly to grapevine stocks, some trees died throughout the year thus leaving more and more gaps in tree rows compared to the theoretical planting scheme (**Figure 47**). In addition, in 2016, likewise in the previous years, the *Sorbus domestica* trees showed signs of water stress during summer drought. Starting mid-July, many leaves in the upper part of their canopy turned yellow to brown and defoliated. It concerned about a third of the total canopy, from visual estimate (**Figure 49**).

Figure 49: Vegetative development of grapevine (*Vitis vinifera* cv. *Grenache*) and trees (*Sorbus domestica*) in 2016, in the plots B3 and B4 at Domaine de Restinclières. Photos: J.Grimaldi

IV.3 Experimental campaign

IV.3.1 Overall sampling strategy

In 2015, a short campaign of micro-climatic measures was carried out at Lagardère (32), from grapevine ripening to harvest (**Figure 50**). Then in 2016, three campaigns were carried out respectively at Lagardère (32), at Lapouyade (33) and at Restinclières (34) from grapevine budburst to harvest. This time, both on site measurements and remote sensing approaches were used. The targeted variables aim at describing the heterogeneity in space and time of the microclimate and their consequences on the climatic functioning of the air-soil-vegetation continuum. The morphological characteristics of the vegetation were also punctually assessed through *in situ* and remotely sensed acquisitions. In addition, data concerning the phenology and the yield of grapevine were collected from work in tandem with technical institutes, namely the IFV[10] at Lagardère and Lapouyade, and with CA 34[11] at Restinclières. The space and time sampling strategy for collecting the ensemble is complementary as it combines time series records at each site, time series records spread at a selection of vine stocks within each study vineyards and instantaneous maps of very high resolution in space (**Figure 51**).

[10] IFV: Institut Français de la Vigne – The experimental campaigns were supervised by Thierry Duffourcq and Marc Vergnes which are warmely thanked for their contributions.

[11] CA 34: Chambre d'Agriculture de l'Hérault – The experimental campaign was supervised by William Trambouze which is warmely thanked for his contribution.

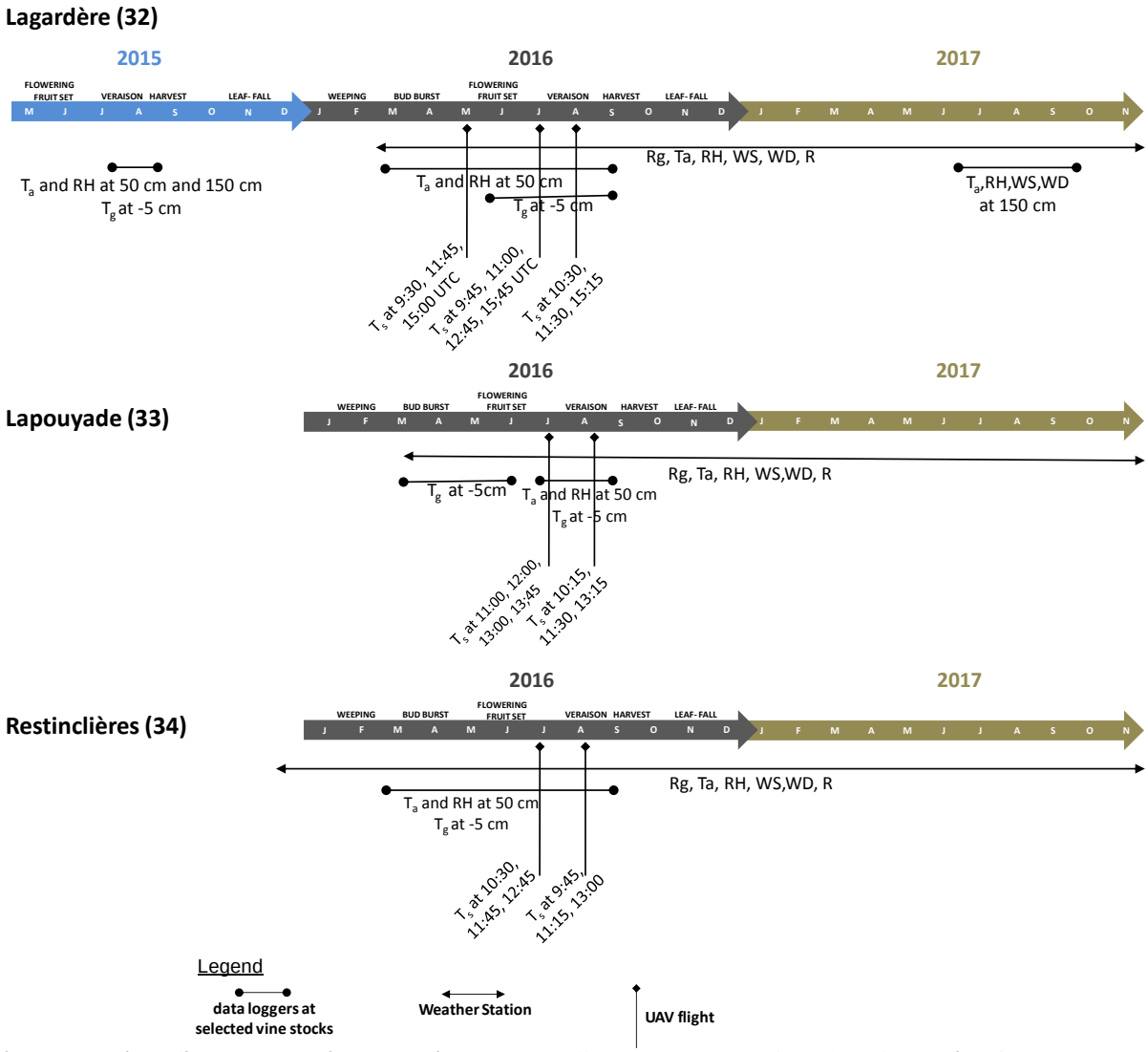

Figure 50: Microclimate measuring campaigns at Lagardère (32), Lapouyade (33) and Domain of Restinclières (34). Abbreviations: T_g: ground temperature, T_a: air temperature, RH: Relative humidity, WS: Wind speed, WD: Wind direction, R: Rainfalls, T_s: Surface temperature

The collected data set covers state variables from three compartments, the atmosphere, the vegetation and the ground. An exhaustive list of collected data and specifications is given in **Annex B**. In the air compartment, meteorological records were taken by a meteorological station at each study site. In addition, air temperature and relative humidity were recorded inside the grapevine canopy at a selection of sampled stocks. In the soil compartment, soil temperatures were recorded in the root zone also at a selection of sampled stocks while structural characteristics were mapped once, using conductivity technology. In the vegetation compartment, the architecture, the biomass and the surface temperatures of grapevine and trees were mapped through Unmanned Aerial Vehicle (UAV) flights which were performed three times in total at Lagardère (32), and twice at Lapouyade (33) and at Domain of Restinclières (34) (**Figure 50**). In addition, grapevine phenological development and yield and berry composition at harvest were assessed at a selection of vine stocks.

The following sections give sensor specifications and explain the protocols that were used for collecting data, sorted by type.

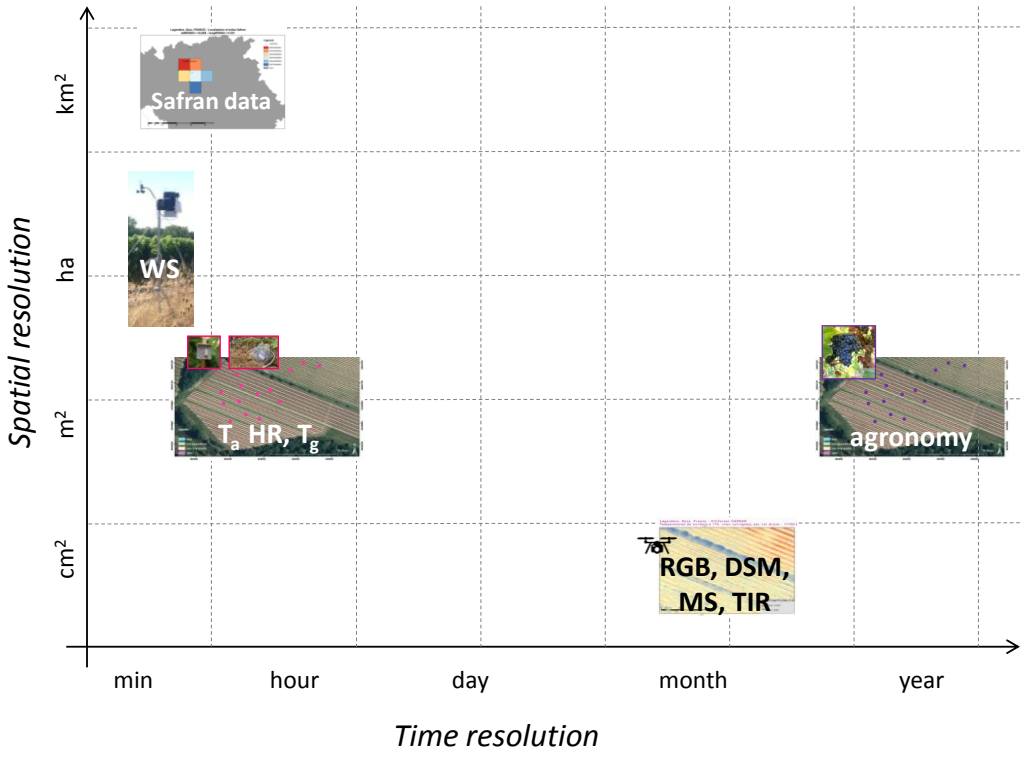

Figure 51: Space and time resolution or representativeness of the climatic and agronomic data sets. Abbreviations: *WS*: Weather Station, T_a: Air temperature in vine canopy, *RH*: relative humidity in vine canopy, T_g: ground temperature, *RGB*: Red-Green-Blue orthophotos, *DSM*: Digital Surface Model, *MS*: Multispectral image, *TIR*: thermal infrared image.

IV.3.2 Meteorological data

IV.3.2.1 Data sources

In 2016, meteorological stations located at Lagardère (32), at Lapouyade (33) and at Restinclières (34) provided records of sun radiation, wind speed and wind direction, air temperature, relative humidity and precipitations at an hourly frequency or higher (**Table 6**).

At Lagardère (32) and at Lapouyade (33), the weather stations were funded by the CASDAR Vitiforest Project and their installation within the study plots was done as part of this thesis. The Vantage Pro 2 sensor suite was installed at 2 m high on a pole, cabled to a GSM console. Particular care was put on cabling the sensors to the console, on calibrating the wind vane, on controlling the horizontality of the pyranometer and rain gauge and on tying up the pole with wire cables running from the ground in order to prevent the whole from a fall. Also the pyranometer and rain gauge were regularly cleaned up throughout the year. Once operational, the remote transmission of data by CAIPOS GSM device never stopped so far and has been very useful. It notably allowed an easy sharing with researchers and viticulturists and a rapid capacity of adaptation to meteorological events.

At Restinclières (34), thanks to a partnership with INRA UMR System[12], a meteorological data set recorded by two local weather stations was made accessible (**Table 6**). Moreover, at each study sites, SAFRAN data[13] were used for two purposes:

1. in order to compare the meteorological trends in 2015 and 2016 to the average ones since 1990;
2. in order to check the validity of the records taken with local weather stations.

SAFRAN data are produced by Météo France (The National Center of Meteorological Research, CNRM) from the interpolation of records in real time and homogeneous climatic zones (Le Moine 2002). They are provided at both daily and hourly time steps and per tiles with a spatial resolution of 8 km[14] (Pagé 2008). Though SAFRAN hourly time step data would have been more precise, the daily time step data were used for validation, since the first type of time series was only partially available (from 2015/08 to 2016/07).

[12] Data collection and pre-processing was realized by Lydie Dufour, which I warmly thank for her dedicated care.

[13] The authors acknowledge Météo-France for supplying the data and the HyMeX database teams (ESPRI/IPSL and SEDOO/Observatoire Midi-Pyrénées) for their help in accessing the data.

[14] Data extraction at study sites was realized using a Python script developed at CESBIO by Mireille HUC.

Table 6: Meteorological data source and properties – *Res*: Resolution, *Acc.* Accuracy - * The time period correspond to the selected one for the purpose of this work.

Study site applications	Time period*	Data type	Location	Variables	Res.	Acc.	Range	freq	Source
Lagardère (32)	2016	**Weather station** Vantage Pro 2 station + pyranometer #6450 from Davis© at 2m high cabled on CaipoBase GSM data logger CAIPOS©	on site at 2m 0° 19' 14,513" E 43° 49' 34,996'' N	Rg $T_{air\ avg}$ RH_{avg} WS WD R	1 W/m^2 0.1 °C 1% 0.5 m/s 1° 0.2 mm	± 5 % ± 0.5 °C ± 3 % ± 1 m/s ± 3° ±0.20 mm	0 to 1 800 W/m^2 -40 to 60 °C 0 to 100 % 1 to 67 m/s 0 to 360° 0 to 999 mm	10'	Vitiforest – data teletransmission http://caipos.com/CaipoWeb/Weather/index
	1990 to 2016	**SAFRAN tiles**	Extraction at 0.30024 lat 43.83950 long (WGS 84) 8km * 8km	Tmax, Tmin, Tavg R ET_0	8 km * 8 km interpolation, of records taken by more than a thousand stations spread out in France			daily	Meteo France (Le Moine 2002)
	2015 and 2016	**Weather station**	Auch – Lamothe 43°41'20" N ; 0°36'04" E	Patm → calculation of ET0 WD in 2016 → correction of measure				1h	Meteo France Meteorological station Météo France # 32013005 source: Infoclimat : https://www.infoclimat.fr/observations-meteo/archives/1er/aout/2015/auch-lamothe/07622.html
Lapouyade (33)	2016	**Weather station** Vantage Pro 2 station + pyranometer #6450 from Davis© at 2m high cabled on CaipoBase GSM data logger CAIPOS©	on site at 2m 0° 17' 29,417'' E 45° 5' 9,559'' N	Rg $T_{air\ avg}$ RH_{avg} WS WD R	1 W/m^2 0.1 °C 1% 0.5 m/s 1° 0.2 mm	± 5 % ± 0.5 °C ± 3 % ± 1 m/s ± 3° ±0.20 mm	0 to 1 800 W/m^2 -40 to 60 °C 0 to 100 % 1 to 67 m/s 0 to 360° 0 to 999 mm	10'	Vitiforest – data teletransmission http://caipos.com/CaipoWeb/Weather/index
	1990 to 2016	SAFRAN data		Tmax, Tmin, Tavg R ET_0	8 km * 8 km interpolation, of records taken by more than a thousand stations spread out in France			daily	Meteo France (Le Moine 2002)
Restinclières (34)	2016	Campbell sensors cabled on CR1000© data logger, (Campbell Scientific Europe, Campbell park, UK)	On site (*A2* field) 3° 51' 43,2" E 43° 42' 18" N	Rg $T_{air\ avg,\ max,\ min}$ $T_{g\ avg,\ max,\ min}$ $RH_{max,\ min}$ WS WD R				1 h	INRA UMR System – contact: Lydie DUFOUR
	1995 to 2016	Meteo France station ID 34172005	Lavalette, (43.39°N, 3.52°E)	Rg $T_{air\ avg,\ max,\ min}$ $RH_{max,\ min}$ WS R ET_0				1 day	Meteo France via AGROCLIM contact: Lydie DUFOUR
	1990 to 2016	SAFRAN data		Tmax, Tmin, Tavg R ET_0	8 km * 8 km interpolation, of records taken by more than a thousand stations spread out in France			daily	Meteo France (Le Moine 2002)

IV.3.2.2 Vintages 2015 and 2016 at study sites

Lagardère (32)

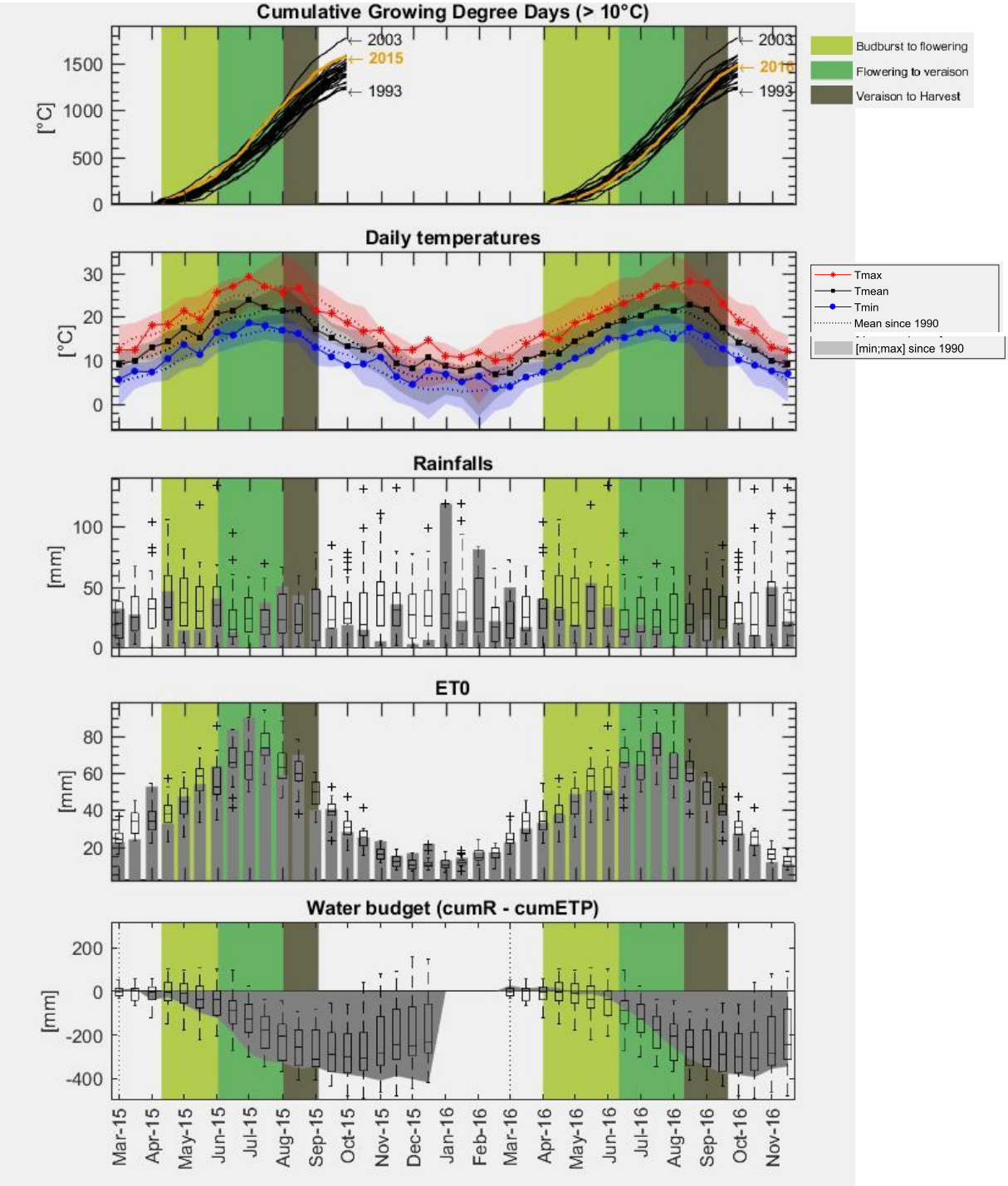

Figure 52: Climatic context in 2015 and 2016 and means since 1990 at Lagardère (32). From top to bottom are shown the time series of the cumulated degree days from 1st April to 30th Sept., the daily mean and extreme temperatures (T), the cumulated rainfalls (R), the cumulated reference evapotranspiration (ET0) and the water budget. Values were average / calculated over half-months - Data sources: SAFRAN daily data (Météo France)

At Lagardère (32), vintage 2015 faced one of the warmest spring and first half of summer since 1990 (**Figure 52**). The very high temperatures combined with unusually low rainfalls provoked a

pronounced drought all along the period from grapevine budburst to flowering. Then important rainfalls occurred in August and temperatures went back in the averages. From 2015 to 2016, winter was the warmest ever recorded since 1990, which contributed for budburst to happen 10 days earlier in 2016 than in 2015. From budburst to veraison, the cumulated heat and the precipitations were both in the averages from the whole period. Then from veraison to harvest, the berry ripening of 2016 vintage occurred in unusually warm and dry conditions: the last decade of August and the first decade of September were the warmest recorded since 1990, especially at night (**Figure 52**).

Lapouyade (33)

At Lapouyade (33), 2015 vintage had been a particularly dry year marked with unusually warm budburst to ripening period with very few rainfalls (**Figure 53**). The water deficit remained pronounced during veraison as well, though rainfalls became above the average. Then the first half of winter received very few rainfalls while the converse was true during the second half, in January and February 2016.

The 2016 vintage showed a particularly rainy spring while there were unusually very few rainfalls from flowering to berry ripening. Berry ripening occurred under particularly warm conditions during the first weeks. The daily mean and maximum temperatures reached respectively 22 °C and 29 °C in August, which is the highest ever recorded over the past 30 years. Then during the final days of berry ripening, temperatures cooled down back to average due to the comeback of rainfalls.

Restinclières (34)

In 2015, the vegetative growth of grapevine from spring to half summer happened under unusually dry conditions (**Figure 54**). The very high evaporative demand was caused by both very few rainfalls as well as very high temperatures. In July, the daily minimum temperature was 21 °C which was the highest ever reached since 1990. Then from 2015 to 2016, winter was particularly warm which may have contributed to budburst to happen 10 days earlier than in 2015.

In 2016, there were unusually few rainfalls from late spring to the beginning of summer. The month of August was also particularly dry. The temperatures remained in the averages throughout the whole season except in the second half of August where the mean and maximum daily temperatures reached respectively 23.0°C and 30 °C which were the highest values since 1990. As a consequence, the period from veraison to harvest was particularly short for the 2016 vintage.

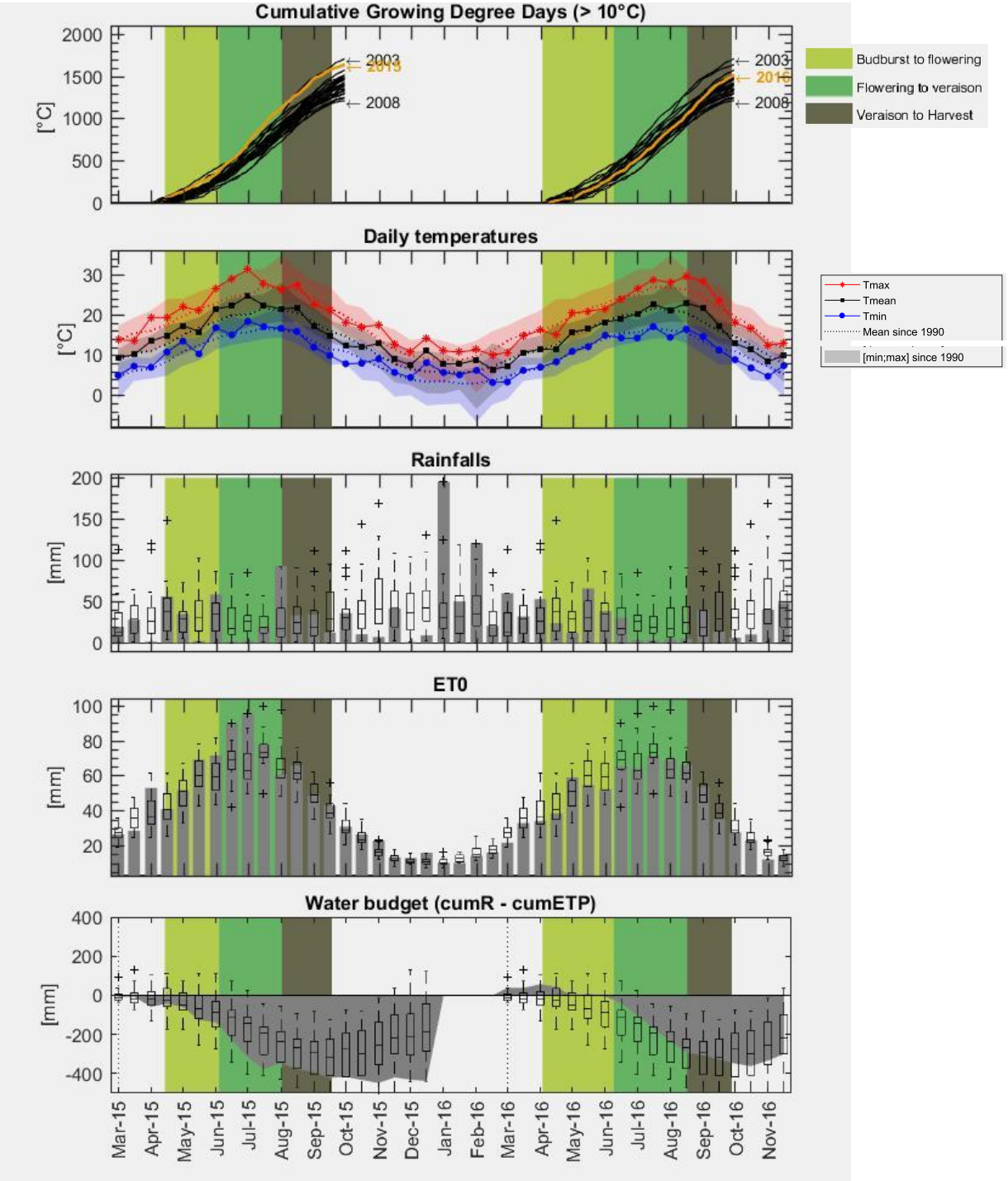

Figure 53: Climatic context in 2015 and 2016 and means since 1990 at Lapouyade (32). From top to bottom are shown the time series of the cumulated degree days from 1st April to 30th Sept., the daily mean and extreme temperatures (T), the cumulated rainfalls (R), the cumulated reference evapotranspiration (ET0) and the water budget. Values were average / calculated over half-months - Data sources: SAFRAN daily data (Météo France)

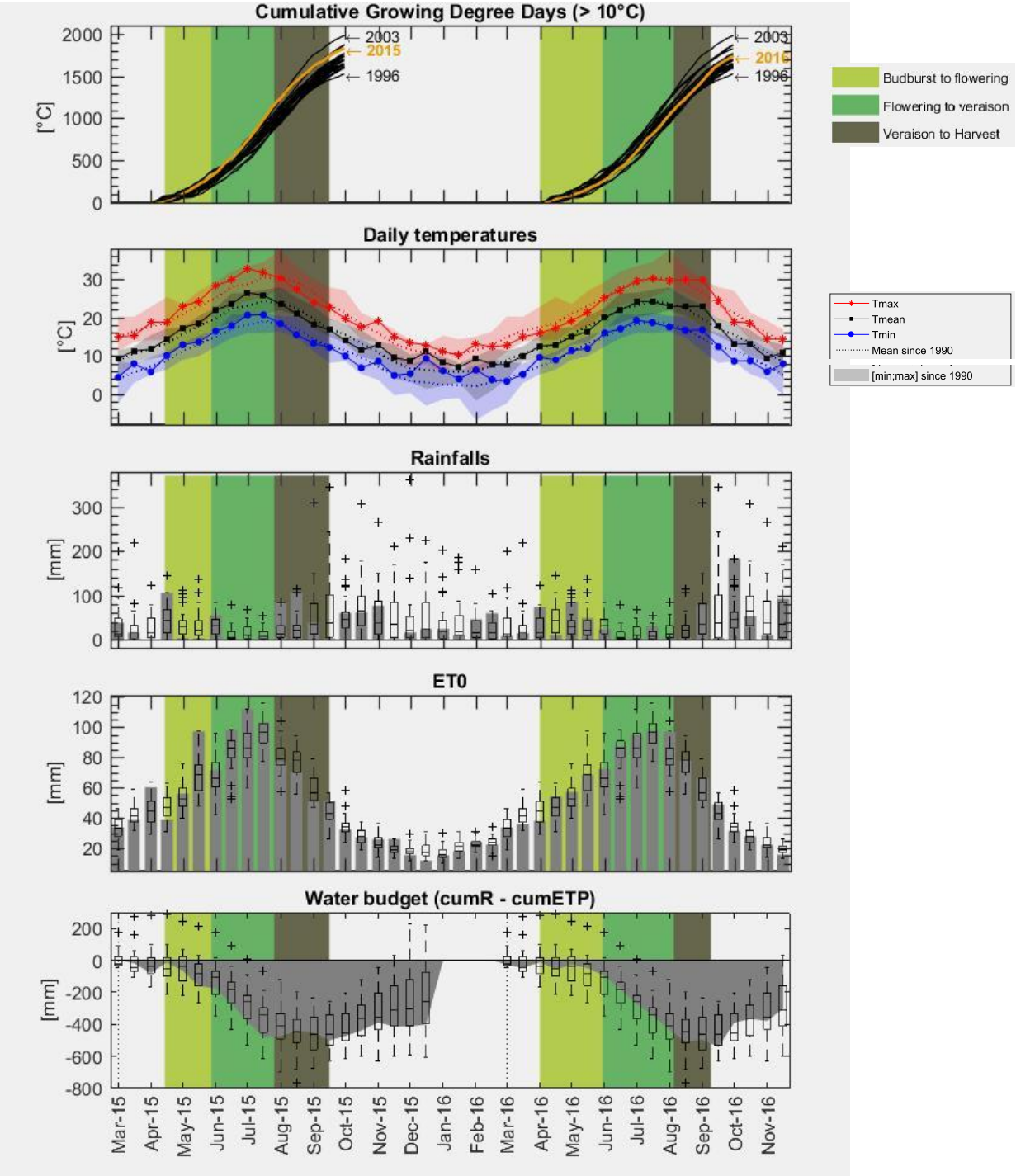

Figure 54: Climatic context in 2015 and 2016 and means since 1990 at Restinclières (34). From top to bottom are shown the time series of the cumulated degree days from 1st April to 30th Sept., the daily mean and extreme temperatures (T), the cumulated rainfalls (R), the cumulated reference evapotranspiration (ET0) and the water budget. Values were average / calculated over half-months - Data sources: SAFRAN daily data (Météo France)

IV.3.3 Distributed measurements of temperature and relative humidity

IV.3.3.1 Objectives

Batches of data loggers recording temperature and relative humidity were placed at Lagardère (32) in 2015 and at Lagardère (32), Lapouyade (33) and Restinclières (34) in 2016. The objectives of these campaigns were to assess the intra-plot heterogeneity of the microclimate and to precise its variability in time throughout the whole vegetative and reproductive cycle of grapevine.

In 2015, the data loggers were placed in order to record the air temperature within the canopy of grapevine and the air and relative humidity below grapevine foliage. Then in 2016, more data loggers were purchased and implemented on site. Time series of air temperature and relative humidity in the bunch area, and of ground temperature in the superficial horizon were all together recorded (**Annex B**).

IV.3.3.2 Data loggers

Two different types of iButton® data loggers were used: i) ***TG*** loggers for recording the **temperature,** ii) and ***TH*** loggers for recording simultaneously the **temperature and the relative humidity** (**Table 7**).

The frequency of the acquisitions was adjusted considering several factors:

i) the time scale at which temperature perceptibly changes, which is estimated at the order of a minute and of an hour for the air and for the ground temperatures respectively,

ii) in order to obtain sufficiently robust statistics at the daily time pace,

iii) so as to limit data collection to a practical maximum frequency of once every 5 weeks, given the available memory of the devices (**Table 7**).

Thus the frequency of data acquisition was set the following way:

- every 20 minutes for measuring the air temperature with TG data loggers,
- every 30 minutes for measuring the ground temperature with TG data loggers,
- and every 15 minutes for measuring the air temperature and relative humidity with TH data loggers.

Parameterization of the acquisitions and data collection were operated using 1-wire viewer®/iButton® software from Maxim integrated[15].

[15] 1-wire viewer®/iButton® is a free application from Maxim integrated available at https://www.maximintegrated.com/en/products/ibutton/software/tmex/download_drivers.cfm

Table 7: Specifications of TG and TH iButton® data loggers.

Data logger	Variables	Resolution	Accuracy	Measurement range	Memory (readings)
TG (iButton® DS1921G)	Temperature	0.5 °C	± 1 °C	-40°C to +85 °C	2048
TH (iButton® DS1923)	Temperature Relative Humidity	0.5 °C 0.5 % RH	± 0.5 °C ± 0.75 % RH	-40°C to +85 °C 0 to 100 % RH	4096 4096

IV.3.3.3 Loggers implementation

In the air, the iButton data loggers were hanged inside shading but aerated electric boxes. The boxes were fixed onto a wooden pole located on the vine rows, between two vinestocks, and were all facing North (**Figure 55 and Figure 56**). In 2015, the boxes containing a TG data logger were positioned at 50 cm above ground, which fell a bit bellow the bunch area, while boxes containing a TH logger were positioned at 150 cm above ground. These latter boxes progressively became surrounded by the vine leaves as the canopy grew up (**Figure 55**). In 2016, boxes with TH loggers were placed in the bunch zone this time in order to closely target the microclimate of berries and TG loggers were placed at -5 cm in the ground on the northern side of vine stocks (**Figure 56**). Though TG loggers were wrapped inside sticker paper for a better water-proofness, the ground was sometimes completely soaked, notably in spring at Lapouyade (33), and which damaged a few loggers (**Figure 56 b3**). In addition, a metallic tube of 5 cm length was used for excavating the ground and placing the logger underground. This manipulation turned out particularly tricky to reproduce identically at every selected vine stocks, notably in the very dry and rocky soil at Restinclières (34). It is identified as a potential source of inter and intra-plot noise in the measures of ground temperature.

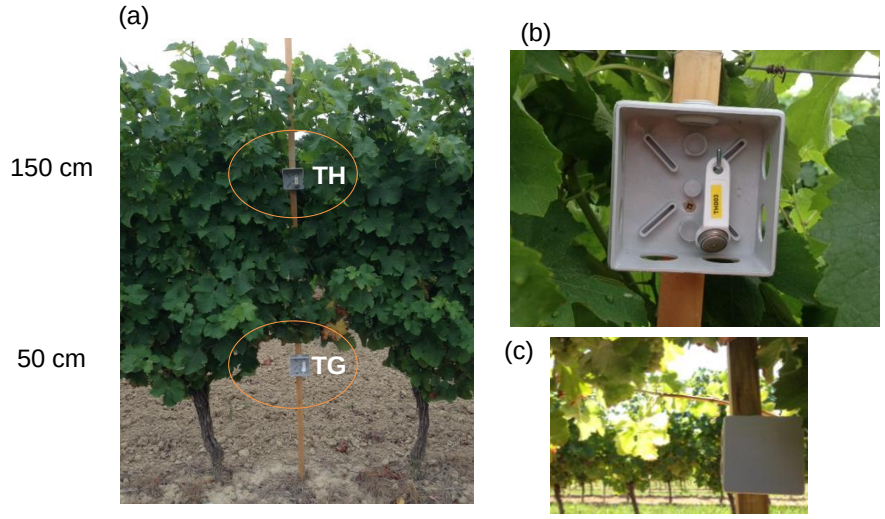

Figure 55: Installation in 2015 of TG and TH iButton® data loggers.

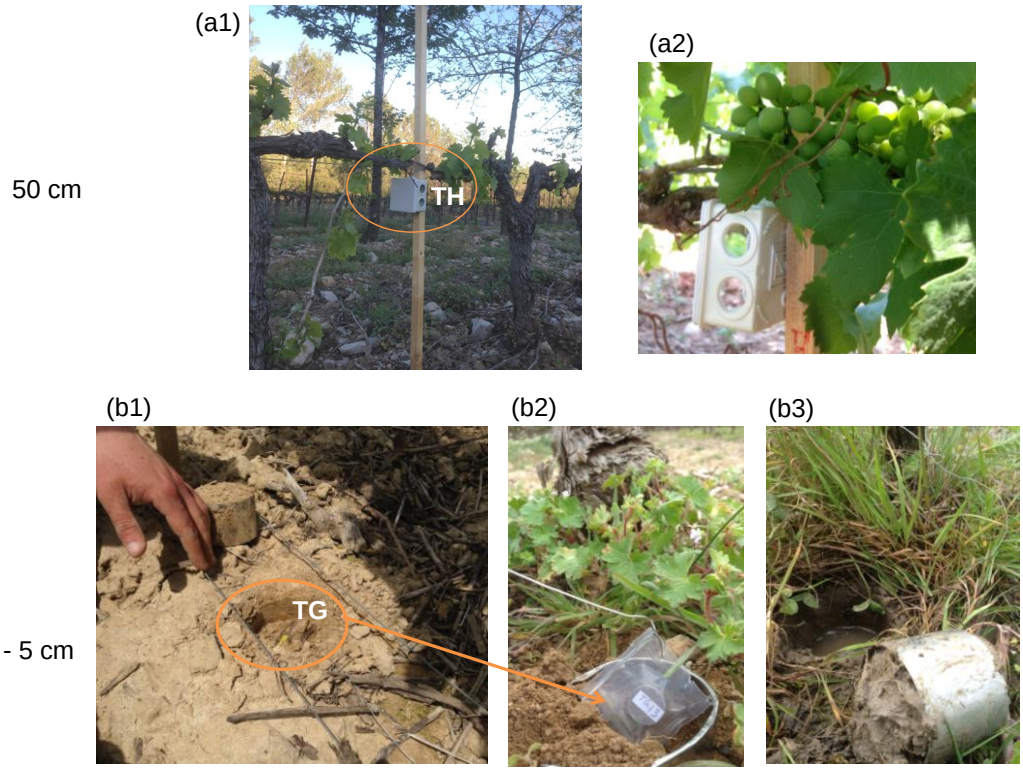

Figure 56: Installation in 2016 of TG and TH iButton® data loggers.

IV.3.3.4 Location of measures within the study vineyards

The data loggers were positioned at a selection of vine stocks within each study vineyard. For each measuring campaign, the selection was made in order to:

i) sample vine stocks located at various distances and sides to the intra plot tree rows,

ii) sample vine stocks located at various distances to the trees eventually surrounding the vineyard,

iii) sample a few vine stocks located far away from the intra-plot tree row to serve as a 'monocropped' reference,

Also, the aerial and underground data loggers were doubled respectively in the electric box and in the ground at two selected vine stocks per study vineyard in order to assess the inherent bias.

At Lagardère (32) in 2015, measures were carried out at 15 selected vine stocks (**Figure 55**): 10 were located in the southern part of the vineyard, around *Sorbus Domestica* and *Sorbus torminalis* tree rows (locations A to J) while 5 were located in the northern part, were there is no intra-plot tree (locations S to W). The measures were duplicated at I and J locations, placing two data loggers per box.

At Lagardère in 2016, the air temperature and the relative humidity were measured from 2016/03/10 to 2016/09/02 at 49 selected vine stocks (**Figure 58**): 44 of them were located in the southern part of the vineyard between *Sorbus Domestica* (C), *Sorbus torminalis* (A) and *Pyrus piraster* (P) tree rows and were organized into 5 transects at right angle with tree rows (AF1 to AF5), while 5 of them were located on the northern part of the vineyard (T1 to T5). The ground temperature

was measured from 2016/05/12 to 2016/09/02 only at 32 locations out of the total selection (**Figure 58**) for the sake of the workforce.

Figure 57: Location of in situ Ta and RH measurements (Δ) from 2015/07/29 to 2015/09/04at Lagardère (32). In I and J locations measurements were duplicated (white Δ)

Site	Name	25	AF1_Cs3
1	T1	26	AF2_Cs2
2	T2	27	AF2_Cs3
3	T4a	28	AF3_Cs2
4	T3	29	AF3_Cs3
5	T5	30	AF2_An2
6	T4b	31	AF1_An2
7	AF3_Cn5	32	AF5_Cs1
8	AF1_Cn2	33	AF4_Cs1
9	AF1_Cn1a	34	AF4_Cs3
10	AF1_Cs1	35	AF4_Cs2
11	AF1_Cs2	36	AF5_Cs2
12	T6	37	AF5_Cs3
13	AF1_Cn1b	38	AF5_An1
14	AF5_Cn3	39	AF5_An2
15	AF3_Cn3	40	AF4_An1
16	AF2_Cn3	41	AF4_An2
17	AF2_Cn2	42	AF3_An2
18	AF3_Cn2	43	AF3_An1
19	AF5_Cn2	44	AF2_An1
20	AF5_Cn1	45	AF3_As1
21	AF3_Cn1	46	AF3_As2
22	AF2_Cn1	47	AF1_Ps1
23	AF3_Cs1	48	AF1_Ps4
24	AF2_Cs1	49	AF3_As3

Figure 58: Location of Ta and RH measurements from 10 from 2016/03/10 to 2016/09/02 at Lagardère (32) (Δ and □) and of Tg measurements (□) from 2016/05/12 to 2016/09/02. In AF3_Cn1 and in T4 locations, the measurements were duplicated (white □).

At Lapouyade (33), *in* situ microclimate measurements were concentrated around the oldest intra-plot tree row named R4 (**Figure 59**). Measurements of ground temperatures (T_g) were carried out in

spring (from 2016/03/25 to 2016/06/11) on a selection of 10 vine stocks divided in two short transects at right angle with R4. Then measurements of air temperature (Ta) and relative humidity (RH) in the bunch area together with measurements of ground temperatures were carried out in summer (from 2016/07/11 to 23/09/2016/09/23) on a selection of 27 vine stocks. These latter locations divide in three W/E oriented transects, namely *A*, *B* and *C*, which are respectively located at a distance of 21 m, 33 m and 34 m from the forest at the southern border of the vineyard. Each transect contains 7 vine stocks located at 0 m to 4.5 m from the tree row and 2 vine stocks located at 30 m away from the tree row, either on the western or on the eastern side (**Figure 59**).

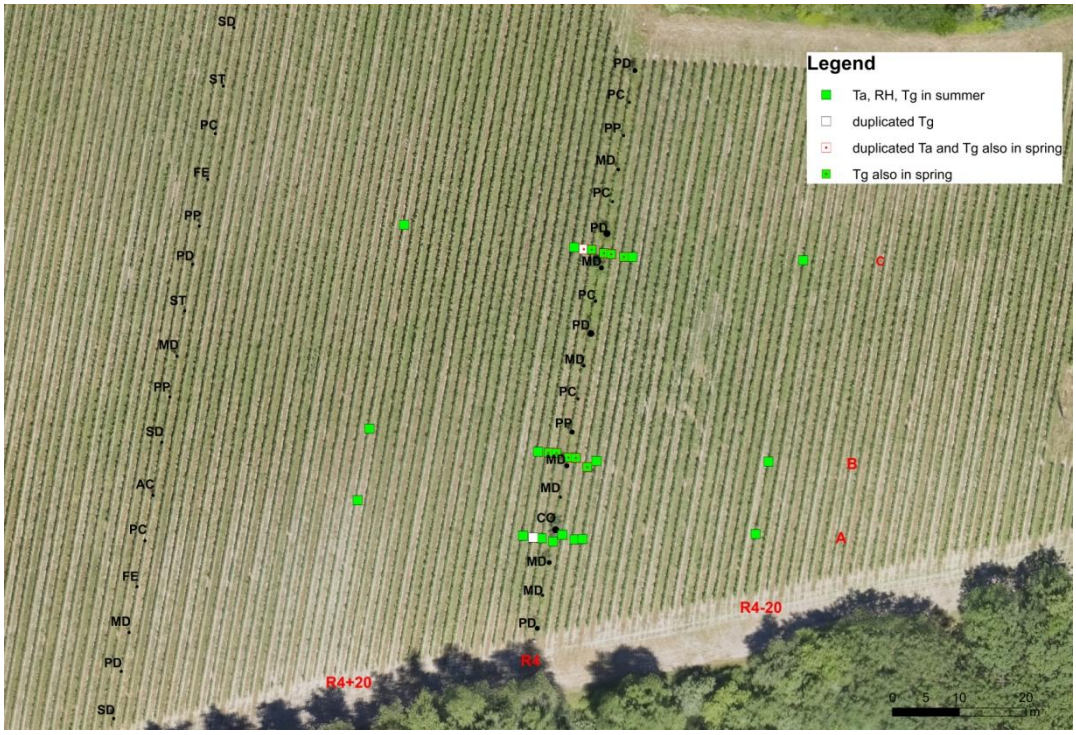

Figure 59: Locations of Ta, RH and Tg measurements (□) from 2016/07/11 to /2016/09/23 at Lapouyade (33). Measurements were duplicated at A_R4+2 and at C_R4+2 locations (white □). Tg was also measured from 2016/03/25 to 2016/06/11 on B_R4-2 to B_R4+3 and on C_R4-2 to C_R4+3 locations (dotted □)

At Restinclières (34), microclimate measurements lasted from 2016/03/01 to 2016/09/09. They were concentrated in the B4 and B3 plots of the Domain, within vine rows planted with the Grenach cultivar (**Figure 60**). The air temperature and relative humidity were measured at 39 selected vine stocks which divide in:

i) one transect in N/S agroforestry vine rows (plot B4) planted at a low density;
ii) three transects in N/S agroforestry vine rows planted at a high density;
iii) one pseudo-transect in the W/E agroforestry vine rows (plot B3) planted at high density;
iv) five vine stocks located in the monocropped area of reference (plot B4 vineRef).

For the sake of the workforce, ground temperatures were only measured at 15 vine stocks among the overall selection. This sub-selection assessed the N/S orientation (plot B4) planted at a high density.

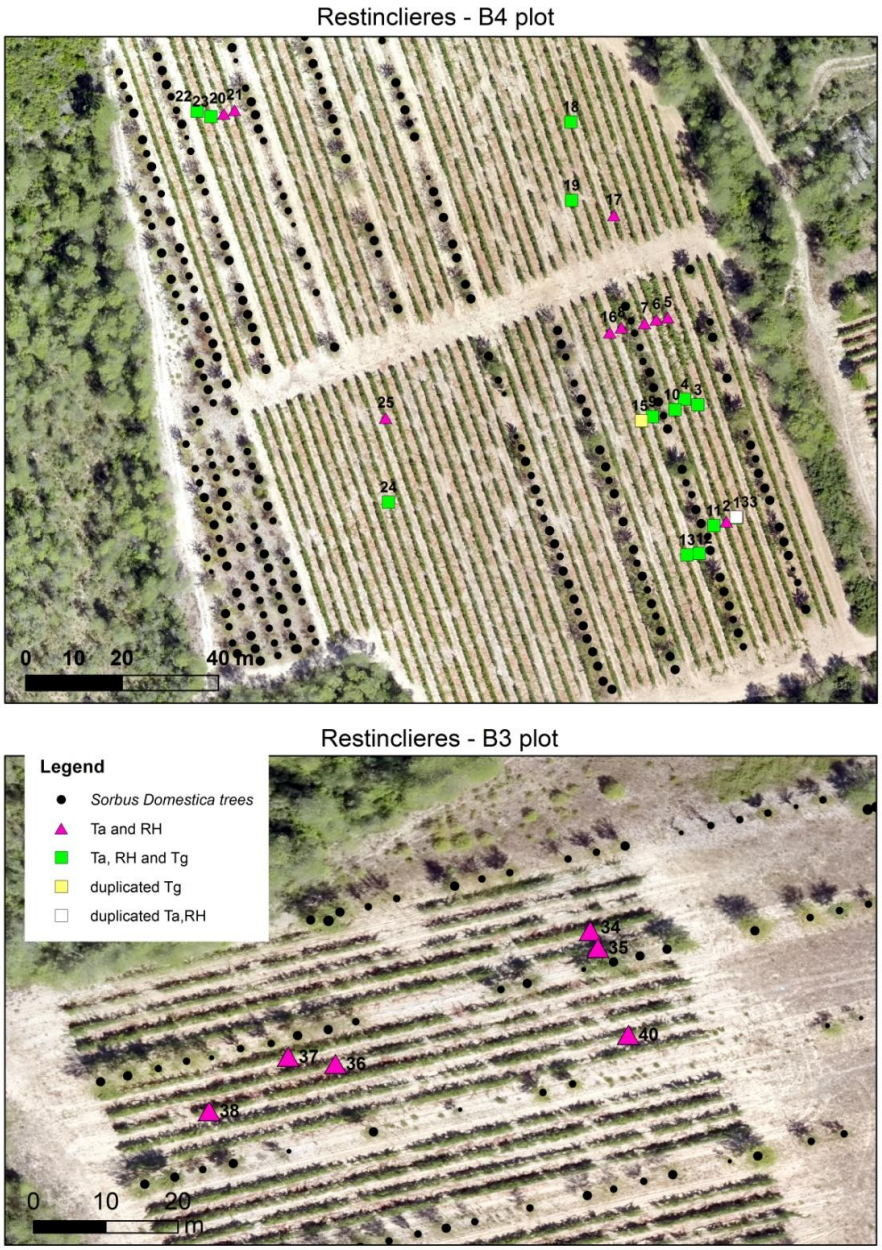

Site	Name		
1	AFB4HD3_Ce3a	17	T3
2	AFB4HD3_Ce2	18	T1
3	AFB4HD2_Ce3	19	T2
4	AFB4HD2_Ce2	20	AFB4BD_Co2
5	AFBAHD1_Ce3	21	AFB4BD_Co1
6	AFB4HD1_ce2	22	AFB4BD_Ce1
7	AFB4HD1_Ce1	23	AFB4BD_Ce2
8	AFB4HD1_Co1	24	T5
9	AFB4HD2_Co1	25	T6
10	AFB4HD2_Ce1	33	AFB4HD3_Ce3b
11	AFB4HD3_Ce1	34	AFB3_Cn2
12	AFB4HD3_Co1	35	AFB3_Cn1
13	AFB4HD3_Co2	36	AFB3_Cs2
14	AFB4HD2_Co2y	37	AFB3_Cs1
15	AFB4HD2_Co2z	38	AFB3_Cs3
16	AFB4HD1_Co2	40	AFB3_Cs4

Figure 60: Location of Ta and RH measurements (Δ) and of Ta, RH and Tg measurements (□) at Restinclières (34) from 2016/03/01 to 2016/09/07. TG data loggers were duplicated in AFB4HD2_Co2 location (yellow □), TH data loggers were duplicated in AFB4HD3_Ce3 (white □).

IV.3.3.5 Data pre-processing

Data loggers generated a .csv file per period of acquisition. The raw data were pre-processed using MATLAB 2016. Firstly, data from each site of measure were concatenated as a single time series using the site name as a unique identifier. Secondly, data from TH data loggers were truncated to only one decimal as the further one which were recorded are artifacts. Thirdly, all the time series from one measuring campaign were aligned according to a time of reference. For this purpose, raw data were interpolated using a spline cubic function (**Figure 61**). The time period of interpolation was set to 30 min for ground temperature measurement and to 10 min for the air temperature and relative humidity measurements. In order to guarantee the robustness of the interpolated values, the absence of missing data was check prior to interpolation. The interpolation was actually performed only when there was at least 1 measured data per hour in the ground temperature raw data and when there were at least 3 measures per hour in the air temperature / relative humidity raw data.

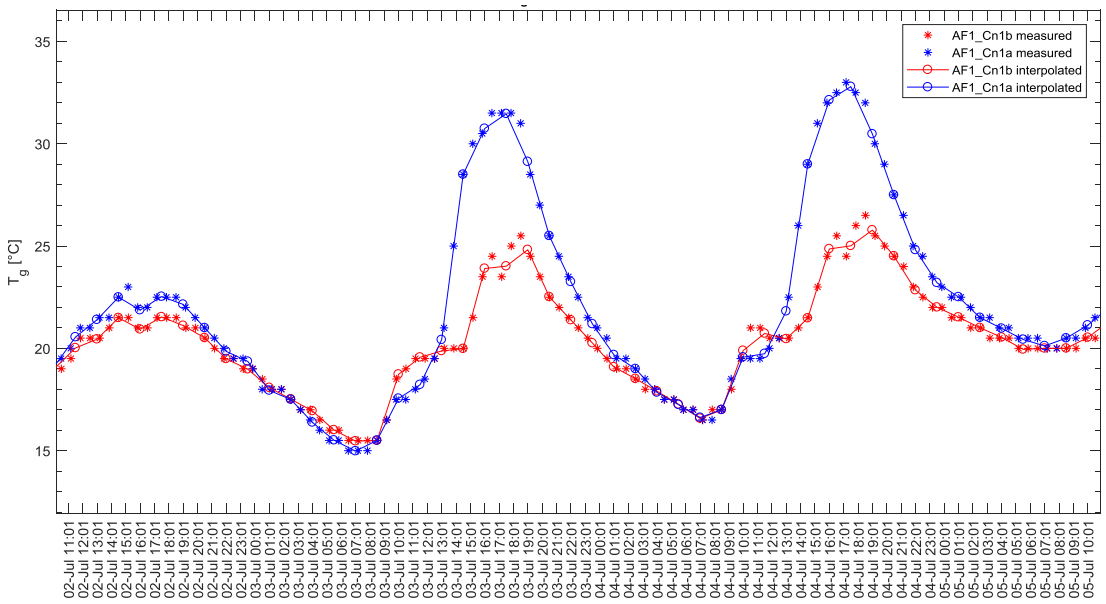

Figure 61: Raw data (*) and interpolated data (o) of ground temperature measured at sites AF1_Cn1b (red) and AF_Cn1a (blue) at Lagardère (32) in 2016

Fourthly, outlier values were eliminated. Indeed, two types of non applicable values appeared in the data:

- Specifically for the ground temperature measurement, data showed a too large daily range when the data loggers accidentally got pulled out from the ground (**Figure 62**). This happened notably when machines passed by grapevine middle row. This latter cause together with TG data loggers turning out of service were the two main causes of data loss (**Table 8**).
- Extremely high values punctually appeared at the date and time of data collection.

Both types of outlier values were removed from the data time series and were replaced by missing values.

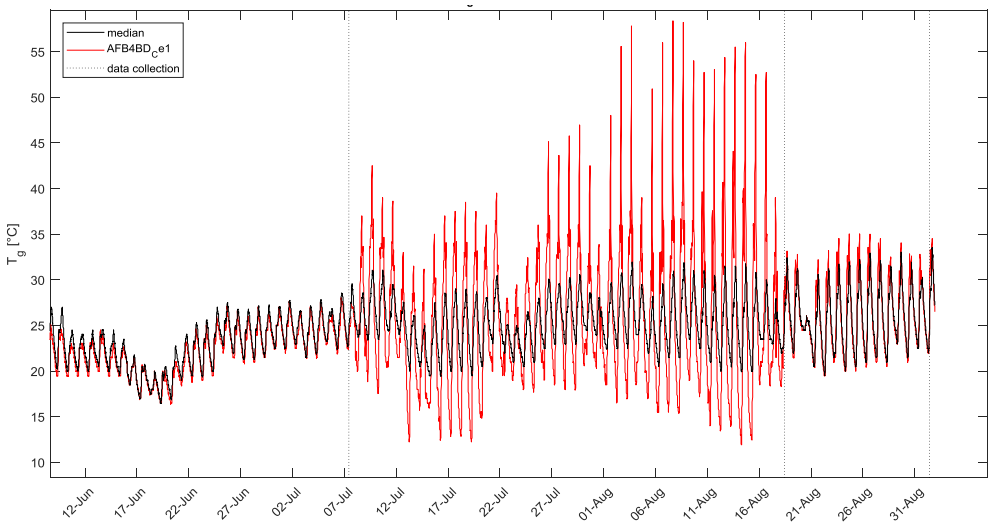

Figure 62: Example of outliers observed within the ground temperature time series measured at site AFB4BD_Ce1 as the data logger was accidentally pulled out from the ground (red). The median temperature serves as a reference (black), from the campaign at Restinclières (34) in 2016.

Table 8: Sources of data loss

		Lagardère (32) 2016	Lapouyade (33) 2016	Restinclières (34) 2016
T_g – TG loggers	Out of ground	5	6	3
	Out of service	3	2	1
	mistake / other			2
	Initial amount	34	28	15
T_a – TH loggers	Out of service			1
	mistake / other	5	2	
	Initial amount	49	28	34
RH – TH loggers	Out of service	1		1
	mistake / other	5	2	
	Initial amount	49	28	33

IV.3.3.6 Intrinsic error

For each experimental campaign, measurements were duplicated at two plots in order to estimate the intrinsic error of measurement. It comprises the contribution from the resolution and accuracy of the devices and from their positioning in the field. In the air; loggers were placed side by side in the same box. The air temperature measured in the bunch zone of grapevine shows difference between twin loggers centered on -0.37 °C and +0.52°C in average (respectively for T4 and AF1Cn1 plots) (**Figure 63a**). This small bias which is of same order than the resolution of sensors suggests that when considering the temperature at two distinct plots, differences smaller than these means should be considered meaningless. The difference of air temperature between twin loggers also shows daily periodic peaks of 1 to 4 °C which seem to be synchronous with the inversion of temperatures at sunrise. Over a day, the difference between twin sensors is the highest when the maximum temperature is reached and to secondary extent when the minimum temperature is reached.

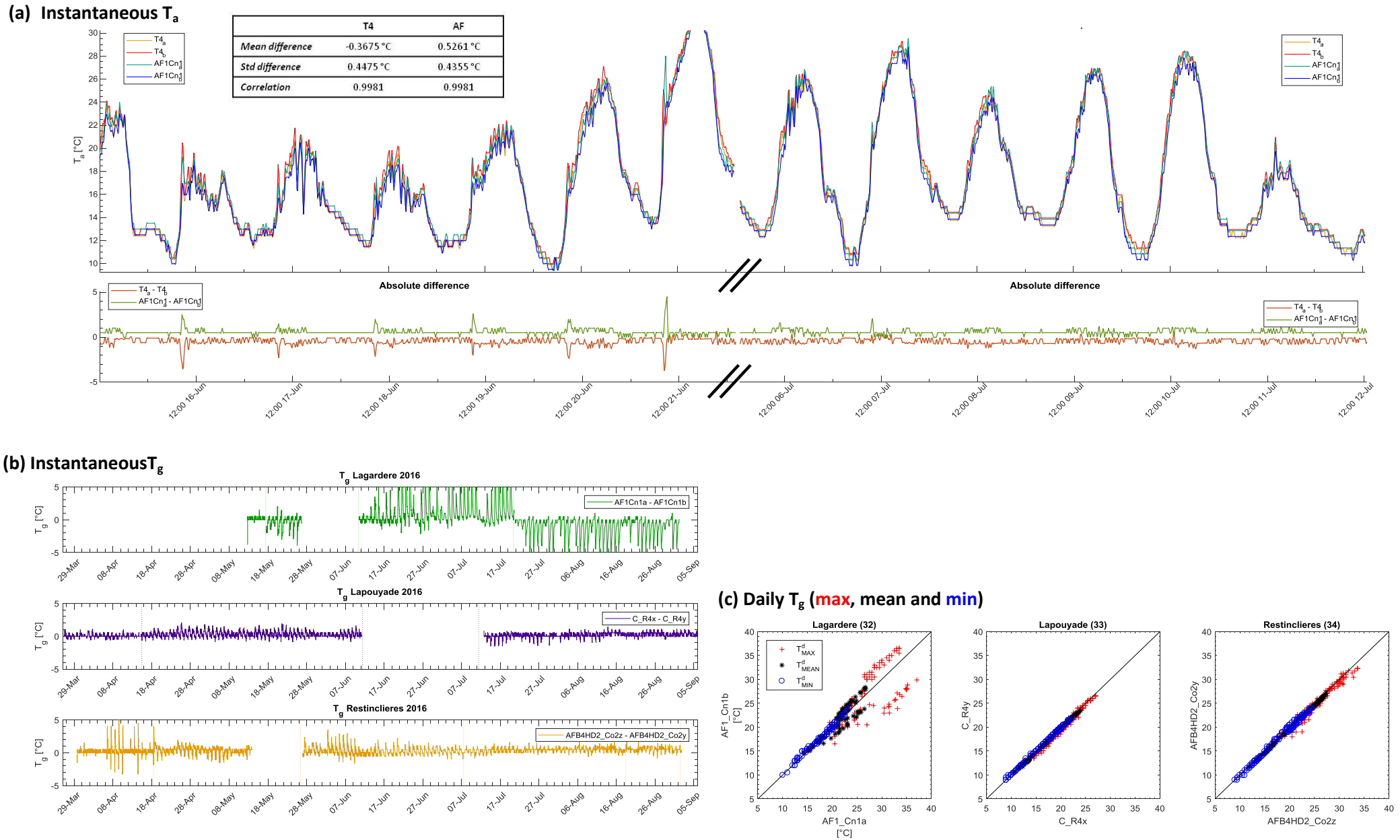

Figure 63: Comparison of measures taken by data loggers forming pairs at duplicated plots. (a) Time series of air temperature at plots *T4* and *AF1Cn1*, and differences between the pairs, Lagardère (32). (b) Ground temperature difference between the pairs of loggers, three study sites (c) Comparison of the daily statistics of ground temperatures between pairs of data loggers, three study sites. The dotted lines mark data collection.

The ground temperature shows differences of 1 to 5 °C between twin loggers and is strongly disturbed at data collection (**Figure 63b**). These disruptions may be explained by difficulties for positioning sensors in the ground at identical depth and in full contact with the above column of dust, depending on the state of the soil at the installation of loggers. They frequently generated differences of more than 5 °C on the maximum daily temperatures (**Figure 63c**). Such important divergences between air temperatures measured at the same vine stocks suggest that further interpretation of the spatial variability of the ground temperature is risky.

IV.3.4 UAV born imagery data set

Though free aerial images with very high spatial resolution (from 5 m to 30 m) and high frequency of revisit (Martimort et al. 2007) are now available from the Sentinel-2 satellite, their spatial resolution remain too loose for the study of vineyards (Hall et al. 2003). More generally, the main limitations for assessing vine morphological properties and functioning from currently available satellite images comes from the heterogeneous structure of vine canopy: thin rows of foliage relatively to the width of middle rows generate a mixed signal in nearly all pixels (Weiss and Baret 2017). Based on this evidence, the acquisition and analysis of images by flying Unmanned Aerial Vehicles (UAV) is highly at stacks and rapidly developing for applications in precision viticulture (Hall et al. 2002). On the one hand, visible stereoscopic images allow building digital elevation models of the vineyards with centimetric resolution. Multispectral images allow the computation of vegetation indices such as the NDVI (normalized difference vegetation index) (Rouse et al. 1974). Their combination has shown promising results for characterizing the morphology and biomass production of grapevines (Hall et al. 2001, 2003; Dobrowski et al. 2002; Caruso et al. 2017; Weiss and Baret 2017). On the other hand, thermal infrared acquisitions are developing in order to improve knowledge regarding grapevine water stress and eventually provide irrigation management tools (Moller et al. 2006; Fuentes et al. 2012; Pou et al. 2014; Bellvert et al. 2014; Santesteban et al. 2017).

Similarly, recent promising results were obtained concerning the characterization of the morphological traits of isolated trees (Zarco-Tejada et al. 2014; Lim et al. 2015) or shelterbelts (Yang et al. 2017) from very high resolution visible images, DEM and multispectral images.

IV.3.4.1 Device properties

A campaign of imagery acquisition was performed using two identical Unmanned Aerial Vehicles (UAV) available at the GEODE research unit, under the supervision of Thomas Houet. The two UAVs are polypropylene flying wings – eBee® from senseFly – with a wingspan of 96 cm (**Figure 64a**). Their propeller is positioned at the back and powered by an electrical battery which allows maximum flight duration of 40 minutes. These UAVs allow a cruise speed ranging from 40 to

90 km/h and present a wind resistance up to 45 km/h. The flight maps were planned prior to take off using eMotion 2 software and the UAV flew in autonomy (**Figure 64b**).

Three different types of sensors were successively placed on board of the UAV, namely a RGB (Red-Green-Blue) digital camera (DSC-WX220 by Sony), a four bands multispectral sensor (multiSPEC 4C from Airinov) and a thermal infrared sensor (thermoMAP from senseFly). Their spectral specifications are given in **Table 9**.

The multispectral sensor requires calibration prior to each flight, which was performed using a target furnished by the constructor.

The thermal infrared sensor by default considers that the emissivity of the observed surface equals $\epsilon = 1$ (blackbody hypothesis). In addition, using a real time acquired measure of the atmosphere temperature, it corrects the measured temperature by subtracting the thermal infrared energy flux which is actually emitted by the column of air between the ground and the sensor.

For the three sensors, positioning targets on the ground was necessary in order to geo-reference the images (**Figure 64c**) – see next section.

Figure 64: UAV acquisition of images using an eBee® flying wing (a) which performed automated flights above study vineyards under the supervision of T. Houet (b). Six square or round aluminum targets of 50 cm length were distributed within each sites as ground control points for georeferencing (c).

Table 9: Specifications of the RGB, the multispectral (MS) and the thermal infrared (TIR) sensors.

	Device	***Spectral bands center (w: width)***	***Resolutions and domain of validity***
RGB sensor	DSC-WX220 (SONY)	$Blue_{RGB}$: 450 nm (w = 85 nm) $Green_{RGB}$: 520 nm (w = 125 nm) Red_{RGB}: 660 nm (w=75 nm)	18 M pixels Accuracy: 255 digital numbers
Multispectral sensor	multiSPEC 4C (Airinov)	$Green_{MS}$: 550 nm (50 nm) Red_{MS}: 660 nm (w = 50 nm) $Red\text{-}Edge_{MS}$: 735 nm (w = 20 nm) NIR_{MS}: 790 nm (w = 60 nm)	1.2 M pixels per sensor Image format : raw irradiance (10 bits tiff)
Thermal Infrared sensor	thermoMAP (senseFly)	TIR: [8 μm – 14 μm]	0.3 M pixels Temperature resolution = 0.1 °C Validity range = [-40 °C – 160 °C]

IV.3.4.2 Image properties

For the three study vineyards, images were acquired on two days of summer which were selected in order to target pre-veraison and post-veraison stages of grapevine (**Figure 50**). At Lagardère (32),

images were also acquired in late spring, at the flowering of grapevine in order to allow comparisons with images of foliage of grapevine and trees under development. The total area covered by the flights was of 16.4 ha at Lagardère (**Figure 65**), of 38.4 ha at Lapouyade (33) **(Figure 66**) and of 22.8 ha at Restinclières (34) **(Figure 67**), and were centered on the study plots. For each day of UAV flight, one RGB acquisition, one multispectral acquisition and three thermal acquisitions (before solar noon, at solar noon and after solar noon) were performed. The flight trajectories and altitudes were each time set in order to generate at least 5 overlapping images everywhere within the flied over areas. In order to retrieve ortho-mosaics, the multiple images were processed in several steps using the pix4D software: i) identification of tie point positions, ii) bundle block adjustment and IV) geolocation adjustment using ground control points. At each acquisition, six ground control points were widely distributed within vineyards over areas using aluminum targets of 0.5 m width (**Figure 64c**). The targets were geo-localized with a precision higher than 0.2 m using a differential GPS (DGPS)[16]. The ground control points that were obtained were imported in pix4D for adjustment and precision assessment.

In addition, because the RGB multiple images presented the highest resolution and percentage of overlap (at least 70 %), they were chosen and used for building a DSM. A dense point cloud was derived from overlapping images using the photogrammetric processing methodology proposed in the Pix4D software, which is based on the structure from motion algorithms (Küng et al. 2011). Then the DSM was interpolated from the dense point cloud applying a triangulation method, with tile merging and a final noise filtering filter.

Also, the NIR and Red bands from the multispectral images were used for computing the NDVI index of vegetation (eq. 1).

$$NDVI = \frac{\rho_{NIR} - \rho_R}{\rho_{NIR} + \rho_R} \qquad \textit{(Rouse et al. 1974)} \qquad [1]$$

with ρ_{NIR} Reflectance in the near infrared wavelength

ρ_R Reflectance in the red wavelength

The final XY resolution of the ortho-mosaics is approximately of 0.03 to 0.05 m for the RGB images and DEMs, of 0.10 m for the multispectral and NDVI images and of 0.25 m for the thermal infrared images. The maxima root mean square error of their georefencing is of same range as their resolution.

[16] I am thankful towards Romain Walcker in charge of the sharing of devices at DIPEE-Ecolab and towards Renaud Marti, Hugo Jantzi and Hugues Barcet from the GEODE research unit for their technical advices.

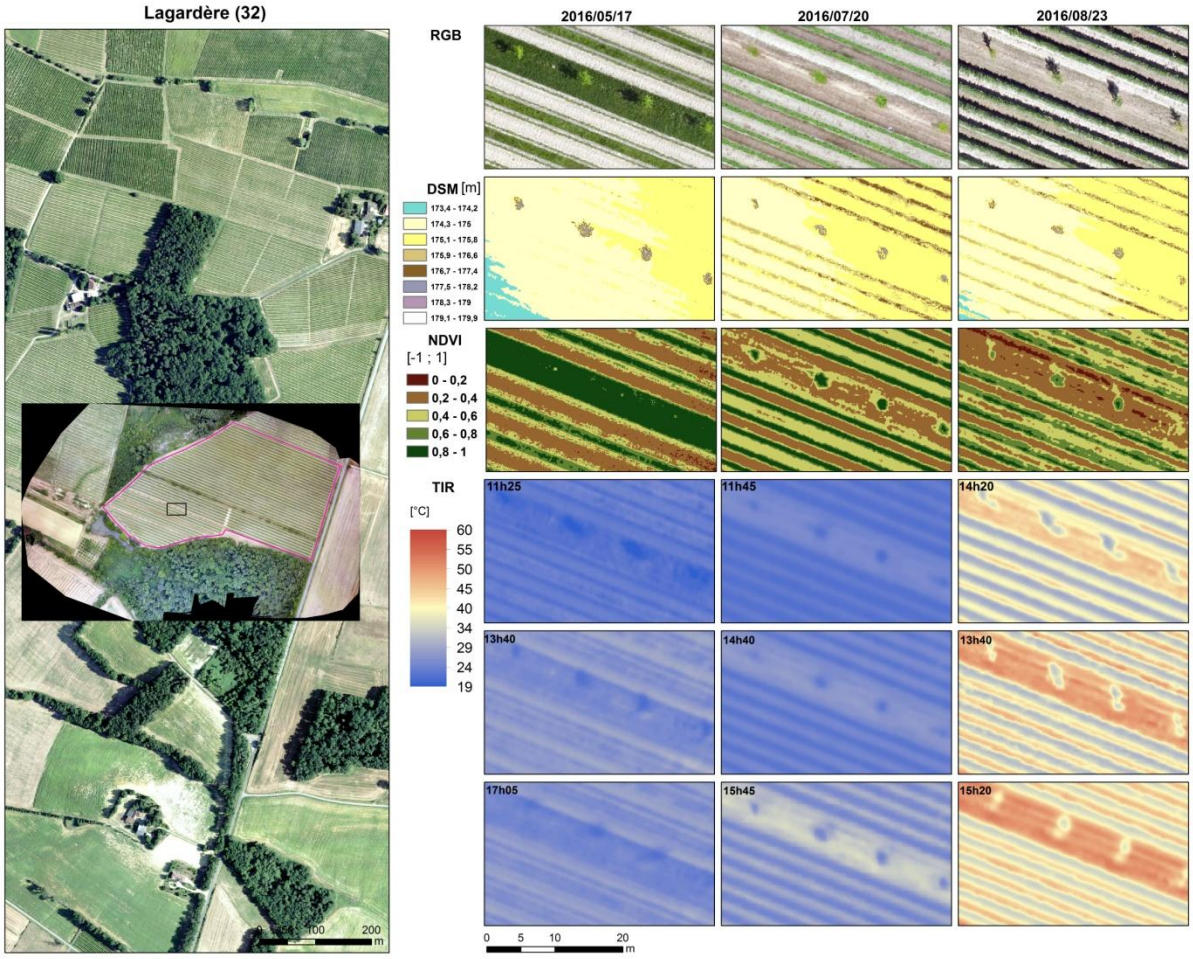

Figure 65: UAV born images taken at Lagardère (32) in 2016. On the left, the image shows the overall extent of the flights with experimental vineyard shown in pink. On the right, the images are zoomed captures from the black rectangle. The hour of the acquisition is given as local time (UTC + 2). Abbreviations: RGB: Red Green Blue camera; DSM: Digital Surface Model; NDVI: Normalized Digital Vegetation Index; TIR: Thermal Infrared. Background picture is from IGN (BDORTHO®50 cm in 2013)

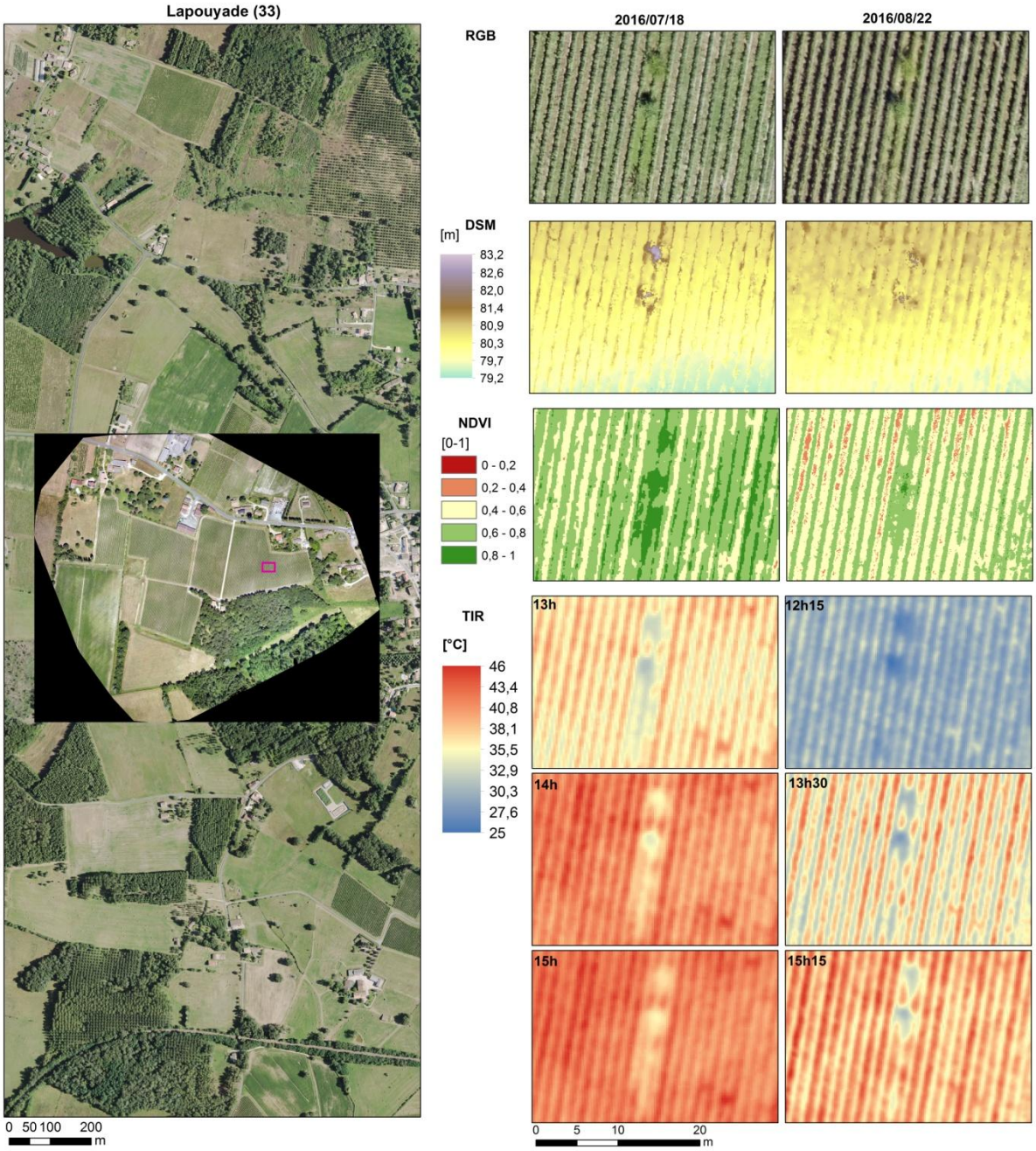

Figure 66: UAV born images taken at Lapouyade (33) vineyard in 2016: overall extent of the flights (left) with zooms on the pink square (right). The hour of the acquisition is given as local time (UTC + 2). Abbreviations: RGB: Red Green Blue camera; DSM: Digital Surface Model; NDVI: Normalized Digital Vegetation Index; TIR: Thermal Infrared. Background picture is from IGN (BDORTHO®50 cm in 2013)

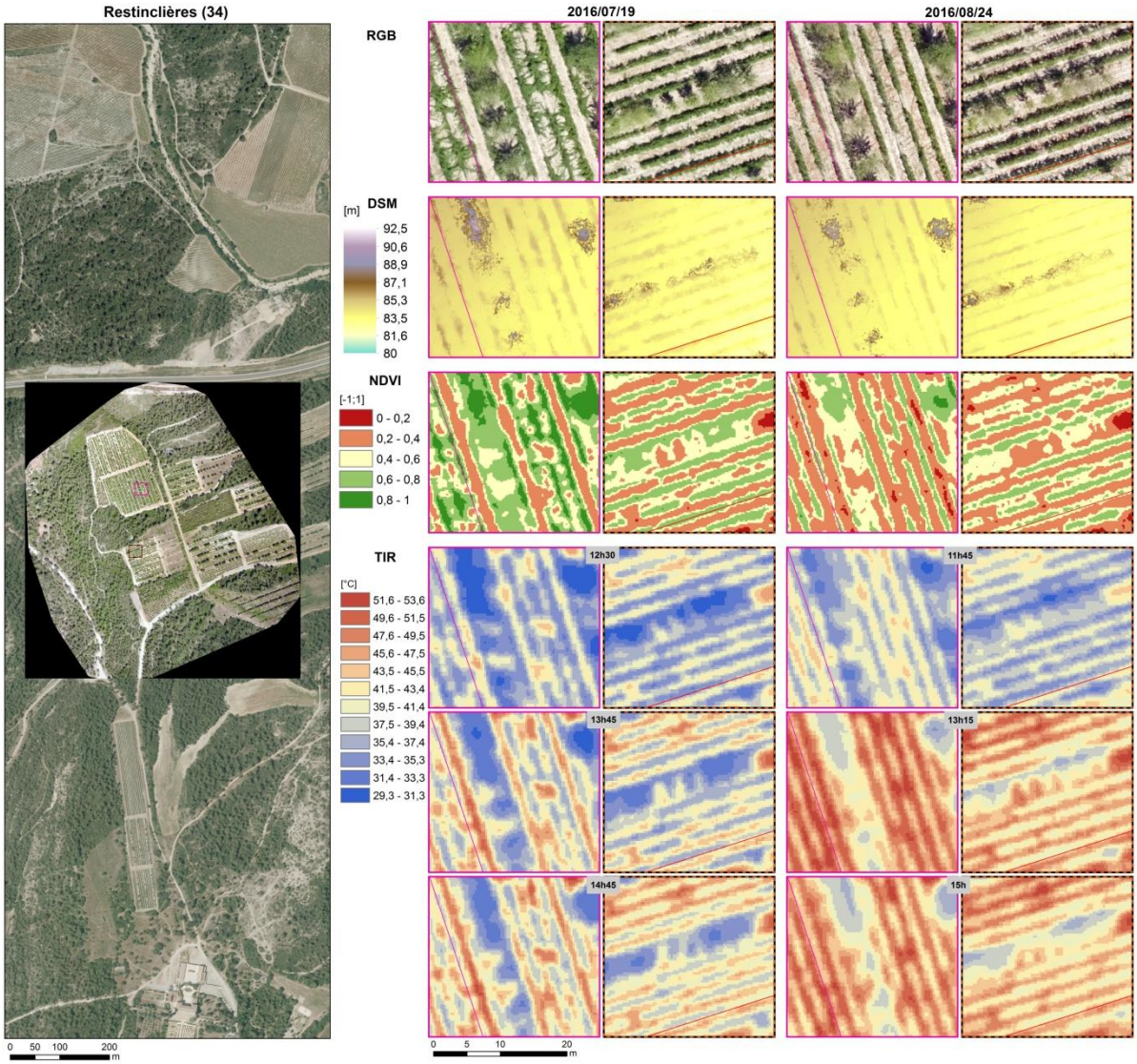

Figure 67: UAV born images taken at Restinclières (34) vineyard in 2016: overall extent of the flights (left) and zooms on the pink square and the orange and black square (right). The lines in zoomed images give example of location of a vine row. The hour of the acquisition is given as local time (UTC + 2). Abbreviations: RGB: Red Green Blue camera; DSM: Digital Surface Model; NDVI: Normalized Digital Vegetation Index; TIR: Thermal Infrared. Background picture is from IGN (BDORTHO®50 cm in 2013)

IV.3.5 Agronomy

The agronomic performances of grapevines were assessed at Lagardère (32), Lapouyade (33) and at Restinclières (34) in 2015 and in 2016. These experiments were supervised respectively by M. Thierry Dufourcq (Institut Français de la Vigne et du Vin, pôle Sud-ouest, France), by M. Marc Vergnes (Institut Français de la Vigne et du Vin pôle Bordeaux-Aquitaine, France) and by M. William Trambouze (Chambre d'agriculture de l'Hérault, Montblanc, France).

For the purpose of this thesis work the data set collected at Lagardère in 2016 was used for comparison with the temperature records. In this objective, sampling strategies were decided collaboratively with Thierry Dufourcq. The following subsections present the main characteristics of this data set.

IV.3.5.1 Phenological stages

Grapevine phenology was followed at each study site. Four different periods seemed the most relevant to distinguish, namely before budburst, from budburst to flowering, from flowering to veraison and from veraison to harvest. The phenological stages were determined at each study sites according to the extended BBCH scale (Lorenz et al. 1995) and are provided in **Table 10**.

Table 10: Phenological stages reported at the study vineyard in 2015 and in 2016 according to the extended BBCH scale of Lorenz et al. 1995.

	Lagardère (32)		*Lapouyade (33)*	*Restinclières (34)*
year	***2015***	***2016***	***2016***	***2016***
Budburst (BBCH 07)	10-Apr.	1-Apr.	14-Apr.	14-Apr.
Flowering (BBCH 65)	2-June	11-June	4-June	28-May
Veraison (BBCH 85)	2- Aug.	11- Aug.	2-Aug.	26-July
Harvest	4-.Sep.	21-.Sep.	18-Sept.	16-Sept.

IV.3.5.2 Sampling strategy

At Lagardère (32) the total amount and weight of cluster per vine were measured by sampling and averaging 5 neighboring vines in a row. The plots were selected at both vineyards according to several lines, each being at right angle to the AF tree rows, in order to cover several distances and orientations to the AF trees and to the forested borders. More precisely at Lagardère (32), 56 plots of 5 vines were harvested in total (**Figure 68**):

- 4 are located in the Northern part of the vineyard or monocropped area;
- 36 are located in the Southern part of the vineyard or AF area and divided in 4 lines at a right angle to the AF tree rows;
- 16 are located at the vine row borders – 6 at the western, 8 at the eastern and 2 at the southern border – in order to value specifically the variability in yield that is due to the specific microclimate at borders plus the increased browsing by deers.

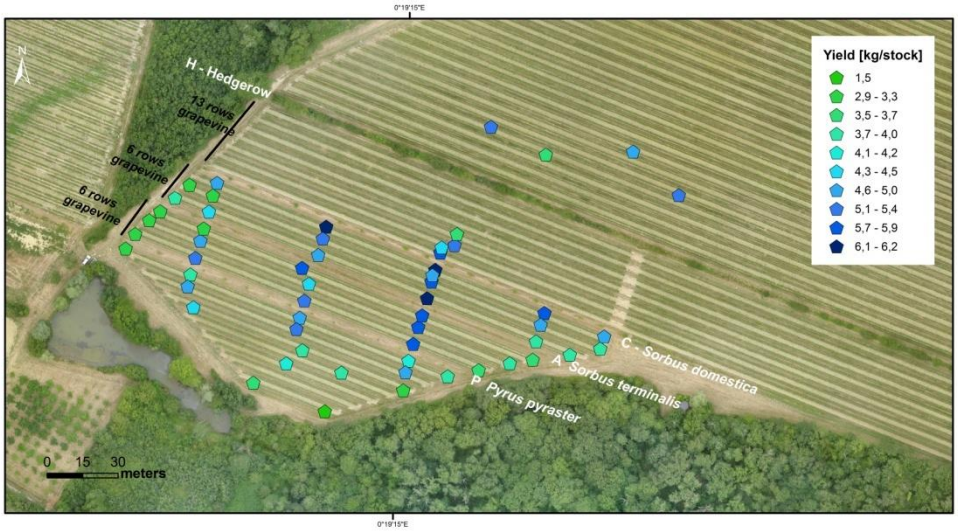

Figure 68: Yield measured at sampled plots in 2016, Lagardère (32) study site.

At Lapouyade (33), similarly to Lagardère (32), sampling plots were constituted of 5 neighboring vines in a row. 50 plots were harvested in total. They were organized in transects of increasing distances to the internal tree rows and to the southern forested hedge.

At Restinclières (34), agronomic measurements were obtained from harvesting single vines distributed at various distances and orientation from the trees. It was concluded that this sampling strategy allows considering the distance and orientation factors from computation of average yield but is not sufficiently robust for spatializing data.

IV.3.5.3 Yield components

According to (Smart and Coombe 1983), yield at the vineyard scale may be written in terms of its components:

$$Yield\ [kg.ha^{-1}] = \ vines\ [ha^{-1}]\ .yield\ [kg.vine^{-1}] \quad (9)$$

$$yield\ [kg.vine^{-1}] = \ clusters\ [vine^{-1}]\ .mean\ cluster\ weight\ [g].0.001 \quad (10)$$

$$clusters\ [vine^{-1}] = nodes\ retained\ [vine^{-1}].\ shoots\ [node^{-1}]\ .\ clusters_S\ [shoot^{-1}] \quad (11)$$

$$cluster\ weight\ [g] = berries\ [cluster^{-1}].mean\ berry\ weight\ [g] + \ rachi\ weight\ [g] \quad (12)$$

with $shoots\ [node^{-1}]$: budburst
$clusters\ [shoot^{-1}]$: fruitfulness

The terms in blue correspond to the variables that were sampled i.e. the total amount and weight of clusters per vine and the mean berry weight. Based on equation **(10)**, we calculated the mean cluster weight.

IV.3.5.4 Berry composition

Berry composition was measured in laboratory from the random collection of 200 berries per plot. The targeted variables concerns the sugar content, the total acidity and aromatic acidity, the polyphenol content and the nitrogen content (**Figure 69**).

	Variable name	***Unit***	***Description***
Quantitative	$Yield$	$kg.vine^{-1}$	Total weight of bunches per vine
	$BunchNb$	$nb.vine^{-1}$	Number of bunches per vine
	$BunchW$	$kg.bunch^{-1}$	Average weight of one bunch computed from $Yield = BunchW * BunchNb$
	$200BerryW$	g	Average weight of 200 berries
Qualitative	$Sugar$	$g.L^{-1}$	Concentration in fermentable sugars
	$TotAcid$	$g.L^{-1}$ H_2SO_4	Titratable acidity (total concentration of free protons and undissociated acids)
	pH		Logarithmic concentration of free protons
	$MalicAcid$	$g.L^{-1}$	Concentration in malic acid
	$TartaricAcid$	$g.L^{-1}$	Concentration in tartaric acid
	TPI		Total polyphenol index measured as the absorbance at 280 nm
	$NitrogenA$	$mg.L^{-1}$	Assimilable nitrogen
	$Potassium$	$g.L^{-1}$	Potassium

Figure 69: Yield parameters and must components measured at harvest in 2016 at Lagardère (32) and Lapouyade (33) by IFV.

IV.4 Characterizing vegetation structure

The review of literature presented in chapter II reveals that the microclimatic contribution from trees and from the overall vegetation depends and varies upon the morphological traits of the vegetation and its spatial arrangement. Remote sensing at very high resolution provides an effective way to characterize the morphological traits of both vineyards (Hall et al. 2002, 2003; Dobrowski et al. 2002; Smit et al. 2016; Weiss and Baret 2017; Poblete-Echeverría et al. 2017) and agroforestry systems under tropical contexts (Ovalle et al. 1996; Lelong et al. 2004, 2014; Gomez et al. 2010; Bégué et al. 2015, 2018; Karlson et al. 2016). The methodology which is proposed in order to describe the vegetation structure in an agroforestry vineyard consist firstly in mapping the land occupation and secondly to characterize the vegetation structure by the use of varied metrics. At each step, several methods were tested. Their main traits and relevance regarding the study of agroforestry vineyards are presented and discussed in the following subsections.

IV.4.1 Land occupation mapping

Two methodologies were tested in order to map the land occupation within and around the study vineyards at a resolution of 10 centimeters. The first one is an object based approach which consisted in segmenting the pixels and selecting the objects that were obtained according to their morphological traits. The second one is based on a supervised classification of the pixels. Both approaches were experimented using the UAV born imagery data set acquired in 2016 at each study vineyard. The resolution of the final map to obtain was chosen as it corresponds to the average size of grapevine leaves and as it was of same range as the resolution of the UAV born images.

IV.4.1.1 Object based approach

Object based image analysis approaches have been increasingly implemented in remote sensing to overcome issues due to pixel heterogeneity and crop variability within fields (Blaschke 2010; Peña-Barragán et al. 2011). It mainly consists in segmenting images into homogenous objects and by the mean time sorting these objects into distinctive classes according to several types of features such as pixel values, contextual information, object features, neighborhood and hierarchical relationships (Baatz and Schäpe 2000).

The whole object based approach which was tested for mapping the land occupation at the study vineyard of Lagardère (32) is illustrated in **Figure 70**.

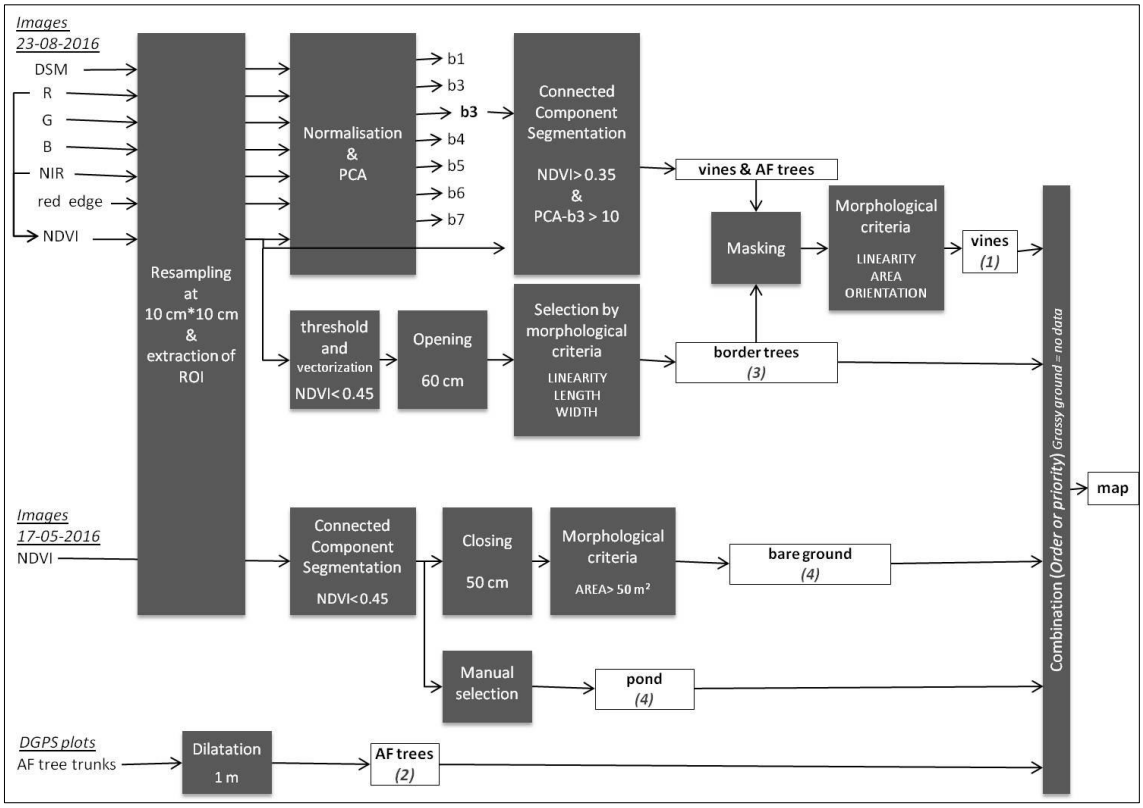

Figure 70: Flow chart of the methodology tested for building the land occupation map of the agroforestry vineyard at Lagardère (32) by an object based approach. Simple text indicates input data, filled boxes indicate treatments and empty boxes indicate vector layers. Abbreviations: AF= agroforestry (refers to rows of trees intercropped between vine rows) - *DSM= Digital Surface Model - ROI= Region Of Interest – PCA = Principal Component Analysis*

Image preparation prior to segmentation and segmentation itself were operated using the open source Orfeo ToolBox (OTB) (CNES 2018) and Geospatial Data Abstraction Library (GDAL) (GDAL/OGR contributors 2018) from a script written in Python. Then shape criteria computation, vector selection and layer combination were operated using ArcGIS software. All images acquired by the RGB and the multispectral sensors during UAV flights were used.

Image preparation mainly consisted in resampling and cropping all images according to an identical grid of reference of 10 cm of resolution. Then, in order to obtain vectors of vine rows, the information contained in the stack of image was summarized through principal component analysis which allowed enhancing contrasts between pixels (**Figure 71**). For example, the second axis from PCA resulted to be very intense in shaded areas while the third axis resulted to be very intense at pixels of foliage. As a consequence, this latter axis was used for performing a segmentation of the pixels. The connected component procedure which was used decides whether two neighboring pixels belong to the same segment according to a user defined criterion which was arbitrary chosen as $PCA_{b3} > 1$. In addition, a masking criterion defined as $NDVI > 0.35$ was applied in order to select the pixels within the image to be actually segmented and thus to reduce computation time. As no decision criteria could be found in order to break the confusion between grapevine foliage and tree foliage, the segmentation resulted in mixed types of vectors, either corresponding to grapevine rows, or to round canopies from trees. Thus, following the segmentation, a selection of the objects only

corresponding to vine rows was made. For this purpose, vectors corresponding to border trees were masked (position criterion) and vectors corresponding to intercropped trees were eliminated according to their low elongation or small areas or absence of preferential orientation, in comparison to that of vine row vectors (morphological criteria). These latter morphological metrics and computation procedure are defined (**Table 11**).

Following equivalent procedure, the vector layers of border trees, of bare ground and of water surface were generated (**Figure 70**). Two types of morphological operations were applied to temporary vectors: (i) in order to eliminate relatively narrow vectors, typically vine rows, an opening consisted in the dilatation of the erosion of the original vectors using a linear structuring element of a given half-width; (ii) in order to merge neighboring objects of a given class, a closing consisted in the erosion of the dilatation of the original binary image.

In addition, a theoretical hull of canopy was built for each tree planted within grapevine rows. For this purpose the plots of individual tree trunk that were marked onsite by DGPS were buffered (dilatation) by an arbitrary radius of 1 m.

At last layers of vectors were combined in order to build the final map. A decreasing order of prior was set in order to manage superimposing conflicts and to label grassy ground as the default land occupation (**Figure 70**).

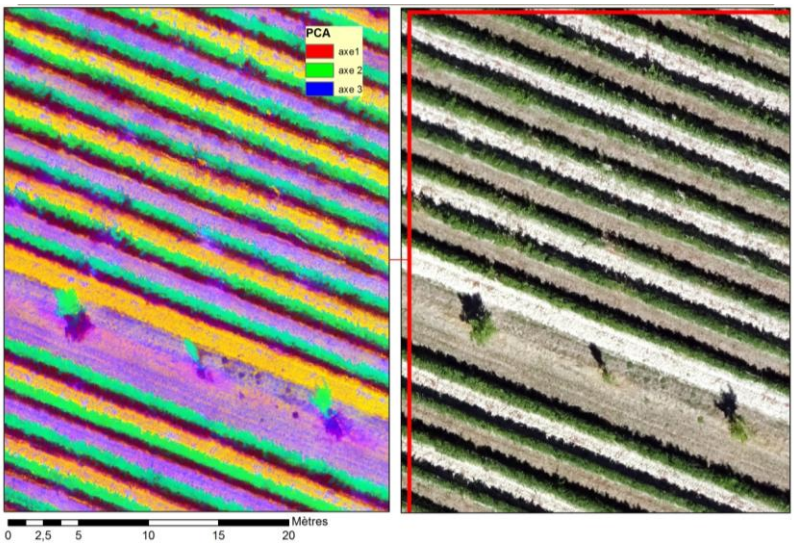

Figure 71: Comparison of the first, second and third axis obtained by principal component analysis (PCA) (left) and visible image acquired by the RGB sensor through UAV flight at Lagardère study vineyard (32) on the 23 Aug. 2016.

Table 11: Definition and implementation of the morphological metrics used for the land occupation mapping through an object based approach.

Morphological metric	Definition and unit	Implementation
AREA	[m^2]	Directly from the vector layer
ELONGATION	$p = \frac{radius\ of\ the\ biggest\ inscribed\ circle}{radius\ of\ the\ smallest\ excribed\ circle}$ p = 0 for a line p = 1 for a circle	1. Generate convex hull (CH) 2. Generate biggest inscribed and smallest excribed circles of CH (with ET GeoWizards plugin of ArcGIS) 3. Radius computation for each layer of circles 4. Spatial join of circle properties to original vector
LENGTH	[m]	1. Generate rectangular hull (RH) 2. Computation of RH length 3. Spatial join of rectangular hull properties to original vector
ORIENTATION	[° clockwise]	1. Generate convex hull (CH) 2. Computation of CH preferential orientation 3. Spatial join of rectangular hull properties to original vector
WIDTH	[m]	Same as length

The land occupation map of Lagardère (32) study vineyard obtained from the object based approach is presented in **Figure 72**. On the one hand, the overall location and areas of each land occupation is well represented. On the other hand, the positioning of grapevine pixels is inaccurate for two reasons: mainly because morphological operations were applied and to lesser impact because information from various dates were combined. In addition, the object based approach that was implemented allowed very poor accuracy in the position of tree foliage. In short, the land occupation map obtained with from object based approach is adapted for describing the overall structure of the vegetation within and around the vineyard. Nonetheless it does not allow an application such as the precise extraction of pixels of grapevine foliage of tree foliage. This latter observation notably raised the methodological issue of filtering the thermal infrared images using an accurate land occupation map at an exact date and at the pixel level. It thus motivated the experimentation of a second approach of land mapping based on supervised classification.

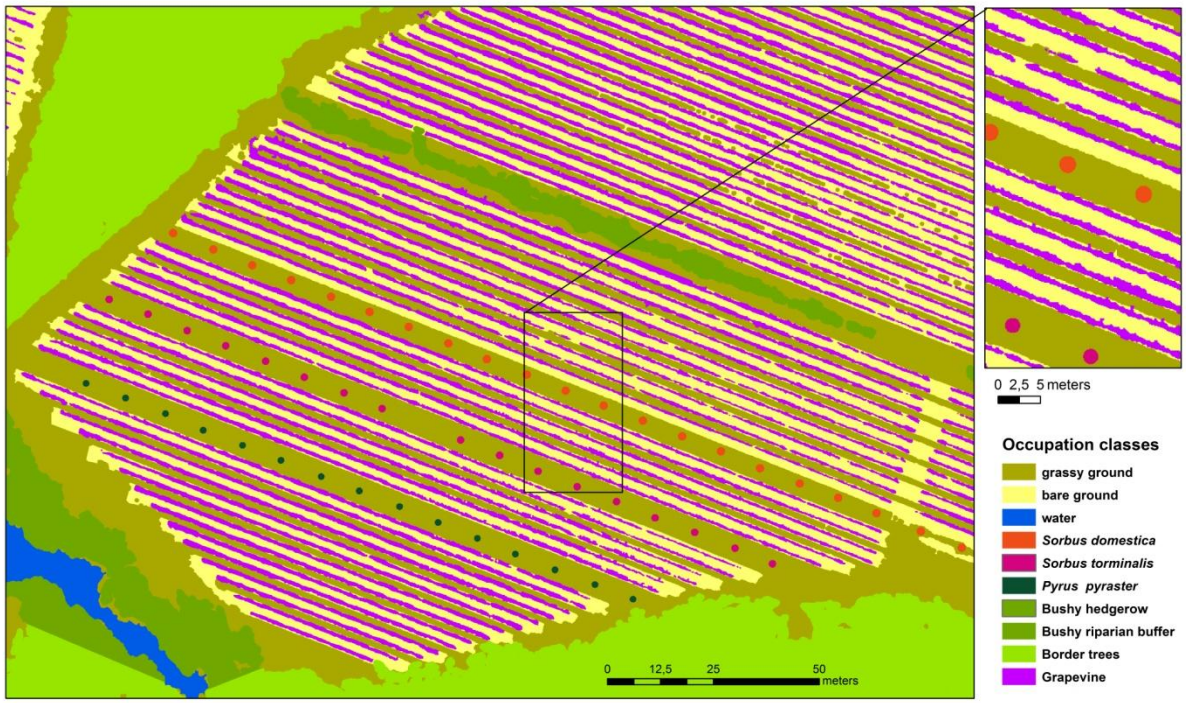

Figure 72: Land occupation map at the agroforestry vineyard of Lagardère in 2016 obtained from object based approach.

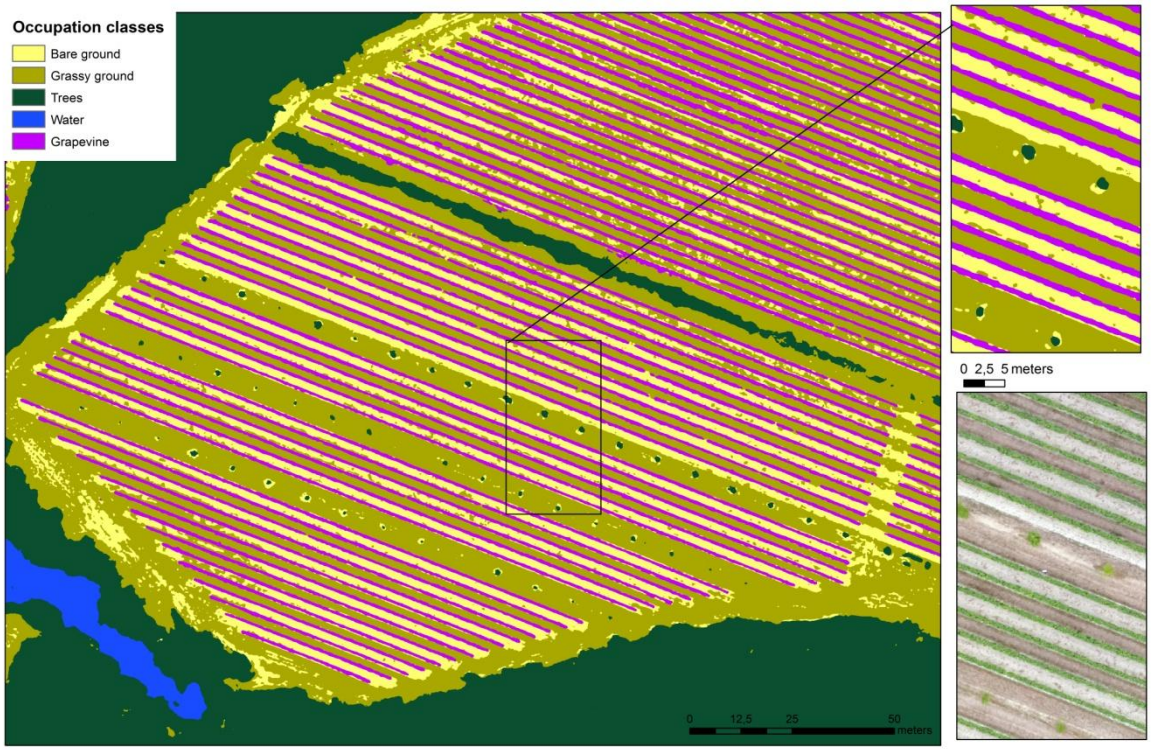

Figure 73: Land occupation map at the agroforestry vineyard of Lagardère on the 20 Jul. 2016 obtained from supervised classification approach

IV.4.1.2 Supervised classification approach

In a recent work, Poblete-Etcheverria et al. (2017) compared four classification methods for mapping the canopy of grapevine using very high resolution RGB images obtained from UAV flights above a vineyard. In their context, grapevine was trained with a vertical trellis systems and the ground was completely bare. These authors compared the performances of the K-means, the artificial neural networks, the random forest and a simple spectral index thresholding method considering three different land occupation classes, namely *Plant*, *Soil* and *Shadow*, and eventually considering additional spectral indexes obtained from the combination of the RGB bands. The best performances of classification of the three classes were obtained with the artificial neural networks just like the random forests methods and when spectral indexes were used together with raw bands as input data.

Following their recommendations a methodology of classification in three steps was implemented and tested on the stack of images obtained for each date and location of image acquisition (**Figure 74**). Data preparation was similar to that by object based approach described in the previous subsection except that two additional spectral indexes, namely the difference index ($2G$) and the green percentage index ($G\%$) - **Table 12** - were computed from the images acquired by the RGB sensor and added to the stack of input images. Classification was performed choosing the random forests method from Breiman (2001). Compared to the artificial neural network method, the random forests best suited our needs as it is much faster for learning samples, requires fewer learning samples, is robust to mislabeled samples and is more robust to parameters. In addition, the random forests method benefitted from a very good expertise developed at CESBIO for its implementation (Pelletier et al. 2016). The overall accuracies of the five maps from five different balanced calibration/validation sampling were of same range (from 0.89 to 0.94), as well as the Fscore of the vine class (from 0.84 to 0.90) (**Annexe E**). It confirms the robustness of the implemented approach. Similarly to the segmentation results, the maps obtained from classification suffered from important confusion between the classes of grapevine and trees (**Annexe E**). As a consequence, post-processing treatments were performed. They consisted firstly in applying a mask of position, as in the previous approach. Secondly, a skeptic position was adopted in order to improve the robustness of the grapevine class: a majority filtering treatment was applied specifically to the vine class so that only grapevine pixels being connected to other grapevine pixels were retained.

Except the building of calibration samples and of position masks, all treatments of the classification approach were performed using the open source Orfeo ToolBox (OTB) (CNES 2018) and Geospatial Data Abstraction Library (GDAL) (GDAL/OGR contributors 2018) and were automated into a single processing script written in Python. Thus the classification approach by far supplants the previous object based approach in terms of rapidity of implementation and reproducibility.

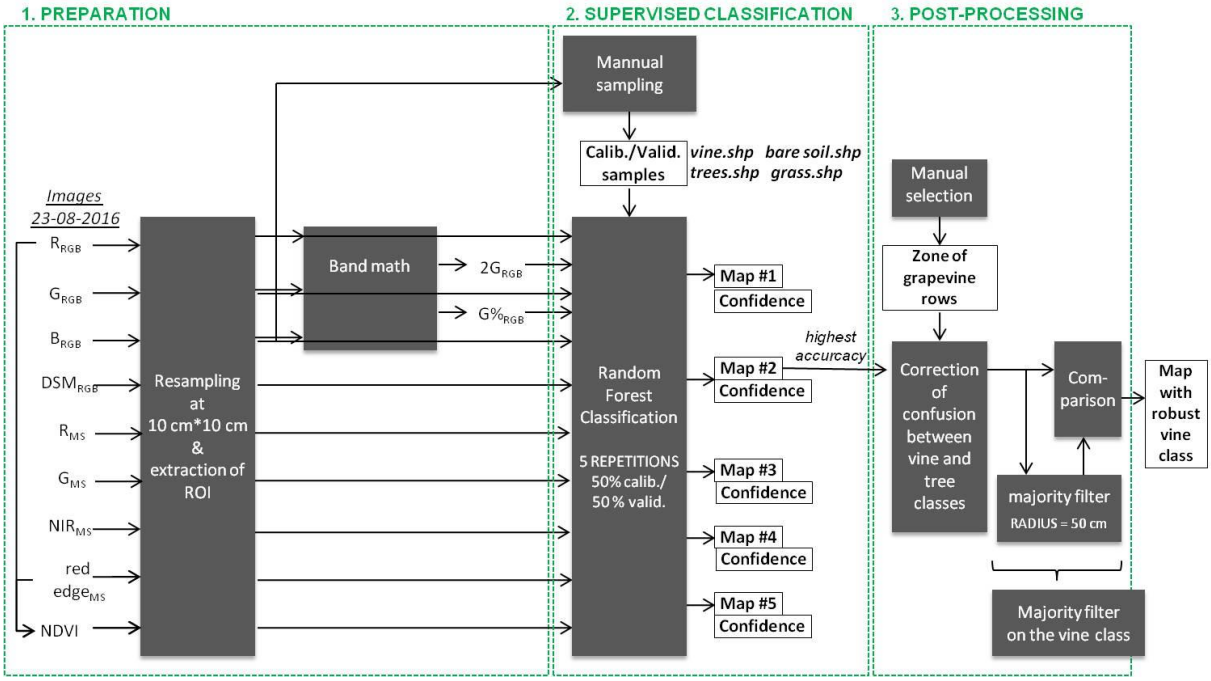

Figure 74: Flow chart of the methodology tested for building the land occupation map of agroforestry vineyards by a supervised classification approach. Simple text indicates input data, grey boxes indicate treatments and white boxes indicate raster maps. The index RGG/MS indicates the type of sensor used for acquiring the input data. Abbreviations: R/G/B = Red Green/Blue – MS = Multi Spectral – NIR = Near Infrared – calib. = calibration – valid = validation – conf = confidence

Table 12: Spectral indexes used among inputs for the classification approach. Abbreviations: DN = Digital Numbers (from 1 to 255) - R/G/B = Red/Green/Blue

Spectral index	*Implementation*	*Recommended by …*
Green percentage index	$G\% = \frac{G_{DN}}{R_{DN} + G_{DN} + B_{DN}}$	… (Richardson et al. 2007; Poblete-Echeverría et al. 2017) for its consistency through the year considering tree leaves.
Difference index	$2G = 2\,G_{DN} - (R_{DN} + B_{DN})$	… (Richardson et al. 2007; Poblete-Echeverría et al. 2017) for its sensitivity to budburst at springtime considering deciduous tree leaves.

The land occupation map of Lagardère (32) study vineyard on the 20 Jul. 2016 obtained by the supervised classification approach is presented in **Figure 73.** The contours of both grapevine and tree canopy follow very closely the RGB image and show a higher precision at the pixel scale compared to the map obtained from object based approach. In addition, the map obtained from the classification approach reveals realistic contrasts in the spans of the trees which are planted within the vine rows.

Nonetheless, the land occupation map of Restinclières study vineyard on the 23 Aug. 2016 reveals several limitations of the classification approach (**Figure 75**). On the one hand, the classification of vine rows oriented NS showed a greater tendency to inaccuracy due to the shadows of grapevine compared to the rows oriented WE whose shadows are more distinctively projected on the ground. On the other hand, the vine rows that were not highly trained with the trellis system where classified as totally full patches of grapevine while the branches of grapevine crossing middle rows actually present a low density of foliage (recall **Figure 49**). This reveals that in this context, the classifying methodology is very conservative and chooses the grapevine class as soon as part of the pixels contains grapevine leaves or stems.

In addition, at Lapouyade (33) and at Restinclières (34) study vineyards, the issue of the confusion between grapevine and tree pixels remained on the vine rows neighboring tree rows even after applying rectangular position masks because tree canopy overlaps that of grapevine in these two vineyards (**Figure 75** and **Figure 76**). Under this configuration, only very accurate but costly masks would be necessary.

Figure 75: Land occupation map at the agroforestry vineyard of Restinclières (34) (plots B4 and B5) on the 24 Aug. 2016 obtained from supervised classification approach. The map is shown as direct raw result from classification, prior to post-processing operations.

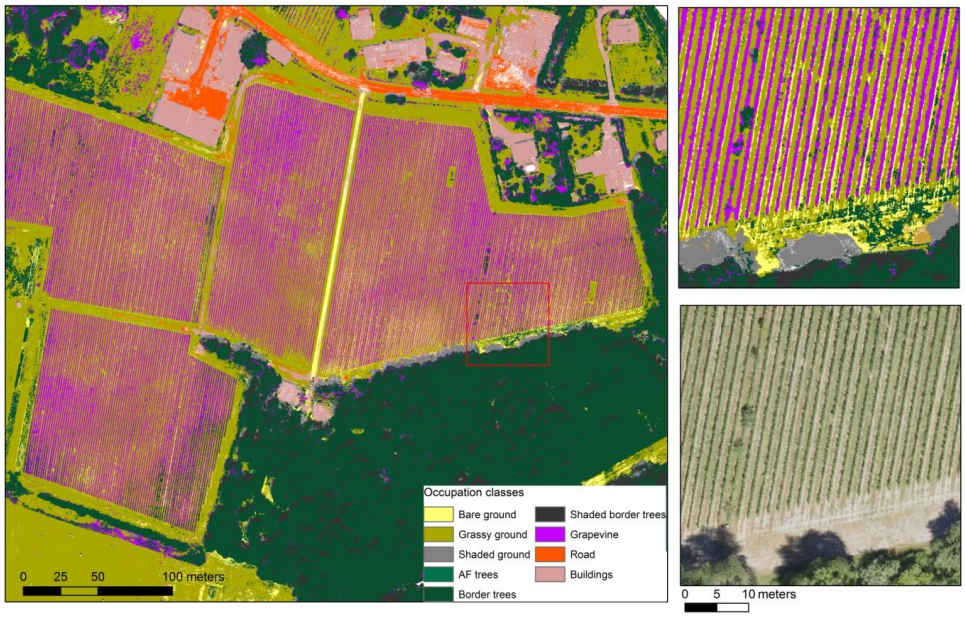

Figure 76: Land occupation map at the study agroforestry vineyard at Lapouyade (33) on the 18 Jul. 2016 obtained from supervised classification approach. The map is shown as direct raw result from classification, prior to post-processing operations.

Adding to the land cover map, the random forests classifier generates a confidence map per class of land occupation. The confidence score is calculated as the ratio of the votes that converged to the majority class, out of the total number of trees (individual learners) that were built by the classifier (Pelletier et al. 2016). The confidence map strengthens the interest of the classification approach for a

pixel by pixel use of the land cover map. For example, when applying an arbitrary threshold of at least 90 % of confidence to the grapevine class, it allows distinctly distinguishing sunny grapevine pixels (which present very high confidence) and the shaded pixels (which present low confidence) from the RGB image (**Annex F**).

IV.4.1.3 Recommendations for methodological improvements

The manual segmentation of the high resolution aerial images resulted to be time consuming and did not allow pixel by pixel applications of the map.

In the case of vineyards with vertically trained vines and non overlapping trees, the supervised classification approach should be retained for its rapidity, generality and precision for applications pixel by pixel. Nonetheless, for a wider applicability to any type of agroforestry vineyards, this method requires improvements. At this state of knowledge, the spectral signatures of grapevine foliage and of tree foliage do not sufficiently differ from one to another for grapevine and trees to be accurately segmented/classified in two different classes. Knowing that in most cases, climatically relevant trees are taller than grapevines, investigations were made concerning the potential contribution from the DSM information. Adding the raw DSM to the input data actually resulted of poor interest according to classification results (from 5 to 9 % of contribution) and did not allow dissociating grapevine and trees in both our segmentation and classification approaches. The main reason may be the noising contribution from the slope of the terrain. In order to overcome this issue, several tests were made notably using vegetation height information derived from the raw DSM. For this purpose, the vegetation height was computed per pixel as the difference between the DSM and the DTM (**Figure 77**). Encouraging results that should be further investigated were obtained using a map of vegetation heights which is entirely derived from the data captured by the RGB sensor on a given date and time (see **Vegetation height**). In addition, the object based approach revealed that trees and vine rows can be distinguished according to their morphological traits in 2D, notably regarding the elongation or preferential orientations. As a consequence, the informative contribution from adding texture features in the input data would be worth assessing too. Encouraging results were notably obtained by Trias-Sanz (2006) and by Peña-Barragán et al. (2011) for the distinctive classification of orchards and vineyards and by Nolan (2015) for the accurate mapping of grapevine rows from high resolution visual/near-infrared images acquired by UAV flights above vineyards.

In addition, our results suggest that the accuracy pixel by pixel of the maps obtained by classification could be improved by considering input data that were all acquired simultaneously by a given sensor. Indeed, the precision of image geo-referencing from reference points positioned on the ground is of same range as the resolution of pixels. In this context, whether mixing input data acquired by differing sensors and at different times of the day actually depletes the precision of the final map compared to the informative gain is a sound hypothesis to test. Following this idea, Nolan (2015) recommends (i) to use an adaptative intervalometer payload system fixed on a multicolor platform

which is capable to adjust image acquisition in real time to ground speed and altitude variations, and (ii) to simultaneously collect the high resolution thermal and multispectral imagery when considering building a map from the multispectral bands in order to mask pixel by pixel the thermal image.

Finally, when two contrasted orientations of the rows combine at a given site, typically at the study vineyard of Restinclières (34), one may recommend to build the calibration samples and to perform classification in two distinct batches.

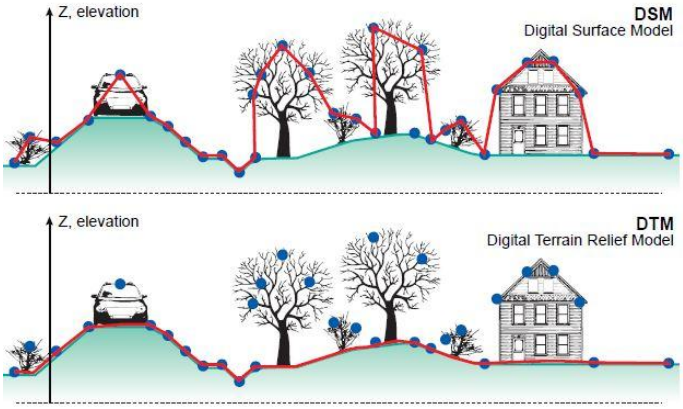

Figure 77: Complementarities of the elevation information provided by a digital surface model (DSM) and a digital terrain model (DTM). Source: www.charim.netdatamanagement32.com

IV.4.2 Selection of metrics for describing the vegetation structure

IV.4.2.1 Conceptual framework

The land occupation map provides a useful tool for documenting the morphology of the vegetation in regards to its microclimatic impacts in agroforestry vineyards. At metric scale, the height of the tree, the density of their canopy and the distances of plantings between grapevine and trees determines the intensity of the interactions between grapevine and trees. At a larger scale, agroforestry practices allow different arrangements of the vegetation in the landscape. When considering the potential impacts of trees in terms of water use, Landsberg (1999) notably distinguishes at least five main categories of arrangements, namely block planting, windbreaks, timberbelts, scattered trees and alley-cropping, with many possible declinations in each case (**Figure 78**).

In order to embrace the diversity and the morphological complexity of agroforestry vineyards, a conceptual framework is proposed which considers mainly two types of morphological parameters further referred as the *internal structure* and the *landscape structure* of the vegetation. On the one hand, the internal structure of the vegetation refers to the morphological traits of individual trees (trunk and foliage heights, foliage porosity, 3D shape, etc.) while its landscape structure refers to their combination in space into a spatial arrangement of specific shape (alley-cropping, network of shelterbelts, scattered trees, etc.). This two leveled distinction is common use for the study of vegetation contributions to ecological processes in a discipline named landscape ecology (Forman and Baudry 1984; Forman and Godron 1986; Burel and Baudry 1999; Gaucherel et al. 2006). In addition,

it has been recommended for the study of the climatic effects from trees in several cases, notably by Burel at al. (1993) for assessing the impact of trees on water runoff, and by Brandle et al. (2004) for the study of the aerodynamic impacts from shelterbelts. In this latter case, the two types of metrics were respectively referred as *internal structure* metrics and *external structure* metrics (**Figure 79**).

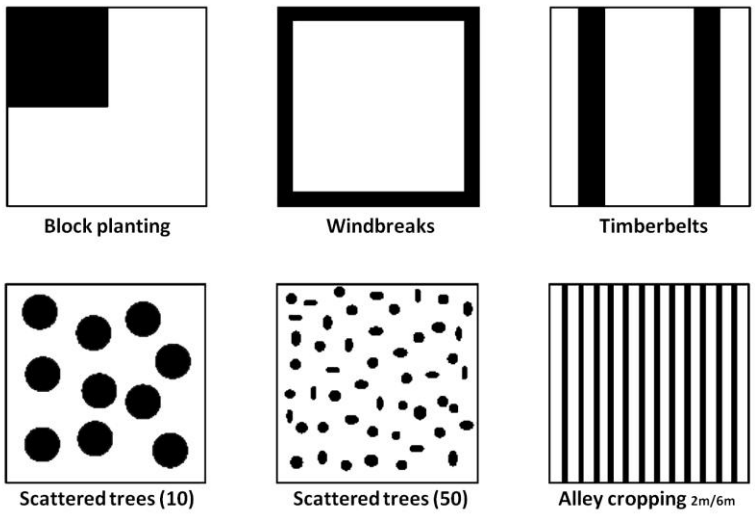

Figure 78: Different arrangements of trees in the landscape. The area of trees , as a fraction of total land area is approximately the same (≈ 25 - 30 %) in each case - From Landsberg (1999), and Stirzaker et al (1996), adapted from Huxley (1985) and Young (1987).

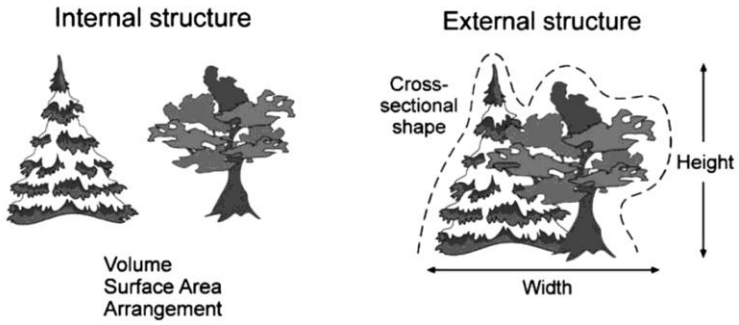

Figure 79: Illustration of the internal (left) and external (right) structure components of two row mixed windbreak. The internal structure consists of the volumes and surface areas of the individual components (leaves/needles, branches and trunks) of the windbreak. The external structure corresponds to the arrangement of the elements as an ensemble. It is characterized by the height, length, orientation, continuity, width and cross-sectional shape of the windbreak. From Brandle et al. (2004)

IV.4.2.2 Internal structure metrics

Vegetation height

Two image analysis methods were tested in order to map vegetation height at the study vineyards (**Figure 80**). The first one further referred as *filtered DSM method* from Zarco-Tejada et al. (2014) only requires a high resolution DSM, while the second one further referred as *DSM-DTM* method requires a high resolution DSM and the corresponding land occupation map.

In addition, in order to furnish reference data, tree heights were measured at a selection of trees within each study vineyards, using a portative laser measuring device. The implementation of the two image analysis methods is presented in the following subsections and then their domain of validity is discussed.

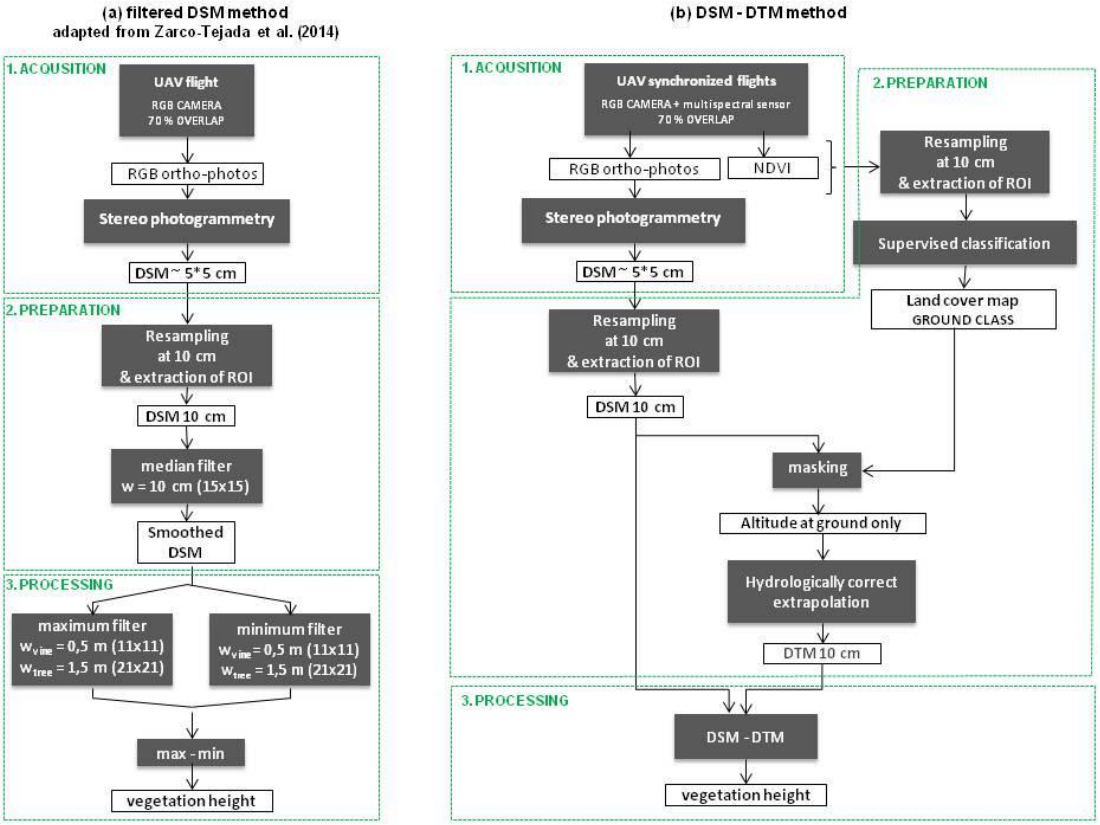

Figure 80: Implementation of the filtered DSM method adapted from Zarco-Tejada et al. (2014) and of the DSM - DTM method for mapping vegetation height in agroforestry vineyards from very high resolution images.

FILTERED-DSM METHOD FROM ZARCO-TEJADA ET AL. (2014)

Zarco-Tejada et al. (2014) retrieved with high accuracy the height of sparse olive trees in an orchard using a very high resolution DSM. This DSM was itself retrieved from the acquisitions of very high resolution visible images with a single UAV flight. Their approach was based on the identification of local maxima likely to correspond to tree tops, and of local minima likely to correspond to the ground height (**Figure 80a**). The processing step was executed as a single line of

bash script using the BandMathX function from the open source Orfeo ToolBox (OTB) (CNES 2018) which allowed extremely short computation times (a few minutes per vineyard). For application to agroforestry vineyards, window sizes for the two kernel filters had to be adjusted to (i) the planting distance between two neighboring trees, (ii) the planting distance between grapevine and trees, and (iii) the average width of the vegetation in place.

The map of vegetation heights obtained at Lagardère (32) from the DSM acquired on the 20 Jul. 2016 is presented for two window width in **Figure 81**. In both cases, the grapevine height ranges between 1.5 and 1.8 m while the trees planted within vine rows reach maximum heights of 3.5 m, 3.0 m and 2.0 m for rows of *Sorbus* domestica, *Sorbus* torminalis and *Pyrus* Pyraster respectively, with very high variability among each species. The filtered DSM method allowed the identification of the maximum height for any class of vegetation which figured within and around the study agroforestry vineyards. Nonetheless, it did not allowed a single synchronous processing but requires plural processing when the vegetation presents heterogeneous spatial extensions, typically when the trees present canopies much wider than grapevine rows. Overall, a window radius of 1.5 m (square filtered of 21x21 pixels) resulted adapted for the identification of the tree heights, while a window radius of 0.5 m (11x11 pixels), allowed identifying the height of the vine rows with more accuracy (**Annexes E and F**). For trees with very wide crowns and notably for forested borders, the width of the filtering window limits the validity of extension of this method. One should note that the BandMathX tool only accept maximum width of 21x21 pixels unless it is readapted in C++ code which was done for testing the contribution from wider filtering windows. In addition, the contours of grapevine foliage, of isolated tree crowns, of copses and woods were modified in the obtained vegetation height maps which do not allow pixel by pixel applications.

DSM-DTM METHOD

The DSM-DTM method consists in retrieving vegetation height as the pixel by pixel subtraction between the DSM and the DTM (recall **Figure 77**). Though it is based on a very simple principle, its implementation at very high resolution and altitudinal accuracy is complex. On the one hand, the DSM was generated by stereo photogrammetry from the overlapping RGB images acquired by drone flight, similarly to the filtered DSM method (**Figure 80b**). On the other hand, several sources of already available DTM were considered at first:

i) the BDTopo25 from IGN, which is an open source elevation map covering all France at a spatial resolution of 25 m;
ii) an elevation map of 7 m resolution acquired in 2015 by the company named GeoCarta using a wandering GPS placed on a quad at the study vineyards of Lagardère (32) and Lapouyade (33).

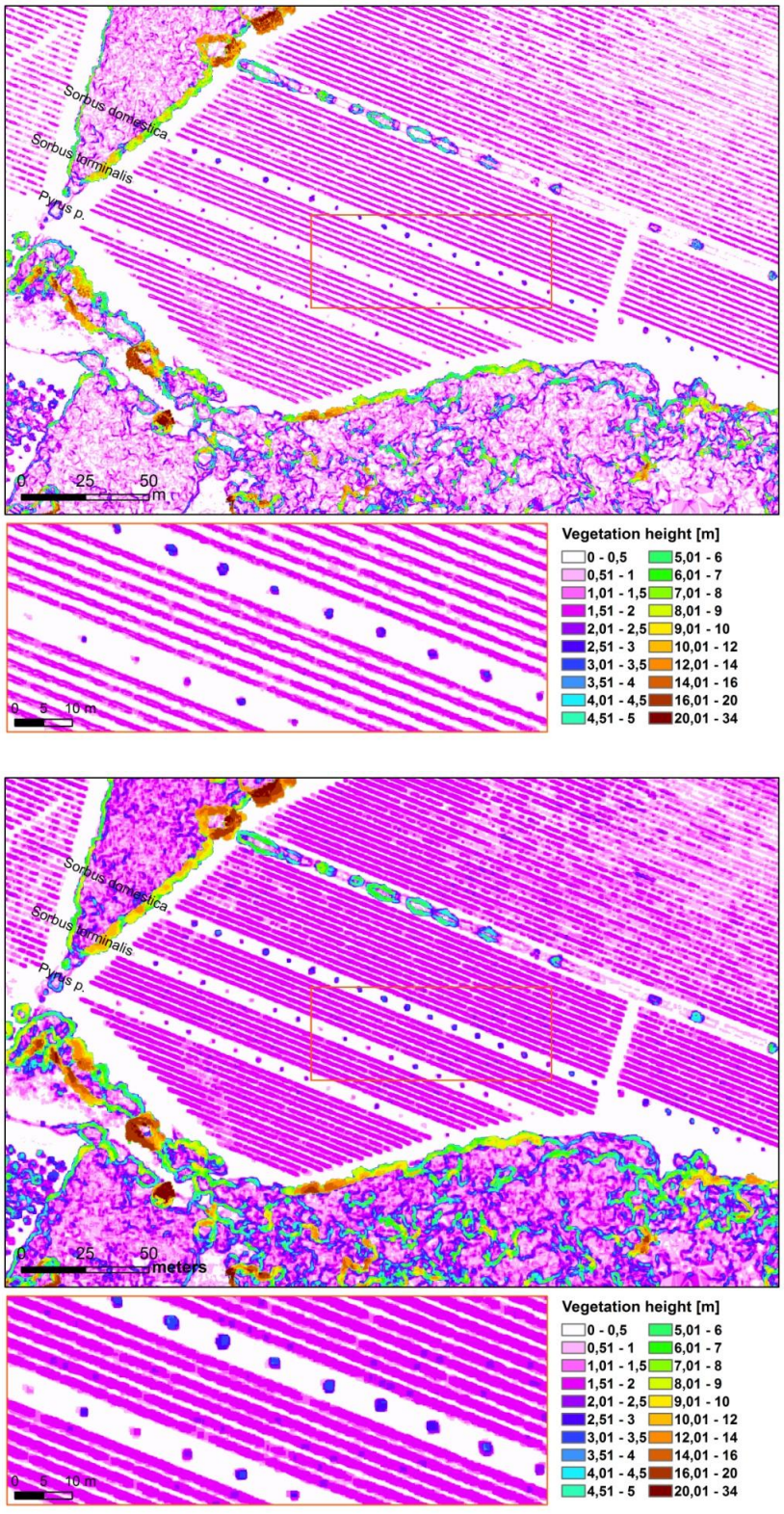

Figure 81: Vegetation height at Lagardère on the 20 Jul. 2016 mapped by the filtered DSM method. Top: A filtering element with a radius of 0.5 m (square of 11x11 pixels) was applied. Bottom: A filtering element with a radius of 1.5 m (square of 21x21 pixels) was applied.

In the first case, the DTM retrieved by extrapolation at 10 cm of the elevation map showed differences of elevation ranging from 1 m to 10 m with the drone born DSM at ground positions. In the second case, the area covered by the elevation map was only limited to the zones with vine rows

but did not cover any of the areas planted with trees. As a consequence, the building of a DTM from the drone born imagery itself became highly at stack. The method which was tested in this thesis consists in building a DTM by extraction of the DSM at zones of ground followed by its extrapolation to the whole area covered by the DSM (**Figure 80b**). For this purpose it is first necessary to retrieve the land occupation map of the vineyard and in particular to map the ground class with accuracy (see **IV.4.1 Land occupation mapping**). Then, the *Topo to raster* interpolation method implemented in ArcGIS software was chosen for its ability to follow abrupt changes in terrain such as steps between vine middle rows or ditches, and accurately integrate contour data (Hutchinson 1988; Hutchinson et al. 2011; Esri 2018). The final confrontation of the DSM and DTM was operated using the BandMathX function of the open source Orfeo ToolBox (OTB) (CNES 2018).

Figure 82 and annex E shows the estimated heights respectively at Lagardère and Restinclieres study vineyards. The heights of grapevine and of the trees planted inside the vineyards show similar trends and variability as that estimated with the filtered DSM method. Nonetheless, net improvements are observed concerning the estimation of the height of the forest trees neighboring the vineyard. This is notably effective for vegetated hedges which are surrounded by patches of bare ground on all their sides, otherwise the accuracy of estimation decreases with the distance to bare ground. In addition, the generated height maps respect the contours of the vegetation and allow pixel by pixel applications. The variability in height within the crown of isolated trees is notably documented with greater realism than with the filtered DSM method.

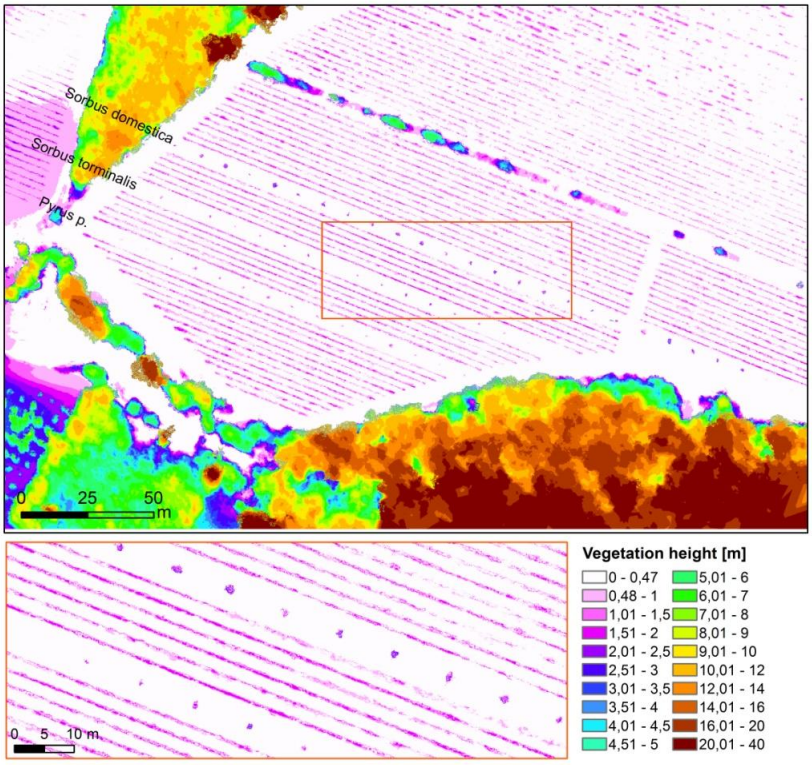

Figure 82: Vegetation height at Lagardère study vineyard on the 20 Jul. 2016 mapped by DSM-DTM method.

DOMAINS OF VALIDITY

In order to assess the validity of the two methods, the estimated heights of isolated trees were extracted from the two sourced maps and confronted with the heights measured at validation trees at Lagardère (32) vineyard (**Figure 83**). For each of the validation trees, residuals were calculated as the difference between the laser-measured tree height and tree height estimated from either the filtered DSM method or the DSM-DTM method. The root mean square error (RMSE) of these residuals was calculated along with the regression fit and the squared correlation coefficient between measured and estimated tree heights. Given the low amounts of reference trees, the determination coefficients resulted very impacted by the behavior of a few points with an outlier tendency. In overall, the linear tendency resulted of same range between the two methods according to the coefficients of correlation. The filtered DSM method showed a slight tendency to underestimate the tree heights while the DSM-DTM method showed a tendency to rather overestimate the tree heights. Considering the tree species contribution revealed that the DSM-DTM method provides more robust estimations of the heights of *Sorbus torminalis* and *Pyrus pyraster* than the filtered DSM method but worsen the mean square error of the estimations for the *Sorbus domestica* species. Three reasons may be involved:

[1] from visible assessment, the canopy of the *Sorbus domestica* trees seems to present the highest intra-crown variability in heights compared to the two other species,

[2] at the collection of reference data, the very small leaves of *Sorbus domestica* made it very difficult to steadily focus the laser on the top leaves – the variability between the 3 repetitions performed at a given tree was the highest which strengthens reasons i and ii;

[3] and the method for extracting the estimated values at reference trees is based on the maximum value of surrounding pixels which reverberates the greatest variability in heights from the DSM-DTM method while the variability from the filtered DSM is intrinsically smoothed.

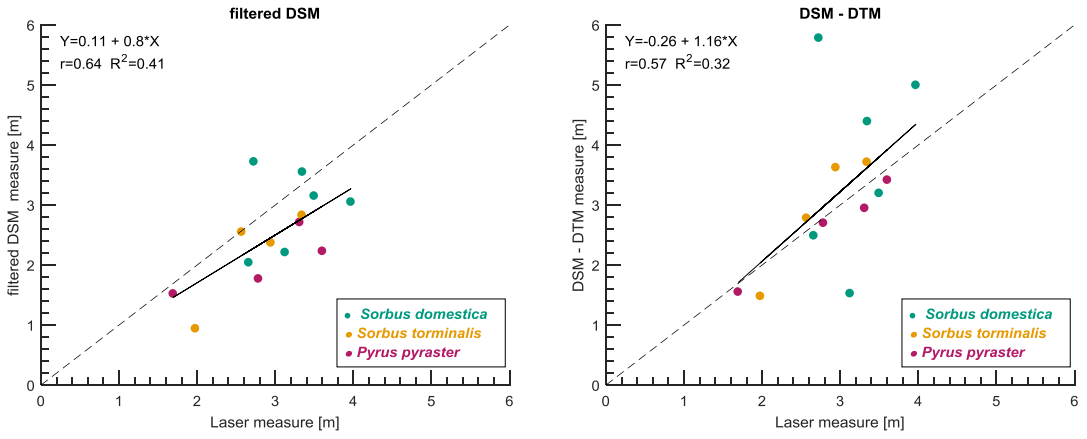

Figure 83: Confrontation of the height of trees at the study vineyard of Lagardère retrieved by filtered DSM method (left) or DSM – DTM method (right) with the reference heights measured by laser. The heights from image analysis were computed as the maximum value of all pixels falling in a distance of 0.5 m, 0.4 m and 0.3 m from tree trunks of respectively Sorbus domestica, Sorbus torminalis and Pyrus pyraster.

Table 4 summaries the advantages and limits of the two image analysis methods that were tested for identifying the height of the vegetation in agroforestry vineyards. The non possible use of the filtered DSM method for pixel by pixel applications stands as the main limitation of this method while the time processing and manual interventions necessary for building the land occupation map in the DSM-DTM method stands as the main limitation of this pixel by pixel method. In terms of perspectives, a "pixel by pixel adaptation" of the filtered DSM method stands as a sound alternative to test. It consists in considering the exact altitude at a given pixel instead of the filtered maximum and subtracting the minimum value computed in a neighboring filter.

Table 13: Recap of the advantages and limits of the filtered DSM method and the DSM-DTM method.

	Filtered DSM method	**DSM – DTM method**
Implementation	Automated and quick	More time-consuming and with potential requirements of manual intervention for generating the land cover map
Vegetation type	Separately considered grapevine rows, isolated trees separately, Hedges Not suitable for copses and forests	Any type of vegetation surrounded by ground
Metrics	Local maximum height	Height per pixel
Applications	Variability assessment per land occupation class (unsaved contours)	Variability assessment pixel by pixel (saved contours)

Canopy density

The canopy density is equally determined by either the density of solid material or the canopy porosity i.-e. the amount of open spaces (Caborn 1957), as cited by (Brandle et al. 2004). Though images acquired with a vertical view cannot provide horizontal information concerning porosity, it was shown in the case of shelterbelts that the porosity of the tree canopy can be estimated using structural variables (Zhu et al. 2004; Torita and Satou 2007) which can themselves be estimated from remote sensing images (Yang et al. 2017). Based on this knowledge, several sources of images were considered for characterizing the porosity of the vegetation in agroforestry vineyards.

The raw land occupation map was first considered for a 2D assessment of the fraction of gaps in tree and grapevine canopies. Nonetheless, in previous subsection, we observed that the classifying methodology tested for generated the land occupation map is very conservative as it chooses the grapevine class for very low density of vine foliage. Similarly, though the foliage of *Sorbus domestica* at the study site of Restincilières (34) was very poorly dense at this time of the year (**Figure 49**), the corresponding pattern in the land occupation map appeared as full patches and as dense in 2D as that of *Pinus pinea* (**Figure 75**). This could be partly explained by the large spatial resolution of the multispectral images that were used in the classification (about 20 cm x 20 cm) relatively to the dimensions of grapevine and tree leaves. In this configuration, the multispectral images include an important amount of mixed pixels of ground and leaves. Consequently, it was concluded that the map produced from the tested supervised classification approach does not provide sufficient information for assessing the porosity of tree foliage in 2D.

On the opposite, the vegetation height maps produced by the DSM – DTM approach provides a pixel by pixel information of the height of the top canopy at a resolution of 10 cm. By applying a threshold these maps allowed mapping and quantifying the amounts of vertical holes in tree and grapevine foliage (**Figure 84**). The maps of foliage gaps reveal the potential contribution from sun flecks and show important intraspecific variability within the study vineyards. In order to assess the validity of this methodological approach, upward hemispheric pictures were captured at a selection of distributed distances to trees within the three study vineyards (**Figure 85**), following a sampling protocol developed at the UMR System[17] specifically for alley-cropped systems and the modeling of light patterns with GLA (Frazer et al. 1999). Some complications were met at picture collection (the big length mode was not systematically activated and two different lengths with very different angles of aperture were alternatively used). They weakened the robustness of the sampling. Thus it was decided to postpone the data analysis which remains to be done so far.

For approaching the 3D density of foliage (the surface or volume area density of leaves), Hall et al. (2003) proposed an empirical method tested on grapevine canopy which highlighted strong correlations between the NDVI at 20 cm of resolution and the vine vigor. Following their recommendations for eliminating pixels of ground and mixed pixels, the distribution of the NDVI was mapped at only pure pixels of foliage. No variability of NDVI was observed at all in the tree canopy which was above 0.8 in all pixels, suggesting that the NDVI at 20 cm of resolution is too binary for documenting internal contrasts of porosity. This conclusion is similar to that from Yang et al. (2017) who compared the relevance of various vegetation indexes for estimating the optical porosity of windbreaks. These authors observed that no index allow to directly estimate the porosity with high accuracy. Intermediate variables involving the LAI, the average tree crown length and width of the windbreak should be considered. In the case of agroforestry vineyards, further methodological investigation and the establishment of empirical relationships between the LAI and spectral indexes, would notably require the collection of biomass data at a selection of reference plots.

[17] Lydie Dufour is greatly thanked for establishing and transmitting this protocol.

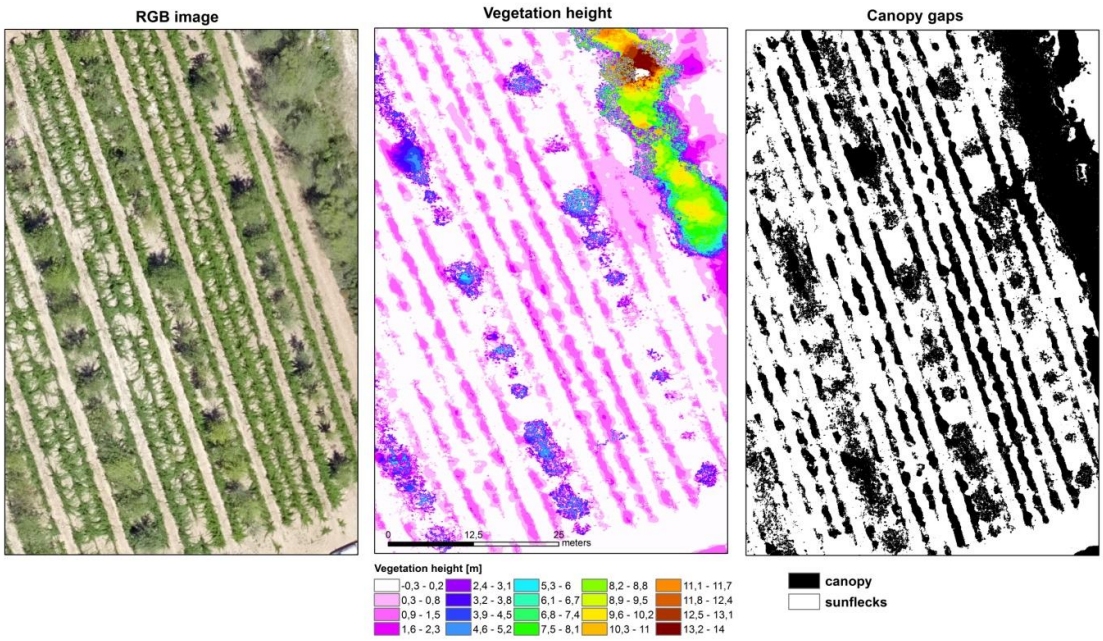

Figure 84: Detection of sunflecks within the canopy of grapevine and trees. Zooms on the RGB image (left), height of the vegetation retrieved by DSM-DTM method (middle) and gaps in canopy (right) at Restinclieres vineyard on the 19 Jul. 2016.

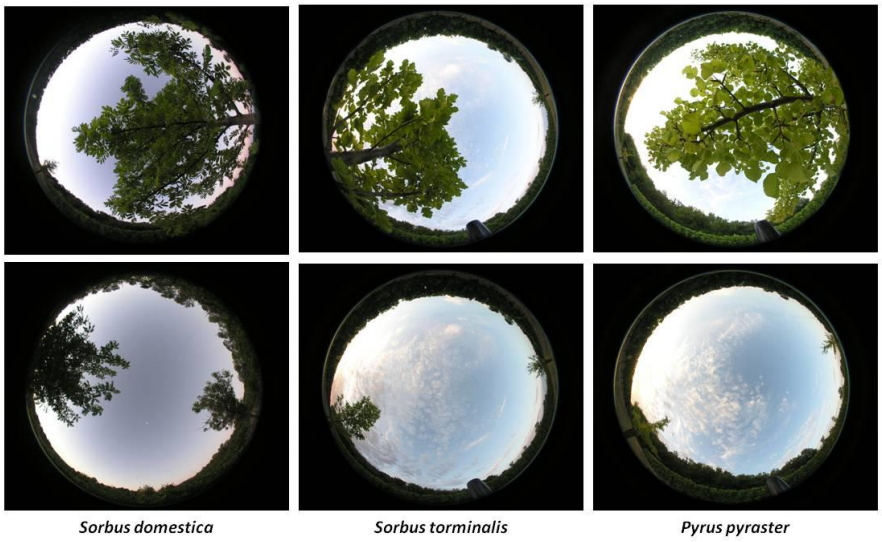

Figure 85: Examples of upward hemispheric pictures captured at the study vineyard of Lagardère (32) using a fish-eye length. Pictures were taken at the tree trunk (top pictures) and at the mid-distance between two trees on the same row (bottom pictures) at 1.2 m above ground

Relative position within grapevine rows: edge and center pixels

Positioning shoots of grapevine as a vertical curtain using trellis system generate important heterogeneity of microclimate within the canopy of grapevine. Leaves positioned at the top, on the sides or eventually in the inner part of the canopy are notably exposed to specific regimes of light (Mabrouk et al. 1997, 2015; Louarn et al. 2008) and wind flow (English et al. 1990). In order to consider the contribution from the spatial position of grapevine leaves within vine rows a classification method was developed and tested using the land cover maps from vineyards with vertically positioned

shoots. Some elements were inspired from the methodology proposed by Hall et al. (2003) for identifying individual vines and extracting shape descriptors.

The algorithm which was developed was automated as a function under MATLAB R2017a. It divides mainly in three steps (**Figure 86**). The first step consists in generating the occupation map of grapevine row and rotating the map into a horizontal orientation of the rows. The second step is the main processing step. Five different classes of pixel position are distinguished, namely a western hedge, eastern edge, northern edge, southern edge or centered position within the rows. For this purpose, West/East/North/South oriented erosions of 2 pixels are generated using linear structuring elements. Then the four different eroded maps of grapevine are together confronted with the original map. In order to reduce the minor classes, typically the W and E edges in WE oriented rows, a majority neighboring filter is applied. Simply the third step consists in rotating the classified map towards its original orientation of the rows. The width of the edge classes can be eventually extended to multiples of two pixels by renewing the processing step on the center class obtained from the first iteration.

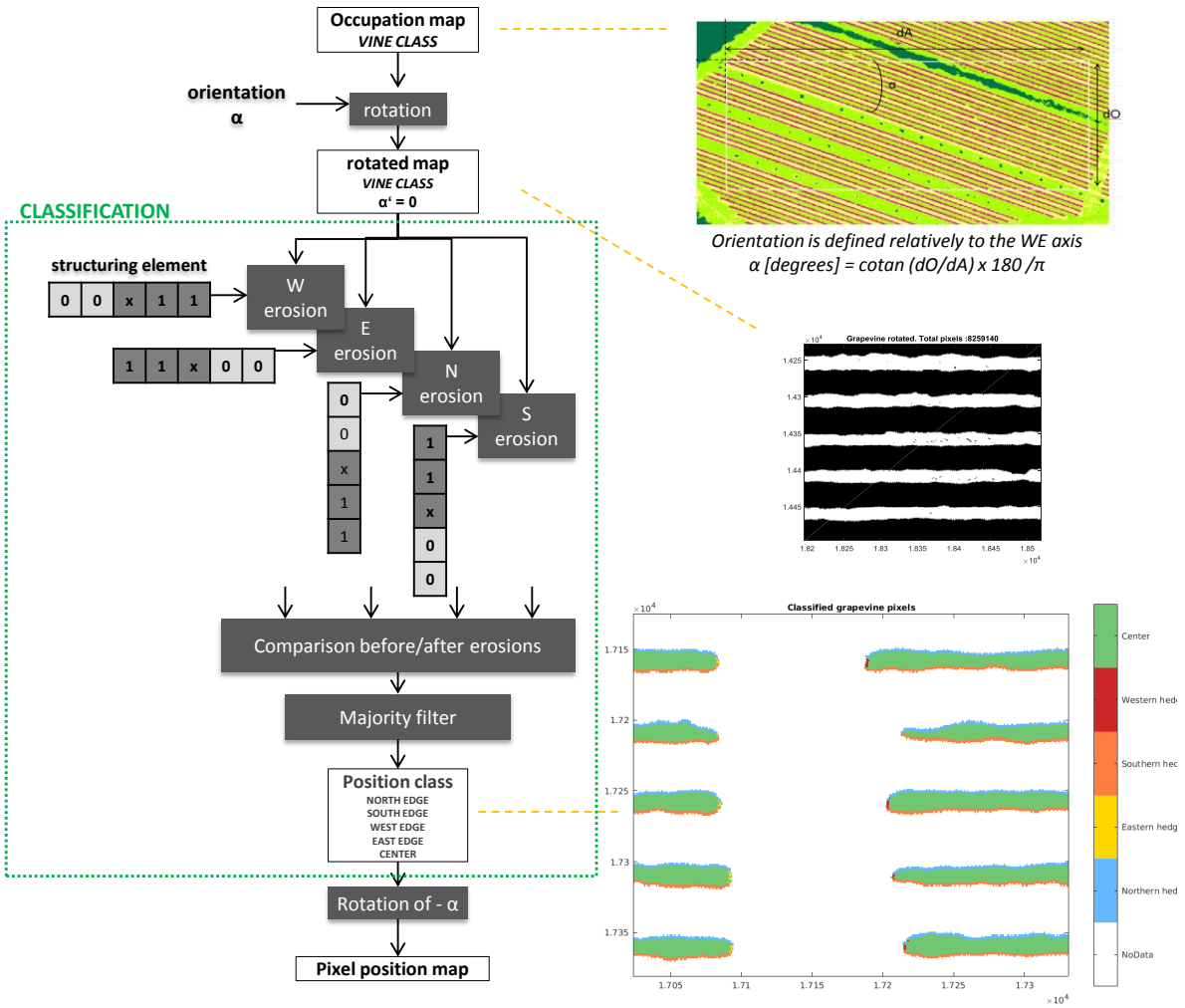

Figure 86: Processing chain for classifying pixel position within grapevine rows.

Figure 87 shows that the classification method gives very satisfying results and is robust to a crenelated aspect of grapevine rows.

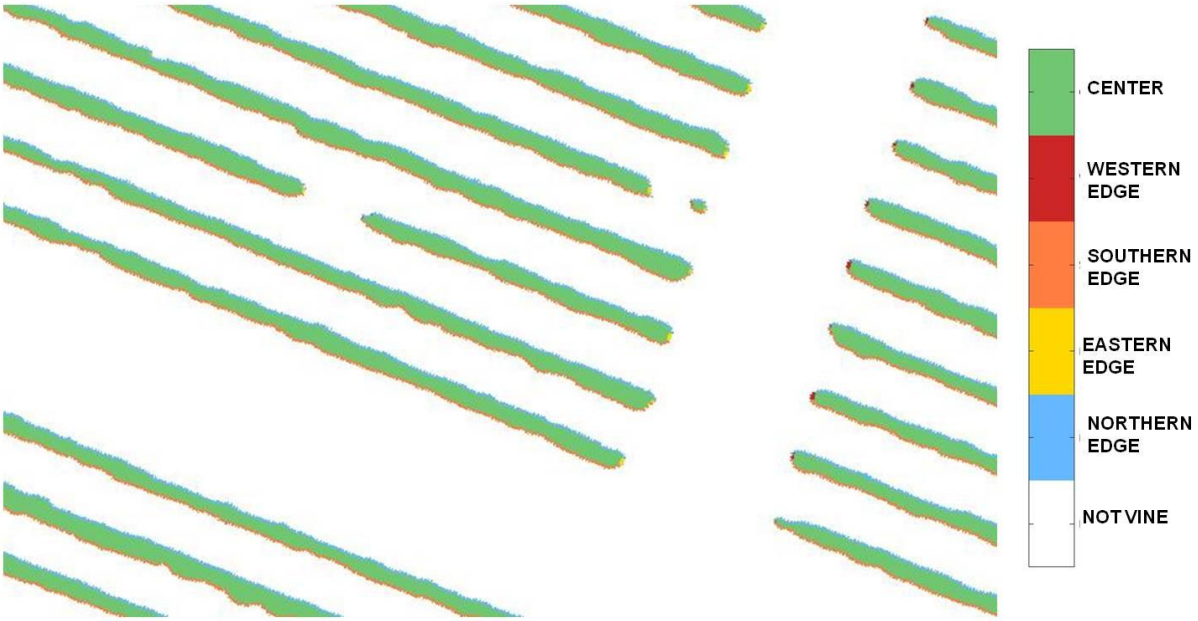

Figure 87: Pixels of grapevine row classified according to their position within vine row, either at one of the western, eastern, southern or northern edge of the row or at the center. From the land occupation map of Lagardère (32) vineyard.

IV.4.2.3 Landscape structure metrics

Row orientation

In order to document the orientation of grapevine and tree rows, the following convention is proposed. First North/South orientations (N/S) and West/East (W/E) orientations are distinguished. In addition, the azimuth angle between the N/S or W/E reference axis is counted positively anti-clockwise or negatively clockwise (**Figure 88**).

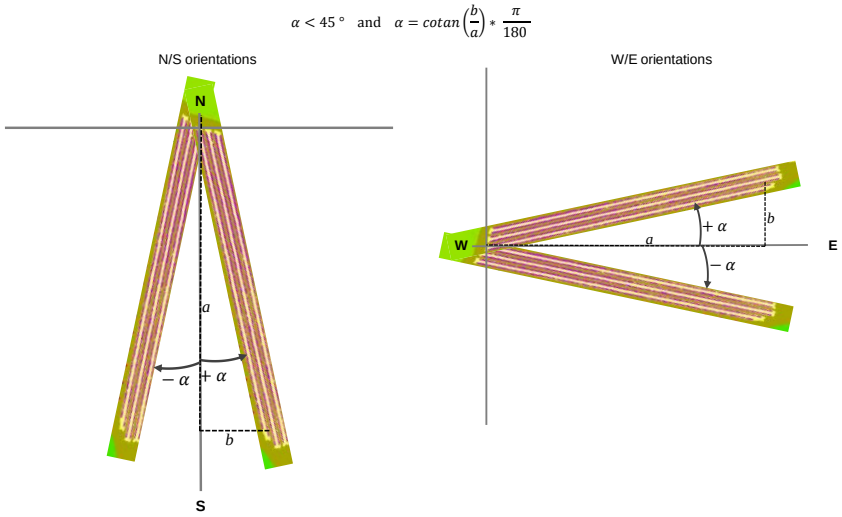

Figure 88: Convention used for documenting the orientation of grapevine and/or tree rows.

2D density

The number of trees per hectare is the most commonly used landscape metrics regarding agroforestry systems since its significance for management purposes and for cost and profits evaluation. Similarly, the density of trees per hectares is generally defined as a single value for the whole agroforestry plantings and gives the fraction of the total land area occupied by trees. It can be derived from a simple proportionality relationship with the number of trees per hectare or more accurately from a land occupation map which integrates the heterogeneity in canopy coverage. Nonetheless, computing a single density of trees for the whole vineyard does not inform either the potential existence of trees at the border of the plot or the spacing between trees, though these two factors highly contribute to the microclimate of the vineyard, notably to the distribution of light, to the air flow regime and to water above and below ground circulation. In order to better assess the vegetation structure in regards to its climatic impacts, the density of trees was mapped within the vineyards considering small to large windows around each pixels. For this purpose, the land occupation map was converted into a binary map of the *tree* class (it includes all tree species within and around vine rows). A resolution of 40 cm was retained as the largest resolution which still allows an accurate representation of the extent and contours of the isolated trees. The density was computed

as the mean amount of tree pixels in a squared neighboring window (eq. 5) using the BandMathX[18] function from the Orfeo ToolBox (OTB) (CNES 2018). Various sizes of neighboring windows were considered ranging from the minimum distance between two trees (~ 8 m) and a maximum of $10\,H$ (~ 80 m), where H is the average height of the trees.

$$D^{n*r}{}_{2D} = \frac{\sum_{i=1}^{n}\sum_{j=1}^{n} x_{ij}}{n^2} \quad [5]$$

with

	D_{2D}	The two dimensional density of tree
	nxn	The dimensions in number of pixels of the neighboring window
	r	The resolution of the raster binary map
	x	Binary map ($x_{tree} = 1\ and\ x_{other} = 0$)

At the study vineyard of Lagardère (32), the density of vegetation showed a large pattern of low density in the north-western part of the vineyard as well as in a triangular zone in the southern part, which both remained effective whatever the window size (**Figure 89**). On the one hand, the density maps obtained with small sizes of neighboring windows gave much credit to the isolated trees planted within vine rows (**Figure 89a**). They stand as a more informative alternative to maps of Euclidian distances. On the other hand, maps of density obtained considering large neighborhoods allows a promising representation of contributions from the trees surrounding the vineyard, notably concerning the circulation of the air flow (**Figure 89b**). Their accurate computation implies acquiring images and building a land occupation map which covers an area extended by the size of the neighboring window.

[18] The maximum window size accepted by the BandMathX function was set to 401 pixels (by default it is 21) and the OTB was manually compiled to allow this modification.

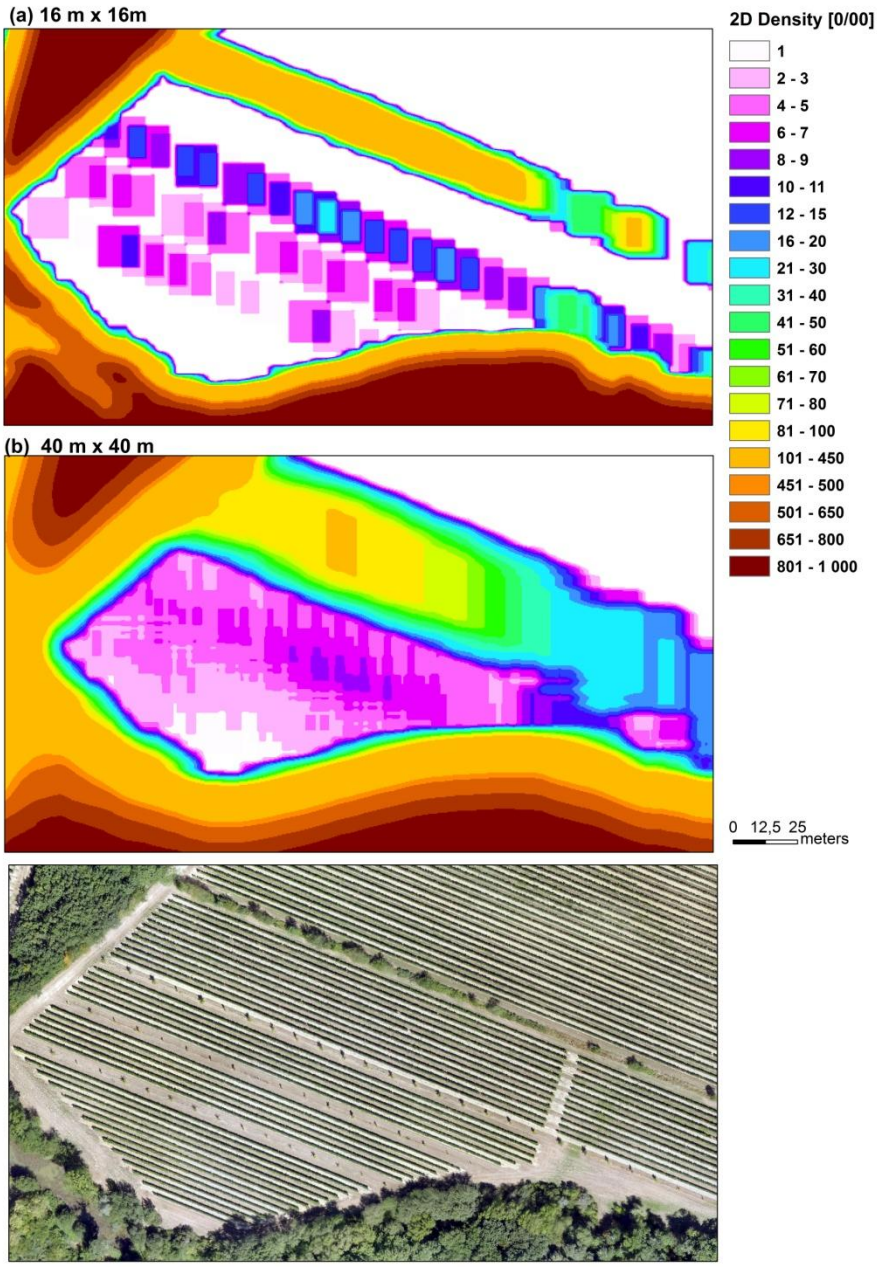

Figure 89: Two dimensional density of trees mapped at Lagardère (32) vineyard. The density was computed within neighboring windows of 16 m x 16 m (a) and 40 x 40 m (b).

In the case of young trees planted in the vicinity of older and taller ones, the 2D density metrics reaches limitations as it will similarly consider two pixels of tree foliage though their height may greatly differ. This represents a source of bias for assessing the vegetation contribution to light interception and to wind sheltering. In this case, improvements could be obtained by weighting the amount of tree pixels by the height of the canopy i.e. by considering the three dimensional density of trees (eq.6).

$$D^{n*r}{}_{3D} = \frac{\sum_{i=1}^{n} \sum_{j=1}^{n} x_{ij} * h_{ij}}{n^2} \quad [6]$$

with $D^{n*r}{}_{3D}$ The three dimensional density of tree in a n*n neighborhood [m]

nxn	The dimensions in number of pixels of the neighboring window
r	The resolution of the raster binary map
x	Binary map ($x_{tree} = 1 \; and \; x_{other} = 0$)
h	The height of the vegetation [m]

Landscape grain

In the six different arrangements represented in **Figure 78**, the 2D density of the trees is approximately the same (about 30 %) in each case (Landsberg 1999), and the 3D density will also be the same if the trees present heights of equivalent magnitude. Nonetheless, the thick gathering of trees will contribute to preferential interceptions of wind flow while scattered trees will increase the overall roughness of the landscape but does not preferentially intercept some of the winds. This highlights that the density is an insufficient metric for informing the compactness of the trees though the consequences in terms of air flow regime circulation may be very different. To face this issue, a landscape metric named the landscape grain is additionally proposed. The landscape grain (LG) was defined by Forman and Gordon (1986) and then successively adapted by Vannier et al. (2011) and by Betbeder et al. (2015) for quantifying the size of the mesh of a hedgerow network ranging from many small elements (fine grain) to larger ones (coarse grain). From a binary map of vegetation, the value of the landscape grain ranges between 0 and 1 and summarizes the rather open structure (high LG) or rather closed structure (low LG) of the landscape (**Figure 90**).

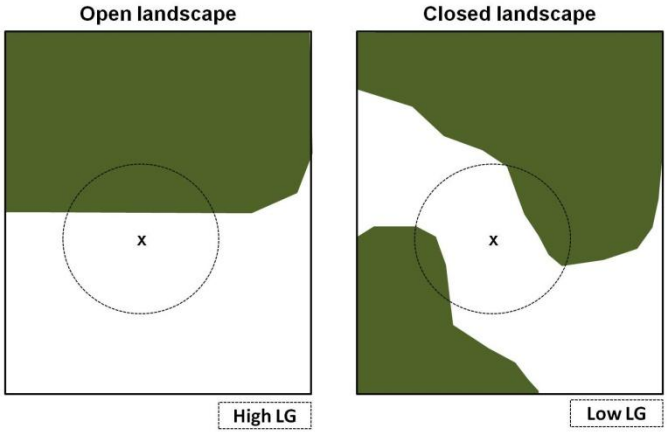

Figure 90: Landscape grain principle. At site x, the density of vegetation (green) computed within the circular window is similar in the two represented landscapes (about 25 %) but the landscape grain is high (close to 1) in the case of an open landscape (left) while it is low (close to zero) in a closed landscape (right).

The LG was computed based on the simplified formula proposed by Betbeder et al. (2015) and using the software Chloe (version beta 23) developed at the SAD-Paysage[19] research unit of INRA (Boussard &Baudry 2014). A first step consisted in computing the distance to the closest tree for every pixel of the raster map. Then distances were sorted into 5 classes:

- class 1 = [0-4 m[- minimum distance from vine an trees,

[19] I greatly thank Jacques Baudry and Julie Betbeder for their scientific advices and technical support for using Chloe.

- classes 2 to 4 = [4-7m[; [7-9.5 m[; [9.5-12 m[- distances to trees of the second, third and fourth vine row neighboring a tree row,
- and class 5 = [12-max[- maximum distance to trees.

Finally the landscape grain wascomputed at all pixels as the ratio of the number of pixels in remote classes out of the number of pixels in close classes considering circular windows of different diameters (15 m, 35 m and 51 m).

Maps of LG at the vineyard of Lagardère study vineyard is given in **Figure 91a**. The vegetation presents an open landscape structure in all the northern part of the vineyard and in a small triangular area located at the southern hedge by the pond. The tree rows generate intermediate closure while the southern and western forested borders generate intense closure. In addition, the contribution from vine rows was also tested by considering the trees and the vine land occupation all together (**Figure 91b**). In this configuration, the landscape grain was the highest where there is no vine row i.e. on tree rows and clearings. This observation suggests that computation of the LG metrics should be adjusted to the type of vegetation in place. In the case of short and poorly dense trees relatively to the vines, including the vine class in the calculation of the landscape grain metrics allows illustrating the generation of corridors by wide rows of young trees.

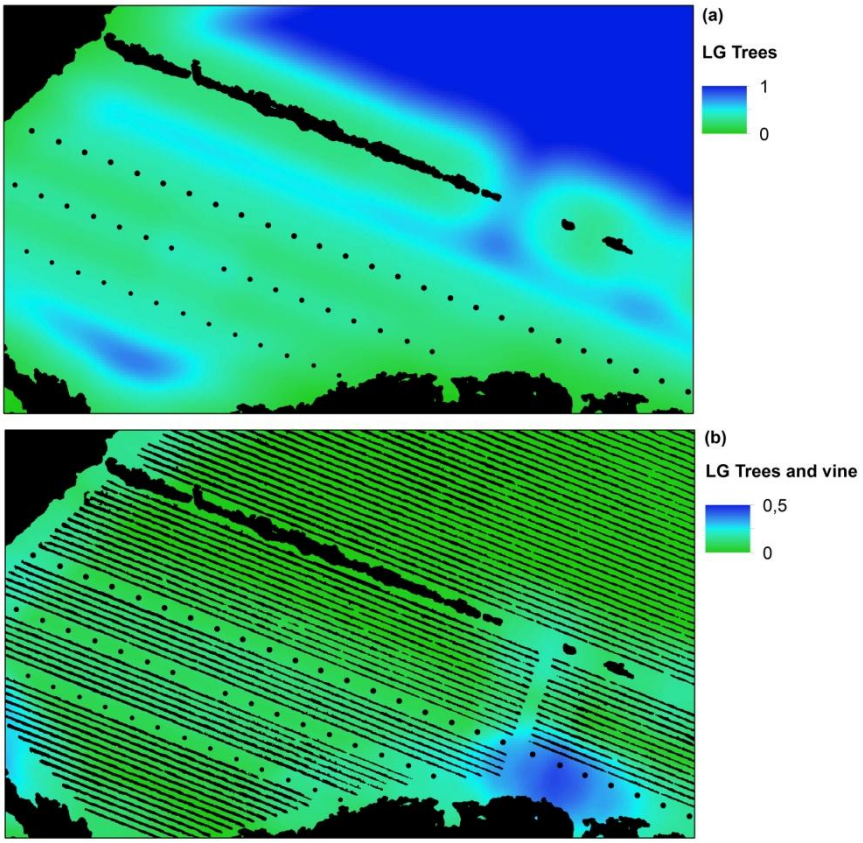

Figure 91: Landscape grain (LG) computed at Lagardère study vineyard considering either distances to trees (top) or distances to trees and vine (bottom). Five classes of distances were considered (thresholdsTREES = 4 m; 7 m; 9.5 m; 12 m and 95 m / thresholdsTREES&VINE = 2 m; 5 m; 10 m; 20 m and 23 m) and a filtering window of 35 m was applied.

IV.5 Conclusions

The three agroforestry vineyards that were selected allow covering a gradient from oceanic, humid continental to Mediterranean climatic contexts. They include diverse vegetation height, arrangement and management practices as well.

An unprecedented data set was collected for documenting their functioning. The main contributions of this phD work consisted in the experimental design and collection of distributed time series of microclimatic variables together with UAV born very high resolution images dedicated to the study of vegetation morphology and functioning. In addition, grapevine phenology and yield parameters were assessed in collaboration with partners from technical institutes. For microclimatic purposes, a new protocol was proposed and tested for distributing the measures in space, within the vineyard. On the one hand, the measures captured within the canopy of grapevine and in the bunch zone are very promising. Focus was made in priority on the temperature variable as it is integrative of both climatic mechanisms and vine response. The results obtained from their analysis will be further developed in chapter V. On the other hand, the measures of temperature taken in the first layer of ground showed poor robustness. Using a UAV for punctually acquiring very high resolution images of the whole vineyards allowed a very complementary coverage of the spatial scale. The image data set includes thermal images of grapevine which will be further analyzed in chapter VII regarding potential water stress patterns.

Based on image analysis, a new methodological approach is proposed for mapping the vegetation and characterizing its morphology and arrangement in agroforestry vineyards. Some of the metrics from landscape ecology which are usually computed at the regional scale were transposed at the scale of the vineyard. A selection of internal structure metrics and landscape structure metrics is proposed for summarizing the morphological traits of the vegetation in regards to its microclimatic impacts. The methods that were developed are the most replicable as possible. For this purpose, toolboxes from the public domain were preferred and processing chains were automated as most as possible.

From the experimental and methodological developments that were presented in this chapter a few technical recommendations can be formulated. The ibutton® sensors are recommended only for measurements in the air but not in the ground. Also, they should preferentially be calibrated in order to remove any systematic errors and should be spatially distributed at a rather high density of plots in order to compensate missing data from human errors at acquisition setting or data collection. The strategy which consisted in duplicating the sensors at a couple of plots per campaign was very informative in regards to data accuracy and robustness. These questions could be further investigated by this time placing the two sensors in two distinct but side by side boxes.

The punctual acquisition of UAV born images is highly complementary to on site data collection. On the one hand, it is very advantaging for its rapidity of collection. On the other hand, particular care must be devoted to accurately geo-reference the images. For this purpose, it is essential to position

targets in all the covered area and at a rather high density (at least one target in each image). Also, maximum resolutions of 5 cm for RGB-DSM images and 10 cm for multispectral and thermal images seems relevant for neutralizing the erroneous contributions from mixed pixels (vine and ground). In addition, several specific recommendations can be made in order to allow pixel by pixel applications from the images, notably mapping canopies:

- The acquisitions with the RGB sensor and the multispectral sensor should be synchronized in time,
- At least two acquisitions at different solar times should be performed during a day,
- Hours of the day should be chosen in regards to the orientation of the rows in order to favor timings when there is no shadow or when the shadows are only projected on the ground but not onto neighboring vegetation.

At last, though image analysis stands as a promising tool for characterizing the landscape structure of the vegetation, it shows limitations for characterizing the internal structure of the vegetation unless complementary data of reference are collected on site: i) capturing either upward hemispherical pictures or lateral pictures of the tree canopy could allow improving estimations of its porosity, and ii) measuring tree heights using a pole would allow validating the robustness/correcting the information which is more easily provided by laser measurements. The land occupation map obtained from this approach is used for modeling purposes in chapter VI.

CHAPTER V
Analysis of temperature patterns at Lagardere (32)

The main objectives of this chapter consist in documenting the space and time variability of temperatures generated by trees in a vineyard and to address its potential impacts on grape and wine production. For this purpose, focus was made on the study vineyard of Lagardere (32) and the experimental data collected at this site were analyzed using a statistical approach. The following content was formatted as a research paper and submitted to the Agricultural and Forest Meteorology journal. The introduction and material sections repeat some of the information already presented in previous chapters of this manuscript in a more succinct way. Then the methodology, the results and discussion and the conclusion sections will be new to the reader.

V.1 Introduction

Assessing the advantages and drawbacks of intercropping trees together with grapevine is of prime importance to support the development of efficient agro-ecological practices in viticulture. Potential microclimatic benefits for intercropping trees in vineyards were early questioned by Desplanques (1958) in regards notably to frost hazard or heat stress. Indeed, because of the specific shape and roughness of woody vegetation, and the high transpiration demand to sustain tree growth, trees alter the microclimate corresponding to variations noticeable at 1 m^2 to 1 ha spatial scale and day to year time scale (Oke 1992; Quenol 2011). The main mechanisms involved are shading (interception of direct sunbeams), sheltering (interference with the air flow) and modifications of the water cycle (Stigter 2015). Two additional mechanisms are also reported in the very vicinity of trees which present very dense and contiguous canopies: the sunny side of their canopy reflects sun beams and thus increases the amount of incoming energy at ground level (Guyot 1989; Brandle et al. 2004); compared to air, trees release an extra amount of radiative heat (thermal infrared emissions) in the sky fraction occupied by their canopy (Chiapale 1975; Guyot 1989). The occurrence and intensity of all these phenomena are driven by three types of factors (Oke 1992): (i) the climate type, (ii) the vegetation structure (tree height, canopy density, multiple tree arrangement), and (iii) the meteorological context (clear sky or overcast sky day, wind speed, wind direction, atmospheric stability, vapor pressure deficit).

Very few references already exist concerning agroforestry vineyard performances and even so concerning their microclimate. To our knowledge, one can exhaustively cite two experimentations reported in the grey literature, both carried out at the agroforestry experimental Domain of Restinclières in southern France (43.7258°N -3.8573°E), under Mediterranean context. In the first study by Goma-Fortin and Trambouze (2009), measurements of irradiance arousing to the leaves of grapevines located at 3.75 m and 6.25 m from ten-year-old *Pinus brutia* were carried out but only over a single day of summer. The second study by Gouttesoulard (2015) assessed the consequences of shading on the air temperatures which was measured inside vine rows, in the bunch zone of grapevine, at either 2.5 m or 3.75 m from trees, depending on the planting density. At the first vine row on the

northern side of trees, their results reported an average depletion of the maxima daily temperatures at veraison of 4 °C and 5.5 °C with respectively *Sorbus domestica* and *Cupressocyparis leylandii* species, considering a West/East oriented plantation. For North/South orientations, an average maximum depletion of 4.5 °C was reported in the morning on the first vine row on the western side of *Sorbus domestica* trees and of 3 °C, in the afternoon on their eastern side. These two references suggest that intercropping trees within a vineyard does generate contrasted microclimate patterns which were due in this case to light interception. Nonetheless, very little is known on the variability of these patterns in time throughout the season and years as well as on their potential impact on the production of grapes.

The study presented in this chapter aims at contributing to better understand the microclimatic impact from agroforestry practices on grape and wine production. In such context, the question arises of how to measure and comprehend tree climatic effects in a systemic way. This study focuses on air temperatures in the bunch zone of grapevine because temperature doubly stands as a key variable: (i) temperature is an integrative variable of the energy and water fluxes between the soil, the vegetation and the atmosphere, and (ii) temperature is involved in most of the physiological, reproductive and chemical processes responsible for the yield (quantitative criterion) and the berry composition for wine making (qualitative criteria) (Jackson and Lombard 1993). The literature concerning the bioclimatology of grapevine suggests that the sensitivity of grapevine to temperatures depends on phenological periods.

Prior to budburst, only extremely low temperatures may damage the ligneous part of the vine while a few successive cold days are necessary for releasing latent buds from dormancy. In spring, activated buds burst as soon as exposed to sufficient heat. The temperature threshold for budburst ranges from 8 °C to 11 °C depending on the grape cultivar (Carbonneau et al. 2015). Once budburst occurred, damages from late frost events are feared notably when air temperatures reaches below 2 °C (Mosedale et al. 2015).

After budburst, latent buds grow from the stalk until they reach the stage of 6 spread out leaves. The sum of active temperatures above 10 °C or growing degree day, shows strong correlation with the vegetative growth speed of grapevine, especially when it is weighted by the length of the day (Tonietto and Carbonneau 2004) and is commonly used for predicting key phenological stages such as budburst and veraison (Parker et al. 2013). Photosynthesis operates from budburst to leaf fall. It directly contributes to the whole plant biomass, notably to the yield, and indirectly to the sugar content in grapes. Light intensity and leaf temperature are the two main environmental factors controlling the photosynthesis efficiency of grapevine leaves (Kriedemann 1968, 1977; Stoev and Slavcheva 1979; Stoev and Slatcheva 1982). The typical photosynthetic light response of grapevine can be separated into two stages: the first at low photon flux densities where photosynthesis occur but is strongly light-limited, and the second at high photon flux densities, where photosynthesis becomes light-saturated. The leaf temperature effect is complementary as it controls both photosynthesis rate and saturation

point, with an optimum estimated at 24°C and 28°C for northern and southern grapevine type respectively (Motorina 1958; Kriedemann and Smart 1971; Greer 2017). Photosynthesis also showed a rapid decline above 35 °C (Kriedemann 1968).

The optimal temperature for grapevine flowering, pollination and germination success ranges between 20°C and 30°C depending on grapevine cultivar. Flowering is shortened when flowers reach quite high temperatures (25 °C – 35 °C), nevertheless pollination may be depleted either if above 35 °C temperatures suddenly occur, or in case of mean temperatures below 14 °C-15 °C (autorhors reviewed by Vasconcelos et al. 2009). Once flower is fecundated, young fruits grow during summer in several phases and the mitotic growth phase is very proportional to growing degree day accumulation (Parker et al. 2013).

Then berry ripening starts at the end of berry growth which matches with the *veraison* stage: sugar accumulates in berries while organic acids are being degraded. Until harvest, temperature and plant water status are the two main contributing factors to the ripening of berry. In addition, secondary metabolites of particular interest are synthesized in berry skins after veraison: anthocyanins, flavonols and tannins are molecules of phenolic type with essential role in the color of grapes and wines, in juice reductive-oxydation mechanisms and in the structure and bitterness of wines. The review of **Downey et al. (2006)** highlights that their synthesis increases with increasing light and most of all increasing berry temperatures but to a certain maximum above which synthesis is inhibited. Blockage of the synthesis is estimated to occur at 30 °C and 35 °C for night and day temperatures respectively (Kliewer and Torres 1972; Azuma et al. 2012). Free aroma compounds or aroma precursors in grapes are also sensitive to light and temperature like pyrazines (Roujou de Boubée et al. 2000), terpenols and norisoprenoids (Reynolds and Wardle 1993; Marais et al. 1999) or rotundone (Zhang et al. 2015).

Adding to the usual strong climatic contribution of microclimate in the yield and in berry quality for wine making, climate change is of prime concern for grape and wine production (Fraga et al. 2012). Average temperatures are increasing as well as the frequency and intensity of extreme events notably of heat weaves and droughts (Pachauri et al. 2015). In many grapevine growing regions around the world, these new trends are already impacting grapevine production (Jones and Webb 2010; van Leeuwen and Darriet 2016): on the one hand, higher temperatures trigger earlier phenological succession which shifts the ripening phase to warmer periods in the summer and thus affects grape composition; on the other hand, increased water stress reduces yields and modifies fruit composition at harvest.

Identifying potential strategies of adaptation to climate change reinforces the importance of assessing the microclimate and the performances of grapevine in agroforestry vineyards. What is the impact of the trees on the microclimate throughout the whole vegetative and reproductive cycle of grapevine? What are the impacts on the yield and on the quality of berries for wine making? Answering these questions is the main objective of this paper. First, we present the study vineyard located in South-Western France and the collected dataset, which gathers measures of air temperature

recorded in 2015 and 2016 in the bunch zone of selected grapevines together with measures of yields and composition of berries at harvest in 2016. Second, we expose the methods for processing the air temperature time series in order to analyze their spatial and temporal variability and their correlations with quantitative and qualitative variables. Third, we present the observed microclimate patterns and discuss their distributions in space and time in regards to the vegetation arrangement. Also the most remarkable correlations observed with components of grapevine yield and of berry quality are described and the domain of validity of our results is discussed. Finally conclusion sums up the main findings of this study and proposes perspectives.

V.2. Material

V.2.1 Study site

A study site of 3.4 ha, located, at Lagardere, in south-western France (43.8264 °N, -0.3507 °E, mean altitude of 175 m above sea level) was selected as an example of modern agroforestry vineyard (**Figure 58a**). It is part of the "*Côtes de Gascogne*" wine region, which is a rural region with varied landscapes gathering crops, pasture, mixed-forests and vineyards (Inglada et al. 2017). The regional topography is made by alluvial hills with gentle slopes separated by valleys which are oriented North/South.

The study vineyard is planted with North-West/South-East oriented rows of *Vitis vinifera* cv. *Sauvignon gris* (white grapes) grafted on 3309C. Vines are spaced by 1 m on a row and by 2.5 m between vine rows, which corresponds to a medium theorical density of 4000 stocks per hectare. The fruit branches of grapevines are pruned (Guyot pruning), their canopy is trained in vertical shoot position by a trellis system and trimmed at 2 m above ground (**Figure 2**).

The north-western part of the study vineyard only contains vine rows, which were planted in 2006, while the south-eastern part contains vine rows and tree rows, which were together planted in 2008 (**Figure** 58**d**). A total of 40 timber wood trees stand within vine rows. They are organized in three rows of same species, namely *Sorbus domestica* further referred as 'C' - for *Cormier* in French – *Sorbus torminalis* as 'A' - for *Alisier* in French - and *Pyrus piraster* as '*P*' for pear tree, separated by six vine rows i.e 19 m. Trees are spaced by 10 m from one to another and by 3.25 m from the immediate northern and southern neighboring vine rows. This agroforestry arrangement corresponds to a theoretical density of 3158 vines and 53 trees per hectare. Trees have been pruned at their trunk once every year in order to shape them as blocks of wood. According to lasermeter measurements performed in 2016, the average height of the trees was 3.8 m, 3.3 m and 3.0 m in row C, A and P respectively.

The northern and southern zones are separated by a ditch and a discontinuous bushy tree hedge. The borders of the plot are occupied by mixed forest (on the North-West, NW, and South-East, SW), by grapevine rows (NE), a road and then a large pasture (E) and by a pond and then a young red oak

planting (SE) (**Figure 58c**). The whole area presents a smooth continuous slope of 3 % which mainly flows from NE to SW, towards the pond (**Figure 58b**).

The soil is a deep silty-clay loam. One out of two grapevine middle rows and tree rows are sown with a grassy cover which is regularly mowed over the vegetative growth season. The bare soil on one out of two grapevine middle rows is mechanically weeded while the bare soil under grapevine rows is chemically weeded.

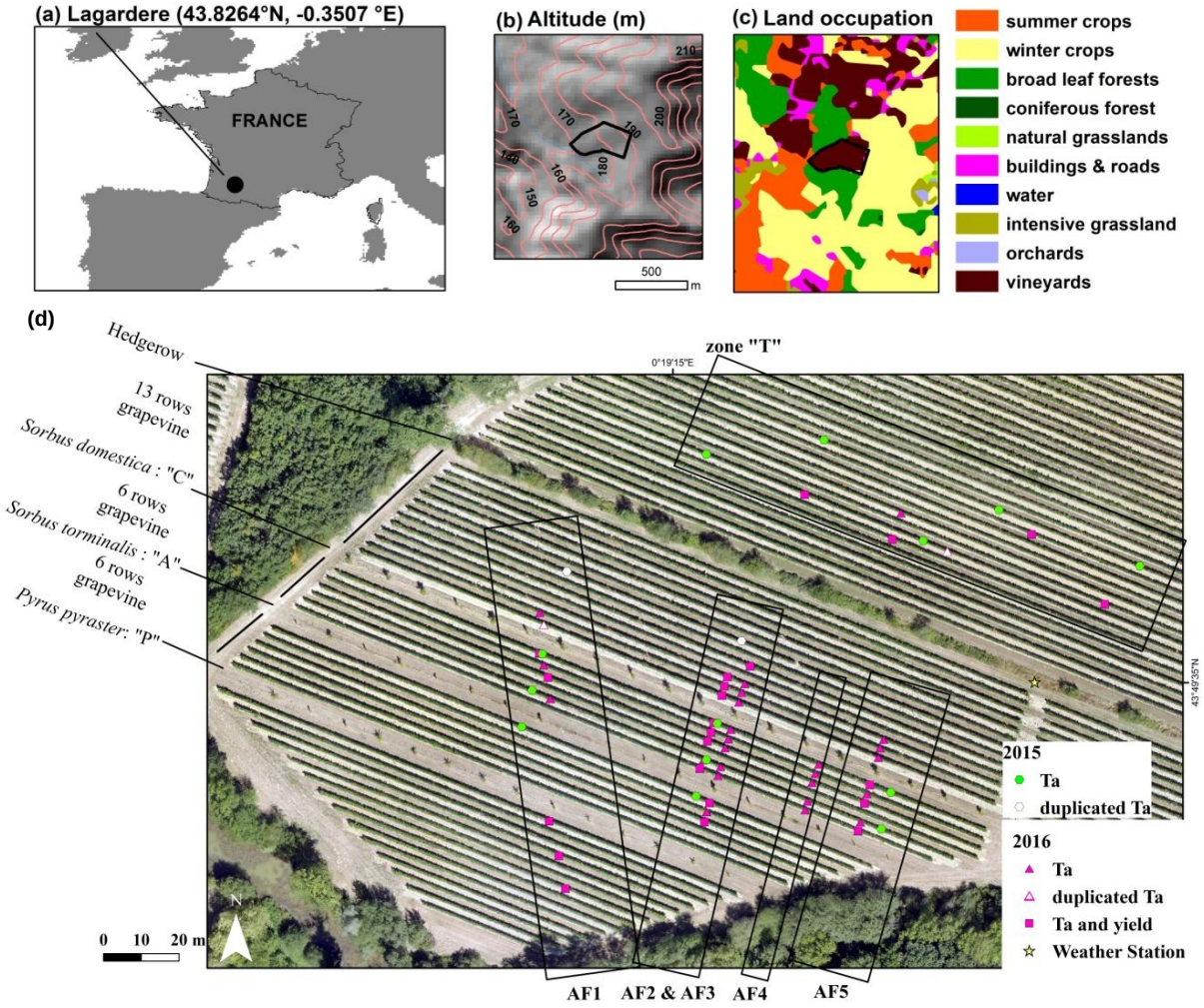

Figure 92: Location (a), topography from BD TOPO 25 m (IGN) (b), land occupation from Inglada et al.(2017)(c) and distribution of experimental plots (d) at the study vineyard in Lagardere, France. Measurements of air temperature (Ta) were carried out simultaneously at 15 plots from 29 Jul. to 2 Sep. 2015 (●) and at 49 plots from 10 Mar. 2016 to 2 Sep. 2016 (▲ and ■). In 2015, the measurements were duplicated at AF1_Cn7 and AF2_Cn7 locations (white ○), while in 2016, they were duplicated at AF3_Cn1 and T4 locations (white △). Also, the grapes from 22 plots (pink ■) were collected as individual batches at harvest in 2016. The names of the plots are given according to their position either in the northern zone "T" or in one of the five southern transects named "AF1" to "AF5". Both T plots and transects are numbered from NW to SE. Tree rows planted with *Sorbus Domestica*, *Sorbus* torminalis and *Pyrus piraster* are designated respectively as *'C', 'A' and 'P'*. Also 'si'/'ni' stands for the ith vine row on either the southern/northern side of a tree row. Background picture was acquired by drone flight on 23 Aug. 2016 by T. Houet.

The regional climate is oceanic to humid continental (Peel et al. 2007). Over the year, the average temperature is 13.1°C and the total cumulated rainfalls are 741 mm. There is no particularly dry season as precipitations are rather fairly distributed throughout the year (**Figure 40**). The regional climatic potentialities for wine production in Lagardere are driven by a heliothermal index of Huglin

that falls in the temperate class and by cool nights plus humid conditions during berry ripening (Tonietto and Carbonneau 2004). Vintage 2015 faced one of the warmest spring and first half of summer since 1990 (**Figure 40**). The very high temperatures combined with unusually low rainfalls provoked a pronounced drought all along the period from grapevine budburst to flowering. Then important rainfalls occurred in August and temperatures went back in the averages. From 2015 to 2016, winter was the warmest ever recorded since 1990, which contributed for budburst to happen 10 days earlier in 2016 than in 2015. From budburst to veraison, the cumulated heat and the precipitations were both in the averages from the whole period. Then from veraison to harvest, the berry ripening of 2016 vintage occurred in unusually warm and dry conditions: the last decade of August and the first decade of September were the warmest recorded since 1990, especially at night (**Figure 40**).

V.2.2 Data set

V.2.2.1 Meteorological records

In 2015, the daily time series of reference evapotranspiration (ET0) was provided by SAFRAN produced by Météo France (Le Moine 2002; Pagé 2008).

In 2016, a weather station was put on site at a height of 2 m above ground (a Vantage Pro 2 sensor suite from Davis, cabled on a GSM consol from CAIPOS). Sun radiation, wind speed and direction, air temperature, relative humidity and precipitations were recorded at a ten minute frequency. In situ meteorological records were combined with a time series of atmospheric pressure recorded at Auch (30 km Southern-East from Lagardere), for computing the daily ET0 according to the FAO Penman-Monteith method (Allen 1998).

V.2.2.2 Distributed temperature measurements

Batches of data loggers from Maxim Integrated (iButton® DS1923 – resolution = 0.5 °C – accuracy = 0.5 °C) were used for recording the air temperature within the study vineyard. Instantaneous temperatures were recorded from 29 Jul. to 4 Sept. 2015 and from 10 Mar. to 2 Sept. 2016, every 15 minutes. Data loggers were hanged inside shaded and naturally ventilated boxes which were positioned in vine rows inside grapevine foliage (1.50 m above ground) in 2015 and in the bunch zone (0.50 m above ground) in 2016 (**Figure 55**).

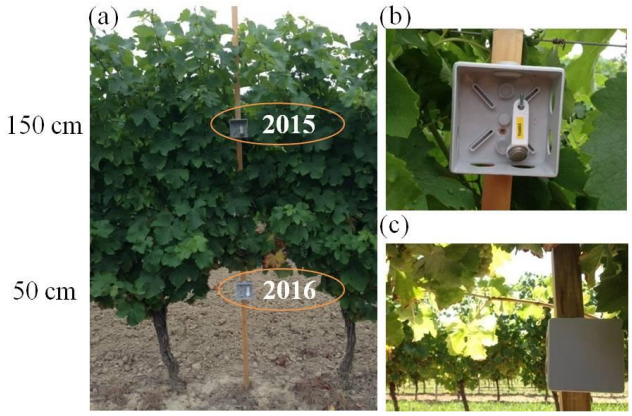

Figure 93: Implementation of iButton® data loggers in grapevine rows for 2015 (top) and 2016 (bottom) experimental campaigns.

Measures were distributed within the study vineyard at a selection of 15 vine stocks in 2015 and 49 vine stocks in 2016, further called "plots" (**Figure 58d**). For the two campaigns, the selection of plots was made in order (i) to sample vine stocks located at various distances and sides to the tree rows, (ii) to sample vine stocks located at various distances to the trees that surround the vineyard, and (iii) to sample a few vine stocks located as far as possible from any tree. The measurement plots were named according to their relative position to trees: '*AF1*' to '*AF5*' – *AF* stands for agroforestry – correspond to five transects of plots running at right angle to the tree rows in the southern zone while 'T1' to 'T6' are individual plots located in the northern zone. Both 'AF' transects and 'T' plots were numbered from West to East i-e by increasing distance from the western forested border. Within *AF* transects, the closest tree is indicated as '*C'* for *Sorbus Domestica*, '*A'* for *Sorbus torminalis* or '*P'* for *Pyrus piraster* and 's*i'*/'n*i*' stands for the ith vine row on either the southern or the northern side of the tree row. For each experimental campaign, measurements were duplicated at two plots in order to estimate the intrinsic error of measurement (contribution from the resolution and accuracy of the devices and their positioning inside boxes). For this purpose two loggers were placed side by side in the same box.

V.2.2.3 Distributed assessment of the yield in grapes and berry components

The yield and composition of the grape bunches were measured in 2016, two days before the vine grower harvested its vineyard. These measurements were carried out at 22 selected plots (**Figure 58d**). At each plot, five consecutive vine stocks located on the same vine row were targeted so as to surround the vine stock where temperature measurement was performed.

A total of ten agronomic variables listed in **Table 14** were considered. They include both quantitative and qualitative traits. On the one hand, the yield and its components (number of bunches per vine and bunch weight) were determined at each selected plot from the collection of all bunches from the 5 consecutive vines. On the other hand, the composition of the must in sugar, acids and polyphenols was determined from a random collection of 200 berries among the 5 consecutive vines.

Variable name	*Unit*	*Description*
$Yield$	$kg.vine^{-1}$	Total weight of bunches per vine
$BunchNb$	$nb.vine^{-1}$	Number of bunches per vine
$BunchW$	$kg.bunch^{-1}$	Average weight of one bunch computed from $Yield = BunchW * BunchNb$
$200BerryW$	g	Average weight of 200 berries
$Sugar$	$g.L^{-1}$	Concentration in fermentable sugars
$TotAcid$	$g.L^{-1}$ H_2SO_4	Titratable acidity (total concentration of free protons and undissociated acids)
pH		Logarithmic concentration of free protons
$MalicAcid$	$g.L^{-1}$	Concentration in malic acid
$TartaricAcid$	$g.L^{-1}$	Concentration in tartaric acid
TPI		Total polyphenol index measured as the absorbance at 280 nm

Table 14: Yield parameters and must components measured at harvest.

V.3 Methods

V.3.1 Processing of temperature records

Temperature data were analyzed following three main steps further called "pre-processing", "period targeting" and "clustering of experimental plots" (**Figure 94**). In short, data pre-processing consisted in retrieving fifteen different variables of interest from the raw time series of temperature. Then, period targeting consisted in subdividing each time series considering (i) four different phenological stages and (ii) two levels of daily evapo-transpiration per stage, either high or low. At last, plot clustering consisted in classifying experimental plots into homogeneous patterns of temperature through performing a non supervised classification for each variable of interest, and then testing the statistical significance of clusters. In total, $15\ variables\ x\ 2\ periods\ =\ 30\ trees$ of classification were obtained from the 2015 records and $15\ variables\ x\ 8\ periods\ =\ 120\ trees$ were obtained from the 2016 temperature records. All these steps were performed using MATLAB R2017a. They are detailed in the three following sections.

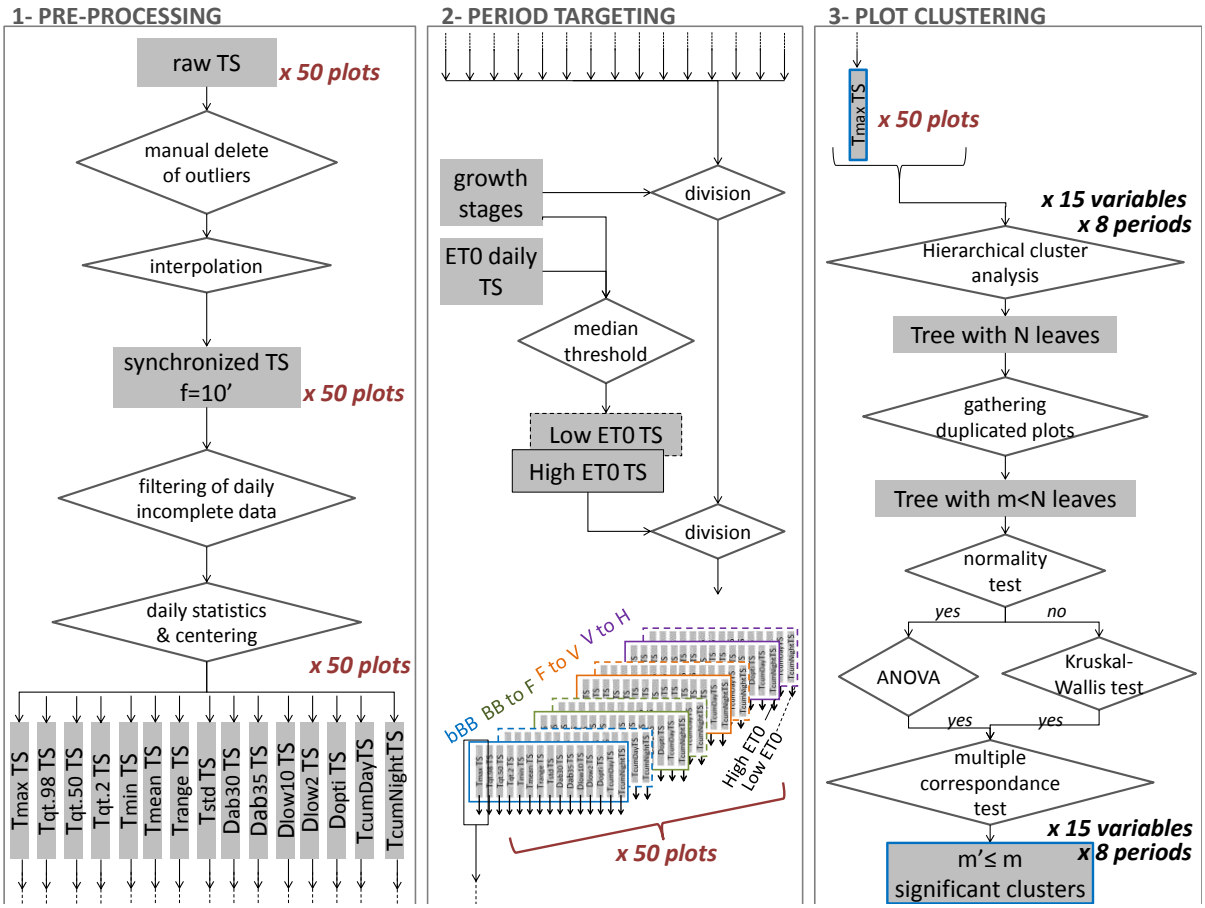

Figure 94: Flow chart of the overall processing of temperature time series. The number of targeted plots and the phenological stages apply for the 2016 campaign. In 2015, temperatures were assessed only at 15 targeted plots and only from veraison to harvest. Abbreviations: *TS*: *time series*, see Table 15 for detail - *f*: frequency – *ETo*: daily cumulated evapotranspiration of reference – *bBB*: before budburst – *BB*: Bud-burst – *F*: Flowering – *V*: Veraison – H: Harvest

Abbreviation	*Variable*	*Unit*
$Tmax$	Daily maximum temperature	°C
$Tqt98$	Daily temperature 98 % quantile	°C
$Tqt50$	Daily median temperature	°C
$Tqt2$	Daily temperature 2 % quantile	°C
$Tmin$	Daily minimum temperature	°C
$Tmean$	Daily mean temperature	°C
$Trange$	Daily pseudo range of temperature $Trange = Tqt98 - Tqt2$	°C
$Tstd$	Daily standard deviation	°C
$Dab30$	Total daily duration above 30 °C	hr
$Dab35$	Total daily duration above 35 °C	hr
$Dlow10$	Total daily duration below 10 °C	hr
$Dlow2sum$	Total daily duration below 2 °C	hr
$Dopti$	Total duration of T> 20°C and 30°C	hr
$TsumDay$	Degree days cumulated during hours of the day (from 8:00 to 19:59)	°C day
$TsumNight$	Degree days cumulated during hours of the night (from 00:00 to 7:59 and from 20:00 to 23:59)	°C day

Table 15: Daily variables retrieved from raw time series of temperature

V.3.1.1 Data pre-processing

Each data logger generated a .csv file per period of acquisition. Data from each plot of measure were concatenated as a single raw time series using the name of each plot as a unique identifier. Then, all the time series were aligned according to a time of reference with a 10 min^{-1} frequency. For this

purpose, raw time series were interpolated using a spline cubic function. In order to guarantee the robustness of the interpolated values, the absence of missing data was checked prior to interpolation and the interpolation was actually performed only when they were at least 3 measures per hour in the raw data. Then, a set of fifteen daily variables detailed in **Table 15** were computed from each raw time series. In order to guarantee their robustness, days of record which presented at least one missing hour of records were eliminated. The last step of data pre-processing consisted in centering each daily time series (substraction of the mean of all plots) in order to eliminate the time correlation between daily observations. **Equation 1** gives the example for centering the $Tmax$ variable.

$$YTmax_i^d = Tmax_i^d - \overline{Tmax^d} \quad \text{Eq. (1)}$$

with $YTmax_i^d$ Centered maximum temperature at plot i on day d
$Tmax_i^d$ Maximum temperature at plot i on day d
$\overline{Tmax}^d$ Mean of the maximum temperatures out of all plots on day d

V.3.1.2 Targeting periods

Complete daily time series were subdivided into shorter periods considering two criteria: the vine growth stage (phenology) and the daily evapotranspiration (ET0). Concerning phenology, four different periods were distinguished, namely before budburst, from budburst to flowering, from flowering to veraison and from veraison to harvest (**Table 10**). The phenological stages of grapevine were reported both in 2015 and in 2016 following the extended BBCH scale (Lorenz et al. 1995)**.** Then for each phenological period, days with high or low ET0 were distinguished. Decision was based on the computation of the median daily ET0 for each phenological period (**Table 10**).

	2015	2016
Prior to budburst (BBCH 07)		10-Mar to 1-Apr. *$ET0_{50\%}$ = 1.68 mm*
from budburst to flowering (BBCH 65)		1-Apr. to 11-Jun. *$ET0_{50\%}$ = 2.94 mm*
from flowering to veraison (BBCH 85)		11-Jun. to 11-Aug. *$ET0_{50\%}$ = 3.88 mm*
from veraison to harvest (end of records)	2-Aug. to 3-Sep. *$ET0_{50\%}$ = 4.02 mm*	11-Aug. to 2-Sep. *$ET0_{50\%}$ = 4.07 mm*
True harvest	4-.Sep.	21-.Sep.

Table 16: Phenological periods and median threshold of evaportranspiration of reference (ET050%) considered in 2015 and 2016. The phenological stages are reported according to the extended BBCH scale of Lorenz et al. 1995.

V.3.1.3 Plot clustering

For each phenological x ET0 period, the *N* experimental plots were agglomerated into clusters of similar patterns by hierarchical cluster analysis, with $N_{2015} = 15$ and $N_{2016} = 50$.

The first step consisted in building a classification tree or 'dendrogram' with *N* leaves. Five different trees were built using respectively (i) the Euclidean distance (similarity metric) and the 'average' i.e. unweighted average distance (grouping criterion), (ii) the Euclidean distance and 'single' i-e the shortest distance criterion, (iii) the Euclidean distance and 'complete' i.e. the farthest distance

criterion, (iv) the Spearman distance and 'average' criterion and (v) the Spearman distance and 'complete' criterion. The degree of fit of each dendrogram to the original data was measured using the cophenetic correlation coefficient (Sokal 1961). The tree obtained with the Euclidean distance and 'average' criterion systematically maximized the cophenetic correlation coefficient and was thus retained to pursue the analysis.

Then a second step consisted in descending the tree in order to divide the plots into a maximum of m clusters. Duplicated plots were used to assess the robustness of the clusters regarding the intrinsic variability: division was forced to stop as soon as duplicated plots appear into distinct clusters.

When at least two clusters $(m > 1)$ were obtained from the above procedure, a third step of validation was carried-out (**Figure 94**). The normality of each population was tested with a Shapiro-Wilk test:

1. When the null hypothesis of normality was conserved with a P-value greater than 5 % then a one-way analysis of variance (ANOVA) was performed in order to compare the means of all the clusters; ANOVA is parametric and tests the null hypothesis $H0: \mu_1 = \mu_2 = \cdots \mu_m$ against $H1: means\ are\ not\ all\ equal$;
2. When the null hypothesis of normality was rejected, a Krustall-Wallis (KW) test was performed in order to compare the medians of all the clusters; This latter is non-parametric and tests the null hypothesis $H0: qt50_1 = qt50_2 = \cdots qt50_m$ against $H1: 'medians\ are\ not\ all\ equal'$.

When H0 was rejected by ANOVA or by KW test, a multiple comparison test was performed to compare pair-wise the group means (after ANOVA) or the average group ranks (after KW test). In both cases, Tukey's honest significant difference criterion ('Tukey test') was used.

V.3.2 Correlation analysis between temperature and agronomic patterns

Correlations between the temperature patterns and the yield characteristics were analyzed considering the 22 plots where both types of variable were assessed in 2016 (**Figure 55**). The analysis followed three steps:

The mean of the daily anomalies was computed for each plot and for each microclimatic variable listed in **Table 15**. The phenological*ET0 time periods were considered separately thus for each climatic variable, height different averages were generated, one for each time period.

Simple linear regressions were performed so as to identify linear models defined as

$$Y^i = {\alpha_p}^{ij} \, (X_p^j - \overline{X_p}) + {\beta_p}^{ij}$$

where Y^i is one of the 10 agronomic variables, X_p^j is one of the 15 temperature variable computed for the period p, and ${\alpha_p}^{ij}$ and ${\beta_p}^{ij}$ are respectively the slope and the intercept coefficients of the linear model.

The coefficient of correlation r and the coefficient of determination R^2 were computed for assessing the robustness of each of the obtained linear models.

V.4.Results and discussion

V.4.1 Analysis of the spatial and temporal behavior of temperature variables

In the following paragraph, the daily statistics of the temperature measured in the bunch zone from two weeks prior to budburst until harvest are compared to that measured at the weather station (2 m above ground) (**Figure 95**).

In 2016, whenever the phenological period, the daily mean temperature ($Tmean$) and the median temperature ($Tqt50$) were very close to the measures at the weather station and did not show any significant variation within the study vineyard (**Figure 95b**). On the opposite, the daily extreme temperatures differed the most from the records at weather station and showed the most variability in space (**Figure 95a&c**). On the one hand, the daily minimum temperature ($Tmin$) and the daily quantile 2 % ($Tqt2$) showed values 1.5 °C cooler than at the weather station on the coldest days of each phenological period (all bottom peaks), especially in spring. The variability between experimental plots of these two variables ranges respectively from 1 °C to 1.5 °C and from 0.5 °C to 1 °C. On the other hand, the daily maxima temperature ($Tmax$) and the daily 98 % quantile ($Tqt98$) were systematically warmer by 1 °C to 5 °C than at the weather station. Their variability in space seemed to increase with the temperature itself as the highest variations were observed from veraison to harvest and could reach 5 °C of amplitude between the sampled plots. Regarding variable correlations, very little differences could be observed between $Tmin$ and $Tqt2$ either in terms of values or variability suggesting that the $Tmin$ variable does not suffer from outlier tendency and is sufficiently informative on its own (**Appendice J**). On the opposite, $Tmax$ was noticeably warmer by 1 °C than $Tqt98$ and presented a higher range of variability between plots suggesting that the two variables, though correlated, convey complementary information.

The daily duration variables all presented seasonal variations and seemed to follow the trend of the extreme temperatures. On the one hand the daily duration below 10 °C ($Dlow10$), which suggested significant interruptions of vegetative growth from budburst to flowering and a few from flowering to harvest could have been predicted from the measure at the weather station (**Figure 95f**). On the other hand, the duration above 30 °C ($Dab30$) was systematically longer than at the weather station and was not always predictable (**Figure 95e**). $Dab30$ suggested some slow down in the photosynthesis process and maybe some breaks in the synthesis of phenolic components in berries to regularly occur from a few days prior to flowering until harvest, with important variations (of 1 to 5 hrs) depending on location within the vineyard. According to the duration below 2 °C ($Dlow2$), a risk of late frost was reported four times after budburst and showed some variability of 30’ to 2.5 hrs between plots

(**Appendice J**). According to the duration above 35 °C ($Dab35$) measured at experimental plots, a risk of heat stress seldom occurred from flowering to veraison but frequently occurred from veraison to harvest, with variations of 1 to 5 hrs between plots (**Appendice J**). Neither of these two risks from extreme temperatures detected in the bunch zone could have been predicted from weather station record.

The daily degrees accumulated over the day ($TsumDay$) and over the night ($TsumNight$) in the bunch zone both showed higher values and synchronized trends with that observed at the weather station. Also, both varied less in space than the daily extreme temperatures and presented some local specific behaviors which appeared as outliers (**Appendice J**). No particular distinction could be seen between the two sums except from veraison to harvest where $TsumNight$ showed a tendency to remain low when $TsumDay$ was actually rising up. This latter observation remains hypothetical as it would need the temperature time series to continue further on until the true harvest of grapevine, which occurred 5 days after temperature measurements stopped.

The daily range of temperatures ($Trange$) and the daily standard deviation ($Tstd$) were very similar in trends. Both systematically showed higher top peaks than at the weather station with +2 °C to +4 °C for $Trange$ (**Figure 95d**) and +0.5 °C to +1°C for $Tstd$. The amplitude of their variability in space is moderate relatively to that of the extreme temperatures and remained almost constant all along the measurement time period.

(a)

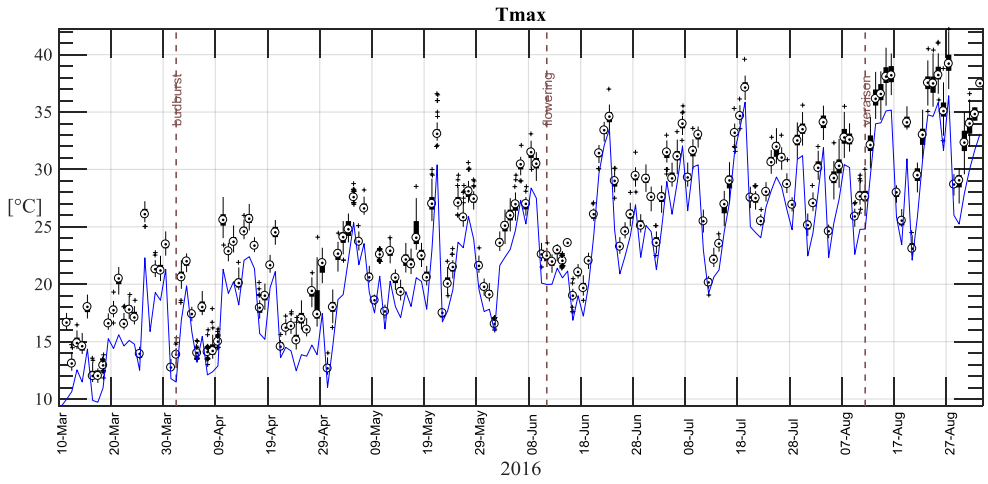
Tmax
budburst
flowering
veraison
[°C]
40
35
30
25
20
15
10
10-Mar
20-Mar
30-Mar
09-Apr
19-Apr
29-Apr
09-May
19-May
29-May
08-Jun
18-Jun
28-Jun
08-Jul
18-Jul
28-Jul
07-Aug
17-Aug
27-Aug
2016

(b)

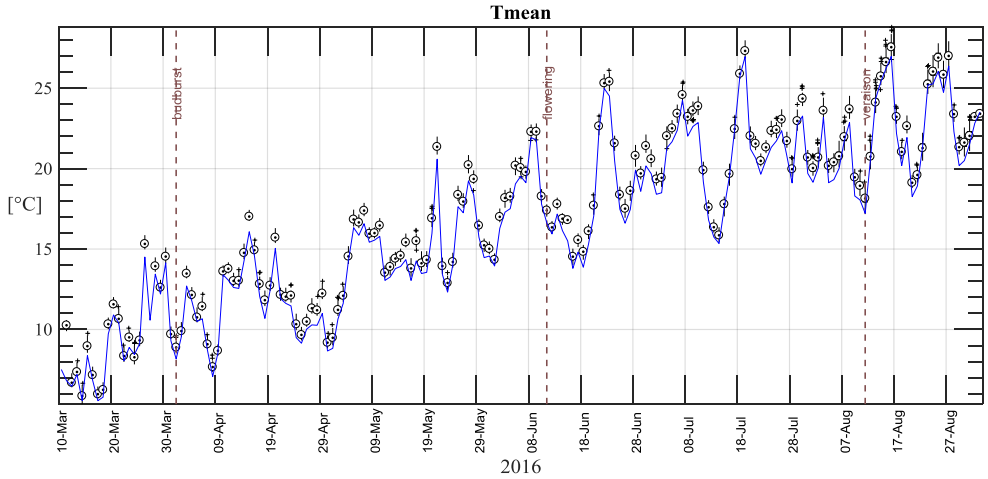
Tmean
budburst
flowering
veraison
[°C]
25
20
15
10
10-Mar
20-Mar
30-Mar
09-Apr
19-Apr
29-Apr
09-May
19-May
29-May
08-Jun
18-Jun
28-Jun
08-Jul
18-Jul
28-Jul
07-Aug
17-Aug
27-Aug
2016

(c)

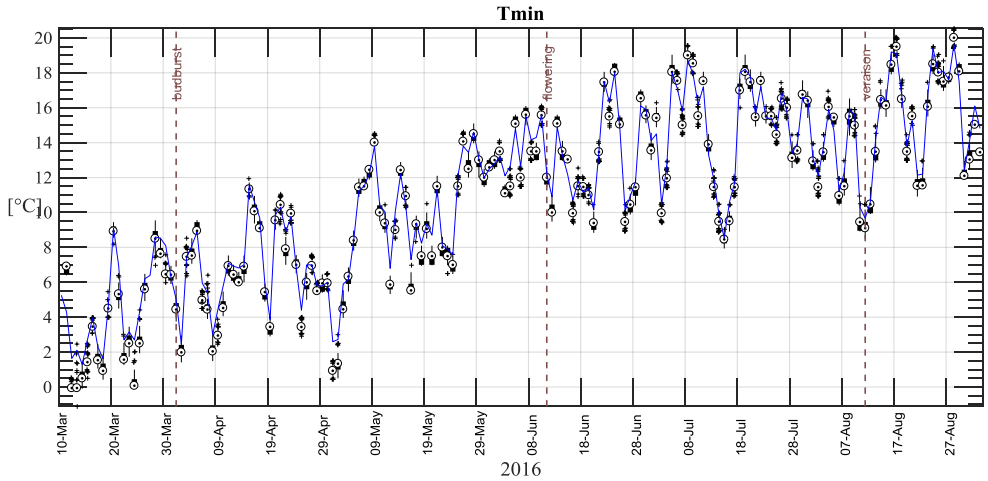
Tmin
budburst
flowering
veraison
[°C]
20
18
16
14
12
10
8
6
4
2
0
10-Mar
20-Mar
30-Mar
09-Apr
19-Apr
29-Apr
09-May
19-May
29-May
08-Jun
18-Jun
28-Jun
08-Jul
18-Jul
28-Jul
07-Aug
17-Aug
27-Aug
2016

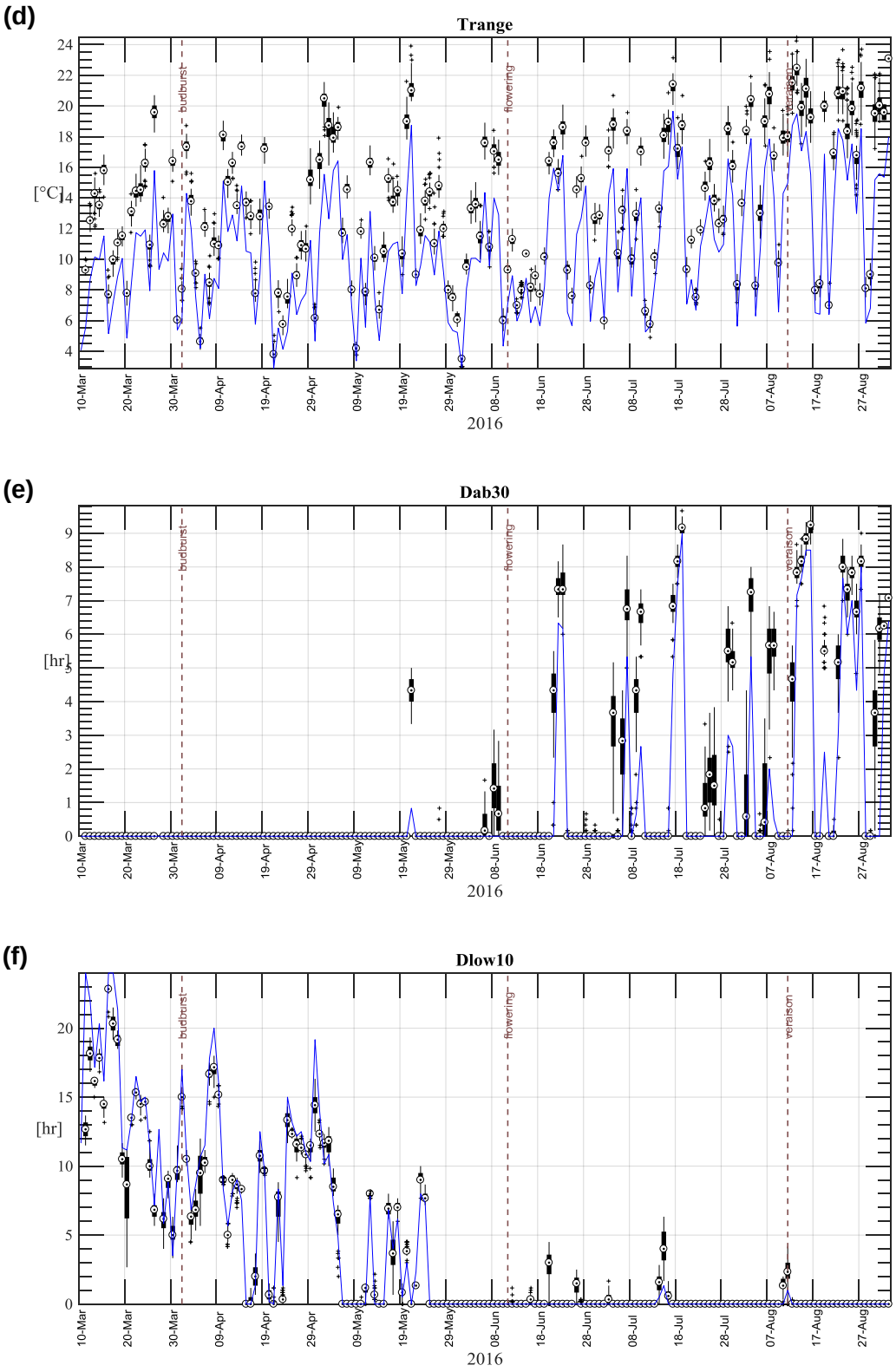

Figure 95: Time series of the daily Tmax (a), Tmean (b), Tmin (c), Trange (d), Dab30 (e) and Dlow10 (f). The blue curve indicates the temperature recorded by the weather station while the box plot indicates the temperatures recorded by the data loggers positioned in the bunch zone of grapevine and distributed at various plots within the vineyard. On each box, the central mark gives the median, the bottom edge gives the 25th percentile and the top edge gives the 75th percentile. The whiskers extend to the most extreme data points not considered as an outlier, and the outliers are individually plotted using the '+' symbol. Whisker extends to approximately +/−2.7σ, with σ the standard deviation.

V.4.2 Overall performance of plot clustering

Table 17 synthesizes the results from clustering of the plots and the associated levels of significance. It confirms that the variables related to extreme temperatures are the most contrasted within the vineyard, allowing the distinction of several clusters of plots. On the opposite, mean and median variables appeared limited for the identification of spatial temperature patterns, due to their few variations within the vineyard (as previously stated). The clustering based on the durations in the extremely low and extremely high temperatures are applicable only respectively in spring and in summer. Also, when applicable, $Dab30$ and even so $Dab35$ showed signs of a low robustness of the statistical test of significance as it may suffer from low to very low repetitions.

	2015				2016					
	from V to H		prior to BB		from BB to F		from F to V		from V to H	
	high ET0	low ET0	High ET0	low ET0	high ET0	low ET0	high ET0	low ET0	high ET0	low ET0
Tmax	15 (3***)	11 (3**)	1	1	15 (2*)	3 (2***)	2 ***	1	1	2 ***
Tqt98	15 (3*)	8 (3**)	2 ***	1	9 (4*)	1	4 ***	1	2 ***	2 ***
Tqt50	1	1	2 ***	1	1	1	1	1	1	1
Tqt2	6 (3*)	4 (2**)	3 ***	4 (3*)	1	1	3 **	1	3 (2***)	3 (2***)
Tmin	6 (3*)	4 (2**)	2 ***	3 ***	1	1	3 ***	1	3 (2***)	2 ***
Tmean	2 ***	2 ***	1	1	1	1	1	1	1	1
Trange	11 (4*)	8 (3*)	4 (3***)	1	4 (2***)	7 (2*)	1	2 ns	1	1
Tstd	14 (3*)	13 (2**)	4 (3***)	3 **	2 ***	2 *	12 (9*)	1	2 ***	2 ***
Dab30	4 (2***)	3 (2*)	NA	NA	1	NA	2 ***	3 ns	6 (4*)	3 (2***)
Dab35	11 (2*)	NA	NA	NA	NA	NA	2 ***	NA	4 (2**)	2 ns
Dlow10	4 ns	2 *	1	1	1	1	1	2 *	1	NA
Dlow2	NA	NA	2 ***	1	1	NA	NA	NA	NA	NA
Dopti	12 (3)	3 ns	1	NA	1	1	4 (3*)	1	2 ***	1
TsumDay	2 ***	2 ***	1	1	1	1	2 ***	1	2 ***	1
TsumNight	3 (2***)	2 **	2 ***	3 ***	1	1	1	2 ***	3 ***	1

Table 17: Number of clusters obtained from the classification of experimental plots and statistical significance of difference in their mean/median. The detail for each variable used for classification is given in Table 15. Significance is expressed either 'ns' if insignificant (pval > 0.05) or *//*** if significant/very significant/highly significant (0.01 < P-value ≤ 0.05 \ 0.001 < P-value ≤ 0.01 \ P-value ≤ 0.001). The number of clusters with significant differences when tested pair-wisely is given in brackets - Abbreviations: *NA*: not applicable – *BB*: budburst - *F*: flowering - *V*: veraison - *H*: harvest**

In 2015, the temperature was recorded at 17 different plots from veraison to harvest. In this case, **Table** 17 shows that most of the clustering analysis stopped very lately. In regards to the total amount of plots, they resulted in a very large amount of clusters whose statistical significance was rejected most of the time. In 2016, the temperature was recorded at 50 different plots. From veraison to harvest, the clustering procedure systematically ceased much sooner and converged on clusters with statistical significance. This comparison suggests that the classification approach and criterion for stopping subdivisions were poorly robust with a low amount of experimental plots while it gained robustness with a high density of sampling.

Sorting days between high and low evaporative demand allowed revealing contrasted results for the periods prior to budburst i-e in spring, from flowering to veraison i-e in the warmest period of summer, and to lesser extent from veraison to harvest (**Table 17**). On the opposite, it made no difference from budburst to flowering. For both the periods of prior to budburst and from flowering to veraison, the gap of ranges between high and low ET0 is relatively important (**Figure 100**). Thus distinguishing high and low daily ET0 may have allowed separating very distinct daily temperatures into two distinct populations.

V.4.3 Seasonal temperature patterns within the study vineyard

V.4.3.1 Before budburst

In 2016, over 21 days before budburst, mainly two contrasted patterns of temperatures appeared within the study vineyard (**Figure 96**). On the one hand, the warmest minimum temperatures of the vineyard were observed at 5 out of the 6 plots located in the Northern part of the vineyard (plots *T2* to *T6*) and most of all at the furthest north-western plots named *T5* and *T6*. The minimum temperatures at these plots were warmer from 0.5 °C to 1 °C than the average of all the plots. On the opposite, the minimum temperatures were the coldest in the southern part of the vineyard but only on days with low evapotranspiration demand. In the first case, the warmer minimum temperatures allowed shorter durations spent below 2 °C (by 30 minutes to 3.5 hours), lower daily ranges of temperature and bigger accumulation of degree days over the night hours. In the second case, colder minimum temperatures may have been responsible for a higher daily variability of temperatures and a lower accumulation of degree days over the night.

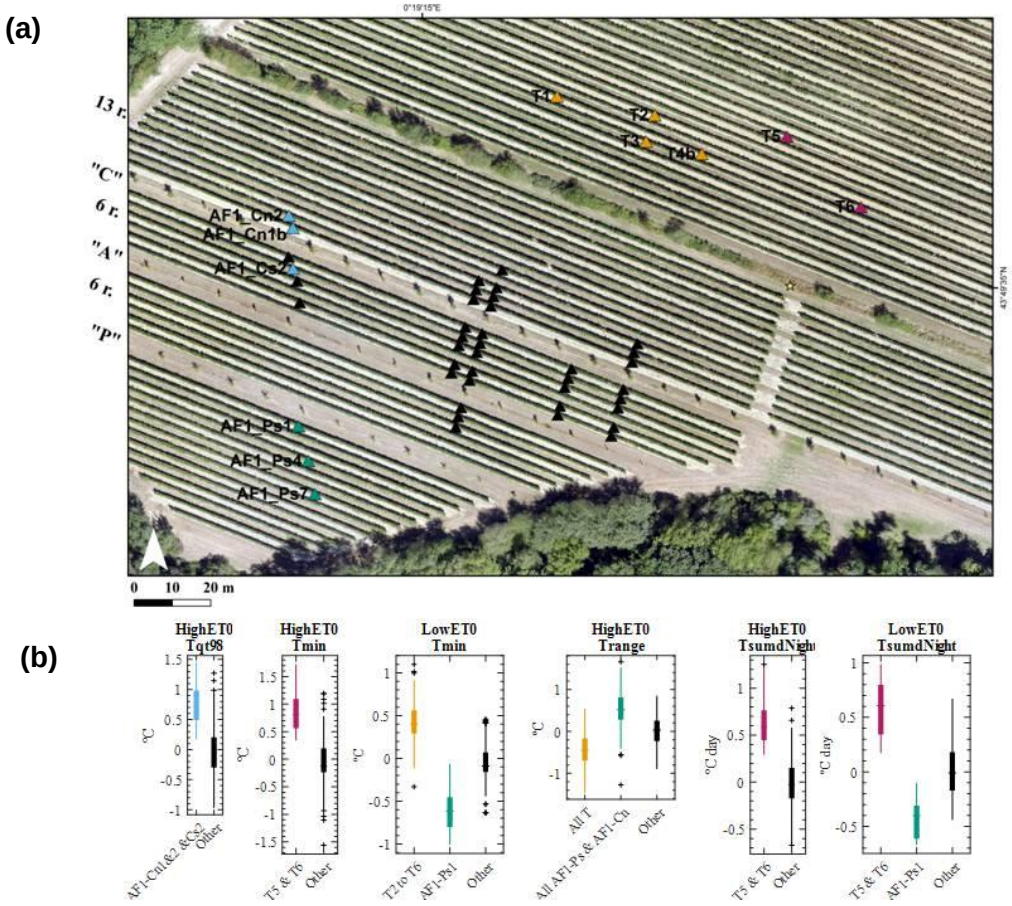

Figure 96: Location of the clusters of plots (a) and corresponding statistics per daily temperature variables (b), considering the period before budburst.

V.4.3.2 From budburst to flowering

In 2016, from budburst to flowering, only few variables led to significantly different clusters within the vineyard, namely the daily maximum temperature and the daily range (**Table 17**). Only slight consistency could be found in the cluster composition. Similarly to the period prior to budburst, all the plots located in the northern part of the vineyard showed a lower daily range of temperature than the rest of the experimental plots, especially on days with low ET0 (**Figure 97b**). Nonetheless no equivalent trend was observed in terms of minima temperature or of risk from late frost damages as both $Tmin$ and $Dlow2$ resulted in no contrasted clusters (**Table 17**). On the opposite, plots at the two extremities of the most western transect (transect "AF1") seems to present the highest daily maximum temperatures and the widest daily ranges in all the vineyard, especially on days with low evaporative demand (**Figure 97a**).

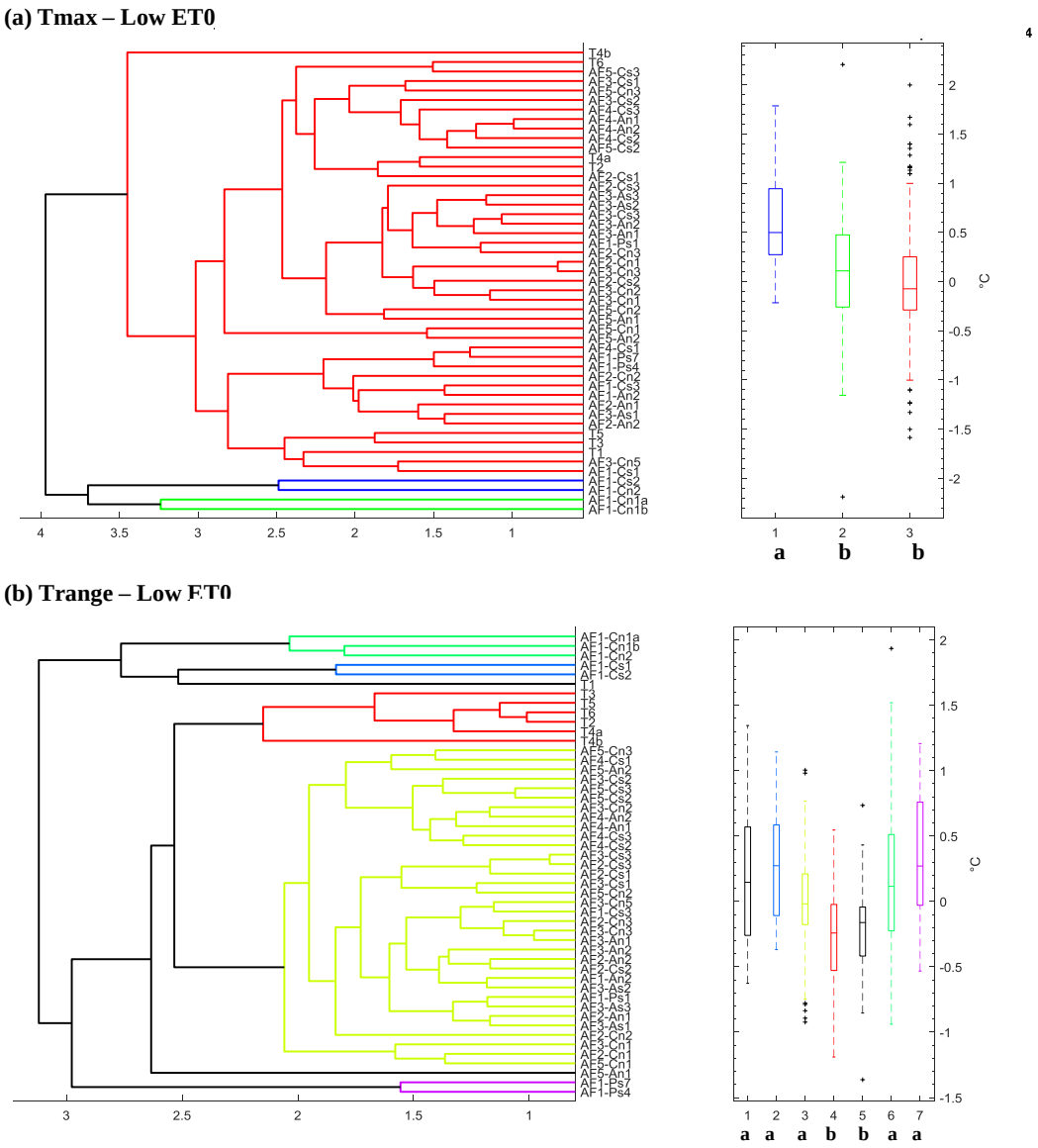

Figure 97: Results of classification of the time series of daily maximum temperature (top) and daily range (bottom) considering days from budburst to flowering with low evaporative demand. The letters a/b indicate clusters with significantly different distributions according to the pair-wise Tukey test.

V.4.3.3 From flowering to veraison

In 2016, three contrasted patterns appeared from flowering to veraison, specifically during the days with high evaporative demand (**Figure 98**). All the plots located on the first southern vine row neighboring a tree row (plots named « xxx - s1 ») showed maxima temperatures cooler by -1 °C than the average. These plots spent durations above 30 °C and durations in the optimum range (20 – 30 °C) which were respectively shorter and longer by about 1 hour than average. The accumulation of degree day at these plots was noticeably lower by day than average while no distinction could be observed by night for this variable. On the contrary, the warmest minimum temperatures were observed at the plots *T5* and *T6* located the furthest north-western part of the vineyard. They were warmer by +0.5 °C to +0.9 °C than average. In addition, the plot AF1-Ps4 located in the furthest southern part showed the highest maxima temperatures, the widest daily ranges and the longest durations spent above 35 °C. No

contrasted patterns were observed when considering the days with low evaporative demand except at the *T5* and *T6* plots where the accumulation of degree days specifically over the night hours was bigger than average, thus confirming previous observations.

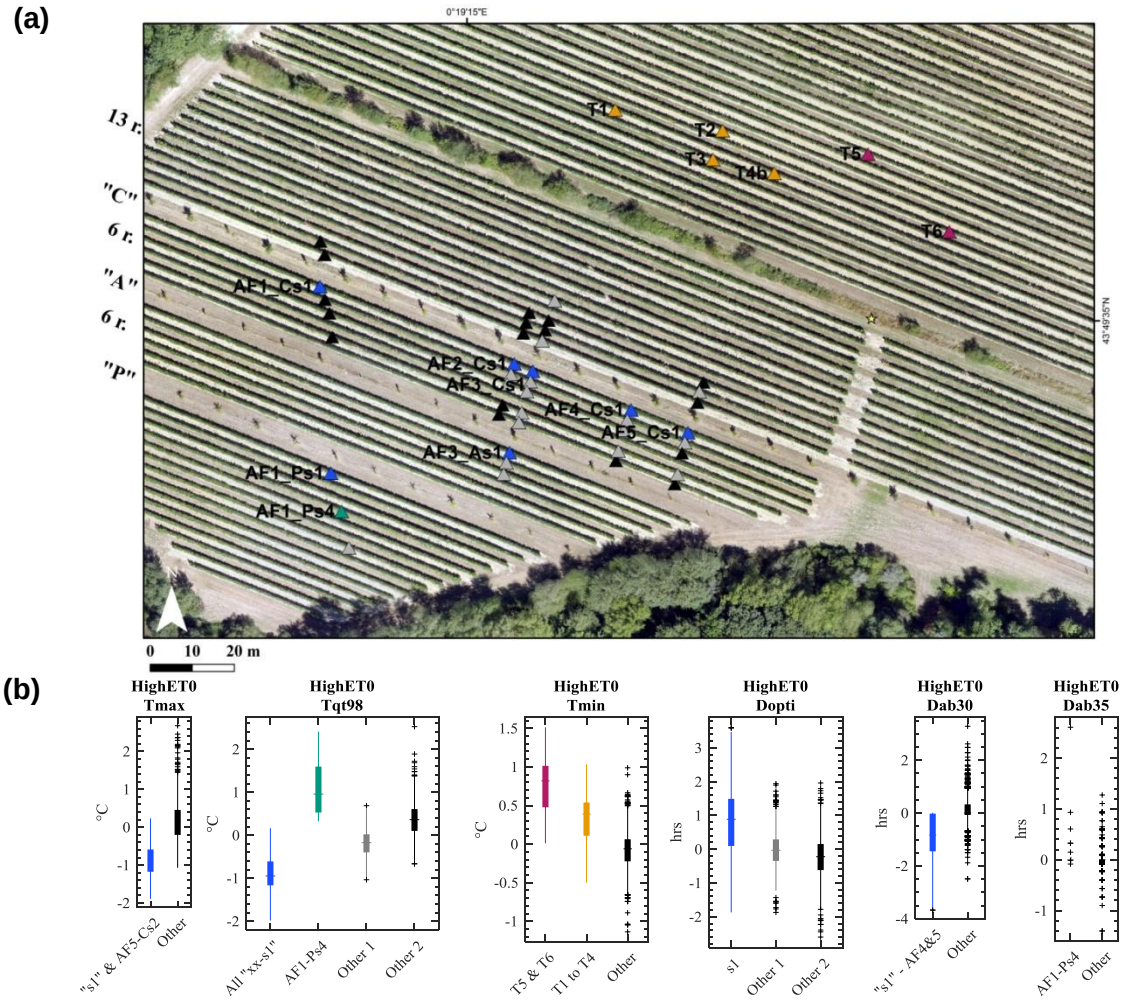

Figure 98: Location of the clusters of plots (a) and corresponding statistics per daily temperature variables (b), considering the period from flowering to veraison.

V.4.3.4 From veraison to harvest

From veraison to harvest in both 2015 and 2016, two main patterns were observed. They applied with the strongest contrast on days with high evaporative demand, while they were less pronounced in terms of distance to the average but still effective on days with low evaporative demand **(Figure 99**).

Similarly to the previous phenological period, all the plots located on the first southern vine row neighboring a tree row (plots named « s1 ») showed a tendency to cooler extreme high temperatures. Indeed, the daily maximum temperatures recorded at these plots were cooler from -0.8 °C to -1.6 °C than the average, the time spent above 30 °C was shorter by -30 min to -1 hour and the time spent above 35 °C was shorter by 1 to 2 hours on days when such extreme occurred (**Figure 99b**). In addition, the daily standard deviation of temperature resulted smaller than average and the time spent at optimum temperature was longer at these plots. The degree day accumulation variables indicated

that most of the differences occurred during the day when an additional amount from +0.6 °C-day to +1.1 °C-day was accumulated at these plots compared to average, while no contrast was observed at night.

On the contrary all the "T" plots, which are located in the northern part of the vineyard, presented a general warmer tendency which is similar to that observed from flowering to veraison: out of all the plots, the warmest maximum temperature were recorded at plots "U","S" and "V" in 2015 (warmer from +0.8 °C to +1.4 °C than average) (**Figure 99a**). Also minimum warmer temperatures from +0.6 °C à +1.1 °C than average were recorded in 2015 and in 2016, and the warmest ones were observed at plots T5 and T6. Consistently, the time spent above 30 °C was longer by +30 min to +1 hour and more degree days were accumulated over the night compared to average.

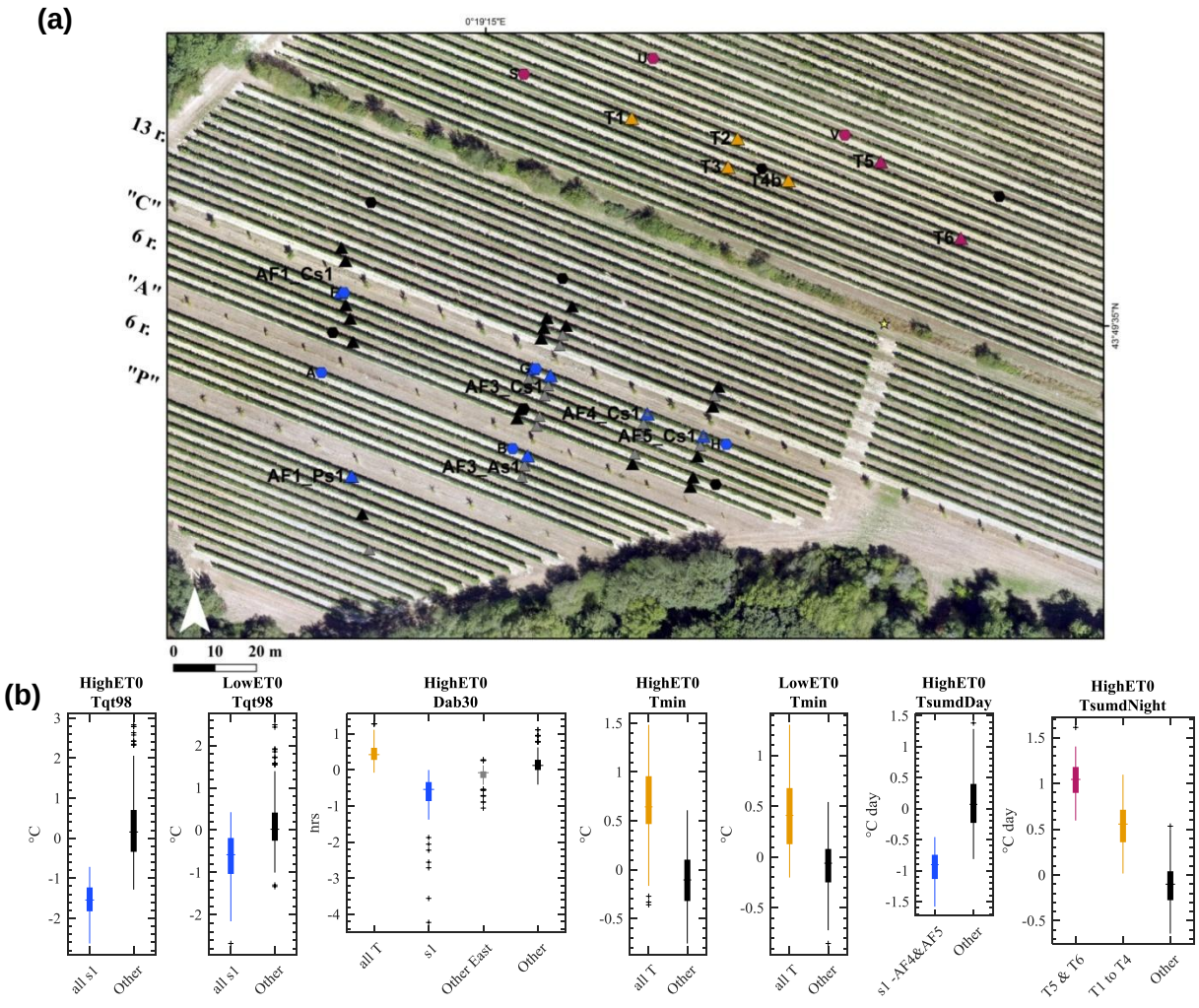

Figure 99: Location of the clusters of plots (a) and corresponding statistics per daily temperature variables (b), considering the period from veraison to harvest.

V.4.4 Contribution of the presence of trees and of meteorological conditions to the microclimate of the vineyard

Local climate conditions can be considered as a distortion of regional climatic trends through the joint contribution of topography, vegetation, water surfaces, urbanized areas and human activities. Indeed, all these land surface parameters locally interact with the air flow and with the energy fluxes between the soil and the atmosphere (Oke 1992). Among multiple factors contributing to microclimate, we discuss here the contribution from agroforestry practices.

V.4.4.1 Contribution from the vegetation arrangement in the landscape

On the one hand, we observed significantly warm minimum temperatures both prior to budburst and during summer in the most north-eastern part of the study vineyard. On the other hand, our analysis suggested cool minimum temperatures at the end of winter, rather warm maximum temperatures from flowering to veraison and large daily ranges of temperatures at both periods in the most south-eastern part of the vineyard. These two contrasted patterns may be explained by a joint contribution from the trees surrounding the vineyard, the preferential wind direction and the topography. Indeed, prior to budburst, there were no leaves either on deciduous trees or on grapevine. Among the climatic mechanisms potentially triggered by trees, only a wind breaking effect and partial shading from the tall and densely ramified perennial parts of trees can be expected. Knowing (i) that high and dense tree copses stand at the western, southern and south-eastern borders of the vineyard (**Figure 58**), (ii) that for all the phenological periods that were considered, the wind preferentially blew from West-South-West and to secondary extent from East (**Figure 100**), and (iii) that the main slope runs from North-East to South-West (**Figure 58**), one may propose the following twofold hypothesis: (1) as soon as some air flow is blowing the furthest North-East part of the vineyard may be the windiest i.e. the most exposed to mixing, while the "AF1" transect and notably its South-Eastern part may be the most isolated in general ; and (2) when no wind is blowing at all, the furthest North-East part of the vineyard may be the most exposed to sun radiation and thus to heat while cold air masses may accumulate/remain stagnant in the down part and near forested zones and/or the pond, for topographical reasons. **Figure 101 a,b,c** considers the instantaneous difference to mean temperatures at the furthest north-western plots and comforts these hypothesis regarding the northern pattern: the warm tendency at this location was the most effective for low rather than for high wind speeds and when the wind blew from SW. On the one hand, the air flow circulating in spring in the North-East zone at night and daybreak must have allowed the air in the bunch zone to heat up the fastest and thus would explained that this zone spent a shorter time at low temperatures. On the other hand, the absence of forested borders in the vicinity of this zone must have induced the stagnation/convection of a warm air mass during the warmest days of summer.

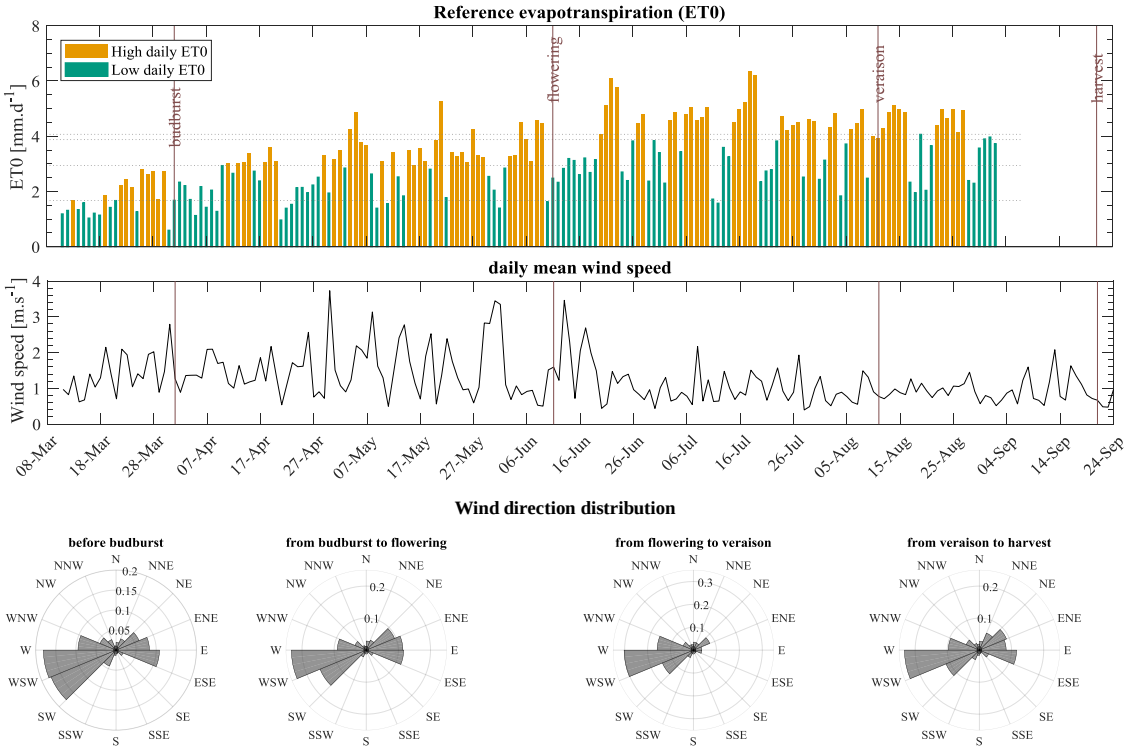

Figure 100: Evolution of the daily reference evapotranspiration (ET0), of the daily mean wind speed measured at 2 m above ground and of the wind direction over the measuring campaign in 2016. For ET0 time series, the dotted horizontal lines indicate the median ET0 per phenological period, namely before budburst, from budburst to flowering, from flowering to veraison and from veraison to harvest. These medians were used for partitioning ET0 as high (above the median) or low (below the median) per phenological period. The circular histograms of wind directions are given as proportions from a raw data captured every 10' by a weather vane positioned on site at 2 m above ground. Abbreviations: N/S/W/E: North/South/West/East.

V.4.4.2 Contribution from the intra-plot tree row

With younger and sparser trees, our study did not show a similar pattern as observed by **Gouttesoulard (2015)** on the northern side of tree rows. On the contrary, our observations revealed that the first vine row neighboring the tree rows on their south-eastern side presented the lowest maximum temperatures of the whole study vineyard and spent significantly shorter time at high temperatures compared to other plots. In our case study, this cooler pattern appeared once the foliage of grapevines and trees were well developed (from vine flowering to harvest) and it was the strongest on days with high evaporative demand. **Figure 101d** considers the instantaneous deviation of the temperature at all the first southern plots according to the temperature at the weather station. It reveals that the low tendency of the temperatures at the first southern plots starts when the air temperature is greater than 25 °C and that the gap increases with the air temperature above this threshold. Since no such pattern was observed either at the first northern vine row or at any other vine row, this pattern seems to result from the joint contribution of grapevine row position and orientation relatively to the tree row. Contrary to the two patterns described in the previous paragraph, this pattern shows no correlation with the wind speed (**Figure 101e&f**). It may eventually prevail for SW oriented wind-speed compared with other orientations but with suspicions as the provoked difference to mean temperature is lower than the thermal sensor accuracy (**Figure 101f**). At this state of knowledge, the

most likely reason for such pattern would be the combination of the shadow from grapevine itself combined with a specific circulation of the air flow within the corridors constituted by the tree rows which are twice wider than the middle row between two vine rows.

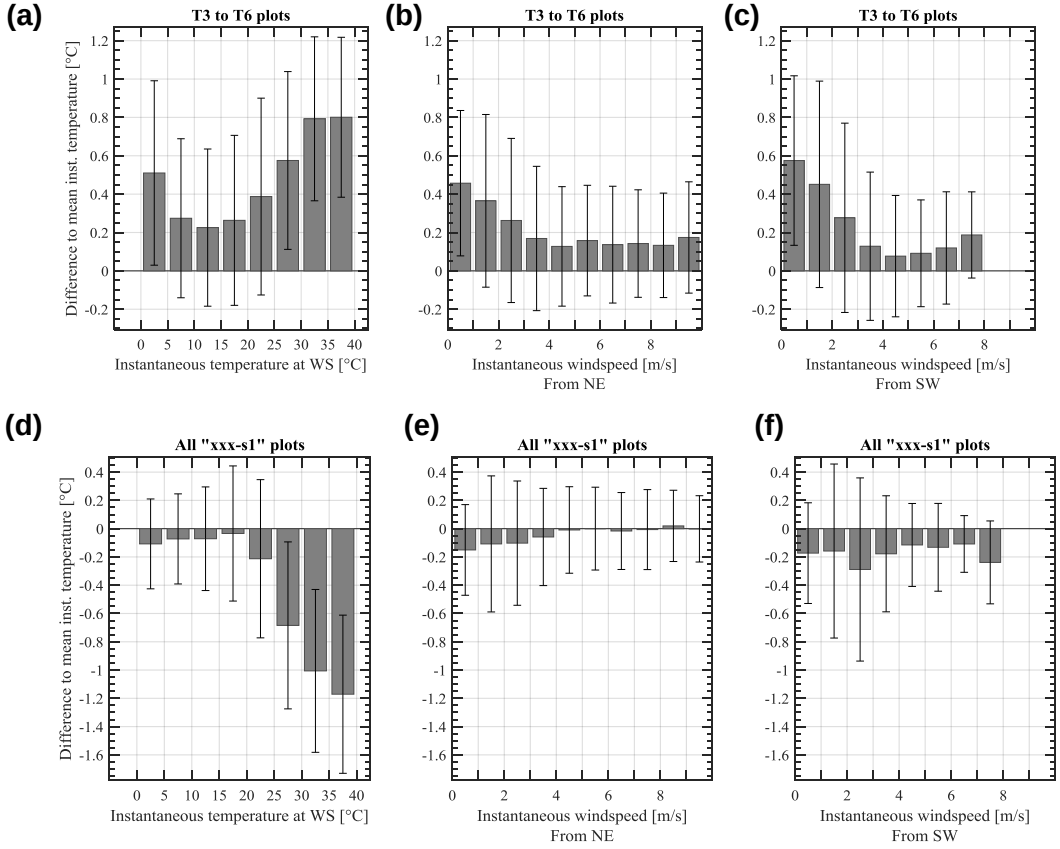

Figure 101: Difference to the mean instantaneous temperature at the further north-west plots (top) or on the southern side of a tree row (bottom) according to the temperature (left), according to the instantaneous wind speed when the wind was blowing from North-East (middle) and according to the instantaneous wind speed when the wind was blowing from South-West (right) at weather station. The mean temperature was calculated considering instantaneous temperatures at all experimental plots. For the top graphics, the time series of the six plots named T3 to T6 were gathered while for the bottom graphics, the time series of the seven plots located on the first southern vine row neighboring a tree row (plots named 'xxx-s1') were gathered. The bar plots give their mean difference to the mean instantaneous temperature and the error-bars give their standard deviation. Orientation 'NE' comprises orientations from NE to ESE and orientation 'SW' comprises orientations from WS to WNW (see Figure 100). Abbreviations: *WS*: weather station – *NE*: North-East – *SW*: South-West.

V.4.4.3 Variability induced by the state of the atmosphere

Distinguishing days of high and low ET0 was chosen in order to consider all together the variability induced by the cloudiness of the sky and the wind speed (Penman 1948; Allen 1998). It added contrast in temperature patterns. Nonetheless, **Figure 100** shows that the daily ET0 integrates many variables and does not allow understanding the sole contribution from the wind speed. Indeed, days with the highest ET0 coincided with both low and intermediate wind speeds. Instead of binary classes of ET0, a distinction between various classes of wind speed and of hours of sunshine was tested using the dataset from 2015. It revealed that the warm pattern of temperatures observed at the furthest North-Eastern plots applies from veraison to harvest in two cases: (i) on days with an average wind speed higher than 1.0 m/s and more than 9 hours of sunshine i-e on completely clear sky days, and (ii) on days with an average wind speed of 1.5 m/s and 3 to 9 hours of sunshine i-e on partially cloudy days. Similarly, in 2016, the pattern of temperature at "xxx-s1" plots occurred over the period from mid-June to beginning of September when the wind speed was rather low but not null. These observations suggest that three types of meteorological conditions may actually be worth distinguishing: (i) days with only a few wind and a clear sky, (ii) days with only a few wind and an overcast sky, (iii) days with strong wind.

V.4.5 Correlations between temperature patterns and agronomy

Figure 102 gives a selection of the highest estimated correlations between the agronomic variables and the temperature variables, again considering this latter per successive phenological periods. The yield in grapes ($Yield$) presents some variability which is correlated with that of the temperatures observed all along the phenological stages, notably because of correlations with the variability of the weight of berries ($200BerryW$) and eventually with the amount of bunches per vine ($BunchW$). The quality of berry for wine making shows some variability which is correlated with that of temperatures regarding three criteria. First, the total acidity is correlated with the lowest temperatures met in the earliest and latest stages, notably because of the variability of the pH and the malic acid, while the tartaric acid showed no significant variability. Second the total polyphenol index (TPI), is correlated with both the high and low temperatures met all along the phenological stages. Third, the concentration in fermentable sugars eventually shows correlations with the range of temperatures in the early stages. Our observations appear consistent with the observations of Dai et al. (2011) who concluded that berry sugar concentration is relatively stable trait for a given cultivar and is less responsive to environmental conditions than organic acids and phenolics. Also, among organic acids in berries, our observations confirm the high sensitivity of malate acid to environmental factors as opposed to the relative stability of the tartaric acid (Archer and Strauss 1989; Dokoozlian and Kliewer 1996; Bergqvist et al. 2001; Koyama and Goto-Yamamoto 2008).

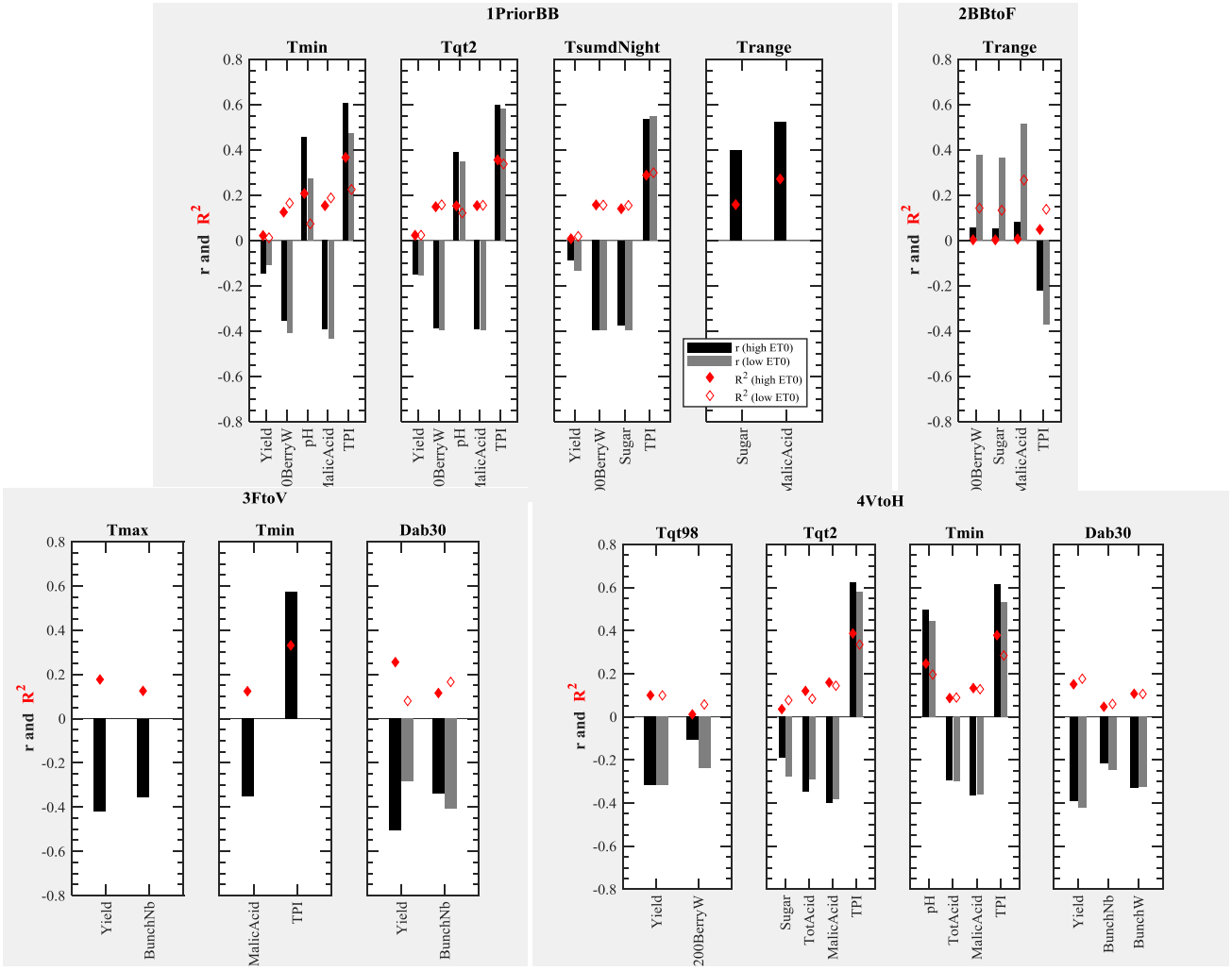

Figure 102: Correlations obtained between the mean centered temperature variables and the agronomic variables. The coefficient of correlation (r) and coefficient of determination (R^2) are given by bars and by diamonds respectively. Four phenological periods were considered, namely prior to budburst ('1PriorBB'), from budburst to flowering ('2BBtoF', from flowering) to veraison (3FtoV and from veraison to harvest of grapevine (4VtoH). Also days with high ETo (black bars and filled diamonds) are distinguished from days with low ETo (grey bars and empty diamonds).

In the previous subsection, the analysis of temperature time series revealed the existence of mainly three contrasted patterns within the study vineyard, namely a cool day pattern along the southern side of tree rows (plots named "xxx-s1"), a warm night pattern at the most open and furthest North-Eastern part of the vineyard ("T3 to T6" plots) and to lesser extent a highly ranged pattern at the isolated furthest south-Eastern part of the vineyard ("Ps-x" plots). The statistics of the yield in grapes and of the composition of berries in 2016 are presented in regards to these patterns in **Figure 103**. Among all plots, the "s1" plots happen to present the highest yield in the vineyard, which is due to an elevated number of bunches per vine together with elevated bunch and berry weights. This is confirmed by the linear model which estimated a depletion of -2.2 bunches per vine when $Tmax_{FtoV}$ reaches 1 °C above the average (**Appendice K**). The "s1" plots also present the highest acidity. In controlled conditions of light and temperature depletion (shading experiments), opposed trends were observed on the yield parameters but similar trends were observed on the acidity **(**Archer and Strauss

1989; Dokoozlian and Kliewer 1996; Bergqvist et al. 2001; Koyama and Goto-Yamamoto 2008). On the opposite, the yield at "T" plots stands amongst the lowest of the vineyard, which is due to remarkably low berry weight this time. Comforting this observation, a negative correlation between the minimum temperatures prior to budburst and from flowering to harvest was found and the linear model estimated a depletion of -15 g of $200BerryW$ per 1 °C deviation of $Tqt2$ and of $TsumNight$. This observation goes against the results of Keller et al. (2010) obtained under artificially increased temperatures of the vine shoots in Spring. They go more in the sense of Petrie and Clingeleffer (2005) who observed a significant impact of the temperature prior to budburst on the inflorescence morphology. In addition, **Figure 103** highlights that the "T" plots also present the lowest total acidity which is due to simultaneously high pH and low concentrations of malic acid while the tartaric acid showed no specific pattern. Consequently, the agronomic pattern at plots "T" could be due to the increased heat at these locations which is responsible for a slight but remarkable depletion of acidity in berries (linear regressions showed slopes of - 0.22 g/L per Celsius degrees of mean centered $Tmin_{FtoV}$). The "T" plots also by far presents the highest total polyphenol index in the vineyard and the mean centered $Tmin_{FtoV}$ explains 57 % of the variability of this variable. This observation matches the observations of (Kliewer and Torres 1972; Bergqvist et al. 2001; Downey et al. 2006; Azuma et al. 2012) and suggest that the warm pattern observed at plots "T" may have been responsible for a net increase of the synthesis in phenols without reaching the limiting thresholds mentioned by these authors and above which synthesis is inhibited. This tendency may have ambiguous impact on the quality of berry for wine making. For white cultivars - which is the case in this study – an elevated concentration in polyphenols is undesirable because (i) it participates in wine astringency, and (ii) it can be involved in some oxidation reactions during wine making process which can in the end decrease the fruity character of the wine (Cheyiner et al. 1990; Reynolds 2010). On the opposite, for red cultivars, phenolic compounds participate in the wine structure and color and are sought after as a full expression of the 'terroir' effect (Vaudour 2002; Vaudour et al. 2015). In this case, experimental results from Haselgrove et al. (2000), Spayd et al. (2002) and Tarara et al (2008) suggest that under microclimate modifications, the composition in anthocyanins can be modified to an even bigger extent than the net quantitative variations. Thus for red cultivars, assessment of the evolution of anthocyanin composition throughout years of agroforestry management would be relevant to further investigate.

Finally, in our study, the "Ps-xx" plots present intermediate yield components, pH or TPI in all the vineyard but remarkably present the highest concentrations in malic acid and in fermentable sugar (**Figure 103**). The mean centered $Trange_{BBtoF}$ explained more than 52 % and 36 % of the variability of the concentration of malic acid and sugar respectively (**Figure 102**). Knowing that the synthesis of organic acids and phenolics only starts during the first phase of development of berries and the accumulation of sugars and the degradation of acids only starts after veraison of berries (Volschenk et

al. 2017), an eventual causal contribution from the temperatures prior to flowering may only be very indirect.

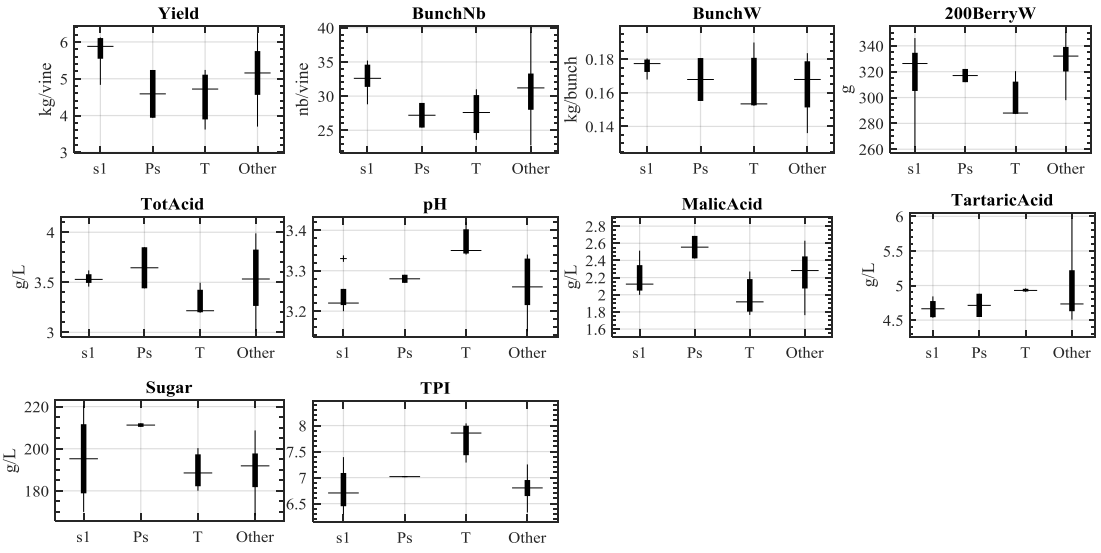

Figure 103: Distribution of the agronomic variables per clusters of plots identified according to their temperature patterns. The cluster '*s1*' gathers all the seven plots located on the first southern vine row neighboring a tree row (plots named 'xxx-s1'), the cluster '*Ps*' gathers the three plots located on the furthest south-eastern part of the vineyard (plots named 'AF1-Psx') and the cluster *'T'* gathers all the four plots located on the furthest north-eastern part (plots named T3 to T6).

V.5 Conclusions

Temperature stands as a key variable for comprehending how trees contribute to the microclimate of a vineyard and how, through this factor, they impact the yield and the quality of grapes. For the first time, temperature measurements were distributed within an agroforestry vineyard, under temperate climate context and were carried out all along the growth stages of the vine from before budburst until harvest.

First, it revealed that trees surrounding the vineyard combined with the topography and the main winds contribute to the heterogeneity of temperatures in the studied vineyard. The most sheltered zones showed a tendency to very large range of temperatures over the days and seasons, while the most open zones formed a warm pattern all along the year. This warm pattern was notably remarkable regarding grape production as it presented a lower risk of frost in spring and extended durations spent at very high temperatures on the warmest days of summer. Second, the presence of height-year-old tree rows planted at 3.25 m from vine rows and oriented NE/SW did not generate a significant shading effect on the northern neighboring vines, most likely because of their limited height and low foliage density. Unexpectedly, it was responsible for a relatively cool pattern, specifically at the first vine row on their southern side, which was the most pronounced on days of high evaporative demand occurring

from flowering to harvest. These patterns were first observed for 2015 vintage and gained robustness from the densely measuring campaign carried out in 2016.

Overall, the temperature showed low correlations either with the yield or the berry quality components measured on 2016 vintage. This may be partly explained by the multiple factors involved beside temperatures. Only a few traits stand out. Concerning quantitative variables, the cold maximum temperatures from veraison to harvest at the southern vine rows next to tree rows coincide with the highest yields, while the highest maximum temperatures observed before the budburst and from veraison to harvest in the northern part of the vineyard (which is the most unsheltered), coincide with the lowest yield. Concerning qualitative variables, the variability in space and time of the temperatures may contribute to the variability observed in both the concentration of malic acid and of polyphenols in general.

These results apply for a relatively young agroforestry vineyard since the growth of the trees and the vine will together continue for at least twenty years. At this stage, the variability induced by the landscape structure of the vineyard is as intense and more extended than that induced by the tree rows which are intercropped within the vine rows.

This study constitutes a valuable reference as it provides detailed order of magnitudes of the possible impacts from trees on the production of grapes in an agroforestry vineyard. In order to better comprehend the interactions between trees and grapevine, further microclimate assessment should consider the trajectory of answer over decades, which may not follow linear trends. In addition, the methodological approach presented in this article could be reused for comparing the climatic contributions from various planting densities and orientations of the rows, in order to meet some of the technical issues raised by vine growers willing to intercrop trees in their vineyard.

CHAPTER VI
3D modeling of the radiative budget of vineyards

VI.1 Introduction

Main objectives

The literature review presented in chapter III highlights that under agroforestry practices, the remaining amount of light available for grapevine directly impacts grapevine biomass production and yield through modulating photosynthesis. In addition, it indirectly impacts both the yield and the grape quality for wine making through contributing to the temperature and the evaporation demand. Controlling shade intensity in order to limit light competition to an acceptable level represents a key component of the design and management of an agroforestry system. Though the importance of the task is well known, its implementation is complex for two main reasons:

1. because the extent and intensity of shading vary a lot according to the internal and landscape structure of the plantation;
2. because the morphology of the vegetation keeps evolving through months and years with the tree phenological cycling, the tree growth and the human interventions (canopy pruning, additional tree planting, tree removals).

This chapter addresses the question of the shading effects of trees within an agroforestry vineyard and the potential consequences on grapevine growth through its modulation of the energy budget available for the plant photosynthesis. Two main objectives are pursued: (1) quantifying the amount of light available for grapevine at (i) the instantaneous time scale or (ii) when cumulated over the whole vegetative growth of grapevine; (2) predicting the shade patterns considering various scenario of tree dimensions and planting arrangement.

Choosing a mechanistic modeling approach

Contrary to Goma-Fortin and Trambouze (2009) who collected on-site measurements of PAR irradiance, and to Duffours (2011) who collected empirically related measures of the vegetation gap fraction, a mechanistic modeling approach is preferred here. Indeed, the diurnal behavior of light interception by tree canopies is complex and depends on numerous variables including canopy architecture, solar angle and the ratio of diffuse to direct radiation. As a consequence on-site measurements of light interception imply many technical limitations in terms of work load which substantially limit the possibilities of generalization. On the contrary, models offer simplified representations of complex processes. In addition, the physical principles regarding radiative transfers at the interface between vegetation, ground and atmosphere are now well known and are formalized into various radiative transfer models, also called physical models. They are capable of accurately represent the interactions that apply in the photosynthetically active radiations. Moreover, well-calibrated models which include precise but reasonable amount of input parameters, notably for describing vegetation properties, enable exploring options for the design and management of

agroforestry systems. Nevertheless, the range of validity of a model inevitably corresponds to that of the cases used for its calibration.

Various models can simulate radiation distribution in vegetated landscapes. Their accuracy (but also complexity) depends on the approach for modeling natural light, for computing flux-tracking and for accurately representing vegetation components. Grau (2012) distinguishes two main categories by increasing levels of complexity:

- **The empirical and semi.e.mpirical models** output mathematical description of incident/intercepted light but do not attempt to explain biophysical parameters and processes in light interception datasets. The semi-empirical models rely on simplified vegetation optical properties and on physical principles of radiative transfer theory.
- The **radiative transfer models or physical models** simulate the propagation of radiation taking into account all the physical mechanisms involved within the atmosphere and the vegetation: emissions, interceptions, multiple scattering and absorptions. Based on the fundamental equations of radiative transfer, they can track the propagation of rays within landscapes which are realistically represented.

In the case of heterogeneous vegetated landscapes, two approaches can be used for modeling the landscape components:

- discretization of the spatial variable into 3D cells (voxels) which are filled with turbid medium,
- and / or juxtaposition of facets or planar individual elements.

Radiative transfer models also differ from one to another according to their mathematical approach for accurately computing multiple scattering with the conservation of energy (CESBIO 2018). One can cite mainly four approaches: the N fluxes method or discrete ordinate method (Verhoef 1985), the radiosity method (Borel et al. 1991), the successive orders of scattering method (Duan et al. 2010) and the Monte Carlo method (Disney et al. 2000).They show advantages and limits depending on the final application for simulating radiative budget (bio-physical, remote sensing, etc) and depending on the degree of anisotropy and of complexity of the landscapes to simulate.

Compared to existing models (listed in **Table 18**), the model DART (Discrete Anisotropic Radiative Transfer) is chosen regarding its ability to simulate radiation propagation in any type of terrestrial landscape as well as remotely sensed images. It is a three-dimensional radiative transfer model developed at CESBIO[20] since 1993 (Gastellu-Etchegorry et al. 1996). Both the turbid and the 3D planar representations of landscape components are allowed with DART and the flux propagation is simulated in all the atmosphere-vegetation system using the N flux method.

[20] DART website: http://www.cesbio.ups-tlse.fr/us/dart.html
DART model was patented in 2003 (PCT/FR02/01181) and licenses are freely distributed for teaching and research purposes by Paul Sabatier University (Toulouse, France)

Table 18: Models of light propagation used for studying light distribution in agroforestry systems. They are sorted by increasing level of complexity according to their characteristics of vegetation representation, of light modeling and of physical accuracy for computing light interception. *Sylvopastoral system* refers to tree + pasture while *alley-cropping* refers to trees + crops –AD: area density ($m^2.m^{-3}$) – LAI: Leaf Area Index ($m^2.m^{-2}$)

Model	Vegetation modeling	Light modeling, scattering and light extinction (LE) computation	Model outputs	Application to agroforestry systems
Light partitioning method from Wallace (1995) (**Annex A**)	*Canopies*: 1D medium filled with mixed canopies. It is characterized by the LAI_i of each canopy component	*LE*: Beer's Law	Fraction of light available at the top of each canopy component	***Mixed-cropped***: Light module of the model GAPS (Rossiter and Riha 1999) → applied on Maize and C4 weeds (Rossiter and Riha 1999)
The simple model of light interception by discontinuous canopies of Jackson and Palmer (1979)	*Trees*: cone / ball / parallelepiped canopies *Crop*: none	*Light*: Global incoming radiation *LE*: Beer's law	Fraction of the incoming light available at ground level over a given period of time (1D time integrated budget)	***Sylvopastoral systems***: It is the light module of the model ALWAYS (Bergez et al. 1999) ***Orchards***: model validation in apple tree orchards (Jackson and Palmer 1972; Jackson 1978)
Gap Light Analyzer GLA (Frazer et al. 1999)	*Trees*: Hemispherical images of tree canopies	*Light*: Global radiation including a diffuse fraction *LE*: Empirical equation of intercepted PAR according to the gap fraction in the canopy images, the global incident radiation and the cloudiness factor	1/ amount of above-and below-canopy (transmitted) direct, diffuse, and total solar radiation incident on a horizontal or arbitrarily inclined surface 2/sunfleck-frequency distribution and daily duration	***Alley-cropping systems***: walnut/cherry/poplar-crops in France (Dupraz et al. 2005)
Light module in WaNuLCAS agroforestry model (Van Noordwjik and Lusiana 1998; Noordwijk et al. 2004)	*Landscape*: Horizontal layers subdivided in 3D cells *Canopies*: All the cells in a given layer are defined by a AD for each type of canopy components (tree leaves, crop leaves, woody parts)	*Light*: Direct light only *LE*: Beer's law applied in each cell of vegetation	Absorbed PAR per horizontal layer of vegetation and per vegetation type (tree/crop)	***Tree-crop-soil interactions***: WaNuLCAS model (Van Noordwjik and Lusiana 1998; Noordwijk et al. 2004)
Hybrid model which was actually used for the first time in 'gap models' FORSKA model (Prentice and Leemans 1990)	*Landscape*: 3D array of cells. *Trees*: ellipsoid turbid medium *Crop*: homogeneous understory turbid layer. Discontinuities in the crop canopy (i.e. sparse canopies) are managed considering the individual plant shade area (m^2), the individual plant leaf area (m^2) and the plant density (plants m^{-2})	*Light*: Global radiation from a standard overcast sky model *Scattering*: One order of scattering from the canopy external envelop (albedo) *LE*: modified Beer's law adapted to crop sparse canopies	Absorbed PAR in each 3D cell of tree canopy or crop. (pseudo 3D instantaneous budget)	***Alley-cropping systems***: light module implemented in the models: 1/ HyPAR → tree-sorghum/millet/maize systems in the dry tropics (Mobbs et al. 1999) 2/ HySAFE (Lecomte and Dupraz 2015) → wheat-walnut agroforestry system in Belgium (Artru et al. 2017) ***Mixed forest***: model calibration (Prentice and Leemans 1990)
RATP model (Radiation, Absorption, Transpiration and Photosynthesis) of Sinoquet et al. (2001)**, initially developed by Sinoquet and Bonhomme** (1992) **and modified by Meloni and Sinoquet** (1997) **to consider three-dimensional heterogeneous canopies**	*Landscape*: 3D array of cells. *Canopies*: Each cell can contain several canopy components (various types of leaves, woody parts, fruits), and is characterized by the AD of every component in the cell	*Light*: discrete beams from direct and diffuse sources *Flux tracking*: radiosities method *LE*: Equation of radiative transfer applied in each cell.	Intercepted PAR flux for each plant component type in each voxel (3D instantaneous budget)	***Sylvopastoral systems***: 1/ Model validation in a young agroforestry planting (Meloni and Sinoquet 1997) 2/ it is the light module implemented in the model TREEGRASS (Simioni et al. 2000)
DART (Discrete Anisotropic Radiative Transfer) (Gastellu-Etchegorry et al. 1996, 2012)	*Landscape:* 3D array of cells including atmosphere layers *Canopies:* same as RATP and/or ensemble or accurate planar 3D objects with optical properties	*Light*: discrete beams from direct and diffuse sources *Flux tracking*: N flux method *LE*: Equation of radiative transfer applied in each cell	Intercepted PAR flux for each plant component type in each voxel (3D instantaneous budget)	***Agroforestry vineyards:*** Grimaldi 2018 – This thesis

Comparison with modeling approaches previsously applied to agroforestry systems

As reviewed in **Table 18**, different types of models have already been used for studying radiation distribution in agroforestry systems. They are sorted by increasing level of complexity according to their level of accuracy for modeling vegetation, for modeling light and for computing light interception respecting physical principals. Together with the RATP model (Sinoquet et al. 2001), DART stands as the most accurate but also the most complex. RATP and DART are the only radiative transfer models listed.

In addition, thanks to the 3D grid representation these two models allow the highest degree of precision for describing the morphology of all the vegetation components, including the internal variability within the canopies of trees and crops. On the opposite, the simple model of light interception by discontinuous canopies of Jackson and Palmer (1979) and the Gap Light Analyzer GLA (Frazer et al. 1999) consider the light budget on a horizontal surface above the crop canopy, which is not represented in their simulations. For representing tree canopies, the analogy with the turbid medium is used in all models except in the Gap Light Analyzer GLA (Frazer et al. 1999). Only DART offers the alternative/complementary 3D objects representation.

A simple Beer's law is used for computing the energy absorbed in every cell of turbid medium except in the RATP and DART models which both also consider multiple scattering. In addition, compared to others, DART allows the most realistic representation of light: it considers both direct and diffuse sourced beams and it models multiple scattering mechanisms. The vegetation in vineyards planted with rows of trellised grapevine is comparable to vertical walls of foliage. In addition, vineyards may also present important variations of topography on short distances. For these two reasons, diffuse solar radiations as well as multiple scattering may be important factors driving the radiation budget within agroforestry vineyards and this justified the choice of the model DART.

Recommendations for modeling trees and grapevine

Concerning trees, a range of sensitivity studies carried out on forest canopies highlighted the importance of 3-D structure for the representation of PAR scattering and absorption (Gastellu-Etchegorry and Trichon 1998; Widlowski et al. 2011). The vertical variability of tree structure notably resulted as a central factor of light distribution (Gibelin et al. 2008; van der Tol et al. 2009; Clark et al. 2011) as reviewed by Morton et al. (2016). Similarly to forests, agroforestry vineyards are characterized by an improtant vertical and horizontal heterogeneity. Using a three-dimensional radiative transfer model offers the possibility to quantify light interactions of such complex canopy arrangements and to output information at the scale of individual leaves. In addition, it is well suited for considering various tree shapes and pruning practices, various tree orientations, spacing and phenological stages, as recommended for agroforestry systems by Dufour et al. (2013).

Concerning grapevine, Smart (1973) showed from experimental design that the morphology of grapevine canopy and grapevine rows arrangement significantly contribute to the energy absorbed by grapevine. The main factors involved are the canopy height, row spacing and row orientation. In addition, meteorological conditions and mostly the partition between direct and diffuse light also has an influence but of secondary importance (Smart 1973). Compared to simpler 1D/2D models, using the 3D model DART allowed representing the architecture in rows and the wall shape of trellised grapevine which intercepts an important amount of the incident light from the vertical lateral sides of its canopy (Mabrouk et al. 1997, 2015). Also, DART allowed taking into account the non negligible implication of the angular distribution of leaves on light interception by plant canopies (Kimes and Kirchner 1983).

For modeling the radiative budget of 'monocropped' vineyards, grapevine was modeled in 3D with two different levels of accuracy (López-Lozano et al. 2011):

- Most studies adopted an actual '2D representation' which considers the canopy of trellised grapevine as parallelepipeds filled with a constant leaf density (Riou et al. 1989; Sinoquet et al. 1992; Mabrouk et al. 1997; López-Lozano et al. 2009).
- A more accurate truly 3D approach was adopted by Louarn et al.(2007, 2008). These authors represented grapevine rows as collections of 3D polygons and calculated the radiative balance at the organ scale using the ARCHIMED software (UMR AMAP CIRAD-INRIA, Montpellier, France) (Dauzat and Eroy 1997). The main difficulty identified in such approach is the availability of a generic but accurate 3D model of grapevine since it greatly depends on grapevine trellis system and canopy management practices (Louarn et al. 2007).

A very informative comparison between the latter 2D and 3D representations was made by López-Lozano et al. (2011). They concluded that the '2D' representation can be valid to calculate light interception and photosynthesis rates, but row dimensions should be optimized. Using the actual maximum boundaries notably led to overestimating the photosynthesis rate of grapevine by 35% in their study, thus they used an empirically reduced height.

For all these reasons, adopting a 3D model seemed of prior relevance for assessing light patterns within an agroforestry vineyard. Nevertheless, as 3D models of grapevine are not easily accessible and are trellis system type-specific, a pseudo 3D representation of grapevine was adopted in first approximation: similarly to the 2D approach, grapevine canopy was modeled as an ensemble of cuboids filled with a constant foliage density, but a realistic variability was introduced on both the width and the height of the rows.

Content of this chapter

The following content of this chapter divides in two parts. Firstly it reminds important notions and presents main functionalities and formalism of the DART model in regards to the modeling objectives. Secondly it describes the simulations that were performed and the results obtained. In

short, a total of five different mock-ups of vineyards were built under the model DART. Three of them correspond to agroforestry arrangements of varied age and row orientations. The two other are ‘monocropped’ vineyards, or conventional vineyards, i.e. sole grapevine rows,with two different orientations. Each of them was used for simulating the 3D radiative budget at various dates and times of the year, spaced by 10 or 5 days, from grapevine budburst to harvest. A time series of meteorological parameters were calibrated in order to match actual meteorological conditions. From space and/or time integration of the model outputs, the cumulated energy absorbed by grapevine was computed and analyzed in regards to the vegetation properties, spatial arrangement and meteorological context of each simulation.

To our knowledge, the model DART had never been used so far for modeling the radiative budget of a vineyard. Through this part of the Ph. D work, the functionalities of the model were put to test in collaboration with DART developers at CESBIO. In addition, no prior references could be found concerning light distribution within agroforestry vineyards. Thus the contribution of the work presented in this chapter is mainly methodological. The strategic choices that were made are detailed and then discussed in regards to their impacts on the radiative budgets. From this first attempt, methodological recommendations are made for pursuing the simulations towards more realistic, more robust and more optimized simulations of the radiative budget of agroforestry vineyards.

VI.2 Material and methods

VI.2.1 Useful definitions

VI.2.1.1 Equation of radiative transfer

Any mass in the universe with a temperature above 0 K exchanges energy through emitting, absorbing and/or scattering electromagnetic waves. Sun light corresponds to the sum of stationary and monochromatic waves with wavelength λ_i (**Figure 19**). The propagation of a stationary and monochromatic electromagnetic wave with wavelength λ at location r, along the direction Ω and of intensity $I(r, \Omega)$ within a medium of temperature T follows the equation of the radiative transfer (Grau 2012):

$$\left[\xi \frac{d}{dx} + \eta \frac{d}{dy} + \mu \frac{d}{dz}\right] I(\lambda, r, \Omega) = -\alpha_e(\lambda, r, \Omega_n).I(\lambda, r, \Omega) + \alpha_a(r, \Omega_n).L_B(\lambda, T) + \int_{4\pi} \alpha_d(r, \Omega).\frac{P(r, \Omega' \rightarrow \Omega)}{4\pi}.I(r, \Omega')d\Omega' \quad [13]$$

with

ξ, η, μ	Cosines of the direction of propagation Ω along axis x, y, z in a Cartesian reference system
$\alpha_a(r, \Omega)$	Absorption coefficient of the medium [m^{-1}]
$\alpha_d(r, \Omega)$	Diffusion coefficient of the medium [m^{-1}]
$\alpha_e(r, \Omega)$	Coefficient of extinction of the medium [m^{-1}]
$P(r, \Omega' \rightarrow \Omega)$	Normalized phase function [sr^{-1}]
$L_B(\lambda, T)$	Radiance of a black body according to Plank's Law $L_B(\lambda, T) = \frac{2h.c^2}{\lambda^5}.\frac{1}{exp\left(\frac{h.c}{k.\lambda.T}\right) - 1}$ [14]
h	Plank constant (h = $6.626.10^{-34}$ J.s)
c	Speed of light in vacuum ($c = 2.9979 . 10^8\ m.s^{-1}$)
k	Stefan Boltzmann constant $k = 1.38\ 10^{-23}\ J.K^{-1}$

The above equation of the radiative transfer gives the variation of the intensity of a wave when crossing a fraction dx, dy, dz of a medium:

- It decreases from absorption (first term),
- It increases from thermal emissions (second term),
- and it increases from diffusion in all the directions (third term).

The radiative transfer equation is very complex to solve analytically as it all together relies on three coordinate variables, on three variables of direction, on temperature variable and on the wavelength variable. Thus physical models of radiative transfers are based on different hypothesis and

adopt simplified theoretical representations of the reality which allows simplifications in the various terms of the equation (Grau 2012).

VI.2.1.2 Energy fluxes

Energy fluxes are quantities of energy propagated from one or multiple sources of emission and eventually intercepted by a surface (Σ) - **Figure 104**. They are defined by their wavelength λ, direction $\Omega(\theta, \phi)$ and sense of propagation. In addition they can be integrated over several wavelengths and/or solid angles. As illustrated in **Figure 104,** the solid angle $d\Omega$ (in sr) along the direction $\Omega(\theta, \phi)$ is the angle in 3D space such as $d\Omega = sin\theta . d\theta . d\Phi$.

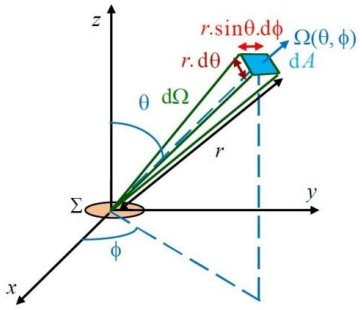

Figure 104: Solid angle dΩ for the direction Ω(θ,ϕ) – from (CESBIO 2018)

Radiance

The radiance $L_\lambda(\Omega)$ is the energy flux along $\Omega(\theta, \phi)$ either intercepted by or propagated from a surface Σ.

Irradiance

The irradiance $E_{\Sigma,\lambda}$ is the incident flux on a surface Σ. It is found by integration of the incoming radiances over all the directions of the upper hemisphere ($2\pi^+$) (**Figure 105**).

$$E_{\Sigma,\lambda} = \int_{2\pi^+} L_{\Sigma,\lambda}(\Omega).|\cos(\theta)|.d\Omega \qquad [W.m^{-2}.\mu m]$$

Irradiation or radiant exposure correspond to the integration of irradiance over a specified time, usually an hour or a day, and will be expressed in $J.m^{-2}$.

Exitance

The exitance $M_{\Sigma,\lambda}$ is the flux that exits a surface Σ. It is found by integration of the outcoming radiances over all the upper hemisphere ($2\pi^+$) (**Figure 105**).

$$M_{\Sigma,\lambda} = \int_{2\pi^+} L_{\Sigma,\lambda}(\Omega).\cos(\theta).d\Omega \qquad [W.m^{-2}.\mu m]$$

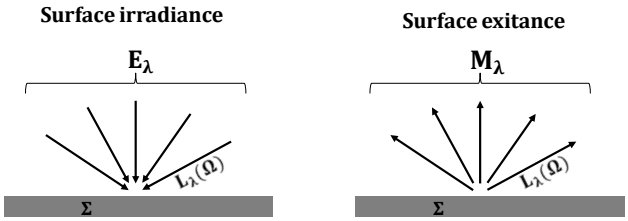

Figure 105: Surface irradiance E_λ (left) and exitance M_λ (right)

Reflectance factor

The reflectance factor $\rho_{\Sigma,\lambda}(\Omega)$ of a surface Σ is proportional to the ratio of the radiance out of the irradiance: $\rho_{\Sigma,\lambda}(\Omega) = \frac{\pi L_{\Sigma,\lambda}}{E_{\Sigma,\lambda}}$.

Lambertian surfaces present isotropic reflectance and radiance, thus in this case, both $\rho_\lambda(\Omega)$ and $E_\lambda(\Omega)$ equal constants. It is a simplified representation as most of natural surfaces scatter incoming radiation into preferential directions (mostly into the specular and the illumination directions).

Phase function

The phase function $T_d(\Omega_s, \Omega_v)$ is defined as the probability for an intercepted photon or flux coming from the direction Ω_s to be scattered into the direction Ω_v.

Direct and diffuse light

Incident light is said of direct type when it is isotropic i.e. when it comes from source direction, while diffuse light is anisotropic, i.e. it comes from an infinity of directions in the sky view angle. The light from the sun is typically anisotropic above the atmosphere. Once it as passed through the atmosphere, it divides into a direct fraction and a diffuse fraction which results from the scattering of light by the atmosphere components.

SKYL or diffuse to total incident light ratio

The 'SKYL' in DART refers to the ratio of diffuse to <u>total</u> irradiance at the bottom of the atmosphere (BOA):

$$SKYL = \frac{E_{BOA}^{diff}}{E_{BOA}^{tot}} = \frac{"sky\ (atmosphere)\ irradiance"}{"total\ (sun + sky)\ irradiance"}$$

From approximation it can be considered equal to the ratio of diffuse to <u>global</u> radiation. This latter can be measured on-site with a pyranometer. The approximation is not recommended when abrupt topographies or vegetation in the vicinity of the sensor also significantlycontribute to the diffuse fraction of light and add to that from the atmosphere.

VI.2.1.3 Latitude and longitude

The latitude Φ of a point P is the angle between a radius drawn from the point to the center of the Earth and a radius drawn from the center of the Earth to the equator (**Figure 106**). Values range from 0° to 90° North and 0° to 90° South (where 0° is the latitude of any point on the equator).

The longitude (L) of a point is the angle between the Greenwich (or prime) meridian and the meridian that passes through the point (**Figure 106**). Values of longitude range from 0° to 90° East and 0° to 90° West (where 0° is the longitude of any point on the Greenwich meridian).

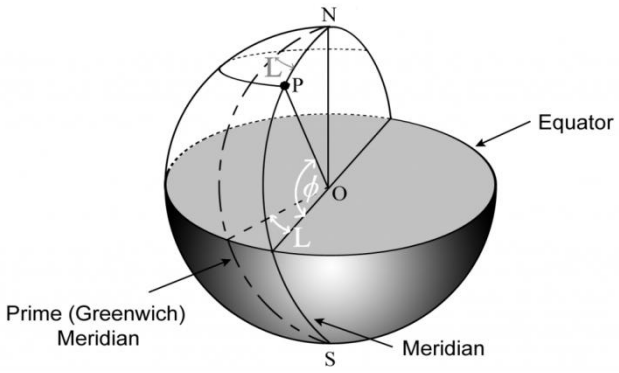

Figure 106: Latitude Φ and longitude L of a point P on the earth's surface – from ITACA, The Sun As A Source Of Energy (www.itacanet.org)

VI.2.1.4 Solar angles: zenith and azimuth

The sun position in the sky viewed from point P on the surface of the Earth is given by the combination of the solar azimuth angle Φ_z, which gives the sun direction, and the solar zenith angle θ_z or its complementary, the solar elevation α, which both define 'how high' the sun is (**Figure 107**).

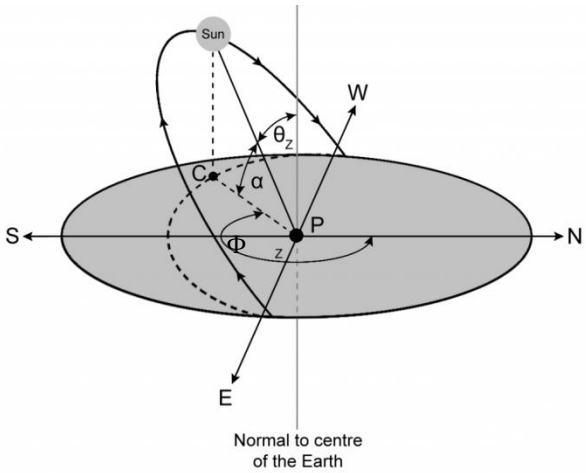

Figure 107: The zenith angle θ_z, the azimuth angle ϕ_z and the altitude angle α of the Sun viewed from point P - from ITACA, The Sun As A Source Of Energy (www.itacanet.org)

VI.2.1.5 Solar time

Solar time is the time provided based on the apparent angular motion of the sun across the sky. Noon solar time is the time when the sun crosses the meridian of the observer. More precisions can be found from Duffie and Beckman (2013).

VI.2.2 DART: a 3D radiative transfer model

VI.2.2.1 Main uses of DART

DART (Discrete Anisotropic Radiative Transfer) model is a three-dimensional radiative transfer model developed at CESBIO[21] since 1993 (Gastellu-Etchegorry et al. 1996). The version used in this work is DART 5.7.0 (version #1011) (CESBIO 2018), whose characteristics and functioning are given in the following section.

DART simulates radiation emissions and propagation in the entire optical domain from visible to thermal infrared wavebands, within natural, agricultural or urban heterogeneous landscapes which include the topography and an atmosphere (**Figure 108**). DART is a physical model as it is based on the fundamental equation of radiative transfer and reproduces the physical mechanisms of absorption, scattering and thermal emission by landscape components (atmosphere, ground, vegetation, etc). It computes the propagation and ray path of radiant light according to the morphological, optical and thermal properties of the landscape components (Gastellu-Etchegorry et al. 2012; Grau 2012).

DART model outputs the remotely sensed images of the simulated landscapes as well as the 3D radiative budget. DART was originally developed for simulating bi-directional reflectance factors and brightness temperatures of 3D natural landscapes and is thus currently widely used by remote sensing specialists for simulating satellite and air-born passive or active (Lidar) optical measures (Gastellu-Etchegorry et al. 2015). One can cite many examples of successful uses of DART for remote sensing applications which concerned woody vegetated landscapes: forest maritime pine plantation (Bruniquel-Pinel and Gastellu-Etchegorry 1998), tropical rain forests (Gastellu-Etchegorry et al. 1999; Barbier et al. 2012), boreal forests (Gastellu-Etchegorry et al. 1999), Norway spruce forest (Malenovsky et al. 2008), TIR signature of olive orchards (Sepulcre-Cantó et al. 2009), reflectance and radiative budget of citrus orchards (Gastellu-Etchegorry et al. 2015; Widlowski et al. 2015).

Concerning simulations of the radiative budget, there are a few recent examples of DART uses for studying light patterns within woody vegetation and evaluating the potential consequences on photosynthesis and productivity: PAR regime in tropical rain forests and in coniferous/deciduous boreal forests (Guillevic and Gastellu-Etchegorry 1999), fraction of absorbed PAR in a sparse shrub tundra of Siberia (Juszak et al. 2017), leaf absorption of PAR in Amazon rain forest (Morton et al.

[21] DART website: http://www.cesbio.ups-tlse.fr/us/dart.html
DART model was patented in 2003 (PCT/FR02/01181) and licenses are freely distributed for teaching and research purposes by Paul Sabatier University (Toulouse, France)

2016). In all these latter studies, DART resulted very useful for taking into account the complex three-dimensional structure of the vegetation and for accurately simulating its impact on the light availability within the canopy and for eventual understory vegetation.

VI.2.2.2 Landscape description in DART: the 3D grid representation

The following content is summarized from Gastellu-Etchegorry et al. (2015), Lauret (2017) and CESBIO (2018).

The 5.7.0 version of DART considers any landscape as an ensemble constituted by an atmosphere, surface elements (vegetation, water, ground, buildings, etc) and a topography (**Figure 108**).

The landscape mock-up is described as a 3D array of cuboids (voxels), which divides vertically in three main parts:

- the upper atmosphere voxels,
- the mid atmosphere voxels,
- and the lower atmosphere and land surface voxels.

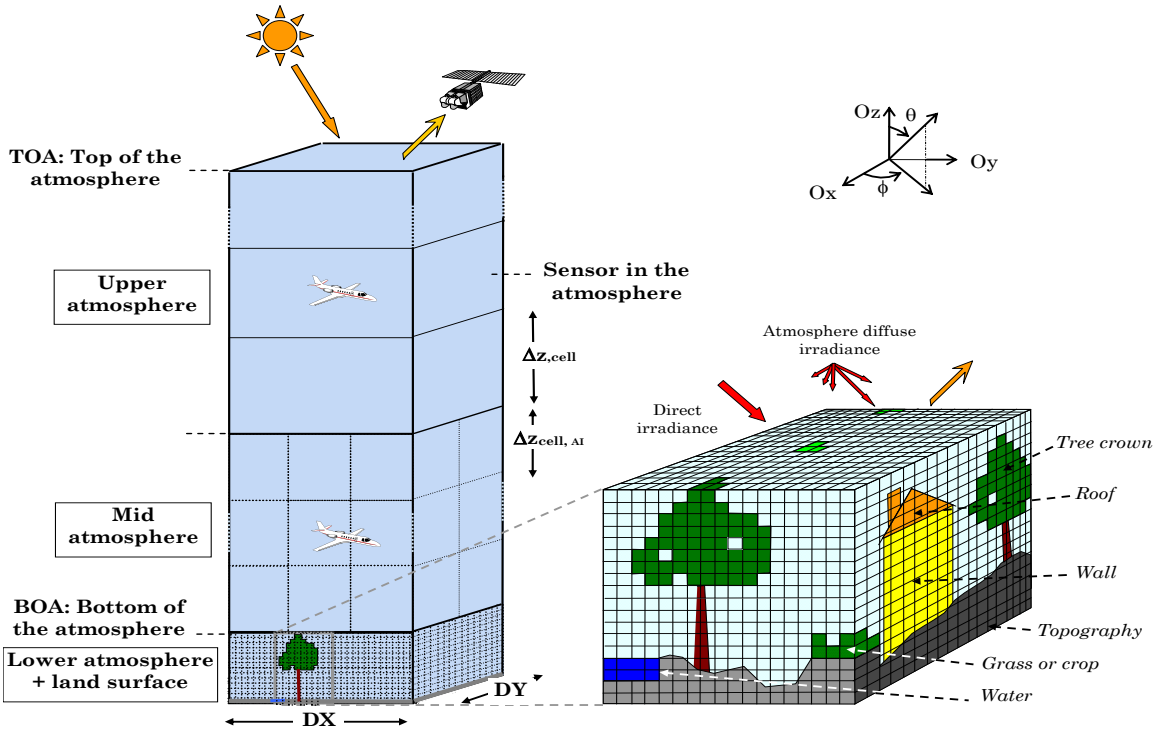

Figure 108: Dart model represents any landscape as a 3D matrix of cuboid cells (voxels) which contains either turbid medium or triangular objects. Together with the information of the location of the site on Earth (latitude, longitude, mean altitude) and the choice of solar angles corresponding to a given day and time of the year, the ensemble constitute a scene. Sensors can eventually be positioned within the scene if willing to simulate images observed from a satellite, an air borne or an in situ view point. – from Gastellu-Etchegory et al. (2012)

Atmosphere description in DART

The size of the upper and the mid atmosphere voxels increases with altitude. These cells contain light-propagating medium characterized by their contents in gas and aerosols and by spectral properties (phase functions, vertical profiles, extinction coefficients, spherical albedo, etc.). These parameters are defined manually or predefined from an atmospheric database, either that available with DART software (Berk et al. 2014), or the dynamic databases provided by the AErosol RObotic NETwork (AERONET) or the European Centre for Medium-Range Weather Forecasts (ECMWF).

Landscape components simulated with turbid or surface elements

Any landscape component located in the land surface voxels (air, vegetation, ground, buildings, etc) can be either described as a turbid medium that fills the entire voxel, or as one or several facets i.e. as surface elements latter called 'triangles'.

On the one hand, the turbid medium analogy is a statistical representation suited for representing matter such as fluids (air, water, etc) or vegetation, assuming homogeneous distribution and infinitesimal size of its components ($d << \Delta X, \Delta Y, \Delta Z$). In DART:

i) a voxel filled with **turbid fluid** contains N types of particles with N densities (particles per m^3). Each type of particle is defined by a cross section (m^2 per particle), a single scattering albedo, a scattering phase function, and thermal properties (if applicable);

ii) a voxel filled with **turbid vegetation** contains leaf/twig elements simulated as infinitely small and flat surfaces defined by a volume density $m^2_{vegetaiton}/m^3_{voxel}$ or area density ($m^2_{vegetation}/m^2_{ground}$), a leaf zenithal angle distribution (leaf azimuthal distribution is assumed uniform), optical properties of Lambertian or specular nature and thermal properties (if applicable).

On the other hand, a facet or 'triangle' is a semi-opaque macroscopic surface positioned within the grid array at precise coordinates. It is characterized by its dimensions, orientation in space (azimuthal and zenithal angles), optical properties (Lambertian, Hapke, or other reflectance functions with a specular component, an isotropic direct transmittance) and thermal properties (if applicable). It is suited for individually representing solid landscape components with dimensions at least equivalent or bigger than the voxel dimensions (typically tree trunks, buildings, etc).

For representing **vegetation** (**Figure 109**), 3D macroscopic objects (e.g. trees) made of a combination of an important but finite amount of triangles of various types (for e.g trunk triangles, bottom/intermediate/upper leaf triangles) can be used. They are either generated with DART or simply imported from vegetation databases. From previous research work and collaborations, DART software database contains several accurate three dimensional representations of crops and trees, such as the accurate model of *fraxinus excelsior* (**Figure 109**).

For representing plant canopies, DART also offers the possibility to generate clouds of triangle leaves of specified dimensions that fills a given voxel, as illustrated on **Figure 109**. The triangle leaves are randomly positioned within the voxel but respect a chosen leaf zenithal angle distribution and a volume density or area density. This representation can be seen as a third representation option, intermediate with the turbid medium analogy and a realistic three dimensional object representation.

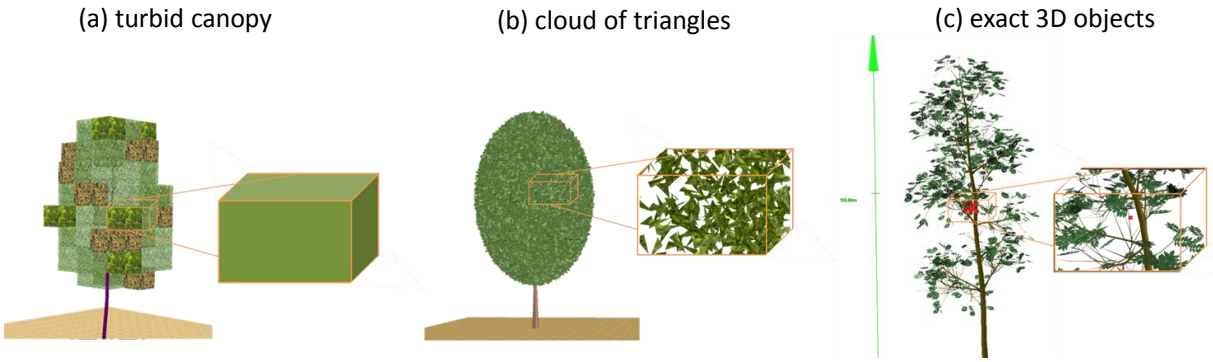

Figure 109: Three possible representations of a tree in DART, (a) as a triangular stem and a canopy made of voxels filled with turbid medium, (b) as a triangular trunk and a canopy made of triangle leaves, or (c) as a 3D object (the image shows the *FraxinusExelsior*.obj available in the RAMI4 database of DART) made by a structurally exact combination of triangles of trunk, branches and leaves type.

Relative localization of landscape components

Within the 3D array, the mock-ups of 3D objects can be positioned either randomly or accurately from relative xyz coordinates provided by the users. Similarly, plots filled with turbid medium or clouds of triangular objects can be set and positioned within the array. Additionally, DART model provides a very useful *land occupation map* tool which enables to generate landscape components of defined geometrical and optical properties by importing a raster file representing the land occupation map.

Topography

DART can add a topography to the scene in two ways, either from a raster file of DEM (Digital Elevation Model) map, or from importing a 3D object to use as DEM. In the first case, the topography is reproduced by filling voxels of ground thus the accuracy of representation is constrained by the XYZ resolutions of the cell array. In the second case, the array of voxels is positioned in space on top of the 3D surface that represents the DEM thus topographical variations are continuous and do not suffer spatial resolution bias.

Solar orientation

DART positions the landscape on the Earth globe from user filled information of latitude, longitude and mean altitude.

A simulation is instantaneous. The position of the sun is set by specifying solar angles corresponding to an exact year, day and time.

The content of the 3D array of cells, plus the information of site location and solar position all together constitute a *scene*.

From finite scenes to continuous landscapes

Because real landscapes are continuous and infinite, simulating the path of solar radiations within a finite or later called 'isolated scene' inevitably induces some border effects which are related to the fact that no interaction with the neighborhood is considered. Regarding this issue, DART proposes to represent landscapes with an *isolated scene mode* but also with two alternative modes:

1. a *repetitive topography* mode: similarly to most of the existing 3D radiative transfer models, DART forces a ray that exits the scene to re-enter the scene by the opposite side. It generates a similar result to that if the landscape components and the topography were juxtaposed infinitely. This method gives very satisfying results with landscapes without topography or with a specific topography where one side is identical to its opposite side within the scene. Nevertheless, in presence of any other kind of topography it generates undesirable discontinuities of topography and thus of illumination and shadows (Gastellu-Etchegorry et al. 2012).
2. a *continuous topography* mode: the scene components are infinitely repeated except the topography which is extended continuously by extrapolation. This singular and very advantaging method implemented in DART generates scenes with an infinite slope. It is very well suited for hilly landscapes.

VI.2.2.3 Light representation and flux tracking computation

Waveband discretization

DART computes the radiation propagation through the entire Earth-atmosphere system represented by a given landscape mock-up. Within the electromagnetic spectrum, DART can manage wavebands from 0.25 to 14 µm. Light can be defined either as a continuous broadband defined by its central wavelength λ_0 and width $\Delta\lambda$ in μm, or it can be discretized in several wavebands. The second option is essential for two reasons. Firstly because within broad spectral ranges such as the whole solar spectrum, both the intensity of solar exitance E_{λ_0} (**Figure 19**) and the optical properties of the earth surface components vary a lot with the wavelength. Concerning optical properties, for example, the reflectance factor ρ_{λ_0} of a deciduous tree leaf is of 10 %, 55 % and 32 % respectively for λ equaling 0.55 μm, 1.0 μm and 1.7 μm. Consequently considering the average exitance and the average reflectance factor over a mono-band of width $\Delta\lambda$ surrounding λ_0 can lead to severe imprecision (eq.

17). On the contrary, discretizing a wide spectral band into *i* shorter intervals within which $E(\lambda)$ and $\rho(\lambda)$ remain nearly constant enables improving the precision of integration (eq. 16). When *i* tends towards the infinite, the error tends to zero as the continuous spectrum of real light can be considered as an infinity of discrete juxtaposed spectral bands (eq. 15).

(reality =continuous) $M_{BOA_{\Delta\lambda}} = \int_{\Delta\lambda} E_{BOA}(\lambda).\rho(\lambda).d\lambda$ [15]

(multi-band simulation) $\approx \sum_i \frac{1}{\Delta\lambda_i}\int_{\Delta\lambda} E_{BOA}(\lambda_i).d\lambda_i \int_{\Delta\lambda_i}\rho(\lambda_i).d\lambda_i \quad \text{with } \Delta\lambda = \sum_i \Delta\lambda_i$ [16]

(mono-band simulation) $\neq \frac{1}{\Delta\lambda}\int_{\Delta\lambda} E_{BOA}(\lambda)d\lambda \int_{\Delta\lambda}\rho(\lambda)d\lambda$ [17]

with

$M_{BOA_{\Delta\lambda}}$	Exitance at the bottom of the atmosphere from a vegetated scene for a spectral width $\Delta\lambda$
E_{BOA}	Solar irradiance
ρ	Reflectance factor of the vegetation considered lambertian
$\Delta\lambda$	Spectral width, discretized in *i* subdivisions of width $\Delta\lambda_i$

Secondly, discretizing light into several discontinuous wavelengths enable simulating acquisitions from multispectral sensors and then combining the outputs for remote sensing applications.

N flux method or discrete ordinate method

For each spectral band λ, DART computes flux-tracking using the N flux or discrete ordinate method. Radiation is restricted to propagate in a finite number N_{dir} *of directions* (Ω_j) with an angular sector width ($\Delta\Omega_j$) in sr. Any set of N_{dir} discrete directions can be selected with $\sum_{j=1}^{N_{dir}} \Delta\Omega_j = 4\pi$. A radiation that propagates along the direction Ω_j at a position *r* is called a source vector $W(\lambda, r, \Omega_j)$. It has three components: i) the total radiation or energy W, ii) the radiation unrelated to leaf biochemistry, iii) the polarization degree associated to first order scattering.

When a source vector reaches landscape components, two different types of interactions occur (Gastellu-Etchegorry et al. 2015):

- volume interactions, within voxels filled with turbid medium (Gastellu-Etchegorry et al. 2004),
- surface interactions when radiation meets a triangle surface element (Gastellu-Etchegorry 2008).

The discrete ordinate method solves the equation of the radiative transfer (eq. 18), by transforming it into N_{dir} differential equations. Considering a Cartesian coordinate system, the equation of the radiative transfer thus becomes:

$$\left[\xi \frac{d}{dx} + \eta \frac{d}{dy} + \mu \frac{d}{dz}\right] L(\lambda, r, \Omega_n) \quad [18]$$

$$= -\alpha_e(\lambda, r, \Omega_n).L(\lambda, r, \Omega_n) + \alpha_a(r, \Omega_n).L_B(T)$$

$$+ \sum_{m=0}^{m=N_{dir}} \alpha_d(\lambda, r, \Omega_n).\frac{P(r, \Omega_m \rightarrow \Omega_n)}{4\pi}.L(\lambda, r, \Omega_m)d\Omega_m$$

with $L(\lambda, r, \Omega_n)$ The radiance flux of spectral length λ at location r in the direction Ω_n

The flux tracking process in the bottom of atmosphere and landscape part of the 3D grid is iterative: the scattered radiation at iteration *i* equals the radiation that was intercepted in iteration *i-1*. The iterative process can end in two ways:

i) either when the difference of exitance at the bottom of the atmosphere between two iterations is lower than a threshold defined by the user,

ii) or when *i* reaches an amount of *N* iterations, also defined by the user.

Breaking the iterative process before the whole energy was scattered, intercepted or absorbed within the bottom of atmosphere layer enables saving a considerable time of computation, for a limited loss of precision. Then, it is possible to activate an extrapolation process in order to estimate the radiative budget and remotely sensed images from an infinity of iterations. The extrapolation of the radiative budget uses coefficients that are calculated from the average radiative budget of all the voxels from the three last iterations.

Steps of computation of the radiative budget

Computation of the radiative budget in the earth surface – atmosphere system follows five steps in DART (**Figure 110**):

- step 1 computes the downward bottom of atmosphere radiances $L_{BOA}(\Omega \downarrow)$ based on the flux tracking of the sun radiations in the upper and mid-atmosphere layers.
- step 2 computes the radiative transfer within the landscape layer by iterative approach using the **N flux method or discrete ordinate method**.
- step 3 computes the retro diffusion in the atmosphere of the upward bottom of atmosphere radiance $L_{BOA}(\Omega \uparrow)$.
- step 4 computes the scattering within the landscape of the energy that was retro diffused from the atmosphere. A single iteration is applied this time but an extrapolation (which is based on step 2) still allows considering multiple scattering.
- Step 5 computes the final scattering of energy between bottom and top of atmosphere and thus the final upward top of atmosphere radiances $L_{TOA}(\Omega \uparrow)$.

Computation of the radiative transfer in the atmosphere may be deactivated by DART users. In this case, simulation of the radiative budget within the scene is performed (step 2) considering the atmosphere as a surface with isotropic downward emissions of the diffuse radiations from the atmosphere (the total irradiance and the SKYL (i.e. the fraction of diffuse radiation from the atmosphere) must be manually set by the user.

Another option offered by DART consists in deactivating the multiple scattering in the atmosphere for accelerating computation time. In this case only steps 1 and 2 are performed (**Figure 110**). It is usually acceptable in terms of precisions unless the blue bands specifically at stakes. This latter configuration was the one adopted for running the simulations described in the following content of this chapter.

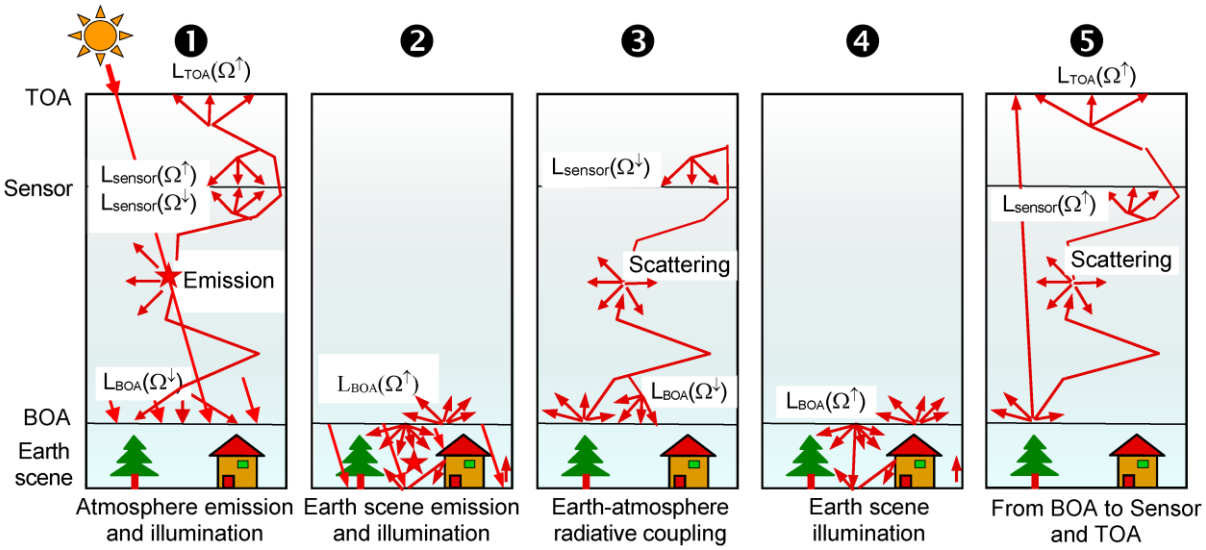

Figure 110: Steps of the DART algorithm which models the radiative transfer of the Earth-atmosphere system- BOA : bottom of atmosphere; TOA : Top of atmosphere; L: radiance: Ω angular direction – from Gastellu-Etchegorry et al. (2015)

VI.2.2.4 DART outcomes

Radiative budget

For each spectral band considered and for each iteration, DART can provide the different terms of the energy budget: absorbed energy, intercepted energy, scattered energy and downward and upward energy. Radiative budget products can be provided in 3D, either per voxel or per triangle. They can also be integrated vertically and projected onto a horizontal surface where they are mapped per cell and eventually per cell and per triangle types. They are given either in $W.m^{-2}.\mu m^{-1}$ or as a fraction of the irradiance at the bottom of atmosphere.

DART accuracy has been verified with ground measurements comparisons and in the RAMI project (Widlowski et al. 2015).

Remotely sensed images

DART can model the optical signals at the entrance of imaging radiometers or laser scanners placed on board of satellites, airplanes, drones or on site devices. For optical signals, DART can generate the reflectance, the radiance factor and/or the brightness temperature of the landscape. Images from satellites/ airplanes can be generated from three different altitude levels: bottom of atmosphere (BOA), top of atmosphere (TOA), or anywhere between BOA and TOA (**Figure 108**). The camera and/or scanner images can be generated with projective and/or orthographic projection considering a user defined viewing directions. In addition, ortho-projected images can also be generated which allows overlaying the georeferenced maps and simulated images.

VI.2.2.5 Informatics

The DART model offers a user-friendly graphic user interface for parameterizing, computing and visualizing the outputs of simulations. Parameterization and/or computation can also be launched by calling the successive modules of DART from a script in bash. For the purpose of this work, it allowed building and testing the simulations from the user-friendly environment, while sequences of simulations where automated in a bash/python script.

A complete simulation procedure can be carried out with four processing modules (Lauret 2017):

i) The *Direction* module computes the discrete directions of light propagation;
ii) The *Phase* module computes the scattering phase functions of all scene and atmosphere elements considering their geometry and optical properties;
iii) The *Maket* module builds the spatial arrangement of atmosphere and landscape elements in the 3D grid (recall **Figure 108**). It divides in two sub modules:
    a. The *atmosphere-maket* module, which fills the upper and mid-atmosphere layers of the grid,
    b. and the *maket* module, which fills the cells of lower atmosphere and landscape;
iv) At last, the module *Dart* computes radiation propagation and interactions. The ray tracking procedure presented in **VI.2.2.3 Light representation and flux tracking computation** is used for simulating the radiation budget and images captured by optical satellite or airborne radiometers.

VI.2.2.6 Key points of the DART model

To sum up, DART can simulate the 3D radiative budget and remotely sensed images of any type of landscapes. It offers a mechanistic (i.e. a realistic) representation of radiation propagation at the earth-atmosphere interface. Main approximations come from the obligation of discretizing the directions of the radiations, the physical space and the spectral range. The resulting impacts can be

managed by the user notably by adjusting the physical resolution of the landscape mock-ups and by slicing the spectrum in intervals according to the desired final accuracy.

VI.2.3 Simulations of the radiative budget of agroforestry vineyards with the model DART

VI.2.3.1 Overall view of the simulations

Five different mock-ups of vineyards were defined (**Figure 111**). The simulation named '*Lagardere AF'* mimics as closely as possible the characteristics of the agroforestry vineyard studied in Lagardère (32). The mock-up corresponds to a square section of 57*57 m from the southern part of Lagardere vineyard, which comprises three monospecies tree rows, separated from each other by six grapevine rows and alternating grassy or bare ground middle rows. Similarly, the simulation named '*NO TREE'* mimics the morphological characteristics that applied in 2016 in a square section located in the northern part of Lagardere vineyard where there is no tree, only grapevine rows (**Figure 113**). The objective is to generate a reference mock-up of a monocropped vineyard with realistic spacing and total grapevine density observed just nearby '*Lagardere AF*' that is not an artificial depletion of the trees from the '*Lagardere AF*' simulation.

The simulation named '*BIG TREES*' aims at assessing the effect of tree height. It represents a future version of Lagardere vineyard, when the trees will have reached a mature height of 1.7 times (*sorbus domestica* and *pyrus pyraster*) to twice (*Sorbus pyralis*) that in 2016.

The simulation named '*BIG TREES N/S*' and its corresponding monocropped reference named '*NO TREE N/S*' aim at assessing the effect of the azimuthal orientation of the rows. They represent imaginary landscapes where topography and vegetation all together have been rotated clockwise by an azimuth of 110°. Rows of grapevine and eventually of trees thus present a Northern-Southern orientation.

All mock-ups of vineyards were built with a xyz resolution of 10 cm. **Figure 111** gives the 3D views of the obtained landscape mock-ups.

In addition, images that would be captured by a satellite in the visible wavebands (a combination of Red Green and Blue bands) on the 25/05/2016 (**Figure 112**) have been simulated. These images enable to check the morphological characteristics of the components in each landscape, as it is uneasy from the sole 3D views of mock-ups (**Figure 111**). They notably confirm that:

- grapevine canopy truly doubled its height in summer scenes compared to that in spring (see the length of grapevine shadows);
- tree 3D objects truly changed dimensions between *Lagardere* AF and *BIG TREES* scenes, with a noticeable impact on the density of the canopies (see the length and the intensity of their shadows);

- applying a rotation coefficient to the sun azimuth angle correctly modify the orientation of the whole vineyards from a NW/SE orientation to a N/S orientation of the rows.

For each mock-up, DART simulations of the radiative budget in the PAR wavelength were run in time-series from the 15-Apr.-2016 to the 12-Sept.-2016, considering this period of time as the vegetative period of grapevine from budburst to harvest.

The atmospheric parameters were set using the meteorological data acquired in Lagardère in 2016 in order to simulate a realistic dataset that then could be compared with surveyed data.

The images shown in **Figure 112** are obtained considering a totally clear sky as the multiplicative factor to apply to the Aerosol Optical Depth (AOD) was set to 0. It was simulated this way in order to show the most intense shadow patches which can occur. Nevertheless atmospheric conditions without any aerosol and a totally clear sky are unrealistic most of the time and especially at the beginning or at the end of the day by this time of the year. The non negligible impact of the cloud cover on the intensity of shade patches is illustrated in **Figure 115**. It agrees with the conclusions of chapter II. For running simulations of the radiative budget of vineyards with realistic meteorological conditions, the multiplicative factor of the aerosol optical depth was adjusted for each date and time. To do so, the global radiation measured in Lagardère in 2016 was used as a reference.

The adopted methodology for building the mock-ups, setting the atmosphere parameters and computing 3D radiative budget products are detailed in the following sub-sections.

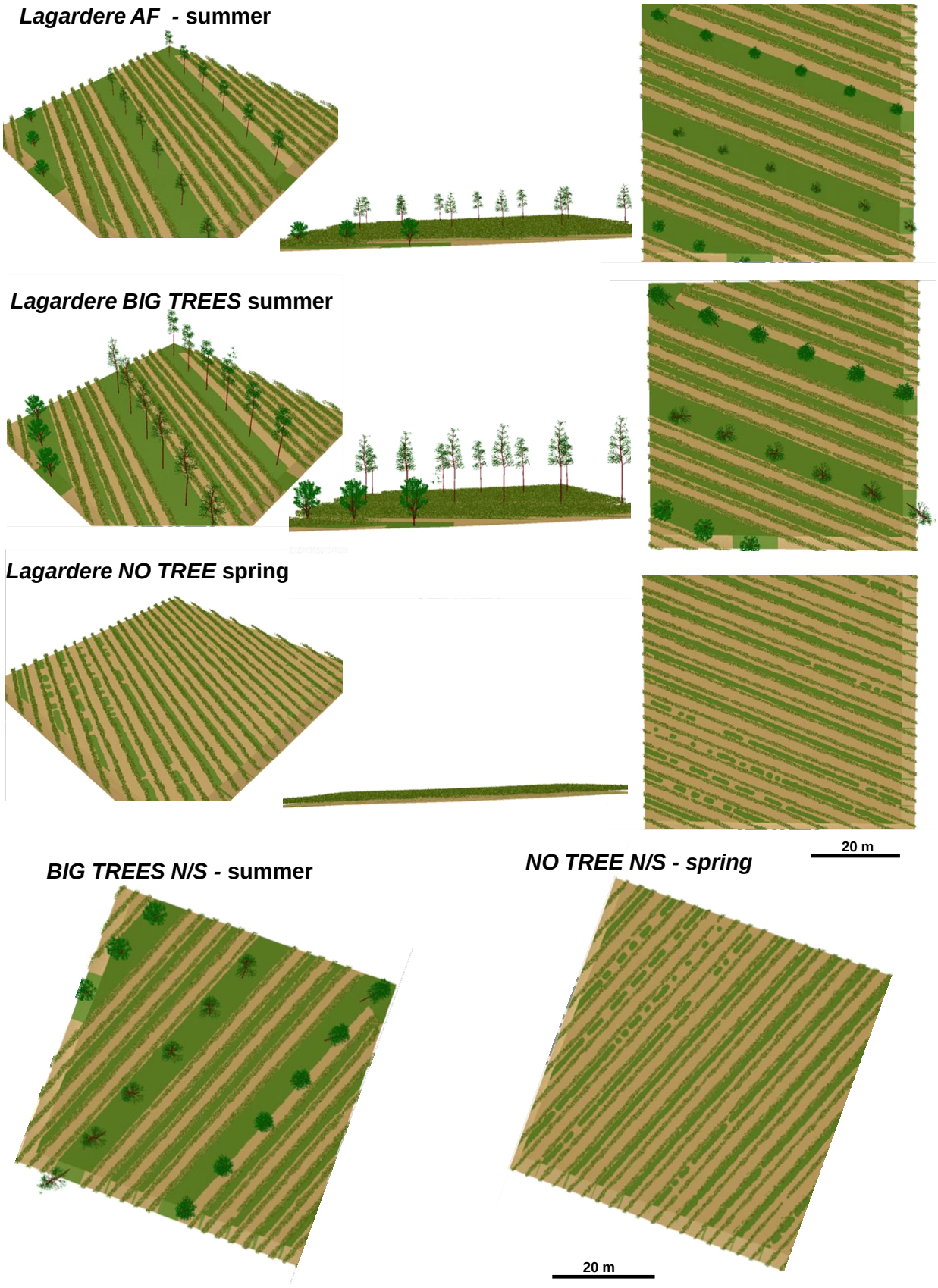

Figure 111 Lateral and aerial (right side and bottom) views of the 3D mock-ups of vineyards built with the model DART. Five different arrangements of the vegetation were considered. In all mock-ups the height of grapevine canopy increased from spring (1 m above ground) to summer (1.5 m above ground).

Figure 112: TWO PAGES show visible RGB images from simulations of the radiance from five different mock-ups of vineyards using the model DART. Images are simulated at nadir on the 25/05/2016 at every couple of hours from 9:00 to 15:00 UTC (local time is UTC + 2 -Solar time is UTC). The three following spectral bands were combined: Red (band center = 0.66 µm – bandwidth = 0.05 µm), Green (center = 0.55 µm – width = 0.05 µm), Blue (center = 0.48 µm – width = 0.06 µm). -

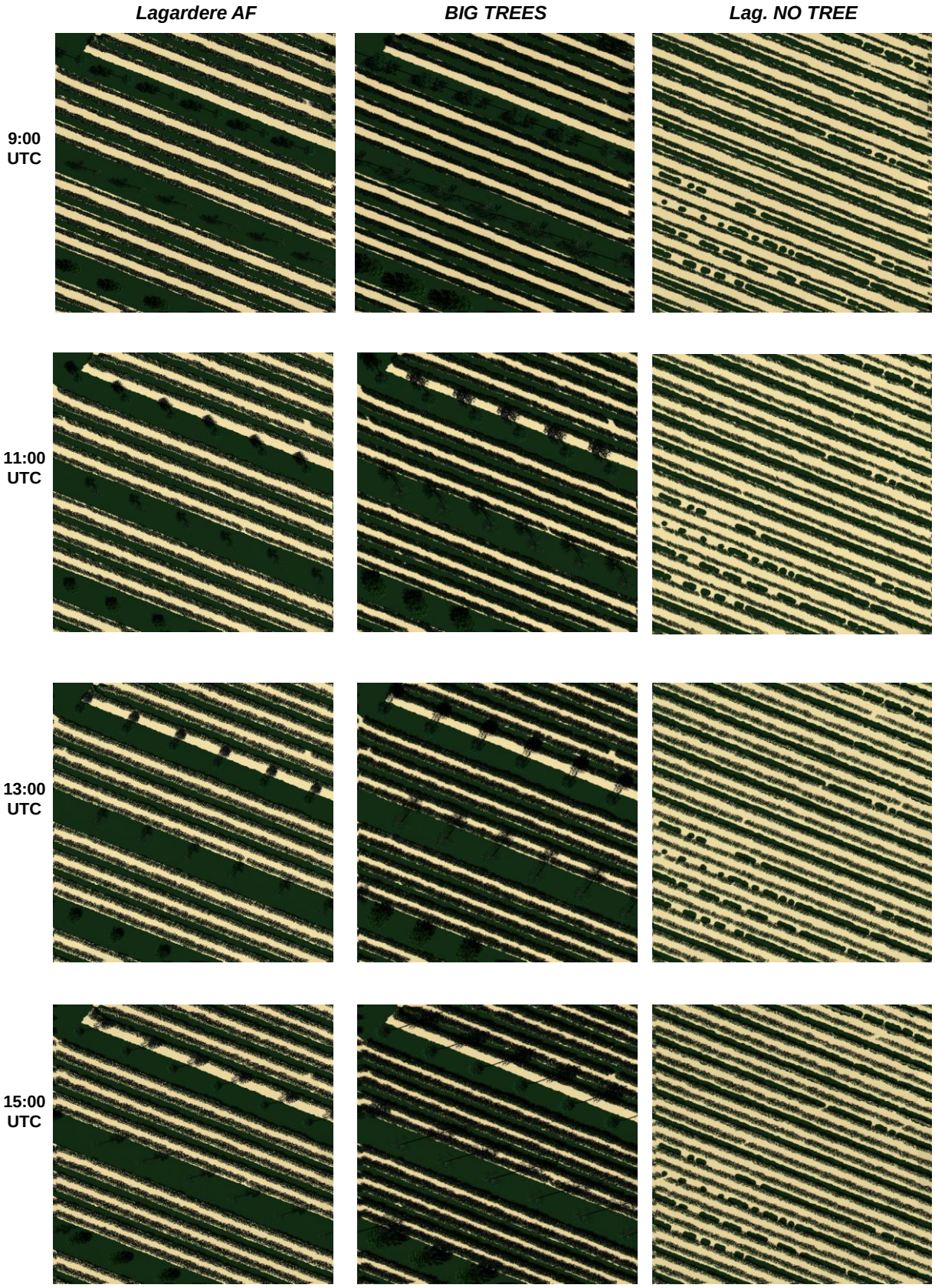

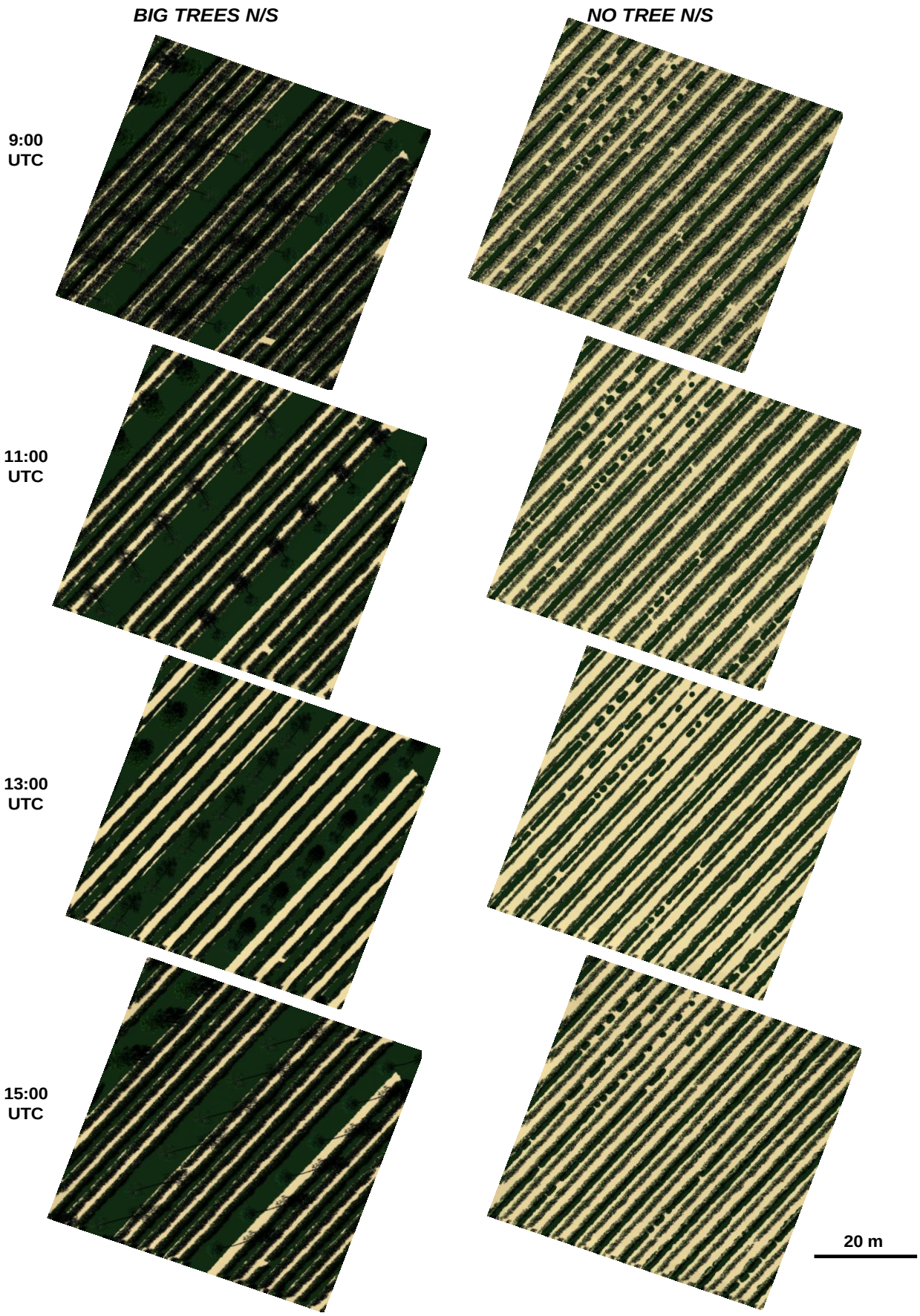
BIG TREES N/S
NO TREE N/S
9:00 UTC
11:00 UTC
13:00 UTC
15:00 UTC
20 m

VI.2.3.2 Light properties

Light was modeled as a single band of wavelength corresponding to the whole photosynthetically active radiation (PAR), i.e. from 0.400 to 0.700 μm. Though the reflectance and transmittance spectra of deciduous leaves vary within the PAR, it was considered that they remain sufficiently constrained within the same range all along the PAR wavelengths for the model to retain their average values. It is a source of moderate inaccuracy while subdividing the PAR into smaller bands would have significantly increased computation time of simulations.

Discretization of light was set to send 100 rays per cell of the grid i.e. the smaller mesh size was set to 0.01.

VI.2.3.3 Components of the 3D mock-ups of vineyards

Dimensions and resolution

All the mock-ups of vineyard presented in **Figure 111** were built using a 3D grid representing the low-atmosphere with a mesh of 0.1 x 0.1 x 0.1 m. Their total length, width and height are summarized in **Table 19**.

Table 19: Dimensions of the mock-ups

Landscape Mock-up	Length (m)	Width (m)	Height (m)
Lagardère AF	*57*	*57*	*11.3*
Big trees	*57*	*57*	*17.9*
No tree	*57*	*57*	*4.9*

Digital Elevation Model

Two main objectives drove the topography representation: (1) using a realistic topography and (2) canceling any contribution of the topography to the variability between mock-ups of vineyards.

Consequently, the same Digital Elevation Model (DEM) was used for parameterizing the topography of each mock-up. As illustrated in **Figure 113**, this DEM is extracted from the Lagardère study site (BD Topo 25 m) and extrapolated at a resolution of 10 cm. The binary rasterized file obtained was then imported in the DEM Generator tool of DART and converted into a planar 3D object. During this process, each square elementary cell of the raster file was converted into a pair of 3D triangles. Knowing the smooth and flat aspect of this DEM (**Figure 113**), a reduction of the number of triangle components of the object DEM was possible and highly recommended in order to reduce the computation time of the mock-ups. This simplification of the 3D geometry was performed under the Blender software imposing a reduction of the number of triangles to 10 % of the initial value. From a visual control (from the DEM 3D view and from a simulation of light interception under

DART), the simplified DEM did not introduce any artefact. At last, the planar 3D object created was imported under DART and used as DEM in every mock-up of vineyards.

In the rotated mock-ups, namely '*Lagardere big trees rotated N/S'* and '*Lagardere no tree rotated N/S*', the main slope ended rotated from the modification of the solar azimuth angle. It mainly faces North in these two mock-ups while it faces Southern-East in all the other.

Land occupation map

For each mock-up, a land occupation map was used for positioning the vegetation and bare ground in the 3D grid representing the lower atmosphere and land surface. It was derived from the object based approach presented in chapter IV, using the stack of visible and multispectral images captured by drone on the 2016/08/23 at Lagardere study site. As illustrated in **Figure 113**, the map presents six different categories of land occupations, namely bare ground, gassy cover, grapevine foliage sitting on top of a bare ground, tree in row 1, tree in row 2 and tree in row 3. The spacing between trees on each tree rows is realistic and registered thanks to DGPS markings (xyz accuracy is 10cm approx.). Two zones were selected: one is located in the southern area of Lagardere vineyard where grapevine rows are intercropped with tree rows; the other is located in the northern part, where there are only grapevine rows but no tree. The two selected areas were respectively used for building the mock-ups of agroforestry vineyards and that of vineyards with no tree. **Figure 113** reveals a slight difference in the width of grapevine rows between the two areas: in average, the width of the grapevine rows seems narrower in the no tree area. In addition, the grassy cover on the middle rows is patchy in some places of the no tree area. All these elements contribute to the spatial heterogeneity in each mock-up.

Information provided by the land occupation map was integrated in DART in two ways:

i) A map of the bare-ground, grass and grapevine coverage was imported for generating plots of ground or vegetation+ground.

ii) Text files providing the relative coordinates of each trees were imported for positioning accurate 3D objects of trees.

The morphological and optical properties of each land occupation class are given in the following sub-sections.

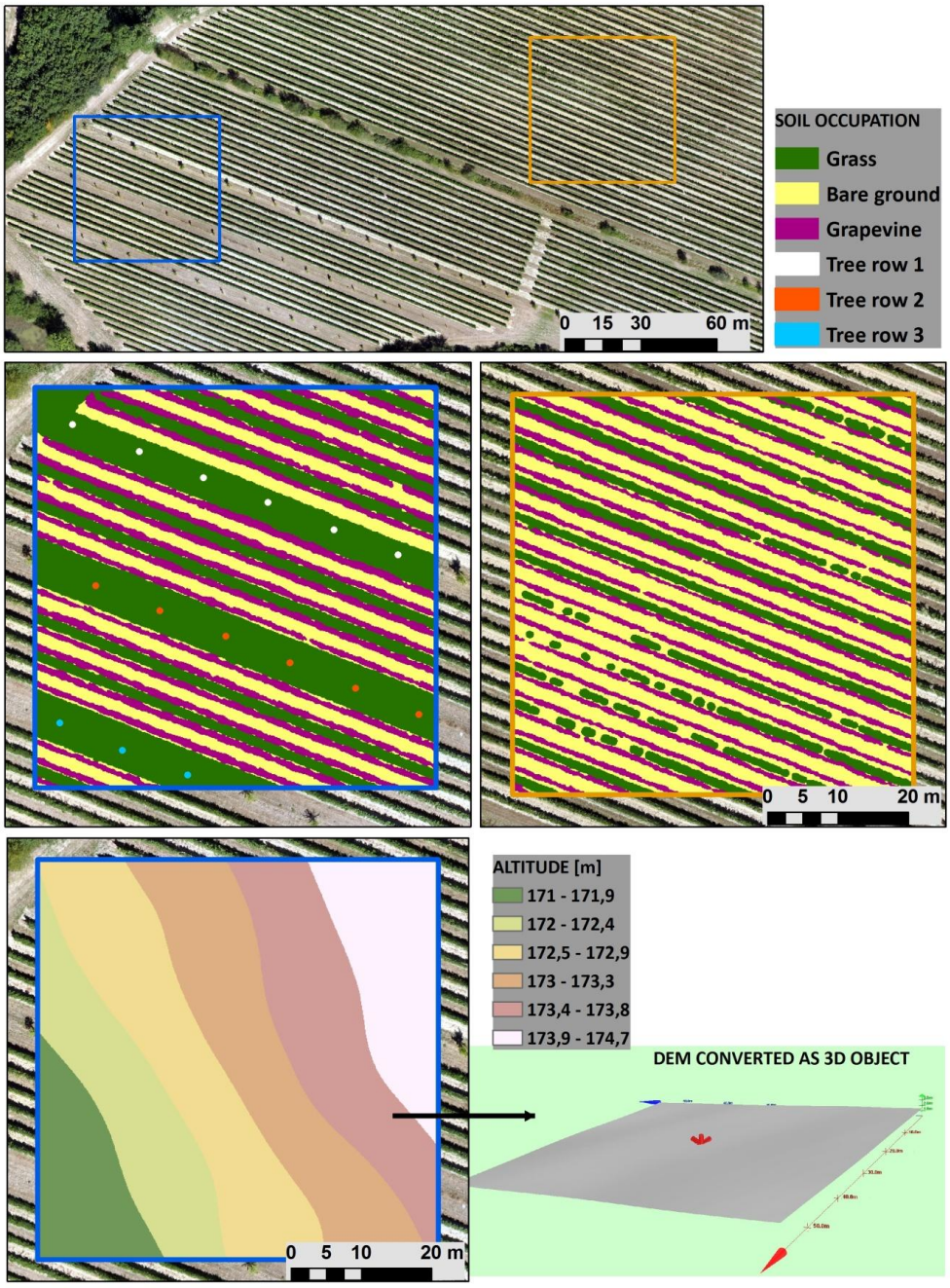

Figure 113: Land occupation maps from Lagardère study site that were used for building mock-ups of agroforestry vineyards (blue area) and monocropped vineyards (orange area) using DART. Rasterized Digital Elevation Model (DEM) was also extracted from the blue area.

The morphological and optical properties of the vegetation varied with mock-ups. **Table 20** summarizes the specifications set for each vegetation type (grapevine foliage, trees, grassy cover) according to simulations and time of the year.

GRAPEVINE

Similarly to López-Lozano et al. (2009), the foliage of vertically trained grapevine was represented in 3D by voxels filled with triangle leaves with an eretophile zenith angle distribution. Defining the geographical XY position of the voxels of foliage according to the land occupation map allowed modeling a realistic variability of the cross section of the vine rows. The trunks of grapevines were not represented, considering it of poor interest in regards to light patterns. Thus the plots of foliage were floating in the air at an height of 0.5 m above ground. The total height of grapevine canopy was set to 0.5 m and 1 m respectively in spring (before 2016/06/01) and in summer (after 2016/06/0). It was lowered by about 12 % compared to the actual heights observed on site, based on the recommendations made by López-Lozano et al. (2011). Also, in order to model realistic variability, variations of grapevine height were artificially introduced by applying a standard deviation of 10 cm to the height of grapevine plots.

Optical properties of grapevine leaves were defined based on the experimental results of Al-Saddik et al. (2017) on *Marselan* and *Chardonnay* cultivars. In their results, grapevine reflectance showed an important variability within the PAR but systematically remained above 0.1. Also it showed rather flat peaks, shaped like downward steps and centered around 0.5 in the near infrared wavelengths. This spectrum was compared with many reflectance spectra available in the lambertian vegetation database of DART. The spectrum of *grass rye* seemed the most similar and was thus chosen for representing grapevine optical properties in the simulations (**Figure 114**).

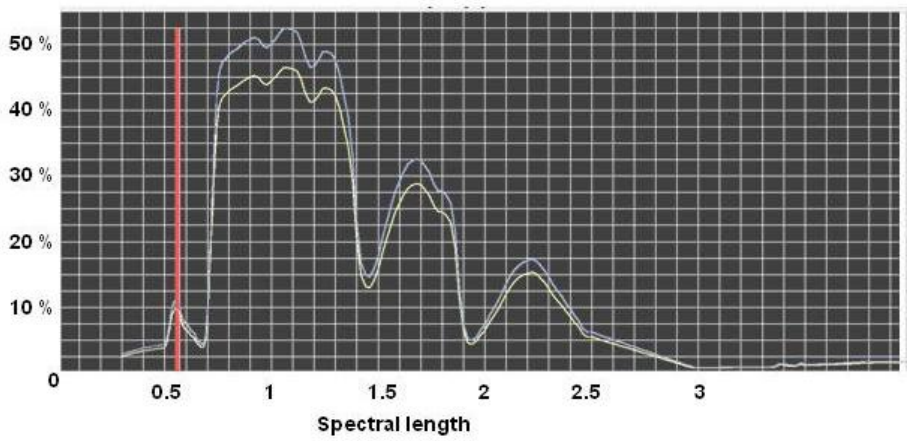

Figure 114: Reflectance (blue) and transmittance (yellow) spectra of *grass rye* in the lambertian vegetation database of DART

TREES

Trees were modeled by accurate 3D objects imported from the DART database. As no mock-up of the tree species present in Lagardère studied vineyard, namely *sorbus domestica*, *sorbus pyralis* or *pyrus piraster*, were available, we chose mock-ups of ash tree (*fraxinus excelsior*), of maple tree (*acer platanoides*) and lemon tree (*Citris sinensis)* instead. Similarly to the tree row #3 in the field, the simulated tree row #3 has a significantly lower tree height than the two other rows. Also it presents a significantly denser canopy while visual observations of the trees on site suggest the converse.

The Leaf Area Index (LAI) of the tree canopies are provided in **Table 20**. They correspond to the area of tree leaves per area of ground located below the trees. They were manually computed according to the following equations:

$$LAI_{tree}^{proj} = \frac{LAI_{tree}^{scene}}{Prop_{tree}} \quad [1]$$

$$Prop_{tree} = \frac{A_{tree}}{A_{scene}} \quad [2]$$

with

LAI_{tree}^{proj}	The LAI of tree canopy calculated per unit area of ground in the vertical projection below the trees. $[m_{leaves}^2 . m_{ground}^{-2}]$
LAI_{tree}^{scene}	The LAI of tree canopy calculated per unit area of ground of the whole scene. $[m_{leaves}^2 . m_{ground}^{-2}]$
$Prop_{tree}$	The proportion of the ground area in the vertical projection of the tree canopy (A_{tree}) out of the total area of the scene (A_{scene})

LAI_{tree}^{scene} was computed by DART per each type of tree using the LAI product proposed by the model DART. Prior to this computation, tree canopy had to be transformed as voxels of turbid medium.

A_{tree} was computed by creating scenes with only trees being represented as 3D objects (DEM and grapevine had to be removed). Then maket.exe was launched for computing the landscape mock-up. Finally the image of the mock-up was observed in the 2D view tool of DART where a 'ground area' tab provided A_{tree}.

The computed LAI revealed an existing be low differences between the LAI of the trees in the *Lagardere* and in the *BIG TREES* simulations. In addition, all the computed values fall below the value of 5 provided as a reference by Eagleson (2005).

GRASSY COVER 2D REPRESENTATION

The grassy cover was modeled only in two dimensions as an accurate representation was considered of negligible interest in regards to light propagation in the simulated scene. It allows limiting the complexity of the mock-ups and thus the computation time of every simulation. Tiles of grassy cover were positioned on top of the DEM according to the land occupation map. The *grass* land

category was set as ‘ground’ instead of ‘vegetation’ in order to delete the vertical dimension. In addition, the spectrum of *grass rye* was applied for reflectance properties (**Figure 114**) and transmittance was set to 0. In order to consider a more realistic reflectance of grassy cover when it has a 3D structure, notably the non negligible contribution of gaps of grounds, a multiplicative factor $f_\rho = 0.745$ as applied to the reflectance of grass rye. This value was calibrated in two steps:

- In a first step, the radiance of a square scene occupied by plots of grassy cover represented in 3D (**Table 20**) was simulated The PAR reflectance of the 3D grassy cover on the 20/07/2016 12:00 UTC was $\rho_{PAR}^{3D} = 7.753\ \%$.
- In the second step, the simulated radiance of the same simulation properties except the grassy cover was represented in 2D with a reflectance factor set to 1. In this case the PAR reflectance measured was $\rho_{PAR}^{2D} = 6.35\%$.

The value of the correcting multiplicative factor was obtained as the following ratio:

$$f_\rho = {\rho_{PAR}^{3D}}\Big/{\rho_{PAR}^{2D}}.$$

The conversion of the grass cover from a 3D representation to a 2D representation significantly reduced the number of triangles composing the mock-ups as it switched from approximately 2.2*10^6 to 1.4*10^6. The computation time of each simulation was changed from about 45 minutes to 20 minutes with this approach.

Table 20: Optical and morphological properties of the landscape components of the five mock-ups of vineyards designed in DART. The LAI are provided per area of ground within the vertical projection of the canopy (and not per area of ground of the total scene). Abbreviations: H: Height from the ground - LAI: Leaf Area Index ($m^2_{leaves}.m^2_{ground}$) - N/S/E/W: North/South/East/West

		Bare ground	Grassy cover	Grapevine	Tree row #1	Tree row #2	Tree row #3	Rows
		Optical properties: *Clay brown* →applied to planar plots	Optical properties calibrated from plots filled with leaves of *grass-rye* H_{top}: 0.1 m LAI: 2.5 Individual leaf area: 0.003 m^2 leaf orientation: erectophile →applied to planar plots	Voxels filled with triangular objects representing leaves Leaf density: 4.5 $m^2.m^{-3}$ Individual leaf area: 0.015 m^2 Leaf orientation: erectophile Optical properties: *grass-rye*	***Fraxinus excelsior*** **(3D accurate object *FREX_Simplified_twig.obj*)**	***Acer platanoides*** **(3D accurate object *ACPL_Simplified_twig.obj*)**	***Citris sinensis*** **(3D accurate object *cisi1.obj*)**	**Orientation**
Vineyard mock-ups	***Lagardere AF***	On one middle row out of two and under grapevine rows	On one middle row out of two and on tree rows	H_{bottom} = 0.5 m H_{top} = 1 m from 15/04 to 31/05 H_{top} = 1.50 m from 1/06 to 12/09	Width (X): 2.66 m Length (Y): 2.73 m Height (Z): 8.22 m LAI: 2.36	Width (X): 2.34 m Length (Y): 2.46 m Height (Z): 7.7 m LAI: 1.29	Width (X): 2.75 m Length (Y): 2.53 m Height (Z): 3.92 m LAI: 3.62	NW/SE (112°)
	BIG TREES	On one middle row out of two and under grapevine rows	On one middle row out of two and on tree rows	H_{bottom} = 0.5 m H_{top} = 1 m from 15/04 to 31/05 H_{top} = 1.50 m from 1/06 to 12/09	Width (X): 3.8 m Length (Y): 3.9 m Height (Z): 13.7 m LAI: 2.56	Width (X): 3.9 m Length (Y): 4.1 m Height (Z): 15.4 m LAI: 2.08	Width (X): 4.5 m Length (Y): 4.14 m Height (Z): 7 m LAI: 4.12	NW/SE (112°)
	Lagardere NO TREE	On one middle row out of two and under grapevine rows	On one middle row out of two	H_{bottom} = 0.5 m H_{top} = 1 m from 15/04 to 31/05 H_{top} = 1.50 m from 1/06 to 12/09	None	None	None	NW/SE (112°)
	BIG TREES N/S	On one middle row out of two and under grapevine rows	On one middle row out of two and on tree rows	H_{bottom} = 0.5 m H_{top} = 1 m from 15/04 to 31/05 H_{top} = 1.50 m from 1/06 to 12/09	Width (X): 3.8 m Length (Y): 3.9 m Height (Z): 13.7 m LAI: 2.56	Width (X): 3.9 m Length (Y): 4.1 m Height (Z): 15.4 m LAI: 2.08	Width (X): 4.5 m Length (Y): 4.14 m Height (Z): 7 m LAI: 4.12	N/S (2°)
	NO TREE N/S	On one middle row out of two and under grapevine rows	On one middle row out of two	H_{bottom} = 0.5 m H_{top} = 1 m from 15/04 to 31/05 H_{top} = 1.50 m from 1/06 to 12/09	None	None	None	N/S (2°)

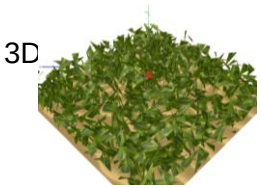


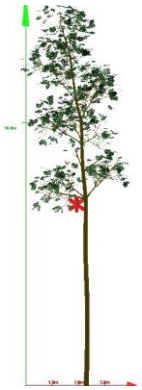
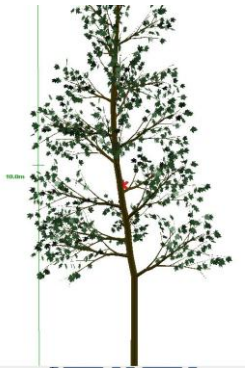
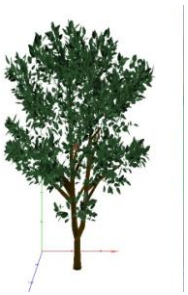

VI.2.3.4 Atmospheric parameters

The state of the atmosphere is an essential parameter of the energy budget at the interface with the earth surface . Firstly, the cloud cover modifies the total amount of solar radiation that arrives to the ground as well as its partition between radiations of direct and diffuse fractions. Secondly, the amount of water vapor and aerosols influences the amount of heat that the atmosphere emits in the TIR wavebands due to the green house effect. In the first case, the cloud cover generates variations in the energy inputs for the surface at a minute to hourly pace, while in the second case the amount of gases generates variations at a daily to seasonal pace. In order to simulate a realistic meteorological time series, a new methodological approach was tested for calibrating the atmosphere properties based on the sole input data of the global solar irradiance measured at Lagardere in 2016. It consisted in modulating the quantity of aerosols for each day and time of simulation. The following sections details and justifies the choices that were made.

Overall optical properties of the atmosphere

Following the instructions of CEBSIO (2018), for all the simulations that were performed:

i. the model of aerosol optical properties named 'rural 23 km', available in DART database, was applied;
ii. the models US Standard 76 were applied for the gas properties and temperature profiles;
iii. the value of the multiplicative factor to apply to the aerosol optical depth was modulated for each day and hour of simulation ($c_{AOD}(t)$) based on the value of the solar global radiation measured by a weather station.

Indeed, the global sun radiation recorded by the weather station at Lagardere in 2016 was the only available data to describe the atmosphere optical properties at the given day and hour of simulation (**Table 6**). The latter approach was previously tested by Landier (2018) for simulations of satellite images in urban context when the information of the partitioning between diffuse and direct sources of irradiance was missing. This author proposed to modulate the multiplicative factor to apply to the aerosol optical depth so as to model all together the variations of the cloud cover, aerosols and water vapor from one date and time of simulation to another. **Figure 115** shows the visual impact of this procedure on the shadow patterns based on simulations of reflectance images with the BIG TREE mock-up of vineyard. It confirms that increasing c_{AOD} has a visible fading impact on shadow patches similarly to dense cloud covers. Shadow patches became nearly inexistent with an AOD factor of 4. These tests also confirmed that similarly to clouds, a high optical density of aerosols leads to a reduction of the total light irradiance simulated at the bottom of the atmosphere and at the same time to an increase of the diffuse to total radiation ratio or *SKYL* (def. **p.219**).

Figure 115: Visual check of the incidence of modifying the multiplicative factor of the Aerosol Optical Depth (c_{AOD}). Simulations of the RGB images were performed on the BIG TREES mock-ups of vineyards on 15/04/2016 15:00 UTC. The total irradiance (E_{TOT}) and the SKYL (diffuse to total irradiance ratio) are given per spectral band

Adjustment of the aerosol optical depth for modeling cloud cover variability

The methodology for adjustment comprised several steps.

First the raw time series of instantaneous R_g taken in $W.m^{-2}$ every 5 to 10' was prepared using MATLAB 2015b®: it was interpolated every minute using a piecewise cubic Hermite interpolating polynomial algorithm and the values corresponding to the days and hours of simulation were exported as a text file.

Second, a mock-up of landscape was built in DART in order to initiate the total irradiance at the bottom of the atmosphere for all simulations. It was very simple as it only contained a square of grassy cover, located at the same latitude, longitude and average altitude of Lagardere vineyard. The whole solar spectra ([250 nm -2800 nm]) was simulated as it corresponds to the spectra of sensitivity of the pyranometer at the study site of Lagardere. For the simulation of irradiance this whole range was segmented into 20 contiguous spectral wavebands, of 127.5 nm width each.

In collaboration with Eric CHAVANON from the DART team at CESBIO, a python script was developed for adjusting the multiplicative factor of the Aerosol Optical Depth (c_{AOD}) for each date and times of simulation (**Annex P**). Simulations of irradiance can be triggered by the python script until the algorithm converges on a simulated irradiance that differs from the measured value by less than a tolerated error rate:

$$\epsilon = \left| \frac{E_{simu}(c_{AOD}^{end}) - E_{mes}}{E_{mes}} \right|$$

The value of ϵ was set to 3 % and the maximum number of iterations allowed to N_{max} = 20. Two cases of non convergence appeared:

i. when E_{simu} remained higher than E_{mes} at the end of the first step and after N_{max} iterations. It generally occurred when the measured irradiance was very low compared to the theoretical clear sky one (by approximation compared to $E_{simu}(1)$). In this case, the tolerance threshold is reconsidered and becomes $\epsilon' = \epsilon * \frac{E_{simu}(c_{AOD}^{i})}{E_{mes}}$

ii. when $E_{simu}(0)$ is lower than E_{mes}. In this case the value $c_{AOD}^{end} = 0$ was retained anyway.

Resulting meteorological time series

The final values of solar global irradiance simulated with DART are shown in **Figure 116**. They strictly follow the daily and seasonal variations of the measured irradiance used for its calibration and show only very few cases of non convergence.

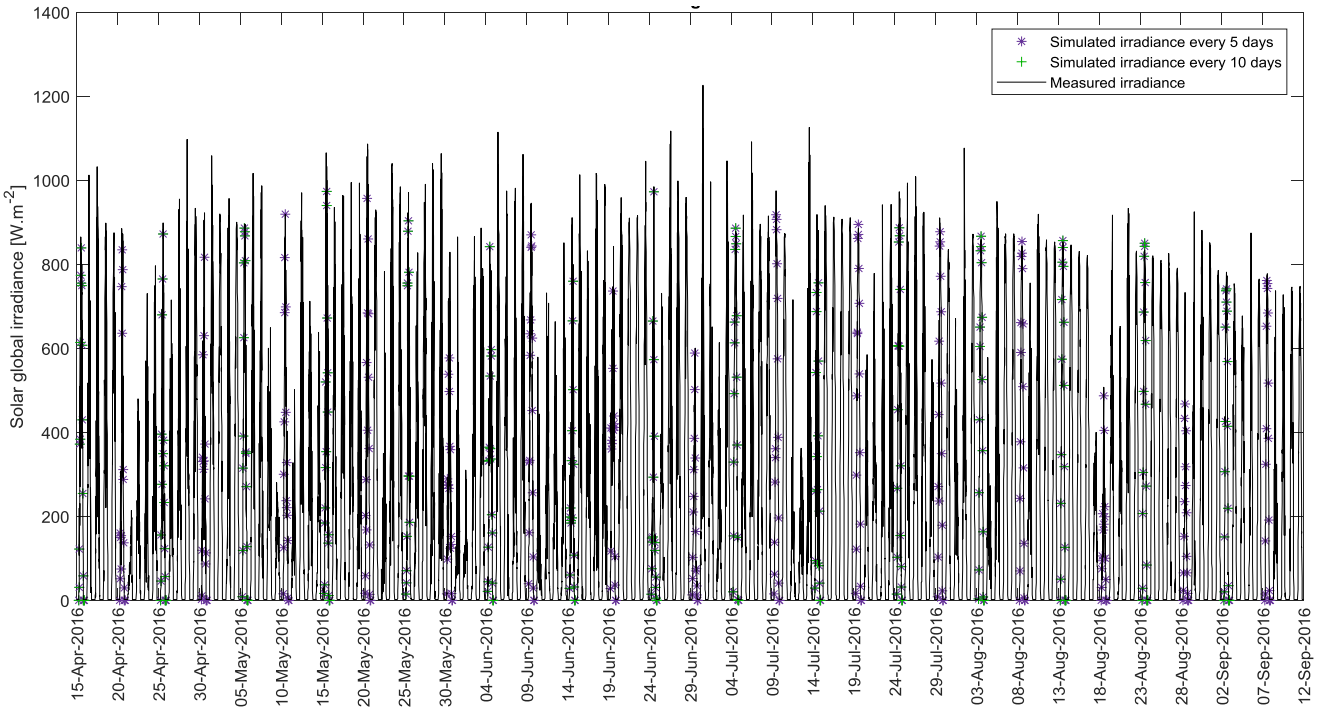

Figure 116: Solar total irradiance measured at Lagardere in 2016 (solid line) and simulated with the DART model (* and +), by adjustment of the multiplicative factor of the aerosol optical depth.

VI.2.3.5 Optimization of computation time

A total of 255 simulations (one date and time) of radiative budget had to be computed for each of the five mock-ups. Several strategies were combined in order to limit the computation time and if possible the RAM necessary for each simulation. They concern vegetation modeling, atmosphere modeling and flux-tracking procedure. The optimized simulation parameters and their impact on the accuracy of the simulation results are presented in the following subsections.

After optimizing the simulation parameters, the computation time for a single simulation was of 15 minutes in average, using 28 CPU of a server.

2D representation of the grass cover

In order to reduce the complexity of the mock-ups, the grassy cover in the middle rows was represented in 2D, according to the methodology described in **Grassy cover 2D representation**. This conversion significantly reduced the number of triangles composing the mock-ups as it switched from approximately $2.2*10^6$ to $1.4*10^6$. The computation time of each simulation was changed from about 45 minutes to 20 minutes with this approach.

Atmosphere discretization

DART gives the possibility to define either automatically or manually the size and number of atmosphere layers (recall **Figure 108**). The cloud cover for each simulation was set by adjusting the multiplicative factor of the Aerosol Optical Depth. This approach implied to manually define the dimensions of the atmosphere layers so it remained identical to the representation that was used for the calibration of the AOD multiplicative factor. The atmosphere is described as layers of mid-atmosphere (MA) and upper-atmosphere (UA) with a default height respectively set to 4 000 m and 80 000 m. Computation time increases with the number of sub-layers N_{MA} and N_{UA} used for representing the two atmospheric zones. The default values in DART are N_{MA} = 8 layers with a thickness of dZ_{MA} = 500 m and N_{UA} = 40 layers with a thickness of dZ_{UA} = 2 000 m. These default dimensions were used for running the simulation of calibration of the AOD multiplicative factor.

Then a sensitivity study was performed in order to identify the maximum thickness of the sub-layers in the mid-atmosphere and in the-upper-atmosphere which does not significantly impact the precision of the simulations compared to the default dimensions (**Table 21**). For this purpose, the total bottom of atmosphere irradiance was simulated with increasing dZ_{MA} and dZ_{UA} while the total heights were remained as default. The simulations were performed on three different dates and times of the year that were selected in order to cover varied configurations of solar angles and/or cloud cover:

- tests A correspond to a completely overcast sky at midday in summer,
- tests B correspond to a completely clear sky at the end of the day in summer,
- tests C correspond to a mitigated sky at midday in spring.

The sensitivity results in **Table 21** showed that the total solar irradiance at the bottom of the atmosphere is very sensitive to the resolution of representation of the mid-atmosphere layers (cf. tests A2 to A4 compared to A1). Consequently the default dimensions for the mid-atmosphere were kept. Nevertheless, a decrease of the number of the sub-layers representing the upper-atmosphere had little impact on the precision of the simulated irradiance and so for every type of meteorological context.

Consequently, the number of upper-atmosphere sub-layers was reduced from 40 to 16which correspond to a width of 5 000 m.

The lower sensitivity of the upper atmosphere representation may be partly explained by the fact that the concentrations in gas and aerosols are much lower in the upper atmosphere than in the mid one.

Table 21: Sensitivity study for optimizing the resolution for modeling the mid- (MA) and the upper- (UA) atmosphere layers. H = Total height - dZ = thickness of each atmospheric layer – E: solar irradiance – ϵ: error rate between the simulated (simu) and the measured (mes) irradiances

TEST A	***18/08/2016 13:00 UTC***		***fAOD = =***	***48***			***E_{mes} :***	***174***	***W.m^{-2}***		
A1 (default)	MA (H = 4000 m)	dZ_{MA} :	500	m	8	layers	E_{simu} :	169.8	W.m^{-2}	Δt:	3'16
	UA (H = 80000 m)	dZ_{UA} :	2000	m	40	layers	ε :	2.4	%		
A2	MA (H = 4000 m)	dZ_{MA} :	1000	m	4	layers	E_{simu} :	134	W.m^{-2}	Δt:	1'40
	UA (H = 80000 m)	dZ_{UA} :	4000	m	20	layers	ε :	23.0	%		
A3	MA (H = 4000 m)	dZ_{MA} :	750	m	5	layers	E_{simu} :	156	W.m^{-2}	Δt:	2'22
	UA (H = 80000 m)	dZ_{UA} :	3000	m	27	layers	ε :	10.3	%		
A4	MA (H = 4000 m)	dZ_{MA} :	500	m	8	layers	E_{simu} :	169.6	W.m^{-2}	Δt:	2'50
	UA (H = 80000 m)	dZ_{UA} :	2500	m	32	layers	ε :	2.5	%		
A5	MA (H = 4000 m)	dZ_{MA} :	500	m	8	layers	E_{simu} :	169.1	W.m^{-2}	Δt:	2'00
	UA (H = 80000 m)	dZ_{UA} :	4000	m	20	layers	ε :	2.8	%		
A6	MA (H = 4000 m)	dZ_{MA} :	500	m	8	layers	E_{simu} :	168.9	W.m^{-2}	Δt:	1'40
	UA (H = 80000 m)	dZ_{UA} :	5000	m	16	layers	ε :	2.9	%		
TEST B	***03/08/2016 18:00 UTC***		***fAOD =***	***0***			***E_{mes}***	***154***	***W.m^{-2}***		
B1 (default)	MA (H = 4000 m)	dZ_{MA} :	500	m	8	layers	E_{simu} :	163	W.m^{-2}	Δt:	31'
	UA (H = 80000 m)	dZ_{UA} :	2000	m	40	layers	ε :	5.8	%		
B2	MA (H = 4000 m)	dZ_{MA} :	500	m	8	layers	E_{simu} :	163	W.m^{-2}	Δt:	20'
	UA (H = 80000 m)	dZ_{UA} :	4000	m	20	layers	ε :	5.8	%		
B3	MA (H = 4000 m)	dZ_{MA} :	500	m	8	layers	E_{simu} :	163.2	W.m^{-2}	Δt:	17'
	UA (H = 80000 m)	dZ_{UA} :	5000	m	16	layers	ε :	6.0	%		
TEST C	***10/04/2016 10:00 UTC***		***fAOD =***	***2***			***E_{mes}***	***698***	***W.m^{-2}***		
C1 (default)	MA (H = 4000 m)	dZ_{MA} :	500	m	8	layers	E_{simu} :	708.1	W.m^{-2}	Δt:	59'
	UA (H = 80000 m)	dZ_{UA} :	2000	m	40	layers	ε :	1.4	%		
C2	MA (H = 4000 m)	dZ_{MA} :	500	m	8	layers	E_{simu} :	708.03	W.m^{-2}	Δt:	34'
	UA (H = 80000 m)	dZ_{UA} :	4000	m	20	layers	ε :	1.4	%		
C3	MA (H = 4000 m)	dZ_{MA} :	500	m	8	layers	E_{simu} :	708.01	W.m^{-2}	Δt:	30'
	UA (H = 80000 m)	dZ_{UA} :	5000	m	16	layers	ε :	1.4	%		

Coupling

The contribution for computing the Earth-Atmosphere coupling step is assessed following the same logic as for the atmosphere representation. In the worst case, removing the coupling phase in flux-tracking computation modified by 3.4 % the instantaneous quantities of energy which is absorbed by grapevine but allowed saving 3’ of computation of the radiative budget. Thus, the quantity of energy which is retro diffused from the atmosphere was considered to be sufficiently low to be ignored and coupling was disabled.

VI.2.4 Repetition of simulations as a meteorologically realistic time series

The year 2016 was used as the reference for calibrating the meteorological parameters at each hour of simulation, based on the total solar irradiance that was measured. The objective was to model a realistic meteorological sequence from budburst to harvest. It raised the two following methodological issues:

- What frequency of days of simulation should be chosen for the meteorological time series to be sufficiently realistic?
- How to automatically calibrate simulations and launch their computation?

VI.2.4.1 Optimization of the frequency of simulations

Simulations were set every hour of the days of simulations. Two frequencies of days of simulation were considered: either every ten days or every five days. The hourly distributions of the solar irradiance measured in Lagardere and simulated with both frequencies were compared (**Figure 117**). It showed that the ten-day-period covers all the range of the measures except at 12h winter time (WT) and at 15h WT where low values and intermediate values of irradiance are misrepresented. It is less the case with the five-day-period.

In addition, **Figure 118** shows the cumulated irradiance obtained in both cases after time integration. The ten-day-period led to overestimate the irradiant energy cumulated from budburst to harvest while the five-day period led to a cumulated budget of same range. Nevertheless overestimation seems mainly due to the simulations performed for August and September. Consequently, a combined time-series of simulation was also tested where the period is 10 days before 13th-Aug.-2016 and is five days after this date. It led to only 3.5 % overestimation of the total cumulated solar irradiance. As a consequence the mixed frequency time series was chosen.

VI.2.4.2 Sequence launcher

A Python script capable of launching the whole simulations as an automatic sequence was prepared and used. Its principle and functioning are explained in **Annex Q**.

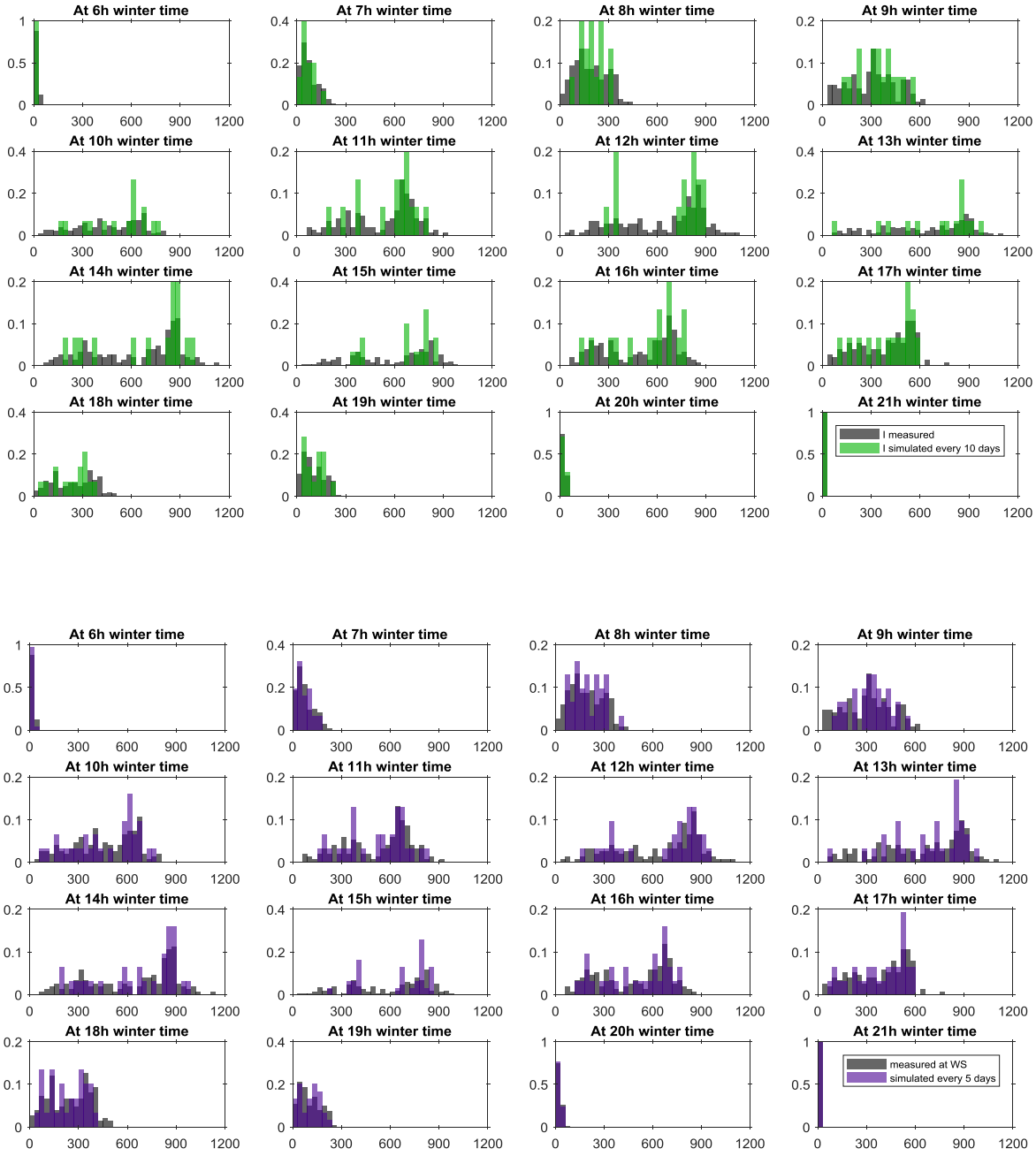

Figure 117: Distribution of the total solar irradiance at each hour of the day from budburst to harvest. The measured irradiance (grey) is compared to the simulations performed every 10 days (green) and every five days (purple).

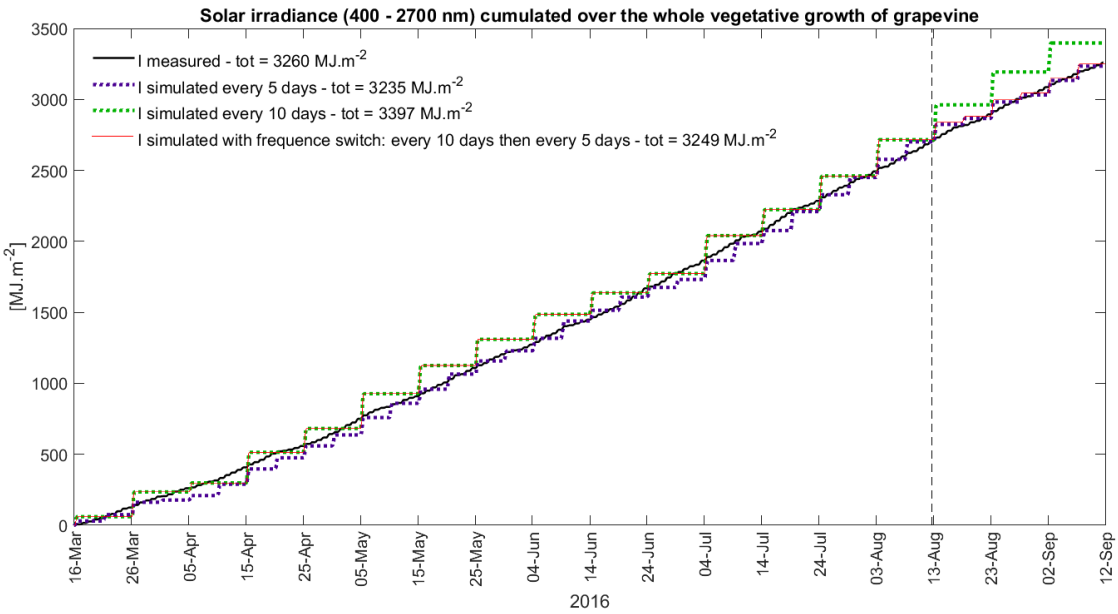

Figure 118: Simulations and measurement of cumulated solar irradiance (400-700 nm) at Lagardère in 2016. Measurements were performed every 10 minutes by the onsite pyranometer (black plot) while simulations were performed with the model DART at every hour of days of simulation. The days of simulation are spaced by either 10 days (green plot) or 5 days (purple plot). A combined time series of simulations is also considered where the frequency of simulation switches from 10 days to 5 days on August the 13th (red plot). The measurement of total cumulated energy from 15/04/2016 to 12/09/2016 reached 2852 MJ.m-2 while for the simulations with a 10 days, 5 days and mixed frequency the simulations reached 3099 MJ.m-2, 2945 MJ.m-2 and 2951 MJ.m-2 respectively.

VI.2.5 Radiative budget products and post-processing

VI.2.5.1 Raw products

Each day and hour of simulation generated the following radiative budget products: intercepted energy, scattered energy and absorbed energy. Simulations were parameterized so as to generate these latter variables in two forms:

1. Vertically integrated;
2. Vertically integrated and per triangle types. This option generated as many binary maps as various types of triangles representing land occupation types. **Figure 120** gives an example of the products obtained with the BIG TREE simulation on the 15/04/2016 at 15h local time.

Only quantities of **energy absorbed by grapevine** are analyzed here.

The radiative budget products of DART are provided in $W.m^{-2}.\mu m^{-1}$ as binary images. They were first converted in $W.m^{-2}$ through multiplying by the PAR spectral width $\Delta\lambda = 0.3\ \mu m$. Then two main post-processing treatments were applied respectively for masking non grapevine pixels and for time integration of the results.

VI.2.5.2 Pixel masking

The objective is to quantify the total energy absorbed by grapevine and document its variations in space and time depending on the vineyard arrangement.

Considered DART outcomes correspond to the sum of the quantities of energy which is absorbed by the triangles of grapevine type which fall at the vertical above each pixel of the image. Thus the raw images show a null value in the pixels which do not present any leaf of grapevine above them (see **Figure 119, first column**).

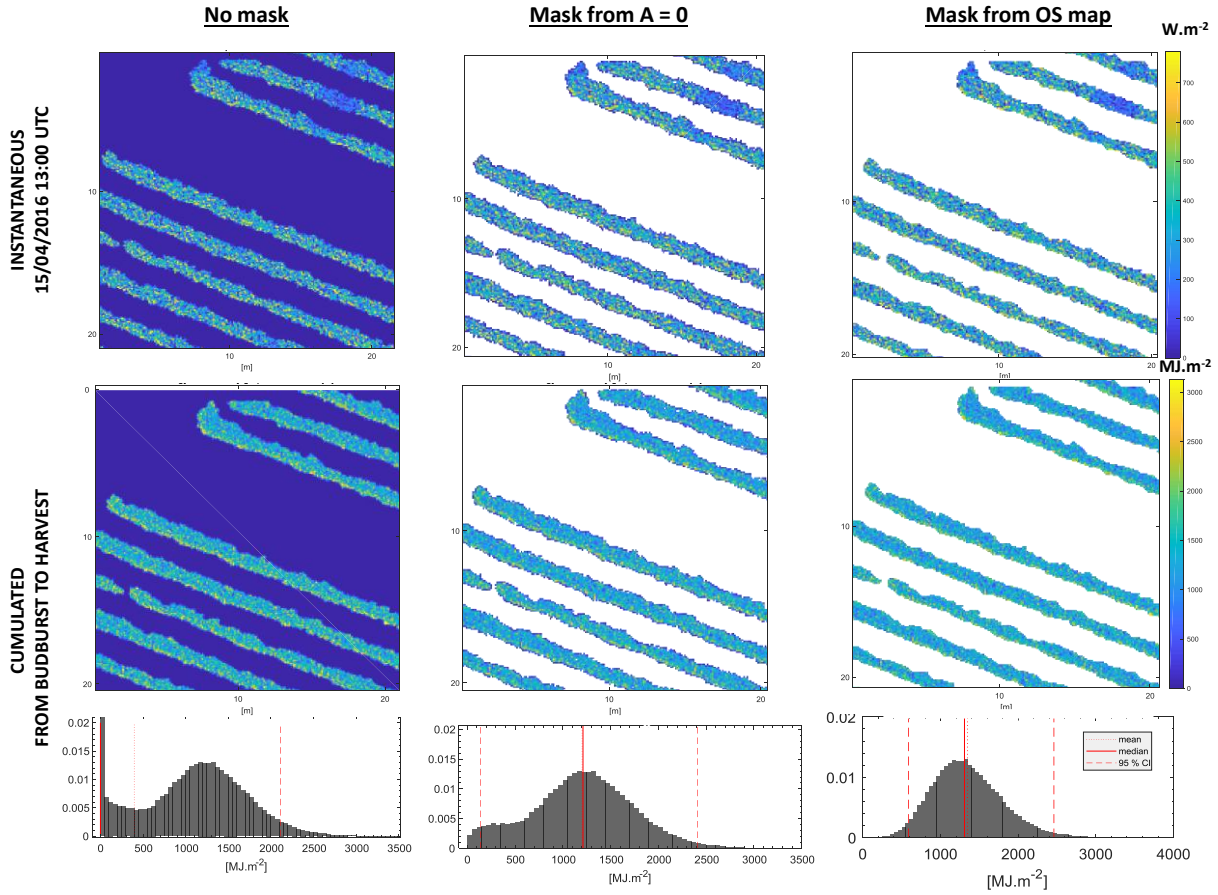

Figure 119: Consequences of pixel masking on the images of instantaneous (first row) and cumulated (second row and distribution) energy absorbed by grapevine. Raw images (first column) are either masked by removing the null values (second column) or by removing the pixels which are not of grapevine type based on the land occupation map of Lagardere vineyard (third column). An artefact remains at the border of grapevine row corresponding to pixels of very low energy. Masking images using the land occupation map highlights that these latter pixels of very low energy actually fall outside from the true vertical projection of grapevine foliage.

When these null values were masked, it enabled to delete pixels in the middle row compared to the unmasked situation. Nevertheless, masking only true null values revealed a systematic surrounding fringe of very low energy values at the border of grapevine rows. When cumulating the absorbed energy through the all growth season, pixels in this fringe created a bump of low but not null pixel values in the distribution of these images (see **Figure 119, second column**). In order to test its relevance, images were masked using the land occupation map. Keeping only pixels labeled as grapevine in the energy budget significantly reduced the total number of pixels compared to that when

applying the mask of null values. The pixels that were cropped were precisely the pixels implied in the border pattern (see **Figure 119, third column**). This comparison highlighted that the pixels of very low energy actually fall outside from the true vertical projection of grapevine foliage. One hypothesis is that this border pattern is an artefact due to the methodology applied in DART for horizontally projecting the radiative budget of a given type of triangle. DART uses flux tracking of downwards vertical rays and the "blurry" effect observed may be due to an authorized slight deviation of rays.

From the latter comparison, it can be concluded that it is necessary to mask all the images obtained using the land occupation map so as to only keep pixels truly corresponding to grapevine.

VI.2.5.3 Time integration

Each simulation outputs instantaneous values of radiative budget expressed in $W.m^{-2} = J.s^{-1}.m^{-2}$. In order to estimate the cumulated quantity of energy absorbed by grapevine through the whole vegetative period from budburst to harvest, the instantaneous values were extrapolated into time integrated budgets, expressed in $J.m^{-2}.period^{-1}$. For this purpose, days of simulation repeat between budburst (considered on 2016/04/15) to harvest (considered on 2016/09/12) are considered and account for the various time pace. From 2016/04/15 to 2016/08/12, days of simulations were spaced by 10 days, then from 13/08/2016 to 12/09/2016 they were spaced by 5 days (recall **VI.2.4.1 Optimization of the frequency of simulations**). During days of simulations, simulations were spaced by 1 hour and began and ended similarly to daylight. The extrapolation was performed by cumulating all the instantaneous energy budgets with a multiplicative factor that considers these various durations. The multiplicative factor equaled $f_{before\ 13-Aug} = 3600\ s.h^{-1} * 10$ and $f_{after\ 13-Aug} = 3600\ s.h^{-1} * 5$ respectively for the time and dates of simulation before or after the 2016/08/13.

Similar approach was applied for computing cumulated energy budgets over days and over each phenological stage of grapevine.

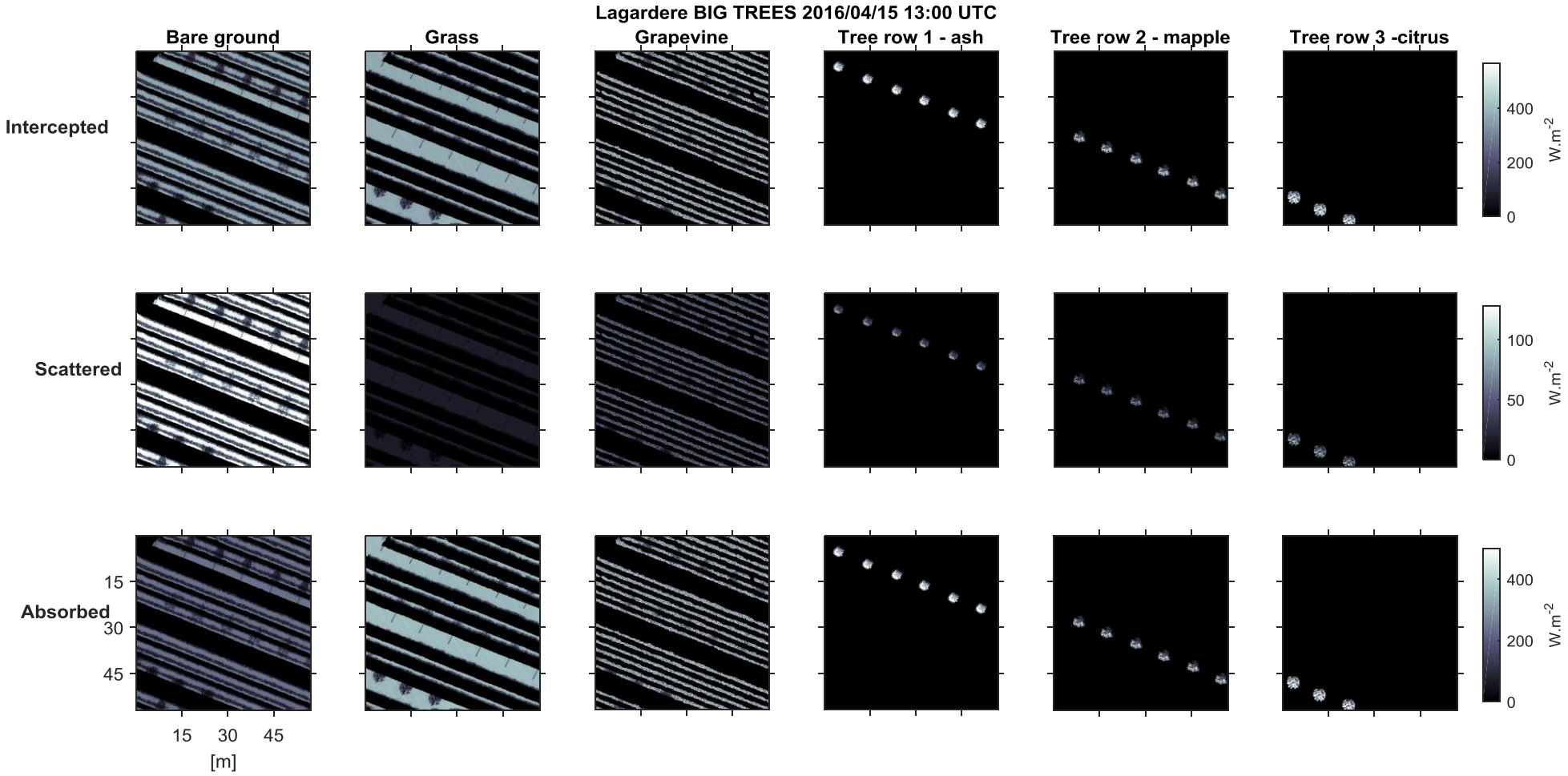

Figure 120: Radiative budget products obtained with the simulation BIG TREES on the 15/04/2016 13:00 UTC. The intercepted (row 1), scattered (row 2) or absorbed (row 3) energy was cumulated vertically and per triangle types (column labels) by the DART model. Time is given in UTC i.e. in solar time, corresponding to minus 2 hours to the local summer tim

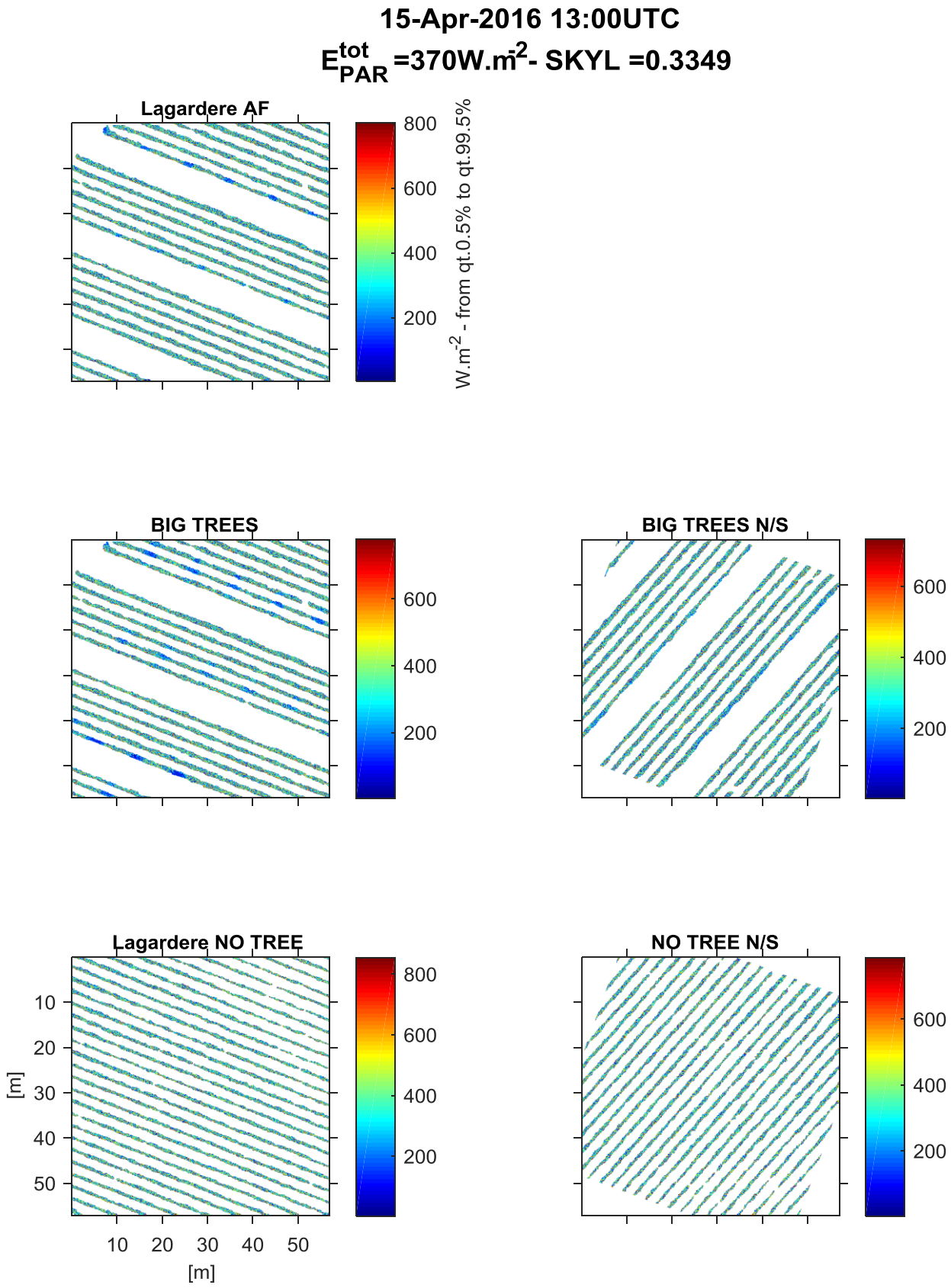

Figure 121: Images and histograms of the 2D cumulated PAR absorbed by grapevine on the 15 April 2016 at 13:00 UTC (minus 2 hours from local time). These maps are the results of 3D radiative budget simulations with the model DART considering successively five different mock-ups of vineyard. The color scale ranges from quintile 0.5% and quintile 99.5% of the image it applies to.

VI.3 Results and discussion

VI.3.1 Instantaneous patterns of light absorption

VI.3.1.1 Variability in time

The quantities of energy absorbed by grapevine were cumulated and projected in 2D. **Figure 122** provides an example of the simulation results obtained on 2016/04/15 at 13:00 UTC, for each of the five mock-ups of vineyard. More images are presented in **Annex L**, notably the daily time serie obtained on the 2016/08/13 and on 2016/08/18. These two latter dates are quite similar in terms of solar declination angle within the year but strongly differ by the meteorological conditions: total irradiance was high at midday on the 2016/08/13 corresponding to a clear sky day while it was very low on 2016/08/18 corresponding to a completely overcast sky. From the images obtained with clear skies (SKYL below 0.8) one can observe patterns of lower absorption which correspond to tree shadows. The length of these patches increases with the height of the trees while their intensities seems proportional to the tree foliage densities. In addition, striking is the very high variability of values between one pixel and the right neighboring ones. This variabiltiy appears in all vineyards no matter their orientations and the agroforestry practices.

The mean and standard deviation of each simulation were computed per vineyard mock-up as well as the average of these values over all the mock-ups. From bud burst to harvest, mainly four different daily trends occurred as illustrated by **Figure 122**:

- Totally clear sky days, e.g. 13th-Aug. 2016
- Mixed days, which divides themselves in two types:
    - Days with constantly alternating sunny and cloudy events (e.g. the 14th July 2016)
    - transition days, with an overcast sky during half on the day and a clear sky during the other half (for e.g on the 14th June 2016);
- Totally overcast days, e.g. 18th-Aug. 2016.

On the one hand, absorbed PAR seems under the direct influence of the total irradiance and grapevine architecture: in average, the PAR absorbed equals $0.81 * E_{PAR}^{tot}$ for the spring mock-ups of grapevine, and equals $1.3 * E_{PAR}^{tot}$, with the summer mock-ups of grapevine, whatever the total irradiance in PAR and whatever the SKYL. On the other hand, the standard deviation seems under the combined influence of the total irradiance and the SKYL: it increases with increasing E_{PAR}^{tot} and decreasing SKYL. For example, in the afternoon on the 13th-Aug. 2016, total irradiance and PAR absorption decreased as the sun zenit angle increased. At the same time, the SKYL importantly decreased, skipping from 72 % to 11 %, which seems to explain a constant increase of the standard deviation of the absorbed PAR. The increase of images variability in case of completely clear skies could be explained by the fact that shadow patches are the most pronounced. In addition, it seems that

high values of absorbed PAR enhances the variability of results between mock-ups of vineyards. In these conditions, the mean PAR absorption in monocropped vineyards (*Lagardere NO TREE* and the *NO TREE N/S*) seem systematically higher than in the simulated agroforetsry vineyards.

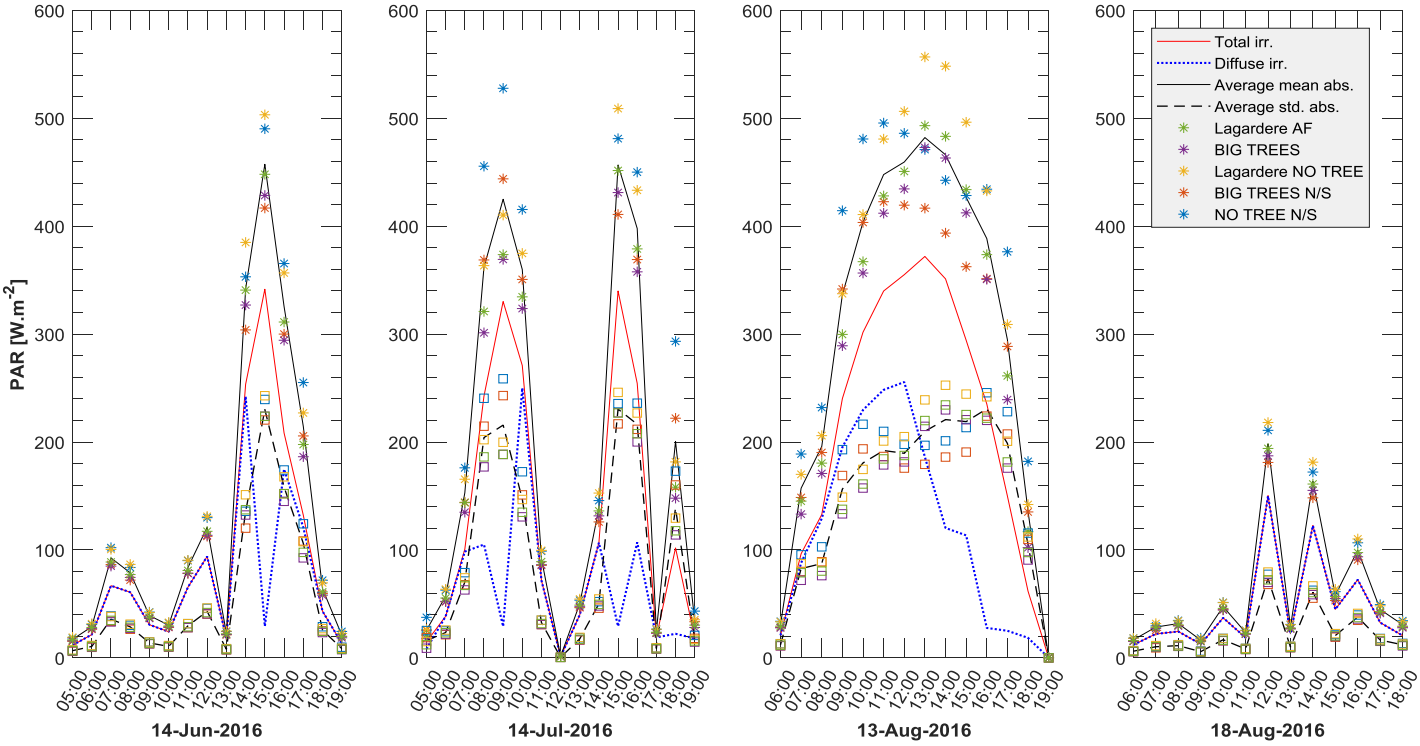

Figure 122: Mean (*) and standard deviation (□) of the energy absorbed by grapevine from simulations on 14/06, 14/07, 13/08 and 18/08. Time is given in UTC (i.e. minus 2 hours from local time). Irr.= irradiance. Abs. = absorbed; PAR = Photosynthetically Active Radiations

The daily statistics of each days of simulation are shown in **Figure 123** and confirm the very important contribution of the meteorology to the absorbed PAR. In all images, the median daily absorbed PAR reproduces the trend observed in the daily PAR (recall **Figure 138**). In addition, some differences can be observed between the different mock-ups during clear sky days of summer and eventually during mixed days of spring: the agroforestry vineyards systematically show lower daily budgets than the monocropped ones (by 20 to 50 %) and their monocropped references: on clear sky days, the daily aborbed PAR is lower (by 20 to 50 %) in agroforestry vineyards than in the monocropped ones. Also the simulation with big trees indicate that, in this configuration, the vine absorbed about 5% less energy than in the case with small trees. The impact of the row orientation is ambigous at this stage: on the one hand, in monocropped vineyards, rows oriented N/S absorbed about 40 % more energy than with a E/W orientation; On the other hand, under agroforestry practices, the the vine in the BIG TREES and E/W oriented configuration, absorbed about 60 % more PAR than in the BIG TREES N/S configuration. All the latter differences do not apply under overcast days which generated low budgets of same range for all mock-ups.

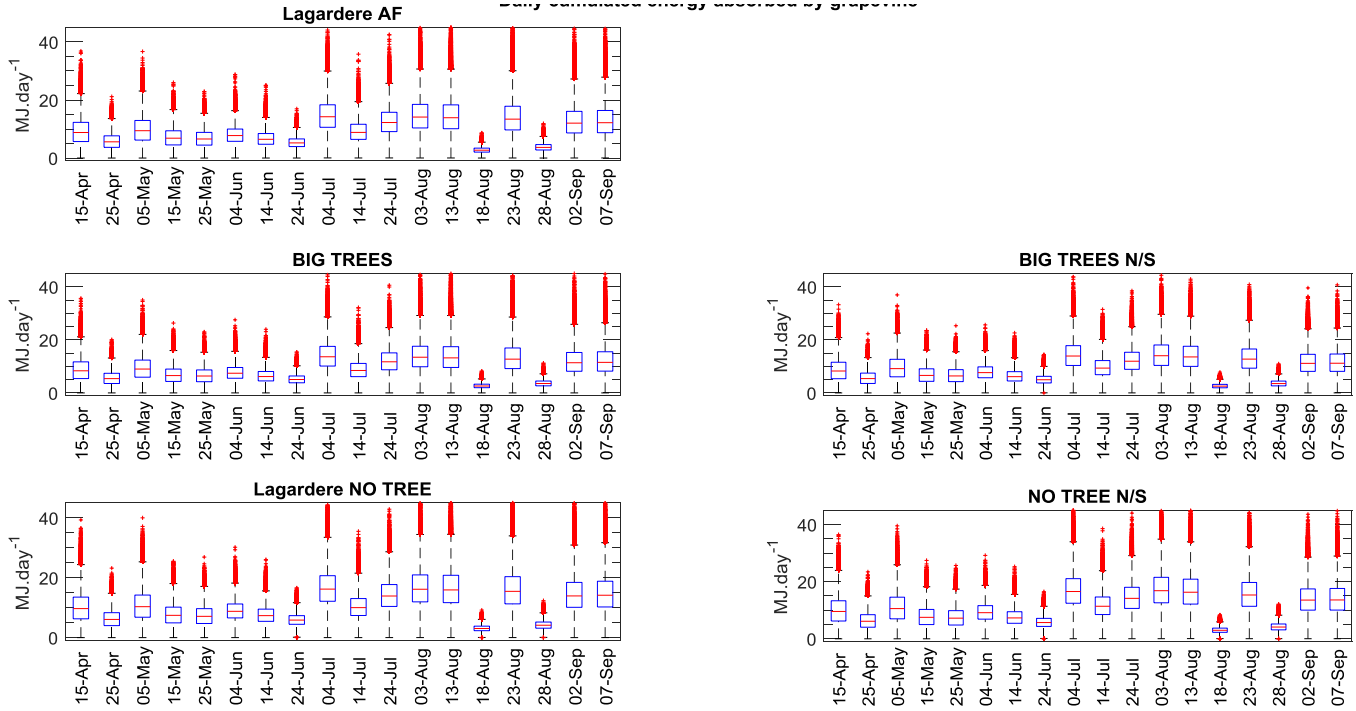

Figure 123: Daily cumulated PAR absorbed by grapevine from simulations with five different mock-ups of vineyard

The daily mean absorbed PAR is provided per phenological stages of grapevine in **Figure 124**. For all the simulated configurations, it is the highest from flowering to veraison, a bit lower from budburst to flowering and it is the lowest from verasion to harvest. Two factors could explain these differences, either the variations in the Earth position around the sun, and/or seasonal differences in cloud cover. As the SKYL remains quite similar between all phenological stages, only the first factor (the declination angle) seems to be involved.

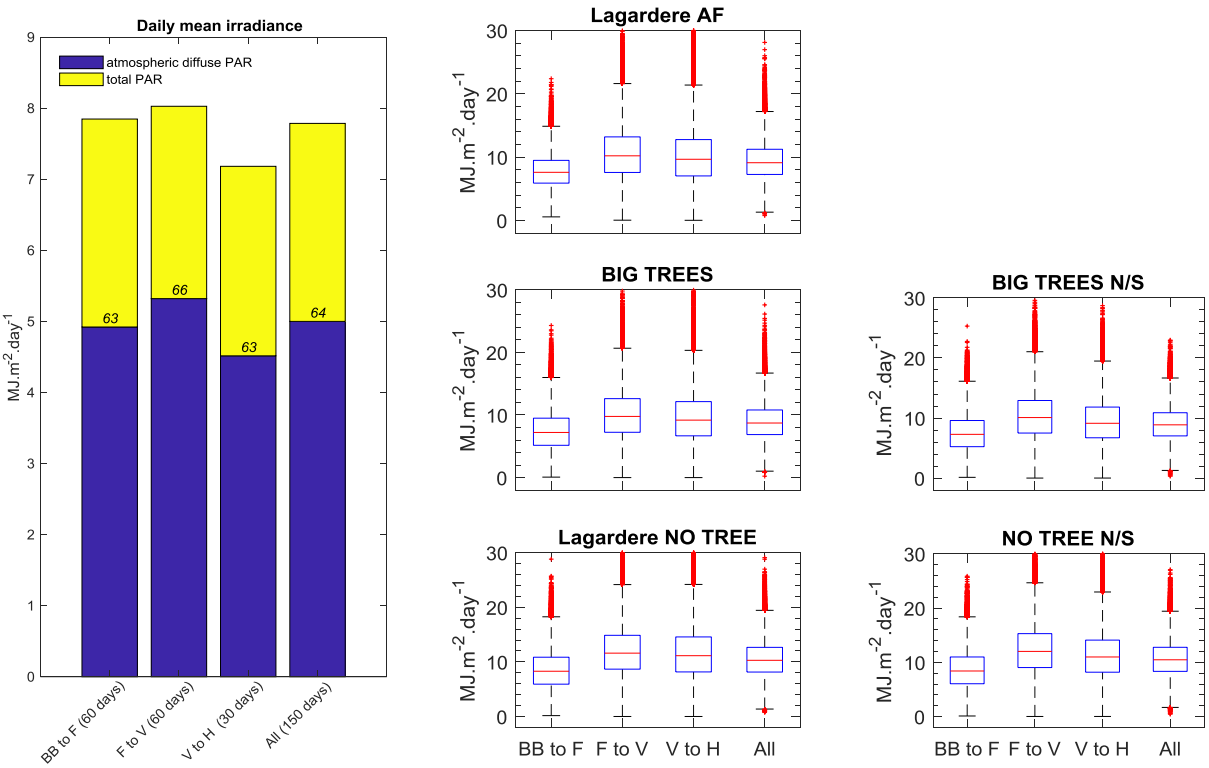

Figure 124: Variations of meteorology (left) and PAR absorbance (right) per phenological stages. SKYL is provided in percents. Abbreviations: the BB to F: Bud burst to flowering; F to V: Flowering to Veraison; V to F: Veraison to harvest; All: from bud burst to harvest.

VI.3.1.2 Contribution of the 3D radiative transfer methodological approach

Choosing a 3D radiative budget model for studying light regime in an agroforestry system was innovative compared to the already tested modeling approaches reviewed in **Table 18**. It notably allowed (i) representing the canopies of grapevine and trees using accurate3D objects, (ii) simulating both the direct and the diffuse fractions of natural lights, and (iii) considering multiple light scattering light. The contribution of the 3D approach using DART was assessed by comparing the simulation results obtained on the 15/04/2016 13:00 UTC with the BIG TREES vineyard mock-up, with that obtained with three modified simulations.

1. The first modified simulation was built in order to simulate the results that would be obtained with a radiative transfer model representing canopies based on the **turbid medium** analogy, typically the RATP model of Sinoquet et al. (2001) (**Table 18**). The leaves of both grapevine and trees were represented as voxels filled with turbid medium. With this representation, the width of grapevine row still follows realistic variations according to the land occupation map. The height of grapevine canopy applied is 50 cm for this date. Similarly to the BIG TREES mock-up, variations were artificially introduced by applying a standard deviation of 10 cm.
2. The second modified simulation was built in order to test the contribution of simulating diffuse sources of light from the atmosphere and multiple scattering. It reproduces the results that would be obtained with a geometric model which represents canopy with **turbid medium**

and which empirically simulates light propagation: **no diffuse radiation and no scattering**. It was performed re-using the latter turbid mock-up (case 1) but light was changed to only direct source (sun) and scattering was not allowed. For this purpose, the total irradiance was maintained at 370 $W.m^{-2}$ for the PAR waveband but the SKYL equals 0 %. In addition, the simulation was stopped at first iteration for preventing scattering of 1^{st} order incident light.

3. The third modified simulation was performed using the same mock-up of vineyard as in the BIG TREES simulation except **that grapevine canopy was transformed in horizontal 2D**. Grapevine was represented as its sole 2D projection on the ground, based on the land occupation map.

Figure 120 gives the quantities of energy that grapevine absorbed in the three latter simulations and in the 'BIG TREES' simulation, which is the reference they all diverge from.

Firstly, concerning vegetation modeling choices, it shows that representing grapevine and tree leaves as cells of turbid medium led to a budget of absorbed energy of similar order of magnitude than when represented by clouds of triangles. The intensity of light depletion in the shadow patches is also of same magnitude. Nevertheless, the turbid medium analogy highly reduced the variability within shadow patches while when representing canopies - both grapevine's and trees' – using accurate 3D objects, it implied a grainy aspect in the absorbed PAR projections. This observation suggests that the simulation of sunflecks highly depends on the chosen approach for representing vegetation canopies. One should note that in the modified simulations #1 and #2, the turbid cells representing tree leaves were quite accurately distributed in 3D as they were distributed by DART respecting accurate 3D models of trees and the size of the voxels is small (of same order as the size of the leaves). In order to investigate more the accuracy of sunflecks modeling, it could be worth simulating the radiative budget with tree canopies represented as full ellipsoids or full conic shapes of constant leaf area densities, i.e. not allowing any sunflecks. In this case, the results obtained would correspond to simulations with the simple model of light transmission of Jackson and Palmer (1979).

Concerning grapevine modeling, using turbid medium cells enhanced the implication of the side and orientation of the vinerows compared to a representation based on clouds of triangles. Indeed, in the first case, the southern and sunny sides of grapevine rows resulted intensively insolated and the northern ones resulted in intense shade. In addition, not taking into account grapevine height (#3: horizontal 2D representation) completely modified the range of values of the absorbed PAR as well as the intensity of energy depletion within the shade patches.

Secondly, concerning light modeling, not considering the diffuse fraction of light and multiple scattering of direct beams completely modified both the range of values of the absorbed PAR and the intensity of energy depletion within the shade patches: the absorbed PAR is reduced by 90 % in average in the BIG TREES reference while it is only reduced by 55 % in the turbid representation.

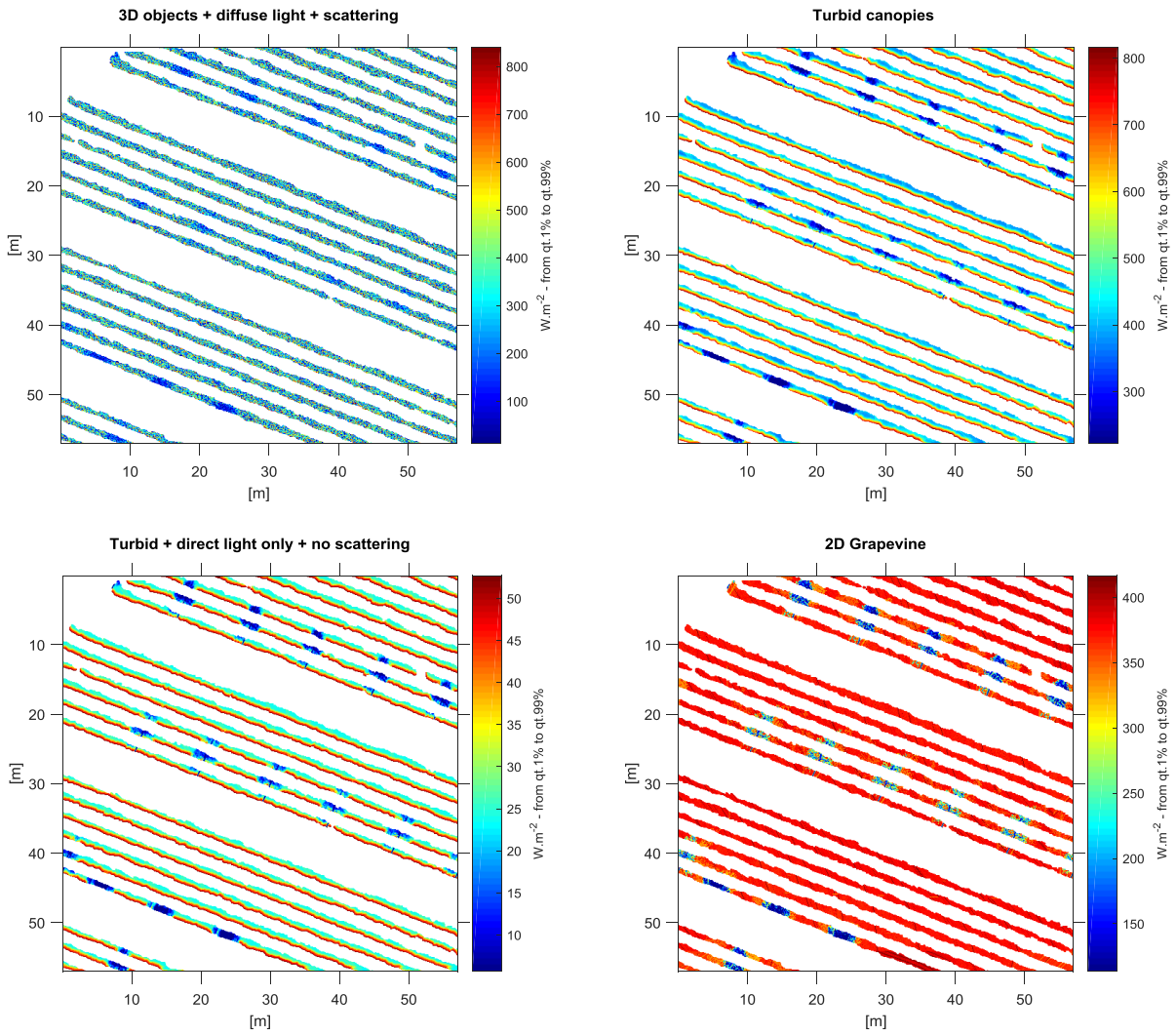

Figure 125: Influence of light and/or vegetation modeling choices on the instantaneous budget of absorbed PAR. Simulations were performed on 15/04/2016 13:00 UTC with a simulated total irradiance = 370 W.m-2. The SKYL = 33 % for all the simulations with diffuse light. The BIG TREES simulation is used as a reference (top left). Three different configurations were considered: 1) the tree and grapevine leaves were changed into voxels of turbid medium (top right); 2) the tree and grapevine leaves were changed into voxels of turbid medium (same as 1) plus light was only direct (SKYL = 0%) and scattering of light was not allowed (bottom left); 3) Same as BIG TREES but grapevine canopy was represented as its sole 2D projection on the ground (bottom right). For each image the color scale ranges from quintile 1 % and quintile 99 % of the image it applies to.

VI.3.1.3 Scene border effects

Shade patches from trees outside mock-ups of the vineyards can be observed. They are an artifact of simulation coming from choosing the infinite slope mode in DART. As mentioned previously (recall **From finite scenes to continuous landscapes**) this mode repeats infinitely the scene of simulation except the topography which is extended infinitely from the slope at the border of the scene. This mode has been activated in order to prevent border artifacts in our simulations. Nonetheless, repeating the simulated images as shown in **Figure 126** brings to the conclusion that it has actually been detrimental as it modified the overall arrangement of the agroforestry plantation in a non controlled way and thus led to patterns of shade on the border of the radiation budget images.

Two strategies of improvements are thought of. Firstly, for an immediate correction, the images produced should be cropped so as to remove the border zones presenting bias from a non realistic neighborhood. Secondly, necessitating more work, simulations should be run again but using the isolated mode. In this mode, because border effects from the sudden interruption of topography could appear, the scene should be extended so as to offer a final extent after border removal, which would be sufficiently representative of the agroforestry planting.

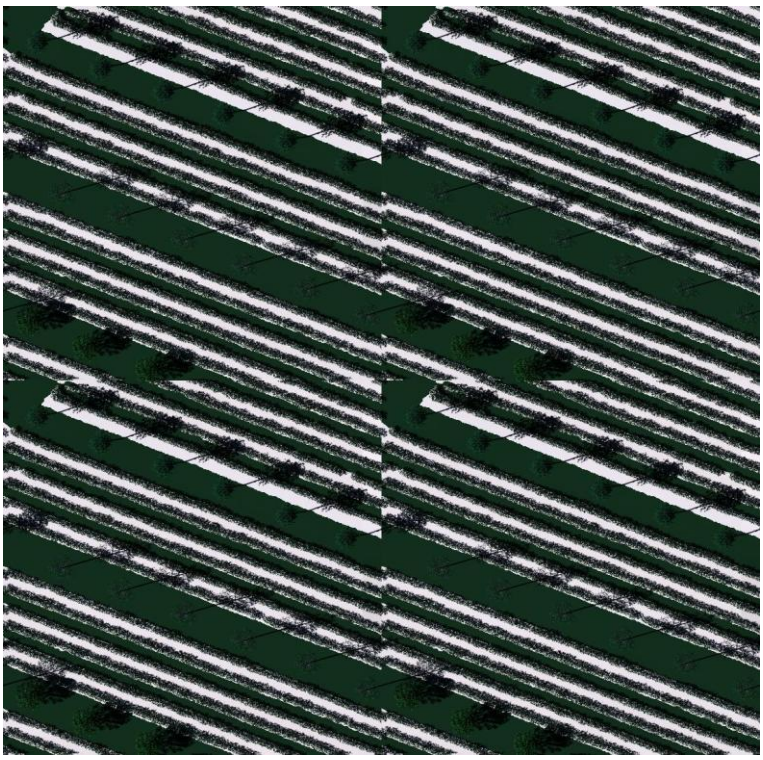

Figure 126: Juxtaposed repetition of the simulated RGB image obtained with the model DART and the BIG TREES mock-up of vineyard at nadir on the 25/05/2016 at 15:00 UTC (local time is UTC + 2 -Solar time is UTC)

VI.3.2 Cumulated budgets of absorbed PAR over the whole vegetative growth of grapevine

VI.3.2.1 Average budgets

Figure 127 shows the 2D maps representing sums of all the energy absorbed by the vertical column of foliage located above each pixel of the map over the simulation period. **Figure 128** shows the statistics and normalized distribution of these latter images. The total quantity of PAR absorbed by grapevine is in average of 1346 $MJ.m^{-2}$, 1409 $MJ.m^{-2}$ and 1581 $MJ.m^{-2}$ respectively in the *BIG TREE*, *Lagardere AF* and *NO TREE* arrangement. In the case of a N/S orientation, the PAR budgets observed were in average of 1360 $MJ.m^{-2}$ and 1600 $MJ.m^{-2}$ respectively for the *BIGTREES N/S* and *NO TREE N/S* arrangement. These observations suggest that the agroforestry vineyards absorbed from 10 to 15 % less energy than the monocropped vineyards. The increase of tree height between *Lagardere AF* and *BIG TREES* reduced the budget in PAR by 4.5 %. These observations apply for all the orientations.

For both monocropped vineyards and agroforestry vineyards, a N/S orientation of the rows showed a total budget very slightly greater than that with a NW/SE orientation (by 1%).

VI.3.2.2 Spatial variability

Striking is the internal variability within all the images: standard deviation is 466 $MJ.m^{-2}$ on average and amounts from 27 to 36 % of the mean cumulated PAR, depending on the vineyard mock-up. Its spatial heterogeneity is expected to be higher in agroforestry vineyards than in monocropped vineyards because of shade from the discontinuous canopies of the tree but the standard deviations observed from simulations with agroforestry vineyards do not exceed that with monocropped ones. Patches of depleted PAR absorption caused by trees appear in the *Lagardere AF*, the *BIG TREES* and the *BIG TREES N/S* images. For example, in the *BIG TREES* image, a patch of important PAR reduction notably appears on the first grapevine row towards north from tree row #3, which is constituted by *Citrus cinensis* trees of 7-m height and dense foliage. In the *BIG TREES N/S* image, a similar patch appears on the first grapevine row towards north from tree row #1, which is constituted by *Fraxinus Excelsior* trees of 13.7-m height. In these patches of low absorption, the cumulated absorbed PAR ranges approximately from 600 to 1300 $MJ.m^{-2}$ and shows again a high variability between one pixel and the neighboring ones.

In addition, based on the conclusions of chapter II, PAR budgets should present a greater heterogeneity with rows oriented NW/SE than when oriented N/S. According to the results in **Figure 128**, this hypothesis works for a monocropped vineyard: the absolute and relative standard deviations of the *NO TREE* distribution are significantly greater than that of the *NO TREE N/*S distribution. Nevertheless, for agroforestry vineyards, the relative and absolute standard deviations actually increase from the *BIG TREES* to the *BIG TREES N/S* budget. This suggests that when grapevine and tree rows combine, the orientation of the rows has a converse impact on the spatial heterogeneity of light absorption by grapevine. In our simulations, the agroforestry arrangement oriented N/S led to less spatial heterogeneity than with a rather E/W orientation. This specificity of agroforestry vineyards compared to other alley cropping-systems might be due to the row structure of grapevine canopy.

At this point, two types of spatial variability can be distinguished:

i) The intrinsic heterogeneity of a vineyard,
ii) The heterogeneity due to agroforestry practices.

Both types are successively investigated in the following sub-sections.

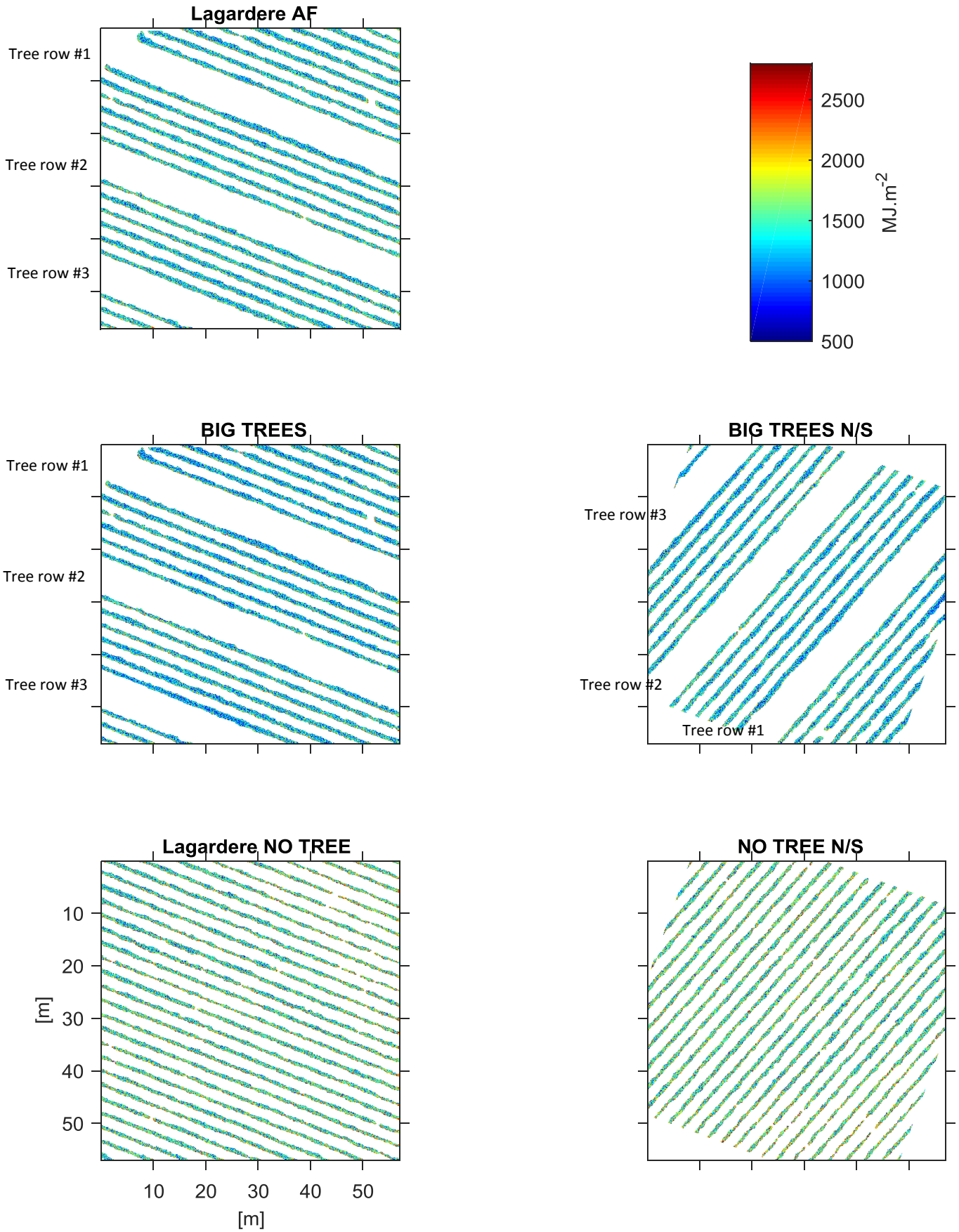

Figure 127: Energy absorbed by grapevine cumulated from budburst to harvest. Five mock-ups of vineyards are compared. In order to generate more contrasts, the color scale is saturated below the minimum 2% percentile of all mock-ups and above the maximum 98 % percentile.

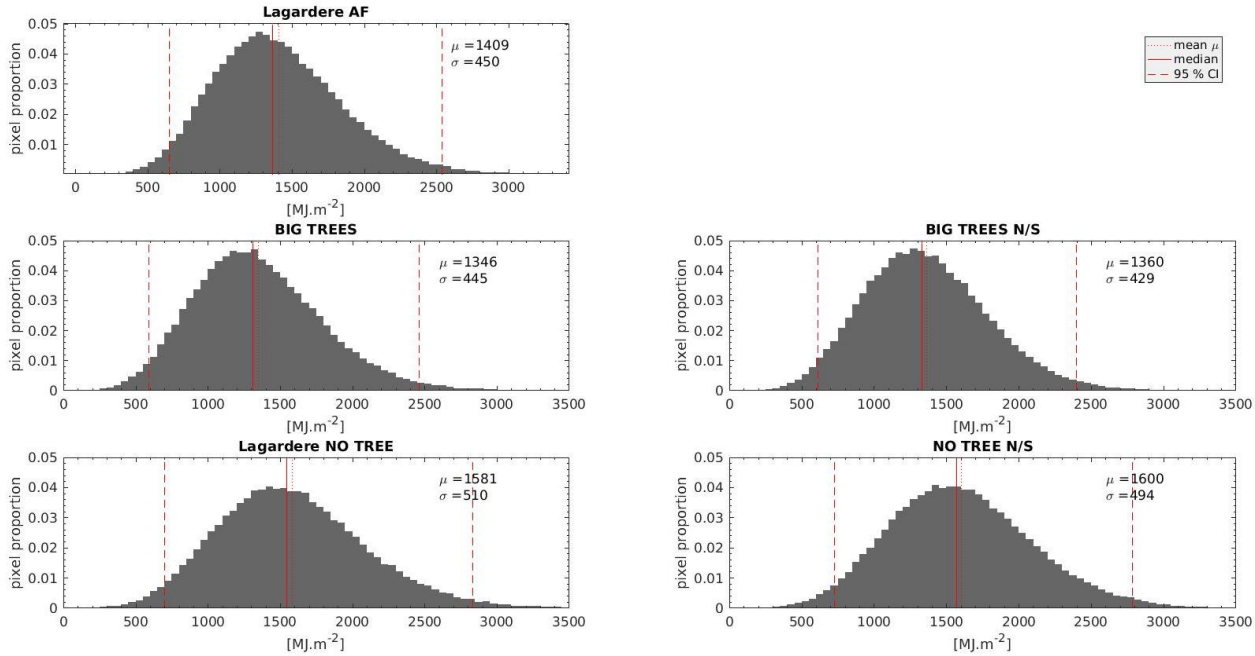

Figure 128: Distributions of the energy absorbed by grapevine over all the season growth and cumulated in 2D. μ: mean – σ: standard-deviation. If expressed as percentages of the mean, standard deviation equals respectively: $\sigma_{Lag.AF} = 32\ \% - \sigma_{BIGTREES} = 33\ \% - \sigma_{Lag\cdot NOTREE} = 32\ \% - \sigma_{BIGTREES_{NS}} = 36\ \% - \sigma_{NOTREE_{NS}} = 27\ \%$.

Intrinsic variability of light regime in a vineyard

All images shown in **Figure 127** present a very high intrinsic heterogeneity which corresponds to variations of the PAR budget between pixels in a same area. They apply no matter the monocropping/agroforestry practices. Three factors explain this intrinsic heterogeneity.

LATERAL POSITION WITHIN A GRAPEVINE ROW

Firstly, part of it seems due to the **lateral position of the leaves within grapevine row**, which is either inside the row or on one of the edges. For leaves on the edges, orientation also seems to contribute. The overall contribution of leaf position within grapevine row was tested by sorting grapevine pixels into five categories: pixels on the edge facing North, South, East, West and in the center of the row (**Figure 129**). The methodology applied for this purpose is presented in chapter IV (**Relative position within grapevine rows: edge and center pixels**). Vine rows with a NW/SE orientation have their leaves classified either in the northern edge, center or southern edge categories, while with a N/S orientation, the western edge, the center and the eastern edge categories dominate. The amounts of energy absorbed per class of leaf position are given in **Figure 130**. In overall, leaves located in the center of the canopy present the lowest budget of absorbed PAR, certainly because of shading by the more external leaves. The leaves located on a northern edge present a budget only greater by 3 % to that of central leaves. Leaves on the southern edge present the greatest budgets, the absorbed PAR being 27 % greater than in the center. The eastern and western edges present intermediate budgets of similar range: both receive about 10 % more PAR than in the center. Thus, the leaf position factor strongly applies for NW/SE orientations of the rows while it shows very less

relevancy with N/S orientations. This observation applies for both the agroforestry/monocropped configurations. The distributions of absorbed PAR per leaf position are provided in **Annex N**. Though differences of PAR regime between classes of leaf position are significant, these distributions show that the heterogeneity is very high within each class. This suggests that additional factors intervene.

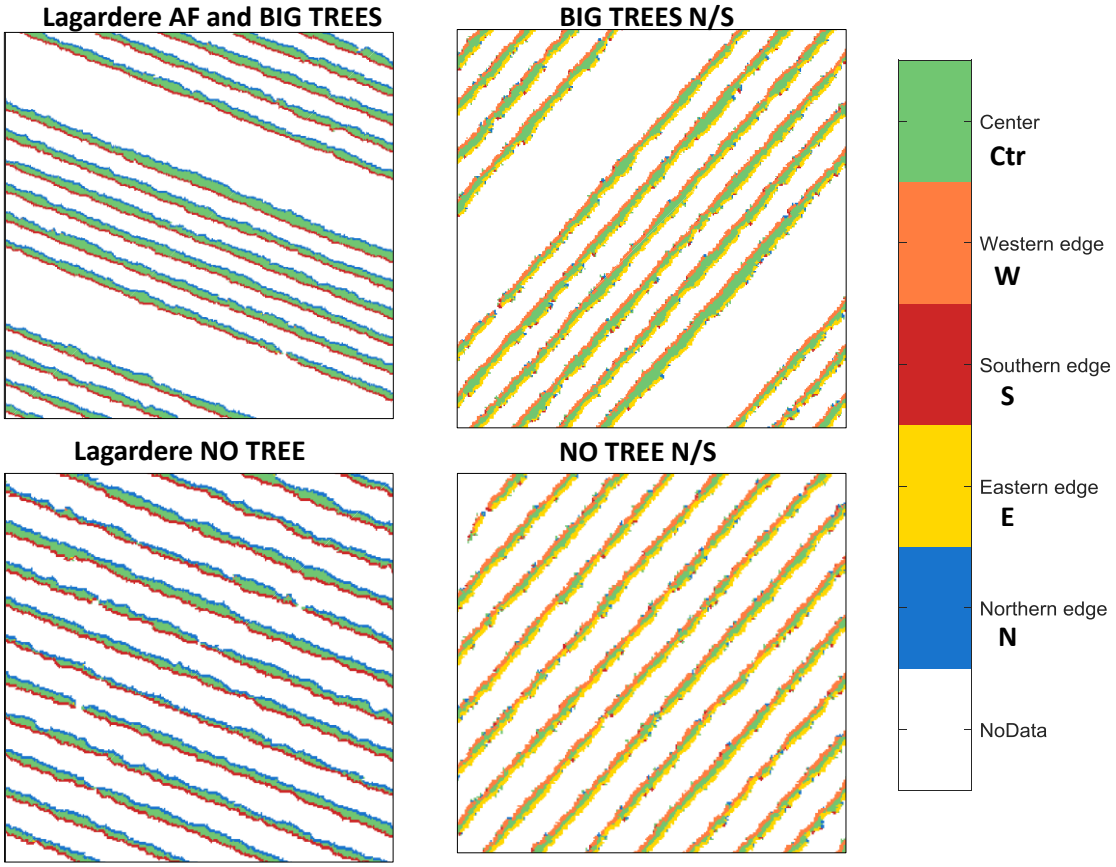

Figure 129: Classification of grapevine pixel position within grapevine rows.

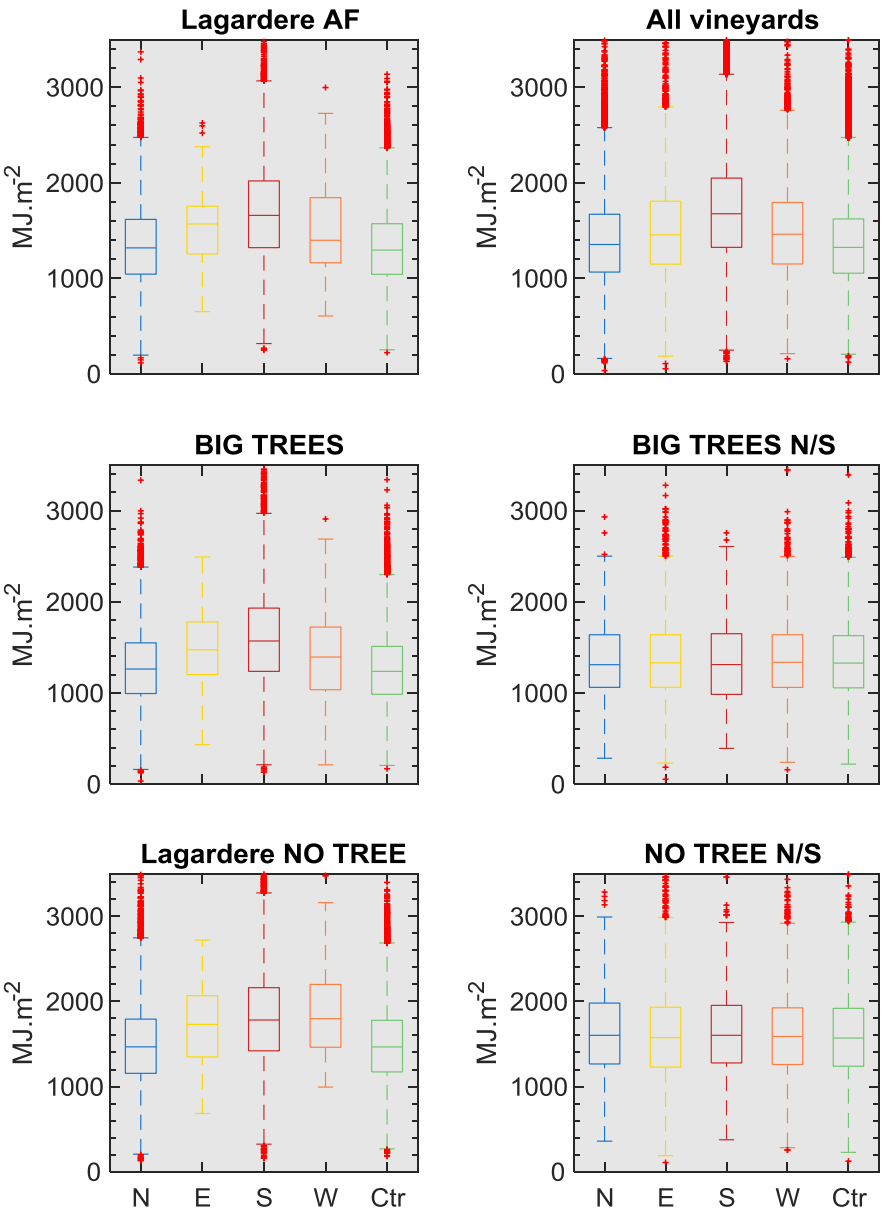

Figure 130: Box plots of the total energy absorbed by grapevine from budburst to harvest considering different positions of the leaves within the canopy, namely N: northern edge, E: eastern edge, S: southern edge, W: western edge, Ctr: center of the row. Results are provided for each mock-up of vineyard used for simulations, as well as for overall, on the top right corner. On each box, the central mark indicates the median, and the bottom and top edges of the box indicate the 25th and 75th percentiles, respectively. The whiskers extend to the most extreme data points not considered outliers, and the outliers are plotted individually using the '+' symbol. Whisker extends to approximately +/−2.7σ, σ being the standard deviation.

WIDTH OF THE ROW

The second factor concerns the **width of grapevine rows**. From **Figure 127**, it seems that the wider the row, the lower the budget of absorbed PAR. This is noticeable by comparing the two budgets from monocropped vineyards, (namely Lagardere NO TREE and NO TREE N/S), where local enlargements of grapevine rows coincide with low budgets of absorbed PAR. This might be related to the amount of leaves at the center of the row, which is basically greater for wide rows than for narrower ones. This observation leads to discuss again the fact that in simulations, the absorbed PAR budget of agroforestry vineyards is systematically lower than for monocropped vineyards, no matter

the tree height. The proportions of pixels falling in the Center class are actually greater by 15 % in the agroforestry cases than in their corresponding monocropped mock-ups. This confirms that the grapevine rows are wider in the mock-ups of agroforestry vineyards than in the mock-ups of monocropped vineyards. This may explain the gap of range between the radiative budgets of agroforestry vineyards and monocropped vineyards obtained from simulations. One can wonder if this source of variability could have been artificially amplified by the morphological representation of grapevine canopy that was adopted in the 3D mock-ups. Indeed, the leaf area density of grapevine leaves was set to 4.5 for all voxels of grapevine canopy, no matter their lateral position within grapevine rows. This representation inevitably led to important shade from external leaves onto the central ones. Nevertheless, according to Louarn et al. (2007), the leaf area distribution of grapevine leaf is rather constant along the horizontal axis which is at right angle to grapevine row. The results of these latter authors applied for various types of trellis systems with shoot positioning, including VSP-2W (Bilateral cordons with two pairs of catching wires), which is the closest to the grapevine architecture simulated. It can be concluded that (i) the variability in PAR budgets due to the width of grapevine row was well represented in our simulations and (ii) and that an increase in the width of grapevine rows, tends to locally deplete the absorption of PAR by grapevine.

ARTIFACTS FROM ANGULAR DISTRIBUTION OF THE LEAVES

A third factor of intrinsic variability may correspond this time to an artefact related to the representation of grapevine leaves in the mock-ups generated with the DART model. Indeed, the absorbed budgets of PAR projected in 2D still shows a grainy aspect when it is considered within homogeneous zones of tree shade, of leaf position within rows or of row width. These random and very high variations from one pixel to its immediately adjacent ones correspond to the many outlier values observed in all instantaneous (**Figure 120**) and time integrated **(Figure 128)** budgets of PAR absorption by grapevine. The hypothesis which is made incriminates the angular orientation of the leaves and more precisely the uniform distribution of the azimuth. Indeed, as illustrated on **Figure 131**, given that the dimensions of grapevine leaves are of same range as the dimensions of voxels and given the leaf area density applied, there are only two to three triangle objects representing grapevine leaves per column of voxels. In this configuration, the angular orientation of a given triangle has very important impact on the overall budget of the column it stands in. Sunflecks thus are very likely to occur. Their representation within grapevine canopy itself may certainly have been strongly and artificially increased in the simulations, compared to reality. Indeed, DART only allows to set a preferential distribution of the zenithal angle of triangle objects, which was set to erectophile, but does not permit to define a prevalence in their azimuth angle, which was thus uniformly distributed in mock-ups (Grau 2012). However, Mabrouk et al. (1997) and Louarn et al. (2007) all underline that due to the strong anisotropy of row canopies, the leaf azimuth strongly depend on the leaf position of the

canopy and that the edge leaves preferentially orientate themselves parallel to the grapevine row border.

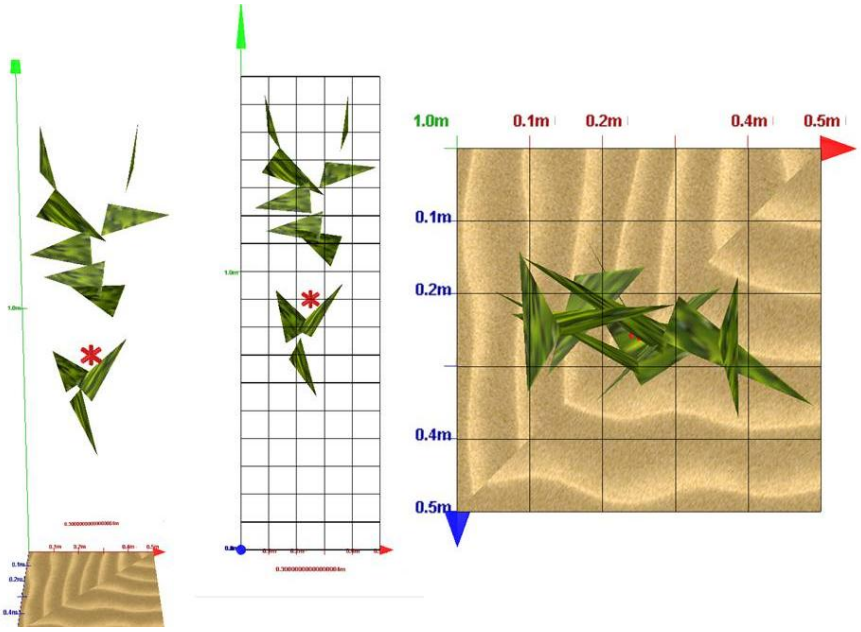

Figure 131: Three dimensional arrangement of grapevine leaves as represented in the mock-ups of vineyards built under the DART model. Zoom on three columns of voxels filled with triangular objects representing grapevine leaves. Their morphological properties are: shape = triangle, area = 0.015 m^2; leaf area density = 4.5 $m^2_{leaves}.m^3$; canopy bottom height = 0.5 m; canopy top height = 1.5 m; XYZ resolution of the voxels = 0.1 m.

Consequently, two strategies for improving the representation of grapevine canopy are identified:

i. Either by adding in the DART model the option of a preferential distribution of the azimuth of leaves.

ii. Or, for even more accuracy (Kimes and Kirchner 1983), by directly providing a 3D mock-up of grapevine rows, i.e. a set of 3D coordinates of the leaves, and eventually woody parts. Some 3D mock-ups of grapevines were notably developed by (Louarn et al. 2007, 2008) who, by this means, showed the great influence of grapevine trellis system and overall architecture on its light regime. They also insist on the fact that mock-ups of individual grapevine stocks do not apply for overall canopies of grapevine structured as rows, which necessitate specific mock-ups.

A more developed comparison between '2D' representation of grapevine canopy (similar to that adopted in this work) and 3D realistic representations can be found in López-Lozano et al. (2011). The importance of leaf area density and angular distribution are questioned all together.

CONSEQUENCES OF A MEAN FILTERING TREATMENT

The very high intrinsic heterogeneity in the radiation budgets obtained by simulations with DART could prevent from detecting contributions of extrinsic contributors to the spatial variability. For this reason, an attempt was made for smoothing the maps by applying a mean filtering treatment. This treatment was applied on a window of 3 x 3 pixels (i.e. 30 cm x 30 cm). The grainy aspect of the

images mostly due to variations of the leaf angular distribution was importantly reduced. On the contrary, the heterogeneity due to variations in leaf position within grapevine rows, to variations of the row width and to the vicinity of trees seem all together enhanced.

Figure 133 shows consequences of the mean filtering treatment on the statistical distribution of the images. The mean filtered distributions confirm the relative differences observed between (i) the short vs. the tall tree agroforestry vineyards and (ii) the agroforestry vs. monocropped vineyards. It also shows more spatial variability with a NW/SE orientation than with a N/S one while orientation seems to impact the mean cumulated energy only very slightly.

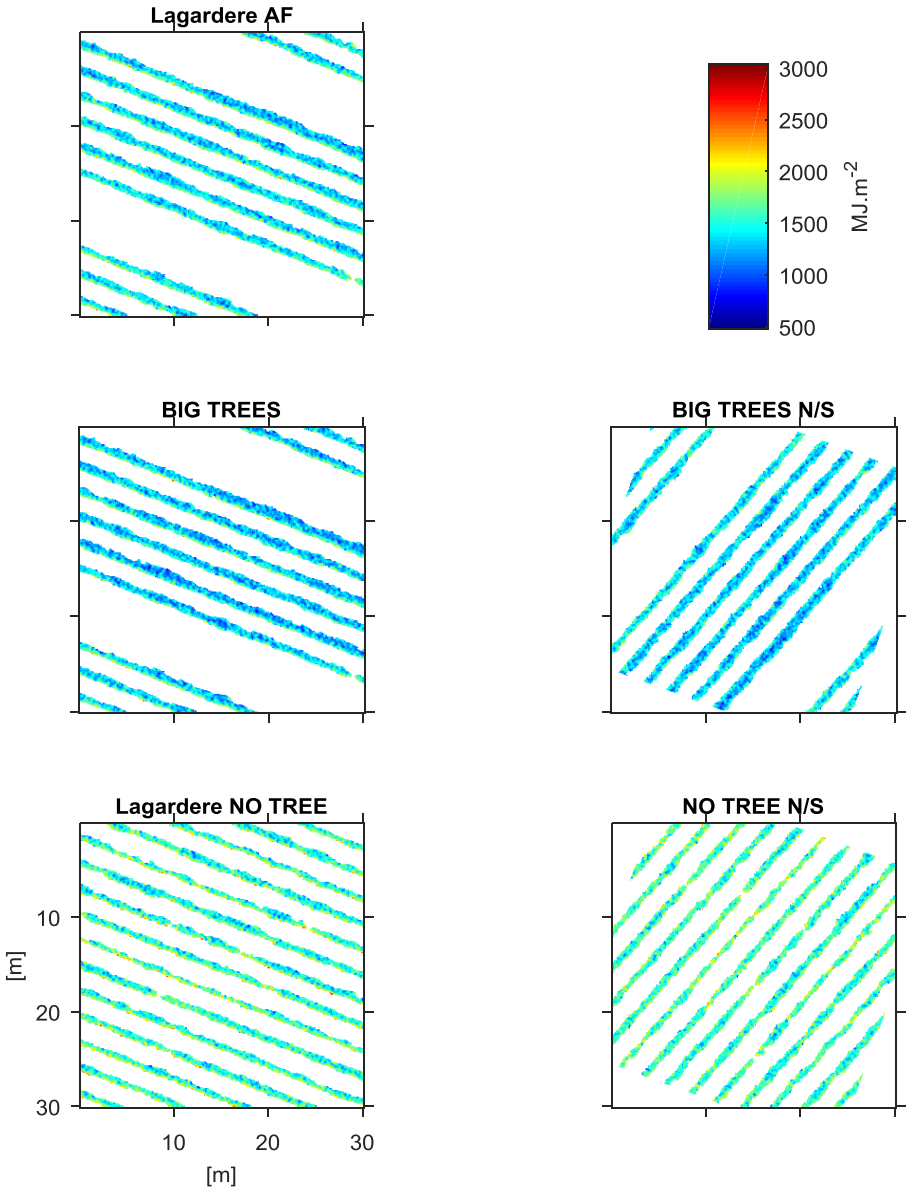

Figure 132: Zooms on the five mean filtered images of cumulated energy budgets from budburst to harvest. The mean filter treatment was applied using a moving window of 3*3 pixels.

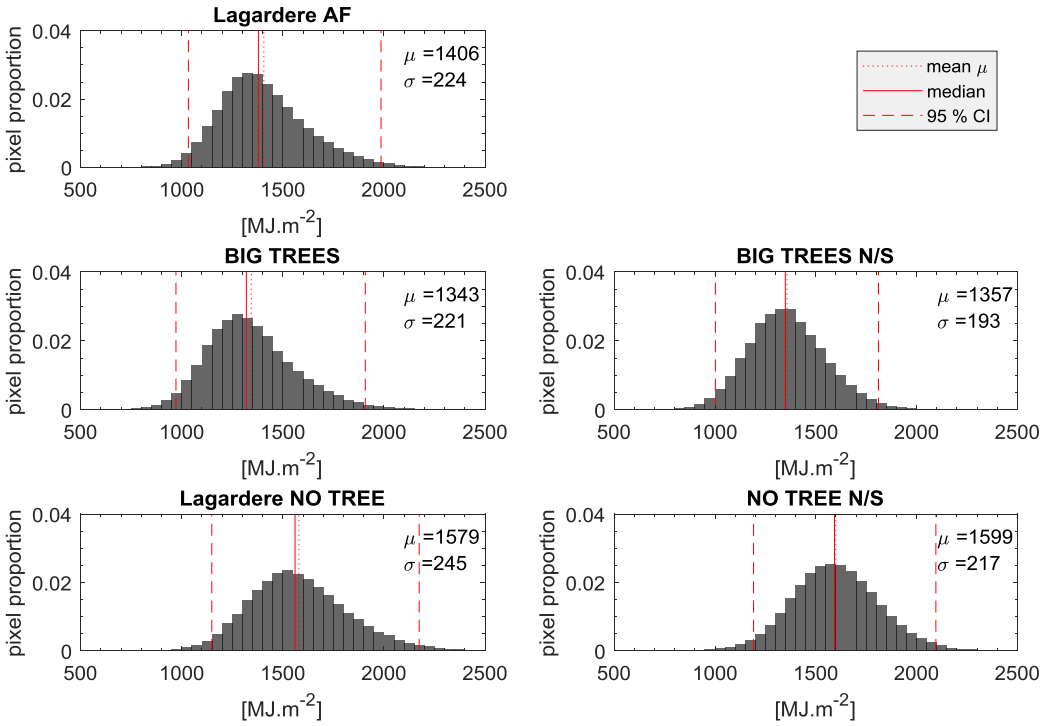

Figure 133: Distribution of the energy budgets cumulated from budburst to harvest after applying a mean filtering treatment with a smoothing window measuring 3 x 3 pixels (30cm x 30cm)

Spatial heterogeneity due to agroforestry practices

This subsection investigates the contribution of the agroforestry practices to the spatial heterogeneity in the radiative budgets of agroforestry vineyards. For this purpose, the cumulated budgets of PAR absorbed from budburst to harvest is compared to two variables, the distance to the trees and the relative orientation to the trees. Given the very high intrinsic heterogeneity in previous results, the following analysis was performed considering the mean filtered values of cumulated energy budgets.

DISTANCE TO THE TREE ROW

Because grapevine is structured in rows, the distance to the trees was considered as a discrete variable corresponding to the row number on a perpendicular transect to the trees. In addition, the orientation of grapevine row, rather on the northern or on the southern side of the tree rows, was taken into account for constituting classes of grapevine rows given their positions relatively to the tree rows. **Figure 134** shows the categorical maps that were built for each type of agroforestry vineyards. Then, the **Figure 135** provides the statistics of the mean filtered cumulated energy budgets per class of grapevine row. In the BIG TREES vineyard, the three southern rows show cumulated budgets slightly greater (by 4 %) than the three northern ones while this doesn't apply with smaller trees (Lagardere AF). Also, from comparison with the BIG TREES N/S vineyard, this latter tendency seems quite specific to the NW/SE orientation but doesn't apply with a N/S one. In addition, in the BIG TREES vineyard, the two first rows on the northern side of the tree rows present slightly lower budgets than

the third one which is more remote, while this difference doesn't appear in the BIG TREES N/S vineyard. In this latter vineyard, only the energy budget of the first south-eastern grapevine row slightly differs from that of the other rows. It shows a budget greater by 3 % to the others which could be due to the fact that the trees are stem pruned and thus the shade of their canopy starts further away than the first grapevine row in this configuration.

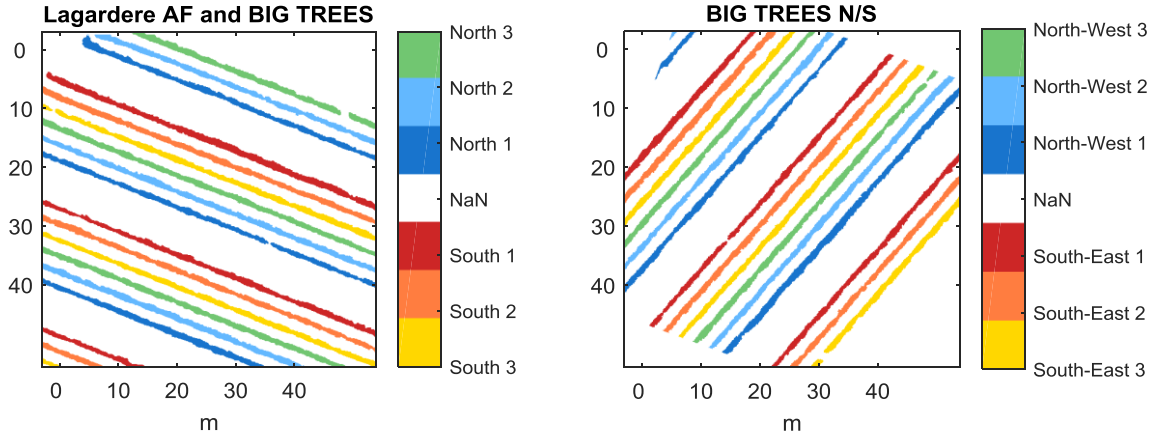

Figure 134: Classification of grapevine pixels per row number to the tree rows.

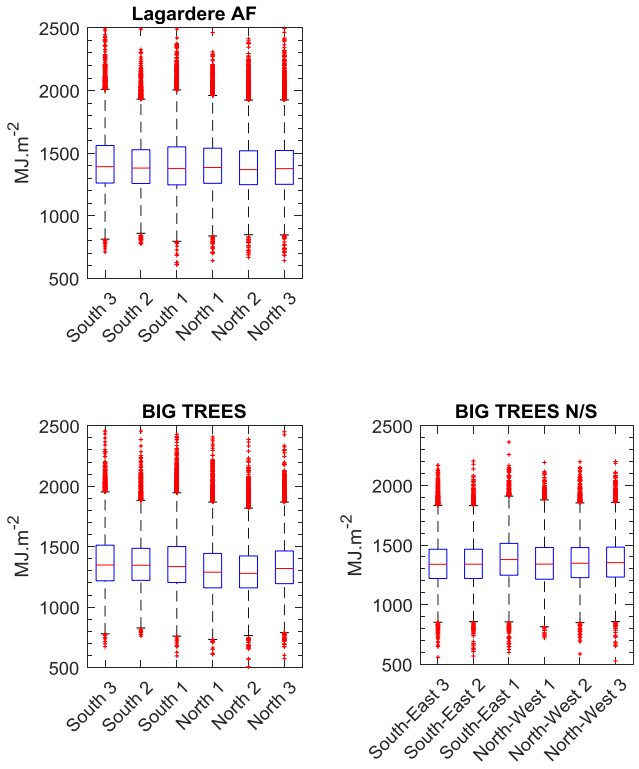

Figure 135: Box plots of the mean filtered cumulated budget in PAR according to the position of grapevine row relatively to the tree row. Results are provided for each case of agroforestry (AF) vineyard simulated. On each box, the central mark indicates the median, and the bottom and top edges of the box indicate the 25th and 75th percentiles, respectively. The whiskers extend to the most extreme data points that were not considered outliers, and the outliers are plotted individually using the '+' symbol. Whisker extends to approximately +/− 2.7σ, σ being the standard deviation.

In this subsection, the importance of grapevine orientation relatively to the trees is questioned. For each mock-up of agroforestry vineyard, grapevine pixels according to six different classes of relative orientation to their nearest tree are classified (**Figure 136**). The Lagardere AF and the BIG TREES vineyards present a majority of S, SW, N and NE orientations while the BIG TREES N/S vineyard mostly presents grapevine pixels with a NW, N, S or SE orientation to the trees.

Then the mean filtered cumulated amounts of energy absorbed are presented per class of relative orientation to the trees in **Figure 137**. No significant effect from a particular orientation class is observed. The higher budget of the NW orientation which appears in the Lagardere AF vineyard seems due to both the very low amount of pixels in this class and to their location on the border of the scene. Nonetheless, when considering all together the agroforestry vineyards that were simulated, the cumulated budget of absorbed PAR is slightly higher for the group of the southern orientations (SE, S and SW) than for the group of the northern ones (NE, NW and NE).

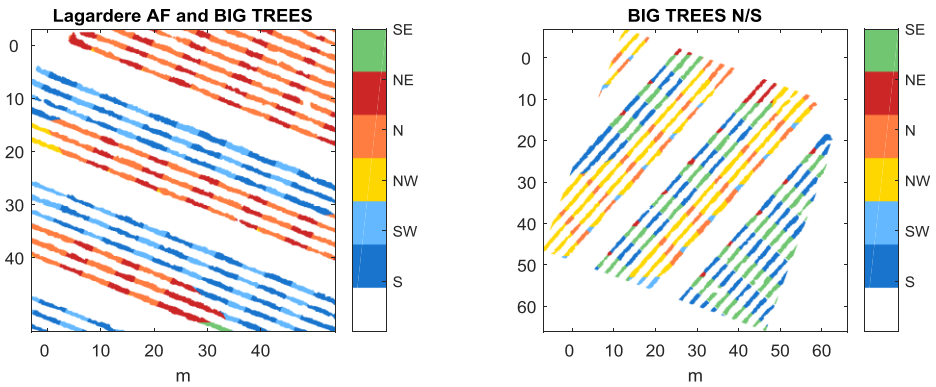

Figure 136: Classification of grapevine pixels according to their relative orientation to the nearest tree. Six different orientations were considered: N: Northern, NW: North-western, NE: North-Eastern, S: Southern, SE: South-Eastern and SW: South-Western

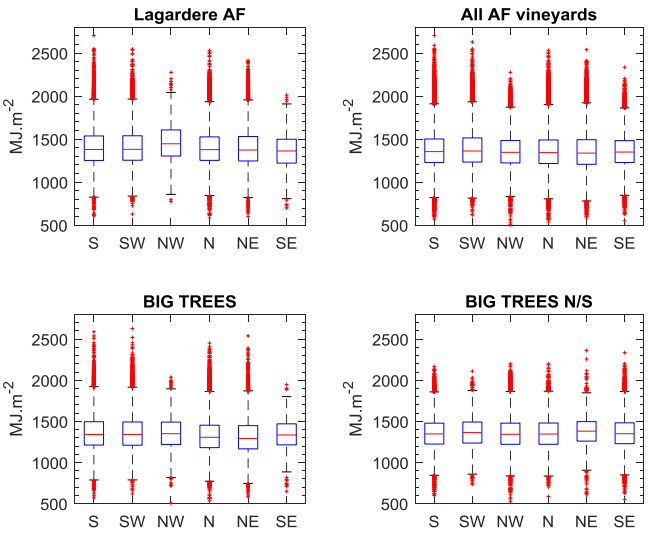

Figure 137: Box plots of the mean filtered cumulated amount of absorbed PAR per orientation to the trees. Results are provided for each case of agroforestry (AF) vineyard simulated and for overall (top right corner). On each box, the central mark indicates the median, and the bottom and top edges of the box indicate the 25th and 75th percentiles, respectively. The whiskers extend to the most extreme data points that were not considered outliers, the outliers are plotted individually as '+'. Whisker extends to approximately +/−2.7σ, σ being the standard deviation.

For assessing the spatial heterogeneity of the PAR budget in agroforestry vineyards variables concerning the distance and the orientation of grapevine relatively to trees were proposed. They were successively confronted to mean filtered budgets of absorbed PAR which led to very little significant results so far. Nonetheless, further investigations seem necessary given a few errors yet identified in this approach. Firstly, the land occupation maps that were used for classifying pixels per distance and per orientation to the nearest tree only considered the area inside the simulated images. Because the infinite slope mode of DART was activated, trees were also present out of the border of the images and should be taken into account. This error could be corrected by two means:

i. either by running again the whole series of simulations but in isolated scene mode,
ii. or by generating the actual land occupation map of the simulated scenes. For this purpose, DART offers the possibility to simulate RGB images and to display them repetitively. Consequently, the repeated images could be uses as a model for positioning the land occupation map according to its actual juxtaposition in the simulated scenes.

VI.3.3 Acceptability of the simulated meteorology

VI.3.3.1 Comparison with reference data

Knowing that the cloud cover has a great influence on the intensity of shading, simulating global and diffuse irradiances in the PAR waveband matching with a realistic time series of meteorological conditions was one of the main objectives. Nonetheless, neither measurements of the diffuse fraction of incident light was available nor the irradiance in the PAR ([400 – 700 nm]). Only data of global solar irradiance ([250 – 2800 nm]) was available from measurements at Lagardere study site. In collaboration with the DART team at CESBIO, a procedure of inversion was tested which consisted in introducing modulations of the multiplicative factor of the aerosol optical depth (AOD).

The simulated global solar irradiance showed in **Figure 116** confirmed that this procedure allows converging to the measured global solar irradiance in most cases. Nonetheless the acceptability of the simulated global PAR irradiance and the $SKYL_{PAR}$ is discussed here.

First, the daily cumulated E_{tot}^{PAR} and E_{diff}^{PAR} which were simulated are given in **Figure 138**. They reveal that the seasonality observed in the measured E_{global}^{solar} was not well reproduced in the PAR wave band. In addition, the simulated SKYL was very high for all days of simulations and presented an important variability from one date to another.

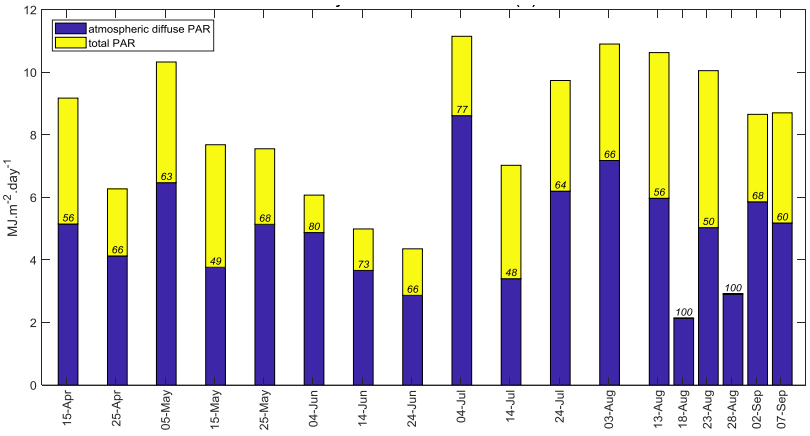

Figure 138: Total and diffuse irradiance at BOA cumulated for each day of simulation. The number indicates the ratio of diffuse irradiance out of the total (SKYL) in percents.

Second, mainly four contrasted cloud cover conditions were identified within the measured global solar irradiance time series, namely (i) fully clear sky, (ii) fully overcast sky, (iii) intermittent clouds and (iv) transitioning sky (**Figure 139**). Except for the fully clear sky days, the c_{AOD} by far exceeded the value of 4 and was forced to very high values, which would be completely unrealistic concentrations for representing only the aerosol concentration. In addition, the simulated ratio of $E_{tot}^{PAR}/E_{tot}^{solar}$ was around 45 % during peaks of clear sky while it surprisingly fell below 5 % when clouds passed in the sky. For example a complete drop of the total PAR irradiance was observed at 14:00 UTC on July 14th (a'Bastille Day' effect ?!').

In order to discuss the acceptability of simulated fraction of diffuse PAR, a comparison was made with the measures acquired by a meteorological station located in Lamasquère (31), at 80 km west from Lagardère (32) vineyard. Lamasquère (31) is one of the long term study site of CESBIO[22] as part of the two observatories named OSR (Regional Space Observatory) (Béziat et al. 2009; Tallec et al. 2013) and ICOS (Integrated Carbon Observation System) (Lafont et al. 2014). It is located in the French department of Haute-Garonne (43°29'47''N, 1°14'16''E, mean elevation of 180 m a.s.l). Measurements of direct and diffuse irradiance in both the solar and the PAR spectra are carried at Lamasquère. A PAR pyranometer (BF5 Sunshine Sensor) records the photosynthetic photon flux density (PPFD) in µmol.s^{-1}.m^{-2}, which was converted into an energy flux in W.m^{-2} using the approximation $1\ W.m^{-2} = 4.57\ \mu\text{mol}.\text{s}^{-1}.m^{-2}$ (Sager and Farlane 1997). On the clear sky day and the fully overcast day selected in **Figure 139**, the global irradiance in the solar spectrum was very similar at Lamasquère (31) and at Lagardère (32), with a systematic overtaking of 10 – 15 % at Lamasquère (31). Nonetheless =, in the case of clear sky day, this tendency was not well reproduced in the PAR spectrum, especially in the early morning (13-Aug-2016) or evening (14 Jun-2016).

[22] Radiation measurements at Lamasquère was funded mainly by ICOS-France. This experimental site benefit from the support and facilities of the Regional Spatial Observatory (OSR), CNRS (Centre National de la Recherche Scientifique), CNES (Centre National d'Etudes Spatiales), University of Toulouse. I am grateful to Franck Granouillac and Bartosz Zawilski for their technical support, and Tiphaine Tallec and Aurore Brut for the data processing

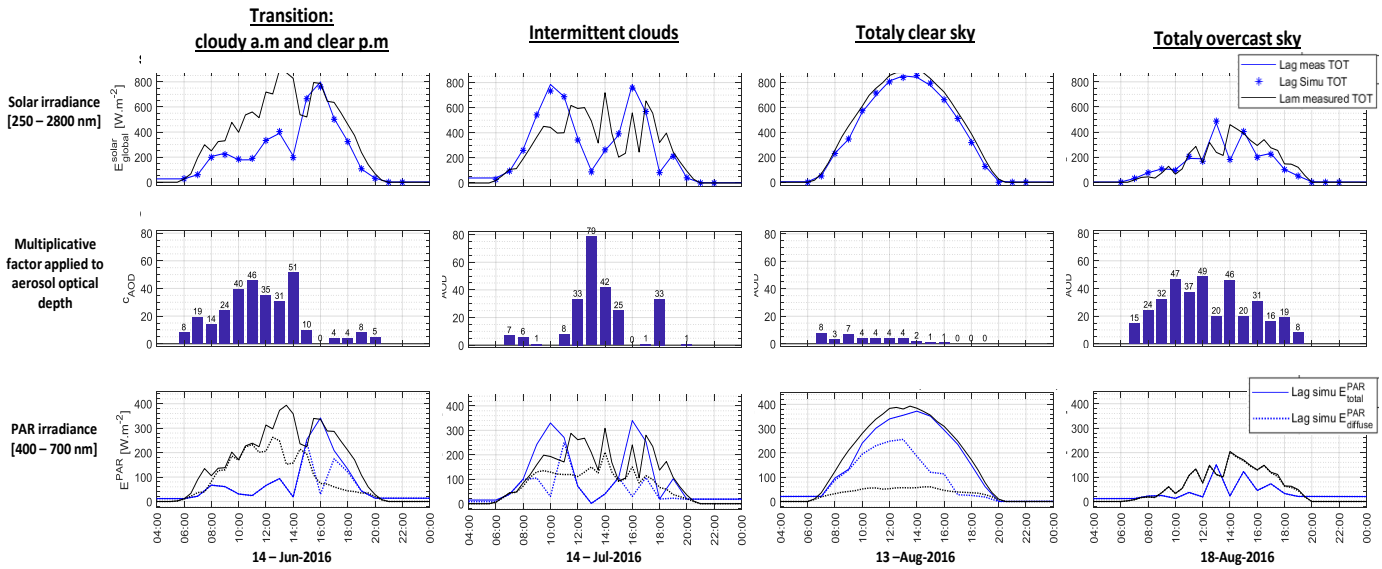

Figure 139: Total (plain lines) and diffuse (dotted lines) irradiances measured/simulated in the solar spectrum (top) and in the PAR spectrum (bottom) at Lagardere study site (blue 'Lag') and at Lamasquère reference site (black 'Lam'). In the middle the histogram gives the values of the values of the c_{aod} obtained from the inversion procedure and used for simulating the irradiance in the PAR at Lagardere.

When considering the whole period of simulation, comparing the two sites suggests that extremely high values of SKYL have been very frequently simulated. This is true at the early or late hours of the days but also in the middle of the day (**Figure 140**). These observations suggest that the budgets of absorbed PAR may have been overestimated in the shade cast of the trees because of a repeated tendency to overestimate the diffuse component of the irradiance on clear sky conditions.

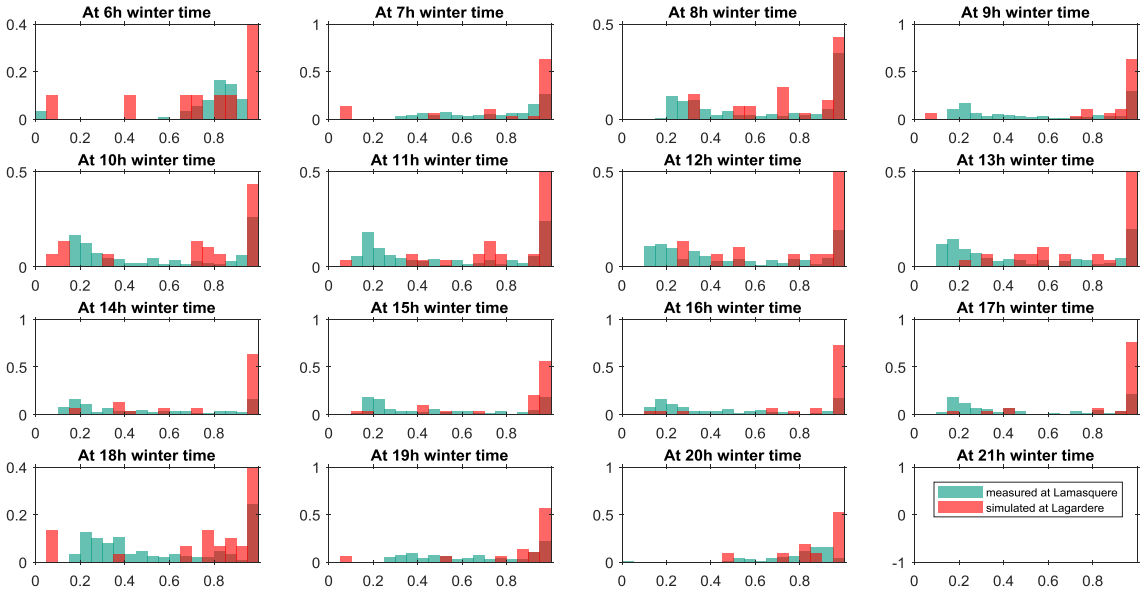

Figure 140: Hourly distribution of the SKYL from DART simulations at Lagardère (32)(red) and of diffuse to global PAR ratio measured at Lamasquère (31) (green), from 16 March 2016 to 12 september

VI.3.3.2 Methodological improvements

The single parameter inversion method described in **Adjustment of the aerosol optical depth for modeling cloud cover variability** led to overestimate the contribution from diffuse PAR, notably on clear sky day, early morning and in the evening. This may be explained by the fact that the spectral behavior of cloud optical depth differs a lot from the spectral behavior of aerosols. Indeed, the spectral variability of the particles in the atmosphere generally depends on the ratio "$\frac{\text{particle interception cross section}}{\text{wavelength } \lambda}$". Thus the interception cross section of aerosols is approximately proportional to λ^{-n}, with n between 0 and 4, depending on the aerosol dimensions and type, whereas the optical depth of clouds, which are made of water droplets, tends to be spectrally constant in all the short wavelengths.In the case of aerosols **Figure 141** shows that $E_{BOA}(\lambda)$ decreases if c_{AOD} increases, and this decrease is larger if sun direction is very oblique (e.g. late afternoon compared to midday). In addition, this decrease is much greater in the short waves than in the long wavelengths, due to the proportionality with λ^{-n}. However, in the case of clouds, the relative decrease of $E_{BOA}(\lambda)$ should be more or less the same at all wavelengths (Chang et al. 2006). It results that modeling clouds impacts by artificially increasing the content of aerosols in the atmosphere led to overestimate the relative decrease of E_{tot}^{PAR}, and consequently tends to underestimate E_{diff}^{PAR}.

From these observations, improvements of the inversion method seemed of prior importance and should take into account the different spectral behaviors of aerosols and clouds. In collaboration with the DART team, a new inversion method was envisaged and is currently under implementation as a new functionality of the model. It consists in adding a new type of particle with the vertical profile of extinction coefficient corresponding to clouds and calling it for inversion. For this purpose, the elements listed in must be introduced in the atmosphere properties section of DART.

Table 22: New parameters to implement in DART for improving the inversion of cloud cover

New parameter	***Description***
cloud_optical_depth_albedo	Table storing cloud optical properties (spectral optical depth, spectral single scattering albedo). The same and structure of the table must be identical to files storing the aerosol optical properties (optical depth, single scattering albedo).
multiplicative factor k_{cloud}	Factor to apply to the cloud optical depth, similarly to the multiplicative factor k_{aero} of the aerosol optical depth.
cloud_density_profile	Table storing the cloud vertical density profile, with the same structure as the table that stores the aerosol vertical density profile.

With this new method; the computation of the vertical profile of cloud extinction coefficient is identical to the present computation of the vertical profile of aerosol extinction coefficient, except that it uses the tables "cloud_optical_depth_albedo" and "cloud_density_profile". In short, the "aerosol / cloud" extinction coefficient per atmosphere layer is computed as:

"aerosol extinction coefficient" + "cloud extinction coefficient" $\forall$ layer

This solution will notably imply several changes for the inversion of the coefficients:

(i) a maximum Max(k_{aero}) should be defined by the user (around 1.5), and

(ii) 2 multiplicative factors (k_{aero}, k_{cloud}) are used, instead of a single one as in the previous inversion method. The method starts with all input parameters of the DART root simulation. The inversion method has 2 steps:

(a) The inversion algorithm searches for k_{aero}. When k_{aero} > Max (k_{aero}) is found, then k_{aero} = Max (k_{aero}) and the algorithm must search for k_{cloud}.

(b) The inversion method iterates on k_{cloud} by dichotomy until it gets $E(k_{aero}, k_{cloud}) \approx E_{measure}$, where $E_{measure}$ is the measured irradiance and $E(k_{aero}, k_{cloud,init})$ is the DART simulated irradiance.

Through repetition of this procedure, the new inversion method gives ($k_{aero}(t)$, $k_{cloud}(t)$) for each time step when $E_{measure}(t)$ is measured.

More sophisticated methods could eventually be designed, such as methods that consider the time variation of $E_{measure}(t)$ in order to assess if the change of E_{BOA} is most probably due to a change of aerosols or clouds.

The modification and testing of these new functionalities haves partly made the object of the current master thesis of Ying Jie Wang. The first results obtained were promising as they allowed important improvements in the simulation of the diffuse fraction of light considering a day with intermediate cloud cover.

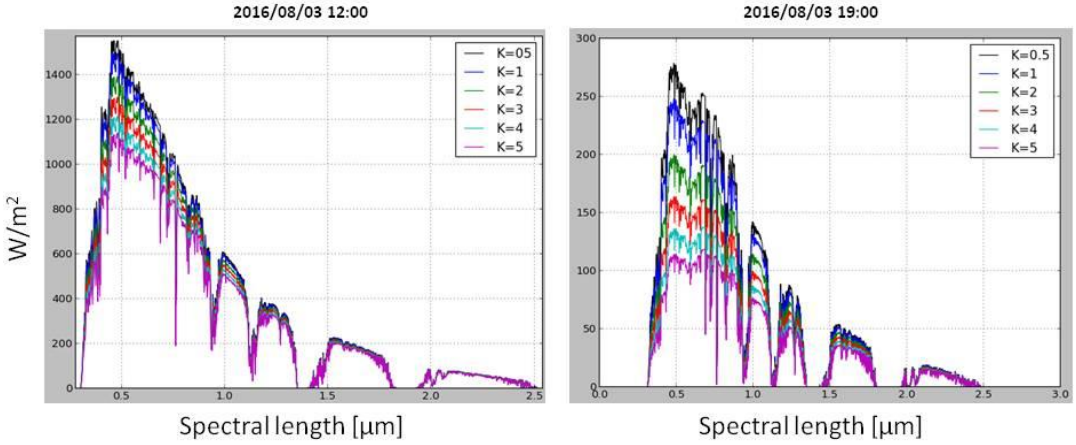

Figure 141: Evolution of the bottom of atmosphere irradiance E_{BOA} (λ) with the spectral length from simulations at 12h (left) and 19h (right) local time in Lagardere on August 3rd, 2016. Six different multiplicative factors K (same as c_{AOD}) were applied to the aerosol optical depth retrieved from the Rural 23km database, thus simulating very clear sky (k = 0.5) to very turbid (k = 5) atmosphere.

VI.4 Conclusions

Scientific and methodological objectives

The work presented in this chapter was driven by two main scientific objectives:

1. Quantifying PAR interception from trees within an agroforestry vineyard and the potential impacts on grapevine photosynthetic activity through the whole vegetative cycle;
2. Assessing the implication of the structure of the vegetation. Two types of factors were considered for this purpose: the vegetation structure responsible for intrinsic heterogeneity within a vineyard and the structure of an agroforestry planting.

In addition, all the methodological choices that were done were driven by the will of considering realistic conditions in terms of vegetation structure, propagation of direct and diffuse light and cloud cover varibility. The 3D radiative transfer model DART developed at CEBSIO was chosen for computing simulations of the radiative budget of agroforestry and monocropped vineyards.

Indeed, the model DART enabled to benefit from useful additional tools, notably for handling an accurate digital elevation model and for positioning vegetation components according to a land occupation map. It can simulate remotely sensed images of the simulated landscapes which added great value to our modeling approach of the radiative budget, notably for checking the morphological parameters of the landscape mock-ups.

Finally a methodology of inversion of the direct and diffuse irradiance in PAR based on the sole measurement of the global solar radiation was tested.

Main results

The simulation outcomes showed that the fraction of absorbed PAR out of the total irradiance is under the direct control of the solar irradiance and the architecture of grapevine: in average out of the five considered arrangements, a multiplicative factor of 0.8 and 1.3 was observed respectively with the spring and the summer mock-up of vine, no matter the meteorological context. The NO TREE mock-ups systematically presented the highest multiplicative factors compared to other arrangements, which may be explained by the absence of tree shade together with lower width of vine rows and thus less shadow from grapevine on itself. Also in all landscape configuration (mocks-up), the heterogeneity of absorbed PAR increased when the ratio of diffuse to total radiation dropped very low, i.e. on completely clear sky conditions, probably because the differences between sunny and shaded patches are enhanced. Through the phenological stages succession, the average daily absorbed PAR is the lowest from veraison to harvest compared to the rest of the cycle. This seemed to be principally due to the seasonal variation of solar declination angle which increases the size of shadow patches by this time of the year.

The absorbed PAR was time integrated i.e. cumulated over the whole period from budburst to harvest. It revealed two main impacts from the trees:

1. Firstly, at the scale of the vineyard, the cumulated absorbed PAR was reduced by 4.5% with simulated mature trees (compared to those in Lagardere study site in 2016).
2. Secondly, the orientation of the rows had very little impact on the total absorbed PAR: vineyards oriented N/S had a PAR greater by only 1% than with a W/E orientation. But more significantly, the orientation of the rows impacted the variability of absorbed PAR within each simulated vineyards. In monocropped vineyards, spatial heterogeneity was greater with a W/E orientation than a N/S one which is due to the row structure of grapevine canopy. Surprisingly, in the agroforestry vineyards, the converse was true: the greater variability was observed with a N/S orientation compared to a rather W/E orientation. This specificity of agroforestry vineyards compared to other alley cropping-systems might be due to the row structure of grapevine canopy combined with the wide tree rows in the arrangements.

Strengths and weaknesses of the simulation results

The simulation results that were obtained present several strengths and weaknesses.

Firstly, the relative accuracy of the results, showed plausible ordering of the simulated radiative budgets. Nonetheless, for the 'Lagardere' arrangement, which is the only yet existing planting out of the five tested arrangement, the absolute accuracy of the results cannot be assessed because the 3D absorbed PAR cannot be measured directly by any type of sensor. On-site placed sensors only allows measuring the incident and reflected light, arousing onto planar surface and gathering the contribution from grapevine and from the grounds (Riou et al. 1989). As a consequence, a sound but only partial validation could be obtained based on the capacities of DART for simulating on-site and air-borne sensors.

Secondly, the meteorological conditions that were simulated are plausible in terms of total cumulated solar irradiance. Nevertheless the inversion method that was used led to frequently and importantly underestimate the direct PAR irradiance and on the contrary to overestimating the diffuse fraction of the PAR irradiance. This error is mainly due to the important attenuation of the PAR wavebands by aerosols, which were used for simulating the cloud impact, while the attenuation from clouds remain more constant whatever the spectral band. This error may have led underestimating the light interception from trees on days with very clear sky.

Thirdly, one of the main novelties of simulations consists in taking into account the intrinsic configurational variability of vineyards. They were notably modeled considering random variations of the height of grapevine canopy, accurate variations of the width of grapevine rows. Following the same logic, grapevine leaves were modeled using triangle objects of realistic size and zenith angle distribution. Still, more accuracy could be gained for modeling grapevine leaves by also setting a

preferential azimuth angle of α degrees, where α is the orientation angle of vine rows. In this configuration, it would more realistically place grapevine leaves vertical and parallel to the external envelop of the rows. Considering natural heterogeneity revealed very varied light patterns within grapevine rows and within areas as small as a single vine stock canopy. This variability may not have appeared if the vineyards had been modeled with a null morphological variability or at lower spatial resolution. In return, this made the results more complex to analyze: no clear tendencies within the maps of energy budgets arised because the pixel amount and variances were both very high.

Main contributions of the chosen approach

Beyond the first order of magnitudes provided by the simulation results, important methodological developments were carried out. For the first time, a 3D radiative budget model allowing 3D realistic modeling of the vegetation was used. The accuracy of light propagation representation (diffuse and direct sources of light, multiple scattering) is one of the main advantages of this modeling approach. Representing grapevine in 3D but with rather simple polygons resulted very informative in regards to the parallelepiped cross section representation used in many modeling of grapevine rows (Riou et al. 1989; Lebon et al. 2003; López-Lozano et al. 2011). In addition, the validity of the method for calibrating the state of the atmosphere (cloud cover, aerosol and water vapor content) was discussed. At this stage, it is not recommended for the study of shadin patterns until modified functions will be implemented. Nonetheless, the new method, similarly to the tested one forces to make several hypothesis concerning the atmosphere properties (choice of atmospheric models, aerosols and vapor content, resolution for representing atmosphere layers, etc) which could not be verified.

Moreover, the methodological developments carried out also concern the landscape modeling. On the one hand, the approach that was developed allows modeling scenes of rather big size at very detailed spatial resolution. On the other hand, it was the first time that the model DART was used for modeling grapevine.

In addition, the repetition of the simulations as a whole time series from grapevine budburst to harvest with adaptation of the frequency of simulations to meteorological variations is one of the main methodological contributions.

This part of the phD work was carried out in collaboration with the developers of the model DART at CESBIO, notably with Jean-Philippe Gastellu-Etchegorry, Nicolas Lauret and Eric Chavanon. Their precious help made it possible to optimize the modeling approach, to detect and correct a few bugs, either concerning simulation parameters, or in the model code. Two suggestions can be made for further developments in the model DART. Firstly, a tool for importing DEM directly as 3D object could be integrated into DART. On the one hand, it is already possible to use a 3D object

as a DEM. On the other hand, Landier (2018) developed a python script for converting a raster DEM into a 3D object. All the technical possibilities being already gathered, the DEM conversion tool would present the interest of suggesting the operation more explicitly as it is very useful for easy modifications of the spatial resolution of the scene.

Secondly, it could be added in DART the possibility to define preferential azimuth distribution of triangle clouds of leaves instead of systematically considering a uniform distribution, just as it possible to do so for the zenithal distribution. This would notably enable DART users to better represent crops/natural vegetation which are structured in rows, for example grapevines with trellised system.

Perspectives

The simulation work presented in this chapter may be considered as a first trial for modeling the radiative budget of agroforestry and monocropped vineyards. It suggests many perspectives of improvements that we further present by decreasing order of priority.

In priority #1, simulations should be freed from the potential bias concerning the meteorological conditions that were simulated. From the former discussion, two improvements can be formulated: the first option will be to test the modified inversion method currently under implementation. The second and more accurate option would be to carry out on site measurements of the diffuse and direct light for the duration of a whole vegetative year. In these conditions, it would benefit doubly to the precision: on the one hand no more hypotheses should be made concerning the atmosphere parameters, and on the other hand, not computing the radiative budget in the atmosphere would save computation time which could be reused for improving the frequency of simulations between budburst and veraison. It could thus allow to cover a more realistic distribution of clear sky/overcast period of time through performing simulations every 5 days.

In priority #2, I think the optical properties of the vegetation, notably of grapevine could be validated and eventually corrected from seasonal variations. For this purpose, two methodologies could be considered. The first option could be to carry out frequent on site measurements of grapevine leaves reflectance and transmittance spectra using a spectrometer. This approach was notably tested on forest trees for simulations with DART by Desmarez (1997). The second option is more generalist and automated. It would consist in calibrating the optical properties of the landscape components based on a comparison of the simulated and the truly captured multispectral images. This new approach was proposed and tested on urban landscape components by Landier et al. (2016; 2017) and Landier (2018). In this context, it allowed estimating the optical properties with a relative error of 1 % in average.

In priority #3, a useful perspective of work would be to build a mock-up of vineyard which would be strictly identical to that of the agroforestry mock-ups that were built but removing the trees. These no tree mock-ups could be use as references for computing pixel to pixel differences in order to better comprehend light interception by trees and potentially for identifying main tendencies that could be

extrapolated in space. Nevertheless, this perspective would be technically complex to implement as it implies reconsidering the representation of grapevine canopy. If the current representation was maintained, the position of grapevine leaves and their angular orientation could greatly differ between one agroforestry mock-up and the no tree reference. This source of important variability would still remain in the simulations.

Finally, for broader perspectives, the simulation work which was initiated provides a first basis of methodological knowledge for the development of a tool of decision support concerning agroforestry vineyards. For a more realistic representation of agroforestry plantings, the size of the simulated scene should be made bigger than the one that was tested because this latter suffers too important bias from scene borders. For modeling bigger scenes with reasonable computation time and RAM, compromises should be made in terms of spatial and temporal resolution of simulations. From the discussion that was carried out concerning grapevine modeling, it can be concluded that the resolution of the 3D grid could be increased to 20-30 cm (instead of 10 cm) only under the conditions of i) maintaining a triangle object representation of grapevine, and ii) of relating grapevine energy budget to the leaf area in each pixel. Once these issues met, the model DART offers infinite possibilities for exploring varied planting arrangements, tree species, tree dimensions, row spacing, orientations, topographies, etc.

CHAPTER VII
Conclusions and perspectives

VII.1 Summary

Agroforestry practices may be a sound strategy towards agroecological and climate-resilient strategies for grape and wine production but have rarely been referenced. The thesis work presented in this manuscript participated in the project Vitiforest aiming to improve knowledge on these systems and focused on the interactions between grapevine and trees through the local impacts of trees on the energy, air and water fluxes. In this context, three objectives were more specifically targeted: (i) documenting the microclimatic impacts from trees in vineyards, (ii) assessing their consequences on grapevine physiology and production and (iii) discussing their impacts according to the morphological characteristics of the vegetation. In addition, this thesis had to propose methodological approaches capable of: (i) assessing the microclimate in a systemic way and (ii) apprehending the intrinsic diversity of contexts and practices and space and time variability in vegetation characteristics.

An important revue of literature was carried out concerning the climatic effects of trees at the local and micro scales, and the sensitivity of grapevine to environmental factors. In addition, three study sites where trees are intercropped with grapevines were selected in Southern France, namely at Lagardere (Gers), Lapouyade (Gironde) and Restinclieres (Prades-Le-Lez, Herault). This sampling allows covering diverse contexts of "terroir" and vegetation structure. Experimental data were collected from vine veraison to harvest in 2015 at the study site of Lagardère (32) and from a few weeks before budburst until harvest in 2016, at the three study sites. The collected data set gathers meteorological records, microclimatic records distributed within the vineyards together with measurements of yield and grape quality for wine making, and a set of drone borne images which covers the optical, near infrared and thermal infrared spectral domains. An image analysis approach was tested in order to describe the vegetation properties in regards to their climatic impacts. In addition, a statistical approach was developed for analyzing the space and time variability of the temperature measured at Lagardère (32) in the bunch zone of the vines and confronting it to the variability of the quantitative and qualitative component of the harvest in 2016. Finally, simulations of the radiative budget of grapevine were performed in 3D, in order to address the specific impacts of trees through light interception. The model DART developed at CEBSIO (Gastellu-Etchegorry et al. 2012) was used for two main reasons: (i) because it is based on physical principles and (ii) because it allows exploring multiple configurations of heterogeneous and vegetated landscapes such as agroforestry vineyards. Compared to the modeling approaches already tested with agroforetsry systems, it allowed (i) representing the canopies of grapevine and trees with accurate realism, (ii) simulating both the direct and the diffuse fractions of natural lights, and (ii) considering all the physical mechanisms involved in radiative budget, notably multiple light scattering. Various three dimensional mock-ups of agroforestry vineyards were built based on the land occupation map of one study vineyard. These mock-ups were used together with a meteorological time series running from

budburst until harvest for parameterization of simulations. The total quantity of energy absorbed by grapevine was cumulated in time over the whole season and was mapped in 2D.

The main results are synthesized and discussed in this conclusion in regards to the initial objectives of this thesis.

VII.2 Main conclusions

VII.2.1 Microclimatic impacts from trees

The review of literature highlighted that trees impact the microclimate of a vineyard due to their higher standing architecture, their denser and more voluminous canopies and eventually through higher evaporation demand and redistribution capabilities from their roots compared to grape vine (*Vitis vinifera*). They mechanically intercept the direct short wave radiations (light) from the sun, slow down and modify the air flow regime and may reduce/redistribute the water resource above and below ground (**Figure 142**).

For experimental purposes, the temperature was targeted in priority because it doubly stands as a key state variable: (i) it is integrative of the energy and water fluxes between the soil, the vegetation and the atmosphere, and (ii) it is involved in most of the physiological, reproductive and chemical processes responsible for the yield (quantitative criterion) and the berry composition for wine making (qualitative criteria). In the study site of Lagardère (32) which is a young and widely spaced agroforestry vineyard, the analysis of the variability of temperatures in space and time revealed that trees surrounding the vineyard combined with the topography and the main winds contribute the most to the heterogeneity of temperatures in this vineyard. The most sheltered zones showed a tendency to very large range of temperatures over the days and seasons, while the most open zones formed a warm pattern all along the year. This warm pattern was notably remarkable regarding grape production as it presented a lower risk of frost in spring and extended durations spent at very high temperatures on the warmest days of summer. Contrary to the already referenced old plantings at Restinclières (34) (Gouttesoulard 2015), the presence of height-year-old tree rows planted at 3.25 m from vine rows and oriented NE/SW did not generate a significant shading effect on the northern neighboring vines in this study case. It is most likely due to the limited height and low foliage density. Unexpectedly, a significantly cool pattern was observed specifically at the first vine rows located on the southern side of these young tree rows, which was the most pronounced on days of summer with high evaporative demand.

The simulated quantities of absorbed PAR throughout its whole vegetative cycle results suggested that the impact from trees on the photosynthesis of grapevine is negligible for all the tested arrangements. Choosing a 3D representation allowed considering the contribution from the architecture of grapevine which seems to importantly impact its light interception regime in general. In addition, the novelty consists in considering a realistic meteorological time series and thus the

contribution from diffuse radiations. Nonetheless, as no information regarding the balance between direct and diffuse radiations was available at the study sites, an adjustment of the quantity of the aerosols in the simulated atmosphere was performed in order to represent the cloud cover. This methodology allowed to accurately simulate the total solar irradiance arousing at the bottom of the atmosphere but tends to unrealistically overestimate the fraction of diffuse radiations in the PAR wavebands which potentially led to underestimating the impacts of shade on days with intermediate cloud cover.

VII.2.2 Consequences on grape and wine production

A review of literature allowed highlighting the light, the temperatures and the plant water status as the major environmental parameters impacting grape and wine production. Both the seasonal dynamics of these variables and the occurrence of extreme events are implied with visible impacts on the succession of phenological stages and eventual physical damages such as frost damages, or scalds from heat and drought stresses. In addition, the sensitivity of grapevine to competition for light or for water is multifactorial and equivocal. Indeed, photosynthesis is a key process as it contributes to the quantitative yield as well as to berry content in sugar and organic acids. It can be limited at low photon flux densities (typically when 9-23 < PFD < 150 $\mu mol\ (photons).m^{-2}.s^{-1}$) but may reach saturation at high photon flux densities (typically above 600 to 1000 $\mu mol.m^{-2}.s^{-1}$, depending on grapevine cultivar) and requires an optimum temperature estimated at 24°C and 28°C for northern and southern grapevine type respectively (Motorina 1958; Kriedemann and Smart 1971; Greer 2017). Light and temperature are also the main contributing factors to the quality of grapes for wine making. Among secondary metabolites, the polyphenols (anthocyanins, flavonols and tannins) are involved in wine color, structure and bitterness. Authors reviewed by Downey et al. (2006) observed that their synthesis increase with increasing light and most of all increasing berry temperatures but to a certain maximum above which synthesis is inhibited. Similarly, a moderate water stress is recognized to be profitable to grapevine production and wine quality while an intense water stress and an early occurrence can affect the net carbon assimilation rate of grapevine and consequently the yield and wine quality (Pellegrino, Lebon et al. 2004).

At the study site of Lagardère (32), the variability of both quantitative and qualitative traits of the yield in 2016 was confronted to the temperature patterns observed the same year from budburst to harvest. Overall, the temperature showed low correlations either with the yield or the berry quality components. This may be partly explained by the multiple factors involved beside temperatures (**Figure 142**). Only a few traits stranded out. Concerning quantitative variables, the cold maximum temperatures from flowering to harvest at the southern vine rows next to tree rows coincided with the highest yields. On the opposite, the highest maximum temperatures observed before budburst and from veraison to harvest in the northern part of the vineyard (which is the most unsheltered), coincided with the lowest yield. In addition, the overall spatial variability of temperatures explained 30 to 50 %

of the variability of some of the qualitative variables, namely the pH, the concentrations of malic acid and of polyphenols in tendencies which went in the sense of most of the references found in the literature concerning the bioclimatology of grapevine.

VII.2.3 Factors of variability: what is the contribution from the vegetation structure?

The review of literature together with our experimental results highlighted mainly two key factors of variability to be considered regarding the microclimatic impacts of trees: (i) the meteorological context and (ii) the structural characteristics of the vegetation.

The meteorological context factor mainly comprises the wind speed and direction, the stability of the atmosphere as well as the cloud cover. The most pronounced spatial variability within vineyards was observed regarding both light and temperature patterns on days with no wind and fully clear skies as shading as well as thermal influence from the ground are the most pronounced in this case. This finding comforts the punctual observations of Gouttesoulard (2015) at Restinclières (34) and allows delimiting the validity domain of these former results. The 3D simulations of the radiative budget notably suggested that shade from the trees become negligible with ratio of diffuse to total irradiance above 50 %. To secondary extent, important variability of temperatures was also observed at the study site of Lagardère (32) on days with a few wind blowing and/or stratified atmosphere. In this context, preferential circulation/stagnation of air mass seems triggered by high forested borders together with topography. In terms of methodology, a classification of days according to their daily ET0 was proposed in order to consider the meteorological factor in an integrative way. It allowed enhancing the time variability of temperatures but alone was not sufficiently informative for differentiating meteorological causes.

The contribution of the morphological traits of the vegetation can be explained using two complementary types of vegetation metrics: internal structure metrics, which describe the morphology of the individual components of the vegetation, and landscape structure metrics, which describe its overall arrangement in space. This conceptual framework has been particularly relevant for understanding the vegetation impact on the air flow, as suggested by Brandle et al. (2004). The computation of the landscape grain metrics (Forman and Godron 1986) was new at the microclimatic scale and allowed considering the trees which are located within vine rows and which surround a vineyard as an ensemble. Indeed this metrics characterizes the closed or open nature of the vegetation arrangement and thus is more informative on the preferential circulation of the wind than the density metric. In addition, at the internal scale, the tree height and foliage density showed the most correlations with the intensity and the extent of light interception from alleys of trees, while at the landscape scale, the orientation of grapevine and tree rows and the 2D/3D density of trees allowed explaining some of the variability in light patterns. For monocropped vine rows (Pieri and Gaudillere 2003; Hunter et al. 2016) as well as for alley-cropped cereals (Leroy et al. 2009), a WE orientation of

the rows (of vine and of trees respectively) generates more variability of light patterns in space and time than a NS orientation. Surprisingly, in the agroforestry vineyards that were modeled, the converse was true, matching with the observations of Duffours (2011): a NS orientation of parallel tree and vine rows showed the greatest contrasts of light absorption in space while the variability was lower with a WE orientation. This specificity of the orientation contribution in agroforestry vineyards might be explained by the straight line and discontinuous structure of grapevine canopy combined with the wideness of the alleys of trees. With a WE orientation, the longest shadows which appear in the early and late hours of the day may cast other trees and not so much neighboring grapevines.

Acquiring and analyzing very high resolution images was new regarding agroforestry systems and resulted as a very advantaging approach to describe the vegetation properties at the two scales of interest. The use of stereoscopic RGB images with no more than 5 cm of resolution is both recommended and self-sufficient for mapping the land occupation and the canopy heights with a pixel by pixel precision. Retrieving an accurate DTM stand as a useful preliminary steps in the two procedures and can be easily managed either from classifying the ground class with Random Forest similarly to Poblete-Echeverría et al. (2017) or through an adaptation of the DSM filtering method from Zarco-Tejada et al. (2014).

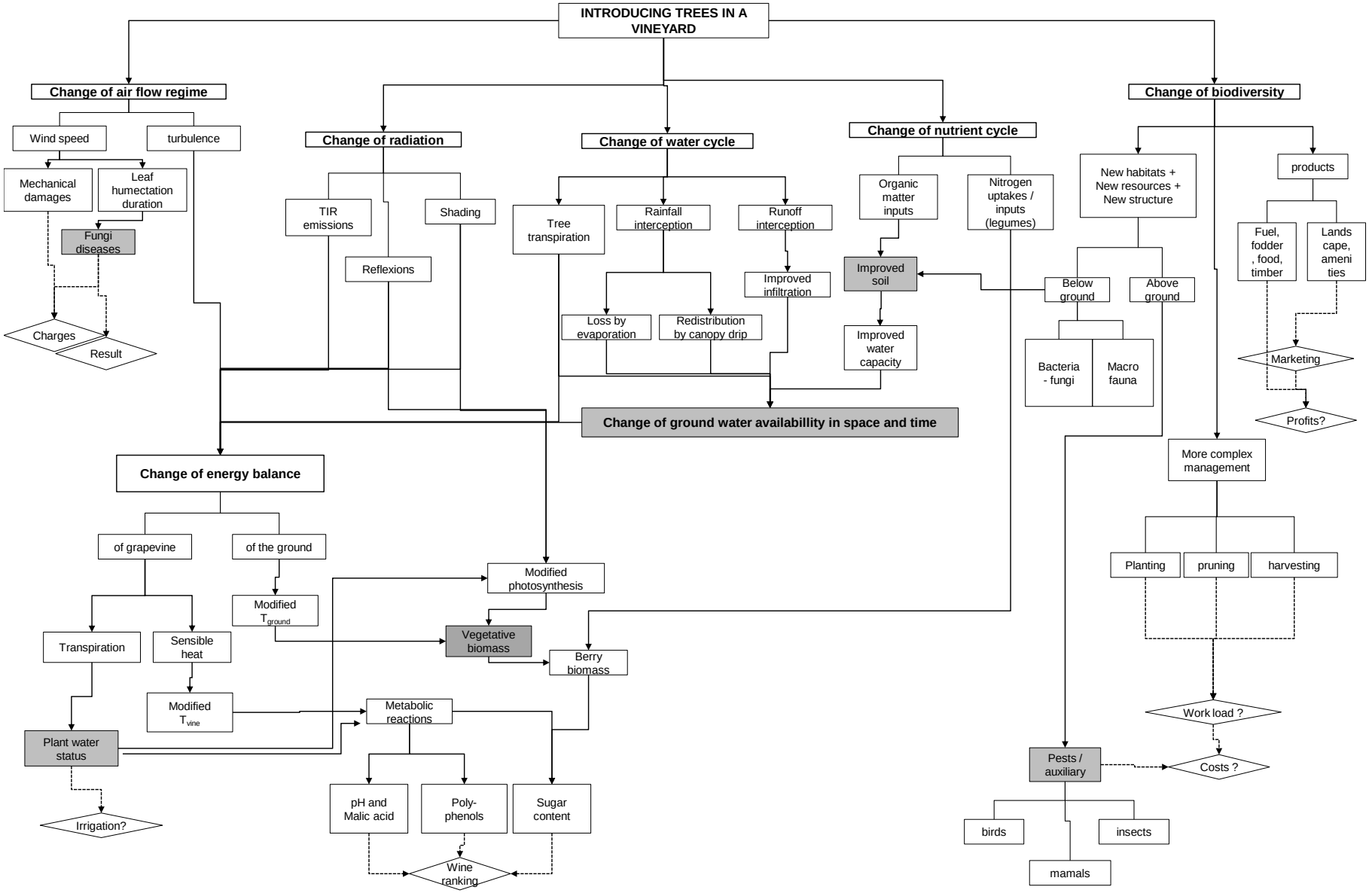

Figure 142: Synthetic diagram summarizing the multiple impacts of trees in a vineyard and the links between them. Rectangular boxes indicate physical and biological consequences while diamond boxes highlights management choices/economic consequences. Bold text highlights the main consequences assuming at least 10 years of tree growth. The arrows represent cause-consequence relationships, with dashed arrows being more hypothetical than solid ones. The remaining lacks of knowledge which should be addressed in priority are identified with grey background.

VII.3 Perspectives

VII.3.1 Further developments of the tested approaches

This thesis provides first references which should be completed by many further perspectives of research.

In first priority, improvements were proposed for simulating the light interception with DART. They notably include a modified approach for modeling clouds which includes the implementation of the phase function of clouds in the model and its activation as an alternative to the increase in aerosol concentrations. The modification of the functionalities of DART has partly made the object of the current master thesis of Ying Jie Wang. The first results obtained are promising as they allowed net improvements in the simulation of the diffuse fraction of light considering a day with intermediate cloud cover. Two objectives should be targeted in priority:

(i) The performances of this new method should be tested using the reference data set from Lamasquère (31) (Haute-Garonne, France, site ICOS), where the diffuse and global fractions of solar and PAR irradiance are measured.

(ii) A new series of c_{AOD} and c_{cloud} multiplicative factors should be calibrated and used for performing again the simulations of the radiative budget of vineyards in order to document the sensitivity of the results to these new parameters.

In addition, the image analysis approach could be further developed in order to calibrate/validate the optical properties of the vegetation which were parameterized. This approach would fully benefit from the ability of DART to simulate reflectance images which can be compared to the drone images acquired in the RGB bands following the recent methodological approach from Landier (2018).

In addition, the water stress status of grapevine stranded as the third key variable to investigate after temperature and light regimes (**Figure 142**). For this purpose, an analysis of the thermal infrared imagery for assessing patterns of grapevine water stress has been initiated but was not mentioned in this manuscript for sake of concision. It implied applying a correction to the raw temperatures acquired by the thermal sensor in order to correct the thermal emissivity of the surface and subtract the fraction of the energy which is actually emitted by the atmosphere and reflected by the ground toward the sensor (**Figure 143**). Confronting the variability of the surface temperature of grapevine leaves (considered at solar noon) with landscape metrics of showed positive correlations with the distance to trees and with the landscape grain and negative correlations with the 2D density of trees. Also, the variability in space of temperature of grapevine leaves at the date and time of the acquisitions (during berry ripening) shows positive correlations with the polyphenol total content and negative correlations with the weight and sugar amount of berries at harvest. Thus this first analysis seems to confirm that

the variability of the temperature of grapevine canopy when observed vertically can be related to the presence and arrangement of trees in a vineyard and is a relevant proxy for assessing plant water status. In order to better inform the plant water status, the computation of the Crop Water Stress Index from Idso et al. (1981) has been tested (**Figure 143**).

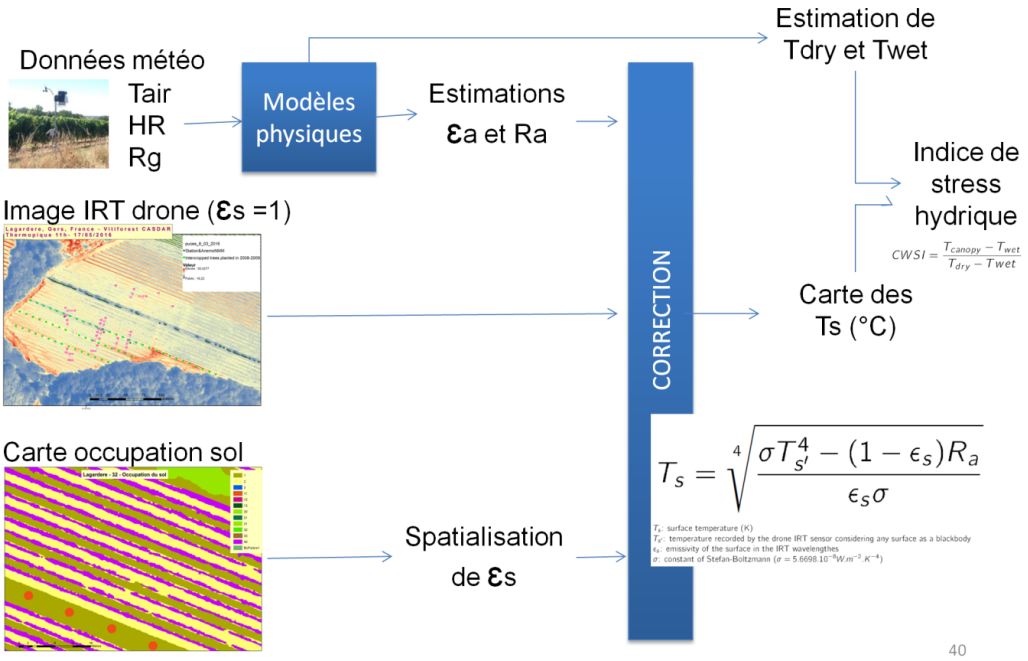

Figure 143: Processing chain applied to TIR images in order to map the Crop Water Stress Index (CWSI) of grapevine.

Figure 144: CWSI on 2016/08/23 – 13h 30 local time. The values correspond to the mean of vine pixels at plots of agronomic sampling, study site of Lagardère (32).

The patterns of CWSI considered during grapevine ripening recalls that observed in temperature patterns (**Figure 144**): the highest values of CWSI appear in the north western part of the vineyard while some of the vines located on the first row on the southern sides of trees, seem to present low

water stress index. Nonetheless, the currently considered CWSI exceeds 1 as its computation as been raising methodological issues. These notably concerned (i) the resolution of the thermal images in regards to the extent of grapevine canopy and (ii) the identification of the T_{wet} and T_{dry} reference temperatures. For this latter purpose, estimations has been tested using the 1D SVAT model SEtHyS (Coudert 2006; Guillevic et al. 2012) which was originally developed for homogeneous crops but showed good performances in orchards under Mediterranean context (Coudert, personal communication). The mock-ups of agroforestry vineyards could be reused for simulating the thermal infrared reflectance of the vegetation. For this purpose, the coupling with a SVAT model would be necessary but could allow a better understanding of the impact of the impact of the architecture of grapevine on its phytoclimate. This approach may allow addressing the technical issues met for the estimation of the T_{wet} and T_{dry} reference temperatures.

Finally in terms of perspectives, the collected data set and the tested methodology will allow widening the scope of references to other contexts of agroforestry vineyards. On the one hand, the two plots targeted at the experimental Domain of Restinclières (34) had already been referenced in the past as part of a long term trial carried out by the Agricultural Council of Herrault (CA 34) but their microclimate had never been assessed in continuity over the whole vegetative cycle of grapevine. On the other hand, the sites of Lagardère (32) and Lapouyade (33) had never been referenced before and benefitted from a multidisciplinary experimental effort during this Ph D work, as being included in the Vitiforest project. A first succinct analysis of the temperature time series recorded at Restinclières (34) suggests that on most days of summer, light interception from the trees decreases the temperatures of the first vine rows neighboring tree rows by 2.5 °C. Following identical statistical approach to that tested at Lagardère (32), the collected data should be further investigated and results should be compared with the references from the former year (Gouttesoulard 2015).

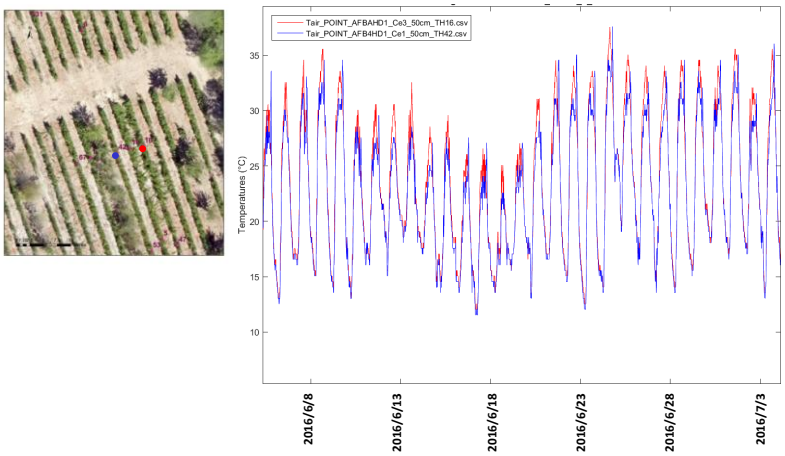

Figure 145: Time series of temperatures recorded in the bunch area of grapevine at the first vine row on the western side of Sorbus Domestica (blue) and at the third vinerow apart from two tree rows (red), Restinclieres, study site plot B4

VII.3.2 Open questions

This thesis leaves some open questions, either because answering them was not the principle objective, or because the answers were more complex than expected.

The soil characteristics and their impacts on the root systems of grapevine and trees will remain an under-referenced world. The review of literature provided in this thesis highlighted their importance for comprehending the effects of trees on the water budget components. As a consequence documenting the properties of the ground in regards to its hydraulic functioning and characterizing the the architecture of the roots at the interface between grapevine and trees could allow a better comprehension of the risks of competition for water. Geophysical approaches such as soil electrical resistivity tomography mapping (Buvat et al. 2014) combined with the sampling of root could be a sound strategy for further investigations. In addition this could allow identifying other factors which contribute to the yield and the composition of berries, notably the competition for nutrients. The competition for nitrogen was assessed by Trambouze and Goma-Fortin (2013) and Trambouze et al. (2017), at the experimental agroforestry domain of Restinclieres, which is marked by shallow soils. These authors report a significant competition for nitrogen for grapevines located at a distance of 2.5 m and 3.25 m from the trees while competition is no longer observed at 4 m from the trees.

The contribution for the architecture of grapevine canopy itself resulted as a key factor of variability in the phytoclimate of grapevine and in its sensitivity to light interception. For sake of concision, this issue led to the methodological choice of only modeling the simple curtain architecture of grapevine which is present at the study vineyard of Lagardere. Nonetheless, comparisons with more horizontal architectures would allow documenting the sensitivity of grapevine light absorption in regards to this factor. Using the land occupation map could be relevant again for simple geometrical architectures but may reach some limitations for representing more complex and bushy architectures such as *gobelet* vines. In these latter cases contribution from LIDAR imagery could be investigated.

VII.4 Final note

Readers of this manuscript must be feeling that though the task was demanding, only a small step was achieved towards a full understanding of the climatic functioning of agroforestry vineyards. Because only few references were available and facing the wide diversity of contexts and practices, this thesis work demanded much humility. How to assess a parameter since everything is changing, from one vineyard to another, within a given plot or even along a unique day of data collection? Does it actually make sense to collect “references” when each case seems peculiar? As I am writing this conclusion, my feeling is that highlighting cases of innovative agroecological practices and creating sharing knowledge groups with professionals are as important as searching for universal answers. As long as research intends to contribute to the development of agroecological and climate-resilient practices, the two following methodological approaches seem particularly relevant to me:

(i) replacing all research results in their context i.e. validity domain,

(ii) and addressing the aims of farmers in regards to their practices.

Very recently, a colleague told me: “Some vine-grower planted trees less than ten years ago, and even though the trees provoke no competition yet, he would like to remove them”. My deep feeling is that *Science* remains somewhat helpless in front of the intrinsic diversity of the living world and the complexity in human choices, and these are particularly at stake in an agroforestry vineyard. Thus, participative or multidisciplinary research may be sound strategies for assessing with more relevance complex and new systems such as agroforestry vineyards.

More personally, this thesis has been a long but very intense and rewarding adventure. It has offered me the opportunity to meet vine – growers and specialists of viticulture. They very kindly taught me the basis of grapevine cultivation and wine making and eventually introduced me to very fine beverages. In addition, I had the chance to meet several scientific and human mentors and I have been trying to follow their steps, deeply motivated by the search for rigor and precision which is the driving force of research. On the short term, this thesis will allow me to join the team of the “RMT Agroforesteries”. Hopefully, this new work experience also dedicated to trees will be as stimulating as this ending thesis.

CHAPITRE VII
Conclusions et perspectives

VII.1 Résumé

La pratique de l'agroforesterie en viticulture pourrait constituer une stratégie intéressante vers des pratiques agro-écologiques et résilientes face aux changements climatiques, mais ses performances et limites ont rarement été documentées. Le travail de thèse présenté dans ce manuscrit a participé au projet Vitiforest visant à améliorer les connaissances sur ces thèmes et est axé sur les interactions entre la vigne et les arbres grâce aux impacts locaux des arbres sur les flux d'énergie, d'air et d'eau. Dans ce contexte, trois objectifs ont été plus spécifiquement ciblés: (i) caractériser l'effet des arbres sur le microclimat d'un vignoble ; (ii) évaluer les répercussions en termes de rendement et de qualité viticole des raisins; (iii) comparer les résultats selon la nature et l'agencement des arbres. De plus, cette thèse devait proposer des approches méthodologiques capables de : (i) évaluer le microclimat de manière systémique et (ii) appréhender la diversité intrinsèque des contextes et des pratiques et la variabilité spatio-temporelle des caractéristiques de la végétation.

Une importante revue de la littérature a été réalisée concernant les effets climatiques des arbres aux échelles locale et micro et la sensibilité de la vigne aux facteurs environnementaux. En outre, trois sites d'étude sur lesquels la vigne est intercalée avec des arbres ont été sélectionnés dans le sud de la France, à savoir à Lagardère (Gers), Lapouyade (Gironde) et Restinclieres (Prades-Le-Lez, Hérault), dans le but d'échantillonner divers contextes de "terroir" et de structure de la végétation. Des données expérimentales ont été collectées sur le site d'étude de Lagardère (32) avant la récolte de 2015 et sur les trois sites d'étude quelques semaines avant le débourrement jusqu'à la récolte en 2016. L'ensemble de données collectées regroupe des enregistrements météorologiques, des mesures microclimatiques enregistrées dans les vignobles, ainsi que des mesures de rendement et de qualité du raisin pour la vinification et un ensemble d'images acquises par drones dans les domaines spectraux du visible, du proche infrarouge et de l'infrarouge thermique. Une approche par analyse d'images a été menée pour décrire les propriétés de la végétation au regard de leurs impacts climatiques. De plus, une approche statistique a été développée pour analyser la variabilité spatio-temporelle de la température mesurée sur le site de Lagardère et la confronter à la variabilité des caractéristiques quantitatives et qualitatives de la récolte 2016. Enfin, des simulations de bilans radiatifs des vignobles ont été réalisées en 3D en utilisant le modèle DART, afin de répondre aux impacts spécifiques des arbres liés à l'interception de la lumière. Le modèle DART développé au CEBSIO (Gastellu-Etchegorry et al. 2012) a été utilisé pour deux raisons principales : (i) parce qu'il repose sur des principes physiques et (ii) parce qu'il permet d'explorer de multiples configurations de paysages hétérogènes et végétalisés. Comparé aux approches de modélisation déjà testées pour l'étude de systèmes en agroforesterie, ce choix de modèle a permis (i) de représenter la canopée de la vigne et des arbres avec un réalisme précis, (ii) de simuler les fractions directes et diffuses composant le rayonnement global incident et les mécanismes impliqués dans le bilan radiatif, notamment les réflexions multiples. Diverses maquettes de vignobles agroforestiers ont été construites en trois dimensions sur la base de la carte d'occupation

du sol du vignoble d'étude de Lagardère (32). Ces maquettes ont été utilisées conjointement, avec une série chronologique météorologique allant du débourrement à la récolte, pour le paramétrage des simulations. La quantité totale d'énergie absorbée par la vigne a été cumulée dans le temps sur toute la saison et a été cartographiée en 2D.

Les principaux résultats sont synthétisés et commentés dans la présente conclusion en regard des objectifs initiaux de cette thèse.

VII.2 Principales conclusions

VII.2.1 Effets microclimatiques des arbres dans un vignoble

La revue de littérature présentée en première partie de ce manuscrit montre que l'impact microclimatique des arbres au sein d'un vignoble est lié à leur port élevé et à leur architecture aérienne, à leur denses et volumineuses canopées et potentiellement à une forte évapotranspiration et/ou capacité de redistribution de l'eau sous-terraine via leurs racines, en comparaison avec celles de la vigne (*Vitis vinifera*). Les arbres interceptent mécaniquement l'énergie de courte longueur d'ondes (lumière), ralentissent les flux d'air et modifient leur régime, et peuvent amoindrir / redistribuer les quantités d'eau disponibles en surface et dans le sol (**Figure 146**).

La température a été préférentiellement ciblée lors du suivi expérimental des sites d'études car celle-ci ressort comme une variable d'état doublement stratégique : (i) elle répond de manière intégrée aux modifications des flux d'énergie, d'air et d'eau au sein du système sol-végétation-atmosphère, et (ii) elle est directement ou indirectement impliquée dans la plupart des mécanismes physiologiques, reproductifs et chimiques qui déterminent le rendement (critères quantitatifs) et la composition des baies pour la vinification (critères qualitatifs). A Lagardère (32), qui est un vignoble d'étude relativement jeune et planté avec de larges espacements, l'analyse des patrons spatio-temporels de températures révèle que les arbres situés en bordure de vignoble (lisières boisées) se combinent avec la topographie et les vents dominants et ensemble engendrent la plus importante variabilité au sein du vignoble. Les zones les plus abritées et enclavées par les arbres présentent de larges amplitudes journalières et saisonnières de température tandis que les zones les plus ouvertes et exposées sont les plus chaudes rencontrées, et ce tout au long de la saison de culture. Pour la production de raisin, ce patron significativement plus chaud que le reste de la parcelle suggère un risque amoindri de gel au printemps mais de plus longues durées passées à des températures supérieures à 30 °C et un risque accru d'échaudage (35 °C) lors des journées estivales les plus chaudes de l'année. Contrairement aux quelques références existantes à Restinclières (34) (Gouttesoulard 2015), les arbres plantés entre les rangs de vigne à Lagardère (à 3,25 m de la vigne, orientation NE/SW) ne génèrent pas d'impact sur les températures de la vigne située sur leur côté Nord. Cela s'explique le plus probablement du fait de la hauteur encore faible (moins de 4 m) des arbres et de leur faible densité de feuillage. Contre toute attente, un patron significativement plus frais se manifeste dans ce vignoble d'étude spécifiquement au

niveau du premier rang de vigne situé au sud des rangées d'arbres. Celui-ci est le plus prononcé en termes de maximum de températures (- 0,8 °C à -1,6 °C par rapport à la moyenne) lors des journées estivales à forte demande évapotranspiratoire.

Les sorties de simulation donnant les quantités de PAR absorbées par la vigne sur l'ensemble des stades du débourrement à la récolte suggèrent un impact négligeable des arbres sur la photosynthèse de la vigne dans toutes les configurations testées. La représentation tri-dimensionnelle de la végétation adoptée pour ces simulations révèle un impact important de l'architecture de la vigne sur sa capacité d'interception de la lumière de manière générale. De plus, la nouveauté de cette approche consiste à considérer une succession météorologique réaliste et ainsi de viser une représentation réaliste de l'apport de la lumière de source diffuse. Cependant, comme aucune donnée renseignant la partition direct/diffus n'était disponible, une méthode d'ajustement de la concentration en aérosols a été testée pour ces simulations afin de représenter la variabilité de la couverture nuageuse. Cette approche permet de forcer le rayonnement global solaire à la valeur mesurée sur site mais a tendance à sous-estimer le PAR et surestimer fortement sa composante diffuse. Ainsi la qualité des résultats de simulation présentés souffre potentiellement d'une sous-estimation de l'ombrage lors des journées présentant une couverture nuageuse modérée.

VII.2.2 Conséquences sur la production vitivinicole

La littérature disponible sur la bioclimatologie de la vigne fait ressortir la lumière, les températures de végétation et le statut hydrique de la plante comme les trois principaux facteurs environnementaux influençant fortement la production de raisin et vin. A la fois les dynamiques temporelles de ces variables et l'occurrence de valeurs extrêmes sont impliquées, générant des impacts sensibles sur la phénologie de la vigne et éventuellement des dommages physiques (gel des bourgeons, échaudage des baies).

De plus, la sensibilité de la vigne à une compétition pour la lumière ou pour l'eau ressort comme plurifactorielle et complexe à appréhender. En effet, la photosynthèse de la vigne est un processus clé qui influence quantitativement la récolte ainsi que sa composition en sucres et en acides organiques. Elle se trouve limitée en cas de faibles flux de photons (9-23 < PFD < 150 $\mu mol\ (photons).m^{-2}.s^{-1}$ environ) mais atteint saturation en cas de flux élevés (supérieurs à 600 - 1000 $\mu mol.m^{-2}.s^{-1}$ selon les cépages). Aussi sa température optimale est estimée entre 24 °C et 28 °C pour des vignes septentrionales et méridionales respectivement (Motorina 1958; Kriedemann and Smart 1971; Greer 2017). Lumière et température sont aussi fortement impliquées dans la qualité des baies pour la vinification. Parmi les métabolites secondaires, les polyphénols (anthocyanes, flavonols et tanins) constituent une vaste famille de molécules impliquées à la fois dans la couleur, la structure et l'amertume des vins. La revue de littérature par Downey et al. (2006) souligne que leur synthèse augmente avec la quantité de lumière incidente et surtout avec la température des baies, jusqu'à atteindre un maximum au delà duquel leurs synthèses sont au contraire inhibées.

De la même façon, un stress hydrique modéré de la vigne est souvent recherché en viticulture afin de bénéficier à la qualité et typicité du vin tandis qu'un stress hydrique sévère, surtout s'il survient dans les stades précoces de la croissance des baies, peut affecter l'efficacité d'assimilation du carbone par la plante et par conséquence les critères à la fois quantitatifs et qualitatifs d'une vendange (Pellegrino, Lebon et al. 2004).

Au sein du vignoble de Lagardère (32), la variabilité des critères à la fois quantitatifs et qualitatifs de la vendange 2016 a été confrontée aux patrons de températures observés la même année depuis le débourrement jusqu'à la vendange. De manière générale, les corrélations observées avec l'un comme l'autre type de critères sont faibles. Cela peut s'expliquer par la multitude de facteurs venant s'ajouter aux températures (**Figure 146**). Seulement certains points semblent se démarquer. Parmi les critères quantitatifs, il s'avère que le patron de plus faibles températures présent de la floraison à la vendange au niveau du premier rang de vigne au sud des allées d'arbres, coïncide avec les plus fortes quantités de raisin récoltées, notamment du fait de poids de baies élevées. Au contraire, les températures journalières les plus chaudes observées avant le débourrement puis de la floraison à la vendange dans la zone Nord-Est du vignoble (qui est la plus ouverte et exposée), coïncide avec les plus quantités récoltées. De plus, la variabilité spatiale générale des températures permet d'expliquer 30 à 50 % de la variabilité observée sur certains critères qualitatifs notamment le pH, la concentration en acide malique et en polyphénols totale, selon des tendances à la hausse ou à la baisse qui recoupent les références trouvées dans la littérature.

VII.2.3 Facteurs de variabilité: quelle contribution de la structure de la végétation ?

La synthèse de littérature ainsi que les résultats expérimentaux présentés dans ce manuscrit soulignent l'importance de deux principaux facteurs de variabilité qui nuancent l'impact climatique des arbres : (i) les conditions météorologiques et (ii) les caractéristiques structurales de la végétation.

L'influence des conditions météo est principalement liée à la vitesse et à la direction du vent, à la stabilité thermique de l'atmosphère ainsi qu'à la couverture nuageuse. Les patrons d'absorption lumineuse et de températures observés en vignobles agroforestiers présentent la plus forte variabilité lors des jours sans vent et au ciel complètement dégagé, notamment du fait que l'ombrage ainsi que les écarts thermiques entre le sol et les basses couches d'air sont les plus prononcés dans ces conditions. Ce résultat recoupe les observations de Gouttesoulard (2015) à Restinclières (34) et permet de cerner le domaine de validité de ces précédents résultats. Les résultats de simulation du bilan radiatif en trois dimensions suggèrent notamment que l'ombrage des arbres considérés devient négligeable pour des rapports d'éclairement diffus sur éclairement total supérieurs à 50 %. Dans une moindre mesure, une importante variabilité des températures est observée à Lagardère (32) lors des journées présentant une très légère vitesse de vent et/ou à atmosphère stratifiée stable. Dans ces conditions, des circulations

préférentielles / la stagnation de masses d'air au sein du vignoble semblent se mettre en place sous l'influence conjointe des bordures boisées et du relief.

En termes de méthodologie, il est proposé de classer les journées selon leur valeur d'ET0 dans le but de prendre en considération de manière intégrée l'influence de la météo. Ce critère permet de faire ressortir avec plus de contraste la variabilité temporelle de l'effet des arbres mais demeure à lui tout seul insuffisamment informatif pour pouvoir distinguer les différentes causes impliquées.

La variabilité liée aux caractéristiques morphologiques de la végétation peut être approchée au moyen de deux types complémentaires de métriques :

(1) les métriques de structure interne qui décrivent la morphologie de chaque constituant individuel de la végétation,

(2) et les métriques de structure paysagère, qui décrivent la disposition de la végétation dans son ensemble.

Comme suggéré par Brandle et al. (2004), cette trame conceptuelle permet notamment de décrire avec pertinence l'importance de la structure de la végétation par rapport à la circulation de l'air. La métrique paysagère du gradient d'ouverture (Forman and Godron 1986) est proposée de manière innovante pour l'échelle microclimatique afin de quantifier le caractère plutôt ouvert ou fermé de la végétation. Elle s'avère pertinente pour intégrer de manière conjointe l'influence des arbres plantés en allée dans le vignoble et de celle tous les arbres présents aux alentours. De plus, parmi les paramètres internes de végétation, la hauteur de la canopée ainsi que la densité du feuillage sont déterminantes concernant l'intensité et l'emprise spatiale de l'ombre des arbres, tandis que parmi les paramètres paysagers, l'orientation des rangs (d'arbres et de vigne) ainsi que la densité 2D/3D permettent d'expliquer une part de la variabilité du régime lumineux au sein des vignobles agroforestiers. Dans le cas de vignobles uniquement plantés de rangs de vignes (Pieri and Gaudillere 2003; Hunter et al. 2016) mais aussi de co-plantations arbre-céréale (Leroy et al. 2009), une orientation Est-Ouest des rangs (respectivement de vigne et d'arbres), génère plus de variabilité spatiale et temporelle de l'irradiance au niveau du feuillage de la culture qu'une orientation North-Sud. De façon inattendue, l'inverse est observé pour des rangs de vignes co-plantés d'allées d'arbres : lorsque les rangs parallèles d'arbres et de vignes sont orientés plutôt NS les simulations 3D d'absorption de lumière par la vigne montrent plus de variabilité qu'avec une orientation à tendance EO. Cette spécificité pourrait s'expliquer par le caractère rectiligne (culture en « rang ») et discontinu de la canopée de la vigne combiné au large écartement des rangs d'arbres. Ainsi, avec une orientation EO, les ombres les plus longues de la journée survenant aux premières et dernières heures du jour, celles-ci doivent venir se projeter essentiellement sur la canopée des arbres voisins et non sur celle de la vigne.

L'acquisition et l'analyse d'images à très haute résolution spatiale par vol drone est prometteuse pour l'étude de systèmes en agroforesterie qui associent plusieurs strates de végétation. Des orthophotographies stéréoscopiques présentant une résolution d'environ 0,05 m permettent à elles-seules de cartographier l'occupation du sol et la hauteur de la canopée avec une précision au pixel près. Une étape préliminaire à ces deux traitements s'avère utile, à savoir la génération d'un modèle numérique de terrain de résolution horizontale de même ordre que les images. Pour cela, deux approches sont à la fois possibles : soit une approche consistant à cartographier le sol par classification non supervisée de type Random Forest similaire à celle de Poblete-Echeverría et al. (2017) ; soit une approche par filtrage du modèle numérique de surface réadaptée de celle proposée par Zarco-Tejada et al. (2014).

VII.3 Perspectives

VII.3.1 Approfondir certaines approches

Cette thèse apporte des premiers résultats et ordres de grandeurs qui méritent d'être approfondis selon plusieurs perspectives de recherches.

En priorité numéro 1, des améliorations sont à apporter quant à la méthode utilisée pour simuler la présence de nuages dans le modèle DART. Celles-ci consistent à ajouter un nouveau formalisme spectral d'« aérosol » qui corresponde mieux au comportement optique des nuages, à savoir une fonction de phase au comportement constant dans les courtes longueurs d'onde. Dans cette optique, la modification des fonctionnalités informatiques de DART a été initiée par l'équipe de ses développeurs et cette nouvelle méthode a été testée par Ying Jie Wang dans le cadre de son stage ingénieur au CESBIO. Les premiers résultats obtenus montrent une amélioration de l'estimation de la fraction diffuse de lumière lors d'une journée ponctuée par le passage intermittent de nuages. Deux objectifs sont identifiés et constitueront une poursuite directe du travail de thèse :

- Les performances de cette nouvelle méthode sont à évaluer en utilisant pour cela les mesures d'irradiance prises à Lamasquère (Haute-Garonne, France, site ICOS) où à la fois le rayonnement diffus et global dans les spectres solaire et du PAR sont mesurés.
- Un nouveau jeu de paramètres (c_{AOD},c_{cloud}) devra être inversé sur la base de la mesure d'irradiance solaire globale à Lagardère puis utilisé pour simuler de nouveau le bilan radiatif des vignobles et discuter la sensibilité des résultats.

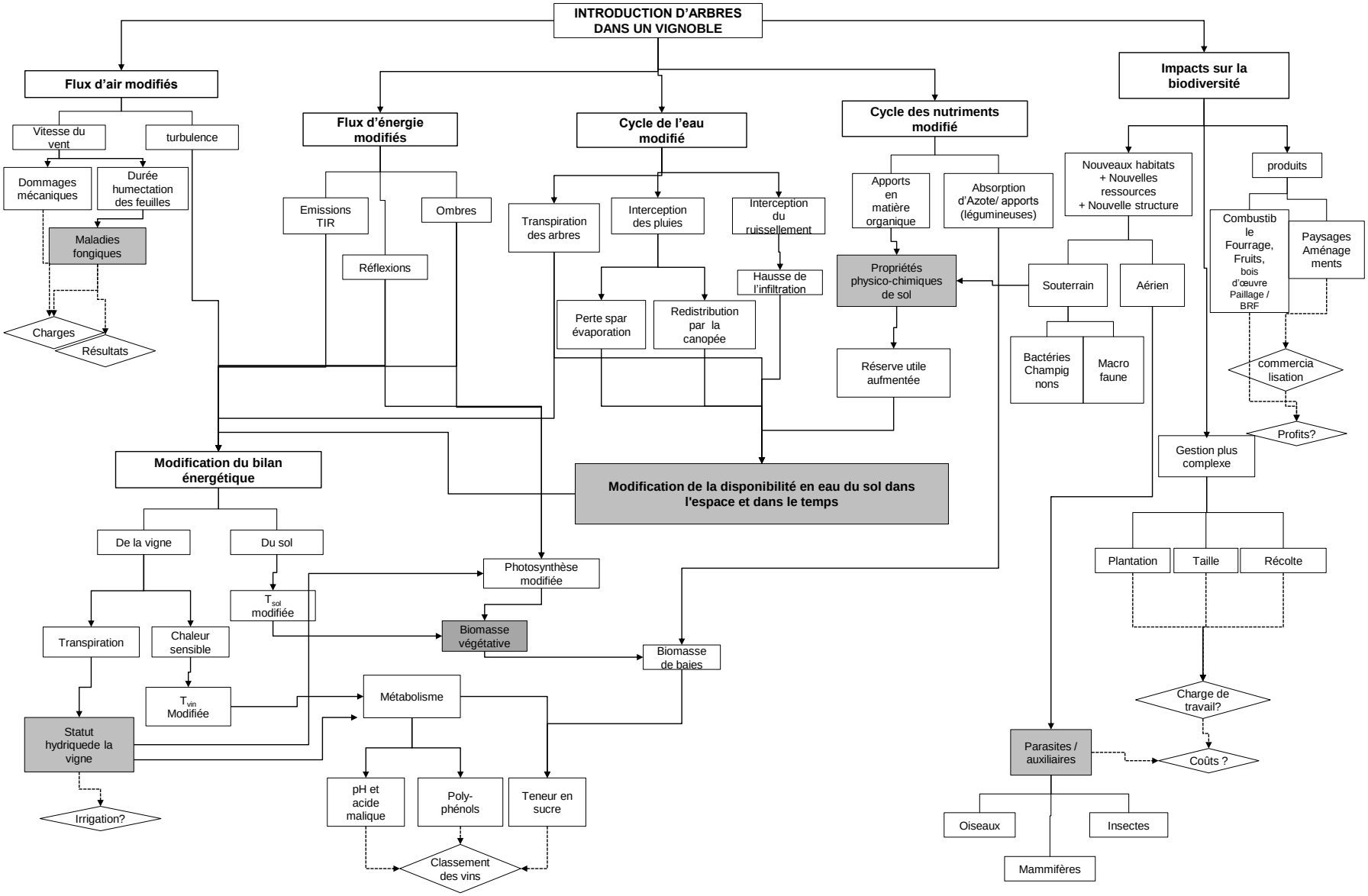

Figure 146: Diagramme synthétique illustrant la multiplicité de conséquences microclimatiques et agronomiques suite à l'introduction d'arbres dans un vignoble et leurs interrelations. Les boites rectangulaires distinguent des conséquences physiques et biologiques tandis que les boites en losange distinguent les conséquences en termes de choix de gestion et résultats économiques. Le texte en gras met en valeur les conséquences les plus marquées si l'on considère une plantation âgée au moins de 10 ans en contexte tempéré. Les flèches indiquent des relations de cause-conséquence, celles étant en pointillées étant plus hypothétiques que celles avec un trait plein. Les principaux manques de connaissances qui devraient être prioritairement ciblés par la recherche sont identifiés par un fond gris.

De plus, l'approche par analyse d'image offre une possibilité d'améliorer la précision des paramètres optiques de végétation renseignés jusqu'ici arbitrairement. En effet, DART offre la possibilité de simuler des réflectances RGB qui pourront être confrontées aux images acquises par drone selon la méthode récemment développée dans le cadre des travaux de thèse de Landier (2018).

En priorité numéro 2, il semble essentiel d'approfondir spécifiquement la question de l'effet des arbres sur le statut hydrique de la vigne (**Figure 146**), celui-ci ressortant comme une variable clé à considérer avec l'impact sur les températures et l'énergie lumineuse. Pour cela, un travail d'analyse des images IRT a été initié au cours de la thèse mais ne figure pas dans ce manuscrit par soucis de concision. Il a notamment consisté à apporter une correction aux images brutes afin d'intégrer (i) l'émissivité réelle de chaque classe d'occupation du sol, et (ii) de soustraire la contribution thermique du rayonnement grande longueur d'ondes qui est émis par la colonne d'air entre le capteur et le sol puis réfléchi par la surface vers le capteur (**Figure 143**). Les températures de la canopée de la vigne aux heures de midi solaire ont été confrontées aux métriques paysagères de végétation montrant des corrélations positives avec la distance à l'arbre, le gradient d'ouverture du paysage, et négatives avec la densité 2D d'arbres. Aussi la variabilité spatiale de la température de la canopée de la vigne observée lors des acquisitions montre des corrélations positives avec la teneur en polyphénols et négatives avec le poids et la teneur en sucre des baies à la récolte. Ainsi ces premiers résultats semblent confirmer que la température de canopée de la vigne observée verticalement présente une certaine variabilité liée à la présence de végétation et peut être un bon proxy du fonctionnement hydrique de la plante. Dans le but d'évaluer avec plus de précision le statut hydrique de la vigne lors des acquisitions et de pouvoir le comparer entre date et entre sites, le calcul d'un indice de stress hydrique (CWSI pour *Crop Water Stress Index*) de Idso et al. (1981) a été testé (**Figure 143**).

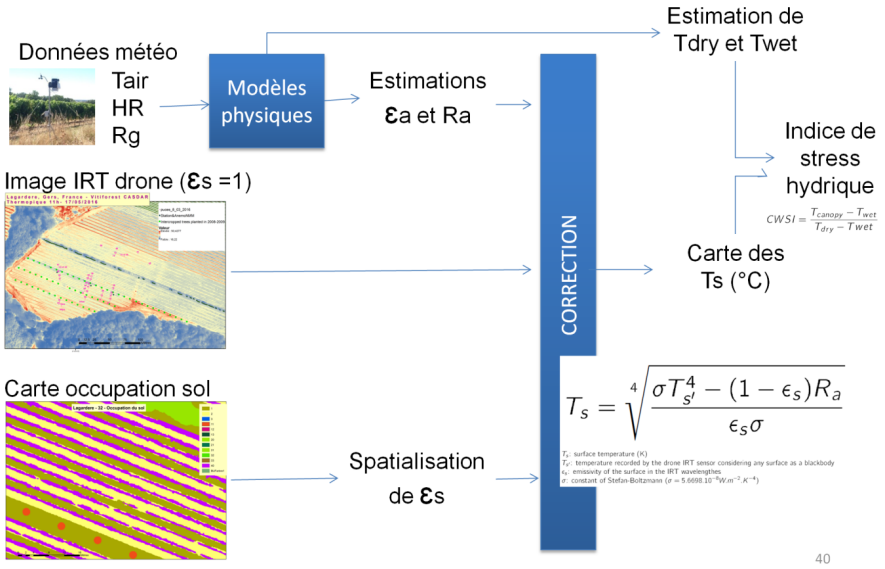

Figure 147: Chaine de traitement appliqué aux images IRT acquises par drone pour le calcul d'un indice de stress hydrique (CWSI) sur la classe vigne.

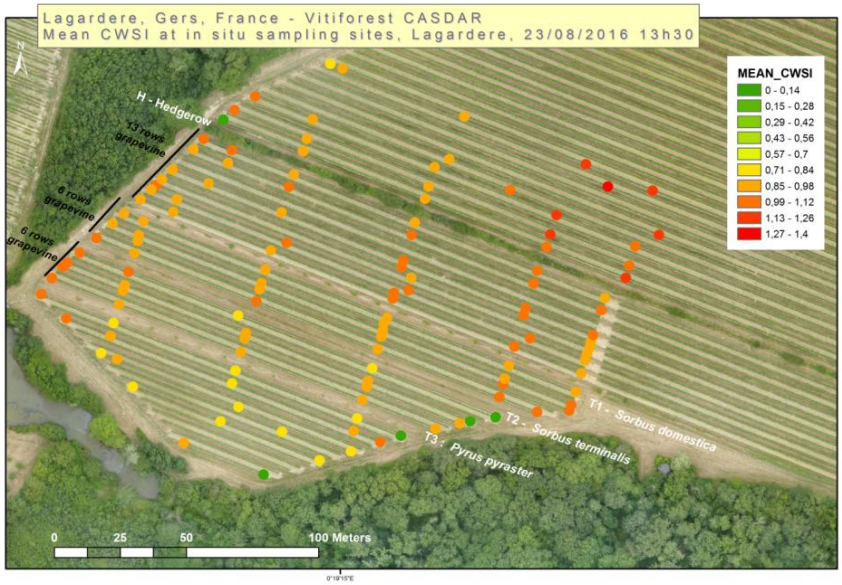

Figure 148: CWSI le 23/08/2016 – 13h 30 heure locale. Les valeurs sont des moyennes calculées sur l'ensemble des pixels de vigne au niveau de chaque placette d'échantillonnage au sol des variables agronomiques, site d'étude de Lagardère (32), France.

Les patrons d'indice de stress mesuré lors de la maturation des baies rappellent les patrons de températures pris dans la zone des grappes (**Figure 144**): les valeurs les plus fortes d'indice de stress apparaissent dans la partie Nord-Ouest de la parcelle, tandis que des valeurs relativement faibles à très faibles se manifestent au niveau des vignes situées sur le premier rang directement au sud des allées d'arbres. Toutefois, les valeurs calculées de CWSI dépassent le seuil théorique maximal de 1 qui s'explique par plusieurs difficultés méthodologiques rencontrées lors de son calcul. Celles-ci concernent (i) la résolution des images IRT (autour de 20 cm) qui est large par rapport à la largeur du feuillage de la vigne (autour de 50 cm), ainsi que (ii) l'estimation des températures de référence T_{wet} et T_{dry} en condition non limitées d'accès à l'eau et en condition de fermeture complète des stomates respectivement. L'estimation de T_{wet} et T_{dry} a en effet été testée via le modèle SVAT à une dimension SEtHyS (Coudert 2006; Guillevic et al. 2012) développé à l'origine pour des couverts homogènes (modèle big leaf) mais qui montre des résultats satisfaisants dans le cas de vergers en contexte Méditerranéen (Coudert, communication personnelle). Les maquettes de vignobles agroforestiers construites avec DART pourraient être réutilisées pour simuler la température de surface de la vigne (simulations d'images IRT), moyennant le couplage avec un modèle de type SVAT. Ceci pourrait permettre de mieux comprendre l'impact de l'architecture de la vigne sur son phytoclimat. Cette approche peut permettre de résoudre les problèmes techniques rencontrés pour l'estimation des températures de référence T_{wet} and T_{dry} qui sont liés à l'ombrage de la vigne sur elle-même.

Enfin, en termes de perspectives, l'ensemble de données collectées et la méthodologie testée permettront d'élargir le champ de connaissance à d'autres contextes de vignobles agroforestiers. D'une part, les deux parcelles ciblées sur le domaine expérimental de Restinclières (34) avaient déjà été référencées dans le passé dans le cadre d'un essai à long terme mené par la Chambre d'Agriculture de

l'Hérault (CA 34) mais leur microclimat n'avait jamais été évalué en continuité sur l'ensemble du cycle végétatif de la vigne. D'autre part, les sites de Lagardère (32) et de Lapouyade (33) n'avaient jamais été référencés auparavant et ont bénéficié d'un effort expérimental pluridisciplinaire dans le cadre du projet Vitiforest auquel cette thèse à participé. Une analyse succincte des suivis de température à Restinclières (34) dans la zone des grappes, suggère que, la plupart des jours d'été, l'interception de la lumière par les arbres diminue de 2,5 ° C les températures des premières rangées de vignes qui avoisinent les rangées d'arbres (**Figure 149**). Une analyse plus approfondie de ces données pourra être conduite suivant une approche statistique identique à celle testée à Lagardère (32), et les résultats pourront être comparés aux références prises l'année précédente (Gouttesoulard 2015).

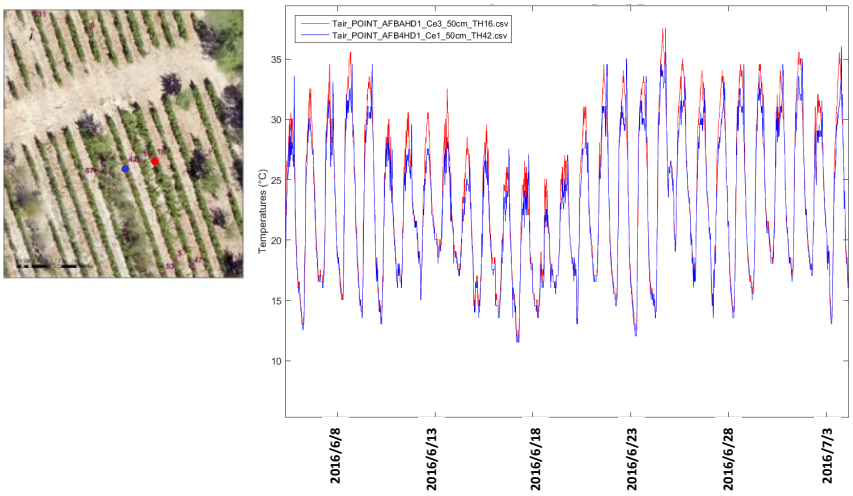

Figure 149 : Séries temporelles de températures enregistrées dans la zone des grappes de vignes constituant le premier rang côté ouest des Cormiers (Sorbus Domestica (courbe bleu) et le troisième rang de vignes à égale distance entre 2 allées d'arbres (rouge), Restinclières (34), parcelle B4.

VII.3.2 Questions ouvertes

Cette thèse laisse quelques questions ouvertes, soit parce que la réponse à ces questions ne faisait pas partie des principaux objectifs, soit parce que leur investigation s'est avérée plus complexe que prévue.

Les caractéristiques du sol et leurs impacts sur les systèmes racinaires de la vigne et des arbres resteront insuffisamment référencés. La revue bibliographique réalisée met en évidence l'importance de ces facteurs pour appréhender l'effet des arbres sur les composantes du bilan hydrique d'un vignoble. Ainsi, documenter les propriétés du sol relatives à son fonctionnement hydrique ainsi que l'architecture des racines dans une zone de voisinage arbre-vigne pourrait permettre de mieux comprendre les risques de concurrence pour l'eau. Des approches géophysiques telles que la tomographie de la résistivité électrique du sol (Buvat et al. 2014) combinée à l'échantillonnage des racines par fosse pourraient constituer une stratégie pour mener ces recherches. En complément, ces approches pourraient permettre un lien avec d'autres facteurs influençant la quantité et la qualité de la

vendange (**Figure 146**) notamment la compétition pour les nutriments (Trambouze and Goma-Fortin 2013; Trambouze et al. 2017).

La contribution climatique liée à l'architecture de la vigne elle-même émerge comme un facteur clé de la variabilité du phytoclimat et de la sensibilité de la vigne à l'ombrage des arbres. Par souci de concision, cette question a conduit au choix méthodologique de ne modéliser que l'architecture en simple rideau correspondant à celle en place à Lagardère. Néanmoins, des comparaisons avec des architectures plus horizontales permettraient de documenter la sensibilité de l'absorption de la lumière vis à vis de ce facteur. L'utilisation de la carte d'occupation du sol pourrait être pertinente là encore pour modéliser des architectures géométriques simples mais pourrait rencontrer certaines limites pour représenter des architectures plus complexes et plus buissonnantes, telles que des vignes en *gobelet*. Dans ces derniers cas, la contribution de l'imagerie LIDAR pourrait être étudiée.

VII.4 Note finale

Bien que la charge de travail fût grande, je pense que le lecteur de ce manuscrit aura compris que le pas est encore petit vers une meilleure connaissance des vignobles en agroforesterie. Face au peu de références et à la grande diversité des contextes et pratiques, la réalisation de cette thèse aura été avant tout, un grand exercice d'humilité. Comment fixer certains paramètres lorsque tout bouge, d'un site à l'autre, au sein d'un même site ou dans le temps même d'une seule journée d'acquisition ? Et pourquoi espérer collecter des « références » alors que tous les cas semblent différents ? A l'heure où j'écris ces lignes, la mise en lumière de pratiques innovantes et la création d'espace d'échanges et de témoignages me semblent tout aussi importants que la quête de réponses universelles. Si la recherche entend aider et accompagner une transition écologique et climato-résiliente de l'agriculture, deux points me paraissent centraux en termes de démarche : (i) replacer les résultats d'étude dans leur contexte et (ii) questionner les objectifs des agriculteurs-rices derrière telle ou telle pratique.

« Les arbres n'ont pas 10 ans, ils ne font ni ombre ni concurrence pour l'azote mais le vigneron veut les abattre… », me disait hier un collègue. Ainsi mon ressenti est que la science « dure » demeure d'une nature aveugle et sourde face à la diversité du vivant et la complexité des choix humains qui se combinent dans un vignoble co-planté d'arbres. Des démarches de recherche participative, collaboratives ou pluridisciplinaires me semblent des voies à davantage emprunter pour aborder avec plus de pertinence des systèmes complexes et émergents tels que les vignobles en agroforesterie.

A titre plus personnel, cette thèse aura été une longue mais intense et riche aventure. J'ai découvert le monde de la viticulture grâce aux viticulteurs-rices du projet Vitiforest et aux collègues d'instituts techniques qui m'ont chaleureusement ouvert leurs portes et au passage initiée à quelques breuvages fort réussis. J'ai également été portée par cette soif de rigueur et de perfectionnement

scientifique qui anime le monde de la recherche, grâce notamment à de très belles rencontres scientifiques et humaines au sein du CESBIO et des laboratoires voisins. A court terme, cette thèse va me permettre d'intégrer l'équipe du RMT Agroforesteries, nouvelle expérience auprès des arbres qui, je pense, sera tout aussi stimulante que celle qui s'achève.

Bibliography

Acevedo-Opazo C, Ortega-Farias S, Fuentes S (2010) Effects of grapevine (Vitis vinifera L.) water status on water consumption, vegetative growth and grape quality: An irrigation scheduling application to achieve regulated deficit irrigation. Agricultural Water Management 97:956–964. doi: 10.1016/j.agwat.2010.01.025

Allen RG (ed) (1998) Crop evapotranspiration: guidelines for computing crop water requirements - FAO56. Food and Agriculture Organization of the United Nations, Rome

Al-Saddik H, Simon J-C, Cointault F (2017) Development of Spectral Disease Indices for "Flavescence Dorée" Grapevine Disease Identification. Sensors 17:2772. doi: 10.3390/s17122772

Amouretti M-C (1988) La viticulture antique : contraintes et choix techniques. Revue des Études Anciennes 90:5–17. doi: 10.3406/rea.1988.4316

Aranda I, Forner A, Cuesta B, Valladares F (2012) Species-specific water use by forest tree species: From the tree to the stand. Agricultural Water Management 114:67–77. doi: 10.1016/j.agwat.2012.06.024

Araujo F, Williams LE, Grimes DW, Matthews MA (1995) A comparative study of young "Thompson Seedless" grapevines under drip and furrow irrigation. I. Root and soil water distributions. Scientia Horticulturae 60:235–249. doi: 10.1016/0304-4238(94)00710-W

Archer E, Strauss HC (1989) Effect of shading on the performance of Vitis vinifera L. cv. Cabernet Sauvignon. South African Journal of Enology and Viticulture 10:74–77

Artru S, Garre S, Dupraz C, et al (2017) Impact of spatio-temporal shade dynamics on wheat growth and yield, perspectives for temperate agroforestry. European Journal of Agronomy 82:60–70. doi: 10.1016/j.eja.2016.10.004

Arya SP (2001) Introduction to micrometeorology, 2nd ed. Academic Press, San Diego

Atkinson D (1983) The growth, activity and distribution of the fruit tree root system. Plant and Soil 71:23–35. doi: 10.1007/BF02182638

Atkinson D (2011) The Distribution and Effectiveness of the Roots of Tree Crops. In: Janick J (ed) Horticultural Reviews. John Wiley & Sons, Inc., Hoboken, NJ, USA, pp 424–490

Austin CN, Wilcox WF (2012) Effects of Sunlight Exposure on Grapevine Powdery Mildew Development. Phytopathology 102:857–866. doi: 10.1094/PHYTO-07-11-0205

Azuma A, Yakushiji H, Koshita Y, Kobayashi S (2012) Flavonoid biosynthesis-related genes in grape skin are differentially regulated by temperature and light conditions. Planta 236:1067–1080. doi: 10.1007/s00425-012-1650-x

Baatz M, Schäpe A (2000) Multiresolution Segmentation: An Optimization Approach for High Quality Multi-scale Image Segmentation. In: Strbla J (ed) Beiträge zum AGIT Symposium Salsburg 2000, (Hrsg.): Angewandte Geographische Informationsverarbeitung, XII, Herbert Wichmann Verlag, Karlruhe. pp 12–23

Bagley WT (1988) 33. Agroforestry and windbreaks. Agriculture, Ecosystems & Environment 22:583–591

Baldy C, Stigter CJ (1998) Agrometeorology of multiple cropping in warm climates. Institut national de la recherche agronomique, Paris

Barbier N, Couteron P, Gastelly-Etchegorry J-P, Proisy C (2012) Linking canopy images to forest structural parameters: potential of a modeling framework. Annals of Forest Science 69:305–311. doi: 10.1007/s13595-011-0116-9

Batish DR (ed) (2008) Ecological basis of agroforestry. CRC Press, Boca Raton, Fla.

Bauerle TL, Richards JH, Smart DR, Eissenstat DM (2007) Importance of internal hydraulic redistribution for prolonging the lifespan of roots in dry soil. Plant, Cell & Environment 0:177–186. doi: 10.1111/j.1365-3040.2007.01749.x

Bayala J, Sanou J, Teklehaimanot Z, Sinclair F (2015) Adaptation of crops to partial shade in mixed cropping systems. In: Ong CK, Black CR, Wilson J (eds) Tree-crop interactions: agroforestry in a changing climate, 2nd edn. CABI, Wallingford, pp 309–325

Bayala J, Wallace JS (2015) The water balance of mixed tree-crop systems. In: Ong CK, Black CR, Wilson J (eds) Tree-crop interactions: agroforestry in a changing climate, 2nd edn. CABI, Wallingford, pp 146–190

Bean A, Alperi RW, Federer CA (1974) A method for categorizing shelterbelt porosity. Agricultural Meteorology 14:417–429

Bégué A, Arvor D, Bellon B, et al (2018) Remote Sensing and Cropping Practices: A Review. Remote Sensing 10:99. doi: 10.3390/rs10010099

Bégué A, Arvor D, Lelong C, et al (2015) Agricultural systems studies using remote sensing. In: Thenkabail PS (ed) Land resources monitoring, modeling, and mapping with remote sensing (Remote Sensing Handbook, 2). Taylor & Francis, Boca Raton, Fla, pp 113–130

Bellvert J, Zarco-Tejada PJ, Girona J, Fereres E (2014) Mapping crop water stress index in a "Pinot-noir" vineyard: comparing ground measurements with thermal remote sensing imagery from an unmanned aerial vehicle. Precision Agriculture 15:361–376. doi: 10.1007/s11119-013-9334-5

Bergez J-E, Etienne M, Balandier P (1999) ALWAYS: a plot-based silvopastoral system model. Ecological Modelling 115:1–17. doi: 10.1016/S0304-3800(98)00153-7

Bergqvist J, Dokoozlian N, Ebisuda N (2001) Sunlight exposure and temperature effects on berry growth and composition of cabernet Sauvignon and grenache in the central San Joaquin Valley of California. American Journal of Enology and Viticulture 52:1–7

Berk A, Conforti P, Kennett R, et al (2014) MODTRAN® 6: A major upgrade of the MODTRAN® radiative transfer code. IEEE, pp 1–4

Betbeder J, Hubert-Moy L, Burel F, et al (2015) Assessing ecological habitat structure from local to landscape scales using synthetic aperture radar. Ecological Indicators 52:545–557. doi: 10.1016/j.ecolind.2014.11.009

Béziat P, Ceschia E, Dedieu G (2009) Carbon balance of a three crop succession over two cropland sites in South West France. Agricultural and Forest Meteorology 149:1628–1645. doi: 10.1016/j.agrformet.2009.05.004

Black CR, Randhawa D, Ong CK (2015) Principles of Resource Capture and Use of Light and Water. In: Ong CK, Black CR, Wilson J, et al. (eds) Tree-crop interactions: agroforestry in a changing climate, Second Edition. CAB International, Wallingford, Oxfordshire. UK ; Boston, MA, USA, pp 57–118

Black TA, Gardner WR, Thurtell GW (1969) The Prediction of Evaporation, Drainage, and Soil Water Storage for a Bare Soil1. Soil Science Society of America Journal 33:655. doi: 10.2136/sssaj1969.03615995003300050013x

Blaschke T (2010) Object based image analysis for remote sensing. ISPRS Journal of Photogrammetry and Remote Sensing 65:2–16. doi: 10.1016/j.isprsjprs.2009.06.004

Bloesch B, Viret O (2008) Stades phénologiques repères de la vigne. Revue suisse de Viticulture Arboriculture Horticulture 40:I–IV

Blouin J (2007) Le dictionnaire de la vigne et du vin. Dunod, Paris

Bonan GB (2008) Forests and Climate Change: Forcings, Feedbacks, and the Climate Benefits of Forests. Science 320:1444–1449. doi: 10.1126/science.1155121

Bonnefoy C (2013) Observation et modélisation spatiale de la température dans les terroirs viticoles du Val de Loire dans le contexte du changement climatique. Université Rennes 2

Borel CC, Gerstl SAW, Powers BJ (1991) The radiosity method in optical remote sensing of structured 3-D surfaces. Remote Sensing of Environment 36:13–44. doi: 10.1016/0034-4257(91)90028-5

Bouby L, Figueiral I, Bouchette A, et al (2013) Bioarchaeological Insights into the Process of Domestication of Grapevine (Vitis vinifera L.) during Roman Times in Southern France. PLoS ONE 8:e63195. doi: 10.1371/journal.pone.0063195

Boussard H (2014) Chloe212 a software for landscape pattern analysis.pdf

Branas J (1974) Viticulture. Broché

Branas J (1970) Données théoriques fondamentales sur le mode de conduite de la vigne. Bulletin of the American Meteorological Society 43:335–346

Brandle JR, Hodges L, Wight B (2000) Windbreak practices. North American agroforestry: An integrated science and practice 79–118

Brandle JR, Hodges L, Zhou XH (2004) Windbreaks in North American agricultural systems. Agroforestry Systems 61:65–78

Breiman L (2001) Random forests. Machine learning 45:5–32

Brenner AJ, Jarvis PG, Van Den Beldt RJ (1995) Windbreak-crop interactions in the Sahel. 1. Dependence of shelter on field conditions. Agricultural and Forest Meteorology 75:215–234

Brooks JR, Meinzer FC, Warren JM, et al (2006) Hydraulic redistribution in a Douglas-fir forest: lessons from system manipulations. Plant, Cell and Environment 29:138–150. doi: 10.1111/j.1365-3040.2005.01409.x

Broome JC, English JT, Marois JJ, et al (1995) Development of an infection model for botrytis bunch rot of grapes based on wetness duration and temperature. Ecology and Epidemiology 85:97–102

Bruniquel-Pinel V, Gastellu-Etchegorry JP (1998) Sensitivity of Texture of High Resolution Images of Forest to Biophysical and Acquisition Parameters. Remote Sensing of Environment 65:61–85. doi: 10.1016/S0034-4257(98)00009-1

Brutsaert W (1982) Energy Fluxes at the Earths Surface. In: Evaporation into the Atmosphere. Springer Netherlands, Dordrecht, pp 128–153

Burel F, Baudry J (1999) Ecologie du Paysage : concept, méthode et application. TEC&DOC

Burel F, Baudry J, Lefeuvre J (1993) Landscape structure and the controle of water runoff. In: Bunce RGH, Ryszkowski L, Paoletti MG (eds) Landscape ecology and agroecosystems. Lewis Publishers, Boca Raton, pp 41–47

Burgess SSO, Adams MA, Turner NC, et al (2001) Tree roots: conduits for deep recharge of soil water. Oecologia 126:158–165. doi: 10.1007/s004420000501

Burgess SSO, Adams MA, Turner NC, Ong CK (1998) The redistribution of soil water by tree root systems. Oecologia 115:306–311. doi: 10.1007/s004420050521

Buvat S, Thiesson J, Michelin J, et al (2014) Multi-depth electrical resistivity survey for mapping soil units within two 3ha plots. Geoderma 232–234:317–327. doi: 10.1016/j.geoderma.2014.04.034

Caborn JM (1957) Shelterbelts and microclimate. H.M. Stationery Office

Calder IR (1986) A stochastic model of rainfall interception. Journal of Hydrology 89:65–71. doi: 10.1016/0022-1694(86)90143-5

Calder IR, Newson MD (1979) Land-use and upland water resources in Britain - a strategic look. Journal of the American Water Resources Association 15:1628–1639. doi: 10.1111/j.1752-1688.1979.tb01176.x

Caldwell MM, Dawson TE, Richards JH (1998) Hydraulic lift: consequences of water efflux from the roots of plants. Oecologia 113:151–161. doi: 10.1007/s004420050363

Calonnec A, Cartolaro P, Naulin J-M, et al (2008) A host-pathogen simulation model: powdery mildew of grapevine. Plant Pathology 57:493–508. doi: 10.1111/j.1365-3059.2007.01783.x

Calonnec A, Latu G, Naulin J-M, et al (2005) Parallel Simulation of the Propagation of Powdery Mildew in a Vineyard. In: Cunha JC, Medeiros PD (eds) Euro-Par 2005 Parallel Processing. Springer Berlin Heidelberg, Berlin, Heidelberg, pp 1254–1264

Carbonneau A (ed) (1992) Agrométéorologie de la vigne en France. Commission of the European Communities, Brussels

Carbonneau A, Casteran P (1986) Essai de systemes de conduite de la vigne pour la production de raisins pourris nobles en bordelais. Connaissance vigne vin 20:17–38

Carbonneau A, Deloire A, Jaillard B (2015) Traité de la vigne: physiologie, terroir, culture. Dunod, Paris

Caruso G, Tozzini L, Rallo G, et al (2017) Estimating biophysical and geometrical parameters of grapevine canopies ('Sangiovese') by an unmanned aerial vehicle (UAV) and VIS-NIR cameras. Vitis 56:63–70

Celette F, Gaudin R, Gary C (2008) Spatial and temporal changes to the water regime of a Mediterranean vineyard due to the adoption of cover cropping. European Journal of Agronomy 29:153–162. doi: 10.1016/j.eja.2008.04.007

Celette F, Ripoche A, Gary C (2010) WaLIS—A simple model to simulate water partitioning in a crop association: The example of an intercropped vineyard. Agricultural Water Management 97:1749–1759. doi: 10.1016/j.agwat.2010.06.008

CESBIO (2018) DART User's manual (5.7.0)

Champagnol F (1984) Elements de physiologie de la vigne et de viticulture générale. Déhan, [Montpellier] Saint-Gely-du-Fesc

Chang C, Salinas S, Liew S, Kwoh L (2006) Spectral reflectance of clouds in multiple-resolution satellite remote sensing images. In: Proceedings of the 27th Asian Conference on Remote Sensing (ACRS), Ulannbaator, Mongolia. pp 9–13

Chazdon RL (1988) Sunflecks and Their Importance to Forest Understorey Plants. In: Advances in Ecological Research. Elsevier, pp 1–63

Chazdon RL, Pearcy RW (1991) The Importance of Sunflecks for Forest Understory Plants. BioScience 41:760–766. doi: 10.2307/1311725

Cheyiner V, Rigaud J, Souquet J-M, et al (1990) Must browing in relation to the behavio of phenolic compounds during axidation. American Journal of Enology and Viticulture 41:346–349

Chiapale JP (1975) A numerical model for estimating the modification of heat budget introduced by hedges. In: Proceedings of international conference. Scripta book co., Dubrovnik, pp 456–466

Chirko CP (1993) Paulownia/winter wheat intercropping: quantifying the relationship between photosynthetically active radiation (PAR) and yield. PhS. dissertation, Michigan State University

Chirko CP, Gold MA, Nguyen PV, Jiang JP (1996a) Influence of direction and distance from trees on wheat yield and photosynthetic photon flux density (Qp) in a Paulownia and wheat intercropping system. Forest ecology and management 83:171–180

Chirko CP, Gold MA, Nguyen PV, Jiang JP (1996b) Influence of orientation on wheat yield and photosynthetic photon flux density (Qp) at the tree and crop interface in a Paulownia—wheat intercropping system. Forest Ecology and Management 89:149–156. doi: 10.1016/S0378-1127(96)03853-4

Choisnel E (1977) Le bilan d'énergie et le bilan hydrique du sol. La Météorologie 6:103–159

Cifre J, Bota J, Escalona JM, et al (2005) Physiological tools for irrigation scheduling in grapevine (Vitis vinifera L.). Agriculture, Ecosystems & Environment 106:159–170. doi: 10.1016/j.agee.2004.10.005

Clark DB, Mercado LM, Sitch S, et al (2011) The Joint UK Land Environment Simulator (JULES), model description – Part 2: Carbon fluxes and vegetation dynamics. Geoscientific Model Development 4:701–722. doi: 10.5194/gmd-4-701-2011

Cleugh HA (1998) Effects of windbreaks on airflow, microclimates and crop yields. Agroforestry systems 41:55–84

CNES (2018) Orfeo ToolBox. https://www.orfeo-toolbox.org/

Contador ML, Comas LH, Metcalf SG, et al (2015) Root growth dynamics linked to above-ground growth in walnut (*Juglans regia*). Annals of Botany 116:49–60. doi: 10.1093/aob/mcv064

Corlett J., Ong CK, Black CR (1989) Microclimatic modification in intercropping and alley-cropping systems. In: Meteorology and agroforestry. ICRAF, Nairobi 9 -13 February 1987, pp 419–430

Coudert B (2006) Apport des mesures de température de surface par télédétection infrarouge thermique pour la modélisation des échanges d'énergie et d'eau à l'interface sol végétation atmosphère. Université de Versailles-Saint Quentin en Yvelines

Crockford RH, Richardson DP (2000) Partitioning of rainfall into throughfall, stemflow and interception: effect of forest type, ground cover and climate. Hydrological Processes 14:2903–2920. doi: 10.1002/1099-1085(200011/12)14:16/17<2903::AID-HYP126>3.0.CO;2-6

Crosbie RS, Wilson B, Hughes JD, McCulloch C (2008) The upscaling of transpiration from individual trees to areal transpiration in tree belts. Plant and Soil 305:25–34. doi: 10.1007/s11104-007-9420-4

Cutter BE, Coggeshall MV, Phelps JE, Stokke DD (2007) Impacts of forest management activities on selected hardwood wood quality attributes: a review. Wood and fiber science 36:84–97

Dai ZW, Ollat N, Gomès E, et al (2011) Ecophysiological, Genetic, and Molecular Causes of Variation in Grape Berry Weight and Composition: A Review. American Journal of Enology and Viticulture 62:413–425. doi: 10.5344/ajev.2011.10116

Darnhofer T, Gatama D, Huxley P, Akunda E (1989) The rainfall distribution at a tree/crop interface. In: Reifsnyder WE, Darnhofer T (eds) Proceedings of ICRAF/WMO/UNEP Workshop on Application of Meteorology to Agroforestry Systems Planting and Management. ICRAF, Nairobi, Kenya, pp 371–382

Dauzat J, Eroy M. (1997) Simulating light regime and intercrop yields in coconut based farming systems. European Journal of Agronomy 7:63–74. doi: 10.1016/S1161-0301(97)00029-4

Dawson TE (1993) Hydraulic lift and water use by plants: implications for water balance, performance and plant-plant interactions. Oecologia 95:565–574. doi: 10.1007/BF00317442

De Parcevaux S, Huber L (2007) Bioclimatologie: concepts et applications. Éditions Quae, Paris

Denyer K, Burns B, Ogden J (2006) Buffering of native forest edge microclimate by adjoining tree plantations. Austral Ecology 31:478–489. doi: 10.1111/j.1442-9993.2006.01609.x

Desmarez V (1997) Modélisation du transfert radiatif et télédétection hyperspectrale pour le suivi temporel de la teneur en chlorophylle d'une forêt tempérée. PhD Thesis, Université Toulouse III Paul Sabatier

Desplanques H (1958) Essay of interpretation of the talian mixed cropping in Italy, essay of interpretation [French titlte: La culture mixte italienne. Essai d'interprétation]. Bulletin de l'Association de géographes français 35:23–37. doi: 10.3406/bagf.1958.7578

Disney MI, Lewis P, North PRJ (2000) Monte Carlo ray tracing in optical canopy reflectance modelling. Remote Sensing Reviews 18:163–196. doi: 10.1080/02757250009532389

Dobrowski S., Ustin S., Wolpert J. (2002) Remote estimation of vine canopy density in vertically shoot positioned vineyards: determining optimal vegetation indices. Australian Journal of Grape and Wine Research 8:117–125. doi: 10.1111/j.1755-0238.2002.tb00220.x

Dokoozlian NK, Kliewer WM (1996) Influence of light on grape berry growth and composition varies during fruit development. Journal of the American Society for Horticultural Science 121:869–874

Downey MO, Dokoozlian NK, Krstic MP (2006) Cultural practice and environmental impacts on the flavonoid composition of grapes and wine: a review of recent research. American Journal of Enology and Viticulture 57:257–268

Duan M, Min Q, Lü D (2010) A polarized Radiative Transfer model based on successive order of scattering. Advances in Atmospheric Sciences 27:891–900. doi: 10.1007/s00376-009-9049-8

Duchêne E, Huard F, Dumas V, et al (2010) The challenge of adapting grapevine varieties to climate change. Climate Research 41:193–204. doi: 10.3354/cr00850

Duffie JA, Beckman WA (2013) Solar engineering of thermal processes / John A. Duffie, William A. Beckman, 4th ed. John Wiley, Hoboken

Duffours C (2011) Contribution of the distance between grapevine and trees to the performances of grapevine under agroforestry practices [French: Influence de la proximité du rang d'arbre sur le comportement de la vigne en système agroforestier]. Master thesis, Montpellier SupAgro & Chambre d'Agriculture de l'Herault

Dufour L, Metay A, Talbot G, Dupraz C (2013) Assessing Light Competition for Cereal Production in Temperate Agroforestry Systems using Experimentation and Crop Modelling. Journal of Agronomy and Crop Science 199:217–227. doi: 10.1111/jac.12008

Dupraz C, Burgess PJ, Gavaland A, et al (2005) Silvoarable Agroforestry for Europe, SAFE project Final Report

Eagleson PS (2005) Ecohydrology: Darwinian expression of vegetation form and function, 1st pbk. ed. Cambridge University Press, Cambridge, UK ; New York, NY

Eastham J, Rose C (1990) Tree pasture interactions at a range of tree densities in an agroforestry experiment. I. Rooting patterns. Australian Journal of Agricultural Research 41:683. doi: 10.1071/AR9900683

Eiseltová M, Pokorný J, Hesslerová P, Ripl W (2012) Evapotranspiration - A Driving Force in Landscape Sustainability. In: Evaporation and Remote Sensing Modeling, InTech. Dr. Ayse Irmak

Ellison D, Morris CE, Locatelli B, et al (2017) Trees, forests and water: Cool insights for a hot world. Global Environmental Change 43:51–61. doi: 10.1016/j.gloenvcha.2017.01.002

Emerman SH, Dawson TE (1996) Hydraulic lift and its influence on the water content of the rhizosphere: an example from sugar maple, Acer saccharum. Oecologia 108:273–278. doi: 10.1007/BF00334651

English JT, Bledsoe AM, Marois JJ, Kliewer WM (1990) Influence of Grapevine Canopy Management on Evaporative Potential in the Fruit Zone. American Journal of Enology and Viticulture 41:137–141

English JT, Thomas CS, Marois JJ, Gubler WD (1989) Microclimates of Grapevine canopies associated with leaf removal and control of botrytis bunch rot. Ecology and Epidemiology 79:395–401

Esri (2018) How Topo to Raster works. In: ArcGIS Pro. https://pro.arcgis.com/en/pro-app/tool-reference/3d-analyst/how-topo-to-raster-works.htm#GUID-989894B7-1C35-4B46-8142-ACF3BFA6553C. Accessed 8 Jan 2018

Evans RJ, Von Caemmerer S (2010) Chapter 1 Light use and leaf gas exchange. In: Munns R, Schmidt S, Beveridge C (eds) Plants in action - Edition 2. Australian Society of Plant Scientists, New Zealand Society of Plant Biologists, and New Zealand Institute of Agricultural and Horticultural Science, pp 1–49

Fabre E (2015) Des vignes entre champs et bois. Le cas de la marge pyrénéenne du vignoble languedocien (milieu XVIIIe-milieu XIXe siècle). In: Marache C, Lachaud S, Bodinier B, Association d'histoire des sociétés rurales (eds) L'univers du vin. Hommes, paysages et territoires. Actes du colloque de Bordeaux (2-5 octobre 2012). pp 373–388

Folorunso OA, Rolston DE, Prichard T, Loui DT (1992) Soil surface strength and infiltration rate as affected by winter cover crops. Soil Technology 5:189–197. doi: 10.1016/0933-3630(92)90021-R

Forman RT, Baudry J (1984) Hedgerows and hedgerow networks in landscape ecology. Environmental management 8:495–510

Forman RTT, Godron M (1986) Landscape ecology. Wiley, New York

Fraga H, Malheiro AC, Moutinho-Pereira J, Santos JA (2012) An overview of climate change impacts on European viticulture. Food and Energy Security 1:94–110. doi: 10.1002/fes3.14

FranceAgrimer (2012) Les chiffres clés de la filière viti-vinicole. Données statistiques 2001/2011. Direction Marchés Etudes et Prospective

Frazer GW, Canham CD, Lertzman KP (1999) Gap Light Analyzer (GLA), Version 2.0: Imaging software to extract canopy structure and gap light transmission indices from true-colour fisheye photographs, users manual and program documentation. Copyright © 1999

Freeman B, Kliewer WM, Stern P (1982) Influence of Windbreaks and Climatic Region on Diurnal Fluctuation of Leaf Water Potential, Stomatal Conductance, and Leaf Temperature of Grapevines. American Journal of Enology and Viticulture 33:233–236

Freeman B, Smart RE (1976) A root obsevation laboratory for studies with grapevines. American Journal of Enology and Viticulture 27:36–39

Fuentes S, De Bei R, Pech J, Tyerman S (2012) Computational water stress indices obtained from thermal image analysis of grapevine canopies. Irrigation Science 30:523–536. doi: 10.1007/s00271-012-0375-8

Fuentes S, Rogers G, Jobling J, et al (2008) A soil-plant-atmosphere approach to evaluate the effect of irrigation/fertigation strategy on grapevine water and nutrient uptake, grape quality and yield. Acta Horticulturae 297–303. doi: 10.17660/ActaHortic.2008.792.34

Füri J (1977) Der Wasserverbrauch und-bedarf de Reben während der Vegetationsperiode. Wein-Wiss 32:77–121

Gadoury DM, Cadle-Davidson L, Wilcox WF, et al (2012) Grapevine powdery mildew (Erysiphe necator): a fascinating system for the study of the biology, ecology and epidemiology of an obligate biotroph: Grapevine powdery mildew. Molecular Plant Pathology 13:1–16. doi: 10.1111/j.1364-3703.2011.00728.x

Galet P (2000) Précis de viticulture. P. Galet, Montpellier

García de Jalón S, Burgess PJ, Graves A, et al (2017) How is agroforestry perceived in Europe? An assessment of positive and negative aspects by stakeholders. Agroforestry Systems. doi: 10.1007/s10457-017-0116-3

Gary C, Metral R, Metay A, et al (2017) Towards an agroecological viticulure: advances and challenges. In: Proceedings of the 20t GiESCO International Meeting. Mendoza, Argentina

Gash JH, Lloyd CR, Lachaud G (1995) Estimating sparse forest rainfall interception with an analytical model. Journal of Hydrology 170:79–86

Gash JHC (1979) An analytical model of rainfall interception by forests. Quarterly Journal of the Royal Meteorological Society 105:43–55

Gastellu-Etchegorry JP (2008) 3D modeling of satellite spectral images, radiation budget and energy budget of urban landscapes. Meteorology and Atmospheric Physics 102:187–207. doi: 10.1007/s00703-008-0344-1

Gastellu-Etchegorry J-P, Demarez V, Pinel V, Zagolski F (1996) Modeling radiative transfer in heterogeneous 3-D vegetation canopies. Remote sensing of environment 58:131–156

Gastellu-Etchegorry J-P, Grau E, Lauret N (2012) DART: A 3D model for remote sensing images and radiative budget of earth surfaces. In: Modeling and simulation in Engineering. pp 29–68

Gastellu-Etchegorry JP, Guillevic P, Zagolski F, et al (1999) Modeling BRF and Radiation Regime of Boreal and Tropical Forests. Remote Sensing of Environment 68:281–316. doi: 10.1016/S0034-4257(98)00119-9

Gastellu-Etchegorry J-P, Lauret N, Yin T, et al (2017) DART: Recent Advances in Remote Sensing Data Modeling With Atmosphere, Polarization, and Chlorophyll Fluorescence. IEEE Journal of Selected Topics in Applied Earth Observations and Remote Sensing 10:2640–2649. doi: 10.1109/JSTARS.2017.2685528

Gastellu-Etchegorry JP, Martin E, Gascon F (2004) DART: a 3D model for simulating satellite images and studying surface radiation budget. International Journal of Remote Sensing 25:73–96. doi: 10.1080/0143116031000115166

Gastellu-Etchegorry JP, Trichon V (1998) A modeling approach of PAR environment in a tropical rain forest in Sumatra: application to remote sensing. Ecological Modelling 108:237–264. doi: 10.1016/S0304-3800(98)00032-5

Gastellu-Etchegorry J-P, Yin T, Lauret N, et al (2015) Discrete Anisotropic Radiative Transfer (DART 5) for Modeling Airborne and Satellite Spectroradiometer and LIDAR Acquisitions of Natural and Urban Landscapes. Remote Sensing 7:1667–1701. doi: 10.3390/rs70201667

Gatti M, Civardi S, Bernizzoni F, Poni S (2011) Long-Term Effects of Mechanical Winter Pruning on Growth, Yield, and Grape Composition of Barbera Grapevines. American Journal of Enology and Viticulture 62:199–206. doi: 10.5344/ajev.2011.10101

Gaucherel C, Giboire N, Viaud V, et al (2006) A domain-specific language for patchy landscape modelling: The Brittany agricultural mosaic as a case study. Ecological Modelling 194:233–243. doi: 10.1016/j.ecolmodel.2005.10.026

Gay LW, Knoerr KR, Braaten MO (1971) Solar radiation variability on the floor of a pine plantation. Agricultural Meteorology 8:39–50. doi: 10.1016/0002-1571(71)90093-8

GDAL/OGR contributors (2018) GDAL/OGR Geospatial Data Abstraction software Library.

Geier-Hayes K, Hayes MA, Basford DD (1995) Detemining individual tree shade length: a guide for silviculturists. U.S. Department of Agriculture, Forest Service, Intermountain Research Station, Odgen, UT

Geoportail (2018) Geological map of France

Ghezehei S, Annandale J, Everson C (2015) Chapter 3: Modelling radiation interception and water balance in agroforestry systems. In: Ong CK, Black CR, Wilson J (eds) Tree-crop interactions, 2nd Edition: agroforestry in a changing climate., 2nd Edition. CAB International, pp 41–56

Gibelin A-L, Calvet J-C, Viovy N (2008) Modelling energy and CO2 fluxes with an interactive vegetation land surface model-Evaluation at high and middle latitudes. Agricultural and Forest Meteorology 148:1611–1628. doi: 10.1016/j.agrformet.2008.05.013

Gladstone EA, Dokoozlian NK (2003) Influence of leaf area density and trellis/training system on the light microclimate within grapevine canopies. VITIS-GEILWEILERHOF- 42:123–132

Glenn DM, Welker WV (1993) Root development patterns in field grown peach trees. Journal of the American Society of Horticultural Sciences 118:362–365

Goma-Fortin N, Trambouze W (2009) Program concerning Agroforestry at Restinclieres. Study report 2009. [French: Programme Intégré de Recherches en Agroforesterie à Restinclières. Rapport d'étude 2009 - Document remis au Conseil Général du Département de l'Hérault]. CA34, Montpellier SupAgro UMR SYSTEM & UMR CBGP, AGROOF

Goma-Fortin N, Trambouze W (2011) Assessement of the interactions between grapevine and trees in agroforestry vineyards [French: Etude des intéractions entre l'arbre et la vigne en agroforesterie] In PIRAT: Integrated research program concerning Agroforestry at Restinclieres. Study report 2011. [French: Programme Intégré de Recherches en Agroforesterie à Restinclières. Rapport d'étude 2011 - Document remis au Conseil Général du Département de l'Hérault]. CA 34, Montpellier, France

Goma-Fortin N, Trambouze W (2012) Study of grapevine and tree interactions under agrofroestry practices. [French: Etude des interactions entre l'arbre et la vigne en agroforesterie.] in PIRAT: Integrated research program concerning Agroforestry at Restinclieres. Study report 2012. [French: Programme Integre de Recherches an Agroforesterie à Restinclières. Rapport d'étude 2012 - Document remis au Conseil Général du Répartement de l'Hérault]. AGROOF, CA 34, INRA, Valhoriz

Gomez C, Mangeas M, Petit M, et al (2010) Use of high-resolution satellite imagery in an integrated model to predict the distribution of shade coffee tree hybrid zones. Remote Sensing of Environment 114:2731–2744. doi: 10.1016/j.rse.2010.06.007

Gommers CMM, Visser EJW, Onge KRS, et al (2013) Shade tolerance: when growing tall is not an option. Trends in Plant Science 18:65–71. doi: 10.1016/j.tplants.2012.09.008

Gouttesoulard C (2015) Assessment of the inter- and intra-lot variability of agronomic performances of grapevine under agroforestry practices [French: Analyse de la variabilité intra et inter parcellaire du comportement agronomique des vignes en agroforesterie]. Master Thesis, ISARA-Lyon & Chambre d'agriculture de l'Hérault

Grant R (1985) The influence of the sky radiance distribution on the flux density in the shadow of a tree crown. Agricultural and Forest Meteorology 35:59–70. doi: 10.1016/0168-1923(85)90074-7

Grant RH (1997) Biologically active radiation in the vicinity of a single tree. Photochemistry and photobiology 65:974–982

Grau E (2012) Modélisation DART du transfert radiatif Terre-Atmosphere pour simuler les bilans radiatif, images de télédétection et mesures LIDAR des paysages terrestres. Université Paul Sabatier-Toulouse III

Greer DH (2017) Temperature and CO2 dependency of the photosynthetic photon flux density responses of leaves of Vitis vinifera cvs. Chardonnay and Merlot grown in a hot climate. Plant Physiology and Biochemistry 111:295–303. doi: 10.1016/j.plaphy.2016.12.015

Grimaldi J, Fieuzal R, Pelletier C, et al (2016) Microclimate patterns in an agroforesrtry intercropped vineyard. In: Celebrating 20 years of innovations in European Agroforestry. Montpellier, France, pp 191–194

Grimaldi J, Trambouze W, Dufourcq T, et al (2017) Can intercropped trees mitigate heat and drought effects on grapevines? A study of microclimate patterns in agroforestry vineyards, Southern France. In: Book of abstracts. Elsevier, Sitges, Spain, pp 104–105

Gross G (1987) A numerical study of the air flow within and around a single tree. Boundary-layer meteorology 40:311–327

Guillevic P, Gastellu-Etchegorry J. (1999) Modeling BRF and Radiation Regime of Boreal and Tropical Forest. Remote Sensing of Environment 68:317–340. doi: 10.1016/S0034-4257(98)00120-5

Guillevic PC, Privette JL, Coudert B, et al (2012) Land Surface Temperature product validation using NOAA's surface climate observation networks—Scaling methodology for the Visible Infrared Imager Radiometer Suite (VIIRS). Remote Sensing of Environment 124:282–298

Guyot G (1989) Les effets aerodynamiques et microclimatiques des brise-vent et des amenagements regionaux. In: Reifsnyder WS, Darnhofer T (eds) Meteorology and agroforestry. ICRAF, Nairobi 9 -13 February 1987, pp 489–520

Guyot G (1999) Climatologie de l'environnement: cours et exercices corrigés. Dunod, Paris

Guyot G (1972) Etude de l'écoulement de l'air au voisinage d'un obstacle poreux en couche limite turbulente (Aerodynamique des brise-vent). These de Docteur Ingenieur, Universite de PARIS V

Guyot G, Verbrugghe M (1976) Etude de la variabitlié spatiale du microclimat à l'échelle parcellaire en zone bocagère. In: Les bocages: histpore, écologie, écnomie. University of Rennes, Rennes, France, pp 131–136

Hall A, Lamb DW, Holzapfel B, Louis J (2002) Optical remote sensing applications in viticulture - a review. Australian Journal of Grape and Wine Research 8:36–47. doi: 10.1111/j.1755-0238.2002.tb00209.x

Hall A, Lamb DW, Louis J, Holzapfel B (2001) Airborne Vineyard Monitoring. In: Blair R., Williams P., Hoj P. (eds) Proceedings of the 11th Australian Wine Industry Technical Conference, Adelaide, Australia. Hyde Park Press, Adelaide, Adelaide, Australia, p 218

Hall A, Louis J, Lamb D (2003) Characterising and mapping vineyard canopy using high-spatial-resolution aerial multispectral images. Computers & Geosciences 29:813–822. doi: 10.1016/S0098-3004(03)00082-7

Hall RH, Calder IR (1993) Drop size modification by forest canopies: measurements using a disdrometer. Journal of Geophysical Research 98:18465–18470

Halleen F, Holtz G (2001) An overview of the biology, epidemiology and control of Uncinula necator (powdery mildew) on grapevine, with reference to South Africa. South African Journal of Enology and Viticulture 22:111–121

Hanson HC (1917) Leaf structure as related to environment. American Journal of Botany 4:533–560. doi: DOI: 10.2307/2435253

Hao X, Chen Y, Li W, et al (2010) Hydraulic lift in Populus euphratica Oliv. from the desert riparian vegetation of the Tarim River Basin. Journal of Arid Environments 74:905–911. doi: 10.1016/j.jaridenv.2010.01.005

Harborne JB, Williams CA (2000) Advances in flavonoid research since 1992. Phytochemistry 55:481–504. doi: 10.1016/S0031-9422(00)00235-1

Haselgrove L, Botting D, Heeswijck R van, et al (2000) Canopy microclimate and berry composition: the effect of bunch exposure on the phenolic composition of Vitis vinifera L cv. Shiraz grape berries. Australian Journal of Grape and Wine Research 6:141–149

Hedrick UP, Booth NO, Taylor OM, et al (1919) Manual of american grape-growing. New York

Heisler GM, De Walle DR (1988) 2. Effects of windbreak structure on wind flow. Agriculture, ecosystems & environment 22/23:41–69

Hockberger PE (2007) A History of Ultraviolet Photobiology for Humans, Animals and Microorganisms¶. Photochemistry and Photobiology 76:561–579. doi: 10.1562/0031-8655(2002)0760561AHOUPF2.0.CO2

Hodges L, Suratman MN (2004) Growth and yield of snap beans as affected by wind protection and microclimate changes due to shelterbelts and planting dates. Hubbard K 39:996–1004

Huglin P (1978) Nouveau mode d'évaluation des possibilites héliothermiques d'un milieu viticole. In: Proceedings of the Symposium International sur l'ecologie de la Vigne. de l'Agriculture et de l'Industrie Alimentaire, Contança, pp 89–98

Hultine KR, Williams DG, Burgess SSO, Keefer TO (2003) Contrasting patterns of hydraulic redistribution in three desert phreatophytes. Oecologia 135:167–175. doi: 10.1007/s00442-002-1165-4

Hunter J., Volschenk CG, Zorer R (2016) Vineyard row orientation of Vitis vinifera L. cv. Shiraz/101-14 Mgt: Climatic profiles and vine physiological status. Agricultural and Forest Meteorology 228–229:104–119. doi: 10.1016/j.agrformet.2016.06.013

Hutchinson MF (1988) Calculation of Hydrologically Sound Digital Elevation Models. In: Third International Symposium on Spatial Data Handling. Sydney, Australia

Hutchinson MF, Xu T, Stein JA (2011) Recent Progress in the ANUDEM Elevation Gridding procedure. In: Hengel T, Evans IS, Wilson JP, Gould M (eds) Geomorphometry, 2011th edn. Redlands, California, USA, pp 19–22

Huxley PA (1985) The tree/crop interface ? or simplifying the biological/environmental study of mixed cropping agroforestry systems. Agroforestry Systems 3:251–266. doi: 10.1007/BF00046958

Idso SB, Jackson RD, Pinter PJ, et al (1981) Normalizing the stress-degree-day parameter for environmental variability. Agricultural Meteorology 24:45–55

Igounet O, Baldy C, Suard B, et al (1995) Thermal regime of the grape (Vitis vinifera L. Syrah gra^pes) during maturation. Influence of the berry coloration, the compactness degree of the grape and the local wind regime. Journal international des Sciences de la Vigne et du Vin 29:193–204

Inglada J, Vincent A, Arias M, et al (2017) Operational High Resolution Land Cover Map Production at the Country Scale Using Satellite Image Time Series. Remote Sensing 9:95. doi: 10.3390/rs9010095

Inoue E (1963) On the turbuilent structure of airflow within crop canopies. Journal of the Meteorological Society of Japan 41:317–326

INRA, CRPF (2000) Agroforesry at Restinclieres, achievements and perspectives [French: Agroforesterie à Restinclières - Réalisations et Perspectives]. Institut National de la Recherche Agronomique, Centre Régional de la Propriété Forestière, Montpellier, France

Jackson D, Lombard P (1993) Environmental and management practices affecting grape composition and wine quality - a review. American Journal of Enology and Viticulture 44:409–430

Jackson JE (1978) Utilization of light resources by High Density Planting (HDP) systems. Acta Horticulturae 61–70. doi: 10.17660/ActaHortic.1978.65.7

Jackson JE, Palmer JW (1979) A simple model of light transmission and interception by discontinuous canopies. Annals of Botany 44:381–383

Jackson JE, Palmer JW (1972) Interception of Light by Model Hedgerow Orchards in Relation to Latitude, Time of Year and Hedgerow Configuration and Orientation. The Journal of Applied Ecology 9:341. doi: 10.2307/2402436

Jackson RB, Sperry JS, Dawson TE (2000) Root water uptake and transport: using physiological processes in global predictions. Trends in Plant Science 5:482–488. doi: 10.1016/S1360-1385(00)01766-0

Jensen M (1954) Shelter effect: investigations into the aerodynamics of shelter and its effects on climate and crops.

Joly D, Brossard T, Cardot H, et al (2010) Types of climates on continental France, a spatial construction. Cybergeo : European Journal of Geography. doi: 10.4000/cybergeo.23155

Jones GV (2003) Paper 4 from the ’Terroir, Geology and wine: a tribute to Simon J. HAYNES session". In: Geoscience Canada

Jones GV, Davis RE (2000) Using a synoptic climatological approach to understand climate-viticulture relationships. International Journal of Climatology 20:813–837

Jones GV, Webb LB (2010) Climate Change, Viticulture, and Wine: Challenges and Opportunities. Journal of Wine Research 21:103–106. doi: 10.1080/09571264.2010.530091

Jones GV, White MA, Cooper OR, Storchmann K (2005) Climate Change and Global Wine Quality. Climatic Change 73:319–343. doi: 10.1007/s10584-005-4704-2

Jones M, Sinclair FL, Grime VL (1998) Effect of tree species and crown pruning on root length and soil water content in semi-arid agroforestry. 201:197–207

Judd MJ, Raupach MR, Finnigan JJ (1996) A wind tunnel study of turbulent flow around single and multiple windbreaks, part I: velocity fields. Boundary-Layer Meteorology 80:127–165

Juszak I, Iturrate-Garcia M, Gastellu-Etchegorry J-P, et al (2017) Drivers of shortwave radiation fluxes in Arctic tundra across scales. Remote Sensing of Environment 193:86–102. doi: 10.1016/j.rse.2017.02.017

Kammer PM, Schöb C, Eberhard G, et al (2013) The relationship between soil water storage capacity and plant species diversity in high alpine vegetation. Plant Ecology & Diversity 6:457–466. doi: 10.1080/17550874.2013.783142

Karlson M, Ostwald M, Reese H, et al (2016) Assessing the potential of multi-seasonal WorldView-2 imagery for mapping West African agroforestry tree species. International Journal of Applied Earth Observation and Geoinformation 50:80–88. doi: 10.1016/j.jag.2016.03.004

Keller M, Tarara JM, Mills LJ (2010) Spring temperatures alter reproductive development in grapevines: Spring temperatures alter reproductive development. Australian Journal of Grape and Wine Research 16:445–454. doi: 10.1111/j.1755-0238.2010.00105.x

Kidd CV, Pimentel D (eds) (1992) Integrated resource management: agroforestry for development. Academic Press, San Diego

Kimes DS, Kirchner JA (1983) Diurnal variations of vegetation canopy structure. International Journal of Remote Sensing 4:257–271. doi: 10.1080/01431168308948545

Kliewer WM, Dokoozlian NK (2005) Leaf area/crop weight ratios of grapevines: influence on fruit composition and wine quality. American Journal of Enology and Viticulture 56:170–181

Kliewer WM, Torres R (1972) Effect of Controlled Day and Night Temperatures on Grape Coloration. American Journal of Enology and Viticulture 23:71–77

Korwar GR, Radder GD (1994) Influence of root pruning and cutting interval ofLeucaena hedgerows on performance of alley croppedrabi sorghum. Agroforestry Systems 25:95–109. doi: 10.1007/BF00705670

Koyama K, Goto-Yamamoto N (2008) Bunch shading during different developmental stages affects the phenolic biosynthesis in berry skins of "Cabernet Sauvignon"grapes. Journal of the American Society for horticultural Science 133:743–753

Kozlowski T. (1976) Water relations and tree improvement. In: Cannell MC., Last FT. (eds) Tree Physiology and Yield Improvement. Academic Press, New York, pp 307–327

Kriedemann P. (1968) Photosynthesis in vine leaves as a function of light intensity, temperature and leaf age. Vitis 7:213–220

Kriedemann P. (1977) Vineleaf photosynthesis. OIV, Oenological and Viticultural Research Institute, Capetown, pp 67–87

Kriedemann P., Buttrose MS (1971) Chlorophyll content and photosynthetic activity within woody shoots of vitis vinifera. Photosynthetica 22–27

Kriedemann P., Smart R. (1971) Effects of irradiance, temperature, and leaf water potential on photosynthesis of vine leaves. Photosynthetica 5:6–15

Küng O, Strecha C, Fua P, et al (2011) Simplified building models extraction from ultra-light UAV imagery. In: International Archives of the Photogrammetry, Remote Sensing and Spatial Information Scien. Cambridge University Press, Cambridge, UK ; New York, pp 217–222

Lafont S, Denis Loustau, Tiphaine Tallec, et al (2014) The French ICOS ecosystem monitoring sites: an overview. Bruxelles, Belgium

Landier L (2018) 3D modeling of the radiative budget of urban landscapes [French Title: Modélisation 3D du bilan radiatif des milieux urbains]. Université Paul Sabatier-Toulouse III

Landier L, Al Bitar A, Lauret N, et al (2016) 3D modeling of radiative transfer and energy balance in urban canopies combined to remote sensing acquisitions. In: Geoscience and Remote Sensing Symposium (IGARSS), 2016 IEEE International. IEEE, pp 6738–6741

Landsberg J (1999) Tree water use and its implications in relation to agroforestry systems. In: Landsberg J (ed) The Ways Trees Use Water. pp 1–31

Landsberg JJ, McMurtrie R (1984) Water use by isolated trees. Agricultural Water Management 8:223–242. doi: 10.1016/0378-3774(84)90055-6

Lange B, Lüescher P, Germann PF (2009) Significance of tree roots for preferential infiltration in stagnic soils. Hydrology and earth system sciences 13:1809

Larry Schwankl, Blaine Hanson, Terry Prichard (1998) Micro-irrigation of Trees and Vines: A Handbook for Water Managers, University of California Irrigation Program, University of California, Davis. US

Lauret N (2017) Modélisation 3D des mesures satellitaires des LiDAR et spectroradiomètres polarimétriques pour l'observation des surfaces terrestres. Université Toulouse III Paul Sabatier

Le Moine P (2002) Description of the analysis of surface fields in France by SAFRAN system [French: Description de l'analyse des champs de surface sur la France par le systeme SAFRAN]. Centre National des Recherches Météorologiques, Météo-France

Le Roux R (2017) Modélisation climatique à l'échelle du vignoble dans un contexte de changement climatique. Géographie, Université Bretagne Loire

Lebon E, Dumas V, Pieri P, Schultz HR (2003) Modelling the seasonal dynamics of the soil water balance of vineyards. Functional Plant Biology 30:699. doi: 10.1071/FP02222

Lecomte I, Dupraz C (2015) Hi-sAFe : un modèle agroforestier obtenu par couplage de STICS avec un modèle arbre

Lee J-E, Oliveira RS, Dawson TE, Fung I (2005) Root functioning modifies seasonal climate. Proceedings of the National Academy of Sciences 102:17576–17581. doi: 10.1073/pnas.0508785102

Leeuwen V, Garnier C, Agut C, et al (2008) Heat requirements for grapevine varieties is essential information to adapt plant material in a changing climate.

Lehmann J, Zech W (1998) Fine root turnover of irrigated hedgerow intercropping in Northern Kenya. Plant and Soil 198:19–31. doi: https://doi.org/10.1023/A:1004293910977

Lelong C, Alexandre C, Dupuy S (2014) Discrimination of tropical agroforestry systems in very high resolution satellite imagery using object-based hierarchical classification: A case-study in Cameroon. South-Eastern European Journal of Earth Observation and Geomatics 2S:255–258

Lelong C, Lesponne C, Lamanda N, et al (2004) Understanding the spatial structure of agroforestry systems using very high resolution remote sensing: An application to cotonut-based systems in Melanesia. Orlando, USA, p 1

Leroy C, Sabatier S, Wahyuni NS, et al (2009) Virtual trees and light capture: a method for optimizing agroforestry stand design. Agroforestry Systems 77:37–47. doi: 10.1007/s10457-009-9232-z

Lilov D, Andonova T (1976) cytokinins, growth, flower and fruit formation in *vitis vinifera* . Vitis 160–170

Lim YS, La PH, Park JS, et al (2015) Calculation of Tree Height and Canopy Crown from Drone Images Using Segmentation. Journal of the Korean Society of Surveying, Geodesy, Photogrammetry and Cartography 33:605–614. doi: 10.7848/ksgpc.2015.33.6.605

Linhoss AC, Siegert CM (2016) A comparison of five forest interception models using global sensitivity and uncertainty analysis. Journal of Hydrology 538:109–116. doi: 10.1016/j.jhydrol.2016.04.011

Livesley SJ, Gregory PJ, Buresh RJ (2000) Competition in tree row agroforestry systems. 1. Distribution and dynamics of fine root length and biomass. Plant and Soil 227:149–161

López-Lozano R, Baret F, Atauri IG de C, et al (2011) 2D approximation of realistic 3D vineyard row canopy representation for light interception (fIPAR) and light intensity distribution on leaves (LIDIL). European Journal of Agronomy 35:171–183. doi: 10.1016/j.eja.2011.06.005

López-Lozano R, Baret F, García de Cortázar-Atauri I, et al (2009) Optimal geometric configuration and algorithms for LAI indirect estimates under row canopies: The case of vineyards. Agricultural and Forest Meteorology 149:1307–1316. doi: 10.1016/j.agrformet.2009.03.001

López-Olivari R, Ortega-Farías S, Poblete-Echeverría C (2016) Partitioning of net radiation and evapotranspiration over a superintensive drip-irrigated olive orchard. Irrigation Science 34:17–31. doi: 10.1007/s00271-015-0484-2

Lorenz DH, Eichhorn KW, Bleiholder H, et al (1995) Growth Stages of the Grapevine: Phenological growth stages of the grapevine (Vitis vinifera L. ssp. vinifera)—Codes and descriptions according to the

extended BBCH scale. Australian Journal of Grape and Wine Research 1:100–103. doi: https://doi.org/10.1111/j.1755-0238.1995.tb00085.x

Lorenz K, Lal R (2014) Soil organic carbon sequestration in agroforestry systems. A review. Agronomy for Sustainable Development 34:443–454

Louarn G, Dauzat J, Lecoeur J, Lebon E (2008) Influence of trellis system and shoot positioning on light interception and distribution in two grapevine cultivars with different architectures: an original approach based on 3D canopy modelling. Australian Journal of Grape and Wine Research 143–152. doi: 10.1111/j.1755-0238.2008.00016.x

Louarn G, Lecoeur J, Lebon E (2007) A Three-dimensional Statistical Reconstruction Model of Grapevine (Vitis vinifera) Simulating Canopy Structure Variability within and between Cultivar/Training System Pairs. Annals of Botany 101:1167–1184. doi: 10.1093/aob/mcm170

Lundgren B (1982) Introduction. Agroforestry Systems 1:3–6. doi: 10.1007/BF00044324

Lyr H, Hoffman G (1967) Growth rate and growth periodicity of tree roots. International Review of Forest Resources 181–236

MAA (2017) Cahier des charges de l'appellation d'origine contrôlée "Bordeaux supérieur"

MAAF (2014) Cahier des charges de l'indication geographique protégée"Côtes de Gascogne." French Ministry of Agriculture, Food and Forestry

MAAF (2017) Cahier des charges de l'appellation d'origine contrôlée Pic Saint-Loup

Mabrouk H, Carbonneau A, Sinoquet H (1997) Canopy structure and radiation regime in grapevine. I. Spatial and angular distribution of leaf area in two canopy systems. Vitis, Journal of grapevine research 36:119–124

Mabrouk H, Sinoquet H, Carbonneau A (2015) Canopy structure and radiation regime in grapevine. 2. Modeling radiation interception and distribution inside the canopy. Vitis-Journal of Grapevine Research 36:125

Madrid F (2015) Etat des lieux de l'agroforesterie viticole en France et en Europe. Master Thesis, Bordeaux Sciences Agro & AgroParisTech

Maetens W, Poesen J, Vanmaercke M (2012) How effective are soil conservation techniques in reducing plot runoff and soil loss in Europe and the Mediterranean? Earth-Science Reviews 115:21–36. doi: 10.1016/j.earscirev.2012.08.003

Magriso Y, Tonchev G (1972) the effect of recharge irriation on the growth, yield and quality of the grapevine variety bolgar. Horticulture and Viticulture Sciences (Sofia) 103–111

Makarieva AM, Gorshkov VG, Li B-L (2013) Revisiting forest impact on atmospheric water vapor transport and precipitation. Theoretical and Applied Climatology 111:79–96. doi: 10.1007/s00704-012-0643-9

Malenovsky Z, Martin E, Homolova L, et al (2008) Influence of woody elements of a Norway spruce canopy on nadir reflectance simulated by the DART model at very high spatial resolution. Remote Sensing of Environment 112:1–18. doi: 10.1016/j.rse.2006.02.028

Malheiro A, Santos J, Fraga H, Pinto J (2010) Climate change scenarios applied to viticultural zoning in Europe. Climate Research 43:163–177. doi: 10.3354/cr00918

Mapa RB (1995) Effect of reforestation using Tectona grandis on infiltration and soil water retention. Forest Ecology and Management 77:119–125. doi: 10.1016/0378-1127(95)03573-S

Marais J, Hunter JJ, Haasbroek PD (1999) Effect of Canopy Microclimate, Season and Region on Sauvignon blanc Grape Composition and Wine Quality. South African Journal of Enology & Viticulture 20:. doi: 10.21548/20-1-2223

Martimort P, Arino O, Berger M, et al (2007) Sentinel-2 optical high resolution mission for GMES operational services. In: 2007 IEEE International Geoscience and Remote Sensing Symposium. IEEE, Barcelona, Spain, pp 2677–2680

Maruti G, Sachin Kumar, Kushalappa CG, Vaast P (2012) Throughfall and Interception Loss in Relation to Different Canopy Levels of Coffee Agroforestry Systems. International Journal of Environmental Sciences 1:145–149

Maseda PH, Fernandez RJ (2006) Stay wet or else: three ways in which plants can adjust hydraulically to their environment. Journal of Experimental Botany 57:3963–3977. doi: 10.1093/jxb/erl127

May P (1965) Reducing inflorescence formation by shading individual Sultana buds. Australian Journal of Biological Sciences 18:463–474

Mc Aneney K, Prendergast P, Judd M, Green A (1992) Observations of equilibrium evaporation from a windbreak-sheltered kiwifruit sheltered orchard. Agriculutral and Forest Meteorology 253–264

Mc Aneney KJ, Salinger MJ, Porteous AS, Barber RF (1990) Modification of an orchard climate with increasing shelter-belt height. Agricultural and forest meteorology 49:177–189

McNaughton K. (1988) 1. Effects of windbreaks on turbulent transport and microclimate. Agriculture, Ecosystems & Environment 22/23:17–39

McPherson RA (2007) A review of vegetation—atmosphere interactions and their influences on mesoscale phenomena. Progress in Physical Geography 31:261–285. doi: 10.1177/0309133307079055

Medrano H, Tomás M, Martorell S, et al (2015) Improving water use efficiency of vineyards in semi-arid regions. A review. Agronomy for Sustainable Development 35:499–517. doi: 10.1007/s13593-014-0280-z

Mekonnen M, Keesstra SD, Stroosnijder L, et al (2015) Soil Conservation Through Sediment Trapping: A Review: Individual, combined and integrated sediment trapping. Land Degradation & Development 26:544–556. doi: 10.1002/ldr.2308

Meloni S, Sinoquet H (1997) Assessment of the spatial distribution of light transmitted below young trees in an agroforestry system. In: Annales des sciences forestières. EDP Sciences, pp 313–333

Mendel M, Hergarten S, Neugebauer HJ (2002) On a better understanding of hydraulic lift: A numerical study modeling hydraulic lift. Water Resources Research 38:1-1-1–10. doi: 10.1029/2001WR000911

Merot P (1999) The influence of hedgerow systems on the hydrology of agricultural catchments in a temperate climate. Agronomie 19:655–669

Merot P, Ruellan A (1980) Pedologie, hydrologic des bocages: characteristiques et incidences de l'arasement des talus boises. Bulletin Technique d'Information - Ministère de l'agriculture et du développement durable

Mette R, Sattelmacher B (1994) Root and nitrogen dynamics in the hedgerow-field crop interface: consequences for land use management. In: Proceedings of the 7th International Symposium of CIEC; Humbold University, Berlin, pp 275–284

Miralles DG, Gash JH, Holmes TRH, et al (2010) Global canopy interception from satellite observations. Journal of Geophysical Research 115:. doi: 10.1029/2009JD013530

Mitchell N, Espie P, Hankin R (2004) Rational landscape decision-making: the use of meso-scale climatic analysis to promote sustainable land management. Landscape and Urban Planning 67:131–140. doi: 10.1016/S0169-2046(03)00034-3

Mobbs DC, Lawson AC, Friend AD, et al (1999) HyPAR Model for Agroforesrty Systems, Model Description for Version 3. Technical Manual. DFID Forestry Research Programme (R5652), UK

Moller M, Alchanatis V, Cohen Y, et al (2006) Use of thermal and visible imagery for estimating crop water status of irrigated grapevine. Journal of Experimental Botany 58:827–838. doi: 10.1093/jxb/erl115

Monteith J, Ong C, Corlett J (1991) Microclimatic-interactions-in-agroforestry-systems. Forest Ecology and Management 31–44

Monteith JL, Szeicz G, Waggoner PE (1965) The Measurement and Control of Stomatal Resistance in the Field. The Journal of Applied Ecology 2:345. doi: 10.2307/2401484

Morlat R, Remoué M, Pinet P (1984) Effects of planting density and soil cultivation practices on the root system of vine. [French title: influence de la densité de plantation et du mode d'entretien du sol sur l'enracinement d'un peuplement de vigne planté en sol favorable]. Agronomie 4:485–491

Morton DC, Rubio J, Cook BD, et al (2016) Amazon forest structure generates diurnal and seasonal variability in light utilization. Biogeosciences 13:2195–2206. doi: 10.5194/bg-13-2195-2016

Mosedale JR, Wilson RJ, Maclean IMD (2015) Climate Change and Crop Exposure to Adverse Weather: Changes to Frost Risk and Grapevine Flowering Conditions. PLOS ONE 10:e0141218. doi: 10.1371/journal.pone.0141218

Mosquera-Losada, M.R., Moreno, G., Pardini, A., et al (2012) Past, Present and Future of Agroforestry Systems in Europe. In: Agroforestry - The Future of Global Land Use, Springer Netherlands. P.K. Ramachandran Nair, Dennis Garrity, pp 285–312

Motorina M. (1958) Photosynthesis and grapevine breathing under the conditions of Moscow region. Izvestija Tinerjazevske poljoprivredne akademije 20

Myburgh PA (2004) Determining grapevine canopy effects on effective rainfall in vineyards. South African Journal of Enology and Viticulture 25:33–35

Nair PKR (1991) State-of-the-art of agroforestry systems. Forest Ecology and Management 45:5–29

Nair PKR (1993) An introduction to agroforestry. Kluwer Academic Publishers in cooperation with International Centre for Research in Agroforestry, Dordrecht ; Boston

Newport (2018) Introduction to Solar Radiation. https://www.newport.com/t/introduction-to-solar-radiation

Nolan AP (2015) Crop monitoring with Unmanned Aerial Vehicles (UAV)

Noordwijk M van, Lawson G, Hairiah K (2015) Chapter 8: Root distribution of trees and crops: competition and/or complementarity. In: Ong CK, Black CR, Wilson J, et al. (eds) Tree-crop interactions: agroforestry in a changing climate, Second Edition. CAB International, Wallingford, Oxfordshire. UK ; Boston, MA, USA, pp 221–257

Noordwijk M van, Lusiana B, Khasanah N 'matul (2004) Wanulcas 3.01: background on a model of water, nutrient, and light capture in agroforestry systems. World Agroforestry Centre : International Centre for Research in Agroforestry, Bogor, Indonesia

Norton RL (1988) Windbreaks: benefits to orchard and vineyard crops. Agriculture, Ecosystems & Environment 22/23:205–213

Oke TR (1992) Boundary layer climates

Oliveira RS, Dawson TE, Burgess SSO, Nepstad DC (2005) Hydraulic redistribution in three Amazonian trees. Oecologia 145:354–363. doi: 10.1007/s00442-005-0108-2

Ollat N, Peccoux A, Papura D, et al (2016) Rootstocks as a component of adaptation to environment. In: Gerós H, Chaves MM, Gil HM, Delrot S (eds) Grapevine in a Changing Environment. John Wiley & Sons, Ltd, Chichester, UK, pp 68–108

Ong CK, Anyango S, Muthuri CW, Black CR (2007) Water use and water productivity of agroforestry systems in the semi-arid tropics. Ann Arid Zone 46:255–284

Ong CK, Corlett JE, Singh RP, Black CR (1991) Above and below ground interactions in agroforestry systems. Forest Ecology and Management 45:45–57. doi: 10.1016/0378-1127(91)90205-A

Ong CK, Huxley PA, C.A.B. International, International Centre for Research in Agroforestry (eds) (1996) Tree-crop interactions: a physiological approach. CAB International in association with the International Centre for Research in Agroforestry, Wallingford, Oxford, UK

Otto J, Berveiller D, Bréon F-M, et al (2014) Forest summer albedo is sensitive to species and thinning: how should we account for this in Earth system models? Biogeosciences 11:2411–2427. doi: 10.5194/bg-11-2411-2014

Ovalle C, Avendaño J, Aronson J, Del Pozo A (1996) Land occupation patterns and vegetation structure in the anthropogenic savannas (espinales) of central Chile. Forest Ecology and Management 86:129–139. doi: 10.1016/S0378-1127(96)03786-3

Pachauri RK, Mayer L, Intergovernmental Panel on Climate Change (eds) (2015) Climate change 2014: synthesis report. Intergovernmental Panel on Climate Change, Geneva, Switzerland

Pagé C (2008) Format of SAFRAN data and desagregation of climatic scenari at CERFACS [French: Format des données SAFRAN et scénarios climatiques désagrégés au CERFACS]. CERFACS (Centre Européen de Recherche et de Formation Avancée en Calcul Scientifique)

Pan D, Gao X, Dyck M, et al (2017) Dynamics of runoff and sediment trapping performance of vegetative filter strips: Run-on experiments and modeling. Science of The Total Environment 593–594:54–64. doi: 10.1016/j.scitotenv.2017.03.158

Parisi AV, Kimlin MG, Wong JCF, Wilson M (2000) Diffuse component of solar ultraviolet radiation in tree shade. Journal of Photochemistry and Photobiology B: Biology 54:116–120. doi: 10.1016/S1011-1344(00)00003-8

Parker A, de Cortázar-Atauri IG, Chuine I, et al (2013) Classification of varieties for their timing of flowering and veraison using a modelling approach: A case study for the grapevine species Vitis vinifera L. Agricultural and Forest Meteorology 180:249–264. doi: 10.1016/j.agrformet.2013.06.005

Parsons PG, Neale R, Wolski P, Green A (1998) The shady side of solar protection. Med J Aust 168:327–330

Pedrosa DLS, Correia Filho WL, Gonçalves JP, et al (2017) Climatic Aptitude Evaluation for Grapevine Cultivation in Pão de Açúcar, Alagoas. Revista Geama 3:229–235

Peel MC, Finlayson BL, McMahon TA (2007) Updated world map of the Köppen-Geiger climate classification. Hydrology and Earth System Sciences 5:1633–1644

Pellek R (1992) Contour hedgerows and other soil conservation interventions for hilly terrain. Agroforestry Systems 17:135–152

Pelletier C, Valero S, Inglada J, et al (2016) Assessing the robustness of Random Forests to map land cover with high resolution satellite image time series over large areas. Remote Sensing of Environment 187:156–168. doi: 10.1016/j.rse.2016.10.010

Peña-Barragán JM, Ngugi MK, Plant RE, Six J (2011) Object-based crop identification using multiple vegetation indices, textural features and crop phenology. Remote Sensing of Environment 115:1301–1316. doi: 10.1016/j.rse.2011.01.009

Penman HL (1948) Natural evaporation from open water, bare soil and grass. In: Proceedings of the Royal Society of London A: Mathematical, Physical and Engineering Sciences. The Royal Society, pp 120–145

Perera M (1981) Shelter behind two-dimensional solid and porous fences. Journal of Wind Engineering and Industrial Aerodynamics 8:93–104

Petrie PR, Clingeleffer PR (2005) Effects of temperature and light (before and after budburst) on inflorescence morphology and flower number of Chardonnay grapevines (Vitis vinifera L.). Australian Journal of Grape and Wine Research 11:59–65. doi: 10.1111/j.1755-0238.2005.tb00279.x

Pieri P, Gaudillere J-P (2003) Sensitivity to training system parameters and soil surface albedo of solar radiation intercepted by vine rows. Vitis 42:77–82

Pinho RC, Miller RP, Alfaia SS (2012) Agroforestry and the Improvement of Soil Fertility: A View from Amazonia. Applied and Environmental Soil Science 2012:1–11. doi: 10.1155/2012/616383

Plate EJ (1971) The aerodynamics of shelter belts. Agricultural Meteorology 8:203–222

Plinius Secundus (Plines l'Ancien) (79) Chapter XXXV. The culture of the vine and the various shrubs that supports it. In: Book XVII The natural history of cultivated trees. pp 200–201

Poblete-Echeverría C, Olmedo G, Ingram B, Bardeen M (2017) Detection and Segmentation of Vine Canopy in Ultra-High Spatial Resolution RGB Imagery Obtained from Unmanned Aerial Vehicle (UAV): A Case Study in a Commercial Vineyard. Remote Sensing 9:268. doi: 10.3390/rs9030268

Pokornỳ J (2001) Dissipation of solar energy in landscape—controlled by management of water and vegetation. Renewable energy 24:641–645

Pou A, Diago M, Medrano H, et al (2014) Validation of thermal indices for water status identification in grapevine. Agricultural Water Management 60–72

Prentice IC, Leemans R (1990) Pattern and Process and the Dynamics of Forest Structure: A Simulation Approach. The Journal of Ecology 78:340. doi: 10.2307/2261116

Prosdocimi M, Cerdà A, Tarolli P (2016) Soil water erosion on Mediterranean vineyards: A review. CATENA 141:1–21. doi: 10.1016/j.catena.2016.02.010

Quenol H (2011) Observation et modélisation spatiale du climat aux échelles fines dans un contexte de changement climatique. Geography. Université Rennes 2, Rennes

Quenol H (ed) (2014) Changements climatiques et terroirs viticoles. Tec & Doc, Paris s.l

Raine JK, Stevenson DC (1977) Wind protection by model fences in a simulated atmospheric boundary layer. Journal of Wind Engineering and Industrial Aerodynamics 2:159–180

Raupach MR, Thom AS (1981) Turbulence in and above Plant Canopies. Annual Review of Fluid Mechanics 13:97–129. doi: 10.1146/annurev.fl.13.010181.000525

Rawls WJ, Gish TJ, Brakensiek DL (1991) Estimating Soil Water Retention from Soil Physical Properties and Characteristics. In: Stewart BA (ed) Advances in Soil Science. Springer New York, New York, NY, pp 213–234

Reifsnyder WE (1989) Control of solar radiation in agroforestry practice. In: Reifsnyder WE, Darnhofer T (eds) Meteorology and agroforestry. ICRAF, Nairobi, Kenya, pp 141–156

Reynolds AG (ed) (2010) Viticulture and wine quality. CRC Press, Boca Raton, Fla.

Reynolds AG, Wardle D (1993) Significance of viticultural and enological practices on monoterpenes flavorants of British Columbia grown Vitis vinifera berries and juices. Viticulture and Eonological sciences 48:194–202

Richardson AD, Jenkins JP, Braswell BH, et al (2007) Use of digital webcam images to track spring green-up in a deciduous broadleaf forest. Oecologia 152:323–334. doi: 10.1007/s00442-006-0657-z

Riou C, Becker N, Sotes R, et al (1994) Le déterminisme climatique de la maturation du raisin: application au zonage de la teneur en sucre dans la Communauté Européenn. Office des Publications Officielles des Communautés Européennes, Luxembourg

Riou C, Valancogne C, Pieri P (1989) Un modèle simple d'interception du rayonnement solaire par la vigne-vérification expérimentale. Agronomie 9:441–450

Ripoche A, Rellier J-P, Martin-Clouaire R, et al (2011) Modelling adaptive management of intercropping in vineyards to satisfy agronomic and environmental performances under Mediterranean climate. Environmental Modelling & Software 26:1467–1480. doi: 10.1016/j.envsoft.2011.08.003

Rivest D, Vézina A (2015) Maize yield patterns on the leeward side of tree windbreaks are site-specific and depend on rainfall conditions in eastern Canada. Agroforestry Systems 89:237–246. doi: 10.1007/s10457-014-9758-6

Roman DT, Novick KA, Brzostek ER, et al (2015) The role of isohydric and anisohydric species in determining ecosystem-scale response to severe drought. Oecologia 179:641–654. doi: 10.1007/s00442-015-3380-9

Ross J (1981) The radiation regime and architecture of plant stands. Springer Netherlands, Dordrecht

Rossi V, Caffi T (2012) The Role of Rain in Dispersal of the Primary Inoculum of *Plasmopara viticola*. Phytopathology 102:158–165. doi: 10.1094/PHYTO-08-11-0223

Rossi V, Caffi T, Giosuè S, Bugiani R (2008) A mechanistic model simulating primary infections of downy mildew in grapevine. Ecological Modelling 212:480–491. doi: 10.1016/j.ecolmodel.2007.10.046

Rossiter DG, Riha SJ (1999) Modeling plant competition with the GAPS object-oriented dynamic simulation model. Agronomy journal 91:773–783

Roujou de Boubée D, Van Leeuwen C, Dubourdieu D (2000) Organoleptic Impact of 2-Methoxy-3-isobutylpyrazine on Red Bordeaux and Loire Wines. Effect of Environmental Conditions on Concentrations in Grapes during Ripening. Journal of Agricultural and Food Chemistry 48:4830–4834. doi: 10.1021/jf000181o

Rouse JW, Haas RH, Schell JA, Deering DW (1974) Monitoring vegetation systems in the Great Plains with ERTS. In: Proceedings of the Third ERTS Symposium, NASA SP-351 1. US Government Printing Office, Washington DC, pp 309–317

Rouzet J, Jacquin D (2003) Development of overwintering oospores of Plasmopara viticola and severity of primary foci in relation to climate*. EPPO Bulletin 33:437–442. doi: 10.1111/j.1365-2338.2003.00670.x

Ruck B, Schmitt F (1986) Flow profile of single-tree boundary flow estimate of deposition probabilities for very fine droplets. Forstwissenschaftliches Centralblatt 105:178–196. doi: 10.1007/BF02741710

Ruiz-Colmenero M, Bienes R, Eldridge DJ, Marques MJ (2013) Vegetation cover reduces erosion and enhances soil organic carbon in a vineyard in the central Spain. CATENA 104:153–160. doi: 10.1016/j.catena.2012.11.007

Rutter AJ, Kershaw KA, Robins PC, Morton AJ (1971) A predictive model of rainfall interception in forests, 1. Derivation of the model from observations in a plantation of Corsican pine. Agricultural Meteorology 9:367–384. doi: 10.1016/0002-1571(71)90034-3

Rutter AJ, Morton AJ, Robins PC (1975) A Predictive Model of Rainfall Interception in Forests. II. Generalization of the Model and Comparison with Observations in Some Coniferous and Hardwood Stands. The Journal of Applied Ecology 12:367. doi: 10.2307/2401739

Sager JC, Farlane CM (1997) Chapter 1 Radiation. Iowa Agricultural and Home Economics Experiment Station, pp 1–30

Santesteban LG, Di Gennaro SF, Herrero-Langreo A, et al (2017) High-resolution UAV-based thermal imaging to estimate the instantaneous and seasonal variability of plant water status within a vineyard. Agricultural Water Management 183:49–59. doi: 10.1016/j.agwat.2016.08.026

Satterlund DR (1983) Forest shadows: how much shelter in a shelterwood? Forest Ecology and Management 5:27–37

Schenk HJ, Jackson RB (2002) Rooting depths, lateral root spreads and below-ground/above-ground allometries of plants in water-limited ecosystems. Journal of Ecology 90:480–494

Schultz HR (1995) Grape canopy structure, light microclimate and photosynthesis. I. A two-dimensional model of the spatial distribution of surface area densities and leaf ages in two canopy systems. VITIS-GEILWEILERHOF- 34:211–216

Schumacher J (2017) How light affects the life of Botrytis. Fungal Genetics and Biology 106:26–41. doi: 10.1016/j.fgb.2017.06.002

Schwartz RC, Fryrear DW, Harris BL, et al (1995) Mean flow and shear stress distributions as influenced by vegetative windbreak structure. Agricultural and forest meteorology 75:1–22

Seguin G (1972) Répartition dans l'espace du système radiculaire de la vigne. Comptes-rendus Hebdomadaires des Séances de l'Académie des Sciences 2178–2180

Sene K (1994) Parameterisations for energy transfers from a sparse vine crop. Agricultural and Forest Meteorology 71:1–18. doi: 10.1016/0168-1923(94)90097-3

Sepulcre-Cantó G, Zarco-Tejada PJ, Sobrino JA, et al (2009) Discriminating irrigated and rainfed olive orchards with thermal ASTER imagery and DART 3D simulation. Agricultural and Forest Meteorology 149:962–975. doi: 10.1016/j.agrformet.2008.12.001

Serra I, Strever A, Myburgh PA, Deloire A (2014) Review: the interaction between rootstocks and cultivars (*Vitis vinifera* L.) to enhance drought tolerance in grapevine: Rootstocks to enhance drought tolerance in grapevine. Australian Journal of Grape and Wine Research 20:1–14. doi: 10.1111/ajgw.12054

Shuttleworth WJ, Wallace JS (1985) Evaporation from sparse crops-an energy combination theory. Quarterly Journal of the Royal Meteorological Society 111:839–855. doi: 10.1002/qj.49711146910

Siau JF (1984) Transport processes in wood. Springer-Verlag, Berlin ; New York

Simioni G, Le Roux X, Gignoux J, Sinoquet H (2000) Treegrass: a 3D, process-based model for simulating plant interactions in tree–grass ecosystems. Ecological Modelling 131:47–63. doi: 10.1016/S0304-3800(00)00243-X

Simonneau T, Lebon E, Coupel-Ledru A, et al (2017) Adapting plant material to face water stress in vineyards: which physiological targets for an optimal control of plant water status? OENO One 51:167. doi: 10.20870/oeno-one.2016.0.0.1870

Sinoquet H, Bonhomme R (1992) Modeling radiative transfer in mixed and row intercropping systems. Agricultural and Forest Meteorology 62:219–240. doi: 10.1016/0168-1923(92)90016-W

Sinoquet H, Le Roux X, Adam B, et al (2001) RATP: a model for simulating the spatial distribution of radiation absorption, transpiration and photosynthesis within canopies: application to an isolated tree crown. Plant, Cell and Environment 24:395–406. doi: 10.1046/j.1365-3040.2001.00694.x

Sinoquet H, Valancogne C, Lescure A, Bonhomme R (1992) Modeling solar-radiation interception in row plantation. 3. Application to a traditional vineyard. Agronomie 12:307–318. doi: 10.1051/agro:19920404

Siqueira M, Katul G, Porporato A (2008) Onset of water stress, hysteresis in plant conductance, and hydraulic lift: Scaling soil water dynamics from millimeters to meters: WATER STRESS AND HYDRAULIC LIFT. Water Resources Research 44:. doi: 10.1029/2007WR006094

Sirven B, Canet A, Arbre et paysage 32 (2016) Le génie de l'arbre. Actes Sud, Arles (Bouches-du-Rhône)

Smart DR, Carlisle E, Goebel M, Nuñez BA (2005) Transverse hydraulic redistribution by a grapevine. Plant, Cell & Environment 28:157–166

Smart RE (1974) Photosynthesis by Grapevine Canopies. The Journal of Applied Ecology 11:997. doi: 10.2307/2401759

Smart RE (1973) Sunlight interception by vineyards. American Journal of Enology and Viticulture 141–147

Smart RE (1985) Principles of Grapevine Canopy Microclimate Manipulation with Implications for Yield and Quality. A Review. American Journal of Enology and Viticulture 36:230–239

Smart RE, Coombe BG (1983) Water relations of grapevines. In: water deficits and plant growth. Academic Press, pp 137–196

Smit JL, Sithole G, Strever AE (2016) Vine signal extraction–an application of remote sensing in precision viticulture. South African Journal of Enology and Viticulture 31:65–74

Smith DM, Jackson NA, Roberts JM, Ong CK (1999) Reverse flow of sap in tree roots and downward siphoning of water by Grevillea robusta. Functional Ecology 13:256–264. doi: 10.1046/j.1365-2435.1999.00315.x

Smucker AJM, Ellis BG, Kang B T (1995) Alley cropping on an Alfisol in the forest savanna transition zone: root, nutrient and water dynamics. In: Alley Framing Reasearch and Development. IITA, Ibadan, Nigeria, pp 103–121

Sokal RR (1961) Distance as a Measure of Taxonomic Similarity. Systematic Zoology 10:70. doi: 10.2307/2411724

Spayd SE, Tarara JM, Mee DL, Ferguson JC (2002) Separation of sunlight and temperature effects on the composition of Vitis vinifera cv. Merlot berries. American Journal of Enology and Viticulture 53:171–182

Stevens RM, Nicholas PR (1994) Root length and mass densities of *Vitis vinifera* L. cultivars "Muscat Gordo Blanco" and "Shiraz." New Zealand Journal of Crop and Horticultural Science 22:381–385. doi: 10.1080/01140671.1994.9513849

Stigter CJ (2015) Agroforestry and micro-climate change. In: Ong CK, Black CR, Wilson J (eds) Tree-Crop Interactions: Agroforestry in a Changing Climate., 2nd Edition. pp 119–145

Stirzaker R, O'Connell D, Prinsley R (1996) Agroforestry and hydrology : What do we need to know? In: Agroforestry and hydrology : What do we need to know? Barton, A.C.T. : Rural Industries Research and Development Corporation, p 16

Stoev K, Slatcheva T (1982) La photosynthèse nette chez la vigne (V. Vinifera L.) et les facteurs écologiques. Connaissance de la vigne et du vin 16:171–185

Stoev K, Slavcheva T (1979) Influence of major ecological factors on photosynthesis of grape leaves. Soviet plant physiology 26:351–354

Sudmeyer R (2002) Tree root morphology in alley systems : a report for the RIRDC/L&W Australia/FWPRDC Joint Venture Agroforestry Program. ACT, Canberra

Sudmeyer R, Flugge F (2005) The economics of managing tree–crop competition in windbreak and alley systems. Australian Journal of Experimental Agriculture 45:1403. doi: 10.1071/EA04155

Sun J, Nishio JN, Vogelmann T (1998) Green light drives CO2 fixation deep within leaves. Plant Cell Physiology 39:1020–1026

Syndicat des Vins Côtes de Gascogne (2018) Côtes de Gascogne. http://www.vins-cotes-gascogne.fr. Accessed 6 Mar 2018

Talbot G, Dupraz C (2012) Simple models for light competition within agroforestry discontinuous tree stands: are leaf clumpiness and light interception by woody parts relevant factors? Agroforestry Systems 84:101–116. doi: 10.1007/s10457-011-9418-z

Tallec T, Béziat P, Jarosz N, et al (2013) Crops' water use efficiencies in temperate climate: Comparison of stand, ecosystem and agronomical approaches. Agricultural and Forest Meteorology 168:69–81. doi: 10.1016/j.agrformet.2012.07.008

Tandonnet J-P, Cookson SJ, Vivin P, Ollat N (2009) Scion genotype controls biomass allocation and root development in grafted grapevine: Scion/rootstock interactions in grapevine. Australian Journal of Grape and Wine Research 16:290–300. doi: 10.1111/j.1755-0238.2009.00090.x

Tarara JM, Lee J, Spayd S, Scagel C (2008) Berry Temperature and Solar Radiation Alter Acylation, Proportion, and Concentration of Anthocyanin in Merlot Grapes. American Journal of Enology and Viticulture 29:235–247

Teklehaimanot Z, Jarvis PG (1991) Direct Measurement of Evaporation of Intercepted Water from Forest Canopies. Journal of Applied Ecology 28:603–618. doi: 10.2307/2404571

Terashima I, Fujita T, Inoue T, et al (2009) Green Light Drives Leaf Photosynthesis More Efficiently than Red Light in Strong White Light: Revisiting the Enigmatic Question of Why Leaves are Green. Plant and Cell Physiology 50:684–697. doi: 10.1093/pcp/pcp034

Thind TS, Arora JK, Mohan C, Raj P (2004) Epidemiology of Powdery Mildew, Downy Mildew and Anthracnose Diseases of Grapevine. In: Naqvi SAMH (ed) Diseases of Fruits and Vegetables Volume I. Kluwer Academic Publishers, Dordrecht, pp 621–638

Tonietto J, Carbonneau A (2004) A multicriteria climatic classification system for grape-growing regions worldwide. Agricultural and Forest Meteorology 124:81–97. doi: 10.1016/j.agrformet.2003.06.001

Torita H, Satou H (2007) Relationship between shelterbelt structure and mean wind reduction. Agricultural and Forest Meteorology 145:186–194. doi: 10.1016/j.agrformet.2007.04.018

Trambouze W, Goma-Fortin N (2013) Agroforestry and viticulture: results of a 11-years study on the production and vigour of the vines. Portugal, pp 514–517

Trambouze W, Gouttesoulard C, Saubion C (2017) Agroforesterie viticole : 20 ans de complantation arbres/vignes, pour quels résultats agronomiques ? In: Actes de la journée Croisons les regards #2. RMT agrofoesteries, Paris, p 28

Trias-Sanz R (2006) Texture Orientation and Period Estimator for Discriminating Between Forests, Orchards, Vineyards, and Tilled Fields. IEEE Transactions on Geoscience and Remote Sensing 44:2755–2760. doi: 10.1109/TGRS.2006.875784

Valente F, David JS, Gash JHC (1997) Modelling interception loss for two sparse eucalypt and pine forests in central Portugal using reformulated Rutter and Gash analytical models. Journal of Hydrology 190:141–162. doi: 10.1016/S0022-1694(96)03066-1

van der Tol C, Verhoef W, Timmermans J, et al (2009) An integrated model of soil-canopy spectral radiances, photosynthesis, fluorescence, temperature and energy balance. Biogeosciences 6:3109–3129. doi: 10.5194/bg-6-3109-2009

Van Eirman J, Karshon R, Razumoval LA, Robertson GW (1964) Windbreaks and shelterbelts Technical not.pdf. WMO, Geneva, Switzerland

van Leeuwen C, Darriet P (2016) The Impact of Climate Change on Viticulture and Wine Quality. Journal of Wine Economics 11:150–167. doi: 10.1017/jwe.2015.21

Van Leeuwen C, Destrac-Irvine A (2017) Modified grape composition under climate change conditions requires adaptations in the vineyard. OENO One 51:147. doi: 10.20870/oeno-one.2016.0.0.1647

Van Leeuwen C, Seguin G (2006) The concept of terroir in viticulture. Journal of Wine Research 17:1–10. doi: 10.1080/09571260600633135

Van Leeuwen C, Trégoat O, Choné X, et al (2009) Vine water status is a key factor in grape ripening and vintage quality for red Bordeaux wine. How can it be assessed for vineyard management purposes? OENO One 43:121–134

Van Noordwjik M, Lusiana B (1998) WaNuLCAS, a model of water, nutrient and light capture in agroforestry systems. Agroforestry Systems 43:217–242. doi: https://doi.org/10.1023/A:1026417120254

Van Rooyen F., Weber H., Levin I (1980) The response of grapes to a manipulation of soil-plant-atmosphere continuum. I. Growth, yield, and quality responses. Agrochemophysica 59–68

Van Zyl JL (1981) Irrigation [Title in Afrikaans:Besproeiing]. In: Burger J, Deist J (eds) In: Viticulture in South Africa [Title in Afrikaans:Wingerdbou in Suid-Afrika]. Stellenbosch, South Africa, pp 234–282

Van Zyl JL, Van Huyssteen L (1980) Comparative studies on wine grapes on different trellising systems: I. Consumptive water use. South African Journal of Enology and Viticulture 1:7–14

Van Zyl JL, Weber HW (1981) The Effect of Various Supplementary Irrigation Treatments on Plant and Soil Moisture Relationships in a Vineyard (Vitis Vinif era var. Chenin Blanc). South African Journal of Enology & Viticulture 2:83–99. doi: 10.21548/2-2-2400

Vannier C (2011) Observation et modélisation spatiale de pratiques agricoles territorialisées à partir de données de télédétection : application au paysage bocage

Vasconcelos MC, Greven M, Winefield CS, et al (2009) The flowering process of Vitis vinifera: a review. American Journal of Enology and Viticulture 60:411–434

Vaudour E (2002) The Quality of Grapes and Wine in Relation to Geography: Notions of Terroir at Various Scales. Journal of Wine Research 13:117–141. doi: 10.1080/0957126022000017981

Vaudour E (2003) Les terroirs viticoles: définitions, caractérisation et protection. Ed. La Vigne : Dunod, Paris

Vaudour E, Costantini E, Jones GV, Mocali S (2015) An overview of the recent approaches to terroir functional modelling, footprinting and zoning. SOIL 1:287–312. doi: 10.5194/soil-1-287-2015

Verhoef W (1985) Light scattering by leaf layers with application to canopy reflectance modeling: The SAIL model. Remote Sensing of Environment 17:165–178

Vigiak O, Sterk G, Warren A, Hagen LJ (2003) Spatial modeling of wind speed around windbreaks. CATENA 52:273–288. doi: 10.1016/S0341-8162(03)00018-3

Vivier MA, Pretorius IS (2002) Genetically tailored grapevines for the wine industry. Trends in Biotechnology 20:472–478. doi: 10.1016/S0167-7799(02)02058-9

Volschenk H, van Vuuren HJJ, Viljoen-Bloom M (2017) Malic Acid in Wine: Origin, Function and Metabolism during Vinification. South African Journal of Enology & Viticulture 27:. doi: 10.21548/27-2-1613

Wagner R (1966) Effets d'un éclairage d'appoint sur la fertilité des bourgeons de la vigne. In: Comptes rendus des séances de l'Académie d'agriculture de France. Paris, pp 670–673

Wallace JS (1995) Towards a coupled light partitioning and transpiration model for use in intercrops and argoforesrty. In: Sinoquet H, Cruz P (eds) Ecophysiology of Tropical intercropping, INRA Editions. Paris, France, pp 153–162

Wallace JS, Roberts JM, Sivakumar MVK (1990) The estimation of transpiration from sparse dryland millet using stomatal conductance and vegetation area indices. Agricultural and Forest Meteorology 51:35–49. doi: 10.1016/0168-1923(90)90040-D

Wang H, Takle ES (1996) On three-dimensionality of shelterbelt structure and its influences on shelter effects. Boundary-Layer Meteorology 79:83–105

Wang H, Takle ES (1997) Momentum budget and shelter mechanism of boundary-layer flow near a shelterbelt. Boundary-Layer Meteorology 82:417–437

Wang W (2012) An Analytical Model for Mean Wind Profiles in Sparse Canopies. Boundary-Layer Meteorology 142:383–399. doi: 10.1007/s10546-011-9687-0

Weiss M, Baret F (2017) Using 3D Point Clouds Derived from UAV RGB Imagery to Describe Vineyard 3D Macro-Structure. Remote Sensing 9:111. doi: 10.3390/rs9020111

Whitmarsh J, Govindjee (1999) The photosynthetic process. In: Singhal G, Renger G, Sopory S, et al. (eds) Concepts in photobiology: photosynthesis and photomorphogenesis. Springer, Place of publication not identified, pp 11–51

Widlowski J-L, Mio C, Disney M, et al (2015) The fourth phase of the radiative transfer model intercomparison (RAMI) exercise: Actual canopy scenarios and conformity testing. Remote Sensing of Environment 169:418–437. doi: 10.1016/j.rse.2015.08.016

Widlowski J-L, Pinty B, Clerici M, et al (2011) RAMI4PILPS: An intercomparison of formulations for the partitioning of solar radiation in land surface models. Journal of Geophysical Research 116:. doi: 10.1029/2010JG001511

Williams K, Caldwell MM, Richards JH (1993) The influence of shade and clouds on soil water potential: The buffered behavior of hydraulic lift. Plant and Soil 157:83–95. doi: 10.1007/BF02390230

Williamson B, Tudzynski B, Tudzynski P, Van Kan JAL (2007) Botrytis cinerea: the cause of grey mould disease. Molecular Plant Pathology 8:561–580. doi: 10.1111/j.1364-3703.2007.00417.x

Willocquet L, Berud F, Raoux L, Clerjeau M (1998) Effects of wind, relative humidity, leaf movement and colony age on dispersal of conidia of Uncinula necator, causal agent of grape powdery mildew. Plant Pathology 47:234–242. doi: 10.1046/j.1365-3059.1998.00242.x

Willocquet L, Clerjeau M (1998) An analysis of the effects of environmental factors on conidial dispersal of Uncinula necator (grape powdery mildew) in vineyards. Plant Pathology 47:227–233. doi: 10.1046/j.1365-3059.1998.00244.x

Winter EJ (1974) Water, soil, and the plant. Macmillan [for the Royal Horticultural Society], London

Woodall GS, Ward BH (2002) Soil water relations, crop production and root pruning of a belt of trees. Agricultural Water Management 53:153–169. doi: 10.1016/S0378-3774(01)00162-7

Yadav JP, Khanna P (1992) Root pruning enhances crop production under *Prosopis cineraria* . Agroforestry Today 4:13–14

Yang X, Yu Y, Fan W (2017) A method to estimate the structural parameters of windbreaks using remote sensing. Agroforestry Systems 91:37–49. doi: 10.1007/s10457-016-9904-4

Yoder CK, Nowak RS (1999) Soil moisture extraction by evergreen and drought-deciduous shrubs in the Mojave Desert during wet and dry years. Journal of Arid Environments 42:81–96. doi: 10.1006/jare.1999.0504

Young A (1987) The environmental basis of agroforestry. In: Reifsnyder WS, Darnhofer T (eds) Proceedings of an Internanional Workshop on the application of meteorology to agroforestry systems planning and management. Nairobi, Kenya, pp 29–48

Zahavi T, Reuveni M, Dimitri Scheglov, Shimon Lavee (2001) Effect of grapevine training systems on development of powdery mildew. European Journal of Plant Pathology 107:495–501

Zarco-Tejada PJ, Diaz-Varela R, Angileri V, Loudjani P (2014) Tree height quantification using very high resolution imagery acquired from an unmanned aerial vehicle (UAV) and automatic 3D photo-reconstruction methods. European Journal of Agronomy 55:89–99. doi: 10.1016/j.eja.2014.01.004

Zhang D, Brandle J, Hodges L (1999) The response of muskmelon growth and development to microclimate modification by shelterbelts. HortSciences 34:64–68

Zhang P, Howell K, Krstic M, et al (2015) Environmental Factors and Seasonality Affect the Concentration of Rotundone in Vitis vinifera L. cv. Shiraz Wine. PLOS ONE 10:e0133137. doi: 10.1371/journal.pone.0133137

Zhang T, Folta KM (2012) Green light signaling and adaptive response. Plant Signaling & Behavior 7:75–78. doi: 10.4161/psb.7.1.18635

Zhu J, Matsuzaki T, Sakioka K (2000) Wind speeds within a single crown of Japanese black pine (Pinus thunbergii Parl.). Forest Ecology and Management 135:19–31. doi: 10.1016/S0378-1127(00)00295-4

Zhu J, Xiu-fen LI, Yutaka G, Matsuzaki T (2004) Wind profiles in and over trees. Journal of Forestry Research 15:305

ANNEXES

List of annexes

A. Calculation of the transpiration from a sparse and discontinuous two species mixed system

As formulated in the review of (Bayala and Wallace 2015).

There has been several attempts for adaptating the 'big leaf' model of transpiration from Penman-Monteith (Monteith et al. 1965) to the mixed canopies of agroforestry systems (Bayala and Wallace 2015). One of the key points is to take into account the light interception mechanisms in place. Also specific Leaf Area Indexes and stomatal resistances have to be introduced. Nevertheless, Wallace et al.(1990) showed that it is also highly essential to take into account the mutual climatic influences of the different components of the system, namely the water and heat fluxes between the upper and lower story of canopy as well as that between the plants and the ground, notably in discontinuous canopies (these latter authors studied alley-cropped millet systems). They adapted the model from Shuttleworth-Wallace (1985) to mixed cropped systems. In comparison to the Shuttleworth-Wallace model, it was found that the Penman-Monteith equation underestimated transpiration when the soil was dry and overestimated it when the soil was wet (Wallace et al. 1990). Equations 1 to 3 provide a mean to estimate transpiration from a two-species canopy when only above-canopy net radiation, temperature and vapour pressure deficit are known (Bayala and Wallace 2015). The total evaporation (λE) of a two-component system with sparse canopies is written as:

$$\lambda E = C_1 PM_1 + C_2 PM_2$$

C_1 and C_2 are coefficients to apply to PM_1 and PM_2 terms, which resemble terms in the Penman-Monteith equation. These take the following format:

$$PM_1 = \frac{\Delta A + {\left[\rho C_P (e_s - e_a) - \Delta r_a^1 (A - A_1)\right]}/{r_a^1 + r_a^a}}{\Delta + \gamma\left[1 + \frac{r_s^1}{r_a^1 + r_a^a}\right]}$$

➔ for PM_2 replace subscript *1* by subscript *2*

A is the total energy available to the mixed canopy, and A_1 and A_2 represent the quantities of energy available to the component species such that:

$$A_1 = f_1 R_n \text{ and } A_2 = f_2 R_n$$

For generating the f_1 and f_2 coefficients, Wallace (1995) proposes the following simple model of light interception which applies Beer's Law and requires the individual values of the extinction coefficient (K) and leaf area index (LAI) for each species and their relative heights (h_1/h_2).

$$f_i = f_i^s + \frac{h_i^2}{h_1^2 + h_2^2}\left(f_i^d - f_i^s\right)$$

with $$f_i^d = 1 - e^{K_i LAI_i}$$

and $$f_i^s = (1 - e^{K_i LAI_i})(e^{K_i LAI_i})$$

The various resistance terms in eq.2 correspond to the bulk leaf boundary layer resistances of the two-component species (r_a^1 and r_a^2) and two the aerodynamic resistance r_a^a between the in-canopy mixing point (D_0) and the reference height (D).

The coefficients C_1 and C_2 are given by:

$$C_1 = \left[\frac{[1 + 1/R_2]}{1/R_1 + 1/R_a}\right]^{-1}$$

where $$R_a = (\Delta + \gamma) r_a^a$$

$$R_1 = (\Delta + \gamma) r_a^1 + \gamma r_s^1$$

➔ for C_2 *and* R_2 , replace subscript *1* by subscript *2*

γ	Psychrometric constant
Δ	Slope of the saturation vapour pressure temperature relationship

$$\lambda E = C_1 PM_1 + C_2 PM_2$$

with $$PM_1 = \frac{\Delta A + {[\rho C_P (e_s - e_a) - \Delta r_a^1 (A - A_1)]}/{r_a^1 + r_a^a}}{\Delta + \gamma\left[1 + \frac{r_s^1}{r_a^1 + r_a^a}\right]}$$

$$A_1 = f_1 R_n$$

$$C_1 = \left[\frac{[1 + 1/R_2]}{1/R_1 + 1/R_a}\right]^{-1}$$

$$R_a = (\Delta + \gamma) r_a^a$$

$$R_1 = (\Delta + \gamma) r_a^1 + \gamma r_s^1$$

➔ for PM_2 A_2 , C_2 *and* R_2 , replace subscript *1* by subscript *2*

λE	Transpiration rate, λ being the latent heat of vaporization of water
R_n	Above canopy net radiation
$e_s - e_a$	Above canopy vapour pressure deficit of the air
γ	Psychrometric constant
Δ	Slope of the saturation vapour pressure temperature relationship
ρ *and* C_P	Density and specific heat of the air
r_s	Mean surface (bulk) resistance of the whole canopy
r_a	Aerodynamic resistance

LAI_i	Leaf area index of the constituents canopy elements (i) [$m^2_{leafarea}.m^2_{soilsurface}$]
$u(z)$	Wind speed a height z above ground
D	zero-plane displacement (recall eq. 2)
$z_{0m} and\ z_{0h}$	Roughness length governing momentum transfer (recall eq. 2) / heat and vapour transfer
z_m	Height of humidity measurement
z_h	Height of wind measurement
k	Von Karman constant

B. Collected data set (French: Jeu de données collecté durant la thèse)

	VARIABLE D'ETAT	LIEUX	CAPTEUR et EMPRISE	DATE / PERIODE	VOCATION DE LA VARIABLE
ATMOSPHERE	Tair (°C) et HR (%)	Lagardère (32)	Station météo (2m)	du 1/03/2016 à aujourd'hui	Bilan radiatif et risque maladies
				f=10min	
			Ibuttons sur 15/50 ceps (zone des grappes)	du 29/07 au 4/09/2015 et du 10/03 au 2/09/2016	Dynamiques et valeurs extrêmes
			d=0,5°C – f=15min		Indices agrométéo
		Lapouyade (33)	Station météo (2m) - f=10min	du 25/03/2016 à aujourd'hui	
			Ibuttons sur 27ceps (zone des grappes)	du 11/07/2016 au 23/09/2016	
			d=0,5°C		
		Restinclières (34)	Station météo INRA (2m) - f=1h	du 1/01/2016 à aujourd'hui	
			Ibuttons sur 30 ceps (zone des grappes)	du 1/03/2016 au 7/09/2016	
		Lacapelle (46)	Station météo (2m)	du 2/04/2016 à aujourd'hui f=10min	
		Barran (32)	Station météo (2m) – f=1h	En continu (station Auch-Lamothe)	
			Ibuttons sur 42 points (1m)	Mars, puis 7/06 au 11/07/2016	
		Aalbecke (Bel)	Station infoclimat (Auch) (2m) – f=1h	2012 à aujourd'hui	
			Ibuttons sur 36 points (0.6h)	du 7/04 au 6/07/2016	
	U vitesse et direction (ref parcelle)	Lagardère (32)	Station météo (2m)	du 1/03/2016 à aujourd'hui	Bilan radiatif
			Anémomètres x 3 ceps (2m)	du 21/07/2016 au 30/07/2016	Cartographie champs de vent
				f=10sec	
		Lapouyade (33)	Station météo (2m)	du 25/03/2016 à aujourd'hui	
		Restinclières (34)	Station météo (2m)	du 1/01/2016 à aujourd'hui	
		Lacapelle (46)	Station météo (2m)	du 2/04/2016 à aujourd'hui f=10min	
		Barran (32)	Station météo (Auch) 2m)	En continu	
		Aalbecke (Bel)	Station (2m) et 36 points x 1 journée	du 7/04 au 6/07/2016	Cartographie champs de vent
	Rg (ref parcelle)	Lagardère (32)	Station météo	du 1/03/2016 à aujourd'hui	Bilan radiatif
		Lapouyade (33)	Station météo	du 25/03/2016 à aujourd'hui	
		Restinclières (34)	Station météo INRA	du 1/01/2016 à aujourd'hui	
		Lacapelle (46)	Station météo (2m)	du 2/04/2016 à aujourd'hui f=10min	
		Barran (32)	Station météo (Auch) 2m	En continu	
		Aalbecke (Bel)	Station météo (Lille) 2m	En continu	
VEGETATION	Trad (carte aérienne)	Lagardère (32)	Drone capteur IRT (8 - 14 µm) résolution : 20cm	le 17/05/2016 à 11h, 13h30 et 17h	Stress hydrique : situation non limitante
				le 20/07/2016 à 11h45, 13h, 14h30 et 15h45	Stress hydrique : situation non limitante
				le 23/08/2016 à 12h15, 13h30 et 15h15	Stress hydrique : stress fort
		Lapouyade (33)		le 18/07/2016 à 13h, 14h, 15h et 15h45	Stress hydrique
				le 22/08/2016 à 12h15, 13h30 et 15h15	Stress hydrique max
		Restinclières (34)		le 19/07/2016 à 12h30, 13h45 et 14h45	Stress hydrique
				le 24/08/2016 à 11h45, 13h15 et 15h	Stress hydrique max
	Images aériennes multispectrales => NDVI	Lagardère (32)	Drone capteur R G RedEdge PIR résolution : 30cm	le 17/05/2016	Occupation du sol : sol enherbé Biomasse et rendement : vigne très peu développée
				le 20/07/2016 (non décomposable)	
				le 23/08/2016	Occupation du sol : herbe sèche et sol nu Biomasse et rendement : max de végétation
		Lapouyade (33)		le 18/07/2016	
				le 22/08/2016	
		Restinclières (34)		le 19/07/2016	
				le 24/08/2016	
	Photos aériennes stéréoscopiques => MNS	Lagardère (32)	Drone capteur RGBPir résolution : 10cm	le 17/05/2016	Occupation du sol Hauteur de végétation : vigne très peu développée
				le 20/07/2016	
				le 23/08/2016	Occupation du sol Hauteur de végétation : max de végétation
		Lapouyade (33)		le 18/07/2016	
				le 22/08/2016	
		Restinclières (34)		le 19/07/2016	
				le 24/08/2016	
	Photo hémisphérique vers le ciel (sous les arbres)	Lagardère (32)	Lentille fish-eye + appareil photo	23/08/2016 : 3 arbres maillage	Interception lumineuse par la canopée Estimation du LAD des arbres
		Lapouyade (33)		22/09 et 23/09/2016 : 22 ceps	
		Restinclières (34)		24/08/2016 : 2 arbres maillage	
	Hauteur d'arbres	Lagardère (32)	Télémètre Laser	23/08/2016 : 15 arbres	Pour validation des images drone
		Lapouyade (33)		le 23/09/02016 : 11 arbres + haie	
		Restinclières (34)		le 7/09/2016 : 17 arbres	Pour validation des images drone. Feuillage très clairement
SOL	Tsol (5cm)	Lagardère (32)	Ibutton en 29 ceps d=0,5°C	du 28/04/2016 au 1/09/2016 f= 40 min	Croissance et métabolisme racinaire
		Lapouyade (33)	Ibutton en 12 puis 27 ceps d=0,5°C	du 25/03/2016 au 11/06/2016 puis du 11/07/2016 au 23/09/2016	
		Restinclières	Ibutton en 12 ceps d=0,5°C	du 1/03/2016 au 2/09/2016	
	Résistivité électrique (carte de profil)	Lagardère (32)	ARP®, Geocarta	hiver 2015	Hétérogénéité structurale et de propriétés hydriques du sol : intégration sur tout le profil
		Lapouyade (33)	ARP®, Geocarta	hiver 2015	
		Restinclières (34)	EM38	hiver 2014	

C. Land occupation map at the agroforestry vineyard of Lagardere on the 23 Aug. 2016 obtained from supervised classification approach and then applying a post-processing threshold of 0.9 from confidence map to the grapevine class.

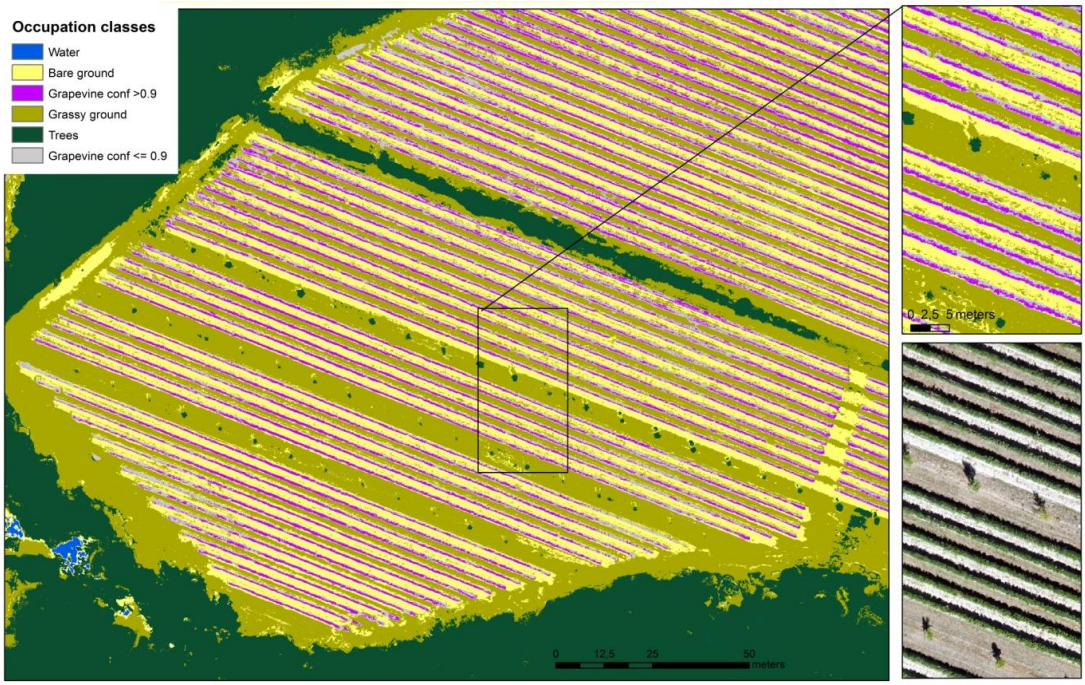

D. Land occupation map at the agroforestry vineyard of Restinclieres on the 21 Aug. 2016 obtained from supervised classification approach and then applying a post-processing combination of maps: only the invariant classes among repetitions of classifications were retained

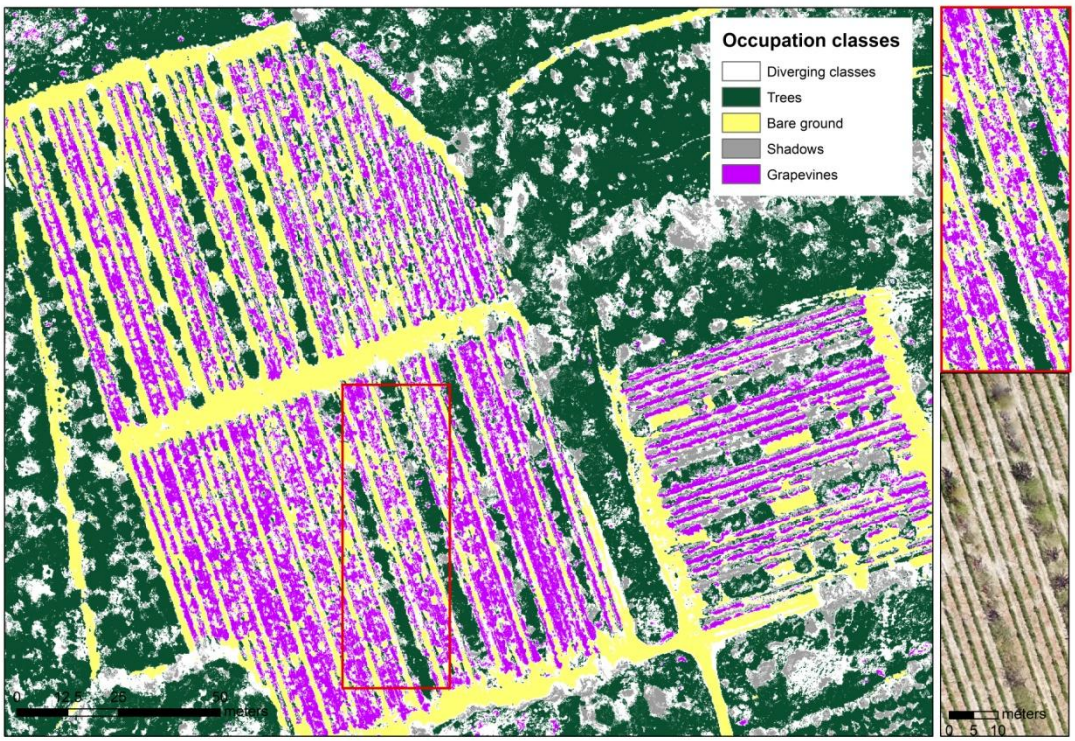

E. Scores of classification: example at Lagardère 08/2016

Overall accuracy: 0.93

Kappa: 0.87

Scores per occupation class

	Precision	Rappel	Fscore
Bare ground	0.64	0.87	0.74
Grass	0.93	0.82	0.87
Trees AF	0.59	0.36	0.45
Border trees	0.98	0.97	0.97
Grapevine	0.84	0.88	0.86
Road	0.92	0.99	0.96

Confusion matrix

		PREDICTION					
		Bare ground	**Grass**	**Trees AF**	**Border trees**	**Grapevine**	**Road**
TRUTH	**Bare ground**	68801	6853	1	1468	1874	0
	Grass	36645	222603	127	5111	2604	3506
	Trees AF	12	627	2032	1271	1664	0
	Border trees	409	9737	1239	101367	21032	0
	Grapevine	1096	470	24	17464	140210	0
	Road	127	48	0	0	0	41963

Contribution of input images

R_{RGB}	13.1 %
G_{RGB}	15.9 %
B_{RGB}	16.5 %
$NDVI_{MS}$	19.7 %
$2G_{RGB}$	17.1 %
$G\%_{RGB}$	17.8 %

F. Filtering of the pixels classified as vine but with a confidence score lower than90 %

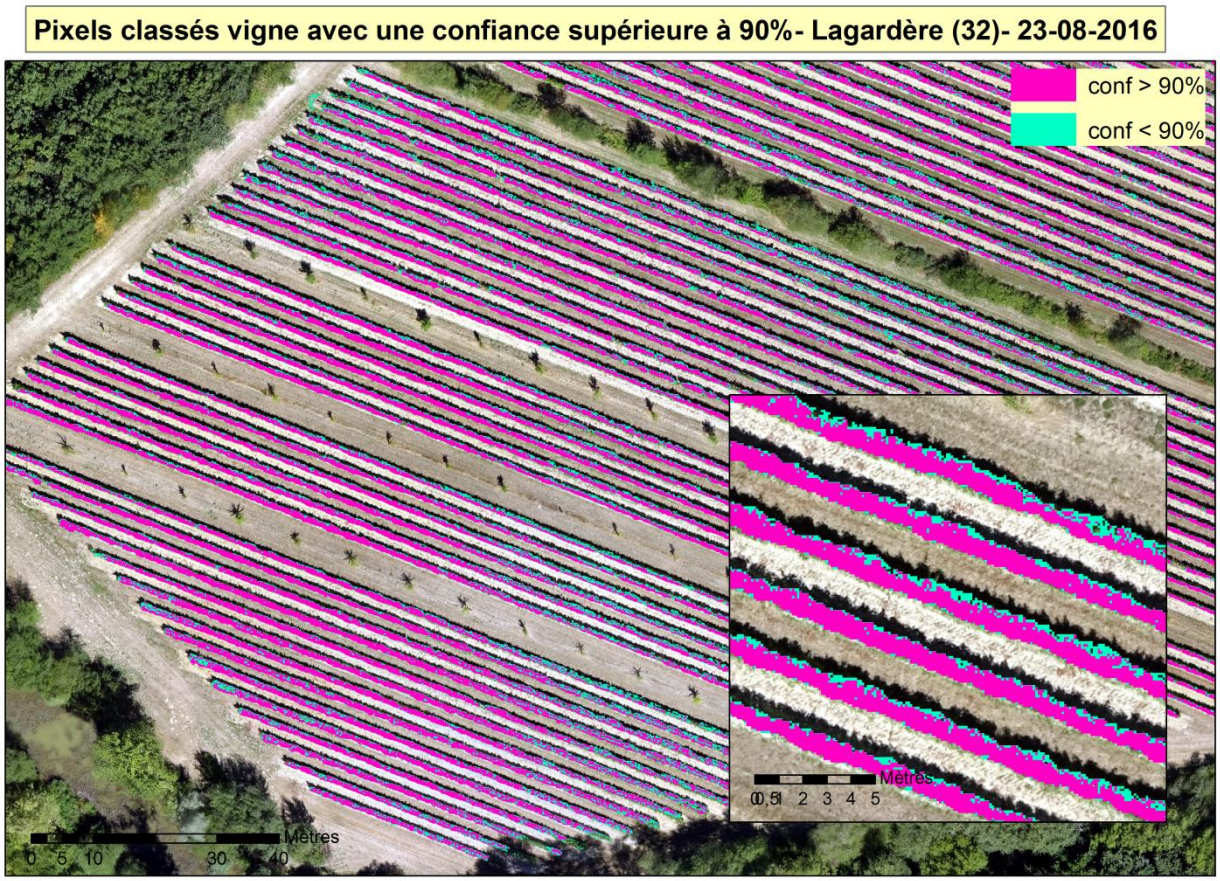

G. Height of vegetation at the study vineyard of Restinclières on the 19 Jul. 2016 obtained by filtered DSM method.

(a) Filtering radius = 50 cm

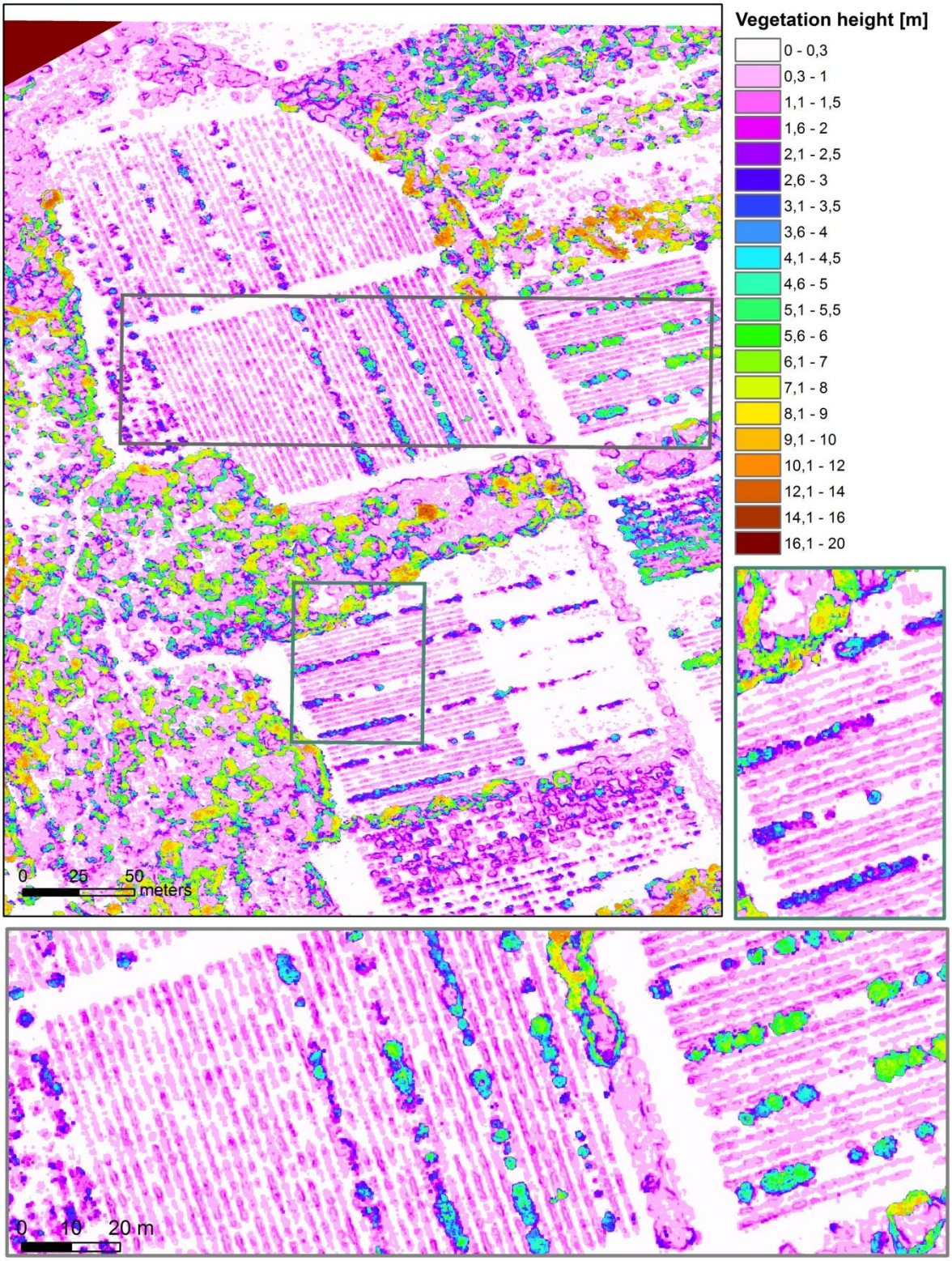

(b) Filtering radius = 150 cm

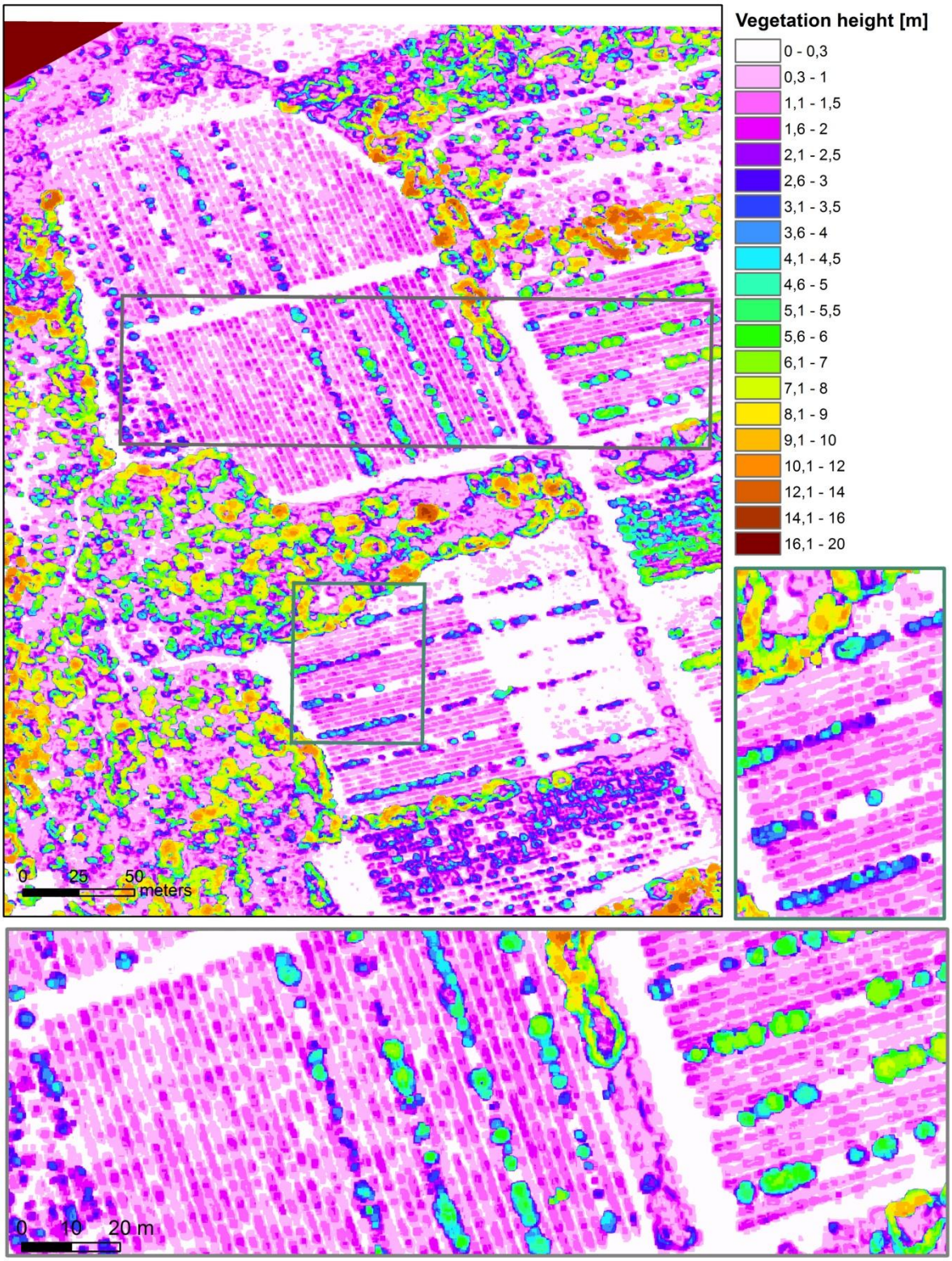

H. Height of vegetation at the study vineyard of Restinclieres on the 19 Jul. 2016 obtained by DSM-DTM method.

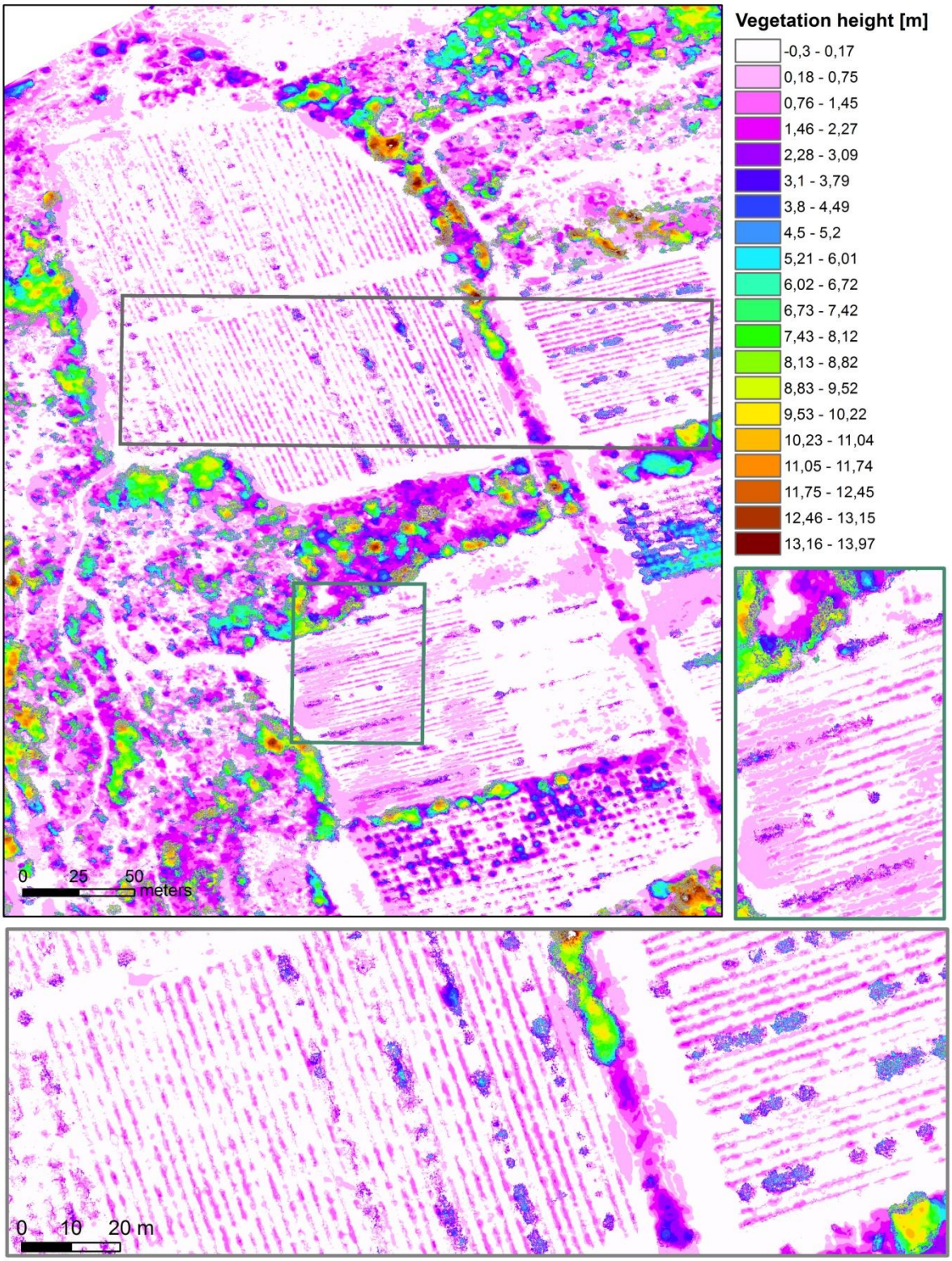

I. Height of vegetation at the study vineyard of Lapouyade on the 22 Aug. 2016 obtained by filtered DSM method.

(a) Filtering radius = 50 cm

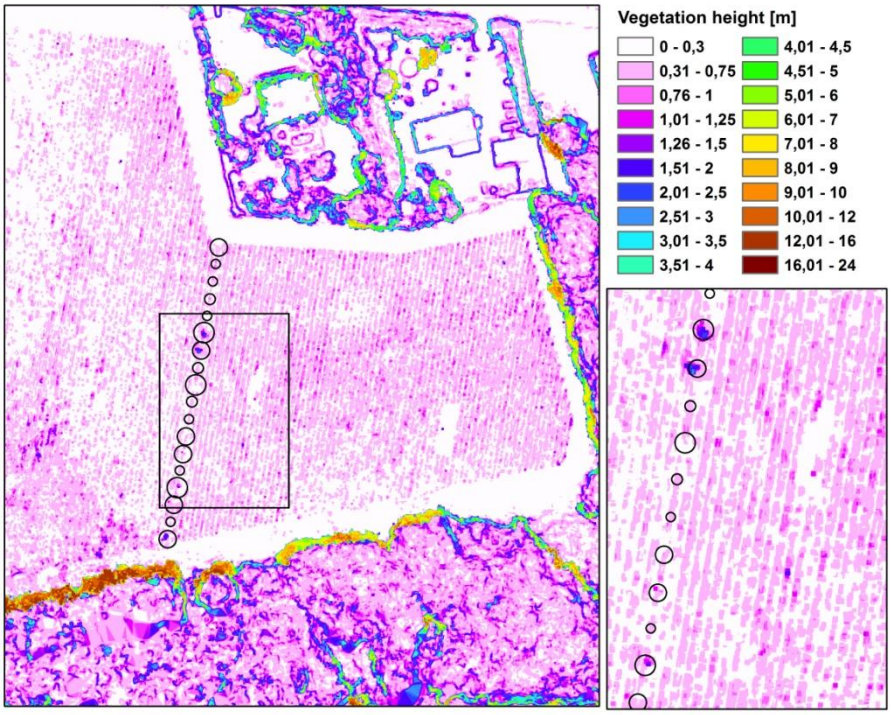

(b) Filtering radius = 150 cm

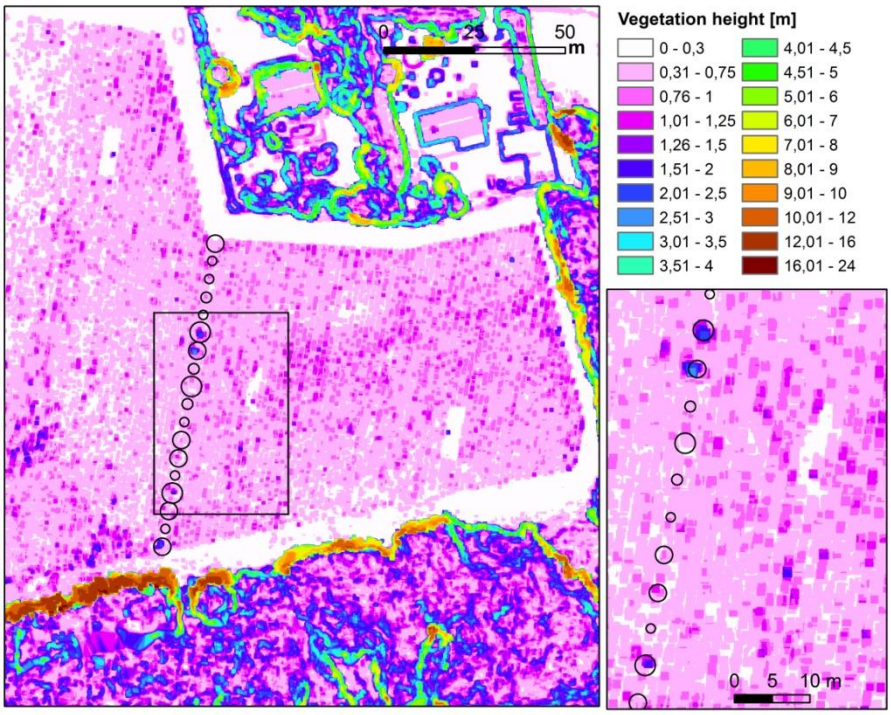

J. Time series of daily variables retrieved from the temperature recorded by on site weather station (blue curve) and by data loggers positioned in the bunch zone of grapevine distributed within the vineyard (box plot).

Fig. A: Time series of daily variables retrieved from the temperature recorded by on site weather station (blue curve) and by data loggers positioned in the bunch zone of grapevine distributed within the vineyard (box plot). On each box, the central mark indicates the median, and the bottom and top edges of the box indicate the 25th and 75th percentiles, respectively. The whiskers extend to the most extreme data points not considered outliers, and the outliers are plotted individually using the '+' symbol. Whisker extends to approximately +/–2.7σ, σ being the standard deviation.

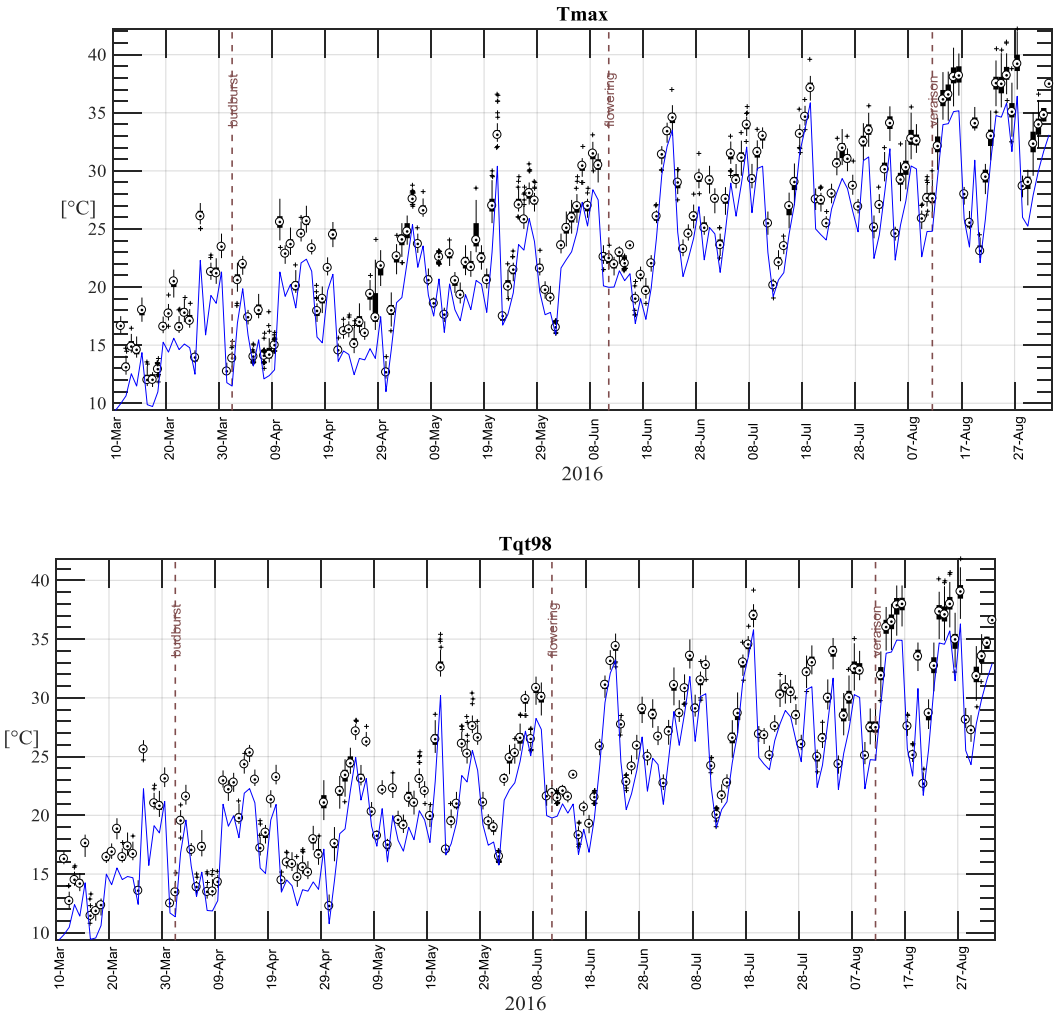

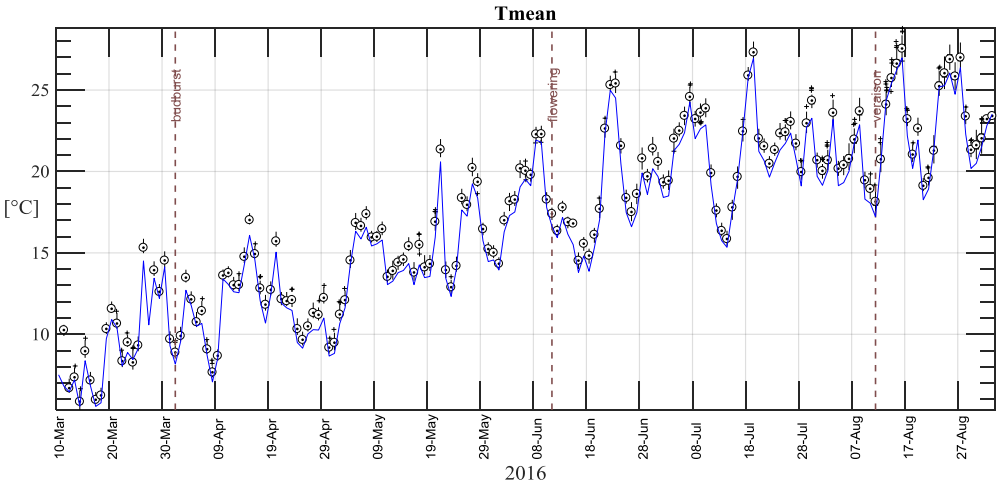
Tmean
budburst
flowering
veraison
[°C]
25
20
15
10
10-Mar
20-Mar
30-Mar
09-Apr
19-Apr
29-Apr
09-May
19-May
29-May
08-Jun
18-Jun
28-Jun
08-Jul
18-Jul
28-Jul
07-Aug
17-Aug
27-Aug
2016

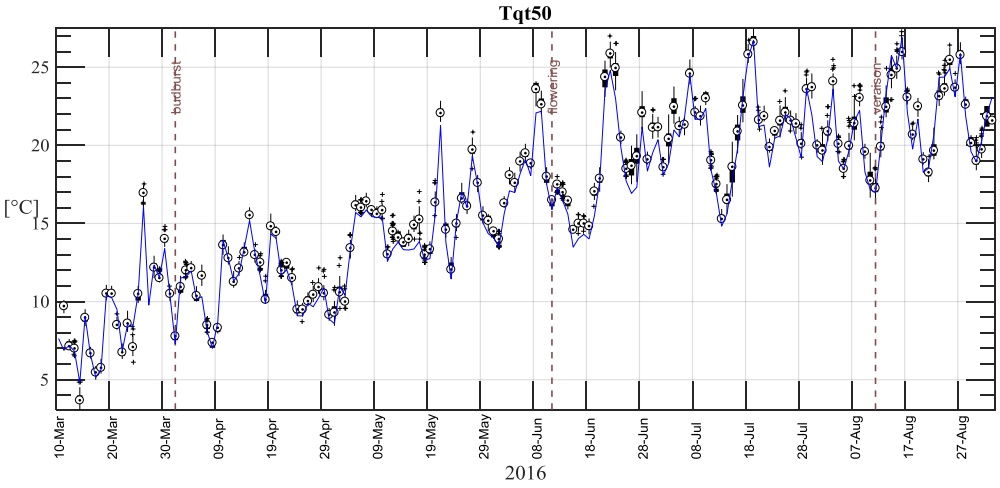
Tqt50
budburst
flowering
veraison
[°C]
25
20
15
10
5
10-Mar
20-Mar
30-Mar
09-Apr
19-Apr
29-Apr
09-May
19-May
29-May
08-Jun
18-Jun
28-Jun
08-Jul
18-Jul
28-Jul
07-Aug
17-Aug
27-Aug
2016

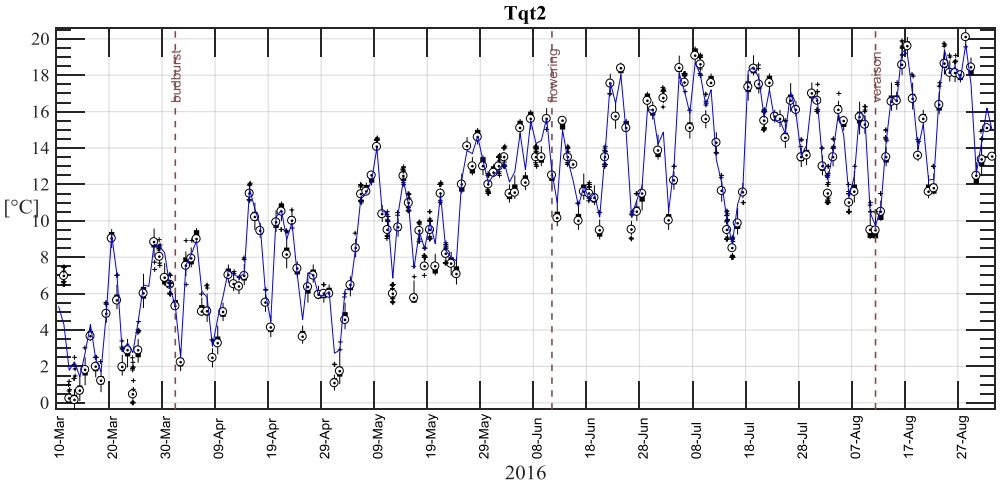
Tqt2
budburst
flowering
veraison
[°C]
20
18
16
14
12
10
8
6
4
2
0
10-Mar
20-Mar
30-Mar
09-Apr
19-Apr
29-Apr
09-May
19-May
29-May
08-Jun
18-Jun
28-Jun
08-Jul
18-Jul
28-Jul
07-Aug
17-Aug
27-Aug
2016

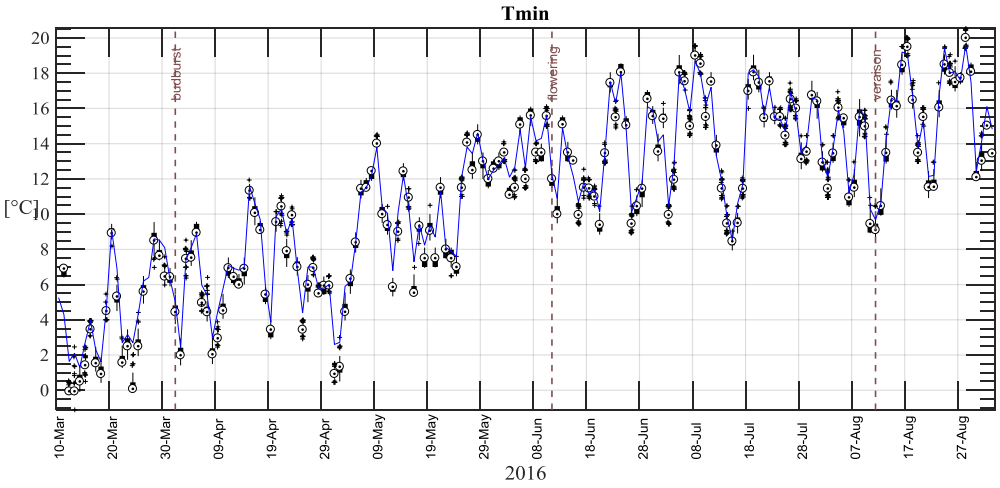
Tmin
[°C]
budburst
flowering
veraison
10-Mar
20-Mar
30-Mar
09-Apr
19-Apr
29-Apr
09-May
19-May
29-May
08-Jun
18-Jun
28-Jun
08-Jul
18-Jul
28-Jul
07-Aug
17-Aug
27-Aug
2016

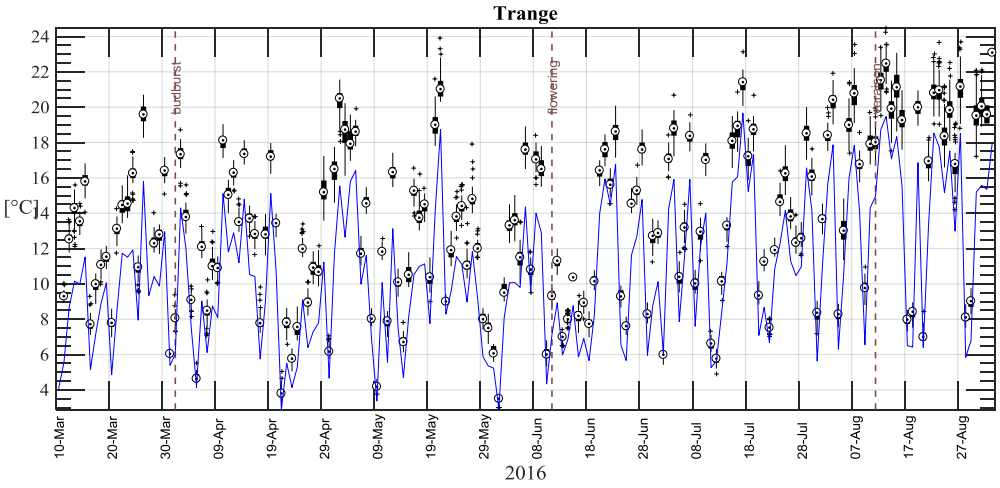
Trange
[°C]
budburst
flowering
veraison
10-Mar
20-Mar
30-Mar
09-Apr
19-Apr
29-Apr
09-May
19-May
29-May
08-Jun
18-Jun
28-Jun
08-Jul
18-Jul
28-Jul
07-Aug
17-Aug
27-Aug
2016

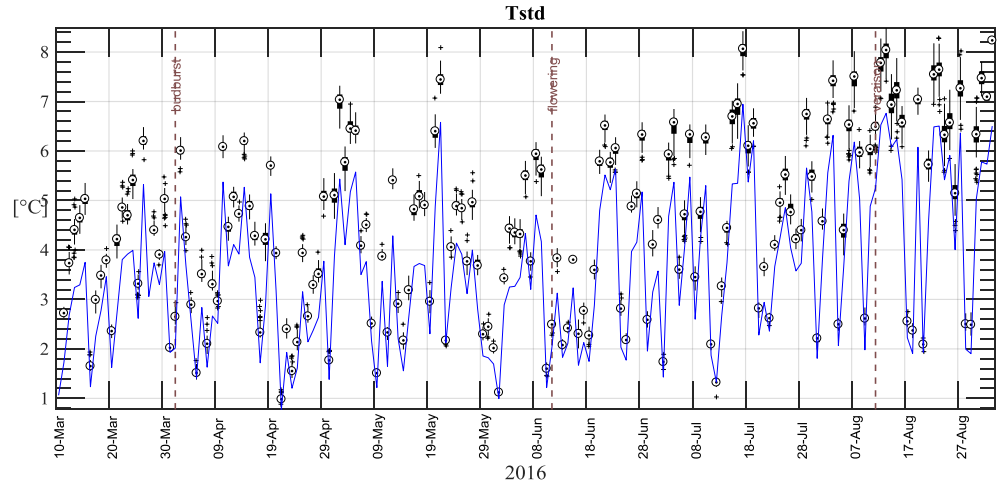
Tstd
[°C]
budburst
flowering
veraison
10-Mar
20-Mar
30-Mar
09-Apr
19-Apr
29-Apr
09-May
19-May
29-May
08-Jun
18-Jun
28-Jun
08-Jul
18-Jul
28-Jul
07-Aug
17-Aug
27-Aug
2016

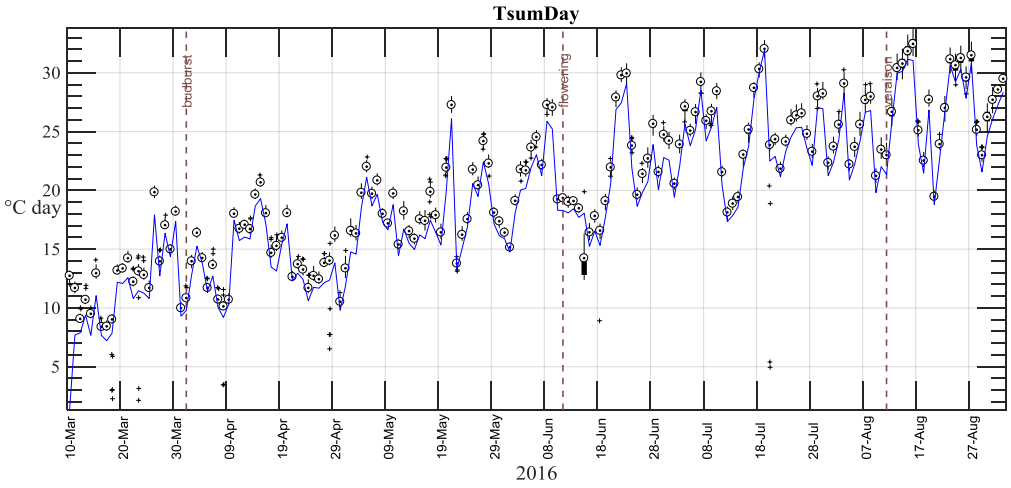
TsumDay
°C day
budburst
flowering
veraison
2016

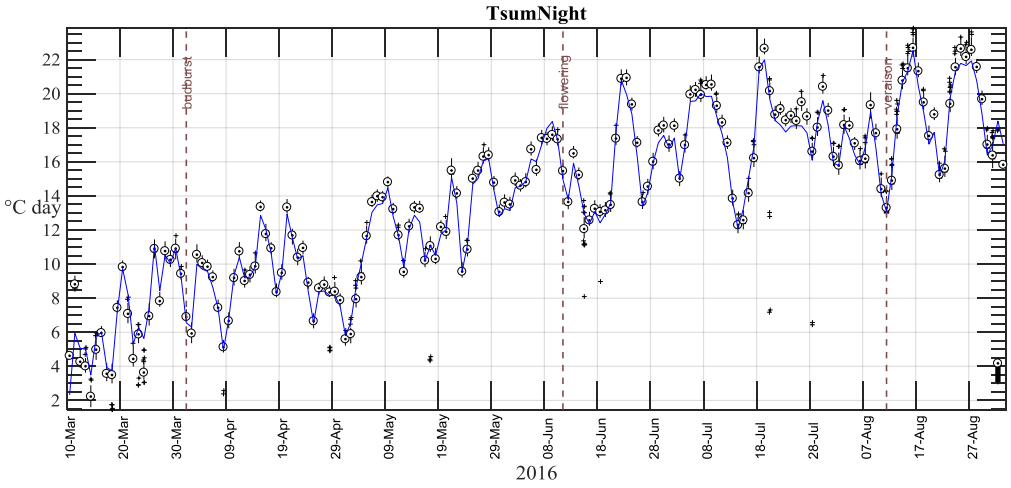
TsumNight
°C day
budburst
flowering
veraison
2016

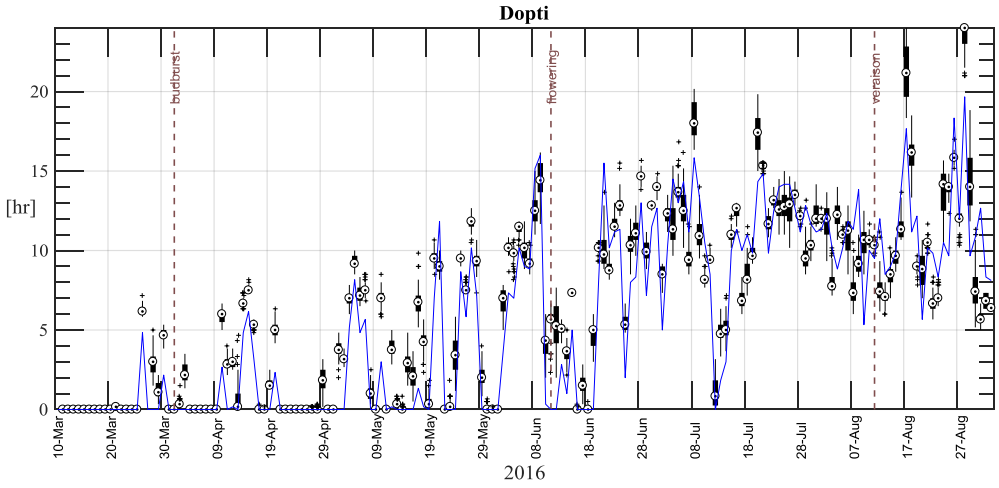
Dopti
[hr]
budburst
flowering
veraison
2016

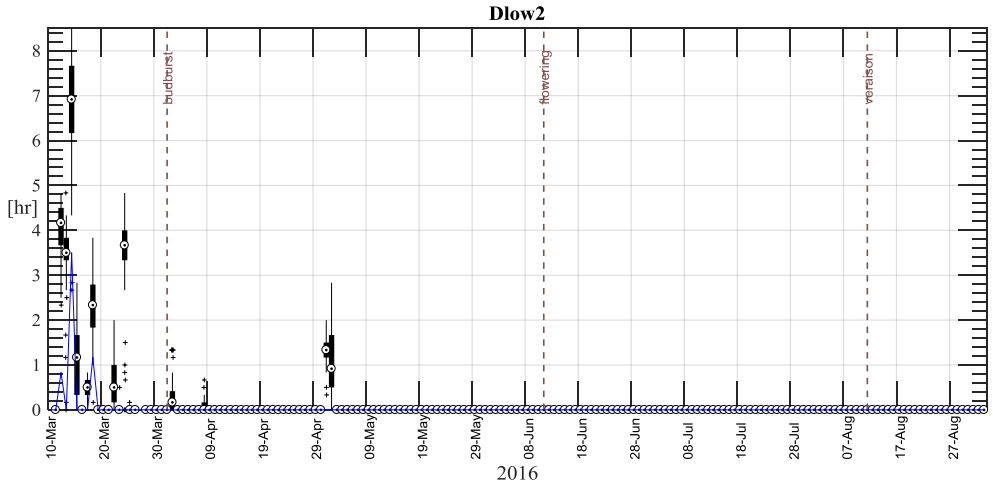
Dlow2
[hr]
budburst
flowering
veraison
2016

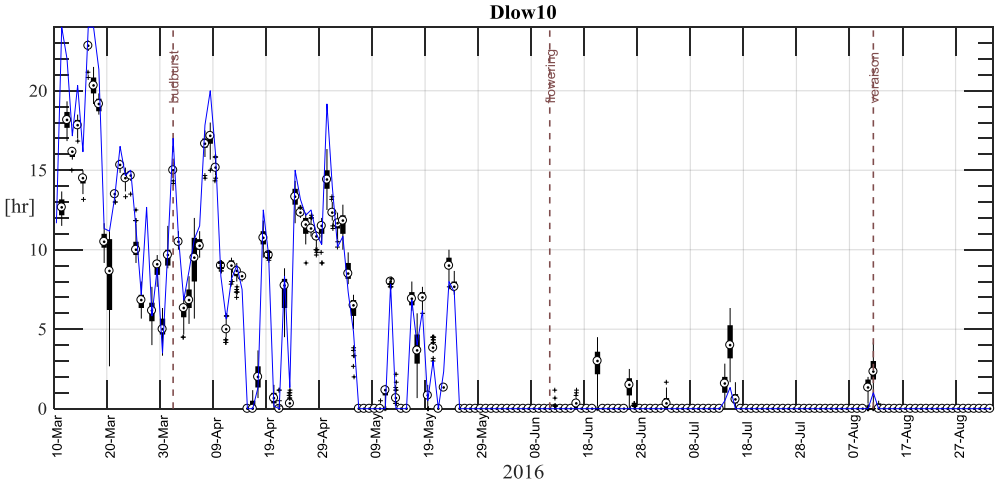
Dlow10
[hr]
budburst
flowering
veraison
2016

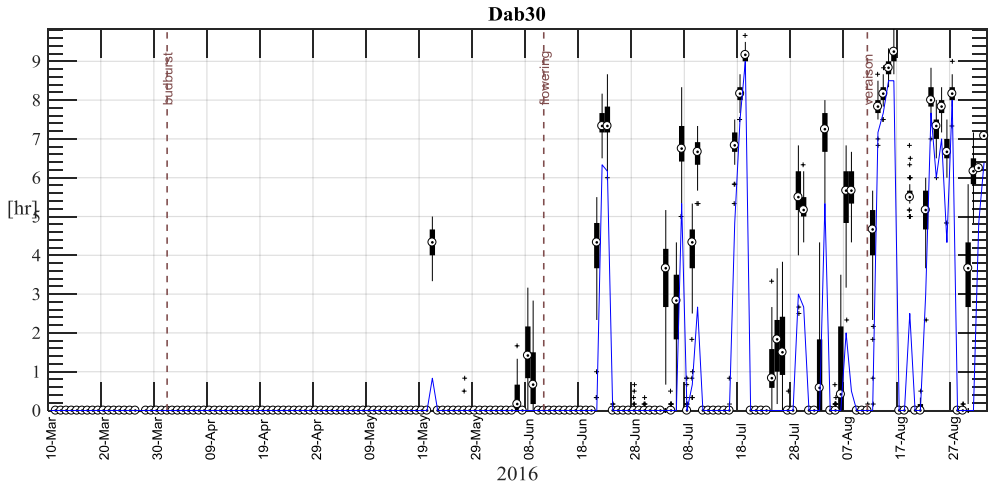
Dab30
[hr]
budburst
flowering
veraison
2016

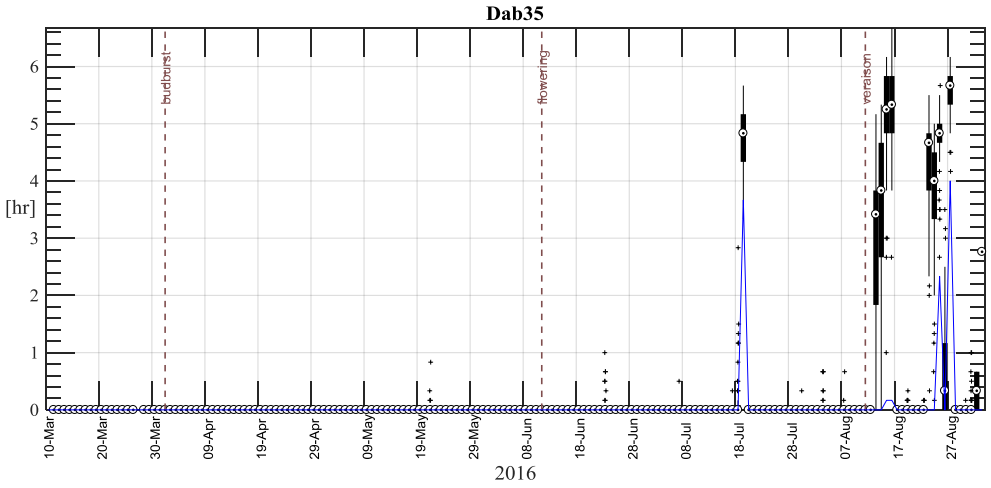
Dab35
budburst
flowering
veraison
[hr]
0
1
2
3
4
5
6
10-Mar
20-Mar
30-Mar
09-Apr
19-Apr
29-Apr
09-May
19-May
29-May
08-Jun
18-Jun
28-Jun
08-Jul
18-Jul
28-Jul
07-Aug
17-Aug
27-Aug
2016

K. Linear models obtained from simple linear regressions between mean centered temperature variables and agronomic variables

			1-Before budburst	2- From budburst to flowering	3-From flowering to veraison	4-From veraison to harvest
Yield	**Tmax**	High ET0	n.a.	Y =0.01(X - $\overline{X}$) +0.01 , r=0, R2 =0	Y =-0.49(X - $\overline{X}$) -0.49 , r=-0.42, R2 =0.18	n.a.
		Low ET0	n.a.	Y =0.06(X - $\overline{X}$) +0.06 , r=0.02, R2 =0	n.a.	Y =-0.42(X - $\overline{X}$) -0.42 , r=-0.33, R2 =0.11
	Tqt98	High ET0	Y =-0.57(X - $\overline{X}$) -0.57 , r=-0.19, R2 =0.04	Y =-0.02(X - $\overline{X}$) -0.02 , r=-0.01, R2 =0	Y =-0.51(X - $\overline{X}$) -0.51 , r=-0.43, R2 =0.18	Y =-0.22(X - $\overline{X}$) -0.22 , r=-0.32, R2 =0.1
		Low ET0	n.a.	n.a.	n.a.	Y =-0.45(X - $\overline{X}$) -0.45 , r=-0.32, R2 =0.1
	Tmed	High ET0	Y =-0.19(X - $\overline{X}$) -0.19 , r=-0.05, R2 =0	n.a.	n.a.	n.a.
		Low ET0	n.a.	n.a.	n.a.	n.a.
	Tqt2	High ET0	Y =-0.32(X - $\overline{X}$) -0.32 , r=-0.15, R2 =0.02	n.a.	Y =-0.87(X - $\overline{X}$) -0.87 , r=-0.38, R2 =0.14	Y =-0.6(X - $\overline{X}$) -0.6 , r=-0.29, R2 =0.09
		Low ET0	Y =-0.37(X - $\overline{X}$) -0.37 , r=-0.15, R2 =0.02	n.a.	n.a.	Y =-0.7(X - $\overline{X}$) -0.7 , r=-0.28, R2 =0.08
	Tmin	High ET0	Y =-0.31(X - $\overline{X}$) -0.31 , r=-0.15, R2 =0.02	n.a.	Y =-0.82(X - $\overline{X}$) -0.82 , r=-0.36, R2 =0.13	Y =-0.59(X - $\overline{X}$) -0.59 , r=-0.31, R2 =0.1
		Low ET0	Y =-0.28(X - $\overline{X}$) -0.28 , r=-0.11, R2 =0.01	n.a.	n.a.	Y =-0.75(X - $\overline{X}$) -0.75 , r=-0.29, R2 =0.08
	Tmean	High ET0	n.a.	n.a.	n.a.	n.a.
		Low ET0	n.a.	n.a.	n.a.	n.a.
	Trange	High ET0	Y =0.06(X - $\overline{X}$) +0.06 , r=0.02, R2 =0	Y =0.21(X - $\overline{X}$) +0.21 , r=0.08, R2 =0.01	n.a.	n.a.
		Low ET0	n.a.	Y =0.95(X - $\overline{X}$) +0.95 , r=0.24, R2 =0.06	Y =0.66(X - $\overline{X}$) +0.66 , r=0.16, R2 =0.02	n.a.
	Tstd	High ET0	Y =-0.79(X - $\overline{X}$) -0.79 , r=-0.1, R2 =0.01	Y =0.28(X - $\overline{X}$) +0.28 , r=0.03, R2 =0	Y =-1.29(X - $\overline{X}$) -1.29 , r=-0.34, R2 =0.12	Y =-0.8(X - $\overline{X}$) -0.8 , r=-0.33, R2 =0.11
		Low ET0	Y =0.5(X - $\overline{X}$) +0.5 , r=0.05, R2 =0	Y =2.21(X - $\overline{X}$) +2.21 , r=0.13, R2 =0.02	n.a.	Y =-1.97(X - $\overline{X}$) -1.97 , r=-0.3, R2 =0.09
	Dab30	High ET0	n.a.	n.a.	Y =-0.68(X - $\overline{X}$) -0.68 , r=-0.51, R2 =0.26	Y =-0.67(X - $\overline{X}$) -0.67 , r=-0.39, R2 =0.15
		Low ET0	n.a.	n.a.	Y =-22.45(X - $\overline{X}$) -22.45 , r=-0.28, R2 =0.08	Y =-1.13(X - $\overline{X}$) -1.13 , r=-0.42, R2 =0.18
	Dab35	High ET0	n.a.	Y =8.59(X - $\overline{X}$) +8.59 , r=0.06, R2 =0	Y =-4.58(X - $\overline{X}$) -4.58 , r=-0.36, R2 =0.13	Y =-0.4(X - $\overline{X}$) -0.4 , r=-0.42, R2 =0.17
		Low ET0	n.a.	n.a.	n.a.	Y =-7.81(X - $\overline{X}$) -7.81 , r=-0.28, R2 =0.08
	Dlow10	High ET0	n.a.	n.a.	n.a.	n.a.
		Low ET0	n.a.	n.a.	Y =4.84(X - $\overline{X}$) +4.84 , r=0.48, R2 =0.23	n.a.
	Dlow2	High ET0	Y =0.8(X - $\overline{X}$) +0.8 , r=0.24, R2 =0.06	n.a.	n.a.	n.a.
		Low ET0	n.a.	n.a.	n.a.	n.a.
	Dopti	High ET0	n.a.	n.a.	Y =0.5(X - $\overline{X}$) +0.5 , r=0.34, R2 =0.11	Y =-0.01(X - $\overline{X}$) -0.01 , r=-0.01, R2 =0
		Low ET0	Y =-3.45(X - $\overline{X}$) -3.45 , r=-0.07, R2 =0	n.a.	n.a.	n.a.
	TsumdDay	High ET0	n.a.	n.a.	Y =-0.93(X - $\overline{X}$) -0.93 , r=-0.47, R2 =0.22	Y =-0.53(X - $\overline{X}$) -0.53 , r=-0.41, R2 =0.17
		Low ET0	n.a.	n.a.	n.a.	n.a.
	TsumdNight	High ET0	Y =-0.24(X - $\overline{X}$) -0.24 , r=-0.09, R2 =0.01	n.a.	n.a.	Y =-0.52(X - $\overline{X}$) -0.52 , r=-0.28, R2 =0.08
		Low ET0	Y =-0.37(X - $\overline{X}$) -0.37 , r=-0.13, R2 =0.02	n.a.	Y =-1.18(X - $\overline{X}$) -1.18 , r=-0.33, R2 =0.11	n.a.

			1-Before budburst	2- From budburst to flowering	3-From flowering to veraison	4-From veraison to harvest
BunchNb	**Tmax**	High ET0	n.a.	Y =0.82(X - $\overline{X}$) +0.82 , r=0.08, R2 =0.01	Y =-2.19(X - $\overline{X}$) -2.19 , r=-0.35, R2 =0.13	n.a.
		Low ET0	n.a.	Y =0.95(X - $\overline{X}$) +0.95 , r=0.05, R2 =0	n.a.	Y =-1.39(X - $\overline{X}$) -1.39 , r=-0.21, R2 =0.04
	Tqt98	High ET0	Y =0.1(X - $\overline{X}$) +0.1 , r=0.01, R2 =0	Y =1.04(X - $\overline{X}$) +1.04 , r=0.1, R2 =0.01	Y =-2.26(X - $\overline{X}$) -2.26 , r=-0.36, R2 =0.13	Y =-0.59(X - $\overline{X}$) -0.59 , r=-0.16, R2 =0.03
		Low ET0	n.a.	n.a.	n.a.	Y =-1.52(X - $\overline{X}$) -1.52 , r=-0.21, R2 =0.04
	Tmed	High ET0	Y =-1.18(X - $\overline{X}$) -1.18 , r=-0.07, R2 =0	n.a.	n.a.	n.a.
		Low ET0	n.a.	n.a.	n.a.	n.a.
	Tqt2	High ET0	Y =-1.06(X - $\overline{X}$) -1.06 , r=-0.1, R2 =0.01	n.a.	Y =-4.71(X - $\overline{X}$) -4.71 , r=-0.38, R2 =0.15	Y =-3.31(X - $\overline{X}$) -3.31 , r=-0.32, R2 =0.1
		Low ET0	Y =-1.63(X - $\overline{X}$) -1.63 , r=-0.13, R2 =0.02	n.a.	n.a.	Y =-3.26(X - $\overline{X}$) -3.26 , r=-0.25, R2 =0.06
	Tmin	High ET0	Y =-1.71(X - $\overline{X}$) -1.71 , r=-0.16, R2 =0.02	n.a.	Y =-4.36(X - $\overline{X}$) -4.36 , r=-0.36, R2 =0.13	Y =-3.03(X - $\overline{X}$) -3.03 , r=-0.31, R2 =0.1
		Low ET0	Y =-1.66(X - $\overline{X}$) -1.66 , r=-0.12, R2 =0.01	n.a.	n.a.	Y =-3.5(X - $\overline{X}$) -3.5 , r=-0.26, R2 =0.07
	Tmean	High ET0	n.a.	n.a.	n.a.	n.a.
		Low ET0	n.a.	n.a.	n.a.	n.a.
	Trange	High ET0	Y =1.66(X - $\overline{X}$) +1.66 , r=0.12, R2 =0.01	Y =2.6(X - $\overline{X}$) +2.6 , r=0.2, R2 =0.04	n.a.	n.a.
		Low ET0	n.a.	Y =3.6(X - $\overline{X}$) +3.6 , r=0.18, R2 =0.03	Y =3.84(X - $\overline{X}$) +3.84 , r=0.17, R2 =0.03	n.a.
	Tstd	High ET0	Y =-1.26(X - $\overline{X}$) -1.26 , r=-0.03, R2 =0	Y =9.38(X - $\overline{X}$) +9.38 , r=0.19, R2 =0.04	Y =-3.39(X - $\overline{X}$) -3.39 , r=-0.17, R2 =0.03	Y =-1.81(X - $\overline{X}$) -1.81 , r=-0.14, R2 =0.02
		Low ET0	Y =14.03(X - $\overline{X}$) +14.03 , r=0.28, R2 =0.08	Y =7.51(X - $\overline{X}$) +7.51 , r=0.08, R2 =0.01	n.a.	Y =-5.38(X - $\overline{X}$) -5.38 , r=-0.16, R2 =0.02
	Dab30	High ET0	n.a.	n.a.	Y =-2.43(X - $\overline{X}$) -2.43 , r=-0.34, R2 =0.12	Y =-1.92(X - $\overline{X}$) -1.92 , r=-0.22, R2 =0.05
		Low ET0	n.a.	n.a.	Y =-171.6(X - $\overline{X}$) -171.6 , r=-0.41, R2 =0.17	Y =-3.36(X - $\overline{X}$) -3.36 , r=-0.24, R2 =0.06
	Dab35	High ET0	n.a.	Y =40.94(X - $\overline{X}$) +40.94 , r=0.06, R2 =0	Y =-27.57(X - $\overline{X}$) -27.57 , r=-0.41, R2 =0.17	Y =-1.35(X - $\overline{X}$) -1.35 , r=-0.28, R2 =0.08
		Low ET0	n.a.	n.a.	n.a.	Y =-24.62(X - $\overline{X}$) -24.62 , r=-0.17, R2 =0.03
	Dlow10	High ET0	n.a.	n.a.	n.a.	n.a.
		Low ET0	n.a.	n.a.	Y =24.24(X - $\overline{X}$) +24.24 , r=0.46, R2 =0.21	n.a.
	Dlow2	High ET0	Y =4.17(X - $\overline{X}$) +4.17 , r=0.24, R2 =0.06	n.a.	n.a.	n.a.
		Low ET0	n.a.	n.a.	n.a.	n.a.
	Dopti	High ET0	n.a.	n.a.	Y =1.74(X - $\overline{X}$) +1.74 , r=0.22, R2 =0.05	Y =-0.44(X - $\overline{X}$) -0.44 , r=-0.04, R2 =0
		Low ET0	Y =54.78(X - $\overline{X}$) +54.78 , r=0.2, R2 =0.04	n.a.	n.a.	n.a.
	TsumdDay	High ET0	n.a.	n.a.	Y =-3.97(X - $\overline{X}$) -3.97 , r=-0.38, R2 =0.14	Y =-1.76(X - $\overline{X}$) -1.76 , r=-0.27, R2 =0.07
		Low ET0	n.a.	n.a.	n.a.	n.a.
	TsumdNight	High ET0	Y =-0.74(X - $\overline{X}$) -0.74 , r=-0.05, R2 =0	n.a.	n.a.	Y =-2.87(X - $\overline{X}$) -2.87 , r=-0.3, R2 =0.09
		Low ET0	Y =-1.89(X - $\overline{X}$) -1.89 , r=-0.13, R2 =0.02	n.a.	Y =-4.91(X - $\overline{X}$) -4.91 , r=-0.26, R2 =0.07	n.a.

			1-Before budburst	2- From budburst to flowering	3-From flowering to veraison	4-From veraison to harvest
BunchW	**Tmax**	High ET0	n.a.	Y =0(X - $\overline{X}$) +0 , r=-0.08, R2 =0.01	Y =0(X - $\overline{X}$) +0 , r=-0.15, R2 =0.02	n.a.
		Low ET0	n.a.	Y =0(X - $\overline{X}$) +0 , r=-0.07, R2 =0.01	n.a.	Y =0(X - $\overline{X}$) +0 , r=-0.2, R2 =0.04
	Tqt98	High ET0	Y =-0.02(X - $\overline{X}$) -0.02 , r=-0.33, R2 =0.11	Y =0(X - $\overline{X}$) +0 , r=-0.11, R2 =0.01	Y =0(X - $\overline{X}$) +0 , r=-0.16, R2 =0.03	Y =0(X - $\overline{X}$) +0 , r=-0.25, R2 =0.06
		Low ET0	n.a.	n.a.	n.a.	Y =0(X - $\overline{X}$) +0 , r=-0.19, R2 =0.04
	Tmed	High ET0	Y =0(X - $\overline{X}$) +0 , r=0.04, R2 =0	n.a.	n.a.	n.a.
		Low ET0	n.a.	n.a.	n.a.	n.a.
	Tqt2	High ET0	Y =0(X - $\overline{X}$) +0 , r=-0.11, R2 =0.01	n.a.	Y =0(X - $\overline{X}$) +0 , r=-0.05, R2 =0	Y =0(X - $\overline{X}$) +0 , r=-0.03, R2 =0
		Low ET0	Y =0(X - $\overline{X}$) +0 , r=-0.06, R2 =0	n.a.	n.a.	Y =0(X - $\overline{X}$) +0 , r=-0.09, R2 =0.01
	Tmin	High ET0	Y =0(X - $\overline{X}$) +0 , r=-0.01, R2 =0	n.a.	Y =0(X - $\overline{X}$) +0 , r=-0.06, R2 =0	Y =0(X - $\overline{X}$) +0 , r=-0.08, R2 =0.01
		Low ET0	Y =0(X - $\overline{X}$) +0 , r=0.01, R2 =0	n.a.	n.a.	Y =0(X - $\overline{X}$) +0 , r=-0.1, R2 =0.01
	Tmean	High ET0	n.a.	n.a.	n.a.	n.a.
		Low ET0	n.a.	n.a.	n.a.	n.a.
	Trange	High ET0	Y =-0.01(X - $\overline{X}$) -0.01 , r=-0.15, R2 =0.02	Y =-0.01(X - $\overline{X}$) -0.01 , r=-0.12, R2 =0.02	n.a.	n.a.
		Low ET0	n.a.	Y =0.01(X - $\overline{X}$) +0.01 , r=0.1, R2 =0.01	Y =0(X - $\overline{X}$) +0 , r=-0.01, R2 =0	n.a.
	Tstd	High ET0	Y =-0.02(X - $\overline{X}$) -0.02 , r=-0.16, R2 =0.02	Y =-0.04(X - $\overline{X}$) -0.04 , r=-0.21, R2 =0.04	Y =-0.02(X - $\overline{X}$) -0.02 , r=-0.3, R2 =0.09	Y =-0.01(X - $\overline{X}$) -0.01 , r=-0.3, R2 =0.09
		Low ET0	Y =-0.06(X - $\overline{X}$) -0.06 , r=-0.33, R2 =0.11	Y =0.01(X - $\overline{X}$) +0.01 , r=0.04, R2 =0	n.a.	Y =-0.03(X - $\overline{X}$) -0.03 , r=-0.23, R2 =0.05
	Dab30	High ET0	n.a.	n.a.	Y =-0.01(X - $\overline{X}$) -0.01 , r=-0.32, R2 =0.1	Y =-0.01(X - $\overline{X}$) -0.01 , r=-0.33, R2 =0.11
		Low ET0	n.a.	n.a.	Y =0.2(X - $\overline{X}$) +0.2 , r=0.13, R2 =0.02	Y =-0.02(X - $\overline{X}$) -0.02 , r=-0.33, R2 =0.11
	Dab35	High ET0	n.a.	Y =0.07(X - $\overline{X}$) +0.07 , r=0.03, R2 =0	Y =0(X - $\overline{X}$) +0 , r=0.02, R2 =0	Y =0(X - $\overline{X}$) +0 , r=-0.28, R2 =0.08
		Low ET0	n.a.	n.a.	n.a.	Y =-0.11(X - $\overline{X}$) -0.11 , r=-0.22, R2 =0.05
	Dlow10	High ET0	n.a.	n.a.	n.a.	n.a.
		Low ET0	n.a.	n.a.	Y =0.02(X - $\overline{X}$) +0.02 , r=0.13, R2 =0.02	n.a.
	Dlow2	High ET0	Y =0(X - $\overline{X}$) +0 , r=0.05, R2 =0	n.a.	n.a.	n.a.
		Low ET0	n.a.	n.a.	n.a.	n.a.
	Dopti	High ET0	n.a.	n.a.	Y =0.01(X - $\overline{X}$) +0.01 , r=0.21, R2 =0.04	Y =0(X - $\overline{X}$) +0 , r=0.04, R2 =0
		Low ET0	Y =-0.38(X - $\overline{X}$) -0.38 , r=-0.4, R2 =0.16	n.a.	n.a.	n.a.
	TsumdDay	High ET0	n.a.	n.a.	Y =-0.01(X - $\overline{X}$) -0.01 , r=-0.21, R2 =0.04	Y =-0.01(X - $\overline{X}$) -0.01 , r=-0.27, R2 =0.07
		Low ET0	n.a.	n.a.	n.a.	n.a.
	TsumdNight	High ET0	Y =0(X - $\overline{X}$) +0 , r=-0.04, R2 =0	n.a.	n.a.	Y =0(X - $\overline{X}$) +0 , r=-0.03, R2 =0
		Low ET0	Y =0(X - $\overline{X}$) +0 , r=-0.02, R2 =0	n.a.	Y =-0.01(X - $\overline{X}$) -0.01 , r=-0.14, R2 =0.02	n.a.

			1-Before budburst	2- From budburst to flowering	3-From flowering to veraison	4-From veraison to harvest
200BerryW	Tmax	High ET0	n.a.	Y =-9.81(X - $\bar{X}$) -9.81 , r=-0.23, R2 =0.05	Y =-3.34(X - $\bar{X}$) -3.34 , r=-0.1, R2 =0.01	n.a.
		Low ET0	n.a.	Y =-2.79(X - $\bar{X}$) -2.79 , r=-0.04, R2 =0	n.a.	Y =-7.24(X - $\bar{X}$) -7.24 , r=-0.21, R2 =0.04
	Tqt98	High ET0	Y =-23.85(X - $\bar{X}$) -23.85 , r=-0.37, R2 =0.14	Y =-10.02(X - $\bar{X}$) -10.02 , r=-0.21, R2 =0.05	Y =-3.65(X - $\bar{X}$) -3.65 , r=-0.11, R2 =0.01	Y =-2(X - $\bar{X}$) -2 , r=-0.11, R2 =0.01
		Low ET0	n.a.	n.a.	n.a.	Y =-9(X - $\bar{X}$) -9 , r=-0.24, R2 =0.06
	Tmed	High ET0	Y =-28.75(X - $\bar{X}$) -28.75 , r=-0.39, R2 =0.15	n.a.	n.a.	n.a.
		Low ET0	n.a.	n.a.	n.a.	n.a.
	Tqt2	High ET0	Y =-17.41(X - $\bar{X}$) -17.41 , r=-0.39, R2 =0.15	n.a.	Y =-22.27(X - $\bar{X}$) -22.27 , r=-0.35, R2 =0.12	Y =-18.17(X - $\bar{X}$) -18.17 , r=-0.34, R2 =0.12
		Low ET0	Y =-27.12(X - $\bar{X}$) -27.12 , r=-0.4, R2 =0.16	n.a.	n.a.	Y =-25.71(X - $\bar{X}$) -25.71 , r=-0.39, R2 =0.15
	Tmin	High ET0	Y =-15.84(X - $\bar{X}$) -15.84 , r=-0.35, R2 =0.12	n.a.	Y =-21.78(X - $\bar{X}$) -21.78 , r=-0.34, R2 =0.12	Y =-15.57(X - $\bar{X}$) -15.57 , r=-0.31, R2 =0.1
		Low ET0	Y =-29.26(X - $\bar{X}$) -29.26 , r=-0.41, R2 =0.16	n.a.	n.a.	Y =-22.95(X - $\bar{X}$) -22.95 , r=-0.33, R2 =0.11
	Tmean	High ET0	n.a.	n.a.	n.a.	n.a.
		Low ET0	n.a.	n.a.	n.a.	n.a.
	Trange	High ET0	Y =8.67(X - $\bar{X}$) +8.67 , r=0.16, R2 =0.02	Y =3.12(X - $\bar{X}$) +3.12 , r=0.05, R2 =0	n.a.	n.a.
		Low ET0	n.a.	Y =31.52(X - $\bar{X}$) +31.52 , r=0.38, R2 =0.14	Y =21.65(X - $\bar{X}$) +21.65 , r=0.19, R2 =0.03	n.a.
	Tstd	High ET0	Y =32.67(X - $\bar{X}$) +32.67 , r=0.19, R2 =0.04	Y =-0.5(X - $\bar{X}$) -0.5 , r=0, R2 =0	Y =8.61(X - $\bar{X}$) +8.61 , r=0.08, R2 =0.01	Y =2.91(X - $\bar{X}$) +2.91 , r=0.05, R2 =0
		Low ET0	Y =81.85(X - $\bar{X}$) +81.85 , r=0.31, R2 =0.09	Y =133.15(X - $\bar{X}$) +133.15 , r=0.37, R2 =0.14	n.a.	Y =-10.33(X - $\bar{X}$) -10.33 , r=-0.06, R2 =0
	Dab30	High ET0	n.a.	n.a.	Y =-6.74(X - $\bar{X}$) -6.74 , r=-0.18, R2 =0.03	Y =-9.94(X - $\bar{X}$) -9.94 , r=-0.22, R2 =0.05
		Low ET0	n.a.	n.a.	Y =-172.92(X - $\bar{X}$) -172.92 , r=-0.08, R2 =0.01	Y =-7.08(X - $\bar{X}$) -7.08 , r=-0.1, R2 =0.01
	Dab35	High ET0	n.a.	Y =-204.86(X - $\bar{X}$) -204.86 , r=-0.06, R2 =0	Y =-60.87(X - $\bar{X}$) -60.87 , r=-0.17, R2 =0.03	Y =-2.23(X - $\bar{X}$) -2.23 , r=-0.09, R2 =0.01
		Low ET0	n.a.	n.a.	n.a.	Y =-69.4(X - $\bar{X}$) -69.4 , r=-0.09, R2 =0.01
	Dlow10	High ET0	n.a.	n.a.	n.a.	n.a.
		Low ET0	n.a.	n.a.	Y =80.62(X - $\bar{X}$) +80.62 , r=0.29, R2 =0.08	n.a.
	Dlow2	High ET0	Y =30.88(X - $\bar{X}$) +30.88 , r=0.43, R2 =0.18	n.a.	n.a.	n.a.
		Low ET0	n.a.	n.a.	n.a.	n.a.
	Dopti	High ET0	n.a.	n.a.	Y =-6.83(X - $\bar{X}$) -6.83 , r=-0.17, R2 =0.03	Y =-13.6(X - $\bar{X}$) -13.6 , r=-0.26, R2 =0.07
		Low ET0	Y =-253.79(X - $\bar{X}$) -253.79 , r=-0.18, R2 =0.03	n.a.	n.a.	n.a.
	TsumdDay	High ET0	n.a.	n.a.	Y =-16.34(X - $\bar{X}$) -16.34 , r=-0.3, R2 =0.09	Y =-6.83(X - $\bar{X}$) -6.83 , r=-0.2, R2 =0.04
		Low ET0	n.a.	n.a.	n.a.	n.a.
	TsumdNight	High ET0	Y =-23.26(X - $\bar{X}$) -23.26 , r=-0.4, R2 =0.16	n.a.	n.a.	Y =-17.66(X - $\bar{X}$) -17.66 , r=-0.36, R2 =0.13
		Low ET0	Y =-30.97(X - $\bar{X}$) -30.97 , r=-0.39, R2 =0.16	n.a.	Y =-39.29(X - $\bar{X}$) -39.29 , r=-0.39, R2 =0.15	n.a.

			1-Before budburst	2- From budburst to flowering	3-From flowering to veraison	4-From veraison to harvest
Sugar	**Tmax**	High ET0	n.a.	Y =-6.02(X - $\overline{X}$) -6.02 , r=-0.18, R2 =0.03	Y =-3.73(X - $\overline{X}$) -3.73 , r=-0.18, R2 =0.03	n.a.
		Low ET0	n.a.	Y =-1.16(X - $\overline{X}$) -1.16 , r=-0.02, R2 =0	n.a.	Y =-8.96(X - $\overline{X}$) -8.96 , r=-0.4, R2 =0.16
	Tqt98	High ET0	Y =-1.87(X - $\overline{X}$) -1.87 , r=-0.04, R2 =0	Y =-5.84(X - $\overline{X}$) -5.84 , r=-0.16, R2 =0.03	Y =-3.98(X - $\overline{X}$) -3.98 , r=-0.18, R2 =0.03	Y =-3.67(X - $\overline{X}$) -3.67 , r=-0.3, R2 =0.09
		Low ET0	n.a.	n.a.	n.a.	Y =-10.6(X - $\overline{X}$) -10.6 , r=-0.43, R2 =0.19
	Tmed	High ET0	Y =-13.99(X - $\overline{X}$) -13.99 , r=-0.25, R2 =0.06	n.a.	n.a.	n.a.
		Low ET0	n.a.	n.a.	n.a.	n.a.
	Tqt2	High ET0	Y =-12.21(X - $\overline{X}$) -12.21 , r=-0.35, R2 =0.12	n.a.	Y =-9.66(X - $\overline{X}$) -9.66 , r=-0.23, R2 =0.05	Y =-6.57(X - $\overline{X}$) -6.57 , r=-0.19, R2 =0.04
		Low ET0	Y =-17.18(X - $\overline{X}$) -17.18 , r=-0.4, R2 =0.16	n.a.	n.a.	Y =-12.04(X - $\overline{X}$) -12.04 , r=-0.28, R2 =0.08
	Tmin	High ET0	Y =-9.26(X - $\overline{X}$) -9.26 , r=-0.27, R2 =0.07	n.a.	Y =-9.93(X - $\overline{X}$) -9.93 , r=-0.24, R2 =0.06	Y =-6(X - $\overline{X}$) -6 , r=-0.18, R2 =0.03
		Low ET0	Y =-20.19(X - $\overline{X}$) -20.19 , r=-0.44, R2 =0.19	n.a.	n.a.	Y =-13.13(X - $\overline{X}$) -13.13 , r=-0.29, R2 =0.09
	Tmean	High ET0	n.a.	n.a.	n.a.	n.a.
		Low ET0	n.a.	n.a.	n.a.	n.a.
	Trange	High ET0	Y =16.88(X - $\overline{X}$) +16.88 , r=0.4, R2 =0.16	Y =2.31(X - $\overline{X}$) +2.31 , r=0.05, R2 =0	n.a.	n.a.
		Low ET0	n.a.	Y =23.4(X - $\overline{X}$) +23.4 , r=0.37, R2 =0.13	Y =3.61(X - $\overline{X}$) +3.61 , r=0.05, R2 =0	n.a.
	Tstd	High ET0	Y =58.68(X - $\overline{X}$) +58.68 , r=0.45, R2 =0.2	Y =1.61(X - $\overline{X}$) +1.61 , r=0.01, R2 =0	Y =-12.55(X - $\overline{X}$) -12.55 , r=-0.18, R2 =0.03	Y =-11.89(X - $\overline{X}$) -11.89 , r=-0.28, R2 =0.08
		Low ET0	Y =56.79(X - $\overline{X}$) +56.79 , r=0.34, R2 =0.11	Y =100.4(X - $\overline{X}$) +100.4 , r=0.36, R2 =0.13	n.a.	Y =-47.94(X - $\overline{X}$) -47.94 , r=-0.42, R2 =0.17
	Dab30	High ET0	n.a.	n.a.	Y =-7.19(X - $\overline{X}$) -7.19 , r=-0.29, R2 =0.09	Y =-12.45(X - $\overline{X}$) -12.45 , r=-0.42, R2 =0.17
		Low ET0	n.a.	n.a.	Y =272.65(X - $\overline{X}$) +272.65 , r=0.19, R2 =0.04	Y =-12.44(X - $\overline{X}$) -12.44 , r=-0.27, R2 =0.07
	Dab35	High ET0	n.a.	Y =73.25(X - $\overline{X}$) +73.25 , r=0.03, R2 =0	Y =-0.07(X - $\overline{X}$) -0.07 , r=0, R2 =0	Y =-5.28(X - $\overline{X}$) -5.28 , r=-0.32, R2 =0.1
		Low ET0	n.a.	n.a.	n.a.	Y =-42.8(X - $\overline{X}$) -42.8 , r=-0.09, R2 =0.01
	Dlow10	High ET0	n.a.	n.a.	n.a.	n.a.
		Low ET0	n.a.	n.a.	Y =33.22(X - $\overline{X}$) +33.22 , r=0.18, R2 =0.03	n.a.
	Dlow2	High ET0	Y =17.57(X - $\overline{X}$) +17.57 , r=0.32, R2 =0.1	n.a.	n.a.	n.a.
		Low ET0	n.a.	n.a.	n.a.	n.a.
	Dopti	High ET0	n.a.	n.a.	Y =5.08(X - $\overline{X}$) +5.08 , r=0.19, R2 =0.04	Y =3.99(X - $\overline{X}$) +3.99 , r=0.11, R2 =0.01
		Low ET0	Y =-71.78(X - $\overline{X}$) -71.78 , r=-0.08, R2 =0.01	n.a.	n.a.	n.a.
	TsumdDay	High ET0	n.a.	n.a.	Y =-10.25(X - $\overline{X}$) -10.25 , r=-0.29, R2 =0.08	Y =-7.95(X - $\overline{X}$) -7.95 , r=-0.36, R2 =0.13
		Low ET0	n.a.	n.a.	n.a.	n.a.
	TsumdNight	High ET0	Y =-16.89(X - $\overline{X}$) -16.89 , r=-0.37, R2 =0.14	n.a.	n.a.	Y =-7.63(X - $\overline{X}$) -7.63 , r=-0.24, R2 =0.06
		Low ET0	Y =-19.58(X - $\overline{X}$) -19.58 , r=-0.39, R2 =0.15	n.a.	Y =-19.08(X - $\overline{X}$) -19.08 , r=-0.29, R2 =0.09	n.a.

			1-Before budburst	2- From budburst to flowering	3-From flowering to veraison	4-From veraison to harvest
TotAcid	Tmax	High ET0	n.a.	$Y = -0.11(X - \overline{X}) - 0.11$, r=-0.17, R2 =0.03	$Y = -0.03(X - \overline{X}) - 0.03$, r=-0.09, R2 =0.01	n.a.
		Low ET0	n.a.	$Y = 0.1(X - \overline{X}) + 0.1$, r=0.09, R2 =0.01	n.a.	$Y = -0.07(X - \overline{X}) - 0.07$, r=-0.16, R2 =0.03
	Tqt98	High ET0	$Y = 0.01(X - \overline{X}) + 0.01$, r=0.01, R2 =0	$Y = -0.07(X - \overline{X}) - 0.07$, r=-0.1, R2 =0.01	$Y = -0.03(X - \overline{X}) - 0.03$, r=-0.09, R2 =0.01	$Y = -0.02(X - \overline{X}) - 0.02$, r=-0.1, R2 =0.01
		Low ET0	n.a.	n.a.	n.a.	$Y = -0.08(X - \overline{X}) - 0.08$, r=-0.17, R2 =0.03
	Tmed	High ET0	$Y = -0.2(X - \overline{X}) - 0.2$, r=-0.18, R2 =0.03	n.a.	n.a.	n.a.
		Low ET0	n.a.	n.a.	n.a.	n.a.
	Tqt2	High ET0	$Y = -0.12(X - \overline{X}) - 0.12$, r=-0.18, R2 =0.03	n.a.	$Y = -0.24(X - \overline{X}) - 0.24$, r=-0.32, R2 =0.1	$Y = -0.22(X - \overline{X}) - 0.22$, r=-0.35, R2 =0.12
		Low ET0	$Y = -0.21(X - \overline{X}) - 0.21$, r=-0.25, R2 =0.06	n.a.	n.a.	$Y = -0.23(X - \overline{X}) - 0.23$, r=-0.29, R2 =0.08
	Tmin	High ET0	$Y = -0.16(X - \overline{X}) - 0.16$, r=-0.24, R2 =0.06	n.a.	$Y = -0.23(X - \overline{X}) - 0.23$, r=-0.31, R2 =0.1	$Y = -0.18(X - \overline{X}) - 0.18$, r=-0.3, R2 =0.09
		Low ET0	$Y = -0.23(X - \overline{X}) - 0.23$, r=-0.26, R2 =0.07	n.a.	n.a.	$Y = -0.25(X - \overline{X}) - 0.25$, r=-0.3, R2 =0.09
	Tmean	High ET0	n.a.	n.a.	n.a.	n.a.
		Low ET0	n.a.	n.a.	n.a.	n.a.
	Trange	High ET0	$Y = 0.19(X - \overline{X}) + 0.19$, r=0.23, R2 =0.05	$Y = 0.03(X - \overline{X}) + 0.03$, r=0.04, R2 =0	n.a.	n.a.
		Low ET0	n.a.	$Y = 0.34(X - \overline{X}) + 0.34$, r=0.27, R2 =0.07	$Y = 0.34(X - \overline{X}) + 0.34$, r=0.25, R2 =0.06	n.a.
	Tstd	High ET0	$Y = 0.57(X - \overline{X}) + 0.57$, r=0.22, R2 =0.05	$Y = 0.4(X - \overline{X}) + 0.4$, r=0.12, R2 =0.02	$Y = 0.08(X - \overline{X}) + 0.08$, r=0.06, R2 =0	$Y = -0.04(X - \overline{X}) - 0.04$, r=-0.05, R2 =0
		Low ET0	$Y = 1.31(X - \overline{X}) + 1.31$, r=0.4, R2 =0.16	$Y = 1.36(X - \overline{X}) + 1.36$, r=0.25, R2 =0.06	n.a.	$Y = -0.23(X - \overline{X}) - 0.23$, r=-0.11, R2 =0.01
	Dab30	High ET0	n.a.	n.a.	$Y = -0.04(X - \overline{X}) - 0.04$, r=-0.09, R2 =0.01	$Y = -0.07(X - \overline{X}) - 0.07$, r=-0.13, R2 =0.02
		Low ET0	n.a.	n.a.	$Y = -3.41(X - \overline{X}) - 3.41$, r=-0.13, R2 =0.02	$Y = -0.15(X - \overline{X}) - 0.15$, r=-0.18, R2 =0.03
	Dab35	High ET0	n.a.	$Y = -11.61(X - \overline{X}) - 11.61$, r=-0.24, R2 =0.06	$Y = -0.18(X - \overline{X}) - 0.18$, r=-0.04, R2 =0	$Y = -0.05(X - \overline{X}) - 0.05$, r=-0.15, R2 =0.02
		Low ET0	n.a.	n.a.	n.a.	$Y = 1.23(X - \overline{X}) + 1.23$, r=0.14, R2 =0.02
	Dlow10	High ET0	n.a.	n.a.	n.a.	n.a.
		Low ET0	n.a.	n.a.	$Y = 0.74(X - \overline{X}) + 0.74$, r=0.23, R2 =0.05	n.a.
	Dlow2	High ET0	$Y = 0.28(X - \overline{X}) + 0.28$, r=0.26, R2 =0.07	n.a.	n.a.	n.a.
		Low ET0	n.a.	n.a.	n.a.	n.a.
	Dopti	High ET0	n.a.	n.a.	$Y = 0.04(X - \overline{X}) + 0.04$, r=0.09, R2 =0.01	$Y = 0.01(X - \overline{X}) + 0.01$, r=0.02, R2 =0
		Low ET0	$Y = 3.9(X - \overline{X}) + 3.9$, r=0.23, R2 =0.05	n.a.	n.a.	n.a.
	TsumdDay	High ET0	n.a.	n.a.	$Y = -0.08(X - \overline{X}) - 0.08$, r=-0.13, R2 =0.02	$Y = -0.08(X - \overline{X}) - 0.08$, r=-0.2, R2 =0.04
		Low ET0	n.a.	n.a.	n.a.	n.a.
	TsumdNight	High ET0	$Y = -0.16(X - \overline{X}) - 0.16$, r=-0.18, R2 =0.03	n.a.	n.a.	$Y = -0.21(X - \overline{X}) - 0.21$, r=-0.36, R2 =0.13
		Low ET0	$Y = -0.23(X - \overline{X}) - 0.23$, r=-0.24, R2 =0.06	n.a.	$Y = -0.13(X - \overline{X}) - 0.13$, r=-0.11, R2 =0.01	n.a.

			1-Before budburst	2- From budburst to flowering	3-From flowering to veraison	4-From veraison to harvest
pH	Tmax	High ET0	n.a.	Y =0.02(X - $\overline{X}$) +0.02 , r=0.14, R2 =0.02	Y =0.03(X - $\overline{X}$) +0.03 , r=0.29, R2 =0.08	n.a.
		Low ET0	n.a.	Y =0.03(X - $\overline{X}$) +0.03 , r=0.09, R2 =0.01	n.a.	Y =0.03(X - $\overline{X}$) +0.03 , r=0.28, R2 =0.08
	Tqt98	High ET0	Y =0.09(X - $\overline{X}$) +0.09 , r=0.33, R2 =0.11	Y =0.02(X - $\overline{X}$) +0.02 , r=0.11, R2 =0.01	Y =0.03(X - $\overline{X}$) +0.03 , r=0.3, R2 =0.09	Y =0.01(X - $\overline{X}$) +0.01 , r=0.19, R2 =0.03
		Low ET0	n.a.	n.a.	n.a.	Y =0.03(X - $\overline{X}$) +0.03 , r=0.29, R2 =0.09
	Tmed	High ET0	Y =0.07(X - $\overline{X}$) +0.07 , r=0.25, R2 =0.06	n.a.	n.a.	n.a.
		Low ET0	n.a.	n.a.	n.a.	n.a.
	Tqt2	High ET0	Y =0.07(X - $\overline{X}$) +0.07 , r=0.39, R2 =0.15	n.a.	Y =0.1(X - $\overline{X}$) +0.1 , r=0.51, R2 =0.26	Y =0.09(X - $\overline{X}$) +0.09 , r=0.52, R2 =0.27
		Low ET0	Y =0.08(X - $\overline{X}$) +0.08 , r=0.35, R2 =0.12	n.a.	n.a.	Y =0.09(X - $\overline{X}$) +0.09 , r=0.44, R2 =0.2
	Tmin	High ET0	Y =0.08(X - $\overline{X}$) +0.08 , r=0.46, R2 =0.21	n.a.	Y =0.1(X - $\overline{X}$) +0.1 , r=0.49, R2 =0.24	Y =0.08(X - $\overline{X}$) +0.08 , r=0.5, R2 =0.25
		Low ET0	Y =0.06(X - $\overline{X}$) +0.06 , r=0.27, R2 =0.07	n.a.	n.a.	Y =0.1(X - $\overline{X}$) +0.1 , r=0.44, R2 =0.2
	Tmean	High ET0	n.a.	n.a.	n.a.	n.a.
		Low ET0	n.a.	n.a.	n.a.	n.a.
	Trange	High ET0	Y =-0.04(X - $\overline{X}$) -0.04 , r=-0.19, R2 =0.04	Y =-0.03(X - $\overline{X}$) -0.03 , r=-0.12, R2 =0.01	n.a.	n.a.
		Low ET0	n.a.	Y =-0.09(X - $\overline{X}$) -0.09 , r=-0.27, R2 =0.07	Y =-0.06(X - $\overline{X}$) -0.06 , r=-0.16, R2 =0.03	n.a.
	Tstd	High ET0	Y =-0.14(X - $\overline{X}$) -0.14 , r=-0.21, R2 =0.04	Y =-0.1(X - $\overline{X}$) -0.1 , r=-0.13, R2 =0.02	Y =0.02(X - $\overline{X}$) +0.02 , r=0.07, R2 =0.01	Y =0.02(X - $\overline{X}$) +0.02 , r=0.08, R2 =0.01
		Low ET0	Y =-0.28(X - $\overline{X}$) -0.28 , r=-0.33, R2 =0.11	Y =-0.25(X - $\overline{X}$) -0.25 , r=-0.18, R2 =0.03	n.a.	Y =0.08(X - $\overline{X}$) +0.08 , r=0.15, R2 =0.02
	Dab30	High ET0	n.a.	n.a.	Y =0.04(X - $\overline{X}$) +0.04 , r=0.32, R2 =0.1	Y =0.04(X - $\overline{X}$) +0.04 , r=0.27, R2 =0.07
		Low ET0	n.a.	n.a.	Y =2.37(X - $\overline{X}$) +2.37 , r=0.34, R2 =0.12	Y =0.07(X - $\overline{X}$) +0.07 , r=0.32, R2 =0.1
	Dab35	High ET0	n.a.	Y =1.19(X - $\overline{X}$) +1.19 , r=0.1, R2 =0.01	Y =0.28(X - $\overline{X}$) +0.28 , r=0.26, R2 =0.07	Y =0.02(X - $\overline{X}$) +0.02 , r=0.29, R2 =0.08
		Low ET0	n.a.	n.a.	n.a.	Y =0.22(X - $\overline{X}$) +0.22 , r=0.09, R2 =0.01
	Dlow10	High ET0	n.a.	n.a.	n.a.	n.a.
		Low ET0	n.a.	n.a.	Y =-0.42(X - $\overline{X}$) -0.42 , r=-0.48, R2 =0.23	n.a.
	Dlow2	High ET0	Y =-0.13(X - $\overline{X}$) -0.13 , r=-0.45, R2 =0.2	n.a.	n.a.	n.a.
		Low ET0	n.a.	n.a.	n.a.	n.a.
	Dopti	High ET0	n.a.	n.a.	Y =-0.02(X - $\overline{X}$) -0.02 , r=-0.16, R2 =0.03	Y =0.02(X - $\overline{X}$) +0.02 , r=0.11, R2 =0.01
		Low ET0	Y =0.09(X - $\overline{X}$) +0.09 , r=0.02, R2 =0	n.a.	n.a.	n.a.
	TsumdDay	High ET0	n.a.	n.a.	Y =0.06(X - $\overline{X}$) +0.06 , r=0.35, R2 =0.12	Y =0.03(X - $\overline{X}$) +0.03 , r=0.3, R2 =0.09
		Low ET0	n.a.	n.a.	n.a.	n.a.
	TsumdNight	High ET0	Y =0.07(X - $\overline{X}$) +0.07 , r=0.32, R2 =0.1	n.a.	n.a.	Y =0.08(X - $\overline{X}$) +0.08 , r=0.51, R2 =0.26
		Low ET0	Y =0.08(X - $\overline{X}$) +0.08 , r=0.32, R2 =0.11	n.a.	Y =0.08(X - $\overline{X}$) +0.08 , r=0.27, R2 =0.07	n.a.

			1-Before budburst	2- From budburst to flowering	3-From flowering to veraison	4-From veraison to harvest
TartaricAcid	Tmax	High ET0	n.a.	Y =0.15(X - $\overline{X}$) +0.15 , r=0.16, R2 =0.03	Y =0.13(X - $\overline{X}$) +0.13 , r=0.23, R2 =0.05	n.a.
		Low ET0	n.a.	Y =0.19(X - $\overline{X}$) +0.19 , r=0.11, R2 =0.01	n.a.	Y =0.11(X - $\overline{X}$) +0.11 , r=0.19, R2 =0.03
	Tqt98	High ET0	Y =0.47(X - $\overline{X}$) +0.47 , r=0.33, R2 =0.11	Y =0.22(X - $\overline{X}$) +0.22 , r=0.21, R2 =0.04	Y =0.14(X - $\overline{X}$) +0.14 , r=0.24, R2 =0.06	Y =0.1(X - $\overline{X}$) +0.1 , r=0.29, R2 =0.08
		Low ET0	n.a.	n.a.	n.a.	Y =0.14(X - $\overline{X}$) +0.14 , r=0.22, R2 =0.05
	Tmed	High ET0	Y =0.24(X - $\overline{X}$) +0.24 , r=0.15, R2 =0.02	n.a.	n.a.	n.a.
		Low ET0	n.a.	n.a.	n.a.	n.a.
	Tqt2	High ET0	Y =0.23(X - $\overline{X}$) +0.23 , r=0.23, R2 =0.06	n.a.	Y =0.14(X - $\overline{X}$) +0.14 , r=0.12, R2 =0.01	Y =0.14(X - $\overline{X}$) +0.14 , r=0.15, R2 =0.02
		Low ET0	Y =0.17(X - $\overline{X}$) +0.17 , r=0.14, R2 =0.02	n.a.	n.a.	Y =0.21(X - $\overline{X}$) +0.21 , r=0.18, R2 =0.03
	Tmin	High ET0	Y =0.18(X - $\overline{X}$) +0.18 , r=0.18, R2 =0.03	n.a.	Y =0.14(X - $\overline{X}$) +0.14 , r=0.13, R2 =0.02	Y =0.15(X - $\overline{X}$) +0.15 , r=0.18, R2 =0.03
		Low ET0	Y =0.09(X - $\overline{X}$) +0.09 , r=0.07, R2 =0.01	n.a.	n.a.	Y =0.22(X - $\overline{X}$) +0.22 , r=0.18, R2 =0.03
	Tmean	High ET0	n.a.	n.a.	n.a.	n.a.
		Low ET0	n.a.	n.a.	n.a.	n.a.
	Trange	High ET0	Y =-0.01(X - $\overline{X}$) -0.01 , r=-0.01, R2 =0	Y =0.16(X - $\overline{X}$) +0.16 , r=0.13, R2 =0.02	n.a.	n.a.
		Low ET0	n.a.	Y =-0.26(X - $\overline{X}$) -0.26 , r=-0.14, R2 =0.02	Y =-0.18(X - $\overline{X}$) -0.18 , r=-0.09, R2 =0.01	n.a.
	Tstd	High ET0	Y =-0.01(X - $\overline{X}$) -0.01 , r=0, R2 =0	Y =0.99(X - $\overline{X}$) +0.99 , r=0.21, R2 =0.04	Y =0.53(X - $\overline{X}$) +0.53 , r=0.29, R2 =0.09	Y =0.35(X - $\overline{X}$) +0.35 , r=0.31, R2 =0.1
		Low ET0	Y =1.27(X - $\overline{X}$) +1.27 , r=0.27, R2 =0.07	Y =-0.91(X - $\overline{X}$) -0.91 , r=-0.11, R2 =0.01	n.a.	Y =0.55(X - $\overline{X}$) +0.55 , r=0.18, R2 =0.03
	Dab30	High ET0	n.a.	n.a.	Y =0.23(X - $\overline{X}$) +0.23 , r=0.36, R2 =0.13	Y =0.3(X - $\overline{X}$) +0.3 , r=0.37, R2 =0.14
		Low ET0	n.a.	n.a.	Y =-4.82(X - $\overline{X}$) -4.82 , r=-0.13, R2 =0.02	Y =0.43(X - $\overline{X}$) +0.43 , r=0.35, R2 =0.12
	Dab35	High ET0	n.a.	Y =-5.32(X - $\overline{X}$) -5.32 , r=-0.07, R2 =0.01	Y =0.98(X - $\overline{X}$) +0.98 , r=0.16, R2 =0.03	Y =0.14(X - $\overline{X}$) +0.14 , r=0.32, R2 =0.1
		Low ET0	n.a.	n.a.	n.a.	Y =0.67(X - $\overline{X}$) +0.67 , r=0.05, R2 =0
	Dlow10	High ET0	n.a.	n.a.	n.a.	n.a.
		Low ET0	n.a.	n.a.	Y =-0.88(X - $\overline{X}$) -0.88 , r=-0.18, R2 =0.03	n.a.
	Dlow2	High ET0	Y =-0.23(X - $\overline{X}$) -0.23 , r=-0.14, R2 =0.02	n.a.	n.a.	n.a.
		Low ET0	n.a.	n.a.	n.a.	n.a.
	Dopti	High ET0	n.a.	n.a.	Y =-0.17(X - $\overline{X}$) -0.17 , r=-0.24, R2 =0.06	Y =0.01(X - $\overline{X}$) +0.01 , r=0.01, R2 =0
		Low ET0	Y =14.24(X - $\overline{X}$) +14.24 , r=0.58, R2 =0.33	n.a.	n.a.	n.a.
	TsumdDay	High ET0	n.a.	n.a.	Y =0.25(X - $\overline{X}$) +0.25 , r=0.26, R2 =0.07	Y =0.19(X - $\overline{X}$) +0.19 , r=0.31, R2 =0.1
		Low ET0	n.a.	n.a.	n.a.	n.a.
	TsumdNight	High ET0	Y =0.27(X - $\overline{X}$) +0.27 , r=0.21, R2 =0.04	n.a.	n.a.	Y =0.12(X - $\overline{X}$) +0.12 , r=0.14, R2 =0.02
		Low ET0	Y =0.16(X - $\overline{X}$) +0.16 , r=0.11, R2 =0.01	n.a.	Y =0.38(X - $\overline{X}$) +0.38 , r=0.22, R2 =0.05	n.a.

			1-Before budburst	2- From budburst to flowering	3-From flowering to veraison	4-From veraison to harvest
MalicAcid	Tmax	High ET0	n.a.	Y =-0.14(X - $\overline{X}$) -0.14 , r=-0.22, R2 =0.05	Y =-0.03(X - $\overline{X}$) -0.03 , r=-0.09, R2 =0.01	n.a.
		Low ET0	n.a.	Y =0.12(X - $\overline{X}$) +0.12 , r=0.11, R2 =0.01	n.a.	Y =-0.08(X - $\overline{X}$) -0.08 , r=-0.2, R2 =0.04
	Tqt98	High ET0	Y =0.05(X - $\overline{X}$) +0.05 , r=0.05, R2 =0	Y =-0.1(X - $\overline{X}$) -0.1 , r=-0.15, R2 =0.02	Y =-0.03(X - $\overline{X}$) -0.03 , r=-0.09, R2 =0.01	Y =-0.04(X - $\overline{X}$) -0.04 , r=-0.18, R2 =0.03
		Low ET0	n.a.	n.a.	n.a.	Y =-0.1(X - $\overline{X}$) -0.1 , r=-0.23, R2 =0.06
	Tmed	High ET0	Y =-0.36(X - $\overline{X}$) -0.36 , r=-0.33, R2 =0.11	n.a.	n.a.	n.a.
		Low ET0	n.a.	n.a.	n.a.	n.a.
	Tqt2	High ET0	Y =-0.26(X - $\overline{X}$) -0.26 , r=-0.39, R2 =0.15	n.a.	Y =-0.26(X - $\overline{X}$) -0.26 , r=-0.34, R2 =0.12	Y =-0.25(X - $\overline{X}$) -0.25 , r=-0.4, R2 =0.16
		Low ET0	Y =-0.31(X - $\overline{X}$) -0.31 , r=-0.39, R2 =0.16	n.a.	n.a.	Y =-0.3(X - $\overline{X}$) -0.3 , r=-0.38, R2 =0.14
	Tmin	High ET0	Y =-0.26(X - $\overline{X}$) -0.26 , r=-0.39, R2 =0.15	n.a.	Y =-0.26(X - $\overline{X}$) -0.26 , r=-0.35, R2 =0.12	Y =-0.22(X - $\overline{X}$) -0.22 , r=-0.37, R2 =0.13
		Low ET0	Y =-0.36(X - $\overline{X}$) -0.36 , r=-0.43, R2 =0.19	n.a.	n.a.	Y =-0.29(X - $\overline{X}$) -0.29 , r=-0.36, R2 =0.13
	Tmean	High ET0	n.a.	n.a.	n.a.	n.a.
		Low ET0	n.a.	n.a.	n.a.	n.a.
	Trange	High ET0	Y =0.43(X - $\overline{X}$) +0.43 , r=0.52, R2 =0.27	Y =0.07(X - $\overline{X}$) +0.07 , r=0.08, R2 =0.01	n.a.	n.a.
		Low ET0	n.a.	Y =0.64(X - $\overline{X}$) +0.64 , r=0.52, R2 =0.27	Y =0.45(X - $\overline{X}$) +0.45 , r=0.33, R2 =0.11	n.a.
	Tstd	High ET0	Y =1.27(X - $\overline{X}$) +1.27 , r=0.51, R2 =0.26	Y =0.45(X - $\overline{X}$) +0.45 , r=0.14, R2 =0.02	Y =0.08(X - $\overline{X}$) +0.08 , r=0.06, R2 =0	Y =-0.1(X - $\overline{X}$) -0.1 , r=-0.13, R2 =0.02
		Low ET0	Y =1.61(X - $\overline{X}$) +1.61 , r=0.52, R2 =0.27	Y =2.61(X - $\overline{X}$) +2.61 , r=0.49, R2 =0.24	n.a.	Y =-0.24(X - $\overline{X}$) -0.24 , r=-0.11, R2 =0.01
	Dab30	High ET0	n.a.	n.a.	Y =-0.06(X - $\overline{X}$) -0.06 , r=-0.14, R2 =0.02	Y =-0.14(X - $\overline{X}$) -0.14 , r=-0.27, R2 =0.07
		Low ET0	n.a.	n.a.	Y =0.28(X - $\overline{X}$) +0.28 , r=0.01, R2 =0	Y =-0.17(X - $\overline{X}$) -0.17 , r=-0.2, R2 =0.04
	Dab35	High ET0	n.a.	Y =-8.69(X - $\overline{X}$) -8.69 , r=-0.18, R2 =0.03	Y =-0.21(X - $\overline{X}$) -0.21 , r=-0.05, R2 =0	Y =-0.06(X - $\overline{X}$) -0.06 , r=-0.21, R2 =0.04
		Low ET0	n.a.	n.a.	n.a.	Y =1.93(X - $\overline{X}$) +1.93 , r=0.22, R2 =0.05
	Dlow10	High ET0	n.a.	n.a.	n.a.	n.a.
		Low ET0	n.a.	n.a.	Y =0.71(X - $\overline{X}$) +0.71 , r=0.22, R2 =0.05	n.a.
	Dlow2	High ET0	Y =0.43(X - $\overline{X}$) +0.43 , r=0.4, R2 =0.16	n.a.	n.a.	n.a.
		Low ET0	n.a.	n.a.	n.a.	n.a.
	Dopti	High ET0	n.a.	n.a.	Y =0.05(X - $\overline{X}$) +0.05 , r=0.1, R2 =0.01	Y =0.04(X - $\overline{X}$) +0.04 , r=0.06, R2 =0
		Low ET0	Y =2.34(X - $\overline{X}$) +2.34 , r=0.14, R2 =0.02	n.a.	n.a.	n.a.
	TsumdDay	High ET0	n.a.	n.a.	Y =-0.1(X - $\overline{X}$) -0.1 , r=-0.16, R2 =0.02	Y =-0.12(X - $\overline{X}$) -0.12 , r=-0.29, R2 =0.08
		Low ET0	n.a.	n.a.	n.a.	n.a.
	TsumdNight	High ET0	Y =-0.34(X - $\overline{X}$) -0.34 , r=-0.39, R2 =0.16	n.a.	n.a.	Y =-0.25(X - $\overline{X}$) -0.25 , r=-0.43, R2 =0.19
		Low ET0	Y =-0.33(X - $\overline{X}$) -0.33 , r=-0.37, R2 =0.13	n.a.	Y =-0.23(X - $\overline{X}$) -0.23 , r=-0.2, R2 =0.04	n.a.

			1-Before budburst	2- From budburst to flowering	3-From flowering to veraison	4-From veraison to harvest
TPI	Tmax	High ET0	n.a.	Y =0.14(X - $\overline{X}$) +0.14 , r=0.13, R2 =0.02	Y =0.17(X - $\overline{X}$) +0.17 , r=0.26, R2 =0.07	n.a.
		Low ET0	n.a.	Y =0.46(X - $\overline{X}$) +0.46 , r=0.24, R2 =0.06	n.a.	Y =0.19(X - $\overline{X}$) +0.19 , r=0.28, R2 =0.08
	Tqt98	High ET0	Y =0.97(X - $\overline{X}$) +0.97 , r=0.58, R2 =0.34	Y =0.19(X - $\overline{X}$) +0.19 , r=0.15, R2 =0.02	Y =0.19(X - $\overline{X}$) +0.19 , r=0.28, R2 =0.08	Y =0.08(X - $\overline{X}$) +0.08 , r=0.2, R2 =0.04
		Low ET0	n.a.	n.a.	n.a.	Y =0.27(X - $\overline{X}$) +0.27 , r=0.35, R2 =0.13
	Tmed	High ET0	Y =0.88(X - $\overline{X}$) +0.88 , r=0.47, R2 =0.22	n.a.	n.a.	n.a.
		Low ET0	n.a.	n.a.	n.a.	n.a.
	Tqt2	High ET0	Y =0.7(X - $\overline{X}$) +0.7 , r=0.6, R2 =0.36	n.a.	Y =0.75(X - $\overline{X}$) +0.75 , r=0.58, R2 =0.34	Y =0.68(X - $\overline{X}$) +0.68 , r=0.62, R2 =0.39
		Low ET0	Y =0.83(X - $\overline{X}$) +0.83 , r=0.58, R2 =0.34	n.a.	n.a.	Y =0.79(X - $\overline{X}$) +0.79 , r=0.58, R2 =0.34
	Tmin	High ET0	Y =0.7(X - $\overline{X}$) +0.7 , r=0.61, R2 =0.37	n.a.	Y =0.74(X - $\overline{X}$) +0.74 , r=0.58, R2 =0.33	Y =0.63(X - $\overline{X}$) +0.63 , r=0.62, R2 =0.38
		Low ET0	Y =0.71(X - $\overline{X}$) +0.71 , r=0.47, R2 =0.23	n.a.	n.a.	Y =0.75(X - $\overline{X}$) +0.75 , r=0.53, R2 =0.28
	Tmean	High ET0	n.a.	n.a.	n.a.	n.a.
		Low ET0	n.a.	n.a.	n.a.	n.a.
	Trange	High ET0	Y =-0.34(X - $\overline{X}$) -0.34 , r=-0.24, R2 =0.06	Y =-0.32(X - $\overline{X}$) -0.32 , r=-0.22, R2 =0.05	n.a.	n.a.
		Low ET0	n.a.	Y =-0.8(X - $\overline{X}$) -0.8 , r=-0.37, R2 =0.14	Y =-0.47(X - $\overline{X}$) -0.47 , r=-0.2, R2 =0.04	n.a.
	Tstd	High ET0	Y =-1.29(X - $\overline{X}$) -1.29 , r=-0.29, R2 =0.09	Y =-1.04(X - $\overline{X}$) -1.04 , r=-0.19, R2 =0.04	Y =0.05(X - $\overline{X}$) +0.05 , r=0.03, R2 =0	Y =0.01(X - $\overline{X}$) +0.01 , r=0.01, R2 =0
		Low ET0	Y =-1.64(X - $\overline{X}$) -1.64 , r=-0.3, R2 =0.09	Y =-2.36(X - $\overline{X}$) -2.36 , r=-0.25, R2 =0.06	n.a.	Y =0.37(X - $\overline{X}$) +0.37 , r=0.1, R2 =0.01
	Dab30	High ET0	n.a.	n.a.	Y =0.28(X - $\overline{X}$) +0.28 , r=0.38, R2 =0.14	Y =0.32(X - $\overline{X}$) +0.32 , r=0.34, R2 =0.11
		Low ET0	n.a.	n.a.	Y =4.37(X - $\overline{X}$) +4.37 , r=0.1, R2 =0.01	Y =0.51(X - $\overline{X}$) +0.51 , r=0.35, R2 =0.12
	Dab35	High ET0	n.a.	Y =-14.65(X - $\overline{X}$) -14.65 , r=-0.18, R2 =0.03	Y =1.8(X - $\overline{X}$) +1.8 , r=0.25, R2 =0.06	Y =0.13(X - $\overline{X}$) +0.13 , r=0.25, R2 =0.07
		Low ET0	n.a.	n.a.	n.a.	Y =1.6(X - $\overline{X}$) +1.6 , r=0.11, R2 =0.01
	Dlow10	High ET0	n.a.	n.a.	n.a.	n.a.
		Low ET0	n.a.	n.a.	Y =-2.83(X - $\overline{X}$) -2.83 , r=-0.5, R2 =0.25	n.a.
	Dlow2	High ET0	Y =-1.11(X - $\overline{X}$) -1.11 , r=-0.59, R2 =0.35	n.a.	n.a.	n.a.
		Low ET0	n.a.	n.a.	n.a.	n.a.
	Dopti	High ET0	n.a.	n.a.	Y =0.01(X - $\overline{X}$) +0.01 , r=0.01, R2 =0	Y =0.37(X - $\overline{X}$) +0.37 , r=0.34, R2 =0.11
		Low ET0	Y =13.81(X - $\overline{X}$) +13.81 , r=0.47, R2 =0.22	n.a.	n.a.	n.a.
	TsumdDay	High ET0	n.a.	n.a.	Y =0.5(X - $\overline{X}$) +0.5 , r=0.45, R2 =0.21	Y =0.24(X - $\overline{X}$) +0.24 , r=0.35, R2 =0.12
		Low ET0	n.a.	n.a.	n.a.	n.a.
	TsumdNight	High ET0	Y =0.82(X - $\overline{X}$) +0.82 , r=0.54, R2 =0.29	n.a.	n.a.	Y =0.63(X - $\overline{X}$) +0.63 , r=0.62, R2 =0.38
		Low ET0	Y =0.89(X - $\overline{X}$) +0.89 , r=0.55, R2 =0.3	n.a.	Y =0.97(X - $\overline{X}$) +0.97 , r=0.48, R2 =0.23	n.a.

L. Images of instantaneous energy absorbed by grapevine from DART simulations at various days and times from grapevine budburst to harvest

The color scale used for printing each of the following images ranges from quintile 0.5% and quintile 99.5% of the values in the image. Images are sorted by date and time.

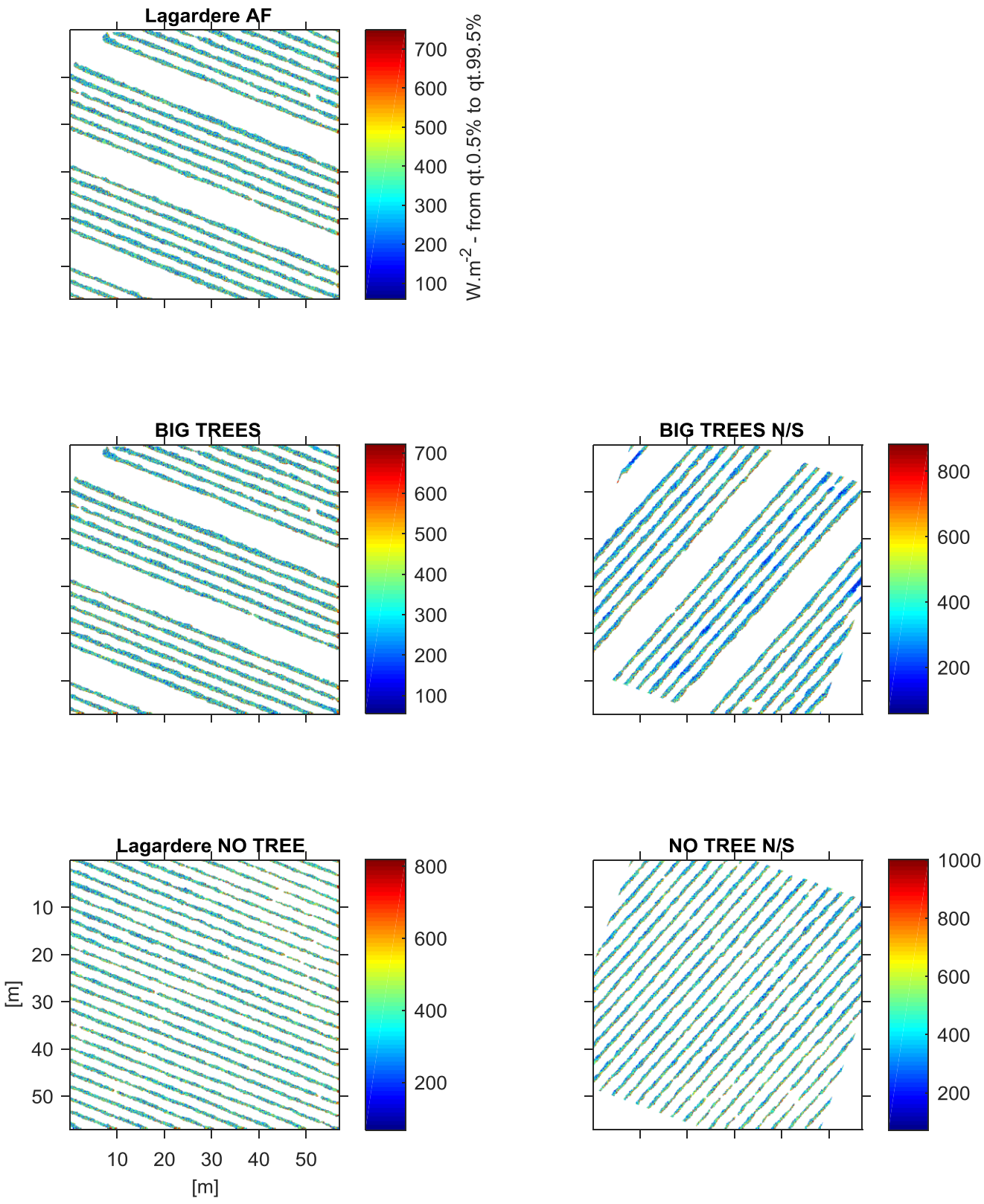
23-Aug-2016 10:00UTC
E^tot_PAR =289W.m^-2- SKYL =0.77318
Lagardere AF
700
600
500
400
300
200
100
W.m^-2 - from qt.0.5% to qt.99.5%
BIG TREES
700
600
500
400
300
200
100
BIG TREES N/S
800
600
400
200
Lagardere NO TREE
800
600
400
200
10
20
30
40
50
[m]
10
20
30
40
50
[m]
NO TREE N/S
1000
800
600
400
200

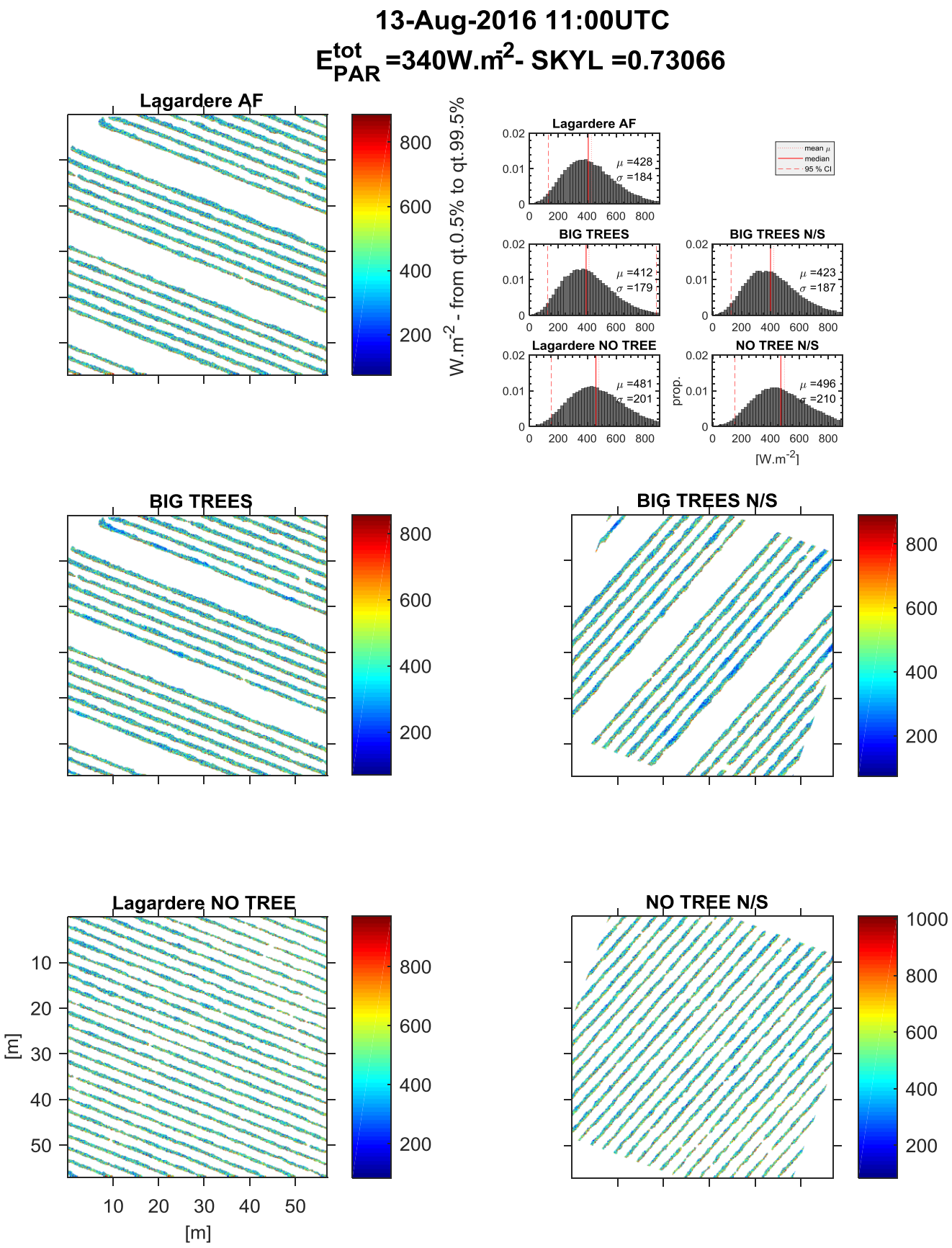
13-Aug-2016 11:00UTC
E_{PAR}^{tot} =340W.m^{-2}- SKYL =0.73066
Lagardere AF
BIG TREES
BIG TREES N/S
Lagardere NO TREE
NO TREE N/S
W.m^{-2} - from qt.0.5% to qt.99.5%
mean μ
median
95 % CI
μ =428
σ =184
μ =412
σ =179
μ =423
σ =187
μ =481
σ =201
μ =496
σ =210
prop.
[W.m^{-2}]
[m]

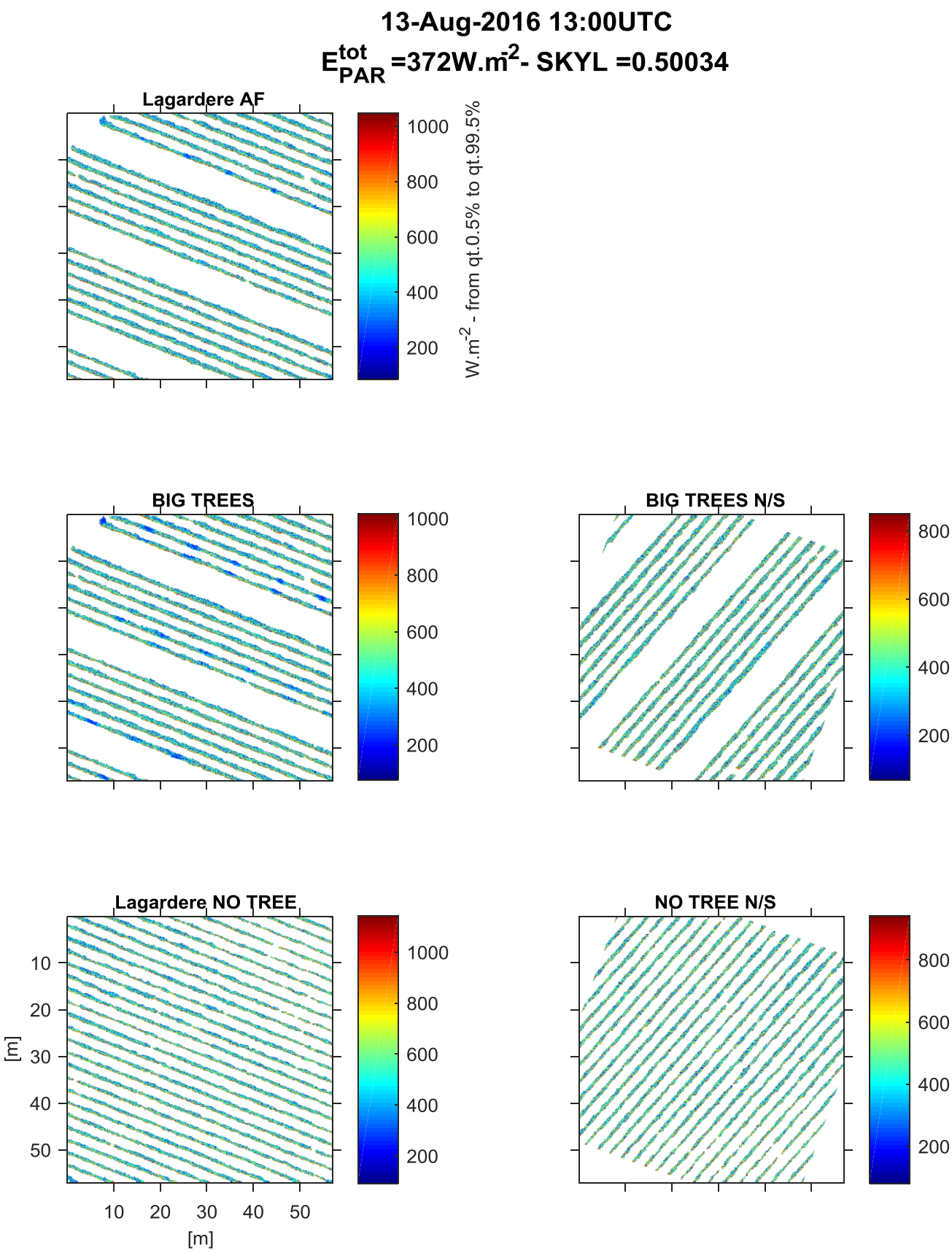
13-Aug-2016 13:00UTC
E^{tot}_{PAR} =372W.m^{-2}- SKYL =0.50034
Lagardere AF
BIG TREES
BIG TREES N/S
Lagardere NO TREE
NO TREE N/S
W.m^{-2} - from qt.0.5% to qt.99.5%
[m]
[m]
10
20
30
40
50
200
400
600
800
1000

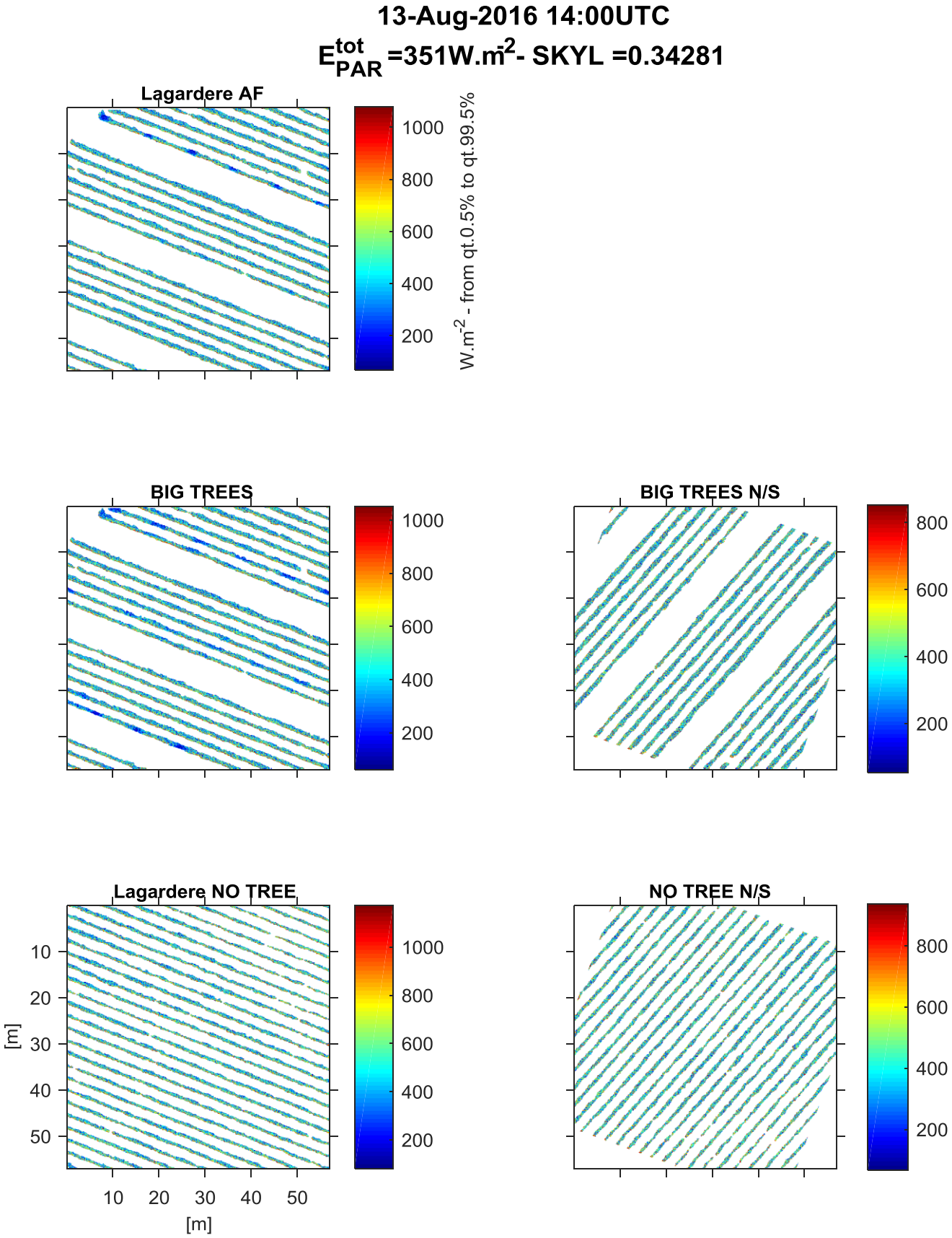
13-Aug-2016 14:00UTC
E^{tot}_{PAR} =351W.m^{-2}- SKYL =0.34281
Lagardere AF
BIG TREES
BIG TREES N/S
Lagardere NO TREE
NO TREE N/S
W.m^{-2} - from qt.0.5% to qt.99.5%
[m]
[m]

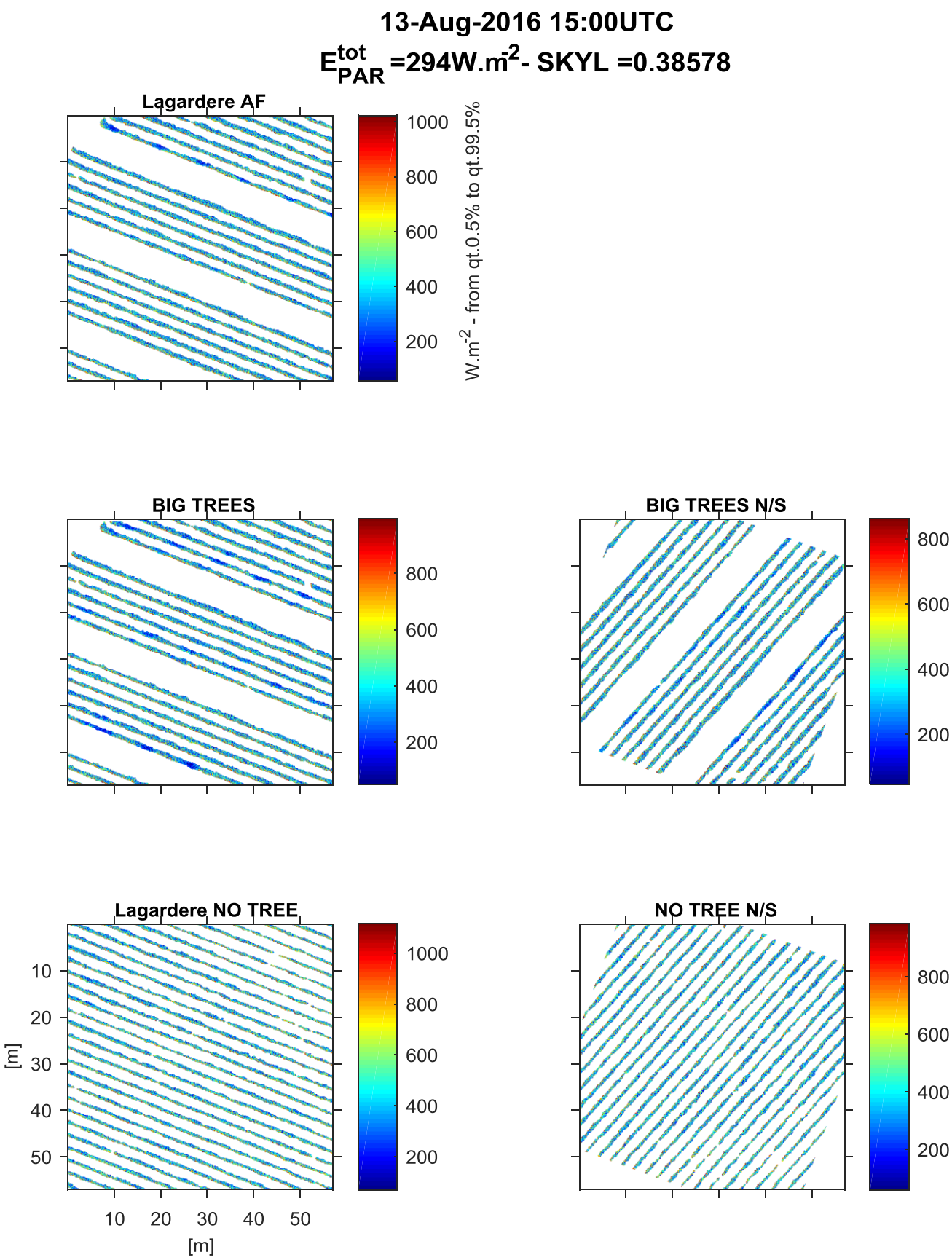
13-Aug-2016 15:00UTC
E^{tot}_{PAR} =294W.m^{-2}- SKYL =0.38578
Lagardere AF
BIG TREES
BIG TREES N/S
Lagardere NO TREE
NO TREE N/S
1000
800
600
400
200
W.m^{-2} - from qt.0.5% to qt.99.5%
10
20
30
40
50
[m]

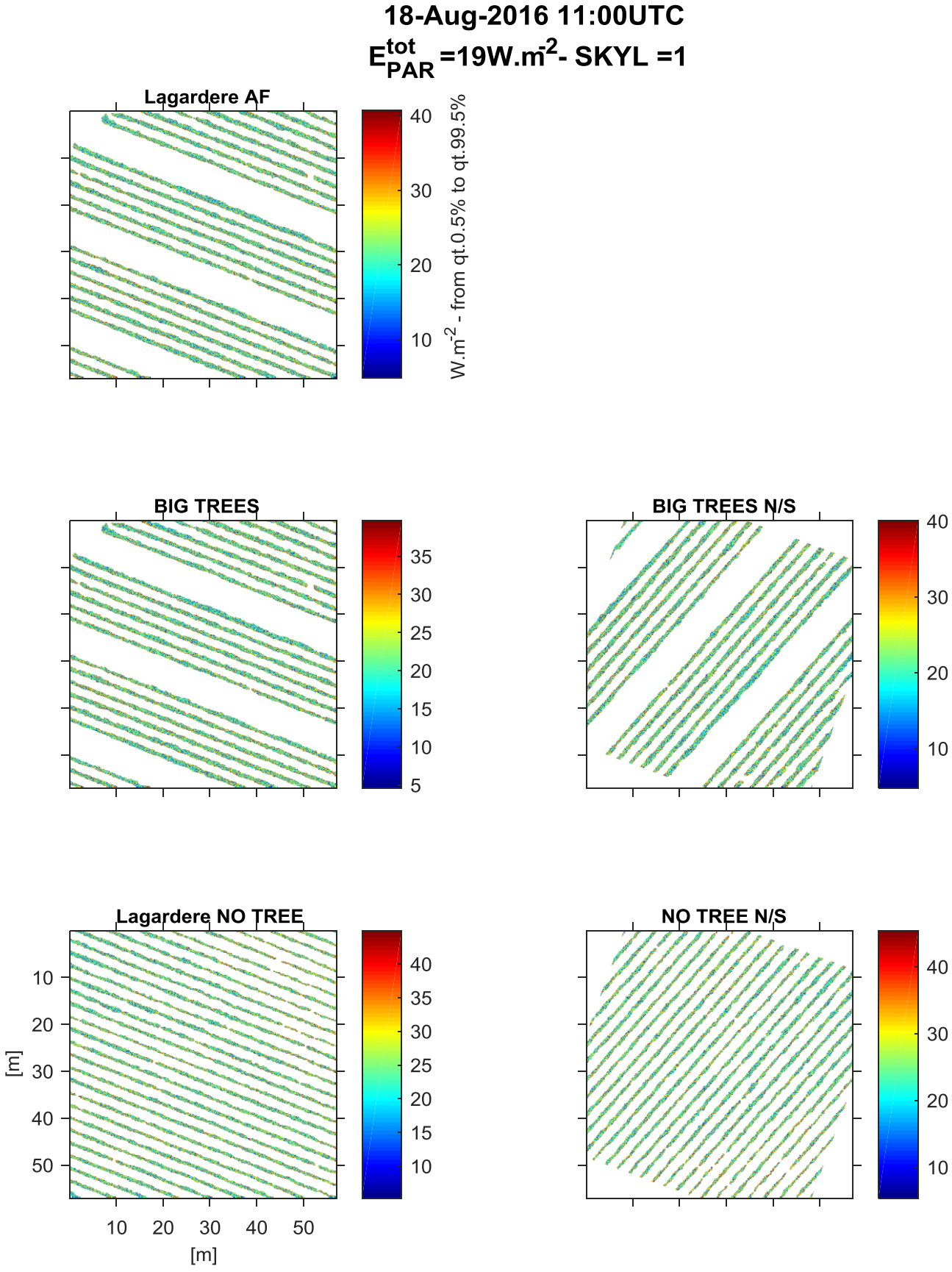
18-Aug-2016 11:00UTC
E^{tot}_{PAR} =19W.m^{-2}- SKYL =1
Lagardere AF
BIG TREES
BIG TREES N/S
Lagardere NO TREE
NO TREE N/S
W.m^{-2} - from qt.0.5% to qt.99.5%
[m]
[m]

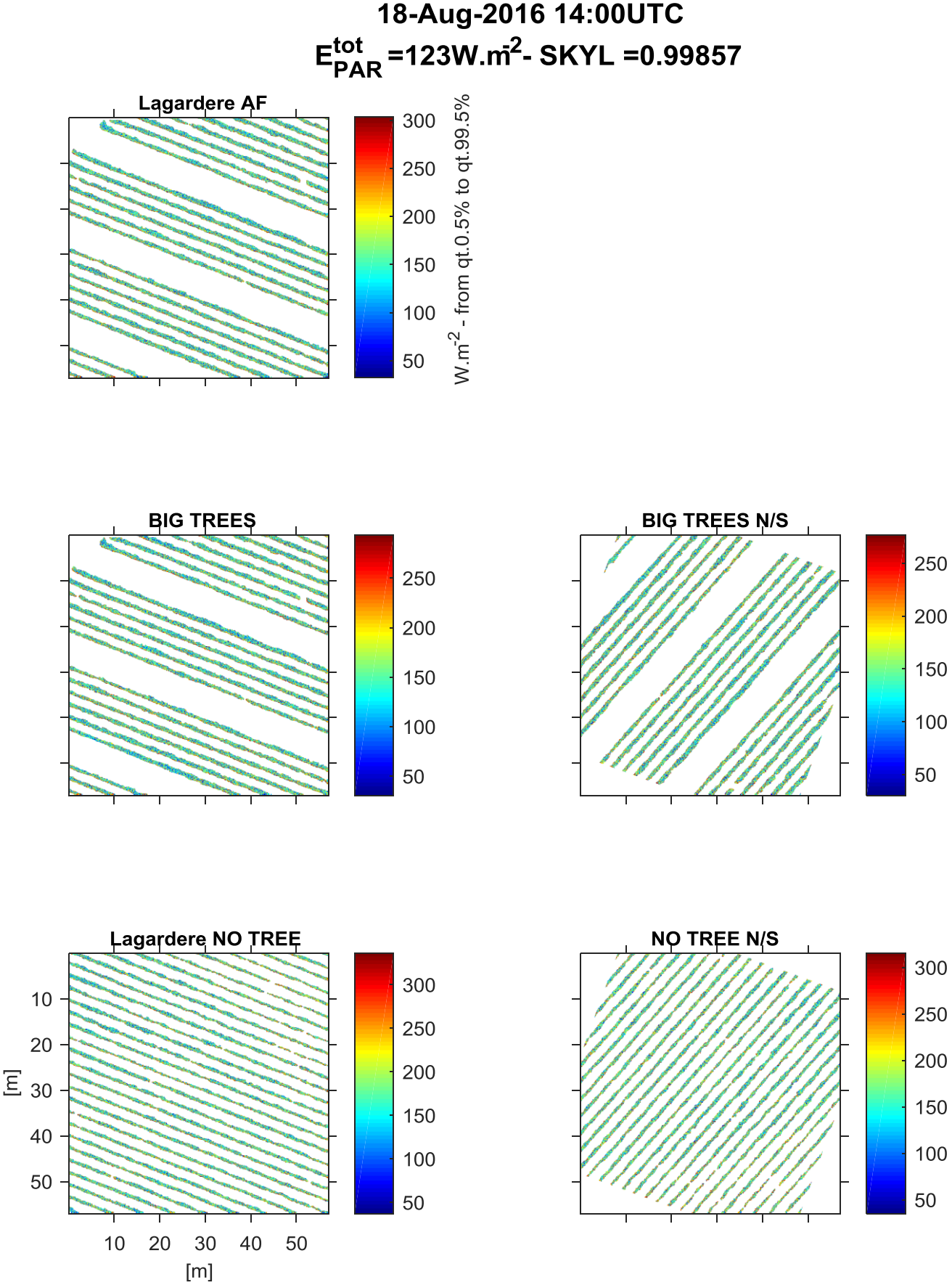
18-Aug-2016 14:00UTC
E^{tot}_{PAR} =123W.m^{-2}- SKYL =0.99857
Lagardere AF
BIG TREES
BIG TREES N/S
Lagardere NO TREE
NO TREE N/S
W.m^{-2} - from qt.0.5% to qt.99.5%
[m]
[m]

M. 3D views of simulations with grapevine canopy modeled as 3D cells of turbid medium or modeled in 2D

Modifications of grapevine representation were performed starting from the simulation 'BIG TREES'. In the first case, grapevine and tree leaves were represented as voxels filled with turbid medium. In the second case grapevine was represented as a 2D planar surface maching with the soil occupation 'grapevine' in the land cover map.

BIG TREES

Tree canopy is a realistic ensemble of 3D planar objects

Grapveine canopy is voxels filled cloud of triangle leaves, positioned according to a land cover map.

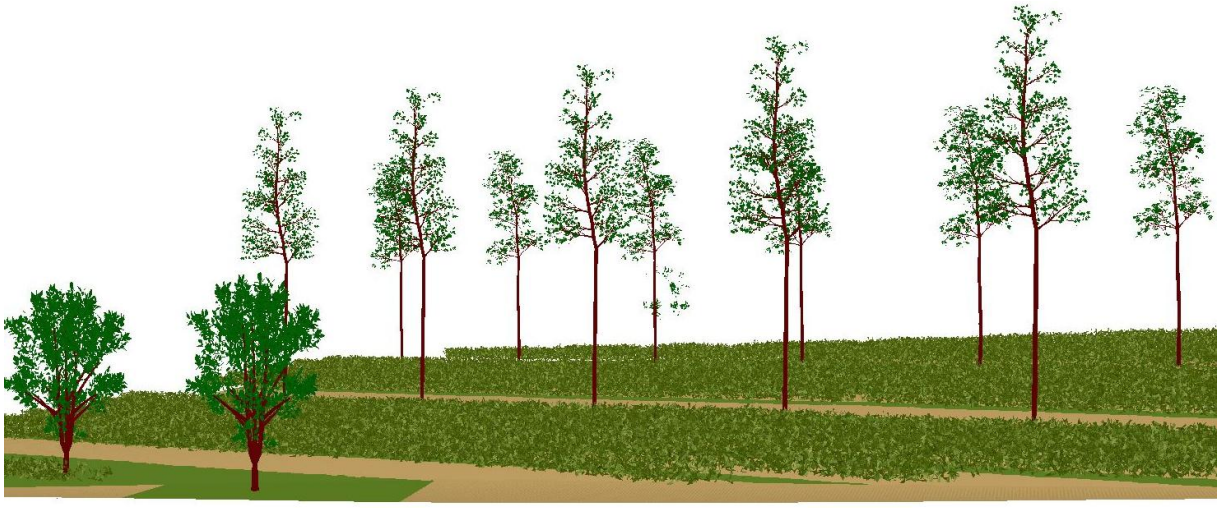

Turbid canopies & no scattering

Grapevine 2D

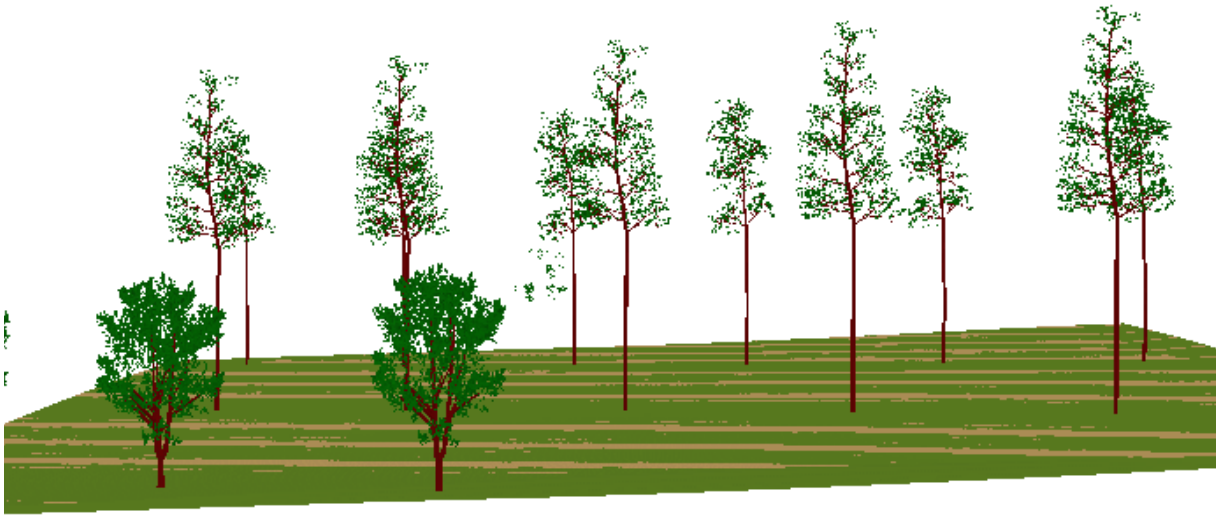

N. Implication of pixel position in light regime for grapevine canopies highly trained with a trellis system

When grapevine canopy is structured as a vertical row, light absorption within a single stock of grapevine present high heterogeneity due to some border effects. The position of the leaves, either on the hedge or inside the canopy combines with the influence of the orientation of the row. As a result, mainly five locations of the leaves can be distinguished: on the edge facing North, on the edge facing South, on the edge facing East, on the edge facing West and in the center of the row. The following figure shows the mean daily quantities of PAR absorbed by grapevine depending on the position within grapevine canopy.

These budgets were obtained from 3D radiative budget simulations with the model DART (Gastellu-Etchegorry et al. 1996). The methodology is exposed in chapter VI of this thesis.

As recalled in the following figure, the budgets obtained gather five different arrangements of vineyards, three being co-planted with trees, two being monocropped with only grapevine rows. The arrangements that were considered also differ in row orientations, both N/S and NW/SE orientations were considered.

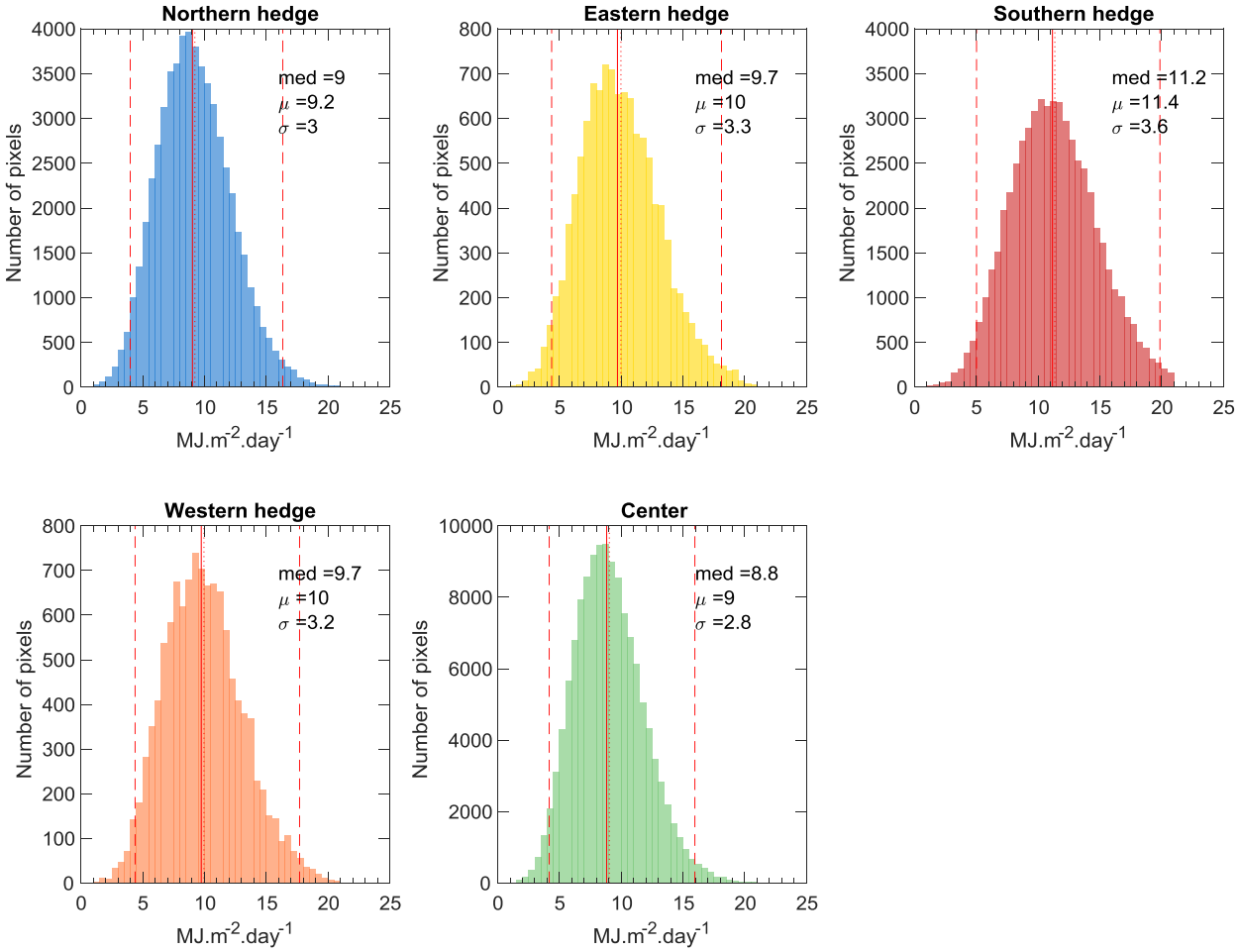

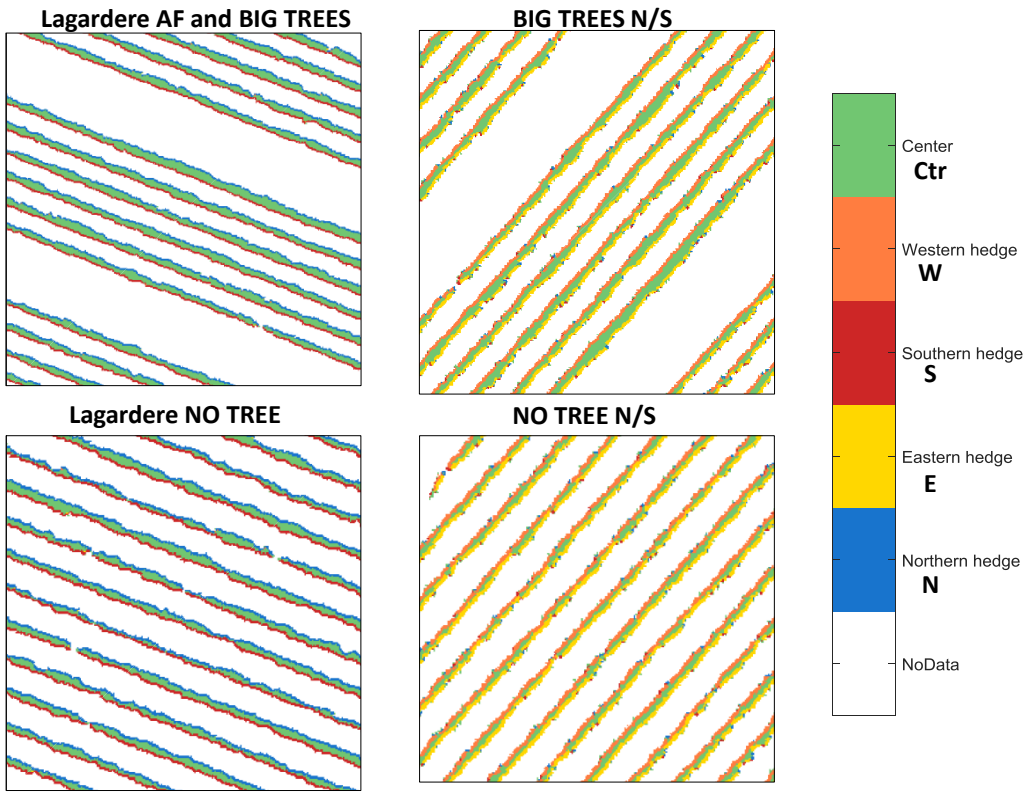
Lagardere AF and BIG TREES
BIG TREES N/S
Lagardere NO TREE
NO TREE N/S
Center
Ctr
Western hedge
W
Southern hedge
S
Eastern hedge
E
Northern hedge
N
NoData

O.Raw and smooth irradiance measured in Lagardere to use as inputs for calibrating the multiplicative factor of AOD in radiative budget simulations

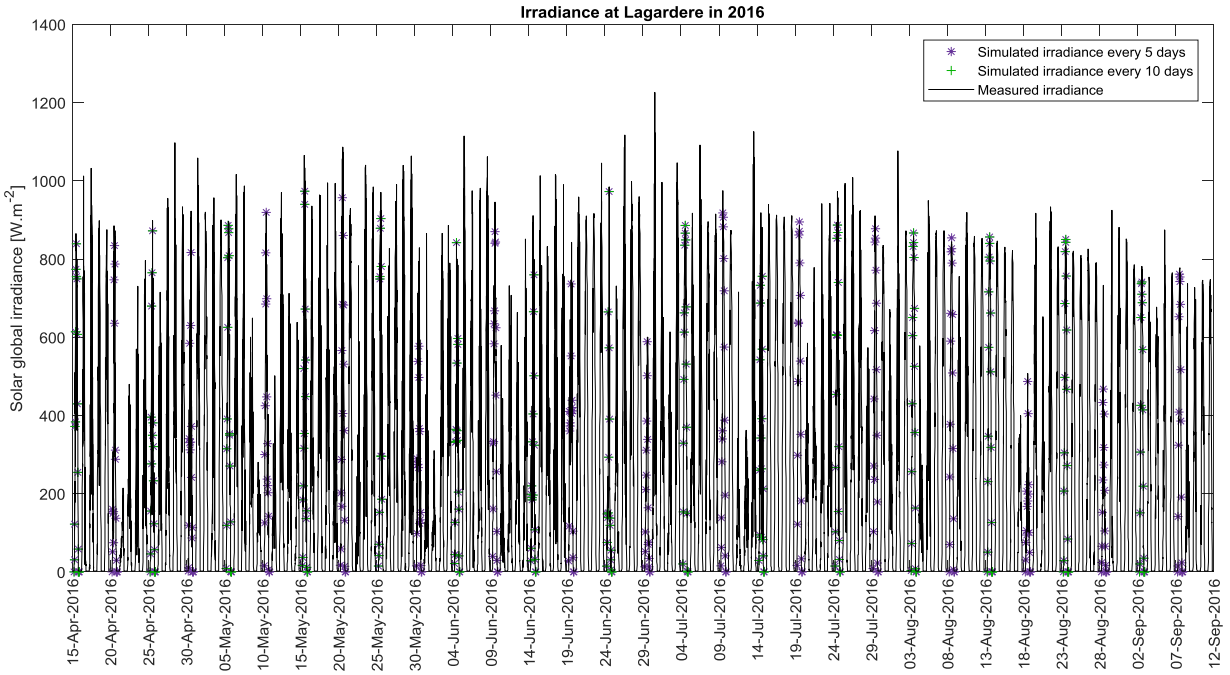

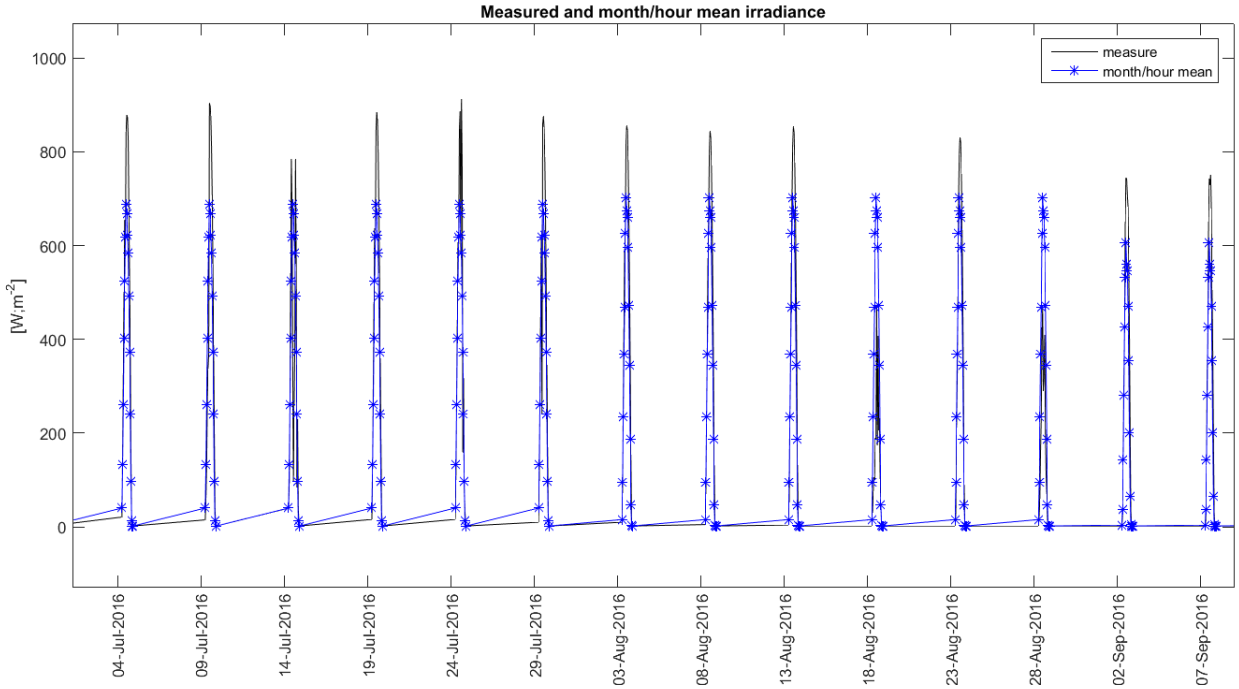

P. Python script for calibration of the multiplicative factor of the Aerosol Optical Depth (AOD) – by E. CHAVANON

P.1 Principal

In collaboration with Eric CHAVANON from the DART team at CESBIO, a python script was developed for adjusting the multiplicative factor of the Aerosol Optical Depth (c_{AOD}) for each date and times of simulation The adjustment procedure uses a text file listing the dates and times of simulations together with the measured solar irradiance and returns a list of c_{AOD}. For converging, the adjustment algorithm starts with a c_{AOD}^{0} set to 1 and works by dichotomy. In a first step, it tries to find a usable pair of c_{AOD}^{0} and c_{AOD}^{i} which enable enclosing the measured irradiance. In a second step, it iteratively narrows the bounds.

P.2 Script

```
##!/usr/bin/env python
#-*-coding: utf8 -*-

# python 3.x print function
from __future__ import print_function
# python 3.x division (allow to treat single '/' division using floating point precision - otherwise '//' would be needed instead in python 2.7)
from __future__ import division

import os
import re
import sys
from xml.dom import minidom, Node

#------------------------------------------------------------------------

#splitter = re.compile("[^0-9a-zA-Z.,-]+")
splitter = re.compile("[^0-9.,-]+")
def cmd_help():
   nb = len(sys.argv[0])
   spc = ""
   for _ in range(nb):
      spc += " "
   print()
   print("   ", sys.argv[0], "simulation_name")
   print("   ",       spc, "measure_data_file")
   print("   ",       spc, "[-e epsilon]")
   print("   ",       spc, "[-ee epsilon]")
   print("   ",       spc, "[-m max_iteration]")
   print("   ",       spc, "[-f not_found_value]")
   print("   ",       spc, "[-i initial_aod_factor]")
   print("   ",       spc, "[-r result_file]")
   print("   ",       spc, "[-d dart_path]")
   print("   ",       spc, "[-t min_date max_date]")
   print()
```

```
        print("   simulation_name          : name of simulation ; may be a path relative to simulation path")
        print("   measure_data_file        : filename of input data ; may be a path relative to simulation path")
        print("                            : col 1: measured irradiance [W/m2]")
        print("                            : col 2: Year")
        print("                            : col 3: Month")
        print("                            : col 4: Day")
        print("                            : col 5: Hour")
        print("                            : col 6: Minute")
        print("                            : col 7: Second")
        print("                            : col 8: maximum irradiance [W/m2] - optional. default = measured irradiance")

        print()
        print("   --- Optional parameters ---")
        print()
        print("   -d dart_path             : default empty => DART_HOME is queried from system environment")
        print("   -e epsilon               : default 0.05")
        print("   -ee epsilon              : default 0.05")
        print("   -f not_found_value       : default -9999.99")
        print("   -i initial_aod_factor    : default None, i-e it uses AOD value from simulation input file")
        print("   -m max_iteration         : default 20")
        print("   -r result_file           : default <simulation_name>.result.txt")
        print("   -t min_date max_date     : default \"0000 00 00\" \"9999 12 31 23 59 59\"")
        print()

    def init(path=""):
        DART_HOME = path
        DART_HOME = os.path.expanduser(DART_HOME)

        # if default path is empty, query DART_HOME from system environment
        if len(DART_HOME) == 0:
            try:
                DART_HOME = os.environ['DART_HOME']
            except KeyError:
                DART_HOME = None

        if DART_HOME is None:
            raise EnvironmentError("You need to set DART_HOME path, either by setting the variable above or
through system environment.")

        try:
            DART_LOCAL = os.environ['DART_LOCAL']
        except KeyError:
            ini = open(os.path.join(DART_HOME, "config.ini"), "r")
            drc = open(ini.readlines()[0].rstrip('\n'), "r")
            for line in drc:
                line = line.strip()
                if len(line) > 0 and not (line[0] == '#' or line[0:3] == 'REM') and "DART_LOCAL" in line:
                    DART_LOCAL = line.split('=')[1]
                    break
            ini.close()
```

```
        drc.close()

    DART_TOOLS = os.path.join(DART_HOME, "tools", "linux")
    return DART_HOME, DART_LOCAL, DART_TOOLS

class AODFileReader(object):
    """
    """
    def __init__(self, path):
        self.path = path
        self.fd = None

    def __del__(self):
        self.close()

    def __iter__(self):
        return self

    def __next__(self):
        return self.next()

    def open(self):
        self.fd = open(self.path, 'r')

    def close(self):
        if not self.fd is None:
            self.fd.close()
            self.fd = None

    def readline(self):
        if not self.fd is None:
            line = self.fd.readline()
            while len(line.strip()) == 0:
                line = self.fd.readline()
                if len(line) < 1:
                    raise StopIteration()
            return line.strip()

    def next(self):
        if not self.fd is None:
            line = None
            while line is None:
                line = splitter.split(self.readline())
                try:
                    return float(line[0]), [int(line[i]) for i in range(1,7)], float(line[7]), float(line[8]), float(line[9])
                except ValueError:
                    line = None
                except:
                    raise StopIteration()
```

```
class InputFileReader(object):
   """
   """
   def __init__(self, path):
      self.path = path
      self.fd = None

   def __del__(self):
      self.close()

   def __iter__(self):
      return self

   def __next__(self):
      return self.next()

   def open(self):
      self.fd = open(self.path, 'r')

   def close(self):
      if not self.fd is None:
         self.fd.close()
         self.fd = None

   def readline(self):
      if not self.fd is None:
         line = self.fd.readline()
         while len(line.strip()) == 0:
            line = self.fd.readline()
            if len(line) < 1:
               raise StopIteration()
         return line.strip()

   def next(self):
      if not self.fd is None:
         line = None
         while line is None:
            line = splitter.split(self.readline())
            try:
               if len(line) > 7:
                  return float(line[0]), float(line[7]), [int(line[i]) for i in range(1,7)]
               else:
                  return float(line[0]), float(line[0]), [int(line[i]) for i in range(1,7)]
            except ValueError:
               line = None
            except:
               raise StopIteration()

def get_coupl_irradiance(output_path, spectral_bands):
   total = 0.0
```

```
        with open(os.path.join(output_path, "simulation.properties.txt"),'r') as file:
            for line in file:
                if "dart.band" in line and "COUPL.irradiance" in line:
                    line = line.split(":")
                    band = int(line[0].split(".")[1].replace("band", ""))
                    irradiance = float(line[1])
                    total += irradiance * spectral_bands[band][1]
        return total

    def read_spectral_bands(input_path):
        tag = minidom.parse(os.path.join(input_path,
"phase.xml")).documentElement.getElementsByTagName('SpectralIntervalsProperties')
        return [ (float(b.getAttribute('meanLambda')), float(b.getAttribute('deltaLambda'))) for b in tag ]

    def get_aod_factor(input_path):
        tag = minidom.parse(os.path.join(input_path,
"atmosphere.xml")).documentElement.getElementsByTagName('AtmosphericOpticalPropertyModel')
        aod = float(tag[0].getAttribute('aerosolOptDepthFactor'))
        return aod

    def set_aod_factor(input_path, value):
        xml_path = os.path.join(input_path, "atmosphere.xml")
        xml = minidom.parse(xml_path)
        tag = xml.documentElement.getElementsByTagName('AtmosphericOpticalPropertyModel')
        tag[0].setAttribute('aerosolOptDepthFactor', str(value))
        with open(xml_path, 'w') as fd:
            xml.writexml(fd, indent='', newl='')

    def set_date(input_path, date):
        xml_path = os.path.join(input_path, "directions.xml")
        xml = minidom.parse(xml_path)
        tag = xml.documentElement.getElementsByTagName('ExactDateHour')
        tag[0].setAttribute('year', str(date[0]))
        tag[0].setAttribute('month', str(date[1]))
        tag[0].setAttribute('day', str(date[2]))
        tag[0].setAttribute('hour', str(date[3]))
        tag[0].setAttribute('minute', str(date[4]))
        tag[0].setAttribute('second', str(date[5]))
        with open(xml_path, 'w') as fd:
            xml.writexml(fd, indent='', newl='')

    def write_results(outfile, date, measured_irradiance, aod_factor, simulated_irradiance):
        r = simulated_irradiance / measured_irradiance if measured_irradiance > 0.0 else 0.0

outfile.write("%s\t%04d\t%02d\t%02d\t%02d\t%02d\t%s\t%s\t%s\n"%(str(measured_irradiance),date[
0],date[1],date[2],date[3],date[4],date[5],str(aod_factor),str(simulated_irradiance),str(r)))
        outfile.flush()

    def run_simulation(simulation, DART_TOOLS):
        if os.path.isfile("run.log"):
```

```
        os.remove("run.log")
    old_pwd = os.getcwd()
    os.chdir(DART_TOOLS)
    for step in [ "dart-directions.sh", "dart-phase.sh", "dart-maket.sh", "dart-only.sh" ]:
        rc = os.system("bash " + step + " " + simulation + " >> " + old_pwd + os.sep + "run.log 2>&1")
        if rc > 0:
            os.chdir(old_pwd)
            sys.exit(1)
    os.chdir(old_pwd)

#-------------------------------------------------------------------------------

def main(simulation_name,
         measure_data_file,
         epsilon1 = 0.05,
         max_iteration = 20,
         not_found_value = -9999.99,
         initial_aod_factor = None,
         result_file = None,
         dart_path = "",
         min_date = "0000 00 00",
         max_date = "9999 12 31 23 59 59",
         epsilon2 = 0.05):
    """
    """
    DART_HOME, DART_LOCAL, DART_TOOLS = init(dart_path)

    simulation_path = os.path.join(DART_LOCAL, "simulations", simulation_name)

    if not os.path.exists(measure_data_file):
        measure_data_file = os.path.join(simulation_path, measure_data_file)

    if result_file is None:
        result_file = os.path.join(simulation_path, simulation_name + ".result.txt")
    elif not os.path.exists(result_file):
        result_file = os.path.join(simulation_path, result_file)

    sim_input_path = os.path.join(simulation_path, "input")
    sim_output_path = os.path.join(simulation_path, "output")

    # Lower bound for AOD factor range is initially 0.0
    # Upper bound is either fixed by parameter or retrieved from the simulation
    ksim = get_aod_factor(sim_input_path)
    if initial_aod_factor is None:
        initial_aod_factor = ksim
    else:
        ksim, initial_aod_factor = initial_aod_factor, ksim

    if ksim <= 0.0:
        ksim = 1.0
```

```
            print("Simulation's AOD factor is 0.0... upper bound forced to 1.0")

        print("Initial AOD factor range => [0.0, %f]"%(ksim))

        # Read spectral band informations (lambda mean & delta lambda)
        bands = read_spectral_bands(sim_input_path)

        # Create lut output file
        outfile = open(result_file, "w")

outfile.write("E_measured\tYEAR\tMONTH\tDAY\tHOUR\tMINUTE\tSECOND\tAOD_FACTOR\tE_simulated\tE_
simulated/E_measured\n")
        outfile.flush()

        # Open input measure file
        ifr = InputFileReader(measure_data_file)
        ifr.open()

        # Iterate through input measure file
        for i, line in enumerate(ifr):

            measured_irradiance, ref_irradiance, date = line

            # check date range constraint
            d = "%4d %02d %02d %02d %02d %02d"%(date[0],date[1],date[2],date[3],date[4],date[5])
            if d < min_date or d > max_date:
                continue

            # increase epsilon if measured irradiance is above reference irradiance
            epsilon = epsilon1 if (measured_irradiance >= ref_irradiance or measured_irradiance == 0.0) else
epsilon1 * (ref_irradiance / measured_irradiance)

            # setup current date in DART simulation
            set_date(sim_input_path, date)

            print("%d."%i, "Processing %4d/%02d/%02d %02d:%02d.%02d  . . .  Measured irradiance = %0.1f . Ref
irradiance = %0.1f . Epsilon =
%f"%(date[0],date[1],date[2],date[3],date[4],date[5],measured_irradiance,ref_irradiance,epsilon))

            k0 = 0     # Initial lower bound for AOD factor
            ki = ksim   # Initial upper bound for AOD factor
            stepB = True
            iteration = 1
            irradiance0 = None

            # step A : try to find a usable range enclosing k such as
            #         k0 < k < ki
            #         with
            #         simulated_irradiance(k0) > measured_irradiance
            #         and
```

```
        #       simulated_irradiance(ki) < measured_irradiance
        #
        # in this step we consider (mainly) the uppper bound:
        # - get simulated irradiance for upper bound
        # - if simulated irradiance meet the desired approximation level => we have found our AOD factor (=
upper bound)
        # - else if simulated irradiance is below measured irradiance
        #       - if this is the first iteration, retrieve simulated irradiance with k = k0 (0.0)
        #       - if simulated irradiance is still below measured irradiance with k = 0.0, we won't succeed =>
stop
        #       - else we have a propoer range that encloses AOD factor => go to step B to refine our
approximation
        # - else continue to next iteration using:
        #       lower bound = upper bound
        #       upper bound = n * upper bound
        while True:
            set_aod_factor(sim_input_path, ki)
            print("    - A%d => k [%f,%f]  . . .  Simulated irradiance = "%(iteration,k0,ki), end='')
            sys.stdout.flush()
            run_simulation(simulation_name, DART_TOOLS)
            irradianceI = get_coupl_irradiance(sim_output_path, bands)
            print(irradianceI)
            # check if simulated irradiance is within the approximation error for aod factor ki
            if abs((irradianceI - measured_irradiance) / measured_irradiance) < epsilon:
                stepB = False
                break
            elif ki == 0.0 and abs((irradianceI - measured_irradiance) / measured_irradiance) < epsilon2:
                stepB = False
                break
            elif irradianceI < measured_irradiance:
                # go to step B
                break
            else:
                k0 = ki
                if measured_irradiance > 0.0 and (irradianceI / measured_irradiance) > 2.0:
                    ki *= irradianceI / measured_irradiance
                else:
                    ki *= 2.0
                irradiance0 = irradianceI
                iteration += 1
                if iteration > max_iteration:
                    ki = not_found_value
                    stepB = False
                    break

        # if irradiance0 is None, we stopped at 1st iteration of step A (initial upper bound's value for k
returned a simulated irradiance below the measured irradiance)
        # => we check if simulated irradiance for initial lower bound (0.0) is over measured irradiance
        #    if not, we won't be able to go any further (unless we meet the tolerance level with k = 0.0)
        if stepB and irradiance0 is None:
```

```
            set_aod_factor(sim_input_path, k0)
            print("    - A%d => k = 0.0  . . .  Simulated irradiance = "%iteration, end='')
            sys.stdout.flush()
            run_simulation(simulation_name, DART_TOOLS)
            irradiance0 = get_coupl_irradiance(sim_output_path, bands)
            print(irradiance0)
            # test if simulated irradiance for k = 0.0 meet tolerance level
            if abs((irradiance0 - measured_irradiance) / measured_irradiance) < epsilon or abs((irradiance0 -
measured_irradiance) / measured_irradiance) < epsilon2:
               ki, irradianceI = k0, irradiance0
               stepB = False
            # simulated irradiances for both bounds are below measured irradiance => we failed to find a
proper range that encloses the AOD factor
            elif irradiance0 < measured_irradiance:
               ki, irradianceI = not_found_value, irradiance0
               stepB = False

         # stop at step A : either we have met the desired approximation error
         #            or there is no lower bound that allow to properly define the range that encloses the AOD
factor...
         if not stepB:
            print("    - k = %f"%ki)
            write_results(outfile, date, measured_irradiance, ki, irradianceI)
            continue

         # step B : try to better approximate k by dichotomy
         while True:
            k = (k0 + ki) * 0.5
            set_aod_factor(os.path.join(simulation_path, "input"), k)
            print("    - B%d => k = %f [%f,%f]  . . .  Simulated irradiance = "%(iteration,k,k0,ki), end='')
            sys.stdout.flush()
            run_simulation(simulation_name, DART_TOOLS)
            irradiance = get_coupl_irradiance(sim_output_path, bands)
            print(irradiance)
            # check if simulated irradiance is within the approximation error for aod factor k
            if abs((irradiance - measured_irradiance) / measured_irradiance) < epsilon:
               break
            # choose bounds between [k,ki] or [k0,k] depending on last simulated irradiance
            if irradiance > measured_irradiance:
               k0, ki = k, ki
               irradiance0, irradianceI = irradiance, irradianceI
            else:
               k0, ki = k0, k
               irradiance0, irradianceI = irradiance0, irradiance
            # next iteration
            iteration += 1
            if iteration > max_iteration:
               k = not_found_value
               break
```

```
        # write step B result
        print("    - k = %f"%k)
        write_results(outfile, date, measured_irradiance, k, irradiance)

    ifr.close()
    outfile.close()

    # restore Simulation's original AOD factor
    set_aod_factor(sim_input_path, initial_aod_factor)

#-------------------------------------------------------------------------------

if __name__ == "__main__":
    if len(sys.argv) < 3:
        cmd_help()
    else:
        # mandatory arguments
        simulation_name = sys.argv[1]
        measure_data_file = sys.argv[2]

        # default values for optional arguments
        epsilon = 0.05
        k0_epsilon = epsilon
        max_iteration = 20
        not_found_value = -9999.99
        initial_aod_factor = None
        result_file = None
        dart_path = ""
        min_date = "0000 00 00"
        max_date = "9999 12 31 23 59 59"

        # optional arguments
        i = 3
        while i < len(sys.argv):
            if sys.argv[i] == '-e':
                i += 1
                epsilon = float(sys.argv[i])
            if sys.argv[i] == '-ee':
                i += 1
                k0_epsilon = float(sys.argv[i])
            elif sys.argv[i] == '-m':
                i += 1
                max_iteration = int(sys.argv[i])
            elif sys.argv[i] == '-f':
                i += 1
                not_found_value = float(sys.argv[i])
            elif sys.argv[i] == '-r':
                i += 1
                result_file = sys.argv[i]
            elif sys.argv[i] == '-i':
```

```
            i += 1
            initial_aod_factor = float(sys.argv[i])
        elif sys.argv[i] == '-d':
            i += 1
            dart_path = sys.argv[i]
        elif sys.argv[i] == '-t':
            i += 1
            min_date = sys.argv[i]
            i += 1
            max_date = sys.argv[i]
        i += 1

    main(simulation_name, measure_data_file, epsilon, max_iteration, not_found_value,
initial_aod_factor, result_file, dart_path, min_date, max_date, k0_epsilon)
```

Q.Python script for launching a sequence of radiative budget simulations with DART

Q.1 Principal and functioning

This script was developed in order to launch simulations of radiative budget under DART as an automatic sequence. It must be launched as a bash command under a Linux operating system where DART is installed. The sequence launcher python script I wrote for this purpose needs at least the two following input parameters:

- the full path where the simulation to launch is stored, this simulation must have been parameterized beforehand under DART interface;
- a text file listing all the dates and times and the corresponding multiplicative factor of Aerosol Optical Depth at which the simulation must be performed.

The script proceeds as a loop over all the rows of the text file provided as input. At each loop turn the script does the three following actions:

1. it sets the final parameters of the simulation;
2. it launches the simulation of the radiative budget by calling the necessary succession of DART modules;
3. it stores simulation outputs in compress format.

For the first step, the script reads the text file provided as input and fills in the date and time of simulation and the multiplicative factor of the aerosol optical depth respectively into the files *atmosphere.xml* et *dart.xml* in the *input* folder of the simulation.

For the second step, the launcher script tests if the landscape mock-up already exists (*maket.txt* file):

i. If it does not yet, the script calls the module "dart-maket.sh" which computes the landscape mock-up. Computation of this sole step takes approximately 15 min under the servers available at CESBIO.

ii. If it already exists, the script only call the sub-module of "dart-maket.sh" called dart-atmosphere-maket.exe which only modifies the upper atmosphere and mid-atmospehre layers of the mock-up. Computation of this sole step takes less than a minute.

For each simulation to be launched, the script calls the module *direction* and the module *phase* in this order, prior to calling the *maket* module. Then it calls the module *dart* for computing the radiative budget.

For the third step, all the outputs from a given simulation are stored, notably the files *simulation.properties.txt* and *dart.txt* which respectively provides information concerning the set of parameters and simulation processing. During simulation back-up, the folder named '*BAND0*', which stores all the PAR radiative budget products in the form of binary images, switches from approximately 500 Mo of data to 20 Mo through a tar.gz compression. A complete sequence of

simulation (255 date and times from the 15/04/2016 to the 12/09/2016), approximately generates 4.5Go of data **in compress format**.

Q.2 Script

```
# -*- coding: utf-8 -*-
"""
Created on Tue Feb 13 08:38:58 2018

@author: grimaldij
"""
#_____________ ReadAODOutput _____________________________
### OBJECTIVES: This script launches a sequence of simulations with dates AOD multiplicative factor (atmospheric parameter) set according to values from an AOD calibration time serie
###STEPS
# 1/ Read AOD calibration time serie file
# 2/ Set simulations with atmospheric parameters with corresponding  AOD paramterer
# 3/ Launch simulation (maket is launched only at first iteration if maket.txt doesn't exist yet)
# 4/ Save a copy of each iteration of output files (dart.txt and simulation.properties.txt) and
    BAND0 to BANDN folders in path SimulationPath/IterationDateHeure/
# NB : Code calls the following home made functions from irradiance_spectra_LUT_v4:
#   - set_date
#   - set_AOD_factor
#   - read_spectral_bands
#   - AODFileReader
### PARAMETERS :
#   - dart_path='/home/grimaldij/DART_570v1011'
#   - PathSimu='/home/grimaldij/PROGRAMMES/DART_simu/simulations/'
#   - NameSimuAOD='Lagardere_Atmo_Param_v7'
#   - FileAOD='RESULTS_AOD_2linesTEST.txt'
#               AOD input file format =  10 columns :
#                           E_measured YEAR MONTH DAY HOUR MINUTE SECOND AOD_FACTOR
    E_simulated E_simulated/E_measured
#   - not_found_value=-9999
#   - NameSimuToRun='TESTSimuToRun'
#   - min_date="2016 03 01"
#   - max_date="2016 31 12 23 30 00"
#   - compress=1 or 0
#_____________________________________________________________________


import os,sys,shutil,argparse,re

import irradiance_spectra_LUT_v4 as IrrFunctions

class AODFileReader(object):
  """
  """
```

```
    def __init__(self, path):
        self.path = path
        self.fd = None

    def __del__(self):
        self.close()

    def __iter__(self):
        return self

    def __next__(self):
        return self.next()

    def open(self):
        self.fd = open(self.path, 'r')

    def close(self):
        if not self.fd is None:
            self.fd.close()
            self.fd = None

    def readline(self):
        if not self.fd is None:
            line = self.fd.readline()
            while len(line.strip()) == 0:
                line = self.fd.readline()
                if len(line) < 1:
                    raise StopIteration()
            return line.strip()

    def next(self):
        splitter = re.compile("[^0-9a-zA-Z.,-]+")
        if not self.fd is None:
            line = None
            while line is None:
                line = splitter.split(self.readline())
                try:
                    return float(line[0]), [int(line[i]) for i in range(1,7)], float(line[7]), float(line[8]), float(line[9])
                except ValueError:
                    line = None
                except:
                    raise StopIteration()

def runShadeSimulation(PathSimuToRunOutput,simulation,DART_TOOLS):
    if os.path.isfile("run.log"):
        os.remove("run.log")
    old_pwd = os.getcwd()
    os.chdir(DART_TOOLS)
    # si maket de triangles n'esiste pas
    if not os.path.isfile(os.path.join(PathSimuToRunOutput,'maket.txt')):
```

```
            steps2run=[ "dart-directions.sh", "dart-phase.sh", "dart-maket.sh", "dart-only.sh"]
        else:
            steps2run=[ "dart-directions.sh", "dart-phase.sh", "DART_MaketAtmosphere_only.sh", "dart-
only.sh"]
        for step in steps2run:
            print(step)
            rc = os.system("bash " + step + " " + simulation + " >> " + old_pwd + os.sep + "run.log 2>&1")
            if rc > 0:
                os.chdir(old_pwd)
                sys.exit(1)
        os.chdir(old_pwd)

    def DARTPathInit(path=""):
        DART_HOME = path
        DART_HOME = os.path.expanduser(DART_HOME)

        # if default path is empty, query DART_HOME from system environment
        if len(DART_HOME) == 0:
            try:
                DART_HOME = os.environ['DART_HOME']
            except KeyError:
                DART_HOME = None

        if DART_HOME is None:
            raise EnvironmentError("You need to set DART_HOME path, either by setting the variable above or
through system environment.")

        try:
            DART_LOCAL = os.environ['DART_LOCAL']
        except KeyError:
            ini = open(os.path.join(DART_HOME, "config.ini"), "r")
            drc = open(ini.readlines()[0].rstrip('\n'), "r")
            for line in drc:
                line = line.strip()
                if len(line) > 0 and not (line[0] == '#' or line[0:3] == 'REM') and "DART_LOCAL" in line:
                    DART_LOCAL = line.split('=')[1]
                    break
            ini.close()
            drc.close()

        DART_TOOLS = os.path.join(DART_HOME, "tools", "linux")
        return DART_HOME, DART_LOCAL, DART_TOOLS

    def
StoreOutputFilesDuringSeq(PathStorageFolder,SimuOutputFolder,SeqIterationID,Files2savelist,Folders2savelist
,compress):
        folderForStoringIteration=os.path.join(PathStorageFolder,SeqIterationID)
        if not os.path.exists(folderForStoringIteration):
            os.makedirs(folderForStoringIteration)
            print('Simulation ' +SeqIterationID+' outputs will be saved at newly created folder:')
```

```
            print(folderForStoringIteration)
        else:
            print('Simulation ' +SeqIterationID+' outputs will be saved at already existing folder:')
            print(folderForStoringIteration)

        for file2copy in Files2savelist[:]:
            print('copied :'+file2copy)
            shutil.copy(os.path.join(SimuOutputFolder,file2copy),folderForStoringIteration)

        for folder2copy in Folders2savelist[:]:
            if compress=="1":
                archiveName=folder2copy+'tar.gz'
                print('copied: '+folder2copy+' to: '+ archiveName)

shutil.make_archive(os.path.join(folderForStoringIteration,folder2copy),'gztar',SimuOutputFolder,folder2copy)
            else:
                print('copied :'+folder2copy)

shutil.copytree(os.path.join(SimuOutputFolder,folder2copy),os.path.join(folderForStoringIteration,folder2copy
))
        return()

    ###  MAIN CODE
    if __name__ == '__main__':

        if len(sys.argv) == 1:
            prog = os.path.basename(sys.argv[0])
            print('      '+sys.argv[0]+' [options]')
            print("     Aide : ", prog, " --help")
            print("        ou : ", prog, " -h")

            sys.exit(-1)

        else:
            usage = "usage: %prog"
            parser = argparse.ArgumentParser(description = "This script launches a sequence of simulations with
dates AOD multiplicative factor (atmospheric parameter) set according to values from an AOD calibration time
serie")
          parser.add_argument('-pDART',dest='dart_path', action='store', help='Path of DART HOME (not
mandatory - default is /disk2/grimaldi/DART570_v1011)',default='/disk2/grimaldi/DART570_v1011',required =
False)
          parser.add_argument('-pSimu',dest='PathSimu', action='store', help='Path to folder storing all
simulations (not mandatory, default is
/disk2/grimaldi/PROGRAMMES/DART_Simu/simulations)',default='/disk2/grimaldi/PROGRAMMES/DART_Simu
/simulations',required = False)
          parser.add_argument('-sAOD',dest='NameSimuAOD', action='store', help='Name of simulation that
contains the AOD calibration input file',required = True)
          parser.add_argument('-fAOD',dest='FileAOD', action='store', help='AOD input file name - ex :
RESULTS_AOD_2linesTEST.txt - format : 10 columns - first line is headers : E_measured YEAR MONTH DAY
```

```
HOUR MINUTE SECOND AOD_FACTOR        E_simulated E_simulated/E_measured - separator is tab - it main contain empty lines', required = True)
        parser.add_argument('-nan',dest='not_found_value', action='store', help='Value use for NaN in AOD input file (default is -9999)', default=-9999, required = False)
        parser.add_argument('-s2run',dest='NameSimuToRun', action='store', help='Name of simulation to run in sequence', required = True)
        parser.add_argument('-dmin',dest='min_date', action='store', help='Date from which to start simulation - default="1900 01 01 00 00 00"', default="1900 01 01 00 00 00",required = False)
        parser.add_argument('-dmax',dest='max_date', action='store', help='Date from which to start simulation - default = "2100 12 31 23 59 59"', default="2100 12 31 23 59 59",required = False)
        parser.add_argument('-comp',dest='compress', action='store', help='Compress output folders- default = 0', default=0 ,required = False)


        args = parser.parse_args()

        dart_path=args.dart_path
        PathSimu=args.PathSimu
        NameSimuAOD=args.NameSimuAOD
        FileAOD=args.FileAOD
        not_found_value=args.not_found_value
        NameSimuToRun=args.NameSimuToRun
        min_date=args.min_date
        max_date=args.max_date
        compress=args.compress

    # ---------- PARAM----------------------------------------
    # dart_path='/home/grimaldij/DART_570v1008'

    # PathSimu='/home/grimaldij/PROGRAMMES/DART_simu/simulations/'
    # NameSimuAOD='Lagardere_Atmo_Param_v7'
    # #FileAOD='RESULTS_AOD_Lagardere_AtmoParamv7_AllSerie5days_From20160315_To_20160915.txt'
    # FileAOD='RESULTS_AOD_2linesTEST.txt'

    # not_found_value=-9999
    # min_date="2016 03 01"
    # max_date="2016 31 12 23 30 00"

    # #NameSimuToRun='Lagardere_v18'
    # NameSimuToRun='TESTSimuToRun'
    # compress=1
    #_____________________________________________________________________________
        print('###### START #####"')
        #----SET DART PATHS ---
        DART_HOME, DART_LOCAL, DART_TOOLS = DARTPathInit(dart_path)

        #---PREPARE OUTPUTS FOLDER AND FILES FOR STORING ---
        PathFolderSavedSequence=os.path.join(PathSimu,NameSimuToRun,'SAVED_SEQUENCE')
        if not os.path.exists(PathFolderSavedSequence):
                os.makedirs(PathFolderSavedSequence)
```

```
                print('#---CREATED FOLDER FOR SAVING SEQUENCE OF OUTPUTS:')
                print(PathFolderSavedSequence)
        else:
                print('#--- SEQUENCE OUTPUTS WILL BE SAVED IN: ')
                print(PathFolderSavedSequence)

        PathSimuToRunInput=os.path.join(PathSimu,NameSimuToRun,'input')
        PathSimuToRunOutput=os.path.join(PathSimu,NameSimuToRun,'output')

        # Files in SimuOutput that will be stored before sequence next iteations
        Files2savelist=['dart.txt','simulation.properties.txt']

        # Folders in SimuOutput that will be stored before sequence next iteations
        bands=IrrFunctions.read_spectral_bands(PathSimuToRunInput)
        Folders2savelist=[ 'BAND'+str(i) for i in range(0,len(bands))]

        # ---- IMPORT AOD CALIBRATED DATA ---
        print('# Reading AOD input file:')
        PathFileAOD=os.path.join(PathSimu,NameSimuAOD,FileAOD)

        if not os.path.exists(PathFileAOD):
                print('AOD input file does not exists:')
                print(PathFileAOD)
        else:
                print(PathFileAOD)
                AODfr=AODFileReader(PathFileAOD)
                AODfr.open()
                #---- ITERATE THROUGH AOD FILE ---
                TabAODCalibration=[]
                for line in AODfr:
                        TabAODCalibration.append(line)
                #
                AODfr.close()

        # ---- SET AND RUN SIMULATION ITERATION, THEN STORE OUTPUT BEFORE NEXT ITERATION ---
        for line in TabAODCalibration:
                #
                measured_irradiance, date, AOD, simulated_irradiance = line[:-1]
                #
                # check date range constraint
                d = "%4d %02d %02d %02d %02d %02d"%(date[0],date[1],date[2],date[3],date[4],date[5])
                if d < min_date or d > max_date:
                        continue
                #
          # If dark (during night): no simulation
                if simulated_irradiance == 0.0:
                        print('### Skipped date/time ',date,' as simulated irradiance equals
',str(simulated_irradiance))
                        continue
          #
```

```
                print('### Calibrating simu: ')
                # set date simu to run
                IrrFunctions.set_date(PathSimuToRunInput,date)
                print('DATE:', date)
                #
                # Set AOD in simu to run
                # ---> set AOD = 0 in case simu irradiance wasn't null but didn't meet epsilon prim constraint
                if simulated_irradiance >0 and AOD==not_found_value:
                        AOD=0
                        print('### Modified AOD from '+str(not_found_value)+' to ')
                IrrFunctions.set_aod_factor(PathSimuToRunInput,AOD)
                print('AOD factor:', AOD)
                #
                # Run simulation
                print('Running: ')
                runShadeSimulation(PathSimuToRunOutput,NameSimuToRun,DART_TOOLS)

                # Store broadband output images (absorbed energy per triangle)
                DateAsSeqID=d.replace(' ','')

        StoreOutputFilesDuringSeq(PathFolderSavedSequence,PathSimuToRunOutput,DateAsSeqID,Files2save
list,Folders2savelist,compress)

        print('###### THE END #####"')
    #-----------------end----------------------------------------
```